E-ISSN: 2547-958X

FMD

FEN VE MÜHENDİSLİK DERGİSİ

DOKUZ EYLÜL ÜNİVERSİTESİ MÜHENDİSLİK FAKÜLTESİ FEN ve MÜHENDİSLİK DERGİSİ (FMD)

DOKUZ EYLUL UNIVERSITY ENGINEERING FACULTY JOURNAL OF SCIENCE AND ENGINEERING (JSE)

CILT 27
SAYI 79
OCAK 2025

VOLUME 27
ISSUE 79
JANUARY 2025

Dokuz Eylül Üniversitesi Mühendislik Fakültesi Fen ve Mühendislik Dergisi
Dokuz Eylul University Faculty of Engineering Journal of Science and Engineering
Elektronik/Online ISSN: 2547-958X

Dergi Sahibi / Journal Owner: Dokuz Eylül Üniversitesi
Elektronik Yayın Yapan / Electronic Publisher : DEÜ Mühendislik Fakültesi
Mühendislik Fakültesi Adına Yayın Sahibi / Publisher on Behalf of the Faculty of Engineering : Prof. Dr. Azize AYOL
CİLT / VOL: 27 SAYI / NO: 79 YIL / YEAR: 2025

Baş Editör/Editor-in-Chief

Doç.Dr. Serkan EKER	Çevre Mühendisliği, Dokuz Eylül Üniversitesi, İzmir, Türkiye Department of Environmental Engineering, Dokuz Eylül University, İzmir, Türkiye

Editörler Kurulu/Editorial Board

Doç. Dr. Mine ANTEP	Kimya Bölümü, Dokuz Eylül Üniversitesi, İzmir, Türkiye Department of Chemistry, Dokuz Eylül University, İzmir, Türkiye
Prof. Dr. Yusuf ARMAN	Makina Mühendisliği Bölümü, Dokuz Eylül Üniversitesi, İzmir, Türkiye Department of Mechanical Engineering, Dokuz Eylül University, İzmir, Türkiye
Dr. Öğr. Üyesi Ayşe Uğurcan ATMACA	Havacılık ve Uzay Mühendisliği Bölümü, Dokuz Eylül Üniversitesi, İzmir, Türkiye Department of Aerospace Engineering, Dokuz Eylül University, İzmir, Türkiye
Prof. Dr. Derya BİRANT	Bilgisayar Mühendisliği Bölümü, Dokuz Eylül Üniversitesi, İzmir, Türkiye Department of Computer Engineering, Dokuz Eylül University, İzmir, Türkiye
Prof. Dr. Muhammed DENİZ	Fizik Bölümü, Dokuz Eylül Üniversitesi, İzmir, Türkiye Department of Physics, Dokuz Eylül University, İzmir, Türkiye
Prof. Dr. A. Hamdi DELİORMANLI	Maden Mühendisliği Bölümü, Dokuz Eylül Üniversitesi, İzmir, Türkiye Department of Mining Engineering, Dokuz Eylül University, İzmir, Türkiye
Prof. Dr. Mustafa DOĞAN	İnşaat Mühendisliği Bölümü, Dokuz Eylül Üniversitesi, İzmir, Türkiye Department of Civil Engineering, Dokuz Eylül University, İzmir, Türkiye
Prof. Dr. Tolga GÖNENÇ	Jeofizik Mühendisliği Bölümü, Dokuz Eylül Üniversitesi, İzmir, Türkiye Department of Geophysical Engineering, Dokuz Eylül University, İzmir, Türkiye
Doç. Dr. Taner GÖKTAŞ	Elektrik-Elektronik Mühendisliği Bölümü, Dokuz Eylül Üniversitesi, İzmir, Türkiye Department of Electrical and Electronics Engineering, Dokuz Eylül University, İzmir, Türkiye
Prof. Dr. Gülseren KARABAY	Tekstil Mühendisliği Bölümü, Dokuz Eylül Üniversitesi, İzmir, Türkiye Department of Textile Engineering, Dokuz Eylül University, İzmir, Türkiye
Prof. Dr. Mehmet ÖZCANHAN	Bilgisayar Mühendisliği Bölümü, Dokuz Eylül Üniversitesi, İzmir, Türkiye Department of Computer Engineering, Dokuz Eylül University, İzmir, Türkiye
Doç. Dr. Burcu Silindir YANTIR	Matematik Bölümü, Dokuz Eylül Üniversitesi, İzmir, Türkiye Department of Mathematics, Dokuz Eylül University, İzmir, Türkiye
Doç. Dr. Metin YURDDAŞKAL	Metalurji ve Malzeme Mühendisliği Bölümü, Dokuz Eylül Üniversitesi, İzmir, Türkiye Department of Metallurgy and Materials Engineering, Dokuz Eylül University, İzmir, Türkiye
Prof. Dr. Aylin ALIN (İstatistik Editörü / Statistical Editor	İstatistik Bölümü, Dokuz Eylül Üniversitesi, İzmir, Türkiye Department of Statistics, Dokuz Eylül University, İzmir, Türkiye
Dr.Öğr. Üyesi Işıl ÖZCAN (Dil Editörü / Language Editor)	Amerikan Kültürü ve Edebiyatı Bölümü, Dokuz Eylül Üniversitesi, İzmir, Türkiye Department of American Culture and Literature, Dokuz Eylül University, İzmir, Türkiye
Dr. Öğr. Üyesi Celal Cem SARIOĞLU (Teknik Editör / Technical Editor	Matematik Bölümü, Dokuz Eylül Üniversitesi, İzmir, Türkiye Department of Mathematics, Dokuz Eylül University, İzmir, Türkiye
Arş.Gör. Meltem GÜLLÜSAÇ (Teknik Editör / Technical Editor	Matematik Bölümü, Dokuz Eylül Üniversitesi, İzmir, Türkiye Department of Mathematics, Dokuz Eylül University, İzmir, Türkiye

Danışma Kurulu/Editorial Advisory Board

Dr. Öğr. Üye Ömer AYDIN	Manisa Celal Bayar Üniversitesi	Türkiye
Dr. Öğr. Üye Enis KARAARSLAN	Muğla Sıtkı Koçman Üniversitesi	Türkiye
Prof. Dr. Nuri AZBAR	Ege Üniversitesi	Türkiye
Prof. Dr. Filiz DİLEK	Orta Doğu Teknik Üniversitesi	Türkiye
Prof. Dr. Ayhan ALTINTAŞ	Bilkent Üniversitesi	Türkiye
Prof. Dr. Cem CİVELEK	Türk-Alman Üniversitesi	Türkiye
Prof. Dr. Adil BAYKASOGLU	Dokuz Eylül Üniversitesi	Türkiye
Prof. Dr. Gülçin FEYZİOĞLU	Galatasaray Üniversitesi	Türkiye
Prof. Dr. Muzaffer KAHVECİ	Konya Teknik Üniversitesi	Türkiye
Prof. Dr. Alper ILKI	İstanbul Teknik Üniversitesi	Türkiye
Dr. Harris VANGELIS	National Technical University of Athen	Greece
Prof. Dr. Bülent ORUÇ	Kocaeli Üniversitesi	Türkiye
Prof. Dr. Anastasia KİRATZİ	Aristotle University of Thessaloniki	Greece
Prof. Dr. Despina KONTOPOULOU	Aristotle University of Thessaloniki	Greece
Prof. Dr. Gregory TSOKAS	Aristotle University of Thessaloniki	Greece
Prof. Dr. Ivana VASİLJEVİC	University of Belgrade	Serbia
Prof. Dr. Osman CANDAN	Dokuz Eylül Üniversitesi	Türkiye
Prof. Dr. Gültekin TARCAN	Dokuz Eylül Üniversitesi	Türkiye
Prof. Dr. Can GENÇ	İstanbul Teknik Üniversitesi	Türkiye
Prof. Dr. Şebnem DÜZGÜN	Colorado School of Mines	USA
Prof. Dr. Serkan SAYDAM	The University of New South Wales	Australia
Prof. Dr. Cengiz KUZU	İstanbul Teknik Üniversitesi	Türkiye
Doç. Dr. Mehmet Sıddık KIZIL	The University of Queensland	Australia
Prof. Dr. Binnur Gönen KIRAL	Dokuz Eylül Üniversitesi	Türkiye
Prof. Dr. Hasan ÖZTÜRK	Dokuz Eylül Üniversitesi	Türkiye
Prof. Dr. Gürel ÇAM	İskenderun Teknik Üniversitesi	Türkiye
Prof. Dr. Hakan GAŞAN	Osmangazi Üniversitesi	Türkiye
Prof. Dr. Merih SARIIŞIK	Dokuz Eylül Üniversitesi	Türkiye
Prof. Dr. Cevza CANDAN	İstanbul Teknik Üniversitesi	Türkiye
Dr. Öğr. Üyesi Hediye ATİK	Atılım Üniversitesi	Türkiye
Dr. Öğr. Üyesi Sedat TOKGÖZ	Gebze Teknik Üniversitesi	Türkiye
Prof. Dr. Serpil ŞAKİROĞLU	Dokuz Eylül Üniversitesi	Türkiye
Doç. Dr. Ümit AKINCI	Dokuz Eylül Üniversitesi	Türkiye
Prof. Lin Shin TED	Sichuan University	China
Prof. Dr. Mieczyslaw CICHON	Adam Mickiewicz University	Poland
Prof. Dr. Selçuk DEMİR	Dokuz Eylül Üniversitesi	Türkiye

İletişim Adresi / Contact Address
Dokuz Eylül Üniversitesi, Mühendislik Fakültesi Dekanlığı Tınaztepe Yerleşkesi,
Adatepe Mah. Doğuş Cad. No: 207-I / 35390 Buca-İZMİR.

Elektronik Erişim Adresi / Electronic Access Address: https://dergipark.org.tr/tr/pub/deumffmd

Hakemli Dergi **Peer-reviewed Journal**
Dergide yayımlanan makalelerin bilimsel içerik ve dil sorumluluğu yazarlara aittir. The scientific content and language responsibility of the articles published in the journal belong to the authors.
Dergide yayımlanan makaleler kaynak gösterilmeden kullanılamaz. Articles published in the journal cannot be used without proper citation.

Atıf Dizinleri / Citation Indexes

- TR Dizin

Diğer Dizinler / Other Indexes

- EBSCO Resource Database
- Google Scholar
- Academindex
- Asos İndeks

Dergi Sahibi / Journal Owner: Dokuz Eylül Üniversitesi
Elektronik Yayın Yapan / Electronic Publisher : DEÜ Mühendislik Fakültesi
Mühendislik Fakültesi Adına Yayın Sahibi / Publisher on Behalf of the Faculty of Engineering : Prof. Dr. Azize AYOL
CİLT / VOL: 27 SAYI / NO: 79 YIL / YEAR: 2025

İletişim Adresi / Contact Address Dokuz Eylül Üniversitesi, Mühendislik Fakültesi Dekanlığı Tınaztepe Yerleşkesi,
Adatepe Mah. Doğuş Cad. No: 207-I / 35390 Buca-İZMİR.

Elektronik Erişim Adresi / Electronic Access Address: https://dergipark.org.tr/tr/pub/deumffmd

Hakemli Dergi **Peer-reviewed Journal**

Dokuz Eylül Üniversitesi Mühendislik Fakültesi Fen ve Mühendislik Dergisi
Dokuz Eylul University Faculty of Engineering Journal of Science and Engineering
Elektronik/Online ISSN: 2547-958X

İçindekiler/ Contents

DEU FMD 27(79) (2025) 1-10

Dokuz Eylül Üniversitesi Mühendislik Fakültesi Fen ve Mühendislik Dergisi
Dokuz Eylul University Faculty of Engineering Journal of Science and Engineering
Elektronik/Online ISSN: 2547-958X

ARAŞTIRMA MAKALESI / RESEARCH ARTICLE

Magnezya Takviyeli 7075 Alüminyum Alaşımı Matrisli Kompozitlerde Üretim Parametrelerinin Abrasif Aşınma Davranışına Etkisi

Effect of Manufacturing Parameters on Abrasive Wear Behavior in Magnesia Reinforced 7075 Aluminum Alloy Matrix Composites

Muharrem Pul

Kırıkkale Üniversitesi Kırıkkale Meslek Yüksekokulu, Elektrik ve Enerji Bölümü, Kırıkkale, TÜRKİYE
Sorumlu Yazar / Corresponding Author: mpul@kku.edu.tr

Öz

Bu çalışmada 7075 alüminyum alaşımı matrisli, %5, 10, 15 ve 20 oranlarında Magnezya takviyeli kompozitler toz metalürjisi yöntemiyle üretilmiştir. Daha sonra kompozitlerin abrasif aşınma deneyleri gerçekleştirilmiştir. Aşınma deneyleri 40 N yük uygulanarak, 0,9 ms^{-1} hızda, 90 m ve 180 m aşınma mesafelerinde yapılmıştır. Deneylerden elde edilen veriler mikroskop görüntüleriyle birlikte yorumlanmıştır. Farklı MgO takviye oranları, aşınma mesafeleri, sinterleme sıcaklıkları ve sürelerinin kompozitlerin abrasif aşınma davranışı üzerindeki etkileri değerlendirilmiştir. Aşınma mesafesinin iki kat artmasına rağmen aşınma kayıplarının aynı oranda artmadığı daha az meydana geldiği görülmüştür. Kompozit yapıda meydana gelen MgO takviye topaklanmaları ve gözenekliliğin mekanik özellikler üzerinde etkili olduğu değerlendirilmiştir. Aşınmış yüzey morfolojisinin daha çok mikro-sabanlama mekanizması şeklinde gerçekleştiği görülmüştür. Kompozitlerin aşınma davranışı üzerinde en etkili parametrenin MgO takviye miktarı olduğu, sinterleme sıcaklığı ve süresindeki değişimlerin çok önemli oranda etki yapmadığı genel sonucuna varılmıştır.

Anahtar Kelimeler: *Alüminyum Matrisli Kompozit, Al 7075, MgO, Sinterleme, Abrasif aşınma*

Abstract

In this study, composites with 7075 aluminum alloy matrix 5%, 10, 15 and 20 Magnesia reinforced at different ratios were produced by powder metallurgy method. Wear tests were carried out by applying a load of 40 N, at a speed of 0.9 ms^{-1}, at wear distances of 90 m and 180 m. Then, abrasive wear tests of the composites were carried out. The data obtained from the experiments were interpreted together with the microscope images. The effects of different MgO reinforcement ratios, wear distances, sintering temperatures and times on the abrasive wear behavior of the composites were evaluated. It has been observed that although the wearing distance has increased by two times, the wear losses have not increased at the same rate, but have occurred less frequently. It has been evaluated that the MgO reinforcement agglomerations and porosity occurring in the composite structure have an effect on the mechanical properties. It was observed that the eroded surface morphology occurred mostly in the form of micro-ploughing mechanism. It was concluded that the most effective parameter on the wear behavior of the composites is the amount of MgO reinforcement, and that the changes in sintering temperature and time do not have a significant effect.

Keywords: *Aluminum Matrix Composite, Al 7075, MgO, Sintering, Abrasive wear*

EXTENDED ABSTRACT

Introduction

Nowadays, new products emerge every day in all engineering fields, depending on the developments in material science. Particularly, metallic materials have a wider place in engineering applications than others. Aluminum is the most used metal in the world after steel. Aluminum is widely used in many applications due to its properties such as soft, ductile, high electrical conductivity and high corrosion resistance. By adding some alloying elements to pure aluminum, its technical properties can be improved. Especially 7xxx series aluminum alloys are stronger than other aluminum alloys. Aerospace, defense, automotive, medical device, etc. It is preferred in industrial areas. However, despite its many superior features, when compared to steel, it may be insufficient in some engineering applications due to its disadvantages such as low strength and tensile strength and low wear resistance. In recent years, aluminum matrix composites (AMC) in which different materials are reinforced have been developed in order to strengthen aluminum and expand its usage area. The low resistance of aluminum and aluminum alloys to wear is one of the main drawbacks that limits their use. Therefore, studies to increase the resistance of aluminum to abrasion are becoming increasingly important.

For this purpose, Al 7075 alloy, which is known for its high mechanical properties, and MgO particle reinforced composite materials at different rates were produced by powder metallurgy technique at 500°C, 550°C and 600°C sintering temperatures and 90 min and 120 min sintering times. The microstructures of the produced composite samples were examined. Abrasive wear

DOI: https://doi.org/10.21205/deufmd.2025277901

Geliş Tarihi / Received: 30.03.2023
Kabul Tarihi / Accepted: 21.12.2023

tests were carried out to determine wear behavior. The data obtained were evaluated together with optical microscope and scanning electron microscope (SEM) images.

Materials and Methods

In this experimental study, the matrix material was powder Al 7075 alloy with an average particle size of 63 µm, and powder Magnesia with a particle size of 37-105 µm, containing 98% MgO, 1% SiO2, 0.6% FeO and 0.4% CaO, was used as reinforcement element. used. The porosity amounts were determined by density measurements on the composite samples produced in different proportions, and the hardness measurements of all composite samples were made according to the Brinell method. In the last stage of the experimental study, abrasive wear tests were carried out. Al2O3 sandpaper with 400 mesh abrasive grain size was used in the experiments. Wear tests were carried out by applying a load of 40 N, a speed of 0.9 ms^{-1}, and a wear distance of 90 m and 180 m. The wear losses of the composite samples were determined by measuring the weights of the composite samples before and after the experiment with an electronic precision scale. Optical microscope images were taken from all composite sample surfaces subjected to wear testing.

Results and Discussion

As the sintering temperature increased, the thermal diffusion mechanism accelerated. It has been evaluated that there are sudden size changes in the aluminum matrix particles due to increased intergranular bonding and accumulation of the liquid phase by moving in a certain direction, especially at sintering temperatures above 550°C. These changes appear as increases in grain sizes. As a result of the desire of growing grains to move towards the center, larger gaps are formed. In this case, it can be stated that the highest sintering temperature applied, 600°C, is not very suitable in terms of porosity. At all sintering temperatures, the amount of pores decreased slightly as the MgO ratio in the structure increased.

It was observed that wear losses decreased with increasing MgO ratio at both experimental distances. Less wear loss occurred in all MgO reinforced composite samples compared to pure Al 7075 samples. It is understood that wear losses gradually decrease due to the effect of the reinforcing element MgO particles in the composite structure being in a very hard phase. Although there was a fourfold increase in MgO between the 5% MgO reinforced composite and the 20% MgO reinforced composite, there was at most a twofold difference in the increase in wear resistance or decrease in the amount of wear.

At both experimental distances, for temperatures of 500°C and 550°C, it was generally understood that the wear losses in the 120 min sintering time were slightly higher than in the 90 min sintering time. However, it can be stated that the change in sintering time does not cause significant differences in wear losses. The porous structure was more effective in causing the wear losses in composites sintered for 120 min to be higher than for 90 min. The least wear loss was obtained from the 20% MgO reinforced composite sintered at 600°C at both test distances. On the other hand, the highest wear loss occurred in the 5%MgO reinforced composite sample sintered at 600°C. In general, it can be said that the change in sintering temperatures does not have a significant effect on wear losses. It is seen that wear losses also increase as the wear distance increases. However, although there was a 100% difference between the 90 m and 180 m wear distances applied in the experiments, the wear losses did not occur at the same rate. It can be said that the wear mechanism in the form of micro-plowing is effective on the wear surfaces of samples without MgO reinforcement. The wear losses in the 5% MgO reinforced sample, in which the Al 7075 matrix material was included more in the composite structure, were higher than the 20% MgO reinforced sample. In this study, it is understood that the parameter that most affects wear among the composite production parameters is the MgO reinforcement ratio.

When the worn surfaces of pure Al 7075 samples without MgO reinforcement were examined, it was seen that the wear lines were very similar to each other and were thinner and more regular than the wear lines on the surface of the 5% MgO and 20% MgO reinforced samples. The effect of MgO particles in the composite structure was revealed in the formation of deeper and wider wear lines on the surface of MgO reinforced samples. During the experiments, MgO particles that broke away from the composite structure also rubbed on the sample surface and had an abrasive effect. It was evaluated that the scratches and grooves formed on the surfaces were in the form of micro-cutting and micro-plowing, which occurred as a result of the slip between the sample and the rotating abrasive disc.

With the increase of sintering time, hardness values decreased and porosity values increased. Depending on the mechanical behavior of the material, more wear loss occurred in Al 7075, which is the main material of the composite structure. Likewise, the separation of MgO particles in the softened composite structure became easier. It can be said that the wear lines formed during abrasion on the Al 7075 alloy become wider and deeper as the sintering temperature increases. The load applied during the experiments on pure aluminum increased wear and caused ductile fractures on the material surface. Depending on the size of the abrasive particles in the abrasive sandpaper, continuous tearing and plastic deformation occurred. It was determined that while some of the MgO particles that broke off from the structure moved away from the surface, some of them were plastered on the surface and remained in the wear grooves.

As the sliding time in the wear experiment increased, the temperature on the surface increased and the hardness of the matrix material decreased slightly. As a result, the areas subjected to plastic deformation and the lines on the sample surface expanded, causing wear losses to increase.

Conclusion

Al 7075 matrix and 5, 10, 15, 20% MgO particle reinforced composites were successfully produced by powder metallurgy method. Porosity and reinforcement agglomerations within the composite structure had negative effects on mechanical properties. As the MgO reinforcement ratio increased, the hardness values of the composite structure increased and its density decreased. As the sintering temperature increased to 600°C, the hardness values of the composite samples at all reinforcement ratios decreased, while the amount of pores increased. It was evaluated that the most effective parameter on wear losses was the amount of MgO reinforcement. When the wear surface images were examined, it was understood that the effect of the abrasive wear mechanism appeared mostly in the form of micro-plowing, and changes in sintering temperature and time did not create significant differences on the worn surface images.

1. Giriş

Günümüzde malzeme bilimindeki gelişmeler bağlı olarak tüm mühendislik alanlarında her geçen gün yeni ürünler ortaya çıkmaktadır. Özellikle metalik malzemelerin mühendislik uygulamalarındaki yeri diğerlerine göre daha geniştir. Dünyada çelikten sonra en fazla kullanılan metal alüminyumdur. Alüminyum, yumuşak, sünek, yüksek elektriksel iletkenlik ve yüksek korozyon direnci gibi özelliklerinden dolayı birçok uygulamada yaygın olarak kullanılmaktadır [1]. Saf alüminyum içerisine bazı alaşım elementleri katılarak teknik özellikleri geliştirilebilmektedir. Özellikle 7xxx serisi alüminyum alaşımları diğer alüminyum alaşımlarına kıyasla daha güçlüdür. Havacılık, savunma, otomotiv, tıbbi cihaz vb. endüstri alanlarında tercih edilmektedir. Ancak birçok üstün özelliğinin yanında çelikle mukayese edildiğinde, düşük mukavemet ve çekme dayanımı, düşük aşınma direnci gibi dezavantajlarından dolayı bazı mühendislik uygulamalarında yetersiz kalabilmektedir [2, 3]. Son yıllarda alüminyumun güçlendirilmesi ve kullanım alanının daha da yaygınlaştırılması amacıyla içerisine farklı malzemelerin takviye edildiği alüminyum matrisli kompozitler (AMC) geliştirilmektedir. Alüminyum matrisli kompozitler yüksek mukavemet, yüksek sertlik, azaltılmış ağırlık, gelişmiş termal özellikler, yüksek sıcaklık dayanımı, geliştirilmiş sönümleme yetenekleri ve artan aşınma direnci ile takviyesiz alüminyum alaşımlara kıyasla çeşitli avantajları vardır [4]. Genellikle seramik esaslı takviye malzemelerinin kullanıldığı AMC'ler çoğunluğu oluşturmaktadır. Uygulamada Al_2O_3, SiC, B_4C, SiO_2, TiC, TiB_2, ZrO_2, Grafen vb. takviye malzemeleri yaygın olarak kullanılmakta olup literatürde farklı çalışmalar yer almaktadır [5-9]. Bu malzemelerin refrakterlik, yüksek sertlik, yüksek basınç dayanımı, aşınma direnci vb. üstün özellikleri, onları kompozit matrisinde takviye olarak kullanıma uygun hale getirir [10]. Literatürde diğerleri kadar yaygın olmasa da, takviye elemanı olarak kullanılan malzemelerden birisi de magnezyum oksit (MgO)'dir. MgO yüksek erime noktası, yüksek basınç dayanımı, yüksek sertliği ve ayrıca mükemmel termodinamik stabilitesi nedeniyle takviye için uygun bir seçimdir [11]. MgO, erime noktası yaklaşık 2780°C olan refrakter bir malzemedir. MgO, iyi termal şok direnci, yüksek erime noktası, düşük termal iletkenlik ve mükemmel termodinamik kararlılık gibi özelliklere sahiptir. Yoğunluğu, Young modülü ve sertliği sırasıyla 3.58 g/cm3, 320 GPa ve e910 HV'dir [12].

AMC kompozitlerin farklı üretim yöntemleri vardır. Sıkıştırmalı döküm, karıştırmalı döküm, sıvı metal infiltrasyonu, toz metalurjisi, mekanik alaşımlama ve sprey ayrıştırma MMC'leri yapmak için kullanılan tekniklerden bazılarıdır [13]. Yukarda sıralanan sıvı faz döküm yöntemlerinin temel sınırlaması, sıvı Al alaşımları ile seramik parçacıkların zayıf ıslanabilirliğidir. Islanabilirlik, bir sıvının katı bir yüzey üzerinde yayılma yeteneği olarak tanımlanabilir ve bir sıvı ile bir katı arasındaki yakın temasın derecesini temsil eder. Zayıf ıslanabilirlik ise takviye topaklanması eğilimini arttırır ve takviye partiküllerin homojen olmayan dağılımına, yüksek gözenek içeriğine ve düşük mekanik özelliklere neden olur [14]. Toz metalürjisi yönteminin diğer döküm yöntemleriyle karşılaştırıldığında, sinterleme sürecinde takviye parçacıkları ile matris alaşımı arasında daha iyi bağlanmanın olması ve matris yapısını kontrol etmenin daha kolay olması gibi bazı önemli avantajları vardır [15]. Ayrıca sinterlemedeki katı hal difüzyonu, sinterleme sıcaklığı ve süresine bağlı olarak, taneler arası boyun oluşumu ve tane büyümesini sağlayarak malzeme yapısının mekanik özelliklerini geliştirmektedir [16, 17].

Alüminyum ve alüminyum alaşımlarının aşınmaya karşı düşük dirençleri, kullanımlarını sınırlayan olumsuzlukların başında gelmektedir. Dolayısıyla alüminyumun aşınmaya karşı dayanımını arttırmak için yapılan çalışmalar giderek önem kazanmakta ve literatürde yer almaktadır [18, 19]. Alüminyum matrisli ve parçacık takviyeli kompozitlerin aşınma davranışları üzerine yapılan çalışmalarda genellikle, uygulanan yükün, aşınma mesafesinin ve hızının etkileri incelenmiştir. Deney yükünün artması, deney mesafesi ve hızının artması ile aşınma kayıplarının arttığı bilinmektedir. Ayrıca literatürdeki çalışmaların büyük bir bölümünde çelik disk üzerine pimin bastırıldığı pin on disc yöntemi kullanılmıştır. Bu çalışmada literatürden farklı olarak toz metalürjisiyle üretilmiş olan kompozit numunelerin abrasif aşınmasında, MgO takviye miktarı, sinterleme sıcaklığı ve süresinin etkisi araştırılmıştır.

Bu amaçla özellikle yüksek mekanik özellikleriyle bilinen Al 7075 alaşımı ile farklı oranlarda MgO partikül takviyeli kompozit malzemeler toz metalürjisi tekniği ile 500°C, 550°C ve 600°C sinterleme sıcaklığında, 90 min ve 120 min sinterleme süresinde üretilmiştir. Üretilen kompozit numunelerin mikroyapıları incelenmiştir. Aşınma davranışlarını belirlemek amacıyla abrasif aşınma deneyleri gerçekleştirilmiştir. Elde edilen veriler optik mikroskop ve taramalı elektron mikroskobu (SEM) görüntüleriyle birlikte değerlendirilmiştir.

2. Materyal ve Metot

Bu deneysel çalışmada kullanılan ve *Nanografi Nano Technology* firmasından temin edilen matris malzemesi ortalama 63 µm parçacık boyutundaki toz Al 7075 alaşımı ile, *KÜMAŞ Magnesite* firmasından elde edilen ve içeriğinde %98 MgO, %1 SiO2, %0,6 FeO ve % 0,4 CaO olan 37-105 µm parçacık boyutundaki toz *Magnezya* takviye elemanı olarak kullanılmıştır. Toz metalurjisiyle üretilmiş olan Al 7075/MgO kompozit malzemelerin üretim parametreleri Tablo 1'de verilmiştir.

Tablo 1. Toz metalürjisi üretim parametreleri [20].

Table 1. Powder metallurgy production parameters [20].

	Sinterleme Sıcaklıkları		
	500°C	550°C	600°C
Sinterleme Süresi (90 min)	%0 MgO	%0 MgO	%0 MgO
	%5 MgO	%5 MgO	%5 MgO
	%10 MgO	%10 MgO	%10 MgO
	%15 MgO	%15 MgO	%15 MgO
	%20 MgO	%20 MgO	%20 MgO
	500°C	550°C	600°C
Sinterleme Süresi (120 min)	%0 MgO	%0 MgO	%0 MgO
	%5 MgO	%5 MgO	%5 MgO
	%10 MgO	%10 MgO	%10 MgO
	%15 MgO	%15 MgO	%15 MgO
	%20 MgO	%20 MgO	%20 MgO

Üretilmiş olan farklı oranlardaki kompozit numuneler üzerinde yoğunluk ölçümleri yapılarak gözenek miktarları tespit edilmiş ve tüm kompozit numunelerin Brinell yöntemine göre sertlik ölçümleri yapılmıştır. Elde edilen gözeneklilik ve sertlik verileri proje kapsamında yapılan başka bir çalışmada yayınlanmış olup bu çalışmanın esası olan abrasif aşınma davranışlarının yorumlanmasında da dikkate alınmıştır [20].

Bu deneysel çalışmanın son aşamasında abrasif aşınma deneyleri gerçekleştirilmiştir. Deneylerde literatürden farklı olarak, abrasif aşınma mekanizması dikkate alınarak çelik disk yerine 400 mesh aşındırıcı tane boyutunda Al_2O_3 zımpara kağıdı kullanılmıştır. Aşınma deneyleri 40 N yük uygulanarak, 0,9 ms^{-1} hızda, 90 m ve 180 m aşınma mesafesi uygulanarak yapılmıştır. Kompozit numunelerin deney öncesi ve sonrası ağırlıkları 0,0001g hassasiyetindeki elektronik terazi ile ölçülerek aşınma kayıpları belirlenmiştir. Aşınma deneyi uygulanan tüm kompozit numune yüzeylerinden optik mikroskop görüntüleri çekilmiştir.

3. Bulgular ve Tartışma

3.1. Mikroyapı

MgO takviyeli Al 7075 kompozitlerin mikroyapısını incelemek amacıyla ortalama takviye oranı olan %10 MgO takviyeli kompozit numuneden çekilmiş olan taramalı elektron mikroskobu (SEM) görüntüleri Şekil 1'de verilmektedir.

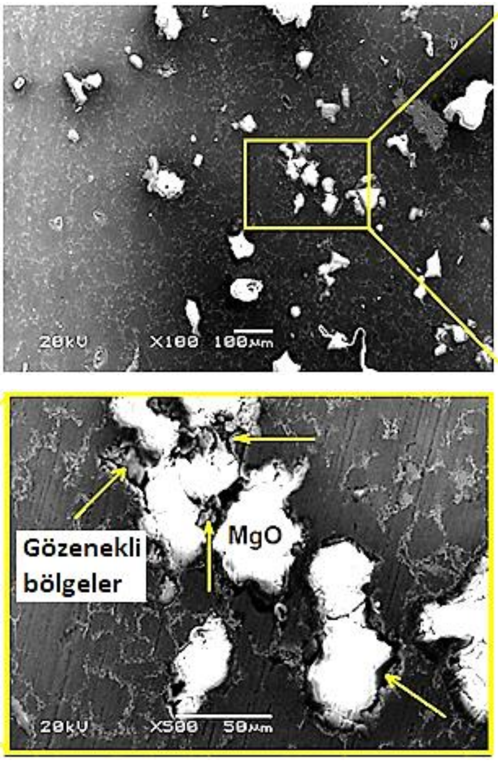

Şekil 1. Kompozit yapı.

Figure 1. Composite structure.

Şekil 1 incelendiğinde, ilk etapta MgO takviye partiküllerinin düzensiz dağılımı dikkat çekmektedir. Diğer önemli husus ise MgO partiküllerinin yan yana gelerek topaklanma eğilimi göstermesidir. MgO topaklanmasının kompozit yapı içerisinde gözenekli bölgelerin oluşmasına da yol açabilmektedir. Literatürde yer alan çalışmalarda, kompozit yapıyı oluşturan malzemelerin çok farklı ısıl davranışları, mekanik özellikleri ve yoğunluk farklılıklarından dolayı porozite oluşumundan bahsedilmektedir [21-24]. Şekil 1'de görüldüğü gibi bir araya gelerek topaklaşan MgO partikülleri arasında erimemiş ve yeterli sinterleme oluşmamış bölgeler yer almaktadır. Çok yüksek ısıl dirence sahip olan refrakter özellikli MgO partikülleri sinterleme sürecinde bir termal bariyer gibi davranarak ısı geçişini engel olmuştur. Dolayısıyla MgO partikülleri arasında kalan bölgelerde boşluklar ve gözenekler meydana gelmiştir. Matris ve takviye parçacıkları arasındaki ıslanabilirlik, metal matrisli kompozitlerin üretiminde karşılaşılan önemli bir problemdir. Matrisin viskozitesi düşükse ve ıslanma ile sistemin serbest enerjisinde bir azalmaya oluşursa, başarılı bir ıslatma oluşmaz. Takviye elemanı olan seramiklerin erimiş metal tarafından ıslanması işlemine, kompozit yapıyı oluşturan malzemelerin yüzey kimyası ve yüzey gerilimi etki etmektedir. Sinterleme sürecinde MgO topaklanmasının olduğu bölgelerde, matris-takviye ara yüzeyindeki ıslatmasının zorlaştığı ifade edilebilir. Başarılı bir ıslatmanın olmaması nedeniyle, kompozit yapıda gözenekli bölgeler meydana gelmektedir.

Gözenekliliğin oluşmasındaki diğer etken ise sinterleme sürecinde matris malzemesi alüminyum partiküllerinin boyun oluşumu ve biri birine bağlanma işleminin başarılı olup olmamasıdır. Sinterleme sıcaklığı ve süresinin artmasıyla birlikte Al 7075 matris tanelerinin biri birine bağlanması ve büyümesi artış göstermektedir. Tam sinterlemenin oluşmadığı ve tüm alüminyum tanelerinin birleşerek tek parça haline gelemediği sinterleme sıcaklıklarında, büyüyen taneler arasındaki boşluklarında daha büyük hacimlere ulaştığı ifade edilebilir. Şekil 2'de sinterleme sırasında sıcaklık artışına bağlı matris elemanının tane yapısındaki değişim ve gözenek (boşluk) durumu sembolik olarak gösterilmektedir. Şekil 2'de sembolize edildiği gibi, sinterleme sıcaklığının artmasıyla termal difüzyon mekanizması da hızlanmaktadır. Özellikle 550°C'nin üzerindeki sinterleme sıcaklıklarında artan taneler arası bağlanma ve sıvı fazın belli yöne doğru hareket ederek birikmesiyle, matris partiküllerinde ani boyut değişiklikleri olabilmektedir. Bu değişiklikler tane boyutlarında büyüme olarak ortaya çıkmaktadır. Büyüyen tanelerin merkeze doğru hareket etme isteği neticesinde daha büyük boşluklar oluşmaktadır (Şekil 2-b). Ancak sinterleme sıcaklığı ve süresi arttırıldıkça sıvı faz daha önce oluşan boşlukları doldurmakta ve sinterleme işleminin sonuna yaklaşılmaktadır. Son aşamada gözenek miktarı minimum seviyeye inerek taneler arası bağlanma tamamlanmış olmaktadır (Şekil 2-c).

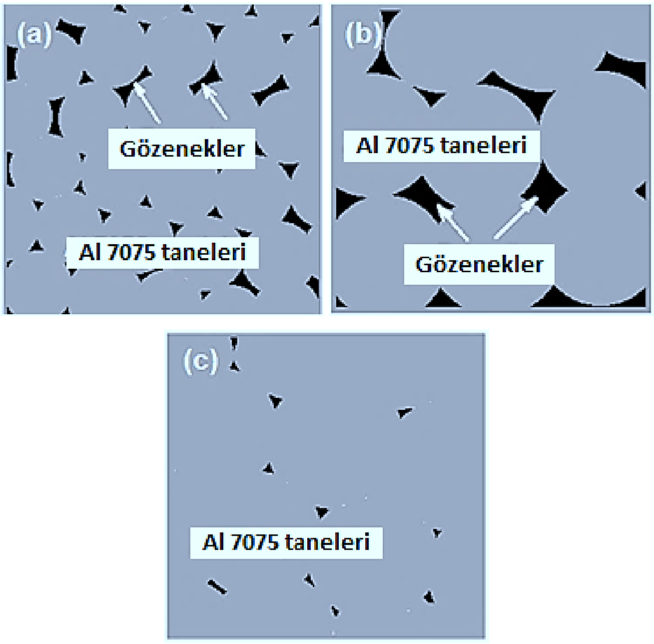

Şekil 2. (a) Düşük sıcaklık 500°C, (b) Yükselmiş sıcaklık 600°C, (c) Tam sinterleme sıcaklığı.

Figure 2. (a) Low temperature 500°C, (b) Raised temperature 600°C, (c) Full sintering temperature.

Bu durumda uygulanan en yüksek sinterleme sıcaklığı olan 600°C'nin porozite açısından çok uygun olmadığı ifade edilebilir. Literatürde benzer sonuçların rapor edildiği çalışmalar yer almaktadır [23, 25]. Diğer taraftan sinterleme süresinin 90 min'dan 120 min'ya çıkmasıyla tüm numunelerin porozite değerlerinde artış olduğu göze çarpmaktadır. Sinterleme süresinin artmasıyla taneler arası bağlanma ve tane büyümesinin arttığı bilinmektedir. Ancak yeterli sinterleme süresi uygulanmayan proseslerde büyüyen taneler arasında tam bağlanmanın olmaması nedeniyle boşluk hacminde büyümeler meydana gelmektedir. Sinterleme süresinin artmasıyla bu durum tersine dönerek artan sıvı faz bu boşlukları doldurarak gözenekliliği azaltmaktadır. Bu durumun sıcaklık artışındaki sebeplerle benzer sebepler olduğu değerlendirilmektedir. Tüm sinterleme sıcaklıklarında yapı içerisindeki MgO oranının artmasıyla gözenek miktarları bir miktar azalmıştır.

3.2. Abrasif Aşınmalar

Al 7075 matrisli %5, 10, 15 ve 20 MgO takviyeli kompozit malzemelerin 40 N yük altında, 400 mesh zımpara üzerinde 90 m ve 180 m aşınma mesafesi uygulanarak yapılan abrasif aşınma deneylerinden elde edilen verilere göre oluşturulan grafikler Şekil 3'te verilmiştir.

3.2.1.MgO oranının aşınmaya etkisi

Şekil 3'teki grafiklere bakıldığında, her iki deney mesafesinde de MgO oranının artışıyla aşınma kayıplarının azaldığı dikkat çekmektedir.

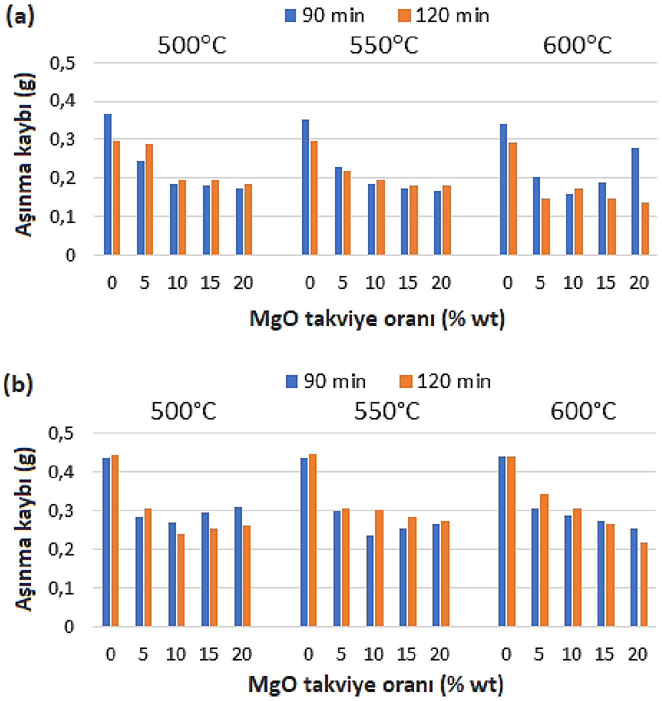

Şekil 3. %5,10, 15 ve 20 MgO takviyeli kompozitlerin numunelerin abrasif aşınma kayıpları (a) 90 m aşınma mesafesi, (b) 180 m aşınma mesafesi.

Figure 3. Abrasive wear losses of composite samples with 5, 10, 15 and 20% MgO reinforcement, (a) 90 m wear distance, (b) 180 m wear distance.

Tüm MgO takviyeli kompozit numunelerde, saf Al 7075 numunelere göre daha az aşınma kaybı meydana gelmiştir. Kompozit yapı içerisindeki takviye elemanı MgO parçacıklarının çok sert fazda olmasının tesiri ile aşınma kayıplarının giderek azaldığı anlaşılmaktadır. Benzer takviye elemanlarıyla üretilmiş alüminyum matrisli kompozitlerin aşınma davranışları üzerine yapılan çalışmalarda, takviye miktarının artmasıyla aşınma direncinin arttığı ve aşınma kayıplarının azaldığı ifade edilmektedir [26-29]. Ancak Şekil 3'teki grafikler incelendiğinde, aşınma direncindeki artışın, MgO artış miktarıyla orantılı olmadığı da anlaşılmaktadır. %5 MgO takviyeli kompozit ile %20 MgO takviyeli kompozit arasında dört kat MgO artışı olmasına rağmen, aşınma direncindeki artış veya aşınma miktarındaki azalış arasında en fazla iki kat farklılık meydana gelmiştir. Hatta 600°C'de sinterlenmiş %20 MgO takviyeli numunede, %5 MgO takviyeli numuneden daha fazla aşınma kaybı oluşmuştur. Parçacık takviyeli metalik kompozitlerde bazen bu tür sıra dışı aşınma davranışları görülmektedir. Bu sıra dışı davranışın farklı sebepleri olmakla birlikte, düzensiz kompozit yapı oluşumları ve homojen olmayan takviye dağılımları önde gelen sebeplerdendir. Yüksek takviye oranıyla birlikte kompozit yapı içerisindeki takviye topaklanması, yüksek gözeneklilik, matris-takviye arasındaki çok düşük ıslatma gibi nedenlerden dolayı aşınma deneyleri sırasında çok fazla miktarda takviye partikülü yapı içerisinden koparak uzaklaşabilmektedir. Bu durumda belli bir orandan sonraki takviye miktarlarında aşınma kayıpları artabilmektedir. Benzer değerlendirmelerin yapıldığı çalışmalar literatürde yer almıştır [30]. Literatürdeki bir çalışmada ise takviye miktarının %10'dan %20'ye çıkmasıyla aşınma direncinde beklenen gelişmenin olmadığı vurgulanmıştır. Bu duruma takviye miktarının artmasıyla birlikte bağıl yoğunluğun düşmesinin neden olduğu belirtilmiştir [31]. Genellikle artan takviye miktarıyla birlikte bazı mekanik özelliklerin artması sonucunda ilk bakışta aşınma direncinin de artacağı düşünülmektedir. Nitekim sertlik değerleri düşük olan %15 MgO takviyeli kompozit numunelerin aşınma kayıpları da fazla olmuştur. Ancak bazı durumlarda takviye miktarı en fazla ve en sert kompozit malzemede aşınma miktarının da arttığı tespit edilmiştir. Bu durumda aşınma özelliklerinin sadece sertlikle ilişkilendirilmesi eksik bir değerlendirme olmaktadır [32]. Fakat takviye elemanı miktarının kompozitin aşınma direnciyle doğrudan ilişkili olduğu söylenebilir [33]. Yapılan bir çalışmada aşınma oranının büyük ölçüde MgO yüzdesinden, ardından sırasıyla yük, kayma mesafesi ve hızdan etkilendiği rapor edilmektedir [34].

3.2.2.Sinterleme parametrelerinin aşınma davranışına etkisi

Şekil 3'teki grafikler incelenmeye devam edilirse, iki deney mesafesinde de, 500°C ve 550°C sıcaklıklar için genel olarak 120 min sinterleme süresindeki aşınma kayıplarının 90 min sinterleme süresine göre bir miktar daha fazla olduğu söylenebilir. 600°C'de ise bazı kararsız aşınma davranışları görülmektedir. Bu durum sinterleme süresinden bağımsız olarak, kompozit yapının düşük sertlik değerleri ve yüksek gözenekliliği ile açıklanabilir. Ancak sinterleme süresindeki değişimin aşınma kayıpları üzerinde kayda değer seviyede farklılıklar oluşturmadığı da ifade edilebilir. Zira sinterleme süresi %33 oranında artmasına rağmen, birkaç numune hariç aşınma kayıplarında çok fazla değişiklik olmamıştır. 120 min süre boyunca sinterlenmiş kompozitlerdeki aşınma kayıplarının, 90 min süreye göre daha fazla olmasında gözenekli yapı daha etkili olmuştur.

Metallerde sinterleme ısıl işlemine etki eden en önemli parametrenin sıcaklık ve süre olduğu bilinmektedir. Ancak içerisinde seramik esaslı partikül takviye edilmiş metalik kompozitlerde, takviye malzemesinin ısıl davranışı da etkili olmaktadır. Şekil 4'teki grafiklerde 500°C, 550°C, 600°C sinterleme sıcaklıklarında, 90 m ve 180 m aşınma mesafesi uygulanarak yapılan deneylerde kompozitlerin aşınma kayıpları verilmiştir.

Şekil 4'teki grafikler incelendiğinde, 80 m aşınma mesafesi ve 120 min sinterleme süresinde 600°C'de sinterlenmiş kompozitlerdeki aşınma kayıplarının 500°C ve 550°C'ye göre bir miktar azaldığı görülmektedir (Şekil 4-a). En az aşınma kaybı iki deney mesafesinde de 600°C'de sinterlenmiş %20 MgO takviyeli kompozitten elde edilmiştir. Diğer taraftan en fazla aşınma kaybı da yine 600°C'de sinterlenmiş %5MgO takviyeli kompozit numunede meydana gelmiştir. Grafiklerde görülen bu istikrarsız değerlerin kompozitin yapısal özelliğinin sebep olduğu değerlendirilmektedir. Her ne kadar sinterleme sıcaklıkları arasında farklılık olsa da, kompozit yapı içerisindeki takviye topaklanması, gözeneklilik ve matris-takviye atasındaki termal uyumsuzluk nedeniyle beklenmeyen malzeme davranışları ortaya çıkmıştır. Dolayısıyla iki grafik genel olarak değerlendirilirse, sinterleme sıcaklıklarındaki değişimin aşınma kayıpları üzerinde önemli bir etkisinin olmadığı söylenebilir. Literatürde yer alan çalışmada benzer sonuç vurgulanmıştır [35].

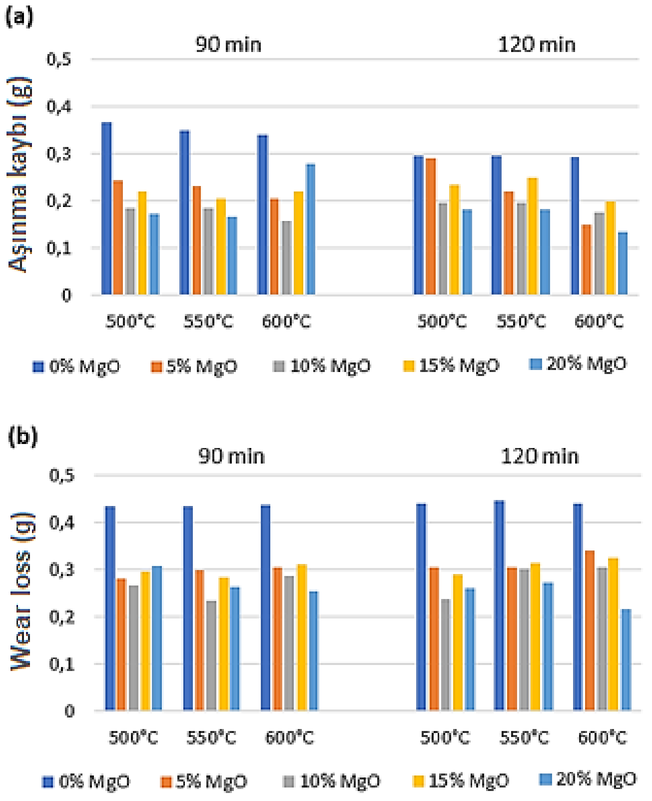

Şekil 4. 500°C, 550°C, 600°C'de sinterlenmiş kompozit numunelerin abrasif aşınma kayıpları (a) 90 m aşınma mesafesi, (b) 180 m aşınma mesafesi.

Figure 4. Abrasive wear losses of composite samples sintered at 500°C, 550°C, 600°C (a) 90 m wear distance, (b) 180 m wear distance.

3.2.3. Deney mesafesinin aşınmaya etkisi

Abrasif aşınma deneylerinde uygulanan 90 m ve 180 m deney mesafelerinin kompozitlerin aşınma davranışlarına etkisini daha net incelemek amacıyla Şekil 5'deki karşılaştırma grafikleri verilmiştir.

Şekil 5'deki grafiklere bakıldığında, aşınma mesafesinin artmasına bağlı olarak aşınma kayıplarının da arttığı görülmektedir. Bu beklenen ve literatürde sıklıkla rastlanan bir sonuçtur [36-40]. Ancak deneylerde uygulanan 90 m ve 180 m aşınma mesafeleri arasında %100 fark olmasına rağmen aşınma kayıpları aynı oranda gerçekleşmemiştir. Aşınma mesafesiyle birlikte aşınma süreside iki katına çıktığından kompozit numunenin aşındırıcı zımpara yüzeyine sürtünmesi artmıştır. Artan sürtünme süresiyle Al 7075 matris üzerindeki sıcaklığın arttığı buna bağlı olarak yumuşayan bir miktar alüminyumun aşınma çizgilerinin ve kopan MgO partiküllerinin oluşturduğu oyuklar içerisine sıvandığı ve yüzeyi terk etmediği değerlendirilmektedir. Bu durumda aşınma kayıplarında sürtünme mesafesindeki miktar kadar artış olmamıştır. Grafikler incelendiğinde 500°C ve 550°C sıcaklıkta sinterlenmiş numunelerde 90 m ve 180 m deney mesafelerindeki aşınma kaybı farklığının ortalama %30 seviyesinde olduğu söylenebilir. 600°C'de ise aşınma mesafesi farkı ile aşınma kaybı farkları arasında daha yakın orantı olduğu görülmektedir.

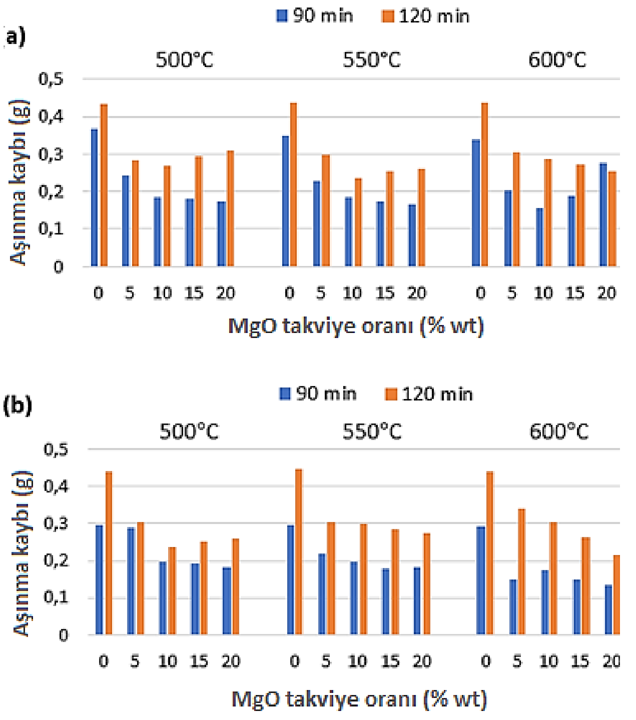

Şekil 5. (a) 90 min sinterleme süresinde, (b) 120 min sinterleme süresinde Al 7075/MgO kompozitlerin aşınma kayıpları.

Figure 5. Wear losses of Al 7075/MgO composites at (a) 90 min sintering time, (b) 120 min sintering time.

Ancak bundan önceki değerlendirmelerde bahsedildiği gibi bazı sıra dışı değerlerde ortaya çıkmıştır. 90 min süreyle 600°C'de sinterlenmiş %20 MgO takviyeli numunede olağan dışı bir aşınma davranışı tespit edilmiştir (Şekil 4a). 180 m kayma mesafesinde, 90 m kayma mesafesinden daha az aşınma kaybı ölçülmüştür. Bu durumun tamamen deneye tabi tutulan numunenin yapısal kusurundan kaynaklandığı ifade edilebilir. 90 m mesafede yapılan bu deneyde numune üzerindeki çok yüksek ve geniş gözenekli bölgenin aşındırıcı zımparaya denk geldiği düşünülmektedir. Bu durumda çok fazla takviye malzemesinin kompozit yapıdan ayrıldığı ve aşınma kaybı değerini aşırı yükselttiği değerlendirilmektedir. Gözeneklilik artışının aşınma miktarlarını doğrudan etkilediği daha önce de ifade edilmiş olup benzer sonuçlar literatürde yer almaktadır [32, 41]. Bazı durumlarda bu tür parçacık takviyeli alüminyum kompozitlerin mekanik özelliklerinin incelendiği deneylerde, sıra dışı sonuçlarla karşılaşılabilmektedir. Şekil 4'te yer alan grafiklerde bu kararsız veya sıra dışı durumlar görülmekte olup nedenleri hakkında yukarıda bazı değerlendirmeler yapılmıştır. Ancak bu kararsız aşınma davranışların altında başka sebeplerinde yatabileceği unutulmamalıdır. Özellikle toz metalürjisi üretim yönteminin en önemli parametresi olan sinterleme işleminde uygulanan sıcaklığın etkisi dikkate alınmalıdır. Kompozit yapıyı oluşturan alüminyum bir metal olup, takviye elemanı olan MgO ise refrakter yapıdaki seramik özellikli bir malzemedir. Bu çok farklı termal özelliklere sahip malzemelerin bir araya getirilmesiyle oluşturulan yeni kompozit yapının çok stabil ve kararlı teknik özellikler göstermemesinin normal olduğu değerlendirilmektedir.

3.3. Aşınmış yüzey morfolojisi

Al 7075 matrisli %5, 10, 15 ve 20 MgO takviyeli kompozit malzemelerin 40 N yük altında, 400 mesh zımpara üzerinde 90 m ve 180 m aşınma mesafesi uygulanarak yapılan abrasif aşınma deneylerinden elde edilen verilere göre oluşturulan grafikler Şekil 3'te verilmiştir

Abrasiv aşınmada yüzeyden malzeme kaybı, yükün etkisi altında aşınma artıkları şeklinde kayan aşındırıcı partiküller ve ayrıca kayma sırasında çevrede sıkışıp kalan toz partiküllerinden kaynaklanır ve aşınmanın kaybolmasına neden olur [42]. Şekil 6'daki yüzey görüntüleri incelendiğinde MgO takviye oranındaki farkın, aşınmış yüzey görüntülerine de yansıdığı dikkat çekmektedir.

MgO takviyesiz numunelerin aşınma yüzeylerinde mikro-sabanlama şeklindeki aşınma mekanizmasının etkili olduğu söylenebilir. Literatürdeki çalışmada benzer aşınma davranışı rapor edilmiştir [11]. Kompozit yapı içerisinde Al 7075 matris malzemesinin daha fazla yer aldığı %5 MgO takviyeli numunedeki aşınma kayıpları, %20 MgO takviyeli numuneye göre daha fazla olmuştur. Şekil 6a, 6d ve 6g'deki yüzeylere bakıldığında Al 7075 matris üzerindeki aşınma çizgilerinin daha geniş ve derin olduğu görülmektedir. Kompozit yapı içerisindeki MgO takviye miktarının aşınma üzerindeki etkisi daha önceki bölümlerde açıklanmıştır. Bu çalışmada da kompozit üretim parametreleri içerisinde aşınmaya en fazla etki eden parametrenin MgO takviye oranı olduğu anlaşılmaktadır. Aşınma yüzeyi görüntülerinin, Şekil 4'deki aşınma kaybı miktarlarını teyit ettiği söylenebilir. Ancak bazı durumlarda yüksek takviye oranının olumsuz etkileriyle karşılaşılmaktadır. Kompozit malzeme içerisindeki takviye parçacıkları alüminyum malzemeye göre daha dayanıklı ve sert olduklarından aşınmaya karşı dirençleri de fazladır. Ancak bu takviye elemanları abrasif aşınma sırasında gevrek ve kırılgan bir davranış gösterebilirler. Deneyler sırasında numune yüzeyine batan aşındırıcı zımpara partikülleri bu gevreklik nedeniyle takviye parçacıklarıyla birlikte önündeki alandan malzeme kaldırmaya çalışmaktadır. Bu durumda takviye miktarı yüksek olan kompozitlerde, azalan matris hacminin uygulanan zorlamaya fazla direnç gösterememesi nedeniyle aşınma kayıplarında artış meydana gelmektedir. 500°C'de 90 min süreyle sinterlenmiş %20 MgO takviyeli Al 7075 kompozitin, 180 m mesafede yapılan abrasif aşınma deneyinden elde edilen aşınma kaybı değerleri yukarıdaki tezi doğrular niteliktedir (Şekil 4). Şekil 9c'deki yüzey görüntüsüne bakıldığında da %20 MgO takviyeli numune yüzeyinde derin aşınma çizgilerinin oluştuğu anlaşılmaktadır.

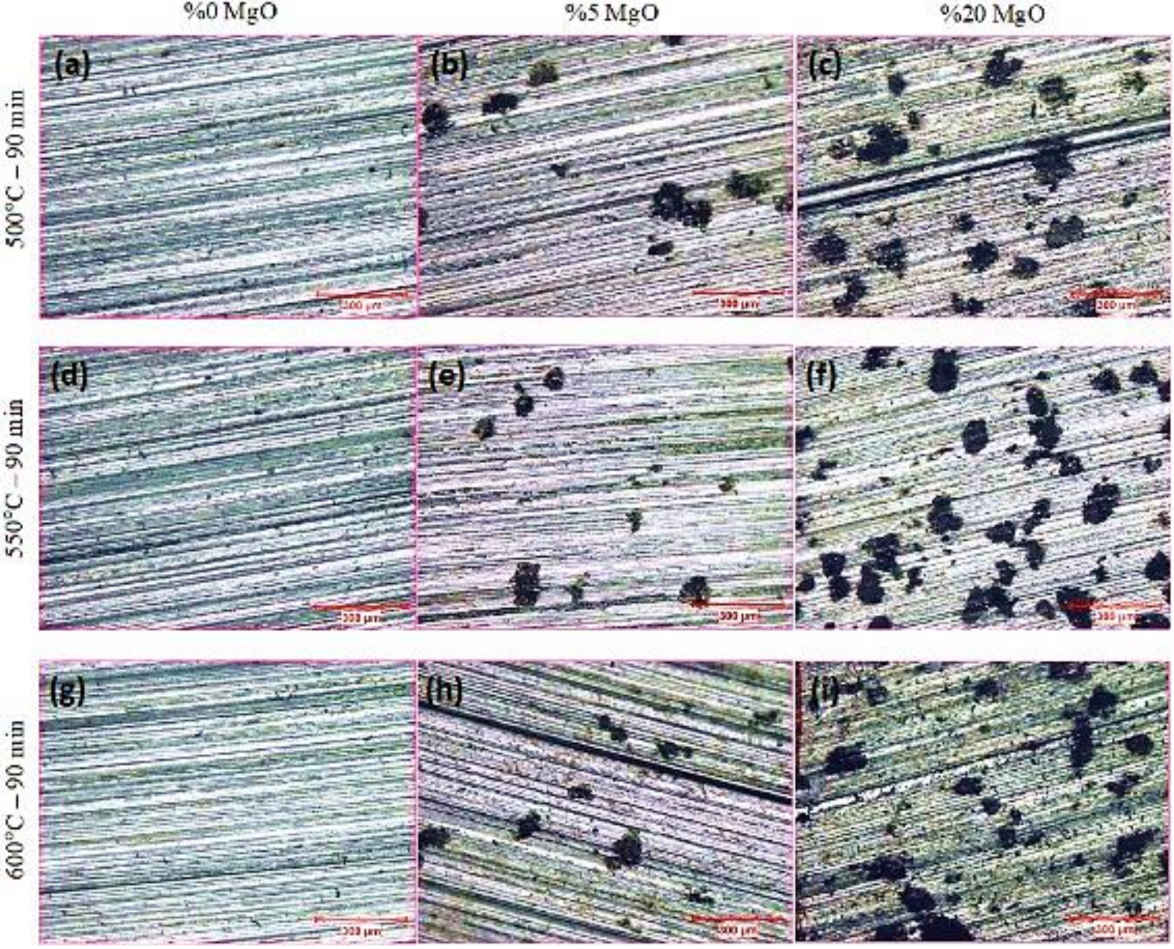

Şekil 6. 90 min süre sinterlenmiş %5 ve %20 MgO takviyeli kompozitlerin aşınmış yüzeyleri.

Figure 6. Worn surfaces of 5% and 20% MgO reinforced composites sintered for 90 min.

Şekil 6'daki MgO takviyesiz saf Al 7075 numunelerin aşınmış yüzeyleri incelendiğinde, aşınma çizgilerinin biri birine çok benzer özellikte olduğu, %5 MgO ve %20 MgO takviyeli numune yüzeyindeki aşınma çizgilerine göre daha ince ve düzenli biçimde görünmektedirler (Şekil 6a, 6d ve 6g). Burada abrasif aşınma deneyi sırasında sadece zımpara üzerindeki aşındırıcı partiküllerin etkisi anlaşılmaktadır. MgO takviyeli numunelerin yüzeyinde oluşan daha derin ve geniş aşınma çizgilerinin oluşmasında ise kompozit yapı içerisindeki MgO partiküllerinin etkisi de ortaya çıkmaktadır. Deneyler sırasında kompozit yapı içerisinden koparak ayrılan MgO tanecikleri de numune yüzeyine sürtünerek ayrıca aşındırma etkisi yapmaktadır. %20 MgO takviyeli numunenin yüksek aşınma kaybına uğramasının sebeplerinden biriside, saf alüminyum numuneden ve %5, %10, %15 MgO takviyeli kompozitlerden daha sert yapıda olmasına rağmen, kopan MgO partiküllerinin ilaveten yaptığı aşındırma etkisidir. Yüzeyler üzerinde oluşan çizik ve oyukların numune ile dönen aşındırıcı disk arasındaki kaymanın bir sonucu olarak oluşan mikro-kesme ve mikro-sabanlama şeklinde olduğu söylenebilir [27].

Aşınmış yüzeylerin görüntüleri incelemeye devam edildiğinde, sinterleme sıcaklıklarının yüzey morfolojisi üzerinde kayda değer ölçüde farklılık oluşturmadığı söylenebilir. 500°C, 550°C ve 600°C'de sinterlenmiş kompozit numunelerin aşınma deneylerinden sonra çekilen mikroskop görüntülerine detaylı olarak bakıldığında, sıcaklığın artmasına bağlı olarak MgO partiküllerinin daha fazla küçük parçacıklara ayrıldığı göze batmaktadır. Bu durumu artan sıcaklıkla beraber yapı içerisindeki gözenekliliğin de artmasıyla ilişkilendirmek mümkündür.

Özellikle 600°C'de sinterlenmiş numune yüzeyindeki çok küçük parçalara ayrılmış MgO tanecikleri dikkat çekmektedir (Şekil 6i). Yüksek miktarda gözeneğin yer aldığı bölgeler içerisinde yer alan çok küçük boyuttaki MgO partikülleri, aşınma deneyi sırasında gözenekli bölgeden ayrılarak numunenin yüzeyine yayılmaktadır. Yine aynı şekilde, en düşük sertlik değerleri 600°C'de sinterlenmiş numunelerden elde edilmiştir. Düşük sertlik değerleri de MgO partiküllerinin kompozit yapı içerisinden daha kolay ayrılmasına neden olmuştur.

Şekil 7'de 120 min süreyle sinterleme yapılan numunelere ait aşınmış yüzey görüntüleri verilmiştir. Görüntülere bakıldığında, Şekil 6'da yer alan 90 min süreyle sinterlenmiş numunelerin yüzey görüntülerinden çok farklılık olmadığı söylenebilir. Ancak daha detaylı bir inceleme yapıldığında, aşınma çizgilerinin bir miktar daha geniş ve derin olduğu anlaşılmaktadır. Zira sinterleme süresinin artmasıyla, sertlik değerleri azalmış ve gözeneklilik değerleri de yükselmiştir. Bu mekanik davranışa bağlı olarak kompozit yapının ana malzemesi olan Al 7075'te daha fazla aşınma kaybı meydana gelmiştir. Aynı şekilde yumuşayan kompozit yapı içerisindeki MgO partiküllerinin ayrılması da daha kolaylaşmıştır. Şekil 7a, 7d ve 7g'deki takviyesiz Al 7075 alaşımı üzerinde abrazyon sırasında oluşan aşınma çizgilerinin sinterleme sıcaklığı arttıkça biraz daha genişleyerek derinleştiği söylenebilir.

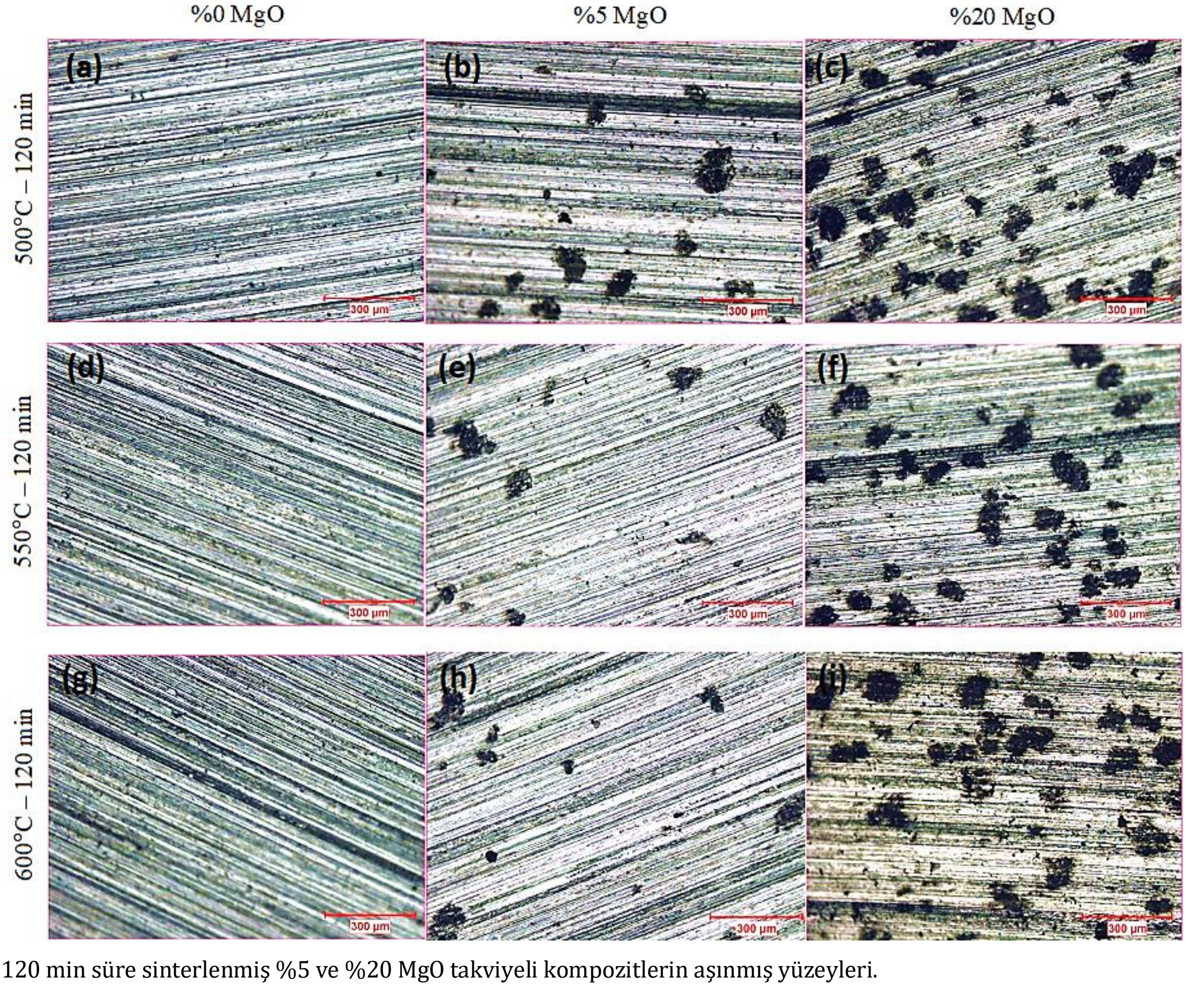

Şekil 7. 120 min süre sinterlenmiş %5 ve %20 MgO takviyeli kompozitlerin aşınmış yüzeyleri.

Figure 7. Worn surfaces of 5% and 20% MgO reinforced composites sintered for 120 min.

Saf alüminyumda deneyler sırasında uygulanan yük, aşınmayı arttırarak malzeme yüzeyinde sünek kırılmalara neden olmuştur. Aşındırıcı zımparadaki aşındırıcı partiküllerin boyutuna bağlı olarak sürekli bir yırtılma ve plastik deformasyon meydana gelmiştir. % 5 MgO ve %20 MgO takviyeli numune yüzeyindeki aşınma çizgilerinin ise daha düzensiz ve farklı genişliklerde olduğu görülmektedir. Aşınma deneyleri sırasında kompozit yapı içerisinden kopan farklı boyuttaki MgO partiküllerinin de yüzeyi çizdiği anlaşılmaktadır. Yapı içerisinden kopan MgO parçacıklarının bir kısmı yüzeyden uzaklaşırken bir kısmının da yüzeye sıvandığı ve aşınma yivlerinin içerisinde kaldığı görülmektedir. Literatürde yer alan çalışmada bu tür seramik takviyeli kompozitlerde artan takviye oranı ile aşındırıcı kaybın sıklıkların arttığını söylenmektedir. Bunun nedeninin, kompozit yapıda bulunan sert takviye fazının büyük ölçüde kırılarak yüzeyi çizmesi ve bunun sonucunda abrasif aşınmanın artması olduğu rapor edilmiştir. Ayrıca aşınma testi sırasında yapıdan kopan donatı partiküllerinin artan donatı oranı ile arttığı ve bunun da aşındırıcı kaybında artışa neden olduğu ifade edilmektedir [35]. Başka çalışmada ise Al_2O_3 takviyeli yüzeyden kopan partiküllerin tekrar yüzeye yapışarak aşınma yüzeylerinde sıvanma tabakaları, çizikler, yırtılmalar ve dökülmeler gibi hasarlara neden olduğu rapor edilmektedir [43].

Bunların dışında 90 min süreyle sinterlenmiş kompozitlerin aşınmış yüzeyleri için yapılan değerlendirmelerin, 120 min süre ile sinterlenmiş olan numuneler için de geçerli olduğu söylenebilir. Ancak kayma süresi arttıkça yüzeydeki sıcaklıkta artarak matris malzemesinin sertliği bir miktar azalacaktır. Bunun sonucunda plastik deformasyona uğramış bölgeler ve numune yüzeyindeki çizgiler de genişleyerek aşınma kayıplarının artmasına neden olacaktır. Literatürdeki bir çalışmada benzer sonuçlar rapor edilmiştir [44].

4. Sonuçlar

Toz metalürjisiyle üretilen Al 7075/MgO kompozitlerin aşınma davranışlarında MgO takviye oranı ve sinterleme parametrelerinin etkisinin araştırıldığı bu çalışmadan elde edilen sonuçlar aşağıda özetlenmiştir.

Al 7075 matrisli ve %5, 10, 15, 20 MgO parçacık takviyeli kompozitler toz metalürjisi yöntemiyle başarılı olarak üretilmiştir.

Kompozit malzemelerin mikroyapıları incelendiğinde yer yer MgO takviye topaklanmaları ve beraberinde gözenekli bölgelerin meydana geldiği görülmüştür. Kompozit yapı içerisindeki gözeneklilik ve takviye topaklanmaları mekanik özellikler üzerinde olumsuz etkiler yaratmıştır.

MgO takviye oranının artmasıyla kompozit yapının sertlik değerleri artarken yoğunluğunda azalmalar meydana gelmiştir. Sinterleme sıcaklığının 600°C'ye çıkmasıyla tüm takviye oranlarındaki kompozit numunelerin sertlik değerleri azalırken gözenek miktarları artış göstermiştir.

Sinterleme sıcaklığı ve süresindeki farklılıkların, kompozit numunelerin aşınma kayıpları üzerinde çok önemli etkisi olmadığı anlaşılmıştır. Aşınma kayıpları üzerinde en etkili parametrenin MgO takviye miktarı olduğu değerlendirilmiştir.

Aşınma deney mesafesinin iki katına çıkarılmasına rağmen aşınma kayıpları aynı oranda gerçekleşmeyip daha az meydana gelmiştir. Bu duruma aşınma yüzeyindeki artan sıcaklıkla birlikte Al 7075 matris malzemesi sıvanmalarının sebep olduğu kanaatine varılmıştır.

Aşınma yüzey görüntüleri incelendiğinde abrasif aşınma mekanizmasının daha çok etkisinin mikro-sabanlama şeklinde ortaya çıktığı, sinterleme sıcaklığı ve süresindeki değişimlerin aşınmış yüzey görüntüleri üzerinde belirgin farklar oluşturmadığı anlaşılmıştır.

Etik kurul onayı ve çıkar çatışması beyanı

Hazırlanan makalede etik kurul izni alınmasına gerek yoktur. Hazırlanan makalede herhangi bir kişi/kurum ile çıkar çatışması bulunmamaktadır.

Teşekkür

Bu çalışma Kırıkkale Üniversitesi Bilimsel Araştırma Projeleri Birimi tarafından 2021/051 numaralı proje kapsamında desteklenmiştir.

Kaynaklar

[1] Dwivedi S.P., Manish Maurya M., Chauhan S.S. 2021. Mechanical, Physical and Thermal Behaviour of SiC and MgO Reinforced Aluminium Based Composite Material, Joint Journal of Novel Carbon Resource Sciences & Green Asia Strategy, Cilt. 8(2), s. 318-327.

[2] Majidiana H., Ghasalia E., Ebadzadeha T., Razavia M. 2016. Effect of Heating Method on Microstructure and Mechanical Properties of Zircon Reinforced Aluminum Composites, Materials Research, Cilt. 19(6), s. 1443-1448.

[3] Mosleh-Shirazi S., Akhlaghi F., Li D.Y. 2016. Effect of graphite content on the wear behavior of Al/2SiC/Gr hybrid nano-composites respectively in the ambient environment and an acidic solution, Tribology International, Cilt. 103, s. 620-628.

[4] Awad A.Y., Ibrahim M.N., Hussein M.K. 2018. Effects of Rice Husk Ash–Magnesium Oxide Addition on Wear Behavior of Aluminum Alloy Matrix Hybrid Composites, Tikrit Journal of Engineering Sciences, Cilt. 25(4), s. 16-23.

[5] El-Sayed M., Sherif, F.H., Latief, H., Junaedi, A.A. 2012. Almajid, Influence of Exfoliated Graphite Nanoplatelets Particles Additions and Sintering Temperature on the Mechanical Properties of Aluminum Matrix Composites, Int. J. Electrochem. Sci., Cilt. 7, s. 4352-4361.

[6] Chintada S., Dora S.P., Kare D. 2021. Mechanical Behavior and Metallographic Characterization of Microwave Sintered Al/SiC Composite Materials – An Experimental Approach, Silicon, Cilt. 10, s. 1-12.

[7] Albert T., Sunil J., Simon Christopher A. 2021. Jegan R., Anand Prabhu P., Selvaganesan M., Preparation and characterization of aluminium-titanium carbide (Al-TiC) composite using powder metallurgy, Cilt. 37(2), s. 1558-1561.

[8] Sadooghi A., Hashemi S.J. 2019. Investigating the influence of ZnO, CuO, Al2O3 reinforcing nanoparticles on strength and wearing properties of aluminum matrix nanocomposites produced by powder metallurgy process, Materials Research Express, Cilt. 6(10), s. 105019.

[9] Sweet G.A.W., Williams B.W., Taylor A. 2020. Hexemer R.L., Donaldson I.W., Bishop D.P., A microstructural and mechanical property investigation of a hot upset forged 2xxx series aluminum powder metallurgy alloy reinforced with AlN,Journal of Materials Processing Technology, Cilt. 284, s. 116742.

[10] Ansary Yar A., Montazerian M. 2009. Abdizadeh H., Baharvandi H.R., Microstructure and mechanical properties of aluminum alloy matrix composite reinforced with nano-particle MgO, Journal of Alloys and Compounds, Cilt. 484, s. 400-404.

[11] John Joshua K., Vijay S.J, Ramkumar P., Kim H.G. 2017. Investigation of Microstructure and Mechanical Properties of AA7068 Reinforced with MgO prepared using Powder Metallurgy, First International Conference on Recent Advances in Aerospace Engineering (ICRAAE), Mart 3-4, Coimbatore, India.

[12] Dwivedi S.P., Maurya M., Chauhan S.S. 2021. Mechanical, Physical and Thermal Behaviour of SiC and MgO Reinforced Aluminium Based Composite Material, Joint Journal of Novel Carbon Resource Sciences & Green Asia Strategy, Cilt. 8(2), s. 318-327.

[13] Khozani B.N., Abuchenari A. 2021. Effects of Mg and MgO Nanoparticles on Microstructural and Mechanical Properties of Aluminum Matrix Composite Prepared via Mechanical Alloying, Journal of Composites and Compounds, Cilt. 3, 91-98.

[14] Kheder A.R.I., Marahleh G.S., Al-Jamea D.M.K. 2011. Strengthening of Aluminum by SiC, Al2O3 and MgO, Jordan Journal of Mechanical and Industrial Engineering, Cilt. 5(6), s. 533-541.

[15] Baghchesara M.A., Abdizadeh H. 2012. Microstructural and mechanical properties of nanometric magnesium oxide particulate-reinforced aluminum matrix composites produced by powder metallurgy method, Journal of Mechanical Science and Technology, Cilt. 26(2), s. 367-372.

[16] Rahimiana M., Ehsania N., Parvinb N. 2009. Baharvandic H.R., The effect of particle size, sintering temperature and sintering time on the properties of Al–Al2O3 composites, made by powder metallurgy, Journal of Materials Processing Technology, Cilt. 209, s. 5387-539.

[17] Konieczny M. 2021. The Effect Of Sintering Temperature, Sintering Time And Reinforcement Particle Size On Properties Of Al-Al2O3 Composites, Composites Theory and Practice, Cilt. 12(1), s. 39-43.

[18] Ahlatci H., Candan E., Çimenoğlu H. 2004. Abrasive wear behavior and mechanical properties of Al–Si/SiC composites, Wear, Cilt. 257, s. 625-632.

[19] Mustafa R.J. 2010. Abrasive Wear of Continuous Fibre Reinforced Al And Al-Alloy Metal Matrix Composites, Jordan Journal of Mechanical and Industrial Engineering, Cilt. 4(2), s. 246-255.

[20] Pul M., Erdem Ü., Türkoz M.B., Yildirim G. 2023. The effect of sintering parameters and MgO ratio on structural properties in Al7075/MgO composites: A review, J Mater Sci., Cilt. 58, s. 664–684.

[21] Wua C., Fang P., Luo G., Chen F., Shen Q., Zhang L., Lavernia E.J. 2014. Effect of plasma activated sintering parameters on microstructure and mechanical properties of Al-7075/B4C composites, Journal of Alloys and Compounds, 615, 276-282.

[22] Baghchesara M.A., Abdizadeh H., Baharvandi H.R. 2010. Microstructure and Mechanical Properties of Aluminum Alloy Matrix Composite Reinforced with Nano MgO Particles, Asian Journal of Chemistry, Cilt. 22(9), s. 6769-6777.

[23] Venkatesh V.S.S., Deoghare A.B.2021. Effect of Sintering Mechanisms on the Mechanical Behaviour of SiC and Kaoline Reinforced Hybrid Aluminium Metal Matrix Composite Fabricated through Powder Metallurgy Technique, Silicon, Cilt. 8.

[24] Xu L., Yue X., Zhang F., Tian Q. 2020. Advance on Al2O3 Particulates Reinforced Aluminum Metal Matrix Composites (Al-MMCs) Manufactured by the Power Metallurgy Techniques- Microstructure and Properties, Advances in Engineering Research, Cilt. 93, s. 99-105.

[25] Aydoğan S.İ., Özer M., Çinici H., Özer A. 2020. Effects of Sintering Temperature on Density and Microstructure of Al-15Si-2,5Cu-0,5Mg/B4C Composites, International Conference on Advanced Materials Science & Engineering and High Tech Devices Applications; Exhibition (ICMATSE 2020), Ekim 2-4 Ekim, Ankara Türkiye.

[26] Sahoo P., Ghosh S. 2011. Tribological Behaviour Of Aluminium Metal Matrix Composites–A Review, Journal Of Tribology Research, Cilt. 2(1), s. 1-14.

[27] Salman K. D. & Abbas H. H. 2020. The Effect of MgO & TiO2 on Wear Behavior of Composite Material. Journal of Mechanical Engineering Research and Developments, CODEN: JERDFO, Cilt. 43(1), s. 288-297.

[28] Tang F., Wu X., Ge S., Ye J., Zhu H., Hagiwara M., Schoenung J.M. 2008. Dry sliding friction and wear properties of B4C particulate-reinforced Al-5083 matrix composites, Wear, 264, s. 555-561.

[29] Rao R.N., Das S. 2010. Effect of matrix alloy and influence of SiC particle on the sliding wear characteristics of aluminium alloy composites, Materials and Design, Cilt. 31, s. 1200-1207.

[30] Pul M., Baydaroğlu V. 2020. Investigation of mechanical properties of B4C/SiC additive aluminum based composites and modeling of their ballistic performances, Journal of Polytechnic, Cilt. 2(2), s. 383-392.

[31] Rahimian M., Parvin N., Ehsani N. 2010. Investigation of particle size and amount of alumina on microstructure and mechanical properties of Al matrix composite made by powder metallurgy, Materials Science and Engineering A, Cilt. 527, s. 1031-1038.

[32] Hasırcı H., Gül F. 2010. B4C /Al Kompozitlerin Takviye Hacim Oranına Bağlıolarak Abrasif Aşınma Davranışlarının İncelenmesi, SDU International Technologic Science, Cilt. 2(1), s. 15-21.

[33] Buytoz S., Eren H. 2007. Effect of Particle Reinforcements on Abrasive Wear Performance of Aluminum Metal Matrix Composites, Science and Eng. J of Fırat Univ. Cilt. 1 (2), s. 209-216.

[34] Rajeshkumar L., Kamalakannan R., Arun Kumar K., Abineesh T. 2018. Dry Sliding Wear Behavior of AA2219 Reinforced with Magnesium Oxide and Graphite Hybrid Metal Matrix Composites, International Journal of Engineering Research & Technology (IJERT), Cilt. 6(7), s. 1-5.

[35] Pul M. 2018. Effect of B4C Reinforcement Ratio and Sintering Temperature on the Mechanical Behavior in Al-B4C Composites, Science of Sintering, Cilt. 50, s. 51-61.

[36] Yıldırım M., Özyürek D. 2018. An Investigation of Wear Behaviors of AA7075 Al Hybrid Composites, High Temp. Mater. Proc., Cilt.37(7), s. 619-624.

[37] Ipek R. 2005. Adhesive wear behaviour of B4C and SiC reinforced 4147 Al matrix composites (Al/B4C–Al/SiC). Journal of Materials Processing Technology, Cilt. 162-163, s. 71-75.

[38] Yashavanth Kumar T., Anil Kumar G., Satheesh J., Madhusudhan T. 2016. A Review On Properties Of Al-B4C Composite Of Different Routes, International Research Journal of Engineering and Technology (IRJET), Cilt. 3(5), s. 860-865.

[39] Karakoç H. 2020. Production of Powder Metal Al7075/B4C/Si3N4 Composite Materials and Investigation of Wear Properties, Journal of Polytechnic, Cilt. 23(4), s. 1141-1151.

[40] Joshua K.J., Vijay S.J., Selvaraj D.P., Ramkumar P. 2017. Influence of MgO particles on Microstructural and Mechanical Behaviour of AA7068 Metal Matrix Composites, IOP Conf. Series: Materials Science and Engineering, Cilt. 247, s. 012011.

Islak S., Çelik H. 2015. Effect of Sintering Temperature and Boron Carbide Content on the Wear Behavior of Hot Pressed Diamond Cutting Segments, Science of Sintering, Cilt. 47, s. 131-143.

[41] Ravi Prakash M., Saravanan R., Nagaral M., Fabrication and Wear Behavior of Particulate Reinforced Metal Matrix Composites-An Overview, IOSR Journal of Mechanical and Civil Engineering (IOSR-JMCE), Cilt. 14(1), s. 10-20, 2017.

[42] Özkan Z., Gökmeşe H., Gökmen U. 2022. Investigation of the Microstructure-Hardness and Wear Performances of Hybrid/Composite Materials Al2O3/SiC Particle Reinforced in AA 7075 Matrix, Science of Sintering, Cilt. 54, s. 1-11.

[43] Megahed M., Attia M.A. 2017. Abdelhameed M., El-Shafei A.G., Tribological Characterization of Hybrid Metal Matrix Composites Processed by Powder Metallurgy, Acta Metall. Sin. (Engl. Lett.), Cilt. 30(8), s. 781-790.

Dokuz Eylül Üniversitesi Mühendislik Fakültesi Fen ve Mühendislik Dergisi
Dokuz Eylul University Faculty of Engineering Journal of Science and Engineering
Elektronik/Online ISSN: 2547-958X

RESEARCH ARTICLE / ARAŞTIRMA MAKALESI

Investigation of the Dose Distribution of ^{32}P Skin Patch Source by GAMOS Monte Carlo Simulation

^{32}P Cilt Yama Kaynağının Doz Dağılımının GAMOS Monte Carlo Simülasyonu ile İncelenmesi

Hakan Epik

Dokuz Eylül Üniversitesi Fen Fakültesi Fizik Bölümü, İzmir, TÜRKİYE
Corresponding Author / Sorumlu Yazar : hakan.epik@deu.edu.tr

Abstract

In recent years, both experimental and theoretical studies on superficial brachytherapy for the treatment of skin cancers have been increasing. The results of experimental and theoretical studies show that the method is promising. The method involves the use of beta-emitting radionuclides. It is crucial to thoroughly understand and investigate the dose characteristics of the radionuclides used for the success of the treatment. In this study, the percent depth dose and transverse dose profiles of the commonly used cancer treatment, the ^{32}P-labeled skin patch source, were examined using the GAMOS Monte Carlo Simulation method. The simulation results obtained are consistent with studies in the literature. The examined 12.5 mm radius skin patch source is suitable for the treatment of skin tumors with sizes ranging from 9.0 to 11.0 mm. By appropriately matching the size of the skin patch source to the size of the skin tumor, both the normal tissue surrounding the tumor and the normal tissue, cartilage, and bone beneath the tumor can be preserved. The ^{32}P skin patch source will be a suitable option for early-stage tumors with a thickness of 1.0-2.0 mm that have not yet reached the deeper layers of the skin tissue. For deeper tumors, radionuclides emitting high-energy beta particles should be utilized.

Keywords: *Phosphorus-32, GAMOS, Superficial Brachytherapy, Skin Patches, Radionuclide*

Öz

Son yıllarda cilt kanserlerinin tedavisinde yüzeysel brakiterapiye yönelik hem deneysel hem de teorik çalışmalar artmaktadır. Deneysel ve teorik çalışmaların sonuçları, yöntemin umut verici olduğunu göstermektedir. Yöntem, beta yayan radyonüklitlerin kullanımını içerir. Tedavinin başarısı için kullanılan radyonüklitlerin doz özelliklerinin iyice anlaşılması ve araştırılması büyük önem taşımaktadır. Bu çalışmada yaygın olarak kanser tedavisinde kullanılan ^{32}P etiketli yama kaynağının yüzde derinlik dozu ve enine doz profilleri GAMOS Monte Carlo Simülasyon yöntemi kullanılarak incelenmiştir. Elde edilen simülasyon sonuçları literatürdeki çalışmalarla tutarlıdır. İncelenen 12,5 mm yarıçaplı cilt yaması kaynağı, boyutları 9,0 ile 11,0 mm arasında değişen cilt tümörlerinin tedavisi için uygundur. Cilt yama kaynağının boyutunun cilt tümörünün boyutuna uygun şekilde eşleştirilmesiyle, hem tümörü çevreleyen normal doku hem de tümörün altındaki normal doku, kıkırdak ve kemik korunabilir. ^{32}P cilt yama kaynağı, henüz cilt dokusunun daha derin katmanlarına ulaşmamış, 1,0-2,0 mm kalınlığındaki erken evre tümörler için uygun bir seçenek olacaktır. Daha derin tümörler için yüksek enerjili beta parçacıkları yayan radyonüklitlerden yararlanılmalıdır.

Anahtar Kelimeler: *Fosfor-32 ,GAMOS , Yüzeysel Brakiterapi, Deri Yamaları, Radyonüklid*

1. Introduction

Skin cancers have been among the most common types of cancer in the last 30 years [1]. There are two main types of skin cancer: melanoma and non-melanoma skin cancer (NMSC). Non-melanoma tumors, including basal cell carcinoma (BCC) and squamous cell carcinoma (SCC), pose the greatest threat to human health despite having a lower probability of occurrence [2, 3]. Various treatment methods, such as surgery, regional treatments, chemotherapy, and radiotherapy, are used in skin cancer treatments based on the type, stage, and location of the skin tumor. Due to the potential for cosmetic complications with surgical methods, radiotherapy stands out as a crucial alternative treatment method. Each method has its own unique advantages and disadvantages. In recent years, alternative superficial brachytherapy methods have been suggested for the treatment of skin cancers, offering the possibility to treat tumors without exposing them to the disadvantages of traditional treatment methods [4]. The superficial brachytherapy method has advantages such as ease of use, simplicity of the treatment procedure, reduction of the dose received through regional dose irradiation, and non-invasiveness. Another benefit is the preservation of healthy tissue and bone underneath the tumor volume by tailoring the size and shape of the patch source used to the size and shape of the skin tumor [5, 6]. In this method, beta (β-) emitting radionuclides with a short penetration depth, such as ^{90}Y, ^{188}Re, ^{166}Ho, and ^{32}P, are preferred.

In the literature, there is an increasing number of both experimental and theoretical studies on patch sources labeled with beta-emitting radionuclides. Pashazadeh et al. presented a patch design loaded with ^{90}Sr radioisotope, which they produced using a 3D printer and medical-grade

DOI: https://doi.org/10.21205/deufmd.2025277902

Geliş Tarihi / Received: 13.02.2024
Kabul Tarihi / Accepted: 11.03.2024

polycaprolactone, tailored to the location and size of the skin tumor [7]. Mukherjee et al, using ^{188}Re-labeled bandages, controlled tumor growth in mice carrying melanoma and found that the tumor size completely regressed at specific radiation doses [8]. Lee et al. treated Bowen's disease and skin cancers using patches impregnated with ^{166}Ho [9]. Salgueiro et al. reported that the design of patches made of silicon or natural rubber labeled with ^{32}P is safe for superficial brachytherapy and achieved complete regression of tumors [10]. Mukherjee et al. tested their ^{90}Y-coated patches to control superficial tumors in mice [11]. Additionally, Saxena and colleagues presented new approaches for preparing ^{90}Y-EGMP patches in superficial brachytherapy [12], and Pashazadeh and colleagues reported the preparation of patches using ^{90}Y microspheres for the treatment of small superficial skin tumors, along with the results of dose calculations [13, 14].

In medical applications, having a good understanding of the dosimetric characteristics of skin patch sources labeled with radionuclides such as ^{90}Y, ^{188}Re, ^{166}Ho, and ^{32}P, which will be used in superficial brachytherapy, is crucial for the success of the treatment. To achieve this goal, in addition to experimental and analytical calculation methods in dose calculations, the Monte Carlo (MC) simulation method based on probability theory is widely used. Obtaining a precise dose distribution with experimental methods is challenging due to the high dose gradient near beta-emitting sources. With MC simulations, these calculations can be performed with high precision. Currently, particle transport codes based on MC such as MCNP [15], EGSnrc [16], PENELOPE [17], FLUKA [18], and GEANT4 [19, 20] are used. In addition to these codes, specifically for users with limited C++ knowledge for special purposes, "Geant4 Application for Tomographic Emission" (GATE) [21] and "GEANT4 based Architecture for Medicine-Oriented Simulations" (GAMOS) [22], which allows users to work with minimal Geant4 knowledge, have been developed.

In this study, the percentage depth dose and transverse dose profiles of a skin patch source labeled with ^{32}P have been investigated using the GAMOS Monte Carlo code.

2. Materials and Methods

In this study, a skin patch source labeled with Phosphorus-32 (^{32}P) radionuclide has been examined. The main physical properties of the ^{32}P radionuclide are presented in Table 1. The spectrum information for the ^{32}P radionuclide is based on RADAR-The Decay Data (2) Figure 1 [23].

Table 1. Physical properties of ^{32}P radionuclide.

Half Life (Day)	E_{max} (MeV)	E_{mean} (MeV)	Range within the tissue (mm)
0.31	0.44	0.97	0.31

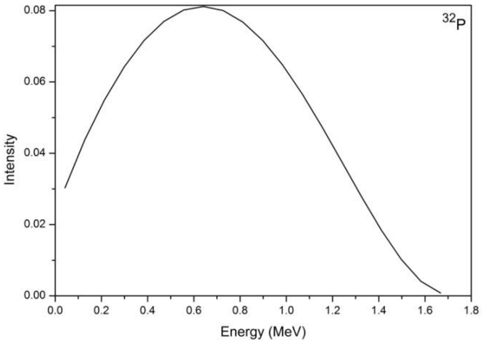

Figure 1. The spectrum of ^{32}P radionuclide.

To simulate the skin patch source labeled with ^{32}P, the GEANT4-based Architecture for Medicine-Oriented Simulations (GAMOS) Monte Carlo code was employed. GAMOS is a Monte Carlo code validated by various researchers and groups, covering applications from radiotherapy to nuclear medicine [22]. The simulation geometry in GAMOS MC was created in ASCII (text) format, as depicted in Figure 2. The patch source has a radius of 12.5 mm and a height of 0.5 mm, protected by an Aluminum shield with a radius of 20.0 mm. To protect the skin, a tissue-equivalent plastic with a thickness of 0.01 mm is present between the generated tissue phantom and the radioactive patch source. The surface where the skin patch source is applied is flat, and there is no air layer between the skin patch source and the skin surface.

The tissue phantom is designed in a rectangular shape with dimensions of 40×40×20 mm^3. To calculate the absorbed dose, the volume of the tissue phantom is filled with voxels of dimensions 0.5×0.5×0.20 mm^3, as shown in Figure 2. The elements and mass fractions of the tissue phantom and tissue-equivalent plastic are provided in Table 2. The densities of the tissue phantom and tissue-equivalent plastic are 1.0 g/cm^3 and 1.127 g/cm^3. When creating the skin patch source, the ^{32}P radionuclide is uniformly distributed throughout the entire volume of the patch source. Beta particles are isotropically emitted from the patch source at an angle of π radians. In MC calculations, the GAMOS electromagnetic physics (GmEMPhysics) package, including low-energy physics, has been employed.

The default production cut-off value in GAMOS is 100 μm for all processes on all materials. The energy threshold value in the tissue phantom is 1.06 keV for gammas and 84.66 keV for electrons. Variance reduction techniques were not used in the calculations. 10^9 particles were used to keep the statistical error below 1.0 %. The dosimetric data within the tissue phantom has been obtained at increments of 0.20 mm from the surface to a depth of 10 mm. Simulation results are in the form of a 3D dose file in the DOSXYZnrc format. The outcomes have been evaluated using a custom code written in MATLAB R2023b (MathWorks, Natick, Massachusetts, USA).

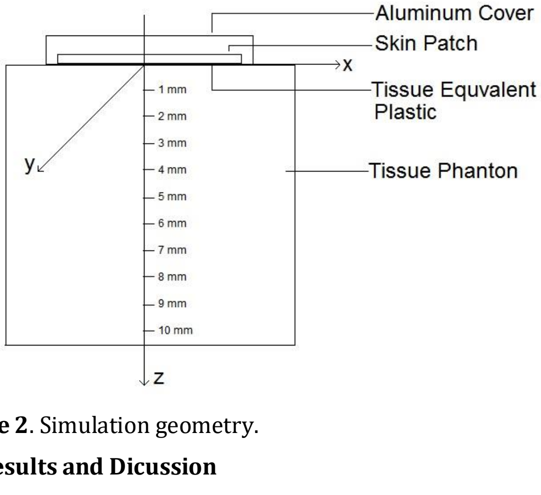

Figure 2. Simulation geometry.

3. Results and Dicussion

The percentage depth dose and normalized dose profiles for 1 mm of the ^{32}P skin patch source are given in Figure 3 [24]. As seen in Figure 3a, there is a sharp decrease in dose with increasing depth. The dose decreases to 90 %, 80 %, and 50 % at depths of R_{90}=0.31 mm, R_{80}=0.44 mm, and R_{50}=0.97 mm, respectively Table 3. This sharp decrease in dose is a desired feature in superficial brachytherapy to preserve normal tissue, bone, and cartilage beneath the target tumor volume.

Table 2. The elements of tissue phantom and tissue equivalent plastic and their mass fractions.

Elements	Tissue Phantom	Tissue Equivalent Plastic
C	0.23219	0.77550
Ca	0.00023	0.01838
H	0.10447	0.10133
N	0.02488	0.03506
O	0.63024	0.05232
F	-	0.01742
Cl	0.00134	
Fe	0.00005	
K	0.00199	
Mg	0.00013	
Na	0.00113	
P	0.00133	

Table 3. Dosimetric parameters of the percent deep dose curve of the ^{32}P patch source.

R_{90} (mm)	R_{80} (mm)	R_{50} (mm)
0.31	0.44	0.97

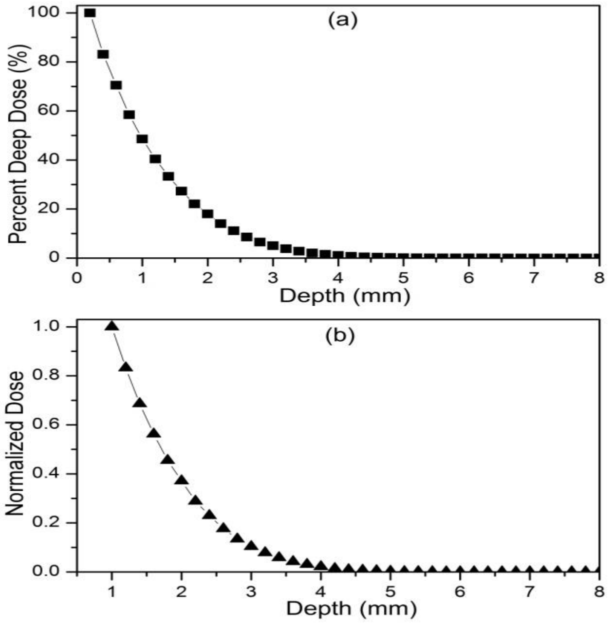

Figure 3. a) Percent deep dose curve of ^{32}P skin patch source, b) Normalized dose curve according to 1.0 mm.

This study's obtained data has been compared with the study conducted by Eduardo et al. Eduardo and colleagues utilized an analytical method and the EGSnrc Monte Carlo code to calculate the dose distributions of ^{32}P and ^{90}Y multichannel skin applicators [25]. The results of Monte Carlo calculations for both studies are presented in Figure 4 and Table 4.

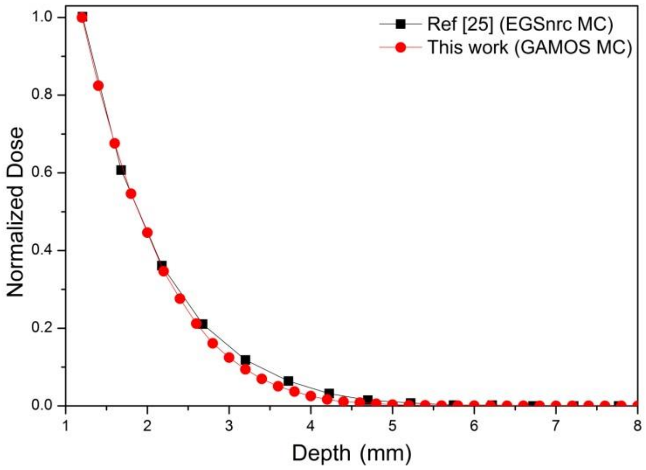

Figure 4. The comparison of the PDD dose distribution. (Curves are normalized to 1.25 mm).

Table 4. Dosimetric parameters of this study and Ref [25].

Depth (mm)	This Study	Ref. [25]
R_{90}	1.32	1.32
R_{80}	1.43	1.44
R_{50}	1.89	1.89

As seen in Figure 4, the results of the two studies are consistent. Beyond 2.2 mm, the maximum difference between the two curves is 2 %. The difference is within reasonable limits. The reasons for this difference lie in the modeling of the tissue phantom in this study and the smaller voxel size of the tissue phantom. Transverse dose profiles of the ^{32}P skin patch source for depths of z=0.2-5.0 mm within the tissue phantom are given in Figure 5.

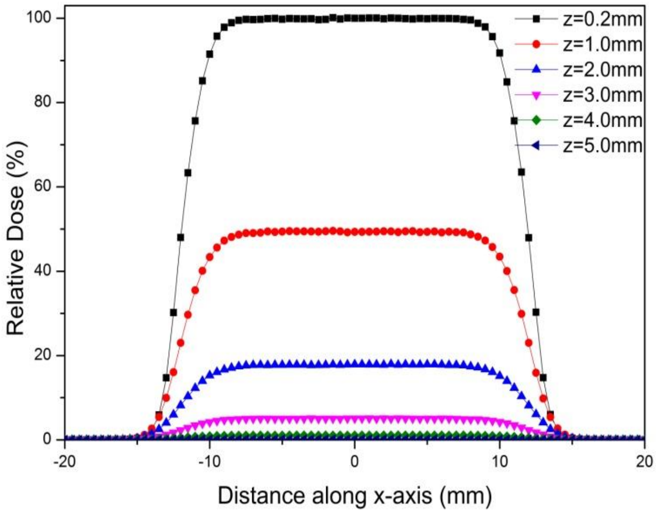

Figure 5. Transverse dose profile of the ^{32}P skin patch source.

The transverse dose profile obtained for a depth of 0.2 mm has symmetry and flatness, which can increase the uniformity of the dose within the target tumor area. The dose value decreases to 40 % at 1.0 mm depth, 17.6 % at 2.0 mm depth and 5.05 % at 3.0 mm depth and after 3.0 mm the dose decrease below 5.0 %. The transverse dose profile of the ^{32}P skin patch source with a radius of 12.5 mm showed that the patch source is suitable for the treatment of skin tumors with a size of 9.0-10.0 mm. Dosimetric parameters of the transverse dose profile are given in Table 5.

Table 5. Dosimetric parameters of the transverse dose profile.

Depth (mm)	Central axis dose value (%)	R_{90} (mm)	R_{80} (mm)	R_{50} (mm)
0.2	100	10.1	10.8	12.0
1.0	49.0	9.79	10.6	11.8
2.0	17.6	9.84	10.5	11.9
3.0	5.05	9.28	10.3	11.7

4. Conclusions

The importance of using skin patch sources labeled with beta-emitting radionuclides in the treatment of superficial skin tumors is clearly evident, especially if there is a bone or cartilage just below the target tumor volume (nose, ear,..). As a result;

- The transverse dose profile of the 12.5 mm radius ^{32}P skin patch source under investigation showed that the patch source is suitable for the treatment of skin tumors with a size of 9.0-11.0 mm. By matching the size and shape of the patch source to the size and shape of the skin tumor, normal tissue surrounding the tumor and normal tissue, bone and cartilage under the tumor volume can be preserved.
- In the treatment of skin tumors with an early stage and a thickness of 1.0-2.0 mm that have not yet spread to the deep layers of the skin tissue, the use of ^{32}P skin patch sources will be a good option for the superficial brachytherapy method.
- In the treatment of deeper-seated skin tumors, it would be appropriate to use skin patch sources labeled with ^{90}Y (2.28 MeV), ^{188}Re (2.12 MeV) radionuclides, which have higher beta energy.

References

[1] International Agency for Research on Cancer. http://www.gco.iarc.fr. (Access Date: 30.01.2024).

[2] Stegman, S. J. 1986. Basal cell carcinoma and squamous cell carcinoma. Recognition and treatment. The Medical Clinics of North America, Vol. 70, p. 95-107. DOI: 10.1016/s0025-7125(16)30971-3

[3] Rass, K., Reichrath, J. 2008. Sunlight, Vitamin D and Skin Cancer. Springer, New York, 162p.

[4] Sedda, A. F., Rossi, G., Cipriani, C., Carrozzo, A. M., Donati, P. 2008. Dermatological high-dose-rate brachytherapy for the treatment of basal and squamous cell carcinoma. Clinical and Experimental Dermatology, Vol. 33, p. 745-749. DOI: 10.1111/j.1365-2230.2008.02852.x

[5] Macey, D. J., Williams, L. E., Breitz, H. B., Liu, A., Johnson, T. K., Zanzonico, P. B. 2001. AAPM Report 71. Medical Physics Publishing, USA, 73 p.

[6] Yeong, C. H., Cheng, M. H., Ng, K. H. 2014. Therapeutic radionuclides in nuclear medicine: current and future prospects. Journal of Zhejiang University Science B, Vol. 15, p. 845. DOI: 10.1631/jzus.B1400131

[7] Pashazadeh, A., Boese, A., Castro, N. J., Hutmacher, D. W., Friebe, M. 2019. A new 3D printed applicator with radioactive gel for conformal brachytherapy of superficial skin tumors. In: 2019 41st Annual International Conference of the IEEE Engineering in Medicine and Biology Society (EMBC), 23-27 July, Berlin, Germany, 6979-6982.

[8] Mukherjee, A., Pandey, U., Sarma, H. D., Gupta, S. K., Ingle, A. D., Pillai, M. R. A., Venkatesh, M. 2003. Bioevaluation of radioactive bandages in a murine model of melanoma. International Journal of Radiation Biology, Vol. 79, p. 839-845. DOI: 10.1080/09553000310001610989

[9] Lee, J. D., Park, K. K., Lee, M. G., Kim, E. H., Rhim, K. J., Lee, J. T., Kim, J. R. 1997. Radionuclide therapy of skin cancers and Bowen's disease using a specially designed skin patch. Journal of Nuclear Medicine, Vol. 38, p. 697-702.

[10] Salgueiro, M. J., Duran, H., Palmieri, M., Pirchio, R., Nicolini, J., Ughetti, R., Zubillaga, M. 2008. Design and bioevaluation of a 32P-patch for brachytherapy of skin diseases. Applied Radiation and Isotopes, Vol. 66, p. 303-309. DOI: 10.1016/j.apradiso.2007.09.008

[11] Mukherjee, A., Pandey, U., Sarma, H. D., Pillai, M. R. A., Venkatesh, M. 2002. Preparation and evaluation of 90Y skin patches for therapy of superficial tumours in mice. Nuclear Medicine Communications, Vol. 23, p. 243-247.

[12] Saxena, S. K., Pandey, A. K., Tandon, P., Chakravarty, R., Reddy, A. V. R., Dash, A., Venkatesh, M. 2009. A novel approach to prepare 90Y EGMP patches for superficial brachytherapy. Applied Radiation and Isotopes, Vol. 67, p. 1416-1420. DOI: 10.1016/j.apradiso.2009.02.059

[13] Pashazadeh, A., Landes, R., Boese, A., Kreissl, M. C., Klopfleisch, M., Friebe, M. 2020. Superficial skin cancer therapy with Y-90 microspheres: A feasibility study on patch preparation. Skin Research and Technology, Vol. 26, p. 25-29. DOI: 10.1111/srt.12758

[14] Dezarn, W. A., Cessna, J. T., DeWerd, L. A., Feng, W., Gates, V. L., Halama, J., Salem, R. 2011. Recommendations of the American Association of Physicists in Medicine on dosimetry, imaging, and quality assurance procedures for 90Y microsphere brachytherapy in the treatment of hepatic malignancies. Medical Physics, Vol. 38(8), p. 4824-4845. DOI: 10.1118/1.3608909

[15] Briesmeister, J. F. 1986. MCNP: A General Monte Carlo Code for Neutron and Photon Transport. Los Alamos, 591p.

[16] Kawrakow, I. 2001. The EGSnrc Code System, Monte Carlo Simulation of Electron and Photon Transport. NRCC Report Pirs, 701s.

[17] Baró, J., Sempau, J., Fernández-Varea, J. M., Salvat, F. 1995. PENELOPE: an algorithm for Monte Carlo simulation of the penetration and energy loss of electrons and positrons in matter. Nuclear Instruments and Methods in Physics Research Section B, Vol. 100, p. 31-46. DOI: 10.1016/0168-583X(95)00349-5

[18] Ferrari, A., Ranft, J., Sala, P. R., Fassò, A. 2005. FLUKA: A Multi-Particle Transport Code. CERN, Switzerland, 387p.

[19] Agostinelli, S., Allison, J., Amako, K. A., Apostolakis, J., Araujo, H., Arce, P., Geant4 Collaboration. 2003. GEANT4—a simulation toolkit. Nuclear Instruments and Methods in Physics Research Section A, Vol. 506, p. 250-303. DOI: 10.1016/S0168-9002(03)01368-8

[20] Allison, J., Amako, K., Apostolakis, J., Araujo, H. A., Dubois, P. A., Asai, M., Yoshida, H. 2006. Geant4 developments and applications. IEEE Transactions on Nuclear Science, Vol. 53, p. 270-278. DOI: 10.1109/TNS.2006.869826

[21] Jan, S., Santin, G., Strul, D., Staelens, S., Assié, K., Autret, D., Morel, C. 2004. GATE: a simulation toolkit for PET and SPECT. Physics in Medicine & Biology, Vol. 49, p. 4543. DOI: 10.1088/0031-9155/49/19/007

[22] Arce, P., Rato, P., Canadas, M., Lagares, J. I. 2008. GAMOS: A Geant4-based easy and flexible framework for nuclear medicine applications. IEEE Nuclear Science Symposium Conference Record, 19-25 October, Germany, 3162-3168.

[23] Keith F. E. 2003. The beta spectra file to use for MCNP code http://www.doseinfo-radar.com/RADARHome.html. (Access Date: 30.01.2024).

[24] TECDOC, I. 2002. Calibration of photon and beta ray sources used in brachytherapy. International Atomic Energy Ageny 66p.

[25] De Paiva, E., Robatjazi, M., Pashazadeh, A. 2022. Calculations of beta radiation doses from multiwell Phosphorus-32 and Yttrium-90 applicators designed to be used in the treatment of superficial skin tumors: comparison of Monte Carlo and analytical methods. The European Physical Journal Plus, Vol. 137, p. 1-7. DOI: 10.1140/epjp/s13360-022-03116-5

DEU FMD 27(79) (2025) 15-21

Dokuz Eylül Üniversitesi Mühendislik Fakültesi Fen ve Mühendislik Dergisi
Dokuz Eylul University Faculty of Engineering Journal of Science and Engineering
Elektronik/Online ISSN: 2547-958X

RESEARCH ARTICLE / ARAŞTIRMA MAKALESI

Lqr-Fuzzy Logic Control of a Quarter Vehicle Model

Çeyrek Taşıt Modelinin Lqr-Bulanık Mantıklı Kontrolcü ile Kontrolü

Omur Can Ozguney

Istanbul University-Cerrahpaşa Faculty of Engineering Mechanical Engineering, Istanbul, TÜRKİYE
Corresponding Author / Sorumlu Yazar : omur.ozguney@iuc.edu.tr

Abstract

In this study, a new control rule was developed using two different control methods, and the results were discussed by applying the developed controller to the quarter vehicle model. A new hybrid controller was designed by considering the advantages of Fuzzy Logic control method and Linear Quadratic Regulator (LQR) control method. Control gain coefficients used in LQR controller were determined by fuzzy logic control method. The developed new controller has been applied to the quarter vehicle model. In the results, control with only Fuzzy Logic controller and developed LQR-Fuzzy Logic controller were compared. It was understood from the results that the developed control method was satisfactory.

Keywords: *Fuzzy Logic Control, LQR Control, Quarter Vehicle Model, Simulation*

Öz

Bu çalışmada iki farklı kontrol yöntemi kullanılarak yeni bir kontrol kuralı geliştirilmiş ve geliştirilen kontrolcü çeyrek taşıt modeline uygulanarak sonuçlar değerlendirilmiştir. Bulanık Mantık kontrol yöntemi ve Lineer Kuadratik Düzenleyici (LQR) kontrol yönteminin avantajları dikkate alınarak yeni bir hibrit denetleyici tasarlanmıştır. LQR denetleyicide kullanılan kontrol kazanç katsayıları bulanık mantık kontrol yöntemi ile belirlenmiştir. Geliştirilen yeni kontrol yasası çeyrek taşıt modeline uygulanmıştır. Sonuçlar kısmında, pasif, sadece bulanık mantıklı kontrolcü ve geliştirilen LQR-Bulanık mantıklı kontrolcü ile elde edilen sonuçlar karşılaştırılmıştır. Geliştirilen kontrol yönteminin tatmin edici olduğu sonuçlardan anlaşılmıştır

Anahtar Kelimeler: *Bulanık Mantıklı Kontrol, LQR Kontrol, Çeyrek Taşıt Modeli, Simulasyon*

1. Introduction

Systems such as robots, vehicles and aircraft are difficult to control due to external disturbances. For this reason, controllers that can absorb both nonlinear behaviors and external disturbances are needed. In recent years, control studies in the field of control generally focus on hybrid controllers developed by using two controllers together. While one controller eliminates nonlinearity in the system, the other controller protects the system against external disturbances. This control method is the result of the development of the classical controller and the newly used controllers. In this study, a new controller was developed by using the LQR and fuzzy logic controllers. Control gain coefficients in the LQR controller are mostly found with the equation in the literature. In this study, gain coefficients in LQR controller were determined by using fuzzy logic controller. Thus, a new control method was obtained by using two different controllers. A quarter vehicle model was used to implement the developed controller. Previous studies were taken as reference for this developed controller.

1.1. Literature review

In this study, a new controller was developed by using two different controllers and this developed controller was applied to a two-degree-of-freedom quarter vehicle model. There are different studies in the literature with Fuzzy Logic controller and LQR controller. These;

Devdutt [1] applied a fuzzy logic controller to a semi-active two-degree-of-freedom quarter vehicle model. In order to see the effectiveness of the study, both time-related and frequency changes of the applied control method were analyzed. Input parameters are designed as passenger seat velocity and secondary suspension system velocity also the output parameter is the controller force. Simulation results showed that the semi-active system using the controller is more effective than passive suspension systems. Palanisamy & Karuppan [2] aimed to design a controller to control the yaw movement of vehicle suspensions. Since active suspension systems are difficult to model, they designed a fuzzy logic controller that can control the unmodeled part of active suspensions by using a fuzzy logic controller. In the fuzzy logic controller, the input parameters are determined as body error and change in error, and the output parameter is determined as control force. They carried out simulations using various road entries and understood that the results were satisfactory. Bhangal & Raj [3] applied fuzzy logic controller to active suspension systems and compared them with passive suspension systems. Also, they applied LQR controller to active suspension systems. The results show that fuzzy logic controller is more effective in reducing the acceleration of sprung mass than LQR controller and passive suspension system. Majdoub et al. [4] focusses on solving the problem of controlling quarter-car semi-active suspension system. To overcome with this problem, they designed an active control system. LQR controller and Lyapunov based control method were used as controllers. Various simulations have been made for the proposed control method.

DOI: https://doi.org/10.21205/deufmd.2025277903

Received: 15.10.2023
Accepted: 16.03.2024

And it has been understood that the developed control method is more stable than passive systems. Rao & Kumar [5] presented Linear Quadratic Regulator (LQR) for quarter car semi active suspension system. In this study, the hydraulic damper was replaced with a magneto-rheological damper and a new controller was designed for the suspension system. With the simulations, it has been understood that the developed controller improves ride comfort.

Nagarkar et al [6] studied modelling and control of nonlinear quarter vehicle model including with seat and driver. PID and LQR controllers are applied to nonlinear quarter vehicle model as a controller. Genetic Algorithm rule is used to determine the cost functions of LQR and PID controllers in this study. From the simulation results, it is understood that it is advantageous to determine the estimation of the gain coefficients with a different control rule. Gokul & Malar [7] demonstrated an adaptive approach for the vehicle suspension system by using the LQR control method. The gain coefficients of the LQR controller were determined using the particle swarm optimization method. In order to prove the accuracy of the results obtained with the simulation, they created an experimental setup using a shaker table and tested the controller. The results showed that the controller they presented is advantageous in terms of road handling and ride comfort. Uddin [8] designed an LQR controller for the quarter vehicle model. Computer simulation was made according to active and passive suspension system. The results show that the developed controller has improved vertical displacement, vertical velocity, and vertical acceleration of the vehicle. Kaleemullah, Faris & Hasbullah [9] designed active suspension systems for quarter vehicle model. Robust H controller, LQR controller and Fuzzy control are compared with passive suspension system. The results showed that the controllers designed in active suspension systems are more successful in road handling and ride comfort. Wei et al [10] developed a hybrid controller for active suspension systems. The proposed controller consists of LQR and modal decomposition control rules. Modal decomposition method also works with the principle of weighting according to the importance of parameters such as neural network. When the results are compared with the passive system, the efficiency of the hybrid controller is understood. Bharali & Buragohain [11] applied three different controllers to a quarter vehicle model with three degrees of freedom. These controllers are PID controller, Linear Quadratic Controller (LQR) and Fuzzy logic controller. They explained the purpose of the study as increasing the ride comfort. As a result of the study, they observed that the fuzzy logic controller is more effective in stability. Divekar & Mahajar [12] aimed to provide ride comfort and road handling and to eliminate the discomforts caused by external disturbances of a vehicle. So that they developed control laws for quarter vehicle model with seat driver. LQR and Fuzzy logic controller have been adapted to this model and different control inputs have been applied to the model. From the results, they have seen that the LQR controller is more successful than the fuzzy logic controller for the step input. Anh [13] studied active suspension systems using PID control and LQR controllers. In this study, the PID controller supports to optimize the vehicle body acceleration and the LQR controller supports to optimize the vehicle body displacement. Rao & Narayanan [14] applied the sky hook damper model to the half vehicle model and examined the differences between LQR controller. From the simulation results, it has been observed that the displacement and velocity values obtained with the LQR controller are close to the skyhook model.

The summary of similar studies in the literature is as follows. Research shows that hybrid controllers are more advantageous. Therefore, a new hybrid control method has been developed by combining LQR and fuzzy logic controllers in this study by recognizing the deficiency in the literature.

There are two important situations for vehicles. The first one is road handling and the second one is ride comfort. It is very difficult to cure these two conditions at the same time. There are many controllers used to control the active suspension system such as PID controller, LQR controller et al. For this, a new controller was designed by considering two different control methods. A hybrid controller is designed using fuzzy logic controller and LQR controller. The control gain coefficients in the LQR control law were determined using a fuzzy logic controller. The input parameters in the fuzzy logic controller are determined as the vertical displacement error of the vehicle and its change with time. The output parameters are LQR gain coefficients (Q,R). The control rule between input and output parameters was determined by trial-and-error method. The effectiveness of the developed controller was obtained by performing simulations with a step path input with an amplitude of 0.01(m).

2. Materials and Methods

In this study, fuzzy logic controller, one of the most important controllers used in artificial intelligence technology, and LQR controller, which is one of the optimal control methods, are combined. LQR is a feedback control method. The control gain coefficients used in this controller are determined by trial-and-error method. A fuzzy logic controller, on the other hand, is a controller used to make predictions. Therefore, a new controller was designed from the combination of these two control methods. A quarter vehicle model was used to properly examine the results.

In the introduction part of this study, previous studies and the purpose of this study are given. In the materials and methods part, the equations of motion of the quarter vehicle model are mentioned. LQR control and Fuzzy Logic Control methods are explained in detail. In the result and discussion chapter, the results of the simulations are given, and the results are discussed. The last section is the discussion section. The advantages of the developed controller are emphasized by examining the results given in the previous section.

2.1. Quarter vehicle model

In Figure 1, two degree of freedom quarter vehicle model is presented.

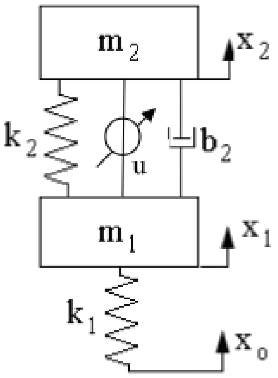

Figure 1. Quarter vehicle model

The equations of motions of the quarter vehicle model demonstrated in Equation 1 and Equation 2. [5]

$$\mathrm{m_1\ddot{x}_1 - b_2(\dot{x}_2 - \dot{x}_1) + k_1(x_1 - x_0) - k_2(x_2 - x_1) = -u} \quad (1)$$

$$\mathrm{m_2\ddot{x}_2 + b_2(\dot{x}_2 - \dot{x}_1) + k_2(x_2 - x_1) = u} \quad (2)$$

In Equation (1) and Equation (2) m1 represents the unsprung mass of the vehicle, m2 represents the sprung mass of the vehicle, and b, k are the damping and stiffness parameters respectively. The numerical parameters of the quarter vehicle model are given in Table 1.

Table 1. Numerical parameters. [14]

Parameter	Unit	Values
m1	kg	36
m2	kg	240
b2	Nsm-1	980
k1	Nm-1	160 000
k2	Nm-1	16000

The state space model of the quarter vehicle model is given below.

$$z_1 = x_1, \qquad z_2 = \dot{x_1}, \qquad z_3 = x_2, \qquad z_4 = \dot{x_2} \quad (3)$$

If Equation 1 and Equation 2 are rewritten using Equation 3;

$$\mathrm{\dot{z_1} = z_2}$$

$$\mathrm{\dot{z_2} = \frac{1}{m_1}[b_2(z_4 - z_2) - k_1(z_1 - x_0) + k_2(z_3 - z_1) - u]}$$

$$\mathrm{\dot{z_3} = z_4}$$

$$\mathrm{\dot{z_4} = \frac{1}{m_2}[-b_2(z_4 - z_2) - k_2(z_3 - z_1) + u]} \quad (4)$$

Using Equation 3, the state space model Equation 5 is obtained.

$$\mathrm{\dot{z}} = [\mathrm{A}]\, z + [\mathrm{B}]\, u + L[x_0]$$

$$\mathrm{y = C}[z] \quad (5)$$

$$A = \begin{bmatrix} 0 & 1 & 0 & 0 \\ \frac{-(k_1 + k_2)}{m_1} & \frac{-b_2}{m_1} & \frac{k_2}{m_1} & \frac{b_2}{m_1} \\ 0 & 0 & 0 & 1 \\ \frac{k_2}{m_2} & \frac{b_2}{m_2} & \frac{-k_2}{m_2} & \frac{-b_2}{m_2} \end{bmatrix}$$

$$\mathrm{B} = \begin{bmatrix} 0 \\ \frac{-1}{m_1} \\ 0 \\ \frac{1}{m_1} \end{bmatrix} \qquad \mathrm{L} = \begin{bmatrix} 0 \\ \frac{k_1}{m_1} \\ 0 \\ 0 \end{bmatrix} \qquad \mathrm{C = [0\ 0\ 1\ 0]} \quad (6)$$

2.2. LQR controller

LQR control method is one of the traditional, optimal control methods like PID controller. Unlike the PID controller, it works on the principle of multiple inputs and multiple outputs. Since it is a feedback control method, most of the control laws currently consider the working principle of the LQR controller.

$$u = K * x \quad (7)$$

In Equation (7), the K is represented as control gain coefficient. In order to optimize the coefficient K in Equation (7), the cost function must be minimized. And the cost function is represented as in Equation (8);

$$J = \int_0^\infty \{x(t)'Qx(t) + u(t)'Ru(t)\}\, dt \quad (8)$$

If Equation 7 substitutes in Equation (8)

$$J = \int_0^\infty x^T(Q + K^T RK)x\, dt \quad (9)$$

In Equation 8, Q and R are the gain coefficients and they should be positive. There are no specific rules for obtaining these coefficients. It's all about trial and error. Therefore, in this study, a fuzzy logic controller that works according to the trial-error principle was used to determine these coefficients. To determine K, assume that there is a constant P;

$$\frac{d}{dt}(x^T Px) = -x^T(Q + K^T RK)x \quad (10)$$

The P value in Equation 6 is determined by the Ricatti equation.

$$PA + A^T - PBR^{-1}P + Q = 0 \quad (11)$$

In Equation 11, A and B represents the state spaces variables of the system.

$$\dot{x} = Ax + Bu \quad (12)$$

The optimum control signal in the LQR controller should be as in Equation 13.

$$u(t) = -R^{-1}B^T P(t)\, x(t) = -Kx(t) \quad (13)$$

The most important part in the LQR controller is to determine the Q and R coefficients. The Q and R coefficients both have specific meanings. While the Q coefficient is adjusted for the response speed of the system, the R coefficient represents the energy consumed in the system.[15] Although there are several methods used to determine the Q and R coefficients, these coefficients are also determined by trial-and-error method.[16] In this study, Q and R coefficients were found with fuzzy logic controller, which is another control method.

2.3. Fuzzy logic controller

Zadeh was the first to come up with this control rule [17]. There are not only clear definitions in this developed control method. While describing any situation, definitions such as true-false, yes-no or 1-0 are made. In fuzzy logic, this is not the case. Intermediate values are also included. For example, when describing a situation, intermediate values other than 1-0 are also included. By means of fuzzy logic, intermediate values are expressed with membership functions. Membership functions can be expressed with geometric shapes such as triangles, trapezoids (Figure 2).

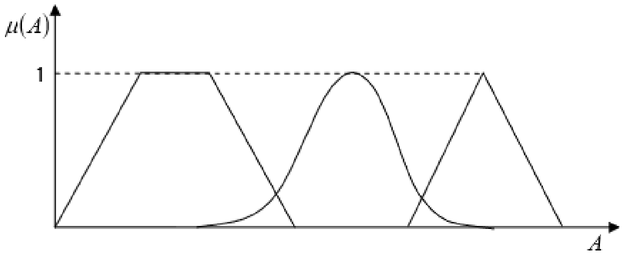

Figure 2. Geometric shapes of membership functions. [18]

Fuzzy Logic Controller consists of fuzzification, rule evaluation and defuzzification steps. First in the fuzzification part, membership functions are defined for the input variables. In the second part, rule table is created along the decision of the relationship between input and output variables. And final part is the fuzzification which the output membership function is converted from fuzzy values to exact values.

The most disadvantage of the LQR controller is that there isn't any clear method for determining the gain coefficients (Q and R) used in the controller. Therefore, in this study, control gain coefficients were determined by fuzzy logic controller. (Figure 3)

In the fuzzy logic controller, first the input and output parameters are determined. Any parameter in the model can be selected as input and output parameters. Rules are written to establish a connection between input and output parameters. These rules can be created by taking reference from previous studies or by trial and error. The trial-and-error method is to obtain the closest desired result according to the simulation results obtained with the membership functions and rules. Membership functions can take different forms. Rules can be created in different ways. These may vary depending on the closeness of the results obtained to the expected results.

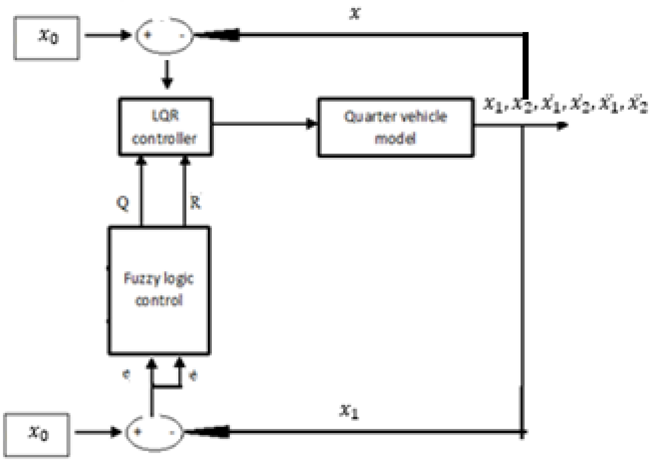

Figure 3. Block diagram of developed control system.

The purpose of the controller is to determine the Q and R gain dynamics in the LQR controller with a fuzzy logic controller. Therefore, system error and its derivative are selected as input. (Figure 4 and Figure 5)

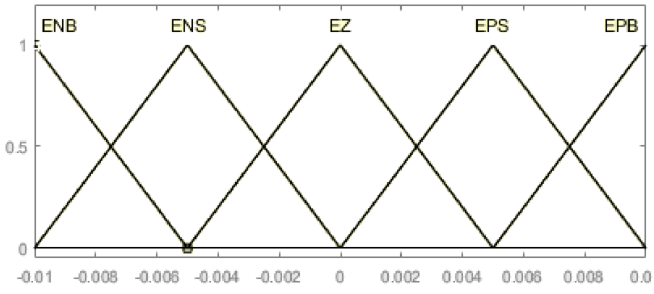

Figure 4. Membership functions of inputs (e).

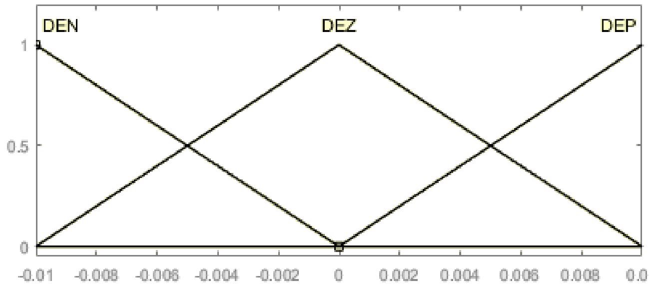

Figure 5. Membership functions of inputs (ė).

In the fuzzy logic controller, the input parameters are determined as the error and its derivative. Error is the difference between the vertical displacement of the vehicle and the road input. Membership functions are determined in a triangular shape between -0.01 and 0.01. Five different membership functions are defined for the error. Also the second input of the fuzzy logic controller is the derivative of the error. Three different membership functions for the derivative of the error are defined. Membership functions are determined in a triangular shape between -0.01 and 0.01.

In this study, the rule table was created by trial and error method. This table can also be created taking into account the literature. But since there isn't any similar study, it was created by trial and error method. (Table 2 and Table 3) The trial and error method proceeds as follows. A random rule was written among the specified inputs. For example, if the error is ENB and the derivative of the error is DEN, the output parameter is selected as QN4. This means that if the error and the time derivative of the error are chosen to be small values, the output Q will also be small. This is directly proportional to the intuition and the knowledge of the expert. The other part of the table was created using this assumption. This rule table was simulated and the results were obtained. Then, a different rule table was created and the results were obtained. The results were obtained by creating this and many similar rule tables, and finally the most desired result was taken into account.

Table 2. Fam table for Q.

e\ ė	DEN	DEZ	DEP
ENB	QN4	QN3	QN2
ENS	QN2	QN2	QN1
EZ	QNZ	QNZ	QNZ
EPS	QP1	QP2	QP2
EPB	QP3	QP3	QP4

Table 3. Fam table for R.

e\ ė	DEN	DEZ	DEP
ENB	RN4	RN3	RN2
ENS	RN2	RN2	RN1
EZ	RNZ	RNZ	RNZ
EPS	RP1	RP2	RP2
EPB	RP3	RP3	RP4

And also output membership functions are shown in Figure 6 and Figure 7.

Figures 6 and 7 show the membership functions of the output parameters Q and R. It is defined as nine triangular membership functions in the range of -1000 and 1000.

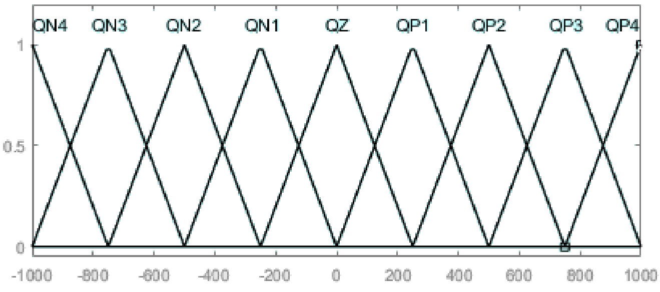

Figure 6. Membership functions of output. (Q)

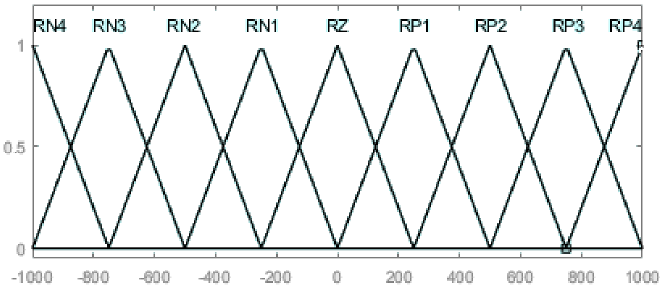

Figure 7. Membership functions of output. (R)

In fuzzy logic control, variables can be defined as anyway. The expression defined as ENB in Figure 4 means E symbolizes error N is negative and B means large. Generally, S (Small), Z (zero), P stands for (positive). The example in Figure 4 is EPS named (Error-Positive-Small). These definitions are completely user's definitions. DE, expressed in Figure 5, represents the derivative of the second input, the error. DEN, DEZ, DEP means derrivative of error small-zero-positive, respectively.

The same is valid for output functions. In Figures 6 and 7, there is a situation where the output membership functions are expressed linguistically. The letter Q at the beginning of the membership functions in Figure 6 represents the Q gain coefficient, and the letter R in Figure 7 represents the R gain coefficient.

In the 2nd and 3rd tables, a relationship has been established between the input and output membership functions. This is called the FAM table. Table 2 is for Q, and Table 3 is for R. For example, if the error (e) is (ENB) in the 2nd table and the derivative of the error ($\dot{\mathbf{e}}$) is DEN, then the gain coefficient Q takes the value of QN4. Or, if the error specified in Table 3 is e (ENS) and the error derivative ($\dot{\mathbf{e}}$) is DEZ, the gain coefficient R takes the value RN2.

3. Results and Dicussion

In order to measure the effectiveness of the developed controller, the proposed controller was applied to the quarter vehicle model and the results were discussed. The most important reason for choosing the quarter vehicle model is that it is possible to make more comfortable comments about the results. The values of the quarter vehicle model are given in Table 1. In Figure 8, the road input is given.

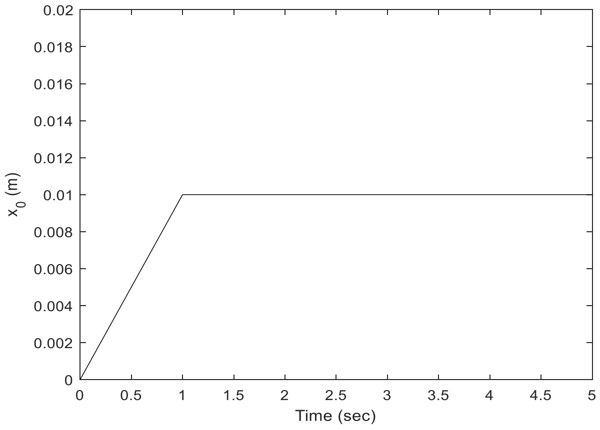

Figure 8. Road input.

The model is simulated for 3 different situations. These are passive Fuzzy Logic controller and LQR-Fuzzy Logic controls. In the fuzzy logic controller, the input membership functions are selected as in Figures 4 and 5. The output function is the controller force. In Figure 9, the displacement of the sprung mass over time is given. With fuzzy logic controller, sprung mass gives better results than passive system. The displacement reaches to the desired position in approximately 2 seconds. And the system oscillates less. LQR-Fuzzy Logic control shows a better result than fuzzy logic controller. With the developed controller, the system reaches the desired position almost without any oscillation.

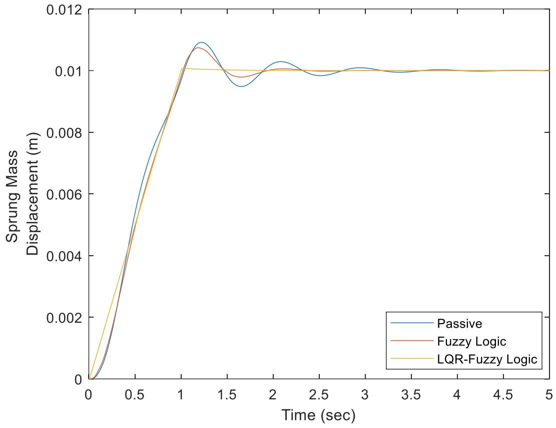

Figure 9. Displacement of the sprung mass over time.

In Figure 10, the displacement error of the sprung mass over time is given. This is the explanatory version of the graph in Figure 9. As can be seen from the figure, the fuzzy logic controller minimized the error faster than the passive system. The error in the developed controller seems to be around 0.1x10^{-3}. This is an indication that a successful result has been achieved.

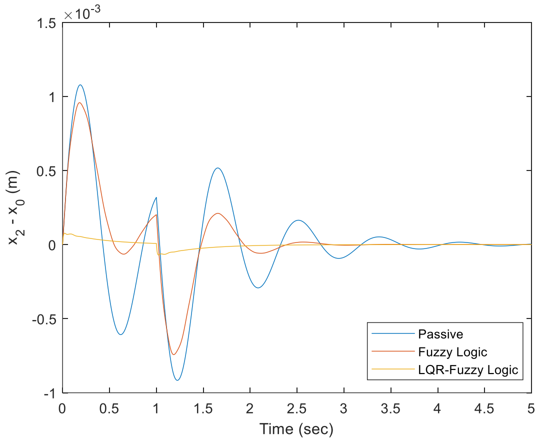

Figure 10. Displacement error of the sprung mass over time.

Figure 11 shows the acceleration of the sprung mass. Acceleration is an important criterion for vehicles, because the more acceleration effect on the vehicle or the later this effect is damped, the more likely it is that the controller has failed. When the figure is examined, it is seen that while the passive system is damped in 4 seconds, the fuzzy logic controller is damped in 2.5 seconds, and the LQR-Fuzzy logic controller is damped in 1.5 seconds. It is understood that while chattering occurs in the fuzzy logic controller, there isn't any chattering in the developed controller and the peak point of the maximum amplitude is 0.02 ms^{-2}.

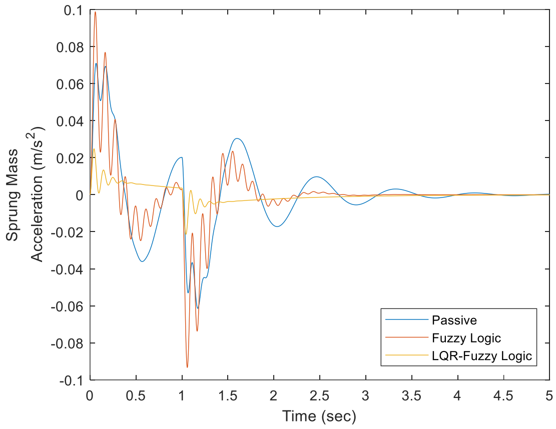

Figure 11. Acceleration of the sprung mass over time.

In Figure 12, tire deflection of the vehicle is given. Tire deflection is an important indicator for road handling. It is seen that the tire deflection is minimized quickly in the developed controller. In passive and fuzzy logic controller, it is understood that the system is minimized later.

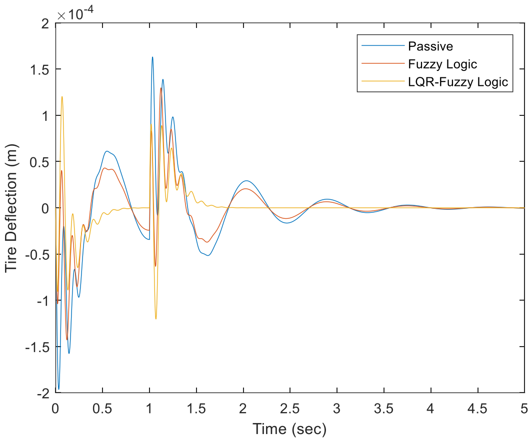

Figure 12. Acceleration of the sprung mass over time.

In the Figure 13 the control forces over time is shown. It is understood that the results are obtained in the expected force range for the quarter vehicle model. It is seen from the figure that the developed controller is more effective with less force.

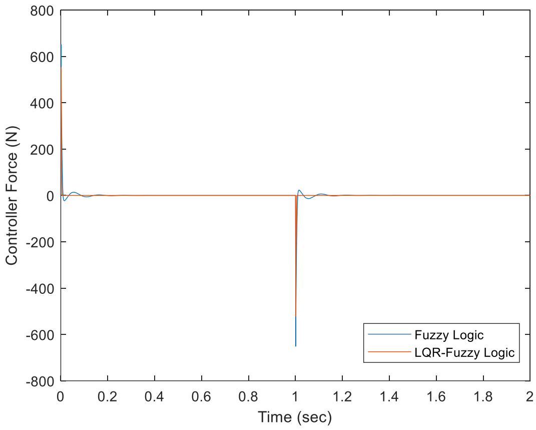

Figure 13. Controller force.

When performing the analytical calculation of frequency analysis, the transfer function of the system is taken into account. In order to find the transfer function of the system, it is necessary to use the equations of the model. Assuming zero initial conditions, The Laplace transform of the system is;

$$(m_1 s^2 + b_2 s + (k_1 + k_2))\, x_1(s) - (b_2 s + k_2)\, x_2(s) = k_1 x_0(s) - u(s) \qquad (14)$$

$$(m_2 s^2 + b_2 s + k_2)\, x_2(s) - (b_2 s + k_2)\, x_1(s) = u(s) \qquad (15)$$

$$\begin{bmatrix} (m_1 s^2 + b_2 s + (k_1 + k_2)) & -(b_2 s + k_2) \\ -(b_2 s + k_2) & (m_2 s^2 + b_2 s + k_2) \end{bmatrix} \begin{bmatrix} x_1 \\ x_2 \end{bmatrix} = \begin{bmatrix} k_1 x_0(s) - u(s) \\ u(s) \end{bmatrix} \qquad (16)$$

$$\Delta = \det \begin{bmatrix} (m_1 s^2 + b_2 s + (k_1 + k_2)) & -(b_2 s + k_2) \\ -(b_2 s + k_2) & (m_2 s^2 + b_2 s + k_2) \end{bmatrix} \qquad (17)$$

From Equation (16) and Equation (17), the transfer function of the system is;

$$G_1(s) = \frac{x_1(s) - x_2(s)}{x_0(s)} = \frac{m_2 k_1 s^2}{\Delta} \qquad (18)$$

$$G_2(s) = \frac{x_1(s) - x_2(s)}{u(s)} = \frac{(m_1 - m_2)s^2 + k_2}{\Delta} \qquad (19)$$

In this direction, when the frequency response of the system is simulated, Figure 14 and Figure 15 are obtained.

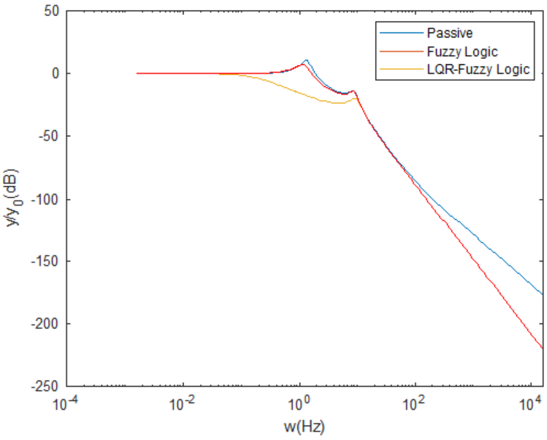

Figure 14. Frequency response of the vertical displacement.

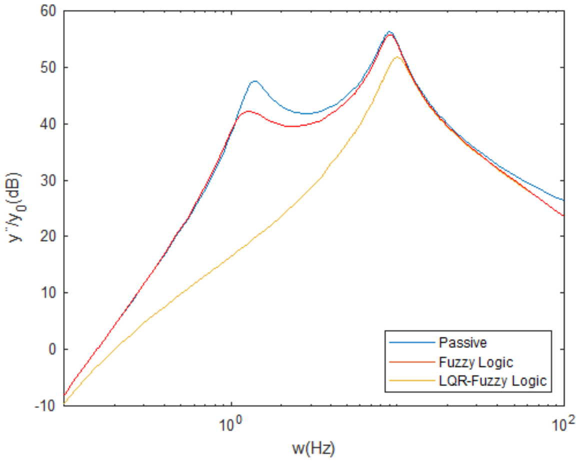

Figure 15. Frequency response of the vertical acceleration.

Figure 14 and Figure 15 show the frequency response of the vertical displacement and acceleration of the vehicle. Frequency response is an important indicator in vehicles in terms of ride comfort. In Figures 14 and 15, the road input was defined as an constant input because frequency is independent of the input parameter. And the systems output is defined as the vertical displacement and vertical acceleration.

The first peak in Figure 14 and Figure 15 shows the frequency response of the vehicle body, and the second peak shows the frequency response of the axle mass. The resonance of the first mass, namely the sprung mass, is around 1 hertz, and the resonance occurs around 10 Hertz, indicate the resonance of the unsprung mass. These frequency values are safe for the proper operation of the vehicle. It is important in terms of ride comfort that the first resonance is suppressed, and the second resonance not increased too much. This indicates that the controller works properly. The frequency responses of the passive system and the fuzzy logic controller system were close to each other. It seems that the fuzzy logic controller has a slight effect on the frequency response. It is understood from Figures 14 and Figure 15 that the developed controller is effective in damping both the body displacement frequency and the peak in the frequency response of acceleration.

4. Conclusions

The most important aim of this study is to design a new hybrid controller using two different controllers. For this, studies in the literature were examined and the most common used controllers in mechanical system design were selected. These are LQR controller and fuzzy logic controller. In the study, the two control gain coefficients Q and R used in the LQR control rule were determined with a fuzzy logic controller. There are different perspectives in the literature on determining the Q and R numbers in the LQR controller. The distinguishing feature of this study comes into play here. With the popularity of artificial intelligence in recent years, fuzzy logic control method has become one of the most used systems. The success of the fuzzy logic controller has been guaranteed by the studies. In this study, the LQR gain coefficients were determined by fuzzy logic control method. In order to determine the efficiency of the developed controller, a quarter vehicle model was selected. When the simulation results are examined, it is understood that an effective controller has been developed. The most important point in the developed controller in this study is the vertical displacement and acceleration of the vehicle. The vehicles displacement reaches to the desired position in approximately 2 seconds in Fuzzy logic controller, however, it is seen that the Lqr-Fuzzy logic controller reaches a steady state immediately. And the system oscillates less in LQR-Fuzzy Logic controller. And the other important point in the study is the acceleration of the sprung mass. When the figure is examined, it is understood that the passive system is damped in 4 seconds, the fuzzy logic controller is damped in 2.5 seconds, and the LQR-Fuzzy logic controller is damped in 1.5 seconds. And It is seen that while chattering occurs in the fuzzy logic controller, there isn't any chattering in the developed controller and the peak point of the maximum amplitude is 0.02 ms^{-2}.

It has been a good reference work for future studies. And in future studies, the effectiveness of the developed controller in this study can be supported by experimental studies. The performance of hybrid controllers developed with different controllers or in different models can be supported by different studies.

Ethics committee approval and conflict of interest statement

This article does not require ethics committee approval. This article has no conflicts of interest with any individual or institution.

References

[1] Devdutt, M. L. 2014. Fuzzy Logic Control of a Semi-Active Quarter Car System. Int. J. Mech. Ind. Sci. Eng, Vol. 8, p. 163-167, DOI: 10.5281/zenodo.1337025

[2] Palanisamy, S., Karuppan, S. 2016. Fuzzy Control of Active Suspension System. Journal of Vibroengineering, Vol. 18 (5), p. 3197-3204. DOI: 10.21595/jve.2016.16699

[3] Bhangal, N. S., Raj, K. A. 2016. Fuzzy Control of Vehicle Active Suspension System. International Journal of Mechanical Engineering and Robotics Research, Vol. 5, p. 144. DOI: 10.18178/ijmerr.5.2.144-148

[4] El Majdoub, K., Ouadi, H., Touati, A. 2014. LQR Control for Semi-Active Quarter Vehicle Suspension with Magnetorheological Damper and Bouc-Wen Model. Int. Rev. Modell. Simulat. IREMOS, Vol. 7(4), p. 703-711.

[5] Rao, K. D., Kumar, S. 2015. Modeling and Simulation of Quarter Car Semi Active Suspension System Using LQR Controller. Proceedings of the 3rd International Conference on Frontiers of Intelligent Computing: Theory and Applications (FICTA), Vol. 1 p. 441-448. DOI:10.1007/978-3-319-11933-5_48

[6] Nagarkar, M. P., Bhalerao, Y. J., Patil, G. J. V., Patil, R. N. Z. 2018. Multi-Objective Optimization of Nonlinear Quarter Car Suspension System–PID and LQR Control, Procedia Manufacturing. Vol. 20, p. 420-427. DOI:10.1016/j.promfg.2018.02.061

[7] Gokul. P. S. Malar. M. K. 2019. A Contemporary Adaptive Air Suspension Using LQR Control for Passenger Vehicles, ISA Transactions, Vol. 93, p. 244-254. DOI:10.1016/j.isatra.2019.02.031

[8] Uddin, N. 2019. Optimal Control Design of Active Suspension System Based on Quarter Car Model. Jurnal Infotel, Vol. 11, p. 55-61. DOI:10.1007/s40430-020-02552-7

[9] Kaleemullah, M., Faris, W, F., Hasbullah, F., 2011. Design of Robust H∞, Fuzzy and LQR Controller for Active Suspension of a Quarter Car Model. 4th International Conference on Mechatronics (ICOM). IEEE, 17-19 May, Kuala Lumpur, 1-6

[10] Wei, X., Li, J. Liu, X. 2013. LQR Control Scheme for Active Vehicle Suspension Systems Based on Modal Decomposition. 25th Chinese Control and Decision Conference (CCDC), 25-27 May, Guiyang, China, 3296-3301

[11] Bharali, J., Buragohain, M. 2016. A Comparative Analysis of PID, LQR and Fuzzy Logic Controller for Active Suspension System Using 3 Degree of Freedom Quarter Car Model. 2016 IEEE 1st International Conference on Power Electronics, Intelligent Control and Energy Systems (ICPEICES). IEEE, 4-6 July, Delhi, India, 1-5

[12] Divekar. A. A. Mahajan, B. D. 2016. Response Optimization and Lqr Based Control for Quarter Car Suspension with Seat-Driver Model. 2016 International Conference on Automatic Control and Dynamic Optimization Techniques (ICACDOT). 9-10 September, Pune, India, 1007-1012

[13] Anh, N. T. 2020. Control an Active Suspension System by Using PID and LQR Controller. International Journal of Mechanical and Production Engineering Research and Development Vol. 10, p. 7003-7012. DOI:10.24247/ijmperdjun2020662

[14] Taskın, Y., Hacıoğlu Y, 2006, Vibration Suppression ofa Vehicle with Fuzzy Sliding Modes, Proceedings of 5th lnternational Symposiurn on Intelligent Manufacturing, 29-31 May, Sakarya, 1132-1140.

[15] Yaren, T. Kizir, S. 2019. LQR Kontrolcü Parametrelerinin Sistem Davranışına Etki Analizi: Çift Çubuklu Ters Sarkaç Sistemi. Konya Mühendislik Bilimleri Dergisi, Vol. 8, p. 175-191. DOI:10.36306/konjes.586958

[16] Zhang, J. Zhang W. 2012. LQR Self-Adjusting Based Control for the Planar Double Inverted Pendulum. International Conference on Applied Physics and Industrial Engineering, Vol. 24, p. 1669 – 1676. DOI:10.1016/j.phpro.2012.02.246

[17] Zadeh, L. A. 1965, Fuzzy sets. Information and Control, Vol. 8, pp. 338-353.

[18] Hacıoğlu, Y. 2004. Bir robotun bulanık mantıklı kayan kipli kontrolü, Yüksek lisans tezi, Makine Mühendisliği, Fen Bilimleri Enstitüsü, İstanbul Üniversitesi, İstanbul, Türkiye.

Dokuz Eylül Üniversitesi Mühendislik Fakültesi Fen ve Mühendislik Dergisi
Dokuz Eylul University Faculty of Engineering Journal of Science and Engineering
Elektronik/Online ISSN: 2547-958X

ARAŞTIRMA MAKALESI / RESEARCH ARTICLE

Tungsten Uzun Çubuk Tipi Penetratörlerin Zırh Çelikleri Üzerindeki Delme Etkinliğinin Penetrasyon Modeller ile İncelenmesi

Depth of Penetration Behaviour Analysis of Tungsten Long-Rod Penetrator Impacting on Armour Steel by Penetration Models

Ahmet Kaan Toksoy

Balistik Koruma Sistemleri Direktörlüğü, Roketsan A. Ş., Ankara, TÜRKİYE
Sorumlu Yazar / Corresponding Author: ktoksoy@roketsan.com.tr

Öz

Uzun çubuk tipi Tungsten penetratörlerin RHA (haddelenmiş homojen) zırh çelikleri üzerine yüksek hız ile çarpması esnasında oluşturduğu penetrasyon zırh sistemlerinin zafiyet analizleri ve balistik verimlerinin belirlenmesi için çok önemlidir. Çalışma kapsamında farklı boy/çap oranlarına (L/D) sahip Tungsten uzun çubuk penetratörlerin yarı sonlu RHA zırh çelikleri üzerinde 665-3500m/s çarpma hızı aralığındaki penetrasyonunu ampirik ve analitik modeller kullanılarak hesaplanmıştır. Bu hesaplamaların yapılabilmesi için Python kodlama dilinde program yazılarak malzeme bilgileri, çarpma hızı ve geometrik özellikleri girdi olarak kullanılmış delme derinliği çıktı olarak elde edilmiştir. Gerçekleştirilen hesaplama sonuçları 150 adet farklı veri noktasını içeren test sonuçları ile karşılaştırılmıştır. Karşılaştırma çalışmaları kapsamında ampirik ve analitik modellerin hesaplama hataları belirlenmiştir. Özellikle ampirik denklemlerin geçerli olduğu L/D değeri için hata oranın düşük olduğu fakat geniş L/D aralığı (10-30) için %9 hata değerine sahip olduğu belirlenmiştir. Bunun yanında Aleksiveeski-Tate modelinin L/D oranı artıkça hata oranının artığı, Walker-Anderson penetrasyon modelinin ise hem tüm L/D değerleri için deney sonuçlarına en yakın değerlerini verdiği hem de L/D değerleri artmasına rağmen hata oranın artmadığı belirlenmiştir.

Anahtar Kelimeler: *Uzun çubuk tipi tungsten penetratör, Yüksek hız penetrasyonu, RHA Zırh Çeliği, Penetrasyon mekaniği*

Abstract

The penetration behavior of Tungsten long rod penetrators on RHA (Rolled-homogenous Armor) steels is very important for vulnerability analysis and ballistic efficiency determination of armor systems. Within the scope of the study, the penetration of Tungsten long rod penetrators with different length to diameter ratios (L/D) on semi-infinite RHA armor steels with various impact velocities between 665-3500 m/s was calculated by using empirical and analytical models. In order to make these calculations, a program was written in Python coding language. Material properties, impact velocity and geometric properties were used as inputs while the penetration depth was obtained as an output. Calculated penetration values were compared with test results for 150 different data points. Also, calculation errors between experimental and empirical/analytical models were determined. It has been found that the error rate was low, especially for the lower L/D values where empirical equations are valid, but for empirical equation which is valid for greater L/D range (10-30) only 9% error rate was achieved. In addition, it was determined that the error rate of the Aleksiveeskii-Tate penetration model increased as the L/D ratio increased, while the Walker-Anderson penetration model gave the closest values to the experimental results for each L/D value and the error rate did not increase even though the L/D values increased.

Keywords: *Tungsten long-rod penetration, High Velocity Impact, RHA Steel, Penetration Mechanics*

EXTENDED ABSTRACT

Introduction

Vulnerability analysis of armored vehicle plays a vital role for modern days land platforms. One of the effective threats on the armored vehicles is long rod penetrators made from heavy metal alloys such as Tungsten or Depleted Uranium. Target effects of these type of threats are widely studied. Studied targets are in wide spectrum from mono-structures such as finite or semi-infinite armour steels, ceramics or multi-layered armour structures to optimize for protection or handling V50 ballistic velocity. Depth of penetration on semi-infinite target, especially on RHA steel, values are required for both ballistic efficiency determination and armor structures vulnerability decisions. Characterization of penetration capability of Long-rod penetrators has been studied based on its geometrical properties such as length to diameter ratio, tip structures. Also, different materials used for DOP characterization of long-rod penetrators on RHA steels. Several empirical equations developed for penetration estimation of penetrators with different L/D ratios. However, each empirical equation is limited with defined velocity range, specific L/D and needs extended data points for constructing them. Analytical penetration models were employed for calculation of penetration behavior of long rod penetrators on both semi-infinite and multi-layered targets.

DOI: https://doi.org/10.21205/deufmd.2025277904

Geliş Tarihi / Received: 23.01.2024
Kabul Tarihi / Accepted: 20.03.2024

Penetration models require material properties such as dynamic yield strength, target resistance stress etc.

Within the scope of the study, the penetration of Tungsten long rod penetrators with different diameter-to-length ratios (L/D) on semi-infinite RHA armor steels with various impact velocities between 665-3500 m/s was calculated using empirical and analytical models. In order to make these calculations, a program was written in Python coding language. Material properties, impact velocity and geometric properties were used as inputs, and penetration depth was obtained as an output. Calculated penetration values were compared with test results for 150 different data points. Also, calculation errors between experimental and empirical/analytical models were determined.

Materials and Methods

Depth of penetration results of Tungsten long-rod impact on semi-infinite RHA steel has been found on literature survey. Related L/D ratios and impact velocity range is summarized in Table 1. Experimental results are collected for long rod penetrators with calibers in between 25mm and 140mm and also specially designed penetrators and sabot package for gas gun launched Figure 1. Totally 150 depth of penetration values for six different L/D has been found and used for this study.

Moreover, empiric equation in literature and newly defined in this study for different L/D ratios of the long rod penetrator was used to calculate of depth of penetration values of Tungsten penetrators impacting RHA steel targets, Equations 1-7 and 12-13. Analytical penetration models Aleksiveeskii-Tate and Walker-Anderson has been explained with details of assumption and material properties of Tungsten and RHA steels in Table 2. Models were also used to estimate the depth of penetration for the comparison with experimental results.

Results and Discussion

Proposed equation by Silsby et. al. [37], Eqn 4, predicts DOP values lower than the experimental results of L/D=10 tungsten long-rod penetrators, Figure 2 (a). On the other hand, Eqn 1 defined by Anderson et al. estimated better DOP values for L/D=10 penetrators. It was observed that both empiric equations, Eqn. 2 and 4, overestimated test results of L/D=15 long rod Tungsten penetrator impact on RHA steel target. Prediction of Eqn. 12 was well aligned with experimental results, Figure 2 (b). It is obvious that there is no DOP data between 1900-2800 m/s impacting velocity for L/D=15 penetrators which decreases estimation capability of empiric equations. Similar results were found for L/D=20 projectile penetration behavior, Figure 2(c). Generally, Eqn. 4 has averagely good estimation tool for penetrator that have L/D ratio over 20, Figure 2(d).

Lanz-Odermatt also proposed an empiric approach for tungsten long rod penetration on RHA steel targets, Eqn 4. Original study only includes calibers between 25 and 140mm of long rod projectiles. In this study, new data points were added to original data set and capability of DOP prediction was checked, Figure 3. Former prediction capability of Lanz-Odermatt equations was calculated as %5 error rate [17]. However, percentage between predicted DOP values over experimental results exceeded 14% especially for L/D=10 projectile penetrator. It is concluded Lanz-Odermatt equation cannot satisfy on estimation of DOP values of L/D values of this study.

Codes created by using Python programming language was used for DOP calculation of both Aleksiveeskii-Tate and Walker-Anderson penetration model for long-rod projectile. Experimental results and calculations were compared, Figure 4. Aleksiveeskii-Tate penetration model predicts L/D=10 tungsten long-rod DOP values higher than experimental results up to 1000m/s impact velocity. A-T model showed good correlation with experimental results when the impact velocities in between 1000 and 2000m/s. However, above the 2000m/s A-T model predicts DOP values lower than experimental results for all L/D range, Figure 4. Unlike Anderson-Tate penetration model, Walker Anderson penetration model predicts DOP results of tungsten long rod projectile impacting on RHA steel targets for all L/D ratios.

DOP Prediction error analysis was made for both empiric and analytic penetration models suggested for prediction of depth of penetration, Table 3. Except for Lanz-Odermatt equation, empiric equations proposed at previous studies for L/D=10 and 20 gave acceptable level of prediction error as 5%. However, this situation found different for proposed equation for L/D=15 long rod penetrator, Eqn 2, which resulted with 14% prediction error. New empiric equations, Eqn 12 and 13, for L/D=15 and L/D=20 values was resulted with less error than previous prediction models. Eqn 4 defined by Silsby et al [37] has been estimated prediction DOP value with 8% error ratio in their study. But adding a new data set for DOP values resulted with slight increasing of error rate as %9. Aleksiveeskii-Tate model generally resulted with higher error rate between 5% and 13.7% which were higher than empiric equations results. However, Walker-Anderson model prediction resulted with maximum 3.3%.

Conclusion

150 different DOP results of Tungsten long rod penetrators impacting on RHA steel targets from various impact conditions such as L/D, impact velocities collected and used for comparison purposes. Empiric and analytic penetration models were also used for calculation DOP values of experimental data points. Especially, time iterative computer codes have been established for analytical penetration models. Lanz-Odermatt empiric equations have good estimation capacity only for the long-rod penetrators defined at their study, which are in between 25-140mm calibers. However, new data DOP results could not be estimated with good approximation. It was found that empirical equations defined for specified L/D ratios of long-rod penetrators resulted with acceptable estimation of DOP values in their boundaries. In this limitation, calculated DOP results gave good approximation when results compared to Aleksiveeskii-Tate analytical penetration model. Error ratio increased with higher L/D ratio in Aleksiveeskii-Tate model. On the contrary, Walker-Anderson penetration model gave the best estimation of DOP value at RHA steels in terms of error between experimental and calculation results.

1. Giriş

Günümüzün muharebe araçları gerek mürettebatını gerek üzerinde taşıdıkları geniş spekturumdaki sensör ve silah sistemleri gibi kritik alt sistemlerinin düşman ateşinden korunması amacı ile özel olarak tasarlanmaktadırlar. Bu amaçla zırh sistemlerinde kullanılan çok farklı malzemelerinin ilgili tehditlere karşı delme analizleri araçların zayıf bölgelerinin ortadan kaldırılması ve zafiyet analizlerinin yapılabilmesi için yaygın olarak yapılmaktadır.

Zafiyet analizlerinin hızlı bir şekilde yapılabilmesi için tehditlerin hedefler üzerinde delme derinliklerinin belirlenmesi büyük öneme sahiptir. Penetrasyon davranışının belirlenmesi amacı ile gerek tehditlerin gerekse hedeflerin geometrik ve malzeme özellikleri araştırılmaktadır [1-2]. Çalışmalar teknolojinin gelişmesi ile beraber monolitik yapılardan çok katmanlı zırh yapılarına doğru gelişmiştir [3]. Bunun yanında penetratör teknolojinde ciddi değişiklikler meydana gelmiştir. Zırh delici sabotlu tehditler (APDS) yerine uzun çubuk tipi sabotlu kanat stabilizeli (APDSFS) tehditler yaygın şekilde zırh sistemlerine karşı kullanılır hale gelmişleridir. Bu tehditler 25mm kalibreden başlayarak 140 mm kalibreye kadar değişiklik göstermektedirler, [4-6].

Zırh delici uzun çubuk tipi penetratörlerde başlangıçta çelik alaşımları kinetik enerjili delicilerin ana malzemesi olarak kullanılırken, toz metalürjisi tekniklerinin gelişmesi ile birlikte yüksek yoğunluğa sahip Tungsten alaşımları veya seyreltilmiş Uranyum gibi malzemeler penetrasyon derinliğinin arttırılması amacı ile tercih edilmişlerdir. Özellikle yüksek yoğunluğa sahip Tungsten vb. alaşımlar 1960 yılından günümüze kadar uzun çubuk tipi penetratörler için yaygın olarak kullanılmaktadır [4,7].

Uzun çubuk tipi penetratörlerin kalibrelerine bağlı olarak boy/çap (L/D) oranları 10-30 değerleri arasında değişiklik göstermektedir. Benzer şekilde hedef vuruş açısının (Obliquity) veya penetratörün atış hattı ile yaptığı açısının (Yaw) değişimi ile yarı sonlu hedeflerin üzerindeki delme derinliklerinin değişimi incelenmiştir [8, 9]. Bu incelemeler ile penetratörlerin malzeme özellikleri kadar geometrik özelliklerinin veya tehdit hedef ilişkisinin penetrasyon üzerindeki etkileri belirlenmiştir.

Bunun yanında uzun çubuk tipi penetratörlerin uç kısımlarının geometrik özelliklerinin delme üzerindeki etkileri de araştırılmıştır [10, 11]. Farklı uç geometrik tasarımlarının özellikle açılı vuruşlarda delme davranışına olan etkileri çalışılmıştır.

Uzun çubuk tipi penetratörlerin yarı sonlu hedefler üzerinde ki delme derinliklerinin sayısal olarak tahmin edilmesi için birçok araştırmacı tarafından ampirik denklemler geliştirilmiştir. Bu ampirik denklemler hesaplama süresi açısından çok hızlı olmak ile beraber elde edilen sonuçların doğruluğu deneysel veri grubunda tanımlanan çarpma hızı, L/D oranı ve hedef malzemesine bağlı kaldığı gözlemlenmiştir [12-14].

Bunlara paralel olarak zamana bağlı analitik çözümleme modelleri ise yarı sonlu hedefler üzerinde uzun çubuk tipi penetratörlerin delme derinliklerinin belirlenmesi için oluşturulmuşlardır [15-17]. Analitik penetrasyon modelleri ampirik tahminleme yöntemlerine göre kompleks matematiksel yöntemleri kullanmalarına rağmen farklı tip penetratörler ve hedef malzemeleri üzerinde elde edilen delme derinliklerinin tahminlenmesinde de kullanılabilmektedirler. Yarı sonlu üzerindeki delme derinliklerinin belirlenmesi zırh sistemlerinin geliştirilmesi açısından çok önemlidir. Bu değerler katmanlı zırh sistemlerinin balistik verimlerinin hesaplanmasında ve zafiyet analizlerine girdi olarak kullanılmaktadır [18-21]. Zafiyet analizlerinde katmanlı zırhın geometrik pozisyonuna bağlı olarak uzun çubuk tipi penetratöre karşı zırhın balistik verimi belirlenerek, zırhın ilgili pozisyonunda delinmenin gerçekleştiğine ya da gerçekleşmediğine sayısal olarak karar verilmesini sağlanmaktadır [3, 22].

Bu çalışma kapsamında farklı çalışmalardan elde edilen uzun çubuk tipi penetratörlerin yarı sonlu hedefler üzerindeki deneysel delme derinlikleri toplanarak karşılaştırma çalışmaları için veri grubu oluşturulmuştur. Çalışmada uzun çubuk tipi penetratörün, boy ve çap oranı bilgisi, yarı sonlu hedefe çarpma hızı ve geometrisi analiz kapsamında hesaplamalar için girdi olarak kullanılmıştır. Uzun çubuk tipi penetratörün malzemesi Tungsten, yarı sonlu hedef malzemenin ise haddelenmiş homojen zırh çeliği (RHA, Rolled Homogeneous Armor Steel) olarak alınmıştır. Veri grubu içerisindeki farklı boy ve çap oranlarına sahip penetratörlerin yarı sonlu hedeflerdeki delme derinlikleri etkinlikleri ampirik ve analitik penetrasyon modelleri ile hesaplanmıştır. Analitik modeller için gerekli hesaplamaların yapılması için zamana bağlı hesaplama yapabilen kod yazılıp her bir veri noktası için çalıştırılarak delme derinlikleri belirlenmiştir. Bu hesaplamalar sonunda ampirik ve analitik penetraston modelleri ile elde edilen delme derinliği sonuçları deneysel veriler ile karşılaştırılmıştır.

2. Materyal ve Metot

2.1. Deneysel Veriler

Analizlerin yapılması amacı ile farklı çap ve boylardaki Tungsten malzemeden üretilmiş uzun çubuk tipi penetratörlerin yarı sonlu RHA hedefler üzerinde gerçekleştirilen çarpışma testleri sonrası elde edilen delme derinleri farklı çalışmalardan toplanmıştır. Bu penetratörler konvansiyonel silah sistemlerinden atılabilen farklı kalibrede üretilen tehditler olduğu gibi gazlı fırlatma sistemlerinden fırlatılmak üzere geliştirilmiş sabotlarla fırlatılan Tungsten malzemelerden üretilmiş penetratörlerdir, Şekil 1. Tehdit L/D oranları, çarpma hızları ve alındıkları kaynak bilgileri Tablo 1'de verilmiştir. Çalışma kapsamında toplamda 150 farklı deney sonucu kullanılmıştır.

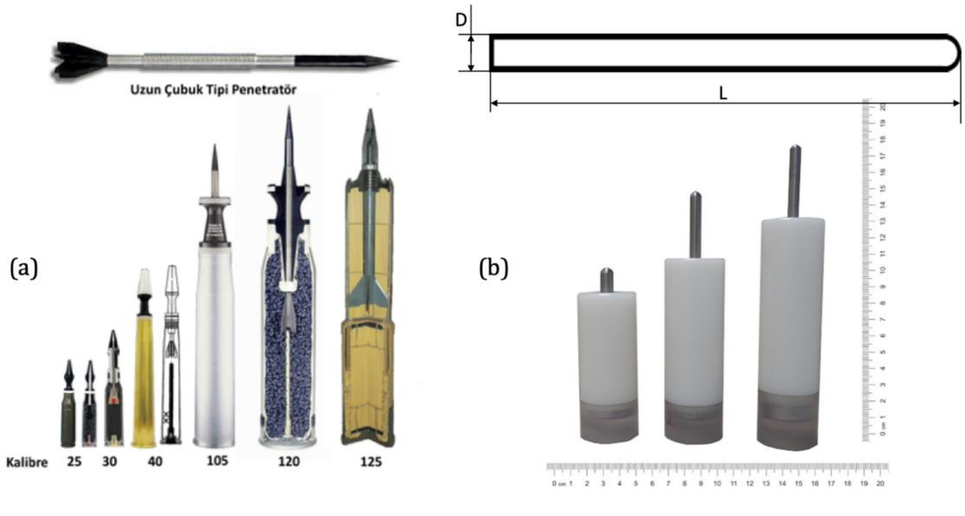

Şekil 1. a) Farklı kalibredeki uzun çubuk tipi penetratörler b) gazlı fırlatma sistemlerinden hedef üzerine atılan uzun çubuk tipi penetratörler.

Figure 1. a) Long rod peneterators with different caliber, b) long rod penetrator and its sabot for gas launching system against target.

Tablo 1. Uzun çubuk tipi penetratörlerin L/D ratio, Çarpma hızı ve veri kaynakları.

Table 1. Information about long rod penetrator L/D ratio , Impact Velocity and data source.

L/D	Çarpma Hız Aralığı (m/s)	Veri Kaynağı	Test Adeti
10	863-1756	[23-28]	54
12	665-1535	[23]	18
14	984-1358	[18], [29]	11
15	1240-2990	[30-32]	21
20	1278-3020	[31,33-36]	34
30	1094-3500	[27,31, 37]	12

2.2. Ampirik Denklemler

Yarı sonlu RHA hedefler üzerinde gerçekleştirilen testler sonucunda elde edilen veriler, penetratörün L/D oranına spesifik olarak hedef üzerindeki penetrasyon ve çarpma hızı arasındaki en uygun ampirik bağıntıyı kurmak üzere kullanılmıştır. Elde edilen ampirik denklemler lineer ilişki içerisinde olduğu gibi hiperbolik veya eksponansiyel olacak şekilde de ifade edilmiştir.

L/D =10 olan Tungsten uzun çubuk penetratörün yarı sonlu RHA çelik hedefler üzerindeki penetrasyon derinliği tahminlenmesi için Woosley ve arkadaşları tarafından oluşturulan ampirik denklem aşağıdaki şekilde verilmiştir [34-35];

$$\frac{P}{L} = 1.06V - 0.712 \tag{1}$$

L/D =15 olan Tungsten uzun çubuk penetratör için; Anderson ve arkadaşları tarafından oluşturulan ampirik denklem aşağıdaki şekilde verilmiştir [13] ;

$$\frac{P}{L} = 0{,}997V - 0.682 \tag{2}$$

Benzer şekilde L/D=20 olan Tungsten uzun çubuk penetratörlerin RHA üzerindeki penetrasyonu için oluşturulan ampirik denklem aşağıdaki denklem verilmiştir [14].

$$\frac{P}{L} = \frac{1.606 \times V^{4.273}}{1.542^{4.273} + V^{4.273}} \tag{3}$$

Silsby ve arkadaşları daha geniş L/D (10-30) aralığı için Tungsten uzun çubuk penetratörün RHA çelik üzerindeki penetrasyon derinliği ve delici boyu ilişkisi için toplamda 100 farklı veri noktası kullanarak aşağıdaki denklemi oluşturmuşlardır, [37].

$$\frac{P}{L} = (1{,}239 + 0{,}00875V)/\left(1 + 117e^{(-3{,}5V)}\right) \tag{4}$$

Denklem 1-3 için geçerli vuruş hız aralığı 800 ve 1750m/s olurken, Denklem 4 için geçerli hız aralığı ise 600 ile 4500m/s arasındadır.

2.2.1.Lanz-Odermatt Ampirik Denklemi

Lanz-Odermatt ampirik denklemi aşağıda verilmiştir [17];

$$\frac{d}{D} = a(L/D)(cos\theta)^m \sqrt{\frac{\rho_p}{\rho_t}} e^{-\frac{c\,R_m}{\rho_p V_i^2}} \tag{5}$$

Bu denklemde L, penetratör uzunluğunu, D ise çapını ifade etmektedir. ⍰ penetratörün hedefe vuruş açısını, $⍰_p$ ve $⍰_t$ penetratör ve hedef malzeme yoğunluklarını, R_m hedef malzemesi çekme mukavemetini, V_i ise penetratörün hedefe vuruş hızını ifade etmektedir. Başlangıçta 105-140mm kalibre APFSDS (Armor-Piercing Fin-Stabilized Discharging Sabot) tipi uzun çubuk tipi penetratörlerden elde edilen veriler kullanılırken, veri kütüphanesi 25-35mm kalibre uzun çubuk tipi penetratörleri de içerecek şeklide genişletilmiştir [45]. Denklem içinde yer alan a sabiti ise aşağıdaki denklem üzerinden hesaplanmaktadır.

$$a\frac{L}{D} = (L/D) + 3.94\left(1 - tanh\frac{L/D-10}{11{,}2}\right) \tag{6}$$

m ve c değerleri Lanz ve Odermatt'ın orijinal çalışmasında 0.745 ve 25.9 gibi sabit değerler iken daha sonra Jeanqartier ve Odermatt [45] tarafından yapılan çalışmada m sabitinin değeri 0.775 olarak belirlenmiş, c sabiti ise aşağıdaki gibi ifade edilmiştir.

$$c = 22.1 + 1.274e^{-8}R_m - 9.47e^{-18}R_m^2 \tag{7}$$

Lanz-Odermatt ampirik denkleminde delici ve hedef malzemesi Tungsten ve RHA zırh çeliği olarak belirlenmiştir. Denklemde kullanılan deneysel veri için L/D aralığı 11-31 değerleri arasında vuruş hızı ise 1100-1900m/s arasında değişmektedir.

Lanz-Odermatt denklemi diğer ampirik denklemlerden hedef malzemenin çekme mukavemetinin ve vuruş açısının denklem içerisinde yer alması nedeni ile farklıdır. Denklem farklı L/D değerleri ve vuruş açılarında gerçekleştirilmiş yarı sonlu çelik malzemelerden elde edilmiş 41 farklı test sonucuna bağlı olarak çıkarılmıştır. Günümüzde yaygın olarak zafiyet analizlerinde kullanılmaktadır [46].

2.3. Aleksveeskii-Tate Penetrasyon Modeli

İki farklı araştırmacı, Aleksiveeskii ve Tate birbirinden habersiz aynı konu üzerinde ve birbirlerine yakın zamanlarda çalışarak uzun çubuk tipi delicilerin yarı sonlu hedefler üzerindeki delme derinliklerini hesaplayan analitik yöntemi geliştirmişlerdir, [15, 16]. Her iki araştırmacı Bernoulli denklemini tek boyutlu penetrasyon davranışını çözmek amacı ile modifiye ederek aşağıdaki şekilde ifade edilmiştir;

$$\frac{1}{2}\rho_p(v-u)^2 + Y_p = \frac{1}{2}\rho_t u^2 + R_t \tag{8}$$

Burada ⍰ delici arka kısmındaki hız, ⍰ hedef içerisindeki penetrasyon hızını, Yp penetrator mukavemetini, Rt ise hedef direncini ifade etmektedir. Yp ve Rt değerleri malzemeye bağlı olarak değişiklik göstermektedir. Yp değeri malzemenin Huguniot Elastik Limit (HEL) ile aynı değerde olduğu belirtilmiştir [15, 47]. HEL değeri ise aşağıdaki şekilde hesaplanmaktadır [41].

$$HEL = Y\,(1-\lambda)/(1-2\lambda) \tag{9}$$

Y malzemenin çekme mukavemeti, λ ise poisson oranıdır. Rt değeri ise malzemenin dinamik çekme mukavemetinin 4 ile 5 katı arasında değişiklik göstermektedir [16]. Penetratör ve hedef yapı malzemeleri olan Tungsten ve RHA için kullanılan Yp ve Rt değerleri Tablo 2'de verilmektedir. Tablo 2'den görüleceği üzere Tungsten ve RHA malzeme için farklı Yp ve Rt değerleri belirli bir aralık içinde değişiklik göstermektedir. Bunun sebebi ise Tungsten ve RHA için kullanılan test numunelerinin üretildiği ana malzeme bloklarının farklı alaşımlardan elde edilmesidir. Örnek olarak penetratör malzemesinin ağırlıkça %91-%93 Tungsten'den veya hedef zırh çeliklerinin ilgili MIL-DTL-12560K [48] standartında belirtilen birçok farklı sınıflardan elde edilmesi olarak verilebilir.

Tablo 2. Tungsten ve RHA malzemeler için Yp ve Rt değerleri.

Table 2. Yp and Rt values for Tungsten and RHA materials.

Penetratör / Hedef Malzeme	Yp (GPa)	Rt (GPa)	Veri Kaynağı
Tungsten	0.8		[38]
	1		[39]
	1,66		[40]
	2		[41]
	1.14		[42-43]
RHA		5,1-5.5	[39]
		4.94	[44]
		4,37	[42]

2.4. Walker-Anderson Penetrasyon Modeli

Walker ve Anderson momentum denklemini belirli kabuller yaparak geliştirmişlerdir [49]. Öncelikle penetratör ve hedef eksenel simetrik olarak tanımlanmıştır. Penetratör ile hedef ara yüzeyinin penetrasyon ile beraber değişimi zamana bağlı olarak, $Z_i(t)$ şeklinde ifade edilmiştir. Penetratörün arka ucunun konumu ise $Z_p(t)$ olarak tanımlanmıştır. Başlangıç zamanında $Z_i(0)=0$ ve $Z_p(0)=-L_0$ olarak kabul edilmiştir, L_0 penetratörün başlangıç uzunluğudur. Araştırmacılar penetratör ve yarı sonlu hedefler üzerinde gerçekleştirdikleri analizleri inceleyerek penetrasyonun analitik olarak modellenmesine yönelik aşağıdaki kabulleri yapmışlardır.

1. Hız profili merkez çizgisi üzerinde hem penetratör hem de hedef için tanımlanmıştır.
2. Penetratörün arka ucu delici içerisinde hareket eden elastik dalga hareketi nedeni ile yavaşlamaktadır. Elastik dalgalar penetratörün arka ucundan geri dönmekte ve penetratör içerisinde oluşan elastik-plastik deformasyon ara kesitinden tekrar geri yansımaktadır.
3. Hedef malzemenin kayma mukavemeti davranışı delinme analizinin yapılabilmesi için tanımlanmıştır.

İlgili kabuller kullanılarak gerçekleştirilen bir seri matematiksel analiz sonrasında Bernoulli denklemi aşağıdaki şekilde oluşturulmaktadır.

$$\rho_P\dot{v}(L-s)+\dot{u}\left(\rho_p s+\rho_t R\frac{\alpha-1}{\alpha+1}\right)+\rho_p\left(\frac{v\dot{-}u}{s}\right)\frac{s^2}{2}+\rho_t\dot{\alpha}\frac{2Ru}{(\alpha+1)^2}= \frac{1}{2}\rho_t(v-u)^2-\left(\frac{1}{2}\rho_t u^2+\frac{7}{3}ln(\alpha)Y_t\right) \quad (10)$$

Denklemde ki s penetratör üzerindeki plastik deformasyon bölgesini, R hedef üzerindeki deformasyon kanalı yarıçapını, α boyutsuz bir parametre olup hedef üzerindeki deformasyon bölge yarı çapını R ile çarpılarak ifade etmeye yarayan bir sabit, Y_t hedef mukavemetini ifade etmektedir. R değeri penetratör ve hedef malzemeye göre değişiklik göstermektedir. Farklı çalışmalarda R değerinin Tungsten penetratörün RHA çelik hedefe çarpma hızına bağlı olarak değişimi ampirik olarak belirlenmiştir [8, 49-50] . Bu kapsamda gerek testlerde elde edilen delinme krater çapı veya sayısal analizlerden elde edilen sonuçlar doğrulama amacı ile kullanılmıştır. Bu çalışmada kullanılan R değerinin çarpma hızına olan değişimi Walker-Anderson tarafından aşağıdaki gibi verilmiştir [49].

$$R=R_P(1+0.287v_0+0.148v_0^2) \quad (11)$$

Denklemde R_p penetratör yarı çapını, v_0 ise penetratörün hedef üzerine çarpma hızını ifade etmektir. Gerek Aleksiveeskii-Tate, gerek Walker-Anderson penetrasyon modeli için kodlar yazılarak Tablo 1'de özetlenen her bir deneye ait L/D oranı ve çarpma hızları için çalıştırılmış ve deneysel sonuçlar ile karşılaştırılmıştır.

3. Ampirik ve Analitik Modeller ile Hesaplanan Delme Derinliklerinin Deneysel Sonuçlar İle Karşılaştırılması

3.1. Ampirik Denklemler

Bölüm 2'de verilen ampirik denklemler kullanılarak L/D=10-30 değerleri için 665-3500 m/s çarpma hızı aralığında delme derinlikleri hesaplanmıştır. Elde edilen delme derinlikleri (P), deneysel veriler ile karşılaştırılmak amacı ile penetratör boyuna oranlanarak (L), çarpma hızına bağlı, karşılaştırılmalı olarak verilmiştir, Şekil 2. Ayrıca, L/D=15 ve L/D=20 olan uzun çubuk tipi penetratörlerin RHA çelik hedef üzerindeki delme derinliğinin hesaplanması için üçüncü dereceden yeni ampirik denklemler oluşturulmuş ve test verileri ile karşılaştırılmıştır. İlgili denklemler aşağıdaki verilmiştir.

L/D=15 olan penetratörler için,

$$\frac{P}{L}=6.332\,10^{-11}\times V^3-7.22\,10^{-6}\times V^2+0.00275\times V-1.96 \quad (12)$$

L/D=20 olan penetratörler için,

$$\frac{P}{L}=2.6510^{-10}\times V^3-2.1710^{-6}\times V^2+0.006\times V-4.30 \quad (13)$$

Şekil 2 (a)'dan görüldüğü üzere L/D=10 olan penetratörler için Silsby ve arkadaşları tarafından oluşturulan Denklem 4 ile hesaplanan değerler deneysel verilerin altında kalmaktadır [37]. Bunun yanında, sınırları daha kesin olarak belirlenen Denklem 1'in bu L/D'ye sahip Tungsten penetratörlerin RHA hedefler üzerindeki penetrasyonunu deneysel verilere oldukça yakın tahmin edildiği görülmektedir. L/D=15 için literatürde verilen ampirik denklemler deneysel sonuçlar ile karşılaştırıldığında yüksek değerler vermektedir, Denklem 2 ve 4 . Bu çalışmada verilen Denklem 12 sonuçları açısından L/D=15 için delme derinliklerini daha iyi hesaplayabildiği görülmüştür. Fakat bu L/D'ye sahip uzun çubuk tipi penetratörler için 1900-2800m/s hız aralığı için yeterli veri olmadığı görülmektedir, Şekil 2(b). Ampirik denklemlerin doğruluğunun artırılması için bu hız aralığında L/D= 15 için deneysel veri elde edilmesi gerekmektedir. L/D=20 için ise Anderson [14] tarafından verilen Denklem 3 deneysel verileri 1500m/s altında kalan çarpma hızları için yeterli doğrulukta hesaplayabilirken bu hızın üzerinde delme değerlerini gerçek test verilerinden düşük olarak hesaplamaktadır, Şekil 2(c). Silsby ve arkadaşları tarafından verilen Denklem 4 ise L/D=20 ve üstü üzerindeki çap boy oranlarını ise yeterli doğrulukta tahmin ettiği görülmektedir. Şekil 2 (c) ve (d).

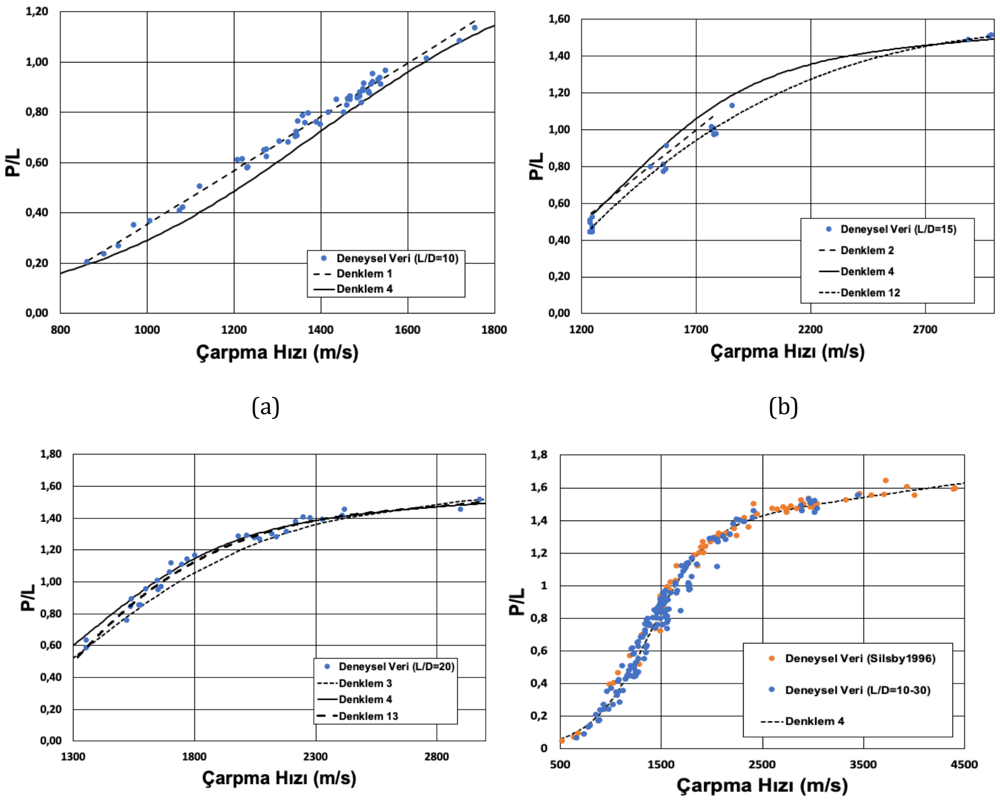

(a) (b)

(c) (d)

Şekil 2. P/L değerlerinin çarpma hızına göre değişimi a)L/D=10, b) L/D=15, c) L/D=20 ve d)L/D= 10-30 değerleri için.

Figure 2. P/L results based on impact velocity for L/D values of a)10, b)15, c) 20 and d) 10-30.

3.2. Lanz-Odermat Ampirik Denklemi

Lanz-Odermatt denklemi 25-140 mm kalibreye sahip uzun çubuk tipi penetratörlerin RHA üzerindeki delme derinliğinin belirlenerek zırh-çelik eşlenik kalınlığının belirlenmesi amacı ile zafiyet analizlerinde sıklıkla kullanılmaktadır. 25-140 mm kalibre uzun çubuk tipi penetratörler için oluşturulan Denklem 5, RHA hedefler üzerindeki penetrasyonu yüksek doğruluk ile hesaplamaktadır, Şekil 3. Lanz-Odermatt'ın yaptığı çalışmada ortaya koyduğu Denklem 5, 25-140 mm kalibreli uzun çubuk tipi tehditlerin RHA hedef üzerindeki penetrasyonunu %5-6 hata oranı ile belirlemektedir [17].

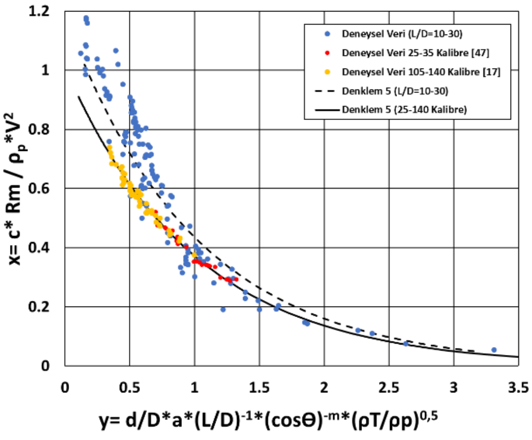

Şekil 3. Denklem 5 sonuçlarının deneysel veriler ile karşılaştırma.

Figure 3. Comparision of Equation 5 with experimental results .

Bu çalışma kapsamında boy çap oranı L/D=10-30 arasında değişen uzun çubuk tipi Tungsten penetratörlerin RHA üzerindeki delme derinliklerinin Denklem 5 ile elde edilen değerlerine bakıldığında ise hedef üzerindeki penetrasyon davranışının hesaplanmasının deneysel veri ile uyuşmadığı görülmektedir. Özellikle L/D =10 olan uzun çubuk tipi penetratörlerin delme derinlikleri için deneysel veri ile hesaplanan değerleri arasında ortalama %14 oranında hata hesaplanmıştır.

Bu açıdan bakıldığında Tablo 1'de oluşturulan veri grubu için Denklem 5'in yeterli hesaplama kapasitesine sahip olmadığı ortaya çıkmaktadır.

3.3. Aleksveeskii-Tate ve Walker-Anderson Analitik Yöntemleri

Aleksveeskii-Tate ve Walker-Anderson analitik modelleri için Python programı kullanılarak zamana bağlı çözüm yapan kodlar yazılmıştır. Hesaplamalar Tablo 1 kapsamında oluşturulan test kütüphanesi içerisinde yer alan her bir veri noktası için yapılmıştır. Elde edilen sonuçlar Şekil 4'te L/D= 10-30 oranına sahip deliciler için çarpma hızına bağlı olarak verilmiştir. Literatüre bakıldığı zaman geniş L/D değer aralıkları için analitik modellerin karşılaştırmaları çok kısıtlı kalmaktadır. L/D=10 oranına sahip uzun çubuk tipi penetratörlerin analiz sonuçları, deneysel verileri ile karşılaştırıldığında 1000m/s çarpma hızlarına kadar Aleksveeskii-Tate modeli deneysel verilere göre penetrasyon derinliklerini daha yüksek hesaplamaktadır. Bunun yanında L/D=10 için Aleksveeskii-Tate modeli kullanılarak yapılan hesaplamalarda uzun çubuk tipi penetratörlerin RHA hedef üzerine 2500m/s ve üstündeki yüksek çarpma hızlarında test değerlerinin hesaplanan değerlerden daha yüksek olduğu görülmüştür.

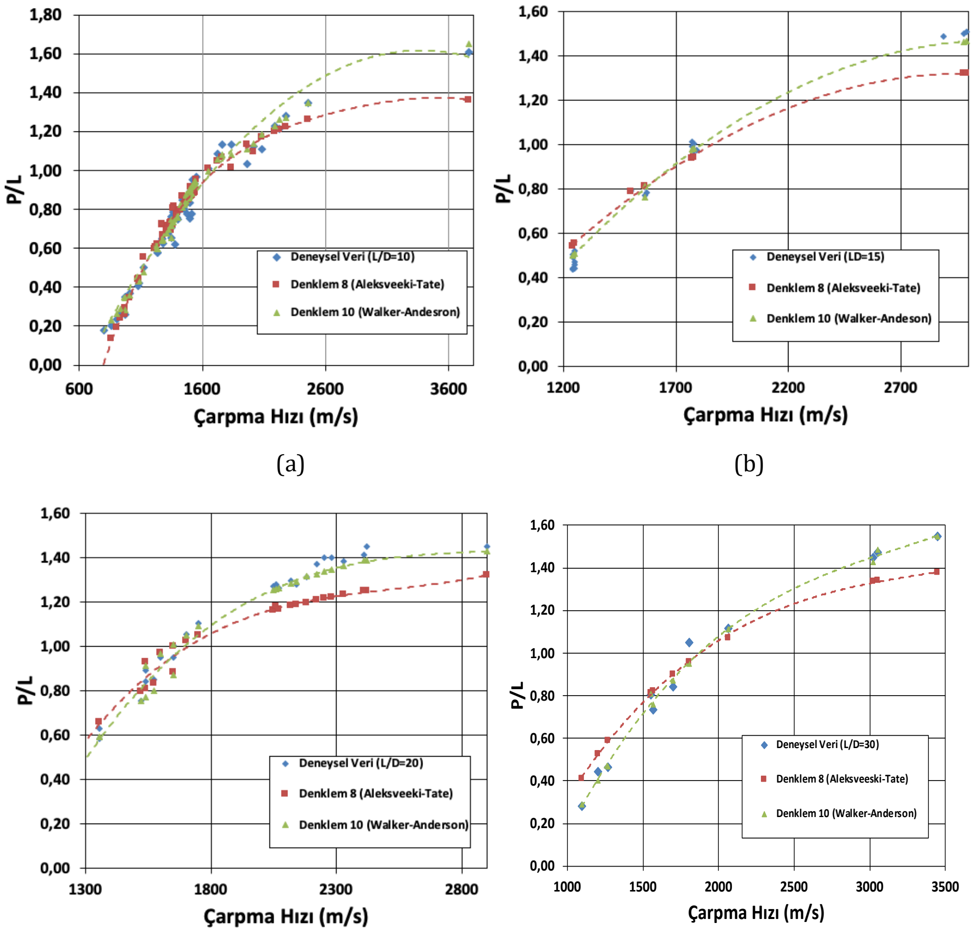

(a) (b)

(c) (d)

Şekil 4. Deneysel ve Analitik Modellerin P/L değerlerinin çarpma hızına göre değişimi a)L/D=10, b) L/D=15, c) L/D=20 ve d)L/D= 10-30 değerleri için.

Figure 4. P/L results of Experimental and Analytic Model based on impact velocity for a)L/D=10, b) L/D=15, c) L/D=20 ve d)L/D= 10-30 values.

Benzer durum L/D=15 olan uzun çubuk tipi penetratörlerin RHA hedef üzerindeki penetrasyonu için de geçerlidir, Şekil 4(b). L/D değeri arttıkça Aleksiveeskii-Tate analitik modelinde yaklaşık 2000 m/s üzerindeki hızlarda hesaplama doğruluğunun düştüğü belirlenmiştir.

Aleksveeskii-Tate modelinden farklı olarak Walker-Anderson modeli ise tüm çarpma hızlarında Tungsten uzun çubuk tipi penetratörün RHA hedef üzerinde oluşturduğu penetrasyon davranışını tüm L/D değerleri için yüksek doğrulukla hesaplayabildiği görülmektedir, Şekil 4(a-d).

Ampirik denklemler ve analitik modellemeler sonucunda hesaplanan Tungsten uzun çubuk tipi penatratörlerin RHA hedef üzerinde oluşturdukları delme derinlikleri deneysel veriler ile hata oranı açısından karşılaştırılması yapılmıştır, Tablo 3. Sayısal olarak bakılınca ampirik denklemler L/D=10 ve 20 için %5 değerinden az bir hata ile hesaplanmaktadır. Fakat L/D=15 için literatürde verilen Denklem 2 %14 gibi yüksek bir hata ile delme derinliklerini hesaplayabilmektedir. Gerek L/D=15 gerek L/D=20 için bu çalışma kapsamında tanımlanan Denklem 12 ve 13 literatürde verilen ampirik denklemlerden daha düşük hesaplama hatasına sahiptir. Silsby ve arkadaşları, [37] tarafından gerçekleştirilen çalışmada hesaplama hatası tüm L/D oranları için %8 iken, yeni veri gruplarının eklenmesi ile tüm L/D değerleri için %9 değerine ulaşmıştır.

Tablo 3. Hata oranları (%).

Table 3. Error ratio (%).

L/D		10	15	20	30
Ampirik Denklemler	1	2,9			
	2		14		
	3			4,6	
	4	9			
	12		5,1		
	13			2,8	
Analitik Modeller	8	5	7	8,8	13,7
	10	2,9	2,4	3	3,3

Analitik penetrasyon modellerinde ise Aleksiveeskii-Tate modelinin hata oranı genel olarak ampirik denklemlerden yüksektir. Ayrıca L/D değerinin artmasıyla hata oranlarının yükseldiği kaydedilmiştir. Walker-Anderson penetrasyon modelinde ise L/D değerlerinin artması ile hata oranlarında artış gözlenmemiştir. Bu neden ile Walker -Anderson modeli zırh yapılarının zafiyet hesaplamalarında hassas sonuçlar elde edilmesini sağlayacağı belirlenmiştir.

4. Sonuçlar

Literatürdeki Tungsten uzun çubuk tipi penetratörlerin RHA zırh çelikleri üzerindeki L/D oranı ve çarpma hızı değişkenlerine bağlı olarak delme derinliği bilgileri toplanmış ve 150 farklı veri noktasından oluşan deneysel veri grubu oluşturulmuştur. Bunun yanında farklı L/D oranları için ampirik denklemler ile elde edilen delme derinlikleri test sonuçları ile karşılaştırılmıştır. Ayrıca analitik penetrasyon modelleri için zamana bağlı çözümleme yapabilen bilgisayar kodu yazılarak benzer şekilde veri grubundaki L/D ve çarpma hızları kullanılarak delme derinlikleri hesaplanmıştır. Yapılan hesaplamalar sonucunda Tungsten malzemeden üretilmiş uzun çubuk penetratörlerin RHA hedef üzerindeki delme derinlikleri Walker-Anderson penetrasyon modeli ile en yüksek doğrulukla hesaplanmıştır. Aleksiveeskii-Tate penetrasyon modelinde ise hesaplanan penetrasyon değerleri ile deneysel veriler arasındaki farkın, L/D değeri ile doğru orantılı olarak arttığı belirlenmiştir. Bunun yanında ampirik denklemler de belirli çarpma aralıklarında ve belirli L/D oranlarında yine yüksek doğruluk oranında hesaplama yapılmasına izin vermektedirler. Ayrıca, Lanz-Odermat ampirik denklemi ile hesaplan değerler bu çalışma kapsamında ele alınan test sonuçları için en düşük doğruluk değerlerine sahiptir. Özellikle ampirik denklemlerin yarı sonu hedefler üzerindeki delme derinliklerinin hesaplanmasında kullanılması esnasında deneysel verilerdeki eksik hız noktalarının tamamlanması gerekmektedir.

Etik kurul onayı ve çıkar çatışması beyanı

Hazırlanan makalede etik kurul izni alınmasına gerek yoktur. Hazırlanan makalede herhangi bir kişi/kurum ile çıkar çatışması bulunmamaktadır.

Kaynaklar

[1] Awerbuch, J. and Bodner, S. R. 1974. Analysis of The Mechanics Of Perforation Of Projectiles In Metallic Plates, Int. J. Solids Struct., Cilt.10, s.671-684, DOI:10.1016/0020-7683(74)90050

[2] Lehr H. F, Wolmand E. 2001. On The Optimal Performance Of Long-Rod Penetrators Subjected To Transverse Accelerations, International Journal of Imapct Engineering, Cilt.26, s.409-420, DOI: 10.1016/S0734-743X(01)00091-4

[3] Reis I., Teixeira-Dias F., Dias-de-Oliveria J., S.2023 Optimisation Strategies for Multi-Layered Armor Plates, International Journal of Modelling and Simulation, s.1-22, DOI: 10.1080/02286203.2023.2167505

[4] Lanz W., Odermatt W., Weihraach G., S. 200, Kinetic Energy Projectiles: Development History, Satet of The Art, Trends. International Symposium on Ballistics, 7-11 May 2001, 1191-1198

[5] Rosset, W.S., S.2001, An Overview of Novel Penetrator Technology, ARL-TR-2395, Army Research Laboratory, Aberdeen Proving Ground, s. 1-30

[6] Balos S., Nikacevic M., Ristic P, Sidanin L. S.2010. Jacketed Long-Rod Penetrators: Problems and Perspectives, Scintific Technical Review, Cilt.60, s.70-75

[7] Keeele M.J., Rapacki E.J.,Bruchey W.J., S.1991. High Velocity Performance of A Uranium Alloy Long Rod Penetrator, BRL-TD-3236, US Armu Ballistic Research Laboratory, s.1-24

[8] Bjerke T.W., Silsby G.F., D.R. Scheffler, Mudd R.M., S. 1992. Yawd long-rod armor penetration. International Journal of Impact Engineering, Cilt.12, s.281-292. DOI:10.1016/0734-743X(92)90473-7.

[9] Anderson C. E., Behner T., Hohler V., S.2013. Penetration as a Function of Target Obliquity and Projectile Pitch. Journal of Aplied Mechanics. Cilt.80, s.1-11.DOI: 10.1115/1.4023342

[10] Yarin A.L., Rubin M. B., Roisman I.V., S.1995, Penetration of a Rigid Projectile Into An Elastic-Plastic Target of Finite Thickness. International Journal of Impact Engineering. Cilt.16. s.801-831. DOI: 10.1016/0734-743X(95)00019-7.

[11] Leonard W. S.1997. The Effect of Nose Shape on Depleted Uranium (DU) Long-Rod Penetration. ARL-TR-1505. Army Resarch Laboratory. Aberdeen Proving Ground.

[12] Wilson L.L., Foster J.C., Jones S.E., Girillis P. S.1989. Experimental Rod Impact Results. International Journal of Impact Engineering. Cilt.8, s.15-25. DOI: 10.1016/0734-743X(89)90028-6.

[13] Anderson C. E., Walker J.D. S.1991. An Examination of Long Rod Penetration, International Journal of Impact Engineering. Cilt.11, s.481-501. DOI: 10.1016/0734-743X(91)90015-8.

[14] Anderson C. E., Walker J.D., Bless S.J., Partom Y. S.1996. On the L/D effect for Long-Rod Penetrators. International Journal of Impact Engineering. Cilt.18, s.247-264. DOI: 10.1016/0734-743X(95)00028-9.

[15] Alekseevskii V. P, S.1966, Penetration Into A Target At High Velocity, Combustion, Explosion and Shock Waves, Cilt.2, s.99-106.DOI: 10.1007/BF00749237.

[16] Tate A., S. 1967. A Theory For The Deceleration of Long Rods After Impact, Journal of Mechanics and Physics of Solids, Cilt.15, s.387-399.DOI: 10.1016/0022-5096(67)90010-5.

[17] Lanz W., Odermatt W.,S.1992. Penetration Limits of Conventional Large Caliber Anti-Tank Guns/Kinetic Energy Projectiles. 13.International Symposium on Ballistics, 1-3 June 1992, 225-233

[18] Huang F., ZHANG L., S.2007. Investigation on Ballistic Performanceof Armor Ceramics Against Long-Rod Penetration. Metallurgical And Materials Transactions A, Cilt.38A. s.2891-2895. DOI: 10.1007/s11661-007-9281-8

[19] Goh W.L, Zheng Y., Yuan J., Ng K.W. S.2017. Effects of Hardness of Steel on Ceramic Armour Module Agaist Long Rod Impact. International Journal of Impact Engineering. Cilt.109, s.419-426. DOI: 10.1016/j.ijimpeng.2017.08.004.

[20] Luo D., Wang Y., Wang F.,Cheng H., Zhu Yu.S.2019. Ballistic Behaviour of Oblique Composite Structure Against Long-Rod Tungsten Projectiles. Materias, Cilt12,s.1-13. DOI: 10.3390/ma12182946

[21] Goh W., Luo B. Zeng. Z, Yuan J. Kee Woei Ng. S.2019. Effect of Hardness and Toughness of Ceramic Armour Module Against Long-Rod Impacts. 42nd International Conference on Advanced Ceramics and Composites: Ceramic Engineering and Science Proceedings, Cilt.39, s.185-198. DOI: 10.1002/9781119543343.ch18

[22] Fellows N.A., Barton P.C. S.1999. Development of Impact model for Ceramic-faced Semi-inifinite Armour. International Journal of Impact Engineering, Cilt.22, s.793-811.DOI: 10.1016/S0734-743X(99)00017-2

[23] Tate A.K. Green E.B., Chamberelain P. G. , Baker R. G. S. 1978. Model Scale Experiments on Long Rod Penetration. 4th Internatonal Symposium on Ballistics, 17-19 Ekim 1978,Monterey, Kanada.

[24] Magness, L.S.. Farrand T. G. S.1990. Deformation Behivour and Its Relationship to the Penetration Performance of High Density KE Penetrators Material. Army Sicence Conference, Durham, NC.

[25] Hohler, V., Schneider E., Stilp A. J., Tham R. S.1978. Length- and Velocity Reduction of High Density Rods Perforating Mild Steel and Armor Steel Plates. 4th Internatonal Symposium on Ballistics, 17-19 Ekim 1978, Monterey, Kanada.

[26] Hohler, V. Stilp A. J. S.1977. Penetration of Steel and High Density Rods in Semi-Infinite Steel Targets. 3rd International Symposium on Ballistics, 23-25 Mart 1977, Karlsruhe, Almanya.

[27] Hohler, V. Stilp A. J. S.1984. Influence of the Length-to-Diameter Ratio in the Range from 1 to 32 on the Penetration Performance of Rod Projectiles. 8th International Symposium on Ballistics, , 23-25 Ekim 1984. Orlando,Amerika

[28] Hohler, V., Stilp A. J. S.1987. Hypervelocity Impact of Rod Projectiles with L/D from 1 to 32. International Journal of Imapct Engineering, Cilt.5, s.323-334, DOI: 10.1016/0734-743X(87)90049-2.

[29] Sentil P.P., Reddy, P.R., Reddy, T.S., Kumar, K.S., Madhu,V., S.2019. Scaled WHA Long Rod Projectile Impact Against Armour Steel. Human Factors and Mechanical Engineering for Defense and Safety, Cilt.3, s.1-8. DOI: 10.1007/s41314-019-0018-4.

[30] Freuh, S., Heine, A., Weber, K.E., Wickert, M. S.2016. Effective depth-of-penetration range due to hardness variation for different lots of nominally identical target material. Defence Technology. Cilt.12, s.171-176. DOI:10.1016/j.dt.2015.10.002.

[31] Sorensen B.R., Kimsey K.D., Silsby G. F., Scheffler D.R. ,Sherrick T. M, De Rosset W. S. 1991. High Velocity Penetration of Steel Target. International Journal of Imapct Engineering, Cilt.11, s.107-119, DOI: 10.1016/0734-743X(91)90034-D

[32] Fras T. S.2021. Experimental and numerical Study on a Non-Experimental Ractive Armour with the Rubber Interlayer Applied Against Kinetic Energy Penetrators-The ‘Bulging Effect’ Analysis. Materials, Cilt.14, s.1-17. DOI: /10.3390/ma14123334

[33] Anderson C.E., Royal-Timmons S. A., S.1997. Ballistic Performance of Confined 99.5% Al_2O_3 Ceramic Tiles, International Journal of Imapct Engineering, Cilt 19,s. 703-713, DOI:. 10.1016/S0734-743X(97)00006-7

[34] Woolsey, P., Mariano, S., Kokidko, D. S.1989. Alternative Test Methodology for Ballistic Performance Ranking of Armor Ceramics

Report No. MTL TR 89-43, U. S. Army Materials Technology Laboratory, Watertown, Massachusetts.

[35] Woolsey, P., Mariano, S., Kokidko, D. S.1990. Progress Report on Ballistic Test Methodology for Armor Ceramics. Proceedings of TACOM Combat Vehicle Survivability Symposium, Gaithersburg, MD, 15 Mart 1990.

[36] Gooch, W.A., Burkins, M.S., Ernst, H-J, Wolf T. S.1995. Ballistic Penetration of Titanium Alloy Ti-6Al-4V. Lightweight Armor Systems Sympossium'95, The Royal Military College of Science, Shrivenham, İngiltere, 28-30 Haziran 1995

[37] Silsby G. F., S.1984. Penetration of Semi-Infinite Steel Targets by Tungsten Long Rods at 1.3 to 4.5km/s. 8th.International Symposium on Ballistics, 23-25 Ekim 1984,Florida, 669-673

[38] Yuan, J., Tan, E.B., S.2014. An Examination of DOP Test of Ceramic Tile Subjected to Long Rod Penetration. Applied Mechanics and Materials . Cilt.566. s. 353-358. DOI: 10.4028/www.scientific.net/AMM.566.353.

[39] Walters, W., Williams, C., S.2005. A Solution of the Alekseevski-Tate Penetration Equations. ARL-TR-3606. Army Research Laboratory, Aberdeen Proving Ground. s.1-50

[40] Zhang, D., Li, J., Wei, X., Feng, K., Wang, Yu, Zhao, J., Xue, D., S.2020. Research on Dynamic Test of Hyper-Velocity Impact Penetration Acceleration Signal. IEEE, Cilt.8, s.194879-194893. DOI: 10.1109/ACCESS.2020.3033676

[41] Lan, B., Wen, H., S.2010. Alekseevskii-Tate revisted: An extension of the Modified Hydrodynamic Theory of Long Rod Penetration. Science China Technological Sciences. Cilt.53, s.1364-1373. DOI: 10.1007/s11431-010-0011-x

[42] Jiao, W.J., Chen, X.W., S.2018. Approximate Solutions of the Alekseevskii-Tate Model of Long Rod Penetration. Acta Mech.Sin. Cilt.34, s.334-348. DOI: 10.1007/s10409-017-0672-9.

[43] Lou, J., Zhang Y., Wang, Z.,Hong, T., Zhang, X., Zhang S., S.2014. Long-Rod Penetration: The Transition Zone Between Rigid and Hydrodynamic Penetration Models. Defecnce Technology. Cilt.10. s.239-244. DOI: 10.1016/j.dt.2014.05.007

[44] Zhiyong, Y., Chen, X. Sç2021. Analysis of Characteristic Parameters of Long-Rod Penetration. Explosion and Shock Waves. Cilt.41, s.1-7. DOI: 10.11883/bzycj-2020-0057

[45] Jeanquartier R., Odermatt W. S.1995. Post Perforation Length and Velocities of KE Projectiles with Single Oblique Targets. 15th International Sympossium on Ballistic. 21-24 Mayıs 1995, Kudüs, s.1-8.

[46] Auten, J. R. S. 2011. A Comparison of Penetration Algorithms: Predictions vs. Test Data For Kinetic Energy Rods, 26th International Symposium On Ballistics, 12-16 Eylül 2011,Miami , s.1522-1533

[47] Tate, A. S.1969. Further Results In The Theory of Long Rod Penetration, Journal of the Mechanics and Physics of Solids, Cilt.17, p 141-150. DOI:10.1016/0022-5096(69)90028-3.

[48] MIL-DTL-12560K, S.2013. Armor Plate , Steel Wrought, Homogeneous (For Use In Combat-Vehicles And For Ammunition Testing).

[49] Walker, J. ,Anderson, C. E. J. S. 1995. A Time-Dependent Model For Long-Rod Penetration. International Journal of Impact Engineering, Cilt.16, s.19-48. DOI: 10.1016/0734-743X(94)00032-R.

[50] Walker, J. ,Anderson, C. E. J. S. 1998. Penetration Modellin of Ceramic and Metal Targets. 36th Aerospace Sciences Meeting&Exhibit. 12-15 Ocak 1998, Reno, s.1-7

DEU FMD 27(79) (2025) 31-37

Dokuz Eylül Üniversitesi Mühendislik Fakültesi Fen ve Mühendislik Dergisi
Dokuz Eylul University Faculty of Engineering Journal of Science and Engineering
Elektronik/Online ISSN: 2547-958X

RESEARCH ARTICLE / ARAŞTIRMA MAKALESI

Evaluation of Sustainable Washing Processes for Fashionable Effects in Denim

Denimde Moda Efektler için Sürdürülebilir Yıkama Proseslerinin Değerlendirilmesi

Ayşe Şevkan Macit

Uşak University, Faculty of Engineering and Natural Sciences, Uşak, TÜRKİYE
Corresponding Author / Sorumlu Yazar : ayse.sevkan@usak.edu.tr

Abstract

Sustainability has become an important issue in every sector today. Effective use of resources is an issue that needs to be emphasized at the global level. Since denim washing processes consume a lot of water, energy, chemicals and time, sustainable processes in this area have gained importance. Various denim washing processes developed in terms of effective use of resources for sustainable methods are applied. Practices may be aimed at reducing water consumption, or may be related to more sustainable chemical consumption. In addition, situations where the process is shortened, waste is reduced or water free processes can come to the fore can also contribute to sustainability. The effects of sustainable processes on fabric properties should also be considered. In this study, denim fabrics with fashionable fading and bleaching effects by different methods were used. Abrasion resistance and bending rigidity properties of denim fabrics with effects obtained by conventional and sustainable methods were investigated comparatively. The results obtained show that among the sustainable processes in the study, there are preferable processes in terms of bending rigidty and abrasion resistance properties.

Keywords: *Denim Fabric, Denim Washing Processes, Sustainability, Bending Rigidity, Abrasion*

Öz

Sürdürülebilirlik konusu günümüzde her sektörde önemli bir hal almıştır. Kaynakların etkin kullanımı global düzeyde üzerinde durulması gereken bir konudur. Denim yıkama işlemleri de çok fazla su, enerji, kimyasal ve zaman tüketimine neden olan süreçler olduğu için, bu alanda da sürdürülebilir uygulamalar oldukça önem kazanmıştır. Sürdürülebilir yöntemler için, kaynakların etkin kullanımı açısından geliştirilen çeşitli denim yıkama işlemleri uygulanmaktadır. Uygulamalar, su tüketimini azaltmaya yönelik olabileceği gibi, daha sürdürülebilir kimyasal madde tüketimiyle de ilgili olabilir. Ayrıca, sürecin kısaltıldığı, atıkların azaltıldığı veya kuru işlemlerin ön plana çıkabileceği durumlar da sürdürülebilirliğe katkı sağlayabilir. Sürdürülebilir proseslerin kumaş özellikleri üzerindeki etkileri de dikkate alınmalıdır. Bu çalışmada, farklı yöntemlerle elde edilmiş olan ve denimde moda olan eskitme ve ağartma efektlerine sahip denim kumaşlar kullanılmıştır. Konvansiyonel yöntemlerle ve sürdürülebilir yöntemlerle elde edilmiş efektli denim kumaşların aşınma dayanımı ve eğilme rijitliği özellikleri karşılaştırmalı olarak incelenmiştir. Elde edilen sonuçlar, çalışmadaki sürdürülebilir prosesler arasında eğilme rijitliği ve aşınma direnci özellikleri bakımından tercih edilebilir süreçlerin bulunduğunu göstermiştir.

Anahtar Kelimeler: *Denim Kumaş, Denim Yıkama Prosesleri, Sürdürülebilirlik, Eğilme Rijitliği, Aşınma*

1. Introduction

Sustainability is an issue of global importance today, and in this context, the effective use of resources is a factor that needs attention in the industrial sense. In terms of sustainability, the textile industry takes many measures to reduce the consumption in the processes. In this context, since denim washing processes consume a lot of water, energy, chemicals and time, the search for sustainable solutions in this regard has gained great importance.

In denim sector, there are fading and bleaching processes that have developed depending on fashion and have been applied for many years. There are dry fading processes such as sand blasting [1], whisker [2], hand sand [3], grinding [3] in denim. Laser process has created an alternative to these processes as a sustainable solution [4]. In addition to the dry fading processes in denim, there are also washing processes for the fading and bleaching effects. Pumice stone washing is one of these methods [5]. This method is one of the conventional methods that has been used for many years. The pumice stone washing process creates a very good worn look effect or fading effect, but the necessity of unloading the stones from machines after the process, the need to the separation of stones and fabric from each other, damage of the stones to the machine over time, the environmental impact of the process are some of the disadvantages of this method. This is not an environmentally friendly process, and the process creates waste in the form of sludge. In addition, wastewater treatment becomes necessity. Some studies on the environmental effetcs of stone washing have been examined [6, 7]. Sustainable solutions such as the use of artificial stones [8], enzyme washing [9, 10], enzyme and stone washing [11] are applied as an alternative to stone washing. For bleaching of denim, denim fabrics are treated with Sodium Hypochlorite [12], Potassium Permanganate [13, 14], Hydrogen Peroxide [15]. Enzyme bleaching [16] and ozone technique processes [17, 18] are sustainable alternatives to

DOI: https://doi.org/10.21205/deufmd.2025277905

Geliş Tarihi / Received: 16.10.2023
Kabul Tarihi / Accepted: 26.03.2024

conventional bleaching processes. Plasma [19, 20] and water jet techniques [4, 21] are also sustainable methods for denim fading.

As sustainability gains importance, various studies examining alternative washing processes in denim appear in literature [7, 22, 23, 24]. In these studies, fabric properties such as tensile strength and color difference [7], tear strength and energy use [22], abrasion resistance and fastness to laundering [23] were examined. In this study, alternative washing processes of denim fabrics were studied. Both conventional and sustainable fading and bleaching processes have been applied to denim fabrics. The effects of sustainably advantageous processes in terms of various fabric performances were investigated. The main aim of the study is determining of abrasion and bending properties of denim fabrics subjected to conventional and sustainable denim fading and bleaching processes. Abrasion and bending properties are two important features for denim fabrics, and in this sense, the results of sustainable processes in terms of these properties are important.

2. Materials and Methods

2.1. Material

Table 1, which includes the properties of the denim fabrics used, is given below.

Table 1. Properties of the denim fabric.

Weaving structure	Weight in grams per square meter (g/m^2)	Raw material	Denim dyeing
Twill (3/1 Z)	480	Cotton	Indigo dyed

Weft yarn count of denim fabrics is Ne 8/1 Open-End and warp yarn count is 6/1 Open-End. Weft density is 18/cm and warp density is 20/cm.

2.2. Method

After weaving of the denim fabrics, they were pre-washed at 50°C for 10 minutes with a dispersing agent made of recycled PET and then the denim fabrics were desized. Then, fading and bleaching effect processes were performed and then test processes were carried out.

2.2.1. Fading and bleaching processes of denim fabrics

After pre-washing and desizing, the fabrics were subjected to fading or bleaching process with 6 different processes. Two of these processes (pumice stone and potassium permanganate spray processes) are conventional methods, while the others are sustainable processes.

Pumice stone washing process is made for fading effect of denim fabrics and this method is a conventional method. Pumice stone is not ecological and it is difficult to dispose of the waste generated by the process. As an alternative to this method, by using stone enzyme (SWE), a fading effect similar to that of pumice stone was obtained, and with this process, the waste in the form of sludge of the pumice stone was eliminated. Because this enzyme dissolves in water, no waste in the form of sludge is formed. As another method, a similar fading effect was obtained in an industrial washing machine using a chemical called ECHO WHITES, with a waterless process. The wet fabric that comes out of the pre-wash is treated with chemicals in the machine without using extra water. The process, which is carried out using ECHO WHITES chemical, is a sustainable method without water and provides an effect similar to the pumice stone fading effect.

The other three methods were applied for bleaching denim fabrics. The first method is the application of potassium permanganate (PP) spray, and a local bleaching is created on the fabric. It is a conventional method and there is a lot of water consumption, it is harmful to health, it has a toxic effect and it is not ecological. The process with chemical substance named PMN/PMK (chemical substitute for PP, PMN main chemical, PMK catalyst) is a locally effective spray application, which is both healthier environmentally friendly product and reduces water consumption by approximately 1/10. The use of this chemical also reduces processing time and this is important in terms of sustainability. Another process with water consumption as low as 1/10, PMN nebulisation, is a water free process. Denim fabric is treated with chemicals in a nebulisation system with nozzles. Denim fabric is bleached by spraying chemical from nozzles.

As can be seen, for fading or bleaching of denim fabrics, sustainable substitutes for conventional methods have been tried both by using stone enzyme or environmentally friendly chemical substance and by reducing or eliminating water consumption. The main purpose of this study is to analyze the results of these sustainable practices in terms of abrasion and bending characteristics, which are of great importance in denim.

Processes and their conditions applied to denim fabrics are given in Table 2.

Table 2. Processes and conditions applied to denim fabrics.

Process	Time *(min.)*	Temperature *(°C)*	Liquor ratio
Pumice Stone	30	50	1/5
SWE (Stone enzyme)	45	50	2 gr/l SWE
ECHO WHITES	30	Water free	%2 ECHO WHITES
PMN Nebulisation	20	Water free	%25
PMN/PMK Spray	-	Water free	%25
PP Spray	-	Water free	%5

After the PP spray process, neutralization is done with sodium metabisulfite for 5 minutes at 50 °C, and the excess PP is removed. Afterwards, the denim fabrics are washed with detergent at 50 °C for 5 minutes and dried at 75-80 °C. Detergent washing and drying is carried out under the same conditions after pumice stone washing, SWE washing, ECHO WHITES washing. After PMN/PMK spray and PMN nebulisation, drying process takes place, then the denim fabrics are washed with detergent and dried once more.

2.2.2. Test procedures of denim fabrics

Following the fading processes, the denim fabrics were exposed to abrasion resistance and bending rigidity tests. Test procedures conducted to denim fabrics are presented Table 3. Before test procedure, the samples were conditioned for 24 h in standard atmospheric conditions (temperature 20 ± 2 °C and relative humidity 65 ± 4%).

Table 3. Test procedures.

Test	Standard	Equipment	Repetition
Abrasion Resistance	TS EN ISO 12947-3 [25]	MESDAN	3
Bending Rigidity	TS 1409 [26]	Test device designed in accordance with the bending rigidity test standard	5

Abrasion behaviors of the denim fabrics were determined by measuring the mass loss amounts of the fabrics after abrasion cycles. Four levels of abrasion cycles 5.000, 10.000, 15.000 and 20.000 were applied to the denim fabrics with 12 kPa weight. Differences in mass loss after 5.000, 10.000, 15.000 and 20.000 abrasion cycles were determined by using fabric weight values before and after abrasion cycles.

On the other hand, the denim fabrics were subjected to bending rigidity test for determining of bending behavior of the denim fabrics in weft and warp direction according to TS 1409 and the formula for calculating bending rigidity with the values obtained in the bending rigidity test is given below.

$$G = 0{,}1\, W\, C^3\ mg.cm \qquad (1)$$

Where,

X=Falling length (cm)

C=X/2 =Bending length (cm)

W=Fabric mass per unit area (g/m^2)

G=Bending rigidity (mg.cm)

Figure 1 shows denim fabrics with their effects after the processes and fabric samples appearances after the abrasion resistance test. Figure 2 shows the microscopic views at 30x magnification of denim fabrics before and after abrasion resistance test. While Figure 1 shows the color changes of denim fabrics after the abrasion resistance test, Figure 2 shows in detail the appearance of the weft and warp yarns on the worn test samples after the test.

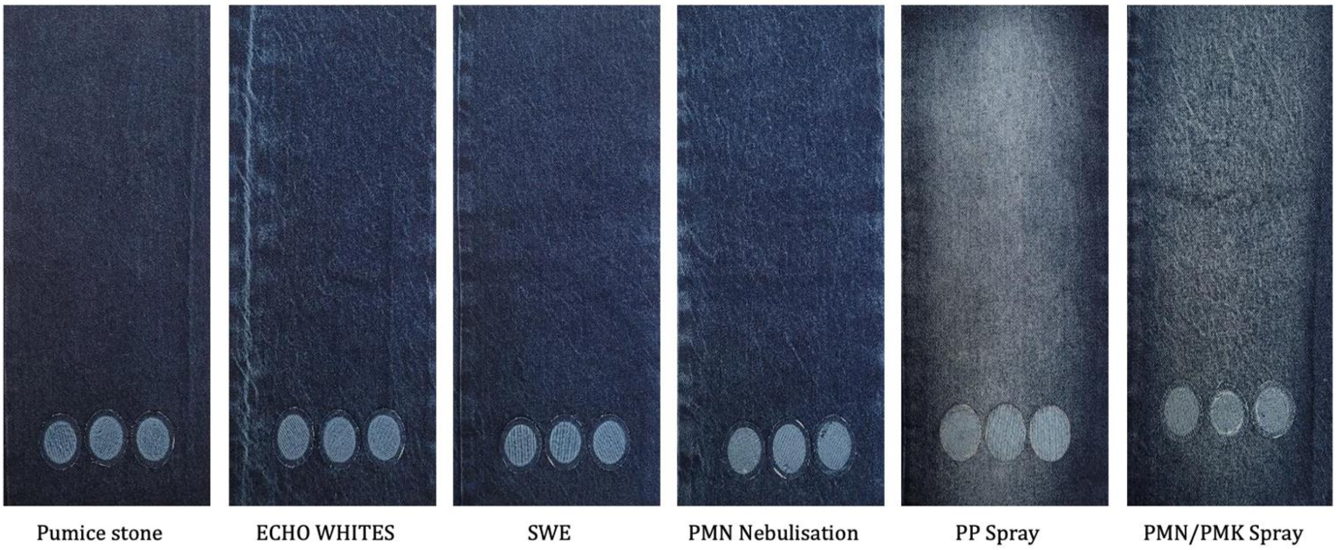

Figure 1. Effects after the processes on denim fabrics and fabric samples appearances after abrasion resistance test.

2.2.3.Statistical Analysis

After the test procedures, the findings were statistically evaluated at 95% confidence level via SPSS program (α=0.05).

3. Results

3.1. Bending Rigidity Test Results

Mass per unit area values of fabrics after processes and bending rigidity test results are given in Table 4.

Mass per unit area values and bending rigidity values in weft and warp direction are shown visually in Figure 3, Figure 4 and Figure 5, respectively.

As seen in Figure 3, the least mass loss was observed after the pumice stone process. It has been observed that the mass loss in fabrics with ECHO WHITES, SWE, PMN nebulisation and PP Spray is close to each other. It was observed after the processes that the highest mass loss is in the fabric to which PMN/PMK Spray is applied.

Table 4. Mass per unit area values of fabrics after processes and bending rigidity test results.

Processes	Mass per Unit Area *(g/m^2)*	Bending Rigidity in Weft Direction *(mg.cm)*	Bending Rigidity in Warp Direction *(mg.cm)*
Pumice Stone	425,89	623,48	745,56
ECHO WHITES	407,80	708,32	867,46
SWE (Stone enzyme)	408,21	651,24	730,21
PMN Nebulisation	413,29	755,19	839,70
PP Spray	412,62	709,86	730,23
PMN/PMK Spray	402,24	741,03	687,98

Pumice stone | Pumice stone after abrasion test | ECHO WHITES | ECHO WHITES after abrasion test

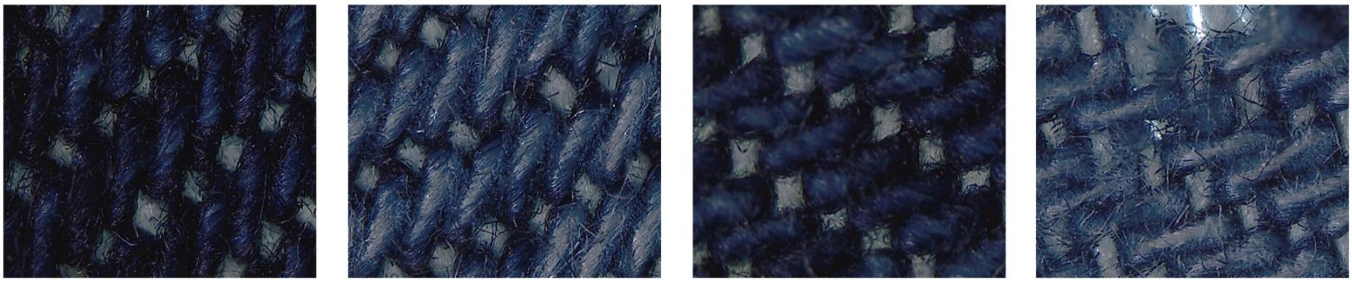

SWE | SWE after abrasion test | PMN Nebulisation | PMN Nebulisation after abrasion test

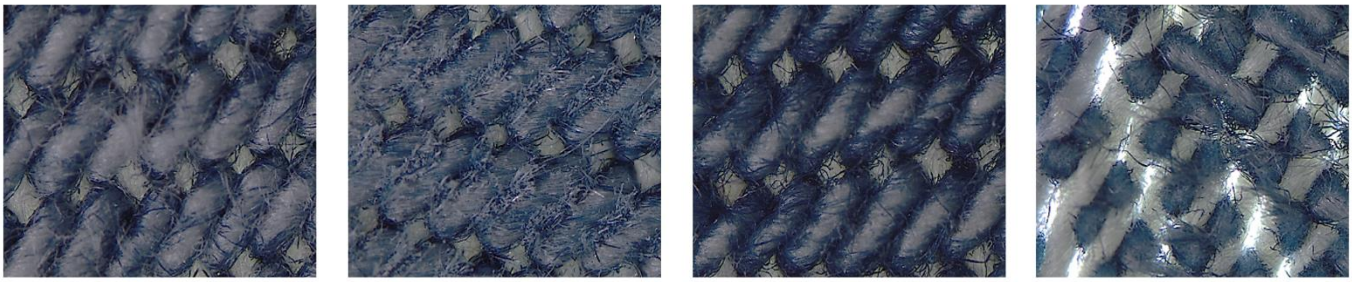

PP Spray | PP Spray after abrasion test | PMN/PMK Spray | PMN/PMK Spray after abrasion test

Figure 2. Microscopic views of denim fabrics before and after abrasion resistance test.

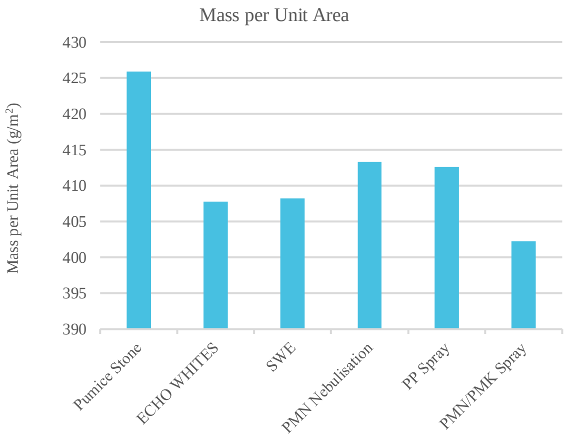

Figure 3. Mass per unit area values of fabrics after processes.

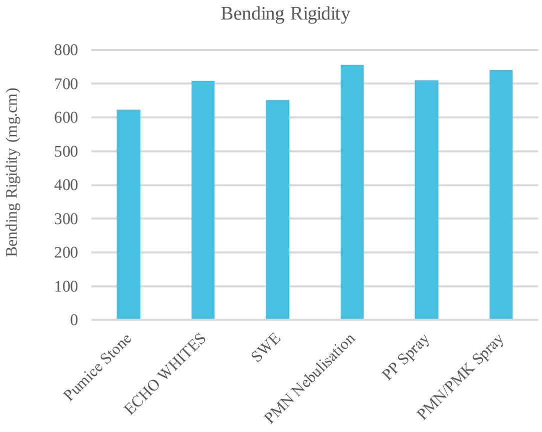

Figure 4. Bending rigidity test results in weft direction.

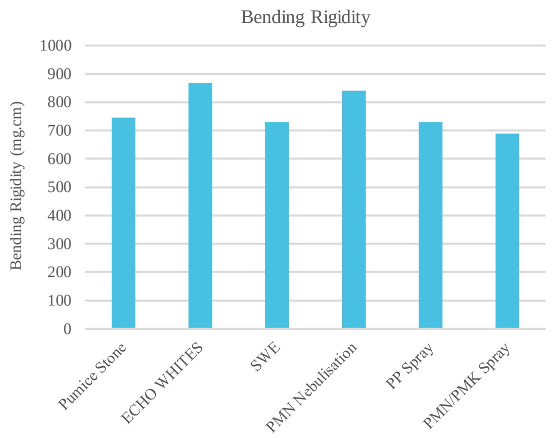

Figure 5. Bending rigidity test results in warp direction.

As seen in Figure 4 and Figure 5, it was determined that the bending rigidity values in the warp direction were slightly higher than in the weft direction. On the other hand, the highest bending rigidity value in weft direction was seen after PMN nebulisation process and this value was followed by PMN/PMK Spray and ECHO WHITES process. The highest bending rigidity value was seen after ECHO WHITES process in warp direction. It was observed that this value was followed by the PMN nebulisation process in warp direction. Also the bending rigidity values of denim fabrics treated with Pumice Stone, SWE and PP Spray were close to each other in both weft and warp direction. In addition, the bending rigidity value of the fabric with PMN/PMK Spray was the lowest value among the fabrics in warp direction. Looking at the statistical evaluation, washing processes and fabric direction have statistically significant effect on bending rigidity (Table 6 and Table 7).

3.2. Abrasion Resistance Test Results

Mass loss ratio values of fabrics after abrasion resistance test are given in Table 5 and mass loss ratio values are shown visually in Figure 6.

Table 5. Mass loss ratio values of fabrics after abrasion resistance test.

Processes	Mass Loss Ratio *(%)* 5.000 cycles	10.000 cycles	15.000 cycles	20.000 cycles
Pumice Stone	2,61	3,04	4,05	4,22
ECHO WHITES	2,53	2,94	4,21	4,38
SWE (Stone enzyme)	2,33	2,89	3,96	4,34
PMN Nebulisation	4,57	6,96	9,15	11,55
PP Spray	2,27	3,21	3,99	4,81
PMN/PMK Spray	15,46	-	-	-

As seen in Figure 6, the mass loss ratio values of SWE, ECHO WHITES and PP Spray processes were close to those of the pumice stone process. Therefore, it would be appropriate to prefer the sustainable SWE and ECHO WHITES processes among these processes.

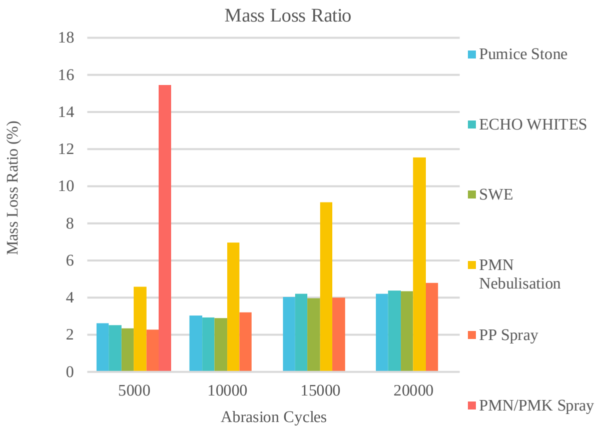

Figure 6. Mass loss ratio values of fabrics after abrasion resistance test.

On the other hand, the mass loss ratio value of the PMN nebulisation process is high, but it does not suffer any degradation until 20000 cycles. When the fabric treated with PMN/PMK Spray was examined at 5000 cycles at abrasion test, it was seen that the sample disintegrated and the test was terminated. The disintegration can also be observed in microscopic views in Figure 2. Besides, in the mass measurements after the processes, the highest mass loss ratio value was observed in this fabric (Figure 3). Statistical analysis show that there is a statistically significant difference for the mass loss ratios after abrasion resistance test according to washing processes and level of abrasion cycles (Table 6).

Table 6. The one-way analysis of variance table for the results.

Property	Factor	F	p-values
Mass loss ratio after abrasion resistance test	Washing processes	23,785	0,000*
	Level of abrasion cycles	6,250	0,001*
Bending rigidity	Washing processes	4,578	0,001*

*: Statistically significant for α=0.05.

Table 7. Independent samples T-Test results for the values.

		Levene's Test for Equality of Variances		t-test for Equality of Means
		F	Sig.	Sig. (2-tailed)
Property	Factor			
Bending rigidity	Fabric direction	1,342	0,252	0,001*

*: Statistically significant for α=0.05.

Besides, results of multiple comparisons of washing methods show that significant difference occur only in PMN Nebulisation from other washing methods. In addition, when the statistical analysis was examined in two groups as conventional and sustainable washing methods, it was observed that the difference between the methods was also found to be statistically significant. PMN/PMK Spray method was not included in the statistical analysis of abrasion property because abrasion test of this method was not completed.

4. Conclusion and Discussion

In this study, conventional and sustainable fading and bleaching processes were applied on the denim fabrics to examine sustainable processes in denim washing. Besides the sustainable properties of these processes, it is aimed to determine the abrasion and bending performances of the denim fabrics subjected to these processes. In this context, abrasion resistance and bending rigidity tests were applied to denim fabrics.

According to the findings; bending rigidity values show that the effect of stone enzyme process SWE on fabric bending rigidity is similar to pumice stone, and in a sustainable sense, it can be said that stone enzyme process can be preferred in terms of bending rigidity. It can be stated that the bending rigidity values of ECHO WHITES and PMN nebulisation processes are slightly high, but they are at a usable level. Therefore, it can be said that these processes will not pose a problem in terms of bending rigidity when used in a sustainable manner. When we look at the two spraying processes that have local bleaching properties, it was observed that the bending rigidity value of the PMN/PMK Spray process, which stands out as sustainable, was lower than the PP Spray process. Otherwise it was observed that the denim fabric treated with PMN/PMK Spray process disintegrated after 5000 cycles at abrasion test. Therefore, it is recommended to try this process under different conditions such as lower chemical substance intensity, shorter spray process time, lower drying temperature and shorter drying process time. In addition, abrasion resistance test show that the mass loss ratio values of SWE, ECHO WHITES and PP Spray processes were close to those of the pumice stone process but while that of PMN nebulisation process is higher. It can be said that the obtained bending and abrasion results depend on the methods and conditions of the applied processes, as well as the chemicals or materials used. Looking at all these comments, considering both bending rigidity and abrasion resistance properties, it can be stated that SWE process, which is one of the sustainable process among these processes with stone enzyme, is the optimum option with similar values to pumice stone. In addition, it seems that ECHO WHITES process also is preferable. PMN nebulisation process may also be preferred, considering that abrasion values are higher.

Since there is a lot of water and chemical consumption in denim washing processes, sustainability studies on this subject are of great importance. As examined in this study, if it provides fabric properties at acceptable levels, the use of sustainable methods that do not produce waste in the form of sludge, minimize water use, also enable water-free processes and increase the use of more environmentally friendly chemicals, should be supported.

For future studies, sustainable processes in denim fabrics with different properties can be tested for different fabric properties. As an alternative to conventional materials, artificial stones and recycled materials can be used for more sustainable processes. For a denim fabric with optimum properties, sustainable processes with less resource consumption can be determined.

Ethics committee approval and conflict of interest statement

Ethics committee approval is not required for this article. There is no conflict of interest with any person/institution in this study.

Acknowledgement

The author thanks to Dr. Ümit CIKCIK, Ahmet Bülbül and ARM Tekstil Boya Kimya San. ve Tic. Ltd. Şti. for supplying denim fabrics.

References

[1] Campaign, C. C. 2011). Fashion Victims-A Report on Sandblasted Denim.

[2] Khoa, T. H. D., Hien, N. T. T., Trung, B. Q., Thach, D. S., & Van Tuong, N. 2021. Application of CO2 laser technology in creating whisker and handsand effects on denim wash. Journal of Science Technology and Food, Vol.21(2), p.62–72.

[3] Periyasamy, A. P., & Militky, J. 2017. Denim processing and health hazards. In Muthu, S. S. (Ed.), Sustainability in denim (1st ed., pp. 161–196). Elsevier. http://doi.org/10.1016/B978-0-08-102043-2.00007-1.

[4] Periyasamy, A. P., & Periyasami, S. 2023. Critical Review on Sustainability in Denim: A Step toward Sustainable Production and Consumption of Denim. ACS Omega, Vol.8(5), p.4472-4490. https://doi.org/10.1021/acsomega.2c06374.

[5] Doshi, R., & Shelke, V. 2001. Enzymes in textile industry-An environment-friendly approach. Indian Journal of Fibre & Textile Research, 26, p.202-205.

[6] Körlü, A. E., Yapar, S., Perinçek, S., Yılmaz, H., & Bağıran, C. 2015. Dye removal from textile waste water through the adsorption by pumice used in stone washing. Autex Research Journal, Vol.15(3), 158-163. https://doi.org/10.1515/aut-2015-0012.

[7] Shibly, M. A. H., Hoque, M. M., & Miah, S. 2021. Development of eco-friendly denim fabric washing by natural resources. International Journal of Textile Science, Vol.10(1), p.1-6. DOI: 10.5923/j.textile.20211001.01.

[8] Sağırkaya, F. S. 2021. Denim'de sürdürülebilir uygulamalar [Sustainable practises in denim]. [Master dissertation, Pamukkale University].

[9] Arjun, D., Hiranmayee, J., & Farheen, M. N. 2013. Technology of industrial denim washing: Review. International Journal of Industrial Engineering & Technology, Vol.3(4), p.25–34.

[10] Köksal, F. 2015. Denim yıkamada renk varyasyonlarının nedenlerinin incelenmesi [The investigation of the causes of color variations in denim laundry (washing) processes]. [Master dissertation, Tekirdağ Namık Kemal University].

[11] Tarhan, M. 2005. Eskitme yöntemlerinin denim mamullerin performans özelliklerine etkisi [Effect of worn out methods on denim products performance properties]. [Master dissertation, Dokuz Eylül University].

[12] Bechtold, T., Maier, P., & Schrott, W. 2005. Bleaching of indigo-dyed denim fabric by electrochemical formation of hypohalogenites in situ. Coloration Technology, Vol.121(2), p.64–68. https://doi.org/10.1111/j.1478-4408.2005.tb00252.x.

[13] Du, W., Zuo, D., Gan, H., & Yi, C. 2019. Comparative study on the effects of laser bleaching and conventional bleaching on the physical properties of indigo kapok/cotton denim fabrics. Applied Sciences, Vol.9(21), p.4662. https://doi.org/10.3390/app9214662.

[14] Siddique, A., Hussain, T., Ibrahim, W., Raza, Z. A., Abid, S., & Nazir, A. 2017. Response surface optimization in discharge printing of denim using potassium permanganate as oxidative agent. Clothing and Textile Research Journal, Vol.35(3), p.204–214. https://doi.org/10.1177/0887302X17701600.

[15] [Choudhury, A. K. R. 2017. Environmental impacts of denim washing. In Muthu, S. S. (ed.), Sustainability in Denim (1st ed., pp. 49–81). Elsevier. https://doi.org/10.1016/B978-0-08-102043-2.00002-2.

[16] Rodríguez-Couto, S. 2012. Laccases for denim bleaching: an eco-friendly alternative. Sigma, 1, p.10–12.

[17] Ben Hmida, S., & Ladhari, N. 2016. Study of parameters affecting dry and wet ozone bleaching of denim fabric. Ozone: Science & Engineering, Vol.38(3),p.175–180. https://doi.org/10.1080/01919512.2015.1113380.

[18] He, Z., Li, M., Zuo, D., & Yi, C. 2018. The effect of denim color fading ozonation on yarns. Ozone: Science & Engineering, Vol.40(5), p.377-384.

[19] Cheung, H. F., Kan, C. W., Yuen, C. W. M., Yip, J., & Law, M. C. (2013). Colour fading of textile fabric by plasma treatment. Journal of Textiles. https://doi.org/10.1155/2013/214706.

[20] Samanta, K. K., Basak, S., & Chattopadhyay, S. K. 2017. Environmentally friendly denim processing using water-free technologies. In Muthu, S. S. (Ed.), Sustainability in denim (1st ed., pp. 319–348). Elsevier. http://doi.org/10.1016/B978-0-08-102043-2.00012-5.

[21] Khalil, E. 2015. Sustainable and ecological finishing technology for denim jeans. AASCIT Communication, Vol.2(5), p.159-163.

[22] İvedi İ, Çay A. 2023. Use of Natural and Synthetic Materials in Denim Washing Process as an Alternative to Pumice Stone. Tekstil ve Konfeksiyon 33(1), 68-76.

[23] Alam, MR, Islam, T, Rahman, M, Antor, MAAN, Rahman, R, Tamanna, TA 2020. Sustainable denim fabric washing with post-used rubber shoe sole: An eco-friendly alternative of Pumice stone. Indian Journal of Science and Technology, Vol.13(48): p.4723-4731. https ://doi.org/10.17485/IJST/v13i48.1974.

[24] Khan MKR, Jintun S. 2021. Sustainability Issues of Various Denim Washing Methods. Textile & Leather Review, Vol.4(2), p.96-110. https://doi.org/10.31881/TLR.2021.01
[25] TS EN ISO 12947-3. Textiles - Determination of the abrasion resistance of fabrics by the Martindale method - Part 3: Determination of mass loss
[26] TS 1409. Stiffness determination of woven textiles.

DEU FMD 27(79) (2025) 38-45

Dokuz Eylül Üniversitesi Mühendislik Fakültesi Fen ve Mühendislik Dergisi
Dokuz Eylul University Faculty of Engineering Journal of Science and Engineering
Elektronik/Online ISSN: 2547-958X

RESEARCH ARTICLE / ARAŞTIRMA MAKALESI

Assessment of an Underground Dams Site Selection in İZMİR Province by Using MAIRCA and EDAS Methods

İZMİR İlinde Kurulacak Olan Bir Yeraltı Barajı için Uygun Lokasyonun MAIRCA ve EDAS Yöntemleri Kullanılarak Belirlenmesi

Muhammet Enes Akpınar [1*], **Mümin Emre Şenol** [2]

[1] İzmir Bakırçay Üniversitesi İktisadi ve İdari Bilimler Fakültesi İşletme Bölümü, İzmir, TÜRKİYE
[2] Manisa Celal Bayar Üniversitesi Mühendislik ve Doğa Bilimleri Fakültesi Endüstri Mühendisliği Bölümü, Manisa, TÜRKİYE

Corresponding Author / Sorumlu Yazar *: enes.akpinar@bakircay.edu.tr

Abstract

Underground dam site selection is the process of selecting locations for dams constructed for the storage and management of groundwater to ensure the sustainable use of water resources. Underground dams store groundwater by utilizing underground aquifers, enabling more efficient and effective utilization of water resources. Particularly, the importance of underground dams has been observed to increase with global warming. They play a crucial role in various aspects, especially during periods of drought, in meeting agricultural irrigation and drinking water needs, among others. The construction of underground dams requires the simultaneous consideration of numerous criteria, thus turning the construction process into a decision-making problem. This decision problem is referred to in the literature as a multi-criteria decision-making (MCDM) problem. In this study, the site selection problem for a underground dam to be established in the province of Izmir has been addressed. In the problem at hand, there are five different alternatives consisting of districts within the province of Izmir and ten different criteria. These criteria and alternatives were determined by experts. In the study, the weights of the criteria were determined using the MAIRCA method, and the EDAS method was used for the selection of alternative locations. As a result of the study, Kınık district was identified as the most suitable alternative among the selected districts.

Keywords: *Underground dam, site selection, multi-criteria decision making, MAIRCA method, EDAS method*

Öz

Yer altı barajı yer seçimi, su kaynaklarının sürdürülebilir şekilde kullanılmasını sağlamak amacıyla yeraltı suyunun depolanması ve yönetimi için yapılan barajların yer seçim sürecidir. Yer altı barajları, yeraltı suyunun doğal rezervuarları olan yeraltı su tabakalarını depolayarak, su kaynaklarının daha verimli ve etkin bir şekilde kullanılmasını sağlar. Özellikle küresel ısınma ile yer altı barajlarının öneminin arttığı gözlemlenmiştir. Özellikle kuraklığın olduğu dönemlerde, başta tarımsal sulama ve içme suyu ihtiyaçlarını karşılamak gibi birçok konuda hayati bir rol oynadığı bilinmektedir. Yer altı barajlarının inşası için çok fazla kriterin eş zamanlı olarak dikkate alınması gerekmektedir. Bu nedenle, inşa süreci bir seçim problemine dönüştürmektedir. Söz konusu seçim problemi ise, literatürde çok kriterli karar verme (ÇKKV) problemi olarak geçmektedir. Bu çalışmada, İzmir ilinde kurulacak bir yer altı barajı için yer seçim problemi ele alınmıştır. Ele alınan problemde, İzmir ilindeki ilçelerden oluşan beş farklı alternatif ve on farklı kriter yer almaktadır. Bu kriterler ve alternatifler karar vericiler tarafından belirlenmiştir. Çalışmada, kriterlerin ağırlıkları MAIRCA yöntemi ile belirlenmiş, alternatif konumların seçiminde ise EDAS yöntemi kullanılmıştır. Çalışma sonucunda belirlenen alternatif ilçeler arasından Kınık ilçesi en uygun alternatif olarak belirlenmiştir.

Anahtar Kelimeler: *Yer altı barajı, yer seçimi, çok kriterli karar verme, MAIRCA yöntemi, EDAS yöntemi*

1. Introduction

Global warming and drought have become increasingly pressing issues worldwide in recent years. Among the possible effects of this problem are the reduction of water resources, decreased agricultural production, ecosystem degradation, increased waterborne diseases, and harm to wildlife. These effects pose serious threats to both humans and natural life [1].

Increased greenhouse gas emissions, deforestation, industrialization, and the usage of fossil fuels are some of the factors contributing to global warming. These elements raise the amount of greenhouse gases in the atmosphere, which raises the earth's temperature. Temperature increases, in turn, increase natural disasters such as droughts and increase the demand for water resources.

Drought, which is a natural consequence of global warming, is a condition that arises from prolonged hot and dry weather conditions. The problem of drought is increasing worldwide, and among its most prominent effects are decreased agricultural production, decreased water resources, and ecological degradation. Drought, especially in regions such as Africa, the Middle East, and Southeast Asia, lower people's quality of life and leads to food security issues [2].

DOI: https://doi.org/10.21205/deufmd.2025277906

Geliş Tarihi / Received: 10.06.2023
Kabul Tarihi / Accepted: 27.03.2024

International cooperation and efforts are crucial to solving the problems of global warming and drought. Reducing greenhouse gas emissions, putting money into renewable energy sources, using water resources sustainably, and taking water conservation measures are a few of these initiatives. These efforts will contribute to both improving people's quality of life and preserving natural life.

Underground dams can be defined as structures built to collect and store groundwater. These dams provide water by using groundwater during periods of low precipitation, thereby reducing the demand for surface water sources during drought periods. Additionally, underground dams contribute to the sustainable use of water since they cause less evaporation and loss than surface water sources [3].

Because underground dams have less of an influence on the environment than surface dams, they are also favored for building. During the construction of surface dams, forests, and habitats are destroyed, agricultural land is damaged, and the lives of indigenous people are negatively affected. However, underground dams minimize these negative effects and contribute to the preservation of natural life. In summary, underground dams offer a solution to the effects of natural disasters such as global warming and drought, promote the sustainable use of water resources, and contribute to the preservation of natural life. Therefore, the construction and use of underground dams are of great importance in terms of the sustainability of water resources [4].

This study addresses an underground dam selection problem. In the problem addressed, a real-life application is made using Multi-Criteria Decision Making (MCDM) techniques. Ten different criteria and five alternative locations were identified by decision-makers in the study. MAIRCA (Multi Atributive Ideal-Real Comparative Analysis) method was used to define the weights of ten criteria. Finally, the results were evaluated using EDAS (Evaluation Based on Distance from Average Solution) method, and the most appropriate alternative was identified. These methods are used to optimize problems. Many different methods are used in the field of optimization [5-8]. In this study, the EDAS method is preferred due to its advantages such as transparency, robustness, flexibility, and not requiring internal inference and reference points when compared to other methods. Besides, MAIRCA method is selected because of its assessing alternative options by comparing their theoretical and empirical ratings. It determines the difference or distance between the actual empirical ratings and the ideal alternatives, utilizing both theoretical and empirical evaluations.

1.1. Literature Review

Numerous studies have been conducted to address the complexity of selecting suitable sites for constructing subsurface dams worldwide. The decision-making process in this domain is intricate due to the involvement of various qualitative and quantitative factors. Consequently, MCDM methods can be employed to tackle this challenge.

Geographic Information Systems (GIS) and MCDM serve as effective tools for spatial analysis and decision-making [9]. MCDM encompasses both conventional and specialized techniques that aid decision-makers in handling the complexities associated with large volumes of intricate information [10].

Finding suitable construction sites for subterranean dams is the main problem because many criteria and aspects need to be considered. Therefore, decision models that account for the significance of various criteria in selecting appropriate dam construction sites are crucial [11,12].

Various methods have been used in the literature to choose ideal sites for dam construction [13]. One of these studies, Rahman et al. [14] focuses on the application of weighted overlay analysis in ArcGIS for selecting an optimal site for a water reservoir. The researchers proposed to select the most suitable sites for the reservoir by integrating multiple criteria using GIS techniques. The study used a weighted overlay methodology, in which weights are given to several variables according to their relative importance. Various criteria, such as land use, slope, soil type, and proximity to water sources, were considered during the analysis. Using ArcGIS software, the researchers combined and analyzed the weighted criteria to generate a suitability map for potential reservoir sites. The integration of multiple criteria and the spatial analysis capabilities of GIS provided a systematic approach to decision-making in identifying suitable locations for water infrastructure projects.

Ajibade et al. [15] utilized integrated techniques of remote sensing (RS) and GIS to analyze and assess potential dam sites. Remote sensing data, such as satellite imagery, was used to extract relevant information about the landscape, including land cover, topography, and hydrological features. GIS tools and spatial analysis techniques were employed to process and integrate the data layers. The findings of the study demonstrated the effectiveness of integrating RS and GIS techniques for dam site selection. The integration of spatial data and analysis capabilities of GIS, along with the information obtained from RS, proved valuable in identifying areas that would be appropriate for building dams.

In another study, Dos Anjos and Cabral [16] aimed to decide appropriate locations for the construction of small dams/reservoirs to enhance water availability and promote agricultural development in the region. The study employed site location analysis techniques to determine optimal sites for small dams/reservoirs. Various factors such as topography, soil characteristics, land use, and hydrological data were considered as criteria for the analysis. The researchers integrated these criteria using GIS and MCDM methods.

In the literature, researchers also utilized MCDM techniques to select suitable places for underground dam construction. For example, in one of the studies, Jozaghi et al. [17] aims to compare the Analytic Hierarchy Process (AHP) and Technique for Order of Preference by Similarity to Ideal Solution (TOPSIS) techniques for dam site selection. The researchers focused on evaluating and comparing the suitability of different potential dam sites by considering multiple criteria. In that study geological factors, hydrological factors, socio-economic factors, and environmental factors are considered. These criteria were integrated into a GIS framework to facilitate the analysis and decision-making process. Findings of the study contribute to understanding the comparative performance of the AHP and TOPSIS techniques in dam site selection. The research demonstrates the potential of GIS-based MCDM methods for supporting decision-making processes in selecting optimal dam sites. In another study, Tsiko and Haile [18] focuses on the integration of fuzzy logic, AHP and GIS model to identify optimal sites for water reservoirs. The study utilized GIS to manage and analyze spatial data related to land cover, slope, drainage patterns, and proximity to water sources. Fuzzy logic was integrated into the analysis to handle the vagueness and ambiguity associated with the criteria. Through pairwise comparisons, the weights of the criteria and their relative relevance were established using the AHP approach. To evaluate the criteria and determine their importance in the selection process, expert opinions were requested. The study's conclusions demonstrated how well GIS, fuzzy logic, and AHP work together to pinpoint the best locations for water reservoirs. The integrated approach facilitated a comprehensive evaluation of multiple criteria, considering both spatial and non-spatial factors, and provided decision-makers with valuable information for informed decision-making in water resource management and infrastructure development. In order to make the process of choosing potential locations for dam construction easier, Minatour et al. [19] sought to offer a thorough framework that integrates several criteria and methods. The goal of this project is to create an integrated MCDM method for choosing a dam location that includes both fuzzy logic and group decision-making. The fuzzy AHP approach was expanded by the researchers to account for group decision-making, and it was then integrated with the VIKOR method. By combining these approaches, it was possible to consider decision-makers subjective opinions and include uncertainty by utilizing fuzzy notions while choosing a site. The group fuzzy AHP technique was used to calculate the weights of various criteria, and VIKOR was utilized to rank the possibilities.

There are numerous MCDM techniques in the related literature. MAIRCA and EDAS are in the group of these techniques. Despite the MAIRCA methos is relatively new, it has received significant attention in the literature. Gigović et al. [20] used the GIS along with the DEMATEL (Decision Making Trial and Evaluation Laboratory), Analytic Network Process (ANP), and MAIRCA methods to determine suitable locations for an ammunition depot. The study evaluated eight locations based on six criteria. In another study, Pamučar et al. [21] assessed bidders in a public procurement tender using interval rough set-based DEMATEL, ANP, and MAIRCA methods. Chatterjee et al. [22] evaluated supplier performance considering green supply chain criteria using rough set-based MAIRCA ANP and DEMATEL methods. Badi and Ballem [23] used rough set-based BWM (Best-Worst Method) and MAIRCA methods to identify the optimal supplier. Pamucar et al. [24] applied DEMATEL and MAIRCA methods to decide where to put a logistics center. Pamučar et al. [25] evaluated water barriers using the interval-valued fuzzy rough set-based MAIRCA method. Arsic et al. [26] used the BWM and rough set-based MAIRCA methodologies to evaluate a restaurant's menu. In Turkish studies related to MAIRCA, Ekinci and Can [27] assessed operators' ergonomic risks using the CRITIC (Criteria Importance Through Intercriteria Correlation) and MAIRCA methods. Haq et al. [28] used MAIRCA method to select sustainable material. Kıran [29] evaluated countries' occupational health and safety performances using the MAIRCA method. Moreover, MAIRCA functions as a valuable mathematical tool and solution approach, providing the flexibility to integrate with other methods. Besides, numerous studies conducted after the EDAS method's creation have attempted to increase its application and reliability by incorporating various uncertainty sets in order to successfully handle challenging real-world issues involving qualitative data.

For example, Yalcin and Uncu [30] investigate the suitability of the EDAS method for the selection of industrial robots. They aim to address the complex decision-making process involved in selecting the most suitable industrial robot among various alternatives. They propose the use of the EDAS method as a MCDM tool to evaluate and rank the alternatives based on multiple criteria. In another study, Veskovic et. al. [31] explores the application of a combined approach using the EDAS and AHP method for evaluating logistics processes. The study applies the combined AHP-EDAS method to evaluate logistics processes in a real-world context. While the EDAS technique is used to assess and rank the alternatives based on their distances from the average solution, the AHP approach is used to determine the weights of various criteria, representing their relative relevance.

To overcome the challenges associated with type-1 fuzzy sets, a novel version of the EDAS methodology was introduced by Kahraman et al. [32]. This modified approach incorporates intuitionistic fuzzy sets, which provide a more advanced framework for addressing the location selection of solid waste disposals. By utilizing the concepts of intuitionistic fuzzy sets, the enhanced EDAS method offers an improved methodology for dealing with the complexities and uncertainties associated with this decision-making problem. Darwis et al. [33] used EDAS method in the selection of the best student. He et. al. [34] propose an extended version of the EDAS method to handle MCDM problems in the context of green supplier selection. The researchers focus on the challenges of decision-making when dealing with probabilistic uncertain linguistic information, which often occurs in real-world situations. They develop an enhanced EDAS method that incorporates probabilistic uncertain linguistic information to enable more accurate and reliable decision-making.

MAIRCA Method

The MAIRCA method, which utilizes linear normalization and possesses a straightforward mathematical framework, is introduced by Pamucar and Lukovac [35]. The core focus of MAIRCA revolves around assessing the differences between theoretical and actual outcomes. Its prominent characteristic is the utilization of a unique linear normalization algorithm that generates reliable results. The main steps of the MAIRCA method include the following:

Step 1. Construct the decision matrix:

Identify the criteria and alternatives.

Create a decision matrix (X) with rows representing alternatives and columns representing criteria.

$$X = \begin{bmatrix} X_{11}\, X_{12} \dots X_{1n} \\ X_{21}\, X_{22} \dots X_{2n} \\ \dots\dots\dots\dots\dots\dots \\ X_{m1}\, X_{m2} \dots X_{mn} \end{bmatrix}$$

$X_{ij}, i = 1,2,\dots,n; j = 1,2,\dots,m$

Step 2. Determine preferences for the alternatives:

The MAIRCA method assumes that decision-makers are neutral in their preferences for selecting alternatives, indicating that all proposed alternatives are considered equally important. The method does not consider any assigned probability values for an alternative selection.

$$PA_i = \frac{1}{m},\ \sum_{i=1}^{m} PA_i \qquad (1)$$

Step 3. Create the theoretical ranking matrix:

The theoretical ranking matrix is calculated by using the following equation.

$$T_p = PA_i\left[t_{p1}\, t_{p2}\ \dots\ t_{p1n}\right] = PA_i[PA_1W_1\ PA_2W_2 \dots PA_nW_n] \qquad (2)$$

Step 4. Create the real ranking matrix:

The real ranking matrix is calculated by using the following equations, use Equation 3 for the benefit type criterion and Equation 4 for the cost type criterion.

$$t_{rij}=t_{pij} * \frac{(X_{ij}-X_{min})}{(X_{max}-X_{min})} \qquad (3)$$

$$t_{rij}=t_{pij} * \frac{(X_{max}-X_{ij})}{(X_{max}-X_{min})} \qquad (4)$$

$$T_r = \begin{bmatrix} t_{r11}\ t_{r12} \cdots t_{r1n} \\ t_{r21}\ t_{r22} \cdots t_{r2n} \\ \cdots\cdots\cdots\cdots\cdots\cdots \\ t_{rm1}\ t_{rm2} \cdots t_{rmn} \end{bmatrix} \quad (5)$$

Step 5. Calculate the Total Gap Matrix:

The total difference matrix is derived by subtracting the theoretical evaluation matrix (Tp) from the actual evaluation matrix (Tr). This process involves subtracting the corresponding values in each cell of Tp from the corresponding values in the Tr to determine the differences between the theoretical and actual assessments for each attribute.

$$G = T_p - T_r = \begin{bmatrix} g_{11}\ g_{12} \cdots g_{1n} \\ g_{21}\ g_{22} \cdots g_{2n} \\ \cdots\cdots\cdots\cdots\cdots\cdots \\ g_{m1}\ g_{m2} \cdots g_{mn} \end{bmatrix} = \begin{bmatrix} t_{p11} - t_{r11}\ t_{p12} - t_{r12} \cdots t_{p1n} - t_{r1n} \\ t_{p21} - t_{p21}\ t_{r22} - \ t_{r22} \cdots t_{p2n} - t_{r2n} \\ \cdots\cdots\cdots\cdots\cdots\cdots \\ t_{pm1} - t_{rm1}\ t_{pm2} - \ t_{rm2} \cdots t_{pmn} - t_{rmn} \end{bmatrix} \quad (6)$$

Step 6. Calculate the criteria function and obtain the rankings:

The criterion function values for each alternative are calculated individually by summing up the difference values, as depicted in Equation 7. This process involves adding the respective difference values across all attributes for a particular alternative, resulting in a single criterion function value that represents the overall performance or evaluation of that alternative.

$$Q_i = \sum_{j=1}^{n} g_{ij} \quad (7)$$

The alternative with the smallest value is determined as the best alternative.

EDAS Method

In a groundbreaking contribution to the literature on Multi-Criteria Decision-Making (MCDM) methods, Keshavarz Ghorabaee et al. [36] introduced the EDAS method as a ranking approach for complex decision-making problems that involve prioritizing multiple criteria among a set of alternatives. The steps of the EDAS method is as follows:

Step 1. Construct the decision matrix:

Identify the criteria and alternatives.

Create a decision matrix (X) with rows representing alternatives and columns representing criteria.

Step 2. Calculate the average solution:

Compute the average value for each criterion across all alternatives.

Calculate the average solution vector (AS) using the equation:

$$\mathrm{AV_j} = \frac{\sum_{i=1}^{n} X_{ij}}{n} \quad (8)$$

where $\mathrm{AV_j}$ is the average solution value for the j-th criterion, n is the total number of alternatives, and $\mathrm{X_{ij}}$ is the value of the i-th alternative on the j-th criterion.

Step 3. Compute the positive distance matrix (PDA) and negative distance matrix (NDA) from the average solution:

If criteria j is a benefit criteria,

$$\mathrm{PDA_{ij}} = \frac{\max(0,(X_{ij} - \mathrm{AV}_j)}{\mathrm{AV}_j} \quad (9)$$

$$\mathrm{NDA_{ij}} = \frac{\max(0,(\mathrm{AV}_j - X_{ij})}{\mathrm{AV}_j} \quad (10)$$

If criteria j is a cost criterion,

$$\mathrm{PDA_{ij}} = \frac{\max(0,(\mathrm{AV}_j - X_{ij})}{\mathrm{AV}_j} \quad (11)$$

$$\mathrm{NDA_{ij}} = \frac{\max(0,(x_{ij} - \mathrm{AV}_j)}{\mathrm{AV}_j} \quad (12)$$

where AV_j is the average solution value for the j-th criterion and $\mathrm{X_{ij}}$ is the value of the i-th alternative on the j-th criterion.

Step 4. Determine the weighted sum of PDA and NDA for all alternatives:

Assign weights to each criterion to reflect their relative importance.

$$\mathrm{SP_i} = \sum_{i=1}^{n} \mathrm{W}_j PDA_{ij} \quad (13)$$

$$\mathrm{SN_i} = \sum_{i=1}^{n} \mathrm{W}_j NDA_{ij} \quad (14)$$

where W_j is the weight of the j-th criterion.

Step 5. Normalize the SP and SN values:

$$\mathrm{NSP_i} = \frac{(\mathrm{SP}_i)}{\max(\mathrm{SP}_i)} \quad (15)$$

$$\mathrm{NSN_i} = 1 - \frac{(\mathrm{SN}_i)}{\max(\mathrm{SN}_i)} \quad (16)$$

Step 6. Calculate the Appraisal Score (AS) value of all alternatives.

$$AS_i = \frac{1}{2}(\mathrm{NSP}_i + \mathrm{NSN}_i) \quad (17)$$

Step 7. Rank the alternatives:

Rank the alternatives based on their AS values.

The alternative with the highest AS value is considered the most favorable.

Through its distinctive normalization procedure, the EDAS method sets itself apart from other conventional techniques like TOPSIS and VIKOR. The best alternative is typically determined by how close it is to the ideal solution and how far it is from the anti-ideal solution, but in practical decision-making situations, having a lower distance from the ideal solution and a higher distance from the anti-ideal solution does not always mean that it is the best option. The best option is chosen using the EDAS method, which instead uses an average solution-based normalizing strategy. The EDAS method is a useful tool for handling complicated decision-making problems because of its departure from conventional methods.

The paper utilizes the EDAS method to evaluate and rank sites for an underground dam construction.

2. Application

In this part, an underground dam site selection problem in Izmir is solved with the proposed method. In this way, the applicability of the integrated method is illustrated. 3 experts determine 10 criteria namely, amount of precipitation (C_1), groundwater level (C_2), flow gradient (C_3), flow distance (C_4), alluvial texture (C_5), distance to villages and agricultural lands (C_6), area of agricultural lands affected by the project(C_7), fault line distance (C_8), engineering opportunities (C_9), evaporation rate (C_{10}) and 5 alternatives namely, Bergama (A_1), Kınık (A_2), Bayındır (A_3), Tire (A_4) and Kiraz (A_5). While C_7 and C_{10} are cost criteria, the others are benefit criteria. These criteria have been determined as the criteria taken into consideration by companies that will invest in dams. At first experts fill in the pairwise comparison matrixes. The pairwise comparison matrixes are illustrated in Table 1-Table3.

Then the arithmetic mean of these three pairwise comparison matrixes is computed. In the pairwise comparison matrix, experts are recommended to use a scale ranging from 1 to 10. In this suggested scale, 1 represents the lowest value, while 10 represents the highest value. The average pairwise comparison matrix is illustrated in Table 4.

After aggregating the expert opinions, the MAIRCA method is utilized the find criteria weights. The obtained criteria weights are given in Table 5.

Table 1. Pairwise comparison matrix of Expert 1.

Criteria	C_1	C_2	C_3	C_4	C_5	C_6	C_7	C_8	C_9	C_{10}
C_1	-	1	1	9	9	5	3	4	5	4
C_2		-	1	5	4	6	5	5	3	3
C_3			-	5	4	3	2	5	2	2
C_4				-	5	5	3	2	2	4
C_5					-	5	4	7	9	10
C_6						-	1	5	3	5
C_7							-	1	8	10
C_8								-	2	3
C_9									-	9
C_{10}										-

Table 2. Pairwise comparison matrix of Expert 2.

Criteria	C_1	C_2	C_3	C_4	C_5	C_6	C_7	C_8	C_9	C_{10}
C_1	-	10	9	8	9	4	5	3	4	4
C_2		-	9	4	3	6	4	4	3	2
C_3			-	4	3	2	1	4	2	2
C_4				-	4	4	2	1	1	3
C_5					-	4	3	6	8	9
C_6						-	1	4	2	4
C_7							-	9	7	9
C_8								-	1	2
C_9									-	8
C_{10}										-

Table 3. Pairwise comparison matrix of Expert 3

Criteria	C_1	C_2	C_3	C_4	C_5	C_6	C_7	C_8	C_9	C_{10}
C_1	-	8	9	7	8	3	1	3	3	2
C_2		-	8	3	3	4	3	3	1	1
C_3			-	3	2	1	2	3	2	2
C_4				-	4	3	2	2	1	2
C_5					-	3	2	5	7	8
C_6						-	2	4	1	3
C_7							-	8	7	8
C_8								-	2	2
C_9									-	6
C_{10}										-

Table 4. Average pairwise comparison matrix

Criteria	C_1	C_2	C_3	C_4	C_5	C_6	C_7	C_8	C_9	C_{10}
C_1	-	9,33	9,33	8	8,66	4	3	3,33	4	3,33
C_2		-	9	4	3,33	5,33	4	4	2,33	2
C_3			-	4	3	2	1,66	4	2	2
C_4				-	4,33	4	2,33	1,66	1,33	3
C_5					-	4	3	6	8	9
C_6						-	1,33	4,33	2	4
C_7							-	9	7,33	9
C_8								-	1,66	2,33
C_9									-	7,66
C_{10}										-

Table 5. Criteria weights

Criteria	Weight	Criteria	Weight
C_1	0.0367	C_6	0.0973
C_2	0.0806	C_7	0.0851
C_3	0.0934	C_8	0.0927
C_4	0.0972	C_9	0.0998
C_5	0.0947	C_{10}	0.0901

Experts also evaluate the alternatives. Experts’ decision matrixes are depicted in Table 6-7-8 respectively.

To aggregate experts’ decision matrixes, geometric mean of the matrixes is computed. The aggregate decision matrix is given in Table 9.

After that, EDAS method is utilized to rank the alternatives. The obtained AS values are illustrated in Table 10. The alternative with the highest value is selected as the best alternative.

Table 6. Expert 1 Decision Matrix

Criteria	A_1	A_2	A_3	A_4	A_5
C_1	8	3	10	9	5
C_2	7	3	9	9	4
C_3	7	1	9	8	4
C_4	6	3	10	8	5
C_5	7	2	8	8	4
C_6	5	4	9	9	4
C_7	5	2	10	7	3
C_8	5	1	10	8	5
C_9	6	2	9	7	4
C_{10}	6	1	9	7	3

Table 7. Expert 2 Decision Matrix

Criteria	A_1	A_2	A_3	A_4	A_5
C_1	7	4	9	10	6
C_2	8	1	9	8	5
C_3	7	2	7	8	5
C_4	6	2	9	9	4
C_5	7	1	8	7	3
C_6	6	3	10	8	5
C_7	9	3	10	8	4
C_8	5	2	10	9	4
C_9	5	1	9	7	3
C_{10}	5	2	10	9	5

Table 8. Expert 3 Decision Matrix

Criteria	A_1	A_2	A_3	A_4	A_5
C_1	7	1	10	8	5
C_2	6	3	10	9	6
C_3	9	2	9	10	6
C_4	8	2	10	9	7
C_5	8	3	10	9	5
C_6	6	1	9	8	5
C_7	5	5	9	8	4
C_8	7	2	8	7	3
C_9	5	3	9	9	5
C_{10}	5	1	9	8	5

Table 9. Aggregate Decision Matrix

	A_1	A_2	A_3	A_4	A_5
C_1	7.318611	2.289428	9.654894	8.962809	5.313293
C_2	6.952053	2.080084	9.321698	8.653497	4.932424
C_3	7.611663	1.587401	8.276773	8.617739	4.932424
C_4	6.603854	2.289428	9.654894	8.653497	5.192494
C_5	7.318611	1.817121	8.617739	7.958114	3.914868
C_6	5.646216	2.289428	9.321698	8.320335	4.641589
C_7	6.082202	3.107233	9.654894	7.651725	3.634241
C_8	5.593445	1.587401	9.283178	7.958114	3.914868
C_9	5.313293	1.817121	9.000000	7.611663	3.914868
C_{10}	5.313293	1.259921	9.321698	7.958114	4.217163

Table 10. Obtained AS Values and Ranking

Alternative	AS value	Rank
A1	0.4830	4
A2	0.5000	1
A3	0.4927	2
A4	0.4846	3
A5	0.4763	5

The alternative A2 is chosen to construct the underground dam.

3. Conclusion

Underground dams are widely acknowledged as facilities designed for storing water beneath the surface, particularly in regions with semi-arid climates. In areas where the utilization of surface water has reached sustainable levels, exploiting groundwater resources emerges as a favorable complementary option. Additionally, in arid regions where surface water is scarce or absent, groundwater serves as the sole available source for domestic needs. Presently, there is increasing emphasis on managing these resources in a sustainable manner. It is evident that establishing boundaries for the development and utilization of groundwater is crucial to ensure its long-term viability and prevent adverse environmental, economic, and social impacts. In the forthcoming decades, the sustainability of surface water resources is anticipated to become a pivotal concern, leading to an inevitable shift towards groundwater utilization.

This study addresses the problem of site selection for an underground dam. Multiple criteria decision-making methods are employed in this study. Firstly, three decision-makers are identified for the study. These individuals determine the criteria required for the selection of an underground dam site. The MAIRCA method is utilized to assign weights to the identified criteria. Subsequently, alternative locations for the dam site are determined using this method. The EDAS method is employed to evaluate the five different alternative locations. Based on the results of the EDAS method, the most suitable location among the five alternatives is selected. The purpose of using MAIRCA and EDAS is to fill the gap in this field because these methods have not been used before. Furthermore, as mentioned in the introduction section, both EDAS and MAIRCA have advantages compared to other methods, such as robustness, flexibility and transparency.

One constraint of this study is that the number of alternatives and experts relatively small. Additionally, future research could explore the use of fuzzy-based algorithms, apart from the methods employed in this study, to provide decision-makers with more flexibility in decision-making.

Author Contribution Statement

All authors are contributed to the paper equally and they have accepted responsibility for the entire content of this manuscript and approved its submission.

References

[1] Jamali, I.A., Olofsson, B., Mörtberg, U., 2013. Locating suitable sites for the construction of subsurface dams using GIS. Environmental Earth Sciences, Vol. 70, pp. 2511-2525.

[2] Kuriqi, A., Pinheiro, A.N., Sordo-Ward, A., Bejarano, M.D., Garrote, L., 2021. Ecological impacts of run-of-river hydropower plants—Current status and future prospects on the brink of energy transition. Renewable and Sustainable Energy Reviews, Vol. 142, p. 110833.

[3] Goran, H., Nilsson, Å., 1986. Ground-Water Dams for Rural-Water Supplies in Developing Countries. Groundwater, Vol. 24(4), pp. 497-506.

[4] Frankl, A., Nyssen, J., De Dapper, M., Haile, M., Billi, P., Munro, R.N., Poesen, J., 2011. Linking long-term gully and river channel dynamics to environmental change using repeat photography (Northern Ethiopia). Geomorphology, Vol. 129(3-4), pp. 238-251.

[5] Kaplan, G., Yildizel, S.A., Memiş, S., Öztürk, A.U., 2018. The optimization of calcareous fly ash-added cement containing grinding aids and strength-improving additives. Advances in Civil Engineering, 2018, pp. 1-9.

[6] Akpınar, M.E., 2021. Unmanned aerial vehicle selection using fuzzy choquet integral. Journal of Aeronautics and Space Technologies, Vol. 14(2), pp. 119-126.

[7] Yıldızel, S.A., Çalış, G., 2019. Design and optimization of basalt fiber added lightweight pumice concrete using taguchi method. Romanian Journal of Materials, Vol. 49(4), pp. 544–553.

[8] Yiğit, M.E., Akpınar, M.E., 2021. Rüzgar türbin kulesi alternatiflerinin çok kriterli karar verme yöntemleri ile değerlendirilmesi. Avrupa Bilim ve Teknoloji Dergisi, No. 23, pp. 386-393.

[9] El-Shirbeny, M.A., Abutaleb, K.A., 2018. Monitoring of water-level fluctuation of Lake Nasser using altimetry satellite data. Earth Systems and Environment, Vol. 2, pp. 367-375.

[10] Baban, S.M., Wan-Yusof, K., 2003. Modelling optimum sites for locating reservoirs in tropical environments. Water Resources Management, Vol. 17, pp. 1-17.

[11] Shirani, K., Dastjerdi, A.S., Rahnamarad, J., 2017. Integration of multi-criteria decision matrix and geographical information system to site selection for an underground dam. Electronic Journal of Geotechnical Engineering, Vol. 22, pp. 3669-3686.

[12] Talebi, A., Zahedi, E., Hassan, M.A., Lesani, M.T., 2019. Locating suitable sites for the construction of underground dams using the subsurface flow simulation (SWAT model) and analytical network process (ANP) (Case study: Daroongar watershed, Iran). Sustainable Water Resources Management, Vol. 5, pp. 1369-1378.

[13] Keskin, A.Ü., Demir, Ş.D., 2018. Amasya Değirmendere Barajında Sulama Alanı ve Baraj Yüksekliği Arasında Ekonomik Analiz. Dokuz Eylül Üniversitesi Mühendislik Fakültesi Fen ve Mühendislik Dergisi, Vol. 20(60), pp. 755-764.

[14] Rahman, N.F.A., Awangku, A.A.H., Tai, V.C., Mohammad, M., Haron, S.H., Khalid, K., Rasid, M., Sharif, S.M., 2021. Site selection of water reservoir based on weighted overlay in ArcGIS (Case study: Bachok, Kelantan). Scientific International (Lahore), Vol. 33(2), pp. 135–139.

[15] Ajibade, T.F., Nwogwu, N.A., Ajibade, F.O., Adelodun, B., Idowu, T.E., Ojo, A.O., Iji, J.O., Olajire, O.O., Akinmusere, O.K., 2020. Potential dam sites selection using integrated techniques of remote sensing and GIS in Imo State, Southeastern Nigeria. Sustainable Water Resources Management, Vol. 6(4), pp. 1–16.

[16] Dos Anjos Luís, A., Cabral, P., 2021. Small dams/reservoirs site location analysis in a semi-arid region of Mozambique. International Soil and Water Conservation Research, Vol. 9(3), pp. 381–393.

[17] Jozaghi, A., Alizadeh, B., Hatami, M., Flood, I., Khorrami, M., Khodaei, N., Ghasemi Tousi, E., 2018. A comparative study of the AHP and TOPSIS techniques for dam site selection using GIS: a case study of Sistan and Baluchestan province. Iran Geosciences, Vol. 8(12), p. 494.

[18] Tsiko, R.G., Haile, T.S., 2011. Integrating geographical information systems, fuzzy logic and analytical hierarchy process in modelling optimum sites for locating water reservoirs: A case study of the Debub District in Eritrea. Water, Vol. 3(1), pp. 254-290.

[19] Minatour, Y., Khazaie, J., Ataei, M., Javadi, A.A., 2015. An integrated decision support system for dam site selection. Scientia Iranica, Vol. 22(2), pp. 319–330.

[20] Gigović, L., Pamučar, D., Bajić, Z., Milićević, M., 2016. The combination of expert judgment and GIS-MAIRCA analysis for the selection of sites for ammunition depots. Sustainability, Vol. 8(4), p. 372.

[21] Pamučar, D., Mihajlović, M., Obradović, R., Atanasković, P., 2017. Novel approach to group multi-criteria decision making based on interval rough numbers: Hybrid DEMATEL-ANP-MAIRCA model. Expert Systems with Applications, Vol. 88, pp. 58-80.

[22] Chatterjee, K., Pamučar, D., Zavadskas, E.K., 2018. Evaluating the performance of suppliers based on using the R'AMATEL-MAIRCA method for green supply chain implementation in the electronics industry. Journal of Cleaner Production, Vol. 184, pp. 101-129.

[23] Badi, I., Ballem, M., 2018. Supplier selection using the rough BWM-MAIRCA model: A case study in pharmaceutical supplying in Libya. Decision Making: Applications in Management and Engineering, Vol. 1(2), pp. 16-33.

[24] Pamučar, D., Lukovac, V., Božanić, D., Komazec, N., 2018. Multi-criteria FUCOM-MAIRCA model for the evaluation of level crossings: Case study in the Republic of Serbia. Operational Research in Engineering Sciences: Theory and Applications, Vol. 1(1), pp. 108-129.

[25] Pamučar, D.S., Ćirović, G., Božanić, D., 2019. Application of interval valued fuzzy-rough numbers in multi-criteria decision making: The IVFRN-MAIRCA model. Yugoslav Journal of Operations Research, Vol. 29(2), pp. 221-247.

[26] Arsić, S.N., Pamučar, D., Suknović, M., Janošević, M., 2019. Menu evaluation based on rough MAIRCA and BW methods. Serbian Journal of Management, Vol. 14(1), pp. 27-48.

[27] Ekinci, E.B.M., Can, G.F., 2018. Algılanan İş Yükü ve Çalışma Duruşları Dikkate Alınarak Operatörlerin Ergonomik Risk Düzeylerinin Çok Kriterli Karar Verme Yaklaşımı ile Değerlendirilmesi. Ergonomi, Vol. 1(2), pp. 77-91.

[28] Haq, R.S.U., Saeed, M., Mateen, N., Siddiqui, F., Ahmed, S., 2023. An interval-valued neutrosophic based MAIRCA method for sustainable material selection. Engineering Applications of Artificial Intelligence, Vol. 123, p. 106177.

[29] Kıran, M.B., 2019. Ülke iş sağlığı ve güvenliği performanslarını değerlendirilmek amacıyla MAIRCA yönteminin dört farklı ağırlıklandırma yaklaşımı ile uygulanması. Master Tezi, Başkent Üniversitesi Fen Bilimleri Enstitüsü.
[30] Yalcin, N., Uncu, N., 2019. Applying EDAS as an applicable MCDM method for industrial robot selection. Sigma Journal of Engineering and Natural Sciences, Vol. 37(3), pp. 779–796.
[31] Vesković, S., Stević, Ž., Stojić, G., Rajilić, S., Vasiljević, M., 2016. Application of fuzzy AHP method for profit analysis of railway operators with PSO. In Conference Paper, RAILCON, Vol. 16.
[32] Kahraman, C., Keshavarz Ghorabaee, M., Zavadskas, E.K., Cevik Onar, S., Yazdani, M., Oztaysi, B., 2017. Intuitionistic fuzzy EDAS method: An application to solid waste disposal site selection. Journal of Environmental Engineering and Landscape Management, Vol. 25(1), pp. 1-12.
[33] Darwis, D., Sulistiani, H., Megawaty, D.A., Setiawansyah, S., Agustina, I., 2023. Implementation of EDAS Method in the Selection of the Best Students with ROC Weighting. Komputasi: Jurnal Ilmiah Ilmu Komputer dan Matematika, Vol. 20(2), pp. 112-125.
[34] He, Y., Lei, F., Wei, G., Wang, R., Wu, J., Wei, C., 2019. EDAS method for multiple attribute group decision making with probabilistic uncertain linguistic information and its application to green supplier selection. International Journal of Computational Intelligence Systems, Vol. 12(2), pp. 1361-1370.
[35] Pamucar, D.V., Lukovac, V.L., 2014. Selection of railway level crossings for investing in security equipment using hybrid DEMATEL-MAIRCA model. In Proceedings of the XVI International Scientific-expert Conference on Railways, Niš, Serbia, 9–10 October, pp. 89–92.
[36] Keshavarz Ghorabaee, M., Zavadskas, E.K., Olfat, L., Turskis, Z., 2015. Multi-criteria inventory classification using a new method of evaluation based on distance from average solution (EDAS). Informatica, Vol. 26(3), pp. 435-451.

DEU FMD 27(79) (2025) 46-53

Dokuz Eylül Üniversitesi Mühendislik Fakültesi Fen ve Mühendislik Dergisi
Dokuz Eylul University Faculty of Engineering Journal of Science and Engineering
Elektronik/Online ISSN: 2547-958X

RESEARCH ARTICLE / ARAŞTIRMA MAKALESI

Performance Comparison of Text Weighting Schemas on NMF-Based Topic Analysis

Metin Ağırlıklandırma Şemalarının NMF-Tabanlı Konu Analizi Alanında Başarımlarının Karşılaştırılması

Tolga Berber *, **Melek Eriş Büyükkaya**

Karadeniz Teknik Üniversitesi, Fen Fakültesi, Bilgisayar Bilimleri Bölümü, Trabzon, TÜRKİYE
Corresponding Author / Sorumlu Yazar *: tolga.berber@fen.ktu.edu.tr

Abstract

Nowadays, it is feasible to analyze text data that is being generated at an exponential rate by transforming it into a sparse matrix of big size using a certain weighting method. A comprehensive text weighting approach consists of three fundamental components: Term Frequency, Document Frequency, and Vector Normalization. The multiplication of these three components yields numerical values that indicate the significance of a word for a text. Nevertheless, the unprocessed state of these values is unsuitable for the semantic analysis of textual material. There are multiple techniques available for this objective, and Topic Analysis, which seeks to identify subjects discussed in extensive text collections, is one of these techniques. The Non-Negative Matrix Factorization (NMF) approach is commonly employed in topic analysis. It involves transforming an input matrix into the product of two or more matrices, using both random and deterministic beginning values. This study involved conducting tests on a dataset of 20,000 articles sourced from Wikipedia, the online encyclopedia, with the aim of investigating the impact of text weighting methods and initial value approaches commonly employed in the literature on the NMF method. The number of clusters to be used in the studies was determined using an analytical procedure, which employed an upper limit. The results indicate that the “lnc” and “nnc” weighting schemes yielded the highest performance in NMF. These findings demonstrate that employing the “lnc” or “nnc” weighting scheme will lead to more favorable outcomes in the domain of topic analysis.

Keywords: *Topic Analysis, Text-Weighting Schemas, Non-negative Matrix Factorization, Performance Comparison*

Öz

Günümüzde üstel bir şekilde üretilen metin verisinin analiz edilebilmesi, bu verinin belirli bir ağırlıklandırma yaklaşımı ile büyük boyutlu seyrek bir matrise çevrilmesi ile mümkün olmaktadır. İdeal bir metin ağırlıklandırma yaklaşımının 3 temel bileşeni bulunmakta olup; bunlar Terim Frekansı, Doküman Frekansı ve Vektör Normalizasyonu bileşenleridir. Bu üç bileşenin çarpımı ile bir kelimenin bir metin için önemini ifade eden sayısal değerler elde edilir. Ancak bu değerlerin ham hali metin verisinin anlamsal olarak analiz edilmesi için uygun değildir. Bu amaçla çeşitli yöntemler bulunmakta olup, büyük metin koleksiyonlarında bahsedilen konuları bulmayı amaçlayan Konu Analizi bu yöntemlerden bir tanesidir. Bu amaçla konu analizinde bir girdi matrisini hem rastgele hem de deterministik başlangıç değeri ile iki veya daha fazla matrisin çarpımına dönüştürmeyi hedefleyen Negatif Olmayan Matris Ayrışımı (NMF) yönteminden sıklıkla faydalanılır. Bu çalışmada, literatürde kullanılan metin ağırlıklandırma yöntemlerinin ve başlangıç değer yaklaşımlarının NMF yöntemi üzerinde etkilerinin bulunması amacıyla, Vikipedi özgür internet ansiklopedisinden elde edilen 20.000 makale üzerinde denemeler yapılmıştır. Denemelerde kullanılacak küme sayısının elde edilmesi için analitik bir yöntem yardımıyla bir üst sınır kullanılmıştır. Elde edilen sonuçlara göre, NMF üzerinde en iyi başarıma “lnc” ve “nnc” ağırlıklandırma şemalarıyla ulaşılmıştır. Buda konu analizi alanında “lnc” veya “nnc” ağırlıklandırma şemalarının kullanılmasıyla daha başarılı sonuçlar elde edileceğini göstermiştir.

Anahtar Kelimeler: *Konu Analizi, Metin Ağırlıklandırma Şemaları, Negatif Olmayan Matris Ayrışımı, Başarım Karşılaştırması*

1. Introduction

Currently, owing to the increasing prevalence of Internet technologies and devices that are able to support them, the most commonly generated form of data is textual data. According to a survey conducted in 2022, around five billion individuals globally and around 63 million individuals in Turkey had at least one account on a social media platform. These individuals dedicate an average of 2 hours and 31 minutes per day to generate textual material on social media [1]. The content generated exclusively on social media platforms has generated a significant increase in data, even on a daily basis. Hence, it is challenging to extract important information from datasets with exceedingly large volumes. In other words, it is feasible to analyze and interpret extensive data by substantially reducing the volume. This allows the implementation of many applications. Various applications, including market research, product feedback, the study of social perception, and prompt handling of complaints and requests, can be effortlessly achieved.

Topic analysis is a technique devised to extract concise and significant information from vast amounts of textual data [2], [3].

DOI: https://doi.org/10.21205/deufmd.2025277907

Geliş Tarihi / Received: 31.01.2024
Kabul Tarihi / Accepted: 02.04.2024

Table 1. Sample view from dataset.

Article Id	Url	Title	Text
12	https://en.wikipedia.org/wiki/Anarchism	**Anarchism**	Anarchism is a political philosophy and movement that is sceptical of authority and rejects all involuntary, coercive forms of hierarchy. Anarchism calls for the abolition of the state, which it holds to be unnecessary, undesirable, and harmful. As a historically…
7676	https://en.wikipedia.org/wiki/Creaky%20voice	**Creaky voice**	In linguistics, creaky voice (sometimes called laryngealisation, pulse phonation, vocal fry, or glottal fry) is a special kind of phonation in which the arytenoid cartilages in the larynx are drawn together; as a result, the vocal folds are compressed rather tightly, becoming relatively slack and compact. They normally…
30266	https://en.wikipedia.org/wiki/Tonyukuk	**Tonyukuk**	Tonyukuk (, , , born c. 646, died c. 726) was the baga-tarkhan (supreme commander) and adviser of four successive Göktürk khagans – Elteriš Qaγan, Qapγan Qaγan, İnäl Qaγan and Bilgä Qaγan. He conducted victorious…

Initially, probabilistic models were commonly employed, although more deterministic approaches are currently being integrated into the methodology. This enables a rapid and effortless overview of textual information. Numerous studies have been published on this topic [4], [5].

Non-negative matrix factorization (NMF) is a method designed to decompose a matrix into a product of two smaller matrices. This facilitates the analysis of the acquired matrices with reduced dimensions. Given this framework, NMF is an iterative method for topic analysis [5]. Despite the deterministic structure of the NMF, the initial values are typically chosen randomly. This reduced the reliability of the method. An approach called non-negative double-singular (NNDSVD) was proposed as a solution to this problem [6]. This approach utilizes singular value decomposition (SVD). For relevant studies, see, for example, [7], [8], [9].

The purpose of utilizing NMF in the domain of topic analysis is to reduce the dimensions of the matrix arising from the process of converting text data into a numeric format. Although NMF is a reliable and efficient technique, its effectiveness is closely tied to the semantic content of the matrix obtained from textual input. Choosing an appropriate strategy will enhance the quality and precision of research, given the various focusing approaches available during the digitization phase of text data [10], [11], [12].

The main contribution of this study is to provide an objective assessment of several text weighting schemas using the NMF topic Modelling approach. Because text weighting is one of the most important factors that directly influences the results of topic modelling, choosing an optimal weighting method will help researchers establish a good starting point. Therefore, a series of experiments were conducted to measure the achievements in the topic analysis of the text weighting approaches defined in the literature, as part of this study. The results were compared in terms of coherence by using the NMF method. The subsequent sections of this paper are structured as follows. second section of the paper presents the dataset and methodologies employed. The third section of the manuscript discusses the experimental findings. In conclusion, the results acquired in the fourth section are consolidated, and suggestions for further research are presented.

2. Related Works

The use of NMF has been an active research area because of its analytical nature. In particular, it has been employed in several academic disciplines such as environmental sciences, medical informatics, and text mining [13]. For example, the NMF method has been used for genetic information extraction [14], [15], [16], [17], [18], to make inferences about textual medical data [19], [20], [21], [22], and pollution discrimination [23], [24], [25]. From a topic analysis perspective, several variants of NMF have been heavily employed in these studies. For instance, NMF and its variants have been used to extract useful insights from tourism sector reviews [26], [27]; health-related textual information [20], [21], [22], [28], [29]; low-source language texts [30], [31]; and accident or disaster analysis from textual data [32], [33]. However, most studies have integrated library-provided functions to preprocess text-weighting schemas. Because weighting is a key factor in topic analysis, using the most accurate text-weighting method is important. Hence, this study aims to close this gap in the literature by providing a comprehensive evaluation of well-known text weighting schemas.

3. Materials and Methods

3.1. Dataset

Studies in the field of topic analysis take advantage of the large amounts of text. The study utilized a version of the Wikipedia Internet Encyclopedia that was generated by the Huggingface group and dated March 1, 2022.

Wikipedia backups its database in XML format for a period of six months and opens it to researchers. However, these data are very difficult to process because they are compressed to 19 GB (open to 86 GB). Huggingface periodically retrieves textual data from Wikipedia and provides it in a JSON-like format (the whole export file is an invalid JSON, but each line is JSON). The study utilized a dataset consisting of 6.458.670 English-language articles that were processed and transformed into JSON format by Huggingface on March 1, 2022 (downloaded from https://huggingface.co/datasets/wikipedia/tree/main/data/20220301.en). We randomly selected 20.000 documents randomly from the Wikipedia Dataset to reduce computation requirements. The random 3 samples of the selected dataset are listed in Table 1.

3.2. Text Preprocessing

To analyze the obtained Wikipedia articles, all words must be represented numerically; hence, pre-processing steps were applied to the obtained data. For the normalization of the articles obtained in the first stage, all characters were translated into lower-case letters. A total of 416.450.007 characters were processed during this phase. Subsequently, characters were eliminated using unicode (universal-coded characters) categories. The KC Normal Form (NFKC), previously proposed by the Unicode consortium, was used at this stage. Then, the characters other than the Unicode category small letter (Ll) or large letter (Lu) and space (Zs) were excluded from the text data, and a total of 392.586.768 characters remained as a result. The resulting documents were split by space character, and a total of 64.535.969 text parts were obtained. Suffixes were removed from the text using the Snowball [34] stemmer, and English stop words were removed from the text. A total of 38.972.617 words were obtained as a result of this phase. There are 516.119 words in our final dictionary. The resulting dictionary digitized 20,000 Wikipedia documents, and the final dimension of the document-term matrix was 20.000 × 516.119.

3.3. Text-Weighting Methods

The raw state of text data is difficult to analyze owing to its various linguistic and contextual characteristics. Therefore, the use of digitized text data is preferred over raw data. The most preferred method for digitizing text data in this area is the Bag of Words (BoW). Using this method, text data are generally translated into large matrices that have a sparse structure and show the relationship between words and documents. The methodologies employed in this approach were determined using the SMART Information Retrieval System created by Cornell University. Within this method, the importance of every word in the documentation comprises of three distinct components. These components consist of the Term Frequency Component (TFC), which quantifies the importance of a word in a document; the document frequency component (DFC), which measures the relevance of a term across the entire text data; and the (VNC), which indicates the process of vector normalization. The final word weight is given by the following equation obtained from the product of these three components:

$$X_{t,d} = TFB_{t,d} \times DFB_t \times VNB \tag{1}$$

Table 2 lists the predefined weighting schemes for the three components used by the SMART information-delivery system.

Table 2. SMART Weighting Components.

TFC		DFC		VNC	
n	$tf_{t,d}$	n	1	n	1
l	$\begin{cases} 1 + log(tf_{t,d}), tf_{t,d} > 0 \\ 0, tf_{t,d} \leq 0 \end{cases}$	t	$log \frac{N_d}{df_t}$	c	$\frac{1}{\sqrt{\sum_{i=1}^{n} w_i^2}}$
a	$0.5 + \frac{0.5 \times tf_{t,d}}{max_t(tf_{t,d})}$	p	$max\left\{0, log \frac{N_d - df_t}{df_t}\right\}$	u	$\frac{1}{u}$
b	$\begin{cases} 1, tf_{t,d} > 0 \\ 0, tf_{t,d} \leq 0 \end{cases}$			b	$\frac{1}{\mathcal{L}_c^{\alpha}}, \alpha < 1$
L	$\frac{1 + log(tf_{t,d})}{1 + log\left(ave_t(tf_{t,d})\right)}$				

where $tf_{t,d}$ indicates the frequency of the word t within the document d; N_d is the total number of documents; df_t is the number of different documents that include the word t; w_i is the element i. of a vector; u is a normalization factor; $\mathcal{L}_c^{\alpha}$ is the average number of words in the text collection; and α is a standardization factor.

This study uses all combinations defined in the SMART notation. However, owing to additional parameters, we excluded "u" and "b" values of VNC.

3.4. Topic Analysis

Topic analysis approaches, which have recently been developed to find topics discussed in large-volume text data, often use reduced matrices through dimension reduction methods. The most preferred dimensional reduction methods for these approaches are the Latent Dirichlet Allocation (LDA) [35] and the NMF [36]. The LDA method is a generative probability model. In this model, two different multivariate probability distributions were used. One of these distributions models the likelihood that any word passes a topic, whereas the other models the probability that any text belongs to a topic. The process of calculating LDA aims to obtain the probability values initially randomly selected, iteratively approaching the actual probability value. Therefore, there may be differences in the results obtained from the LDA calculation. However, the classic NMF method aims to convert a large matrix into the product of two smaller matrices. The structure of this method also involves an iterative calculation process, and the starting point is usually chosen randomly. Unlike LDA, it has been demonstrated that an effective and deterministic starting point can be determined using the classic NMF method, thereby increasing the consistency of the results obtained [6]. Therefore, the success of topic analysis was measured using only the NMF method.

3.5. Non-negative Matrix Factorization (NMF)

In the classical NMF method, the input matrix is divided into two different matrices using a specific approach. A matrix display separated by the classical NMF is

$$\mathrm{X} = \mathrm{WH} \tag{2}$$

where $X \in \mathbb{R}^{m \times n}$ and $x_{ij} \geq 0, 1 \leq i \leq m, 1 \leq j \leq n$ indicate the input matrix, $W \in \mathbb{R}^{m \times r}$ and $w_{ik} \geq 0, 1 \leq i \leq m, 1 \leq k \leq r$ the mixture matrix (base), $H \in \mathbb{R}^{r \times n}$ and $h_{kj} \geq 0, 1 \leq k \leq r, 1 \leq j \leq n$ the coding matrix and the r parameter also the difference size [37].

The classical NMF method aims to find the $\widetilde{W} \approx W$ and $\widetilde{H} \approx H$ separation matrices of the $\tilde{X}$ matrix, which is a prediction of the X matrix. In this case, the differential to be obtained for the matrix $\tilde{X}$ is

$$\tilde{X} = \widetilde{W}\widetilde{H} \tag{3}$$

where $\widetilde{W} \in \mathbb{R}^{m \times r}$ and $\widetilde{\mathrm{H}} \in \mathbb{R}^{\mathrm{r} \times \mathrm{n}}$ are matrices.

NMF is an optimization method. This method uses the objective function of minimizing a certain $D(.,.)$ distance measurement between the matrix $\tilde{X}$ and the input matrix X. This is shown in Equations (4) and (5):

$$\min_{\tilde{X} \in \mathbb{R}^{m \times n}} D(X, \tilde{X}) = \min_{\widetilde{W} \in \mathbb{R}^{m \times r}, \widetilde{H} \in \mathbb{R}^{r \times n}} D(X, \widetilde{W}\widetilde{H}), \tag{4}$$

$$D(X, \widetilde{W}\widetilde{H}) = \frac{1}{2}\left\|X - \widetilde{W}\widetilde{H}\right\|_F^2 = \frac{1}{2}\sum_{i=1}^{m}\sum_{j=1}^{n}\left((X)_{ij} - (\widetilde{W}\widetilde{H})_{ij}\right)^2. \tag{5}$$

Here, $D: \mathbb{R}^{m \times n} \times \mathbb{R}^{m \times n} \rightarrow \mathbb{R}$ is an error function, and the Frobenius norm is indicated by the notation $\|\cdot\|_{\mathrm{F}}^2$.

The r separation dimension is an important parameter in the NMF method. However, the failure to calculate this parameter in advance and to experimentally determine it prolongs the completion time of the work. For example, in most NMF applications, calculation of the appropriate r value is typically performed experimentally and within a wide range of values (approximately 140). In this context, the brute-force approach is used to select the one with the best success value among all r values in the value range. This experimental approach is expressed as

$$\underset{r_{min} < r < r_{max}}{argmax} \; P(X, \widetilde{W}\widetilde{H}) \tag{6}$$

where r_{min}, r_{max} represents a value in the range $r \in \mathbb{N}^+$, and large values of the $P: \mathbb{R}^{m \times n} \times \mathbb{R}^{m \times n} \rightarrow \mathbb{R}$ function indicate high achievement. Researchers can also use natural numbers that have a specific pattern because they can use all natural numbers in this value range. However, $\mathrm{r}_{\mathrm{min}}$, $\mathrm{r}_{\mathrm{max}}$ values do not have an analytical approach to determine, and these values are determined based on the experience of researchers. This is a factor that negatively affects the coherence of work with NMF.

As a general rule, the upper limit of the r parameter is expected to comply with

$$r \ll min(m,n) \tag{7}$$

rule. Here, the expression $\ll$ indicates a radically small r parameter value, whose upper limit is $min(m,n)$, must be used.

Because the NMF method is a low-rank matrix approximation, the element counts of the $\widetilde{W}$ and $\widetilde{H}$ separation matrices obtained by this method are expected to be less than the element count of the X input matrix. Therefore, given the number of elements $(mr + nr)$ of the separated matrices to be obtained with classical NMF, the following inequality must be satisfied:

$$mr + nr < mn. \tag{8}$$

Thus, the upper limit of the separation size is

$$r < \frac{mn}{m+n}. \tag{9}$$

If the input matrix is sparse, the upper limit is

$$r < \frac{nnz(X)}{m+n}. \tag{10}$$

Here $\mathrm{nnz}: \mathbb{R}^{\mathrm{m\times n}} \rightarrow \mathbb{N}^{+}$ denotes the number of elements in a matrix that are different from zero. These two inequalities produce values that are more suitable for estimating the upper boundary of parameter r than inequality (7). In this study, the highest r value that yields the inequality (10) was used [38].

The proposed calculation approaches for the classic NMF method iteratively minimize the objective function in Eq. (5). The most preferred of these approaches is the Frobenius rule's Multiplicative Update Rules (MUR) [36]. In addition to this approach, the steepest gradient descent and Newton-type numerical methods have been proposed [39], [40]. In our study, MUR was preferred because of its widespread use, and this method is shown in Equations (11)–(12).

$$G_w(\widetilde{W}^t, \widetilde{H}^t) = \widetilde{W}^t \otimes \left(X\widetilde{H}'^t \oslash \widetilde{W}^t\widetilde{H}^t\widetilde{H}'^t\right), \tag{11}$$

$$G_h(\widetilde{W}^{t+1}, \widetilde{H}^t) = \widetilde{H}^t \otimes \left(\widetilde{W}^{t+1}X \oslash \widetilde{W}'^{t+1}\widetilde{W}^{t+1}\widetilde{H}^t\right). \tag{12}$$

Here, $\otimes$ is the Hadamard product; $\oslash$ is the Hadamard division; and, G_w and G_h are the functions that update the $\widetilde{W}$ and $\widetilde{H}$ matrices, respectively.

In all these calculation methods, the starting values of the $\widetilde{W}$ and $\widetilde{H}$ matrices were randomly selected from the uniform distribution. This negatively affects the consistency of the $\widetilde{W}$ and $\widetilde{H}$ matrices obtained with NMF applications [41], [42]. In addition, these randomly selected starting values also adversely affect the calculation time of the NMF method [43].

3.6. Non-Negative Double Singular Value Decomposition (NNDSVD)

For the classic NMF method to produce more consistent and faster results, a deterministic starting value approach for $\widetilde{\mathrm{W}}$ and $\widetilde{\mathrm{H}}$, called the NNDSVD, has been suggested and successful results have been obtained [6]. Algorithm 1 presents the algorithm for the NNDSVD method.

Algorithm 1. NNDSVD Algorithm

Input: $\mathrm{X} \in \mathbb{R}_{+}^{\mathrm{m\times n}}, \mathrm{r} < \min(\mathrm{m,n}) \in \mathbb{N}^{+}$

Output: $\widetilde{\mathrm{W}}^{0} \in \mathbb{R}_{+}^{\mathrm{m\times r}}, \widetilde{\mathrm{H}}^{0} \in \mathbb{R}_{+}^{\mathrm{r\times n}}$

```
1    Calculate the single value of the largest r of $X : U,S,V = svd(X,r)$
2    Specify as $\widetilde{W}_{\cdot,1} = \sqrt{s_{1,1}} \times U_{\cdot,1}$ and $\widetilde{H}_{1,\cdot} = \sqrt{s_{1,1}} \times V'_{\cdot,1}$
3    For $\forall j \in [2,r]$
3.1    $x = U_{\cdot,j}$ ve $y = V'_{\cdot,j}$
3.2    $x_+ = \begin{cases} x_i, & x_i > 0 \\ 0, & otherwise \end{cases}, x_- = \begin{cases} -x_i, & x_i < 0 \\ 0, & otherwise \end{cases}, y_+ = \begin{cases} y_i, & y_i > 0 \\ 0, & otherwise \end{cases}$ ve $y_- = \begin{cases} -y_i, & y_i < 0 \\ 0, & otherwise \end{cases}$
3.3    $\mu_+ = \|x_+\|\|y_+\|$ ve $\mu_- = \|x_-\|\|y_-\|$
3.4    $u = \begin{cases} \frac{x_+}{\|x_+\|}, \mu_+ > \mu_- \\ \frac{x_-}{\|x_-\|}, \mu_- \le \mu_+ \end{cases}, v = \begin{cases} \frac{y_+}{\|y_+\|}, \mu_+ > \mu_- \\ \frac{y_-}{\|y_-\|}, \mu_- \le \mu_+ \end{cases}$ and $\sigma = max(\mu_+, \mu_-)$
3.5    $\widetilde{W}_{\cdot,j} = \sqrt{s_{j,j} \times \sigma} \times u$ and $\widetilde{H}_{j,\cdot} = \sqrt{s_{j,j} \times \sigma} \times v'$
```

With this algorithm, it has been demonstrated that the $\widetilde{\mathrm{W}}$ and $\widetilde{\mathrm{H}}$ matrices have non-negative values and decrease the value of the goal function without becoming stuck in local minima [6]. The classical NMF method used in this approach has been confirmed by several studies in which calculations are closer to conclusions in a shorter time and produce consistent results [7], [8], [9].

3.7. Computational Complexity

Owing to the nature of NMF, most algorithms developed to determine the exact factors are NP-Hard. These algorithms, which can be solved in polynomial time, impose certain restrictions on r. In this case the running time complexity of NMF algorithms $O\left((mn)^{cr^2}\right)$ for a constant c, which is a grow exponentially for large values of r [38]. Hence, selecting the most suitable text-weighting scheme is important to reduce the computational requirements of the approach.

3.8. Topic Coherence

Using the results obtained from topic analysis, the maximum weight for each topic was determined using $M = 5, \ldots, 20$ words. There are many methods in the literature that measure the coherence of topics obtained. In these methods, topic coherence is calculated based on a combination of words obtained. The most popular of these methods is called U_{mass}, and the equation is shown in Equation (13) [44].

$$U_{mass} = \sum_{0<i<j\le M} \mathcal{S}(w_i, w_j) = \sum_{0<i<j\le M} \log \frac{\mathfrak{D}(w_i, w_j) + 1}{\mathfrak{D}(w_i)} \tag{13}$$

Here, $\mathfrak{D}(w_i)$ represents the total number of documents passed by the word w_i, and $\mathfrak{D}(w_i, w_j)$ represents the total number of documents passed by the words w_i and w_j together. After calculating the U_{mass} value for all topics obtained, the average of all U_{mass} values are taken so that the overall evaluation of the subject analysis results can be made. This is expressed in Equation (14).

$$C_{U_{mass}} = \frac{1}{r}\sum_{i=1}^{r} U_{mass_i} \tag{14}$$

where $C_{U_{mass}}$ denotes the overall coherence value of the object analysis results, r denotes the number of objects, and U_{mass_i} denotes the U_{mass} value of i. the topic.

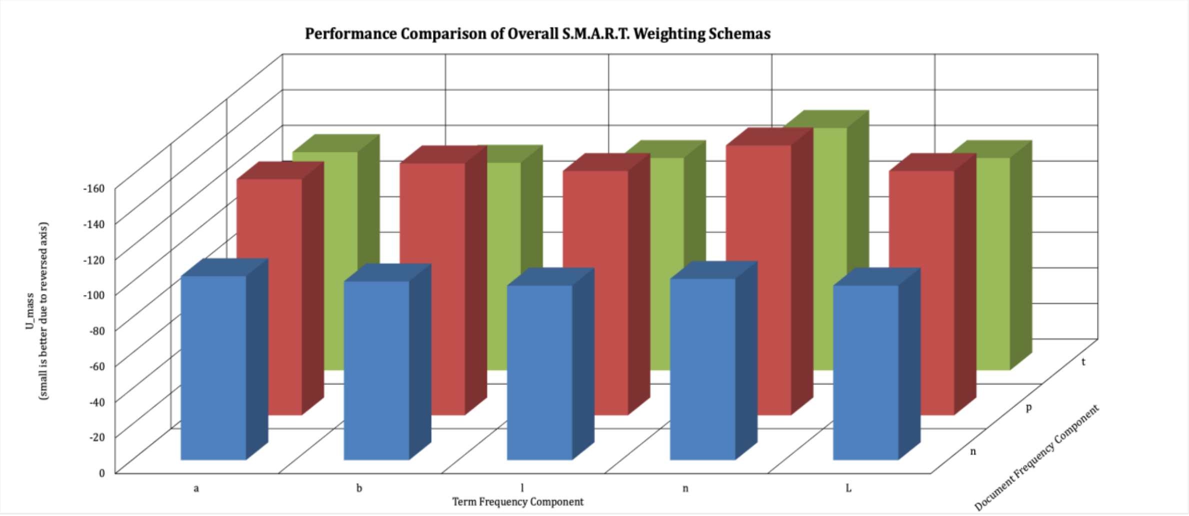

Figure 1. Overall Performances of SMART Component Values.

In the end, the obtaining of large $C_{U_{mass}}$values indicates that the analysis results have a high consistency.

4. Experimental Results

We conducted a series of experiments on the Wikipedia dataset to determine the most effective combination of the SMART components. Although each SMART component has a different impact on generating document-term matrices, they generated document-term matrices with the same number of non-zero elements in our experiments. The overall properties of the obtained document term matrices are listed in Table 3.

Table 3. General Properties of Document-Term Matrix.

Total Number of Documents	6458670
Total Number of Selected Documents	20000
Total Number of Unique Tokens	516119
Total Number of Non-zero Entries in Each Document-Term Matrix	14579095
Sparsity of Each Document Term Matrix	%0.1412

We used these properties to determine the upper limit of topic count. Using equation (10), the upper limit of the topic count was calculated as 27 for our experimental setup.

Because the normalization components u and b require additional parameter estimations, we exclusively used the c-component. In addition, our experimental configuration excludes the n component of term normalization to avoid generating document vectors that are not normalized. In total, we conducted 15 experiments to assess the effectiveness of each combination of word frequency (n, l, a, b, L) and document frequency (n, t, p) components in Topic Analysis, using the Wikipedia dataset.

After the creation of document term matrices for each SMART component, we calculated the W and H matrices using NMF on the GPU code implemented using the CuPy library. We implemented the NNDSVD algorithm to determine the initial values of W and H matrices. We ran all our models on an NVIDIA Quadro P4000 GPU with 8 GB of VRAM. The peak memory usage in each experiment was approximately 300 MB.

The performance of each topic-analysis result was evaluated using U_{mass} coherence measure. We took the average of all topic coherence values to provide an overall comparison between the SMART components. The average U_{mass} values for each pair are presented in Table 4 and Figure 1.

Table 4. Coherence Values of Each Combination.

	n	p	t
a	-103.31	-132.53	-122.59
b	-100.37	-141.47	-116.60
l	-98.01	-137.18	-119.28
n	-101.77	-151.55	-136.15
L	-98.01	-137.18	-119.28

The findings demonstrate that the “n” document frequency component consistently attained the highest coherence scores, irrespective of the TFC while the “p” document frequency component obtained the worst coherence values. Nevertheless, we were unable to determine the particular TFC that achieved the highest coherence scores across all document frequency components. The TFCs “l” and “L” exhibit the highest coherence scores when combined with the document frequency component “n”. The “a” TFC has the highest coherence score with the “p” document frequency component, whereas the “b” TFC has the highest coherence score with the “t” document frequency component. The TFCs “l” and “L” achieved the same values for all experimental setups. In summary, the best configuration of the SMART components for the Wikipedia dataset is the “lnc” configuration.

Because topic analysis is not only a field of study for mathematics but also a field of textual data summarization, coherence scores are insufficient to present textual concepts. To overcome this insufficiency, many researchers have attempted to name these topics. The topic-naming process involves two stages: finding the most effective topic terms and generating a title for the found terms. The first stage is straightforward, but the second stage requires domain expertise and is generally subject to subjective assessment. In our experimental setup, we included a well-known generative artificial intelligence (AI) system to remove subjective naming assessment [45]. Hence, we generated titles objectively. The prompts used to generate the topic titles are given in Table 5.

Table 5. ChatGPT Title Generation Prompt.

Propose a single topic header for the following words:
<comma joined the most effective topic words>

We generated a total number of 405 topic titles using ChatGPT with a given prompt. Some titles produced were the same. For example, our prompt generated “*Japanese History and Culture*” topic titles for 12 of the topics of different SMART components.

Table 6. The First 40 Topic Titles and Their Statistical Properties.

Topic Titles	Frequency	Avg. Coherence Score
Japanese History and Culture	12	-22.23
International Organizations	6	-33.25
Key Terms and Concepts in American Football	6	-64.14
Mathematical Concepts and Terminology	5	-82.30
Various Professions	4	-77.49
Exploring Computer Hardware and Software Components	4	-116.63
Exploring Demographic Statistics and Trends: A Comprehensive Analysis	4	-117.45
Topics in Abstract Algebra	4	-131.25
Exploring Telecommunication Technologies and Services	4	-132.60
Roman Empire and its Key Figures	4	-145.04
Exploring Subatomic Particles and Fundamental Forces in Particle Physics	3	-78.21
International Organizations and Agencies	3	-91.57
Chemical Elements and Compounds	3	-95.82
Topics in Linguistics	3	-104.11
Mathematical Concepts and Structures	3	-114.38
Exploring the Fundamentals of Particle Physics and Quantum Mechanics	3	-116.99
Key Components and Processes in Cellular Biology	3	-119.15
Countries and Territories	3	-129.36
Medieval Empires and Kingdoms	3	-133.63
Logical Reasoning and Mathematical Concepts	3	-144.98
Roman History and Figures	3	-145.84
Medieval Kingdoms and Empires	3	-147.85
Exploring the Roman Empire: History, Calendar, and Cultural Influence	2	-43.63
Exploring Key Terms and Concepts in American Football	2	-53.00
Education and its Impact on Society	2	-56.18
Exploring the Elements: Actinides, Transuranium Elements, and their Properties	2	-61.14
Various Professions and Nationalities	2	-70.64
Economic Indicators and Policies	2	-74.01
Titles, Figures, and Institutions in Historical European Context	2	-78.07
Economic Development and Policies in the European Union: A Comprehensive Analysis	2	-78.99
Key Terms in American Football	2	-80.85
Government and Politics	2	-82.07
Geography and Climate Features	2	-87.18
Exploring the World of Polyhedra and Geometric Shapes	2	-87.41
Key Concepts in Economic Policy and Governance	2	-93.74
Exploring the World of Computing: Software, Hardware, Interfaces, and More	2	-93.82
Phonetics and Phonology: An Exploration of Speech Sounds and Language	2	-95.69
Exploring the World of Music and Entertainment	2	-96.52
Chemical Reactions and Compounds	2	-96.91
Exploring the World of Music: Albums, Instruments, Studios, and More	2	-97.15

The first 40 topics, sorted by coherence scores, are listed in Table 6. According to the results, the majority of the selected Wikipedia titles are related to historical figures and cultural heritage.

Although our approach for generating topic titles produced unbiased titles, some of the generated titles were insufficient because of the large range of topic terms generated. For example, one of the topic of SMART configuration “Ltc” produced “*disambigu, album, unincorpor, surnam, township, indiana, iowa, mathemat, kentucki, uss, softwar, nebraska, missouri, wisconsin, cuisin, ohio, ix, counti, band, entertain*” terms. The generated topic titles for these terms produce 15 different topic titles, as listed in Table 7.

Table 7. Proposed Topic Titles for Example.

Proposed Topic Titles
1. Disambiguation and its importance in information retrieval
2. The significance and impact of albums in the music industry
3. Unincorporated areas and their role in local governance
4. The history and significance of surnames in genealogy and identity
5. Township governance and its role in local administration
6. Exploring the states of Indiana, Iowa, Nebraska, Missouri, and Wisconsin
7. The beauty and complexity of mathematics
8. Kentucky's rich history and cultural heritage
9. The role and impact of the United States Navy's USS (United States Ship) vessels
10. The evolution and importance of software in modern society
11. Exploring the diverse landscapes and attractions of Ohio
12. Understanding the Roman numeral system and its applications
13. County governance and its impact on local communities
14. The power of music and the role of bands in entertainment
15. Exploring the world of entertainment and its various forms

The main cause of this issue is the contextual diversity of the terms that describe the topic. Put simply, the topic encompasses a wide range of themes that are too diverse to be consolidated under a single title. We named this topic as *The Null Topic (TNT)* and used the coherence value of this topic as a threshold to discriminate high quality topics from low quality ones.

According to the TNT Coherence score, the distribution of high-quality topics by DFC (n, p, and t) and TFC (a, b, l, L, and n) of the SMART system is given in Table 8.

Table 8. Distribution of High Quality Topics

	n	p	t
a	25	22	24
b	25	20	24
l	26	21	23
L	26	21	23
n	27	18	24

As a result we could say the most of the high quality topic titles are generated from "n" DFC component. Moreover, all the topics generated by the "n" TFC component in combination with the "n" DFC component were high-quality topics.

5. Conclusions

We conducted a series of experiments to determine the best combination of SMART system components for NMF-based topic analysis tasks. Because the SMART system is still widely used in Topic Analysis tasks, researchers must select the most suitable SMART components to make inferences about textual data. In this work, we have found that the "lnc" and "nnc" SMART configurations work best in terms of Topic Coherence and Topic Quality, respectively. This provides a good starting point for any Topic Analysis task and decreases the time required.

Another contribution of this study is the integration of a generative AI tool into a Topic Analysis task to overcome the subjectivity of topic title generation. We designed a prompt to generate a single topic title for topic terms. This approach provides another opportunity to measure topic quality.

As a side product, we propose a new method to assess topic quality using an automatic coherence thresholding method. This method uses the coherence values of AI-generated titles with more than one alternative. Hence, our approach constructs a basis for the automated objective evaluation of Topic Analysis in terms of topic quality. However, this approach needs to be supported by further analysis.

Ethics committee approval and conflict of interest statement

This study did not require approval from the ethics committee. This article has no conflicts of interest with any individual or institution.

Author Contribution Statement

The first Author contributed to the formulation and implementation of the data analysis techniques, writing of the manuscript, and interpretation of the results. The second author contributed to the literature survey, theoretical foundations, and the writing and interpretation of the results.

References

[1] "Reports & Content — Kepios." Accessed: Aug. 25, 2023. [Online]. Available: https://kepios.com/reports.

[2] Vayansky, I., Kumar, S.A.P., 2020. A review of topic modeling methods. Information Systems, Vol. 94, p. 101582. DOI: 10.1016/J.IS.2020.101582.

[3] Blei, D.M., 2012. Probabilistic topic models. Communications of the ACM, Vol. 55, No. 4, pp. 77–84. DOI: 10.1145/2133806.2133826.

[4] Schachtner, R., 2010. Extensions of Non-negative Matrix Factorization and Their Application to the Analysis of Wafer Test Data. PhD Thesis, Universität Regensburg, Regensburg.

[5] Shen, J., Israël, G.W., 1989. A receptor model using a specific non-negative transformation technique for ambient aerosol. Atmospheric Environment, Vol. 23, No. 10, pp. 2289–2298. DOI: 10.1016/0004-6981(89)90190-X.

[6] Boutsidis, C., Gallopoulos, E., 2008. SVD-based initialization: A head start for nonnegative matrix factorization. Pattern Recognition, Vol. 41, No. 4, pp. 1350–1362. DOI: 10.1016/J.PATCOG.2007.09.010.

[7] Yamashita, A., Nagata, T., Yagyu, S., Asahi, T., Chikyow, T., 2022. Direct feature extraction from two-dimensional X-ray diffraction images of semiconductor thin films for fabrication analysis. Manufacturing Letters, Vol. 2, No. 1, pp. 23–37. DOI: 10.1080/27660400.2022.2029222.

[8] Wang, Z., Yu, Y., 2022. Revealing the spatial and temporal distribution of different chemical states of lithium by EELS analysis using non-negative matrix factorization. Micron, Vol. 154, p. 103213. DOI: 10.1016/J.MICRON.2022.103213.

[9] Lu, H., Zhao, Q., Sang, X., Lu, J., 2020. Community Detection in Complex Networks Using Nonnegative Matrix Factorization and Density-Based Clustering Algorithm. Neural Processing Letters, Vol. 51, No. 2, pp. 1731–1748. DOI: 10.1007/S11063-019-10170-1.

[10] Wang, J., Zhang, X.L., 2023. Deep NMF topic modeling. Neurocomputing, Vol. 515, pp. 157–173. DOI: 10.1016/J.NEUCOM.2022.10.002.

[11] Habbat, N., Anoun, H., Hassouni, L., 2021. Topic Modeling and Sentiment Analysis with LDA and NMF on Moroccan Tweets. Lecture Notes in Networks and Systems, Vol. 183, pp. 147–161. DOI: 10.1007/978-3-030-66840-2_12.

[12] Egger, R., Yu, J., 2022. A Topic Modeling Comparison Between LDA, NMF, Top2Vec, and BERTopic to Demystify Twitter Posts. Frontiers in Sociology, Vol. 7, p. 886498. DOI: 10.3389/FSOC.2022.886498.

[13] Guo, Y.-T., Li, Q.-Q., Liang, C.-S., 2024. The rise of nonnegative matrix factorization: Algorithms and applications. Information Systems, Vol. 123, p. 102379. DOI: 10.1016/j.is.2024.102379.

[14] Takasawa, K., et al., 2024. Advances in cancer DNA methylation analysis with methPLIER: Use of non-negative matrix factorization and knowledge-based constraints to enhance biological interpretability. Experimental & Molecular Medicine. DOI: 10.1038/s12276-024-01173-7.

[15] Chen, D., et al., 2024. Comprehensive analyses of solute carrier family members identify SLC12A2 as a novel therapy target for colorectal cancer. Scientific Reports, Vol. 14, No. 1, p. 4459. DOI: 10.1038/s41598-024-55048-y.

[16] Dey, A., Das Sharma, K., Bhattacharjee, P., Chatterjee, A., 2024. Identification of disease-related biomarkers in time-varying 'Omic data: A non-negative matrix factorization aided multi-level self-organizing map based approach. Biomedical Signal Processing and Control, Vol. 90, p. 105860. DOI: 10.1016/j.bspc.2023.105860.

[17] Shi, Y., Jin, Z., Deng, J., Zeng, W., Zhou, L., 2024. A novel high-dimensional kernel joint non-negative matrix factorization with multimodal information for lung cancer study. IEEE Journal of Biomedical and Health Informatics, Vol. 28, No. 2, pp. 976–987. DOI: 10.1109/JBHI.2023.3335950.

[18] Ramamoorthy, T., Kulothungan, V., Mappillairaju, B., 2024. Topic modeling and social network analysis approach to explore diabetes discourse on Twitter in India. Frontiers in Artificial Intelligence, Vol. 7, p. 1329185. DOI: 10.3389/frai.2024.1329185.

[19] Subbarayudu, Y., Sureshbabu, A., 2024. The detection of community health surveillance using distributed semantic-assisted non-negative matrix factorization on topic modeling through sentiment analysis. Multimedia Tools and Applications. DOI: 10.1007/s11042-024-18321-w.

[20] Choi, D., et al., 2023. WellFactor: Patient Profiling using Integrative Embedding of Healthcare Data. In Proceedings of the 2023 IEEE International Conference on Big Data (BigData), IEEE, pp. 616–625. DOI: 10.1109/BigData59044.2023.10386138.

[21] Ahammad, T., 2024. Identifying hidden patterns of fake COVID-19 news: An in-depth sentiment analysis and topic modeling approach. Natural Language Processing Journal, Vol. 6, p. 100053. DOI: 10.1016/j.nlp.2024.100053.

[22] Zong, L., Yang, Y., Xia, H., Yuan, J., Guo, M., 2023. Elucidating the Impacts of Various Atmospheric Ventilation Conditions on Local and Transboundary Ozone Pollution Patterns: A Case Study of Beijing, China. Journal of Geophysical Research: Atmospheres, Vol. 128, No. 20. DOI: 10.1029/2023JD039141.

[23] Knobel, P., et al., 2023. Socioeconomic and racial disparities in source-apportioned PM2.5 levels across urban areas in the contiguous US, 2010. Atmospheric Environment, Vol. 303, p. 119753. DOI: 10.1016/j.atmosenv.2023.119753.

[24] Westervelt, D.M., et al., 2024. Low-Cost Investigation into Sources of PM2.5 in Kinshasa, Democratic Republic of the Congo. ACS ES&T Air, Vol. 1, No. 1, pp. 43–51. DOI: 10.1021/acsestair.3c00024.

[25] Karamouzi, E., Pontiki, M., Krasonikolakis, Y., 2024. Historical Portrayal of Greek Tourism through Topic Modeling on International Newspapers. In Proceedings, pp. 121–132. Accessed: Mar. 30, 2024. [Online]. Available: https://aclanthology.org/2024.latechclfl-1.13.

[26] Athurugiriya, A.A.A.G., Sumathipala, P., Hemachandra, K.M.T.A., 2023. Development of an Enhanced Quality Score Calculation Method for Accurate Assessment of Hotel Quality. In Proceedings of the 2023 5th International Conference on Advancements in Computing (ICAC), IEEE, pp. 804–809. DOI: 10.1109/ICAC60630.2023.10417334.

[27] Mahmoudi, L., Hossein Shari, M., Bagheri, R., 2024. Exploring Healthcare Research Patterns in Developed and Developing Countries: A Topic Modeling Perspectives. DOI: 10.21203/RS.3.RS-3865906/V1.

[28] Hornback, A., et al., 2023. Latent Topic Extraction as a Source of Labeling in Natural Language Processing. In Proceedings of the 2023 IEEE International Conference on Bioinformatics and Biomedicine (BIBM), IEEE, pp. 4312–4319. DOI: 10.1109/BIBM58861.2023.10385618.

[29] Sweidan, A.H., El-Bendary, N., Elhariri, E., 2024. Autoregressive Feature Extraction with Topic Modeling for Aspect-based Sentiment Analysis of Arabic as a Low-resource Language. ACM Transactions on Asian and Low-Resource Language Information Processing, Vol. 23, No. 2, pp. 1–18. DOI: 10.1145/3638050.

[30] Pallawala, D., Haddela, P.S., 2023. A Comparison of Topic Modeling Techniques for Sinhala. In Proceedings of the 2023 5th International Conference on Advancements in Computing (ICAC), IEEE, pp. 376–381. DOI: 10.1109/ICAC60630.2023.10417327.

[31] Nanyonga, A., Wasswa, H., Wild, G., 2023. Topic Modeling Analysis of Aviation Accident Reports: A Comparative Study between LDA and NMF Models. In Proceedings of the 2023 3rd International Conference on Smart Generation Computing, Communication and Networking (SMART GENCON), 2023. DOI: 10.1109/SMARTGENCON60755.2023.10442471.

[32] Ghaly, M.Z., Laksito, A.D., 2023. Topic Modeling of Natural Disaster in Indonesia Using NMF. In Proceedings of the 2023 8th International Conference on Informatics and Computing (ICIC), IEEE. DOI: 10.1109/ICIC60109.2023.10382064.

[33] Porter, M.F., 1980. An algorithm for suffix stripping. Program, Vol. 14, No. 3, pp. 130–137. DOI: 10.1108/EB046814.

[34] Blei, D.M., Ng, A.Y., Jordan, M.I., 2003. Latent Dirichlet Allocation. Journal of Machine Learning Research, Vol. 3, pp. 993–1022.

[35] Lee, D.D., Seung, H.S., 1999. Learning the parts of objects by non-negative matrix factorization. Nature, Vol. 401, No. 6755, pp. 788–791. DOI: 10.1038/44565.

[36] Paatero, P., 1997. Least squares formulation of robust non-negative factor analysis. Chemometrics and Intelligent Laboratory Systems, Vol. 37, No. 1, pp. 23–35. DOI: 10.1016/S0169-7439(96)00044-5.

[37] Gillis, N., 2020. Nonnegative Matrix Factorization. Philadelphia, PA: Society for Industrial and Applied Mathematics. DOI: 10.1137/1.9781611976410.

[38] Guillamet, D., Vitrì, J., 2002. Non-negative Matrix Factorization for Face Recognition. In Proceedings of the Fifth Catalonian Conference on Artificial Intelligence, Castellon, Spain, pp. 336–344.

[39] Kim, D., Sra, S., Dhillon, I.S., 2007. Fast Newton-type Methods for the Least Squares Nonnegative Matrix Approximation Problem. In Proceedings of the Sixth SIAM Conference on Data Mining, Minnesota, USA, pp. 343–354.

[40] Hofmann, T., 2017. Probabilistic Latent Semantic Indexing. In Proceedings of the 22nd Annual International ACM SIGIR Conference on Research and Development in Information Retrieval, ACM, pp. 211–218.

[41] Kim, H., Park, H., 2008. Nonnegative Matrix Factorization Based on Alternating Nonnegativity Constrained Least Squares and Active Set Method. SIAM Journal on Matrix Analysis and Applications, Vol. 30, No. 2, pp. 713–730. DOI: 10.1137/07069239X.

[42] Belford, M., Mac Namee, B., Greene, D., 2018. Stability of topic modeling via matrix factorization. Expert Systems with Applications, Vol. 91, pp. 159–169. DOI: 10.1016/J.ESWA.2017.08.047.

[43] Mimno, D., Wallach, H.M., Talley, E., Leenders, M., McCallum, A., 2011. Optimizing Semantic Coherence in Topic Models. Association for Computational Linguistics, pp. 262–272. Accessed: Nov. 23, 2023. [Online]. Available: https://aclanthology.org/D11-1024.

[44] OpenAI, 2024. ChatGPT. Version 3.5. Accessed: Jan. 10, 2024.

DEU FMD 27(79) (2025) 54-61

Dokuz Eylül Üniversitesi Mühendislik Fakültesi Fen ve Mühendislik Dergisi
Dokuz Eylul University Faculty of Engineering Journal of Science and Engineering
Elektronik/Online ISSN: 2547-958X

RESEARCH ARTICLE / ARAŞTIRMA MAKALESI

Investigation of Crack Effects on the Nonlinear Vibrations of Microbeams with a Tip Mass in a Magnetic Field

Uç Kütlesi Bulunan Mikrokirişlerin Manyetik Alan Altında Lineer Olmayan Titreşimlerinde Çatlakların Etkilerinin İncelenmesi

Duygu Atcı

İzmir Katip Çelebi University, Faculty of Engineering and Architecture, Department of Mechatronics Engineering, İzmir, TÜRKİYE
Corresponding Author / Sorumlu Yazar : duygu.atci@ikc.edu.tr

Abstract

Microelectromechanical systems (MEMS) are critical members of modern technological devices, due to their applications in various industrial fields. In the physical applications of MEMS, cracks are a common structural problem, affecting the static and dynamic behavior of the system. In this paper, the effects of cracks on microbeams with a tip mass under the influence of a magnetic field have been investigated. The micro-size effect of the beam has been involved into the model by using the modified couple stress theory. The crack has been modeled by using a torsional spring, with the spring coefficient corresponds to the severity of the crack. Thus, the beam has been modeled as consisting of two segments connected by a torsional spring. The equations of motion have been formulated using Hamilton's principle. The obtained equations have been solved by using the method of multiple scales, a perturbation technique. Frequencies regarding both linear and nonlinear vibrations of the microbeams have been examined. The results obtained in this study have been validated by using available numerical results in the literature. The effects of parameters such as crack severity, crack location, tip mass and the magnetic field force on linear and nonlinear vibrations have been presented. The results indicate a significant decrease in the natural frequencies and nonlinear frequencies of microbeams with increasing crack severity.

Keywords: *Nonlinear Vibrations, Cracked Microbeams, Perturbation Techniques, Modified Couple Stress Theory, Method of Multiple Scales*

Öz

Mikroelektromekanik sistemler (MEMS), birçok endüstriyel alana uygulanabilmeleri sayesinde, modern teknolojik cihazların önemli elemanlarından biri haline gelmiştir. MEMS' in fiziksel uygulamalarında sıklıkla ortaya çıkan çatlaklar, sistemin statik ve dinamik davranışlarını etkilemektedir. Bu makalede, manyetik alan etkisi altındaki, uç kütleye sahip mikrokirişler üzerindeki çatlakların etkileri incelenmiştir. Kirişin mikro boyut etkisi, değiştirilmiş çift gerilme teorisi kullanılarak modele dahil edilmiştir. Çatlak, bir burulma yayı kullanılarak modellenmiştir ve burulma yay katsayısı çatlak şiddetine karşılık gelmektedir. Böylece kiriş, burulma yayı aracılığı ile birbirine bağlı iki kısımdan oluşacak şekilde modellenmiştir. Hareket denklemleri Hamilton prensibi uygulanarak oluşturulmuştur. Elde edilen denklemler, bir perturbasyon yöntemi olan çok ölçekli metot kullanılarak çözülmüştür. Mikrokirişlerin hem lineer hem de nonlineer titreşimlerine ilişkin frekansları incelenmiştir. Bu çalışmada elde edilen sonuçlar, literatürde bulunan mevcut sayısal sonuçlar kullanılarak doğrulanmıştır. Çatlak şiddeti, çatlak konumu, uç kütle ve manyetik alan kuvveti gibi parametrelerin lineer ve nonlineer titreşimler üzerindeki etkileri sunulmuştur. Elde edilen sonuçlar, mikrokirişlerin doğal frekansları ve nonlineer frekanslarında, çatlak şiddetinin artmasıyla birlikte önemli ölçüde düşüş olduğunu göstermektedir.

Anahtar Kelimeler: *Nonlineer Titreşimler, Çatlak İçeren Mikrokirişler, Perturbasyon Teknikleri, Değiştirilmiş Çift Gerilme Teorisi, Çok Ölçekli Metot*

1. Introduction

Microelectromechanical systems (MEMS) are significant component in numerous modern technological devices across various industries. Due to their ability to integrate mechanical and electrical functionalities on a micro scale structure, these systems have found applications in fields such as aerospace, automotive engineering, biomedical and health industries. Beam type structures are generally used as the main components of MEMS. Understanding the static and dynamic behavior of these systems is crucial for their reliable operation.

The mechanical characteristics of small sized systems have different properties than macro sized structures [1-2]. Hence, additional elasticity theories have been derived to consider the effects of small size properties on static and dynamic responses. Yang et al. [3] have firstly introduced a couple stress based strain gradient theory, which includes only one additional material length scale parameter. Park and Gao [4] and Ma et al. [5] have employed this theory to the Bernoulli-Euler beam and to Timoshenko beams, respectively. They have predicted decreasing deflections and increasing bending rigidity as the beam size decreases. Kong et al. [6] have investigated the vibrational characteristics of Bernoulli-Euler microbeams. They observed the significant decrease in natural frequencies as the size of the beam increases. Reddy [7] have presented static deflection, free vibration and buckling analyses of functionally graded beams. They have obtained smaller static deflections and increased natural frequencies as the beam thickness increases. Asghari et al. [8] have implemented the modified couple stress theory to static and vibration problems of inhomogeneous

DOI: https://doi.org/10.21205/deufmd.2025277908

Geliş Tarihi / Received: 14.03.2024
Kabul Tarihi / Accepted: 15.04.2024

composite beams, revealing a significant difference between the results of the aforementioned theory and the classical beam theory. Şimşek et al. [9] have investigated the size dependent vibrations of microbeams and predicted the significant effects of the scale parameter on plates.

Nonlinear phenomena also have a profound impact on the dynamics of microstructures as they have complex dynamic responses. Wang et al. [10] have studied the nonlinear free vibrations of microbeam. The predicted nonlinear frequencies obtained by the modified couple stress theory are larger than those obtained from the classical beam model. Ghayesh et al. [11] have investigated nonlinear resonant dynamics of microbeams. In recent years, the researchers have studied through the linear and nonlinear vibrational characteristics of micro [12-13] and nano beams [14-15] by using the modified couple stress theory.

Cracks have been one of the structural problems on small sized structures, which affects the mechanical behaviors significantly. The previous studies in the literature [16-18] have predicted decreasing natural frequencies of the small sized structures, as the crack severity increases. Vibrations of cracked nanobeams have been analyzed by using modified couple stress theory [19] and nonlocal elasticity theory [20]. Larkin et al. [21] have investigated the effects of a crack on microgyroscopes. Free vibration analysis of multi-cracked microbeams [22], functionally graded microbeams [23] and piezoelectric nanobeams [24] have been studied, presenting the significant effects of the cracks on natural frequencies.

In this study, nonlinear vibrations of cracked microbeams under magnetic field force have been investigated. Micro size property of the beam has been involved into the model by using the modified couple stress theory. The crack has been modelled by introducing a torsional spring located at the crack position, where the spring coefficient corresponding to the crack severity. To obtain the approximate solutions for linear and nonlinear transverse vibrations, method of multiple scales, which is a perturbation technique [25] has been employed. The numerical results have been validated by the available results of the literature. The effects of crack severity, the crack location, tip mass parameter and the magnetic field force on natural frequencies and on nonlinear frequencies have been presented. Frequency-response curves have been plotted to demonstrate the nonlinear behavior affected by the crack and the system parameters.

2. Method

Mechanical properties of structures at micro-scale differ from those at the large scale [Fleck-Lam et al]. Modified couple stress theory [Yang et al] is employed in this study to involve the effects of small size of the beam. One additional parameter, which is used to characterize the couple stress is introduced, in addition to two classical Lame parameters. The strain energy of a Bernoulli-Euler beam under small deformation is written as follows [3]:

$$U = \frac{1}{2}\int_0^L (\mathrm{EI} + GAl^2)\, w''^2 dx \tag{1}$$

E is the modulus of elasticity, I is the area moment of inertia, G is the shear modulus and A is the cross-sectional area. w is the transverse displacements of the beam along z-axis, where x is the longitudinal axis. Here, l is the material length scale parameter, introduced by the modified couple stress theory and represents the small size-dependency of the structure. The energy expression regarding the classical beam theory is obtained by setting the parameter l to zero.

2.1. The model of the cracked microbeam with tip mass

In this paper, cantilever microbeams with tip mass under magnetic field force are investigated. The schematic figure of the model, including the crack, is given in Figure 1.

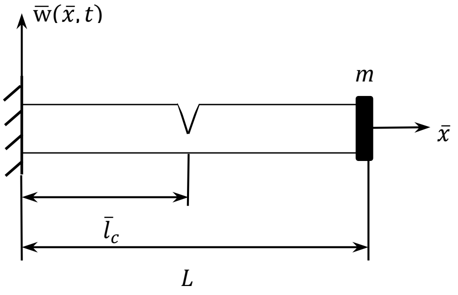

Figure 1. Schematic figure of the cantilever microbeam with tip mass.

Kinetic energy (T) and the strain energy (U) of the cracked microbeam are expressed as:

$$T = \frac{1}{2}\int_0^{\bar{l}_c} \rho A\, \dot{\bar{w}}_1^{\,2} d\bar{x} + \frac{1}{2}\int_{\bar{l}_c}^{L} \rho A\, \dot{\bar{w}}_2^{\,2} d\bar{x} + \frac{1}{2} m \dot{\bar{w}}_2(L)^2 \tag{2}$$

$$\begin{aligned} U = {} & \frac{1}{2}\int_0^{\bar{l}_c} (EI + GAl^2)\bar{w}_1''^2 d\bar{x} + \frac{1}{2}\int_{\bar{l}_c}^{L} (EI + GAl^2)\bar{w}_2''^2 d\bar{x} \\ & + \frac{1}{2} EA \int_0^{\bar{l}_c} \left(\bar{u}_1' + \frac{1}{2}\bar{w}_1'^2\right) d\bar{x} \\ & + \frac{1}{2} EA \int_{\bar{l}_c}^{L} \left(\bar{u}_2' + \frac{1}{2}\bar{w}_2'^2\right) d\bar{x} \end{aligned} \tag{3}$$

The beam is considered in two segments that are divided by the crack. $\bar{w}_1$ and $\bar{w}_2$ are the transverse displacements, $\bar{u}_1$ and $\bar{u}_2$ are the longitudinal displacements of the two segments, respectively. ρ is the mass density, m is the quantity of the tip mass, L is the length of the microbeam, $\bar{l}_c$ is the position of the crack measured from the left end of the beam. The strain energy of the beam includes the size-dependent deformation energy, which is given in Eq. (1).

The microbeam is subjected to an axial magnetic field, leading the Lorentz force expressed as follows [12]:

$$f_m = \eta A H_x^{\,2} \frac{\partial^2 w}{\partial x^2} \tag{4}$$

where η is the magnetic permeability and H_x is the longitudinal magnetic field vector along x-axis.

The kinetic and strain energies of the system satisfy the below expression according to the Hamilton' s principle:

$$\int_{t_1}^{t_2} (\delta T - \delta U)\, dt = 0 \tag{5}$$

Equations of motion of the two segments of the microbeam becomes:

$$\begin{aligned} & (EI + \mu A l^2)\overline{w_1}^{iv} + \rho A \ddot{\bar{w}}_1 \\ & \quad = \eta A H_x^{\,2} \bar{w}_1'' + \frac{EA}{2L}\int_0^{\bar{l}_c} \bar{w}_1'^2\, d\bar{x}.\bar{w}_1' \end{aligned} \tag{6}$$

$$(EI+\mu Al^2)\overline{w_2}^{iv}+\rho A\ddot{\overline{w}}_2 = \eta A{H_x}^2{\overline{w}_2}''+\frac{EA}{2L}\int_{\bar{l}_c}^{L}{\overline{w}_2}'^2\,d\bar{x}.{\overline{w}_2}' \qquad (7)$$

In order to express the equations in a convenient form, the following non-dimensional parameters are introduced and listed in Table 1.:

Table 1. The boundary and the compatibility conditions.

Non-dimensional parameters	
$w=\frac{\overline{w}}{d}$	Transverse displacement
$x=\frac{\bar{x}}{L}$	Longitudinal axis parameter
$t=\frac{\bar{t}}{L^2}\sqrt{\frac{EI}{\rho A}}$	Non-dimensional time parameter
$\gamma=\frac{\mu Al^2}{EI}$	Micro size parameter
$H=\frac{\eta A{H_x}^2L^2}{EI}$	Magnetic force parameter
$\alpha_2=\frac{Ad^2}{I}$	Slenderness of the beam
$l_c=\frac{\bar{l}_c}{L}$	Crack location parameter
$M=\frac{m}{\rho AL}$	Tip mas parameter
$\omega_n=\bar{\omega}_nL^2\sqrt{\frac{\rho A}{EI}}$	Non-dimensional natural frequency

Non-dimensional form of the equations are obtained as follows:

$$(1+\gamma){w_1}^{iv}+\ddot{w}_1+\mu\dot{w}_1 = H{w_1}''+\frac{1}{2}\alpha_2\int_0^{l_c}{w_1}'^2\,dx.{w_1}''+Fcos\Omega t \qquad (8)$$

$$(1+\gamma){w_2}^{iv}+\ddot{w}_2+\mu\dot{w}_2 = H{w_2}''+\frac{1}{2}\alpha_2\int_{l_c}^{1}{w_2}'^2\,dx.{w_2}''+Fcos\Omega t \qquad (9)$$

Transverse excitation with the amplitude F and the frequency Ω and damping effect with the damping constant μ are inserted into the equations additionally.

2.2 Method of Solution

The equations of motion of the microbeam are solved according to the method of multiple scales, a perturbation technique [25]. Time parameter is divided into slow $(T_0=t)$ and fast $(T_1=\varepsilon t)$ scales, where ε is a perturbation parameter in small order. Time derivatives are expressed in terms of these new time parameters as follows:

$$\frac{\partial}{\partial t}=\mathrm{D}_0+\varepsilon D_1 \quad \frac{\partial^2}{\partial t^2}=\mathrm{D}_0{}^2+2\varepsilon D_0D_1+.. \quad D_n=\frac{\partial}{\partial T_n} \qquad (10)$$

The solutions of the two segments of the microbeam are expanded as:

$$w_1(x,t{:}\,\varepsilon)=w_{01}(x,T_0,T_1)+\varepsilon w_{11}(x,T_0,T_1)+O(\varepsilon^2) \qquad (11)$$

$$w_2(x,t{:}\,\varepsilon)=w_{02}(x,T_0,T_1)+\varepsilon w_{12}(x,T_0,T_1)+O(\varepsilon^2) \qquad (12)$$

$O(\varepsilon^2)$ represents the smaller order parameters. Substituting the expanded solutions into Eqs. (8) and (9), the equations can be expressed separately for two orders. Eqs. (13-14) involve the parameters at $O(1)$ and present the linear problem. Eqs. (15-16), presenting the nonlinear problem, includes the $O(\varepsilon)$ parameters and excitation and damping effects which are assumed to be at $O(\varepsilon)$:0

$$(1+\gamma){w_{01}}^{iv}+{D_0}^2w_{01}-H{w_{01}}''=0 \qquad (13)$$

$$(1+\gamma){w_{02}}^{iv}+{D_0}^2w_{02}-H{w_{02}}''=0 \qquad (14)$$

$$(1+\gamma){w_{11}}^{iv}+{D_0}^2w_{11}-H{w_{11}}'' = -2D_0D_1w_{01}+\frac{1}{2}\alpha_2\int_0^{l_c}{w_{01}}'^2dx\,.w_{01}''-\mu D_0w_{01}+Fcos\Omega t \qquad (15)$$

$$(1+\gamma){w_{12}}^{iv}+{D_0}^2w_{12}-H{w_{12}}'' = -2D_0D_1w_{02}+\frac{1}{2}\alpha_2\int_{l_c}^{1}{w_{02}}'^2dx\,.w_{02}''-\mu D_0w_{02}+Fcos\Omega t \qquad (16)$$

The solution of the linear problem can be assumed as $w_{0i}(x,T_0,T_1)=A(T_1)e^{i\omega T_0}Y_i(x)+cc$, for i=1,2. Here, ω is the frequency of vibration and cc refers the complex conjugates. This assumption is substituted into the Eqs. (13-14), resulting the expression:

$$(1+\gamma)Y_i(x)^{iv}-\omega^2Y_i(x)-HY_i(x)''=0 \quad i=1,2. \qquad (17)$$

$Y_i(x)$ can be expressed as the shape functions of the microbeam as follows:

$$\begin{aligned} Y_1(x)&=c_1e^{ir_1x}+c_2e^{ir_2x}+c_3e^{ir_3x}+c_4e^{ir_4x} && 0<x<l_c \\ Y_2(x)&=c_5e^{ir_1x}+c_6e^{ir_2x}+c_7e^{ir_3x}+c_8e^{ir_4x} && l_c<x<1 \end{aligned} \qquad (18)$$

Eq. (18) is substituted into Eq. (17) and obtained that:

$${r_n}^4(1+\gamma)-\ \omega^2-H{r_n}^2=0 \qquad n=1\ldots4. \qquad (19)$$

The unknown coefficients r_1- r_4 are found as:

$$r_n=\mp\sqrt{\frac{-H^2\mp\sqrt{H^4-4(1+\gamma)\omega^2}}{2(1+\gamma)}} \qquad n=1..4 \qquad (20)$$

The boundary conditions of the microbeam with clamped-free ends and the compatibility conditions of the crack location are listed in Table 2. K_t is the torsional spring coefficient, which represents the crack severity.

Eq. (18) is subjected to the boundary and the compatibility conditions. A set of linear equations are obtained as a result. Coefficient matrix of the parameters c_1...c_8 are formed from the set of equations and determinant of the matrix is set to zero to calculate the natural frequencies.

Table 2. The boundary and the compatibility conditions.

Left end	Crack location	Right end
$Y_1(0)=0$	$Y_1(l_c)=Y_2(l_c)$	$Y_2''(1)=0$
$Y_1'(0)=0$	$Y_2'(l_c)-Y_1'(l_c)-K_tY_1''(l_c)=0$	$Y_2'''(1)-M\omega^2Y_2(1)=0$
	$Y_1''(l_c)=Y_2''(l_c)$	
	$Y_1'''(l_c)=Y_2'''(l_c)$	

The nonlinear equations that are given in Eqs. (15-16) have the solution in the following form:

$$w_{1i}(x,T_0,T_1;\varepsilon)=\phi(x,T_1)e^{i\omega T_0}+W(x,T_0,T_1)+cc \qquad i=1,2 \tag{21}$$

The assumed solution and the solutions of the linear problem, $w_{01}(x,T_0,T_1)$ and $w_{02}(x,T_0,T_1)$ are inserted into the nonlinear problem. W includes the non-secular parameters. The substitution results the following expressions for the two segments of the microbeam:

$$\begin{aligned}(1+\gamma)\phi_1^{iv}-\phi_1\omega^2-H\phi_1''&=-2i\omega D_1AY_1(x)\\&+\frac{1}{2}\alpha_2A^2\bar{A}\left[\bar{Y}_1''(x)\int_0^{l_c}Y_1'(x)^2dx\right.\\&\left.+2Y_1''(x)+\int_0^{l_c}Y_1'(x)\bar{Y}_1'(x)dx\right]\\&-\mu Ai\omega Y_1(x)+\frac{F}{2}e^{i\sigma T_1}+NST+cc\end{aligned} \tag{22}$$

$$\begin{aligned}(1+\gamma)\phi_2^{iv}-\phi_2\omega^2-H\phi_2''&=-2i\omega D_1AY_1(x)\\&+\frac{1}{2}\alpha_2A^2\bar{A}\left[\bar{Y}_1''(x)\int_{l_c}^{1}Y_1'(x)^2dx\right.\\&\left.+2Y_1''(x)+\int_{l_c}^{1}Y_1'(x)\bar{Y}_1'(x)dx\right]\\&-\mu Ai\omega Y_1(x)+\frac{F}{2}e^{i\sigma T_1}+NST+cc\end{aligned} \tag{23}$$

NST denotes the non-secular term of the equation. The frequency of excitation is taken as $\Omega=\omega+\varepsilon\sigma$ to ensure the primary resonance, where σ is the tuning parameter. The solvability condition, which eliminates the secular terms, is written as follows:

$$2i\omega D_1A-k_1A^2\bar{A}+\mu Ai\omega-f_1e^{i\sigma T_1}=0 \tag{24}$$

where k_1 and f_1 are obtained as:

$$\begin{aligned}k_1&=\frac{\alpha_2}{4i\omega S}\left[\int_0^{l_c}\bar{Y}_1''(x)\bar{Y}_1(x)\int_0^{l_c}Y_1'(x)^2dx\,dx\right.\\&+\int_{l_c}^{1}\bar{Y}_2''(x)\bar{Y}_2(x)\int_{l_c}^{1}Y_2'(x)^2dx\,dx\\&+2\int_0^{l_c}Y_1''(x)\bar{Y}_1(x)\int_0^{l_c}Y_1'(x)\bar{Y}_1'(x)dx\,dx\\&\left.+2\int_{l_c}^{1}Y_2''(x)\bar{Y}_2(x)\int_{l_c}^{1}Y_2'(x)\bar{Y}_2'(x)dx\,dx\right]\end{aligned} \tag{25}$$

$$f_1=\frac{F}{4i\omega S}\left[\int_0^{l_c}\bar{Y}_1(x)dx+\int_{l_c}^{1}\bar{Y}_2(x)dx\right] \tag{26}$$

where $S=\int_0^{l_c}Y_1(x)\bar{Y}_1(x)dx+\int_{l_c}^{1}Y_2(x)\bar{Y}_2(x)dx$.

Phase-amplitude equations are obtained by substituting the amplitudes as $A=\frac{1}{2}ae^{i\theta}$ and $\bar{A}=\frac{1}{2}ae^{-i\theta}$ into Eq. (24):

$$D_1a=k_{1R}\frac{1}{4}a^3-\frac{\mu}{2}a+2f_{1R}cos\alpha-2f_{1I}sin\alpha \tag{27}$$

$$D_1\alpha=\sigma-k_{1I}\frac{1}{4}a^2-2\frac{f_{1R}}{a}sin\alpha-2\frac{f_{1I}}{a}cos\alpha \tag{28}$$

where $\alpha=\sigma T_1-\theta$. The subscripts R and I denote the real and imaginary components of the terms, respectively. Derivatives of the amplitude and the phase, D_1a and $D_1\alpha$ respectively, converges to zero for a steady-state solution. The tuning parameter σ is solved by using Eq. (28) as follows:

$$\sigma=\frac{1}{4}k_{1I}a^2\pm\sqrt{\frac{4}{a^2}\left({f_{1R}}^2+{f_{1I}}^2\right)-\frac{\mu^2}{4}} \tag{29}$$

The nonlinear frequency of the microbeam is calculated by considering the free and undamped vibrations and setting $f=\mu=0$ in Eq. (29). The obtained frequency is:

$$\omega_{nl}=\omega_n+\frac{1}{4}k_{1I}{a_0}^2 \tag{30}$$

3. Results and Dicussion

In this paper, numerical results of cracked cantilever microbeam with a tip mass are presented. Firstly, obtained results are verified by comparing with the results of the available literature. Then, the results of linear and nonlinear frequencies of the cracked microbeam are given in the following sections.

3.1. Verification of the results

In order to ensure the accuracy of the numerical results of the cracked beam model, non-dimensional frequency parameters, which are obtained in the present study, are compared with the ones of Loya et al. [16]. A simply-supported microbeam is considered with the properties of the beam: $L=100\,h$, $b=10h$, $\rho=8166\,kg/m^3$, $E=207\,GPa$, $\nu=0.3$. Nonlocal parameter is set to zero. The results for the first four modes of vibration are given in the Table 3.

Table 3. Verification of the results. (*M*=0, *H*=0, *l_c*=0.5)

Non-dimensional frequency parameters	K_t=0		K_t=0.065	
	Loya et al [16]	Present study	Loya et al [16]	Present study
1	3.1416	3.14159	3.0469	3.04691
2	6.2832	6.28319	6.2832	6.28319
3	9.4248	9.42478	9.1669	9.16691
4	12.5664	12.5664	12.5664	12.5664

Table 3 (continued)

Non-dimensional frequency parameters	K_t=0.35		K_t=2	
	Loya et al [16]	Present study	Loya et al [16]	Present study
1	2.7496	2.74957	2.0960	2.09598
2	6.2832	6.28319	6.2832	6.28319
3	8.6129	8.61288	8.0730	8.07304
4	12.5664	12.5664	12.5664	12.5664

3.2 Numerical results of the cantilever microbeam with tip mass

In order to investigate the effects of the crack, the microbeam with tip mass under clamped-free boundary conditions are considered. Other parameters regarding the material and size properties are listed as:

$$h=100\ \mu\text{m}\ b=3h,\ L=10\ h,\ \text{E}=1.44\ \text{GPa},\quad \rho=1600\ \text{kg/m}^3,\ \nu=0.38,\ l=17.6\ \mu\text{m} \tag{31}$$

Non-dimensional natural frequencies regarding the first three modes of vibration with respect to the crack severity are presented in Figure 2. Varying crack positions for cantilever microbeams with M=0.1, H=10 are considered. For each mode, natural frequencies decrease with increasing crack severity. For the first mode, the decrease in natural frequency is more significant when the crack is located at l_c=0.25. The effect of crack severity becomes insignificant when the crack location is l_c=0.75, which is close to the free end boundary of the microbeam. In the second mode, the decrease in natural frequencies is more pronounced. Specifically, when the crack is at l_c=0.50, the decrease is greater than when the crack is at l_c=0.25. This is related to the mode shape of the second mode, which gives larger slope at the crack location. For the third mode, the decrease in natural frequency is more remarkable for l_c=0.25 and becomes insignificant as the crack location approaches to the free end of the microbeam.

In Figure 3, the results predicting the effects of tip mass on the first mode non-dimensional natural frequencies are shown. The crack is taken at the midpoint of the beam and the magnetic force parameter is H=10. The results predict a significant increase in natural frequencies as the tip mass parameter increases. Moreover, the effect of the crack is seen more clearly for the microbeam without a tip mass. The presence of the crack becomes less significant as the tip mass parameter increases.

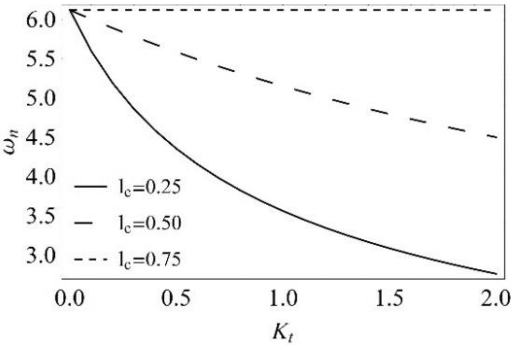

a. 1st mode

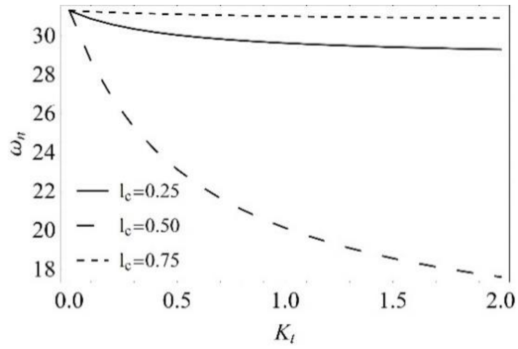

b. 2nd mode

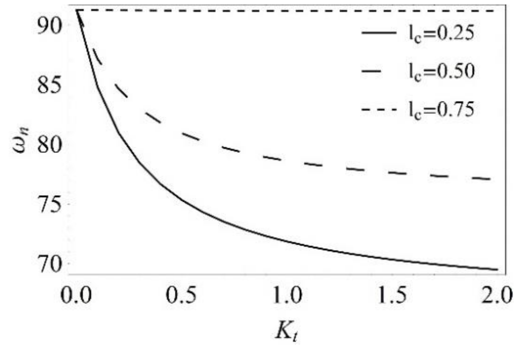

c. 3rd mode

Figure 2. Non-dimensional natural frequencies of cantilever microbeams with varying crack positions.

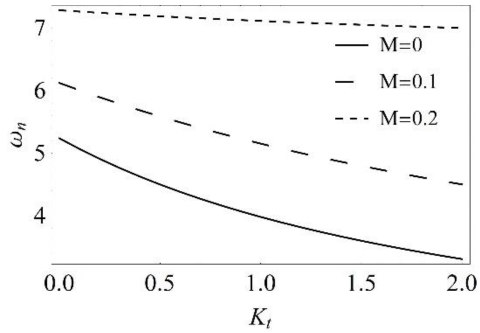

Figure 3. Non-dimensional natural frequencies of cantilever microbeams with varying tip mass values.

Figure 4 shows the non-dimensional natural frequencies with respect to the crack severity for different magnetic force parameters. The microbeams with the crack location l_c=0.5 and with the tip mass parameter M=0.1 are investigated. Increasing natural frequencies are obtained as the magnetic force parameter increases. The effect of the crack severity leads decreasing natural frequencies for all magnetic force parameters. However, the decrease becomes more pronounced when the force parameter increases.

By considering the steady-state free vibration without damping and excitation, nonlinear frequencies are plotted with respect to the amplitude in Figure 5. Cantilever microbeams with M=0.1 and l_c=0.5 and varying crack severity parameters are taken. The nonlinear frequencies decrease significantly as the crack severity increases.

In Figure 6, effects of varying crack location on the first mode nonlinear frequencies are illustrated, by considering the crack severity as K_t=1 and the tip mass parameter M=0.1. The nonlinear frequency increases as the crack location is closer to the free end of the microbeam. Moreover, the nonlinear behavior alters with the increasing amplitudes for different crack locations.

Figure 7 represents the effects of the tip mass of the cracked cantilever microbeam. Nonlinear frequencies are plotted with respect to the amplitude for varying tip mass parameters and for l_c=0.5 and K_t=1. As the tip mass parameter increases, the nonlinear frequencies increases. This result is related to the increasing stiffness of the microbeams with tip mass.

The frequency-response curves of the cracked microbeam having a M=0.1 tip mass are given in Figure 8. The curves corresponding to the different crack severity parameters are obtained by taking l_c=0.5, α_2=3, F=5 and μ=0.1. Increasing nonlinear behavior is observed as the crack severity increases.

Effects of the crack location and the tip mass parameter are demonstrated in Figures 9 and 10, respectively. Frequency-response curves of the first mode vibrations are plotted. In Figure 9, the microbeam has a crack with K_t=1 and tip mass parameter of M=0.1. The curve shows softening behavior for l_c=0.25 and l_c=0.75, whereas a hardening behavior is observed for l_c=0.5. In Figure 10, the beam has a crack at the midpoint with K_t=1. Softening nonlinear behavior is observed for the microbeam without tip mass. However, hardening effect is observed when the tip mass parameter increases.

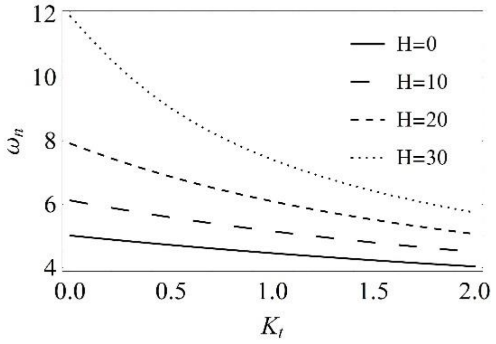

Figure 4. Non-dimensional natural frequencies of cantilever microbeams with varying magnetic force parameters.

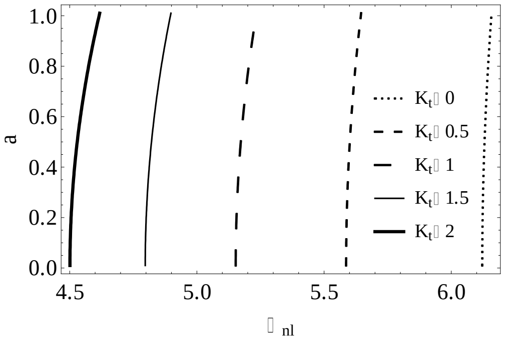

Figure 5. Nonlinear frequencies with respect to the amplitude for varying crack severities.

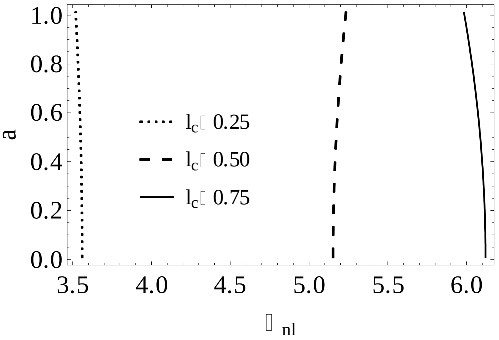

Figure 6. Nonlinear frequencies with respect to the amplitude for varying crack locations.

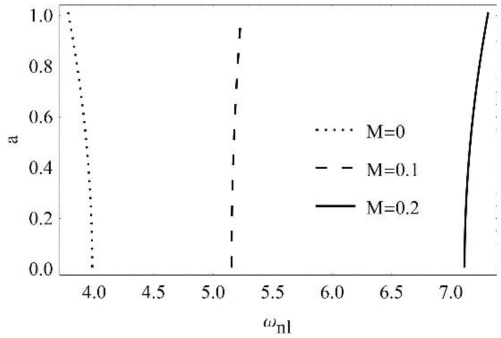

Figure 7. Nonlinear frequencies with respect to the amplitude for varying tip mass parameters.

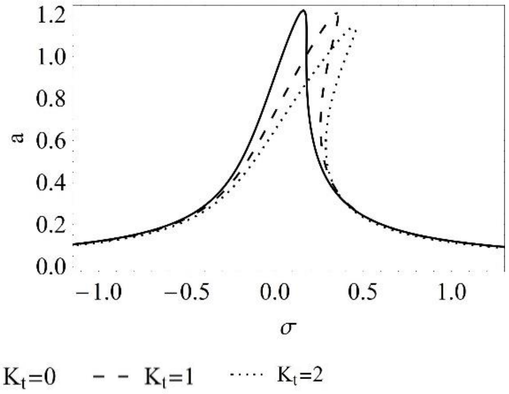

Figure 8. Frequency-response curves of microbeams for varying crack severities.

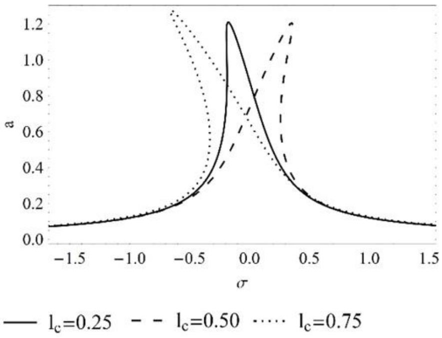

Figure 9. Frequency-response curves of microbeams for varying crack severities.

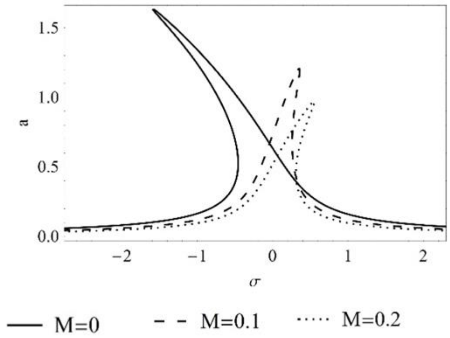

Figure 10. Frequency-response curves of microbeams for varying tip mass parameters.

4. Conclusions

The effects of cracks on nonlinear vibrations of microbeams under a magnetic field have been investigated in this paper. Cantilever microbeams with tip mass attached to the free end have been included. The micro size effect of the beam has been involved into the model by using modified couple stress theory. A material length scale parameter has been included in the strain energy of the microbeam, which describes the small size property. The crack has been modelled by using a torsional spring and the spring coefficient corresponds to the crack severity. The derived equations of motion have been solved by employing the method of multiple scales, which is a perturbation technique. The approximate numerical results regarding both linear and nonlinear vibrations of the cracked microbeams have been obtained. To ensure the accuracy of the results, natural frequencies obtained from this study have been compared with the ones obtained from the literature.

The effects of the crack severity, crack location, magnetic field force, tip mass have been investigated. It is concluded that natural frequencies and nonlinear frequencies decrease significantly as the crack severity increases. The frequency-response curves of the cracked microbeams reveals a change in the nonlinear behavior. As the crack severity increases, hardening characteristic of the curves increases. Additionally, the peak amplitudes decrease with increasing crack severities.

The crack location has been observed as a major parameter, which alters the effects of cracks. For different mode shapes of vibration, sensitivity to crack severity of natural frequencies varies, as the crack location varies. For the first mode, the decrease amount of natural frequencies increases as the crack location is closer to the fixed end of the microbeam. The presence of the crack becomes more critical and effective in such microbeams. On the other hand, for the second mode, the decrease is more pronounced for the microbeam having a crack at the midpoint. This is related to the mode shape of the second mode, resulting larger slope at the crack location. Nonlinear frequencies have also been investigated and it is concluded that the nonlinear frequency decreases as the crack location becomes closer to the fixed end of the beam, in the first mode vibration. Moreover, the frequency-response curves reveal altering nonlinear behaviors with different crack locations.

The presence of the tip mass on the cantilever microbeams leads an increasing effect on the natural frequencies and on the nonlinear frequencies. There is a consistent increase in frequencies with the increasing tip mass parameter. The results show a softening nonlinear behavior for the microbeam without tip mass. However, the frequency-response curves predict a hardening behavior when the tip mass is added. The hardening behavior has an increasing effect as the tip mass parameter is increased. In addition, the peak amplitude of the response decreases as the tip mass parameter increases. This results re related with the increasing stiffness of the microbeam as the tip mass parameter increases.

The influence of the magnetic field has been investigated. As the magnetic force parameter increases, the natural frequencies increases. Specifically, the effect of the crack severity becomes more significant as the magnetic force parameter increases. The findings of this study can provide insights for the real-world applications of MEMS, to estimate the health and performance and to design the micro components of these systems.

Ethics committee approval and conflict of interest statement

This article does not require ethics committee approval. This article has no conflicts of interest with any individual or institution.

References

[1] Fleck, N. A., Hutchinson, J. W. 1993. A Phenomenological Theory for Strain Gradient Effects In Plasticity. Journal of the Mechanics and Physics of Solids, Vol. 41(12), pp. 1825-1857. DOI: https://doi.org/10.1016/0022-5096(93)90072-N

[2] Lam, D. C. C., Yang, F., Chong, A. C. M., Wang, J., Tong, P. 2003. Experiments and Theory in Strain Gradient Elasticity. Journal of Mechanics and Physics of Solids, Vol. 51(8), pp. 1477-1508. DOI: 10.1016/S0022-5096(03)00053-X

[3] Yang, F., Chong, A. C. M., Lam, D. C. C., Tong, P. 2002. Couple Stress Based Strain Gradient Theory for Elasticity. International Journal of Solids and Structures, Vol. 39(10), pp. 2731-2743. DOI: 10.1016/S0020-7683(02)00152-X

[4] Park, S. K., Gao, X. L. 2006. Bernoulli–Euler Beam Model Based on a Modified Couple Stress Theory. Journal of Micromechanics and Microengineering, Vol. 16, pp. 2355-2359. DOI: 0.1088/0960-1317/16/11/015

[5] Ma, H. M., Gao, X. L., Reddy, J. N. 2008. A Microstructure-Dependent Timoshenko Beam Model Based on a Modified Couple Stress Theory. Journal of Mechanics and Physics of Solids, Vol. 56(12), pp. 3379-3391. DOI: 10.1016/j.jmps.2008.09.007

[6] Kong, S., Zhou, S., Nie, Z., K. Wang. 2008. The Size-Dependent Natural Frequency of Bernoulli–Euler Micro-Beams. International Journal of Engineering Science, Vol. 46(5), pp. 427-437. DOI: 10.1016/j.ijengsci.2007.10.002

[7] Reddy, J. N. 2011. Microstructure-Dependent Couple Stress Theories of Functionally Graded Beams. Journal of Mechanics and Physics of Solids, Vol. 59, pp. 2382-2399. DOI: 10.1016/j.jmps.2011.06.008

[8] Asghari, M., Ahmadian, M. T., Kahrobaiyan, M. H., Rahaeifard, M. 2010. On The Size-Dependent Behavior of Functionally Graded Micro-Beams. Materials and Design, Vol. 31, pp. 2324-2329. DOI: https://doi.org/10.1016/j.matdes.2009.12.006

[9] Şimşek, M., Aydın, M., Yurtcu, H. H., Reddy, J. N. 2015. Size-Dependent Vibration of a Microplate Under the Action of a Moving Load Based on the Modified Couple Stress Theory. Acta Mechanica, Vol. 226, pp. 3807-3822. DOI: 10.1007/s00707-015-1437-9

[10] Wang, Y. G., Lin, W. H., Liu, N. 2013. Nonlinear Free Vibration of a Micro Scale Beam Based on Modified Couple Stress Theory. Physica E Low Dimensional Systems and Nanostructures, Vol. 47, pp. 80-85. DOI: 10.1016/j.physe.2012.10.020

[11] Ghayesh, M. H., Farokhi, H., Amabili, M. 2013. Nonlinear Dynamics Of A Microscale Beam Based on the Modified Couple Stress Theory. Composites Part B, Vol. 50, pp. 318-324. DOI: https://doi.org/10.1016/j.compositesb.2013.02.021

[12] Hieu, D. V., Hoa, N. T., Duy, L. Q., Thoa, N. T. K. 2021. Nonlinear Vibration of an Electrostatically Actuated Functionally Graded Microbeam under Longitudinal Magnetic Field. Journal of Applied and Computational Mechanics, Vol. 7(3), pp. 1537-1549. DOI: 10.22055/JACM.2021.35504.2670

[13] Bağdatlı, S. M., Togun, N., Yapanmış, B. E., Akkoca, Ş. 2023. Nonlinear Vibration Of Microbeams Subjected To A Uniform Magnetic Field And Rested On Nonlinear Elastic Foundation. Zeitschrift für Naturforschung A, Vol. 79(1), pp. 17-30. DOI: 10.1515/zna-2023-0225

[14] Togun, N., Bağdatlı, S. M. 2016. Size Dependent Nonlinear Vibration Of The Tensioned Nanobeam Based On The Modified Couple Stress Theory. Composites Part B-Engineering, Vol. 97, pp. 255-262. DOI: https://doi.org/10.1016/j.compositesb.2016.04.074

[15] Atcı, D. 2021. Free Vibrations of Nanobeams under Non-Ideal Supports Based on Modified Couple Stress Theory. Zeitschriftt für Naturforschung A, Vol. 76(5), pp. 427-434. DOI: 10.1515/zna-2020-0335

[16] Loya, J., Lopez-Puente, J., Zaera, R., Fernandez-Saez, J. 2009. Free Transverse Vibrations of Cracked Nanobeams Using a Nonlocal Elasticity Theory. Journal of Applied Physiscs, Vol. 105(4), pp. 044309-9. DOI: 10.1063/1.3068370

[17] Tadi Beni, Y., Jafari, A., Razavi, H. 2015. Size Effect on Free Transverse Vibration of Cracked Nano-Beams Using Couple Stress Theory. International Journal of Engineering, Vol. 28(2), pp. 296-304. DOI: 10.5829/idosi.ije.2015.28.02b.17

[18] Hsu, J. C., Lee, H. L., Chang, W. L. 2011. Longitudinal Vibration of Cracked Nanobeams Using Nonlocal Elasticity Theory. Current Applied Physics, Vol. 11(6), pp. 1384-1388. DOI: 10.1016/j.cap.2011.04.026

[19] Akbaş, Ş. D. 2018. Forced Vibration Analysis of Cracked Nanobeams. Journal of Brazilian Society of Mechanical Science and Engineering, Vol. 40, pp. 392. DOI: 10.1007/s40430-018-1315-1

[20] Roostai, H., Haghpanahi, M. 2014. Vibration of Nanobeams of Different Boundary Conditions with Multiple Cracks Based on Nonlocal Elasticity Theory. Applied Mathematical Modelling, Vol. 38(3), pp. 1159-1169. DOI: 10.1016/j.apm.2013.08.011

[21] Larkin, K., Ghommem, M., Hunter, A., Abdelkefi, A. 2020. Nonlinear Modeling and Performance Analysis of Cracked Beam Microgyroscopes. International Journal of Mechanical Science, Vol. 188, pp. 105965. DOI: https://doi.org/10.1016/j.ijmecsci.2020.105965

[22] Rahi, A., Petoft, H. 2018. Free Vibration Analysis of Multi-Cracked Micro Beams Based on Modified Couple Stress Theory. Journal of Theoretical and Applied Vibration and Acoustics, Vol. 4(2), pp. 205-222. DOI: 10.22064/TAVA.2019.89997.1113

[23] Esen, İ., Özarpa, C., Eltaher, M. A. 2021. Free Vibration of a Cracked FG Microbeam Embedded in an Elastic Matrix and Exposed to Magnetic Field in a Thermal Environment. Composite Structures, Vol. 261, pp. 113552. DOI: 10.1016/j.compstruct.2021.113552

[24] Eghbali, M., Hosseini, S. A., Pourseifi, M. 2022. Free Transverse Vibrations Analysis of Size-Dependent Cracked Piezoelectric Nano-Beam Based on the Strain Gradient Theory under Mechanic-Electro Forces. Engineering Analysis with Boundary Elements, Vol. 143, pp. 606-612. DOI: 10.1016/j.enganabound.2022.07.006

[25] Nayfeh, A. H. 1981 Introduction to Perturbation Techniques. John Wiley, New York, NY, USA. ISBN: 0-471-39917-5.

DEU FMD 27(79) (2025) 62-71

Dokuz Eylül Üniversitesi Mühendislik Fakültesi Fen ve Mühendislik Dergisi
Dokuz Eylul University Faculty of Engineering Journal of Science and Engineering
Elektronik/Online ISSN: 2547-958X

RESEARCH ARTICLE / ARAŞTIRMA MAKALESI

An Adaptive PI Controller Design for Current Control of Brushless DC Motor Drives

Fırçasız Doğru Akım Motor Sürücülerinin Akım Kontrolü için Bir Uyarlamalı PI Kontrolcü Tasarımı

Ceyhun Arslanoğlu *, **Fatih Adıgüzel**

Yıldız Technical University, Faculty of Electrical and Electronics, Department of Control and Automation Engineering, İstanbul, TÜRKİYE
Corresponding Author / Sorumlu Yazar *: ceycanarslanoglu@gmail.com

Abstract

Brushless direct current motor(BLDCM) are used to drive many systems in numerous fields. The control of BLDCM with basic drive techniques is required to obtain the desired output. Although basic drive techniques may be unsatisfactory in meeting these demands, they have found an invariable place for themselves due to their easy-to-use advantages. Due to these reasons, many researchers have focused on how innovative solutions are developed. In this paper, an adaptive PI controller is proposed to control the current of BLDCM drives. This paper aims to design a PI controller with time-varying gains for current regulation. The adaptive PI, improving the steady-state response, is constructed by one adaptation rule and a classical PI. In addition, the stability analysis is proved with Lyapunov theory. To demonstrate the effectiveness of the proposed controller, several simulations are performed with comparisons. The simulations with a classical PI and high-gain current controller comparisons are presented for set-point and sinusoidal references, and 500 rpm and 1500 rpm motor speeds. Comparing the classical PI with adaptive controller, the adaptive controller improves the current performance from 0.3442 to 0.0656 for 500 rpm, and from 0.4703 to 0.1552 for 1500 rpm in RMS of the current errors for 2A reference current. Similarly, the outcomes of comparing the high-gain controller to the adaptive PI show that the designed controller reduces RMS of the currents errors from 0.1853 to 0.1611 for 1500 rpm with 2A reference current, and from 0.1879 to 0.1720 for 1500 rpm with a sinusoidal reference current.

Keywords: *Brushless direct current motor drives, Adaptive control, PI controller, Current control*

Öz

Fırçasız doğru akım motoru(FDAM), sayısız alanda birçok sistemi tahrik etmek için kullanılmaktadır. FDAM temel tahrik teknikleriyle kontrolü, istenilen performansın alınabilmesi için gereklidir. Her ne kadar klasik yaklaşımlar bu talepleri karşılamada yetersiz kalsa da klasik kontrolörler kolay sürüş avantajlarından dolayı kendilerine değişmez bir yer bulmuşlardır. Bu nedenlerden dolayı, birçok araştırmacı yenilikçi çözümlerin nasıl geliştireceği üzerine odaklanmıştır. Bu makalede, FDAM akım kontrolü için uyarlamalı bir PI kontrolcü önerilmektedir. Bu makaledeki amaç, FDAM akım regülasyonu için zamanla değişen kontrolör kazançlarına sahip bir PI kontrolcü tasarlamaktır. Sürekli rejim yanıtını iyileştiren önerilen uyarlamalı PI kontrolcü, bir uyarlama kuralı ve klasik bir PI kontrolcüden oluşmaktadır. Ayrıca, kararlılık analizi Lyapunov teorisi ile kanıtlanmıştır. Önerilen kontrolörün etkinliğini göstermek için karşılaştırmalarla çeşitli simülasyonlar gerçekleştirilmiştir. Klasik PI ve yüksek kazançlı akım kontrolörü ile yapılan benzetimler, sabit ve sinüzoidal referanslar ile 500 rpm ve 1500 rpm motor hızları için karşılaştırmalı olarak sunulmuştur. Klasik PI, uyarlamalı kontrolcü ile karşılaştırıldığında, uyarlamalı kontrol 2A referans akımı için akımlarının hatasının RMS'deki akım performansını 500 rpm hız için 0,3442'den 0,0656'ya ve 1500 rpm hız için 0,4703'ten 0,1552'ye iyileştirmektedir. Benzer şekilde, yüksek kazançlı kontrolcünün uyarlamalı PI ile karşılaştırma sonuçlarında, uyarlamalı kontrolcü, motor akımlarının hatasının RMS'sini 2A referans akımında 1500 rpm hız için 0,1853'ten 0,1611'e ve sinüzoidal referans akımında 1500 rpm hız için 0,1879'dan 0,1720'ye düşürmektedir.

Anahtar Kelimeler: *Fırçasız doğru akım motor sürücüsü, Uyarlamalı kontrol, PI kontrol, Akım kontrol*

1. Introduction

A brushless direct current motor (BLDCM) is an electric motor, which is supplied by a DC voltage source and is commutated electronically without using of any brushes, unlike the conventional DC motor. The definition of BLDCM types is simplified as PMSMs having the trapezoidal-induced emf are known as permanent magnet brushless direct current motors (PMBLDCM) [1]. In recent years, due to its many advantages, such as simple structure, high efficiency, large torque, etc., BLDCM drives have been a viable option in industries like robotics, aerospace, industrial process control, household appliances, and more [2, 3]. Unlike conventional DC motors, PM brushless DC motors are commutated electrically. Thus, it requires continuous information on the rotor position to rotate the motor.

Over the years many control methods have been employed for the control of BLDC motor drives. Due to the fact that BLDC motor is a permanent magnet synchronous motor, vector control methods such as field-oriented control (FOC) [4] and direct

DOI: https://doi.org/10.21205/deufmd.2025277909

Geliş Tarihi / Received: 27.12.2023
Kabul Tarihi / Accepted: 16.04.2024

torque control (DTC) [5], have been quite popular methods. The control of BLDCM drives requires continuous information on the rotor position. However, this can be overwhelming in terms of costs. Therefore, some sensor-less methods including Kalman Filter [6] and Model Predictive Control (MPC) [7], have been employed to that FOC [8], DTC and many other control methods like back-EMF difference estimation methods [9, 10, 11] and back-EMF zero cross detection estimation [12] to exclude the sensors. Each of these methods has its advantages and disadvantages. However, none of them has the simplicity of a classical PI/PID controller.

The PID has been widely used since its introduction in the 1940s during the analog era. Examples of modern digital systems that utilize it include distributed control systems (DCS), supervisory control and data acquisition (SCADA), and digital systems [13]. As the systems advanced through the years, the need for tuning methods was brought along, such as Ziegler-Nichols. Having a simple structure and easy-to-use advantages have made PI/PID controllers be employed in many kinds of systems. However, systems in real life have nonlinearities and uncertainties, which need to be dealt with by an advanced controller. Although Ziegler-Nichols is simple and intuitive, it lacks good stability margins and creates a closed-loop system that is poorly damped. Hence, conventional PID controller struggles to adapt to varying operating conditions, leading to suboptimal performance. To overcome this problem, advanced methods, which are aforementioned, were brought up, implemented, and tested. The outcome of these advanced control methods has shown better performance in terms of trajectory tracking and compensation of nonlinearities, disturbances and even varying load conditions than a conventional PID controller. However, these advanced control methods are quite complicated in structure, and in the sense of computation, they are rather expensive and overwhelming. In practice, to reduce the cost and computational burden, these advanced methods have been undesired. As long as the PI/PID controller can compensate for the effects of nonlinearities, uncertainties parameter variations, etc., it will be the go-to choice for many systems. The synthesis of a universal PI control for nonlinear systems with analytically calculated gains, while guaranteeing stability and transient performance, is an ongoing unresolved topic. If the systems contain actuation failures, external disturbances, and modeling uncertainty, the issue becomes even more complex [14]. Multiple methods have been implemented for the control of nonlinear systems ranging from linearization of nonlinear systems into a linear system, adaptive backstepping control [15], to direct compensation of nonlinear systems by integrating neural networks (NN) with approximation capabilities [16]. Moreover, in [17] with the implementation of feedback linearization, an equivalent linear system for a DC motor was obtained and controlled with a linear quadratic regulator (LQR) to improve the performance. Furthermore, in [18] an adaptive input-output feedback linearization control, which was robust against the variation of motor parameters, for a non-ideal BLDC motor is proposed to generate the reference voltages for three phase voltage source inverter (VSI). In [19], an adaptive deadbeat controller using particle swarm optimization (PSO) and an adaptive neuro-fuzzy interference system (ANFIS) were used collaboratively to achieve a deadbeat response. In [20, 21, 22], fuzzy-based PI/PID controllers have been designed and implemented for the control of the speed of BLDC motors, and the incompetency of conventional PI/PID were alleviated in terms of compensating the side effects of nonlinear systems. In [23], for a class of nonlinear systems, a PI adaptive fuzzy controller has been employed, which ensures stability through Lyapunov theory while ensuring stability and robustness under large and fast varying disturbances. These forenamed algorithms, methods, and techniques have made significant improvements in PI/PID's ability to deal with nonlinear systems and to ensure stability and performance for closed-loop systems. However, there is still much to be discovered in terms of affordability, simplicity, and effectiveness. In [24], a self-tuning PID controller, where the gains of the controller were adjusted online. The adaptation mechanism has been designed based on the Lyapunov approach, ensuring the stability of the designed controller. Moreover, PI/PID controllers have been designed for nonlinear systems with possible sensor and actuation faults, where no linearization and approximation were done and stability was ensured through the Lyapunov approach, with control schemes that are simple in structure and computationally affordable [25, 26, 27]. However, such controllers specifically for BLDCM drives have not been come across in literature.

One of the reasons for the torque ripple in BLDCM drives is the commutation torque ripple which arises from the switching of the model dynamics. To handle this problem, several modified PWM methods are used such as the elimination commutation torque ripple of brushless DC motor with minimum commutation time [28], PWM modulation technique without calculation of commutation time [29], the switched current controller with commutation delay compensation [30], the switched adaptive controller [31]. In this paper, because the updating of the controller gains is considered the system dynamics, the reduction commutation torque is met without an additional controller modification.

The main purpose of this paper is to design an adaptive PI controller to regulate the currents in BLDCM with the elegant presentation of the current model. In the closed-loop nonlinear system containing nonlinearities and uncertainties, the general rule to determine the gains of the PI/PID controller does not exist. The tuning of the controller gains is usually adjusted by the trial-error method and practical concerns in nonlinear systems. However, this paper presents a tuning method for the gain of the PI controller which guarantees that all signals in the closed-loop are bounded aiming that the currents of BLDCM drives regulate in advance. The main philosophy of the structure of the designed controller is first to assign roughly PI controller gains to the BLDCM drives in which the drive is simple but inadequate considering the system performance. Secondly, the system performance is met by time-varying gains of the proposed PI controller which is constructed based on Lyapunov stability despite the system uncertainties, external disturbances, and actuator faults. Finally, the convergence of uniformly ultimately bounded stability of the closed-loop current dynamics is proved in the sense of Lyapunov theory. In addition to the aforementioned advantages of the designed controller, the contributions of this paper can be listed as follows:

1. Although the designed controller for the current control of BLDCM has a fundamental structure, an adaptation rule is employed for the control of the current of BLDCM as if advanced PI controller gains are used in PI control.
2. The controller structure is designed for the control of the conducting period of the motor, however, it is well-known that the BLDCM has a commutation period for each sector of currents. Without an additional controller, the designed controller proceeds due to the adaptation rules in the time-varying controller gain taking into account this switching of system dynamics.

3. The response of the designed controller seems to be a high-gain current controller but it is a controller that consumes less energy and responds easily to a non-linear changing of the system.

To show the effectiveness and viability of the proposed controller, several numerical simulations are carried out by comparing a traditional controller PI and a high-gain controller.

The rest of this paper is organized as follows. In Section 2, some lemmas are introduced to facilitate the understanding of controller design steps in the convergence analysis of the proposed controller. Section 3 gives the dynamic model of the BLDCM drive and its elegant presentation of the implicit current dynamic model. In Section 4, the design steps with the stability analysis of the proposed PI controller are rendered. In Section 5, some computer-based numerical experiments are presented to show the effectiveness of the proposed adaptive controller as to the traditional PI controller and a high-gain current controller. Finally, the conclusions are referred to in Section 6.

2. Preliminaries

This section presents some Lemmas to facilitate the design of the controller to be proposed and the stability analysis of the controller structure.

Lemma 2.1 (Barbalat's Lemma): Let $\alpha(t): [t_0, \infty) \to \mathbb{R}$ be a continuously differentiable scalar function. If $\alpha(t)$ has a finite limit as $t \to \infty$, and $\dot{\alpha}(t)$ is uniformly continuous over $[t_0, \infty)$, then

$$\lim_{t\to\infty} \dot{\alpha}(t) = 0. \tag{1}$$

For Proof of Lemma 2.1, see [32].

Consider a PI controller and we define a filtered variable u which is

$$u(t) = e(t) + \beta \int_0^t e(\tau)d\tau. \tag{2}$$

where $e(t) = x(t) - x^*(t)$ is the error of trajectory tracking and $\beta > 0$ is a design parameter gain to be determined in the implementation of the controller to be designed for the torque loop control of BLDCM drive. We assume here that $e(t)$ is a sufficiently smooth function.

Lemma 2.2: Consider the filtered variable $u(t)$ given in (2). If $\lim_{t\to\infty} u(t) = 0$, then $e(t)$ and $\int_0^t e(\tau)d\tau$ converge asymptotically to zero as $t \to \infty$ with the same decreasing rate with the filtered variable.

Proof: According to Lemma 2.1, it is satisfied that $\lim_{t\to\infty} \dot{u}(t) = 0$ which means that

$$\frac{d}{dt}\left(e(t) + \beta \int_0^t e(\tau)d\tau\right) = 0. \tag{3}$$

Then,

$$\dot{e}(t) + \beta e(t) = 0. \tag{4}$$

The solution of the equation given in (4) can be calculated as follow:

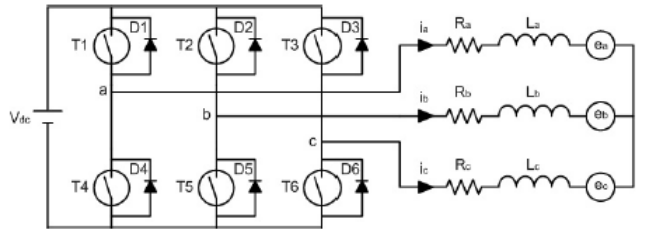

Figure 1. BLDCM Drive. [33]

$$e(t) = \bar{e}_0\, e^{-\beta t} \tag{5}$$

where $\bar{e}_0 = \frac{1}{e_0}$ with a constant initial value e_0, it implies that

$$\begin{aligned}\int_0^t e(\tau)d\tau &= \bar{e}_0 \int_0^t e^{-\beta\tau}d\tau \\ &= -\bar{e}_0\beta e^{-\beta t}.\end{aligned} \tag{6}$$

The proof is thus completed by the same decreasing rate value as that of $u(t)$.

3. Model of BLDCM Drives

In this section, the dynamical model of a three-phase BLDCM drive is presented. In the modeling of the BLDCM drive, some assumptions are taken into account as follows: (1) mutual inductance for each winding is zero, (2) resistances and inductances of three phases are equal, and (3) the neutral motor voltage is neglected. The equivalent circuit model of the BLDCM drive system is shown in Figure 1. The mathematical model of BLDC motor drive can be introduced as follows [34]:

$$L\,\frac{di_a(t)}{dt} = v_a(t) - Ri_a(t) - e_a(t) \tag{7}$$

$$L\,\frac{di_b(t)}{dt} = v_b(t) - Ri_b(t) - e_b(t) \tag{8}$$

$$L\,\frac{di_c(t)}{dt} = v_c(t) - Ri_c(t) - e_c(t) \tag{9}$$

where i_a, i_b, i_c denote the phase currents, v_a, v_b, v_c denote the phase voltages, e_a, e_b, e_c denote the back-EMF voltages, R is the resistance per phase and L is the inductance per phase. Besides, the following equality is satisfied:

$$i_a(t) + i_b(t) + i_c(t) = 0. \tag{10}$$

The differential equation for the mechanical part of the BLDC motor drive is modeled as follows:

$$J\,\frac{d\omega(t)}{dt} = T_e(t) - T_l(t) - \beta\omega(t) \tag{11}$$

where J is the equivalent inertia, ω is the angular velocity of BLDC motor shaft, T_e is generated motor torque and T_l is the load torque. Besides, the motor output torque of the BLDCM can be formalized as follows:

$$T_e(t) = \frac{e_a(t)i_a(t) + e_b(t)i_b(t) + e_c(t)i_c(t)}{\omega(t)}. \tag{12}$$

To achieve the desired output torque, the BLDC motor types need a well-shaped current drive when it is considered the shape of back-EMF signals. However, driving the currents of the motor to be obtained for each phase is not possible in practical applications. In practice, matched and un-matched uncertainties, external disturbances, faults in actuators, and nonlinearities also make the control of currents of the motor difficult. The main aim of this paper is to design a PI regulator for BLDC motor drives that takes the aforementioned drawbacks into account in the torque loop control. To facilitate the controller structure, the current dynamics given in (7)-(9) can be re-written as follows:

$$\frac{di_s(t)}{dt} = f(i_s, e_s) + gv_s(t) \tag{13}$$

where $= \{a, b, c\}$, $f(i_s, e_s) = -\frac{1}{L}Ri_s - \frac{1}{L}e_s$, $g = \frac{1}{L}$, and $v_s = \rho v + v_{un}$ with the definitions that ρ is actuator healthy rate, v is the controller input to be determined by the adaptive PI controller, v_{un} is uncontrollable part of the controller signal v_s given in (13). It is noticed that the controller gain g is a time-invariant unknown coefficient such that $0 \le \underline{g} \le |g| \le \overline{g}$, and ρ and v_{un} are unknown but bounded such that $0 < \underline{\rho} \le \rho \le 1$ and $|v_{un}| \le \overline{v}_{un}$ with unknown $\underline{\rho}$ and $\overline{v}_{un}$ values. Besides, the bounded uncertain function $f(i_s, e_s)$ includes the measurement of currents and back-EMF signals which render some nonlinear effects, and there exists an unknown time-invariant $f_c \ge 0$ and a known nonlinear function $\phi(i_s, e_s) \ge 0$ such that $|f(i_s, e_s)| \le f_c\phi(i_s, e_s)$.

4. Adaptive PI Controller

In this section, an adaptive PI controller is proposed for the torque loop control of BLDC motor drives, where the adaptive PI controller proposed in [26] is utilized for the regulation of the current of BLDCM drives to reduce the effects of the ripples over the output torque. It should be noted that the proposed controller is designed to address actuation failures, other uncertainties, and unknown controller gain. The designed controller diagram is presented in Figure 2.

First, the error expression can be defined as follows:

$$i_{es}(t) = i_s(t) - i_s^*(t) \tag{14}$$

where i_s^* is the desired sufficiently smooth current trajectory with $\frac{d^n i_s^*}{dt^n} \le \overline{i_s^*} \le \infty$. Then, the classical PI controller is

$$v(t) = -k_P i_{es}(t) - k_I \int_0^t i_{es}(\tau)d\tau \tag{15}$$

where k_P and k_I denote the non-negative PI controller gains, and the relationship of two controller gains can be assigned as $k_I = \beta k_P$ where the coefficient β is the controller design parameter. As it is given in (2), a filtered variable can be introduced as follows:

$$f_v(t) = i_{es}(t) + \beta \int_0^t i_{es}(\tau)d\tau. \tag{16}$$

The proposed controller structure is

$$\begin{aligned} v(t) = -(k_P + \Delta k_P(t))i_{es}(t) - (k_I \\ + \Delta k_I(t)) \int_0^t i_{es}(\tau)d\tau \end{aligned} \tag{17}$$

where Δk_P and Δk_I are the time-varying controller gains to be determined by an adaptation rule, however, $\Delta k_I = \beta\Delta k_P$. Utilizing the filtered variable f_v given in (16), the proposed controller structure can be re-expressed as

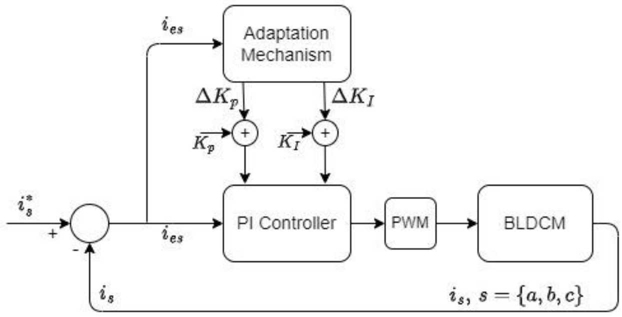

Figure 2. Block Diagram of the Adaptive PI Controller.

$$v(t) = -(k_P + \Delta k_P(t))f_v(t) \tag{18}$$

Then, the derivation of the filtered variable is obtained as

$$\begin{aligned} \frac{df_v(t)}{dt} = f(i_s, e_s) + g\rho v(t) + gv_{un}(t) - \frac{di_s^*(t)}{dt} \\ + \beta i_{es}(t) \end{aligned} \tag{19}$$

and substituting (18) into (19), the equation (19) becomes

$$\begin{aligned} \frac{df_v(t)}{dt} = f(i_s, e_s) - g\rho(k_P + \Delta k_P(t))f_v(t) + gv_{un}(t) \\ - \frac{di_s^*(t)}{dt} + \beta i_{es}(t). \end{aligned} \tag{20}$$

To be able to construct the adaptation rule and to analyze the stability of the system, we assume that the form of the estimation error is $\tilde{\theta}(t) = \theta - \gamma\hat{\theta}(t)$ where γ is a positive adaptation gain to be determined later, and the candidate Lyapunov function can be defined as

$$V(t) = \frac{1}{2}f_v^2(t) + \frac{1}{2\sigma\underline{g}\,\underline{\rho}}\tilde{\theta}^2(t) \tag{21}$$

whose derivative along the filtered trajectory of (16) is

$$\begin{aligned} \dot{V}(t) &= f_v(t)\frac{df_v(t)}{dt} + \frac{1}{\sigma\underline{g}\,\underline{\rho}}\tilde{\theta}(t)\frac{d\tilde{\theta}(t)}{dt} \\ &= f_v^2(t)\big(-g\rho(k_P + \Delta k_P(t))\big) + |f_v(t)|\Big(f(i_s, e_s) + \\ &\quad gv_{un}(t) - \tfrac{di_s^*(t)}{dt} + \beta i_{es}(t)\Big) - \tfrac{\gamma}{\sigma\underline{g}\,\underline{\rho}}\tilde{\theta}(t)\tfrac{d\hat{\theta}(t)}{dt} \\ &\le f_v^2(t)\Big(-\underline{g}\,\underline{\rho}(k_P + \Delta k_P(t)\Big) + \\ &\quad |f_v(t)|\big(f_c\phi(i_s, e_s) + \overline{g}\,\overline{v}_{un}(t) - \overline{i_s^*} + \\ &\quad \beta|i_{es}(t)|\big) - \tfrac{\gamma}{\sigma\underline{g}\,\underline{\rho}}\tilde{\theta}(t)\tfrac{d\hat{\theta}(t)}{dt}. \end{aligned} \tag{22}$$

With the help of defining of $\theta = \max\{\overline{g}\,\overline{v}_{un} + \overline{i_s^*}, f_c, \beta\}$ and $\varphi(i_{es}, e_s) = 1 + \phi(i_s, e_s) + |i_{es}(t)|$, and time varying controller gain $\Delta k_P(t) = \frac{\hat{\theta}\,\varphi^2}{\varphi|f_v| + \epsilon}$, in which $\hat{\theta}(t)$ and ϵ stand for the estimation of the constant of θ and non-negative sufficiently small value respectively, the equation given in (22) becomes

$$\begin{aligned} \dot{V}(t) \le -\underline{g}\,\underline{\rho}k_P f_v^2(t) - \underline{g}\,\underline{\rho}\tfrac{\hat{\theta}(t)\varphi^2(i_{es}, e_s)f_v^2(t)}{\varphi(i_{es}, e_s)|f_v| + \epsilon} + \\ \theta\varphi(i_{es}, e_s)|f_v(t)| - \tfrac{\gamma}{\sigma\underline{g}\,\underline{\rho}}\tilde{\theta}(t)\tfrac{d\hat{\theta}(t)}{dt} \end{aligned}$$

$$\leq -\underline{g}\,\underline{\rho}k_P f_v^2(t) + \left(\theta - \underline{g}\,\underline{\rho}\hat{\theta}(t)\right)\left(\frac{\varphi^2(i_{es},e_s)f_v^2(t)}{\varphi(i_{es},e_s)|f_v|+\epsilon}\right) + \theta\epsilon - \frac{\gamma}{\sigma\underline{g}\,\underline{\rho}}\tilde{\theta}(t)\frac{d\hat{\theta}(t)}{dt} \tag{23}$$

where it is used $\frac{\varphi|f_v|}{\varphi|f_v|+\epsilon} \leq 1$ to obtain the right-hand side of (23). If the estimation error $\tilde{\theta}$ is re-defined as

$$\tilde{\theta}(t) = \theta - \underline{g}\,\underline{\rho}\hat{\theta}(t), \tag{24}$$

where $\underline{g}\,\underline{\rho} = \gamma$, then the inequality given in (23) turns into

$$\dot{V}(t) \leq -\gamma k_P f_v^2(t) + \tilde{\theta}(t)\left(\frac{\varphi^2(i_{es},e_s)f_v^2(t)}{\varphi(i_{es},e_s)|f_v|+\epsilon} - \frac{1}{\sigma}\frac{d\hat{\theta}(t)}{dt}\right) + \theta\epsilon. \tag{25}$$

The adaptation rule can be designed as follows:

$$\frac{d\hat{\theta}(t)}{dt} = -\sigma\kappa\hat{\theta}(t) + \sigma\frac{\varphi^2(i_{es},e_s)f_v^2(t)}{\varphi(i_{es},e_s)|f_v|+\epsilon} \tag{26}$$

where κ is a design parameter, and (25) transforms to

$$\begin{aligned}\dot{V}(t) &\leq -\gamma k_P f_v^2(t) + \kappa\hat{\theta}(t)\tilde{\theta}(t) + \theta\epsilon \\ &\leq -\gamma k_P f_v^2(t) - \frac{\kappa}{2\gamma}\left(\tilde{\theta}^2(t) - \theta^2\right) + \theta\epsilon\end{aligned} \tag{27}$$

where $\hat{\theta}(t)\tilde{\theta}(t) = \frac{1}{\gamma}\left(\theta - \tilde{\theta}(t)\right)\tilde{\theta}(t) \leq \frac{1}{2\gamma}\left(\theta^2 - \tilde{\theta}^2(t)\right)$ is employed by using inequality $2\theta\tilde{\theta}(t) \leq \theta^2 + \tilde{\theta}^2(t)$. Thus,

$$\begin{aligned}\dot{V}(t) &\leq -\gamma k_P f_v^2(t) - \frac{\kappa}{2\gamma}\left(\tilde{\theta}^2(t) - \theta^2\right) + \theta\epsilon \\ &\leq -\delta_1 V(t) + \delta_2\end{aligned} \tag{28}$$

where $\delta_1 = \min\{2k_P\gamma, \kappa\} > 0$ and $\delta_2 = \frac{\kappa}{2\gamma}\theta^2 + \theta\epsilon$. The solving of $\dot{V} \leq -\delta_1 V + \delta_2$ is $V \leq \frac{\delta_2}{\delta_1} + \left(V(0) - \frac{\delta_2}{\delta_1}\right)e^{-\delta_1 t}$ which implies that all signals of the current dynamics of BLDCM drive system are uniformly ultimately bounded (UUB) with the globally attractive set $S = \left\{\left(f_v, \tilde{\theta}\right)\middle| V \leq \frac{\delta_2}{\delta_1}\right\}$. According to Lemma 2.2, the error variable f_v is also UUB. The filtered variable satisfies $|f_v| \leq \sqrt{2\frac{\delta_2}{\delta_1}}$ which means the filtered variable is bounded in a finite time. Hence, the filtered variable converges to a very small neighborhood of origin, and the convergence rate can be tuned by appropriate parameters mentioned in the stability analysis. Moreover, i_{es} and $\int_0^t i_{es}(\tau)d\tau$ are continuous and bounded according to Lemma 2.2, and the value of $\frac{\delta_2}{\delta_1}$ is related to the design parameters, so the error i_{es} converges to a very small neighborhood of origin.

5. Simulation Results

Several numerical simulations have been carried out to assess the performance of the proposed adaptive PI controller. Implementation of the simulation has been done on MATLAB/Simulink. The back-EMF signals are considered to be ideal. Phase inductance and phase resistance of the BLDC are taken as $L = 2.5\ mH$ and $R = 0.58\ \Omega$. Three-phase inverter is fed by a DC voltage source of 48V. PWM is created with the switching frequency of 10kHz and there is no switching loss since the switches are ideal. For the first part of the comparisons, PI controller parameters are chosen as $k_p = 2$, $\beta = 1$, where $k_I = \beta k_p$. Adaptation parameters are assigned $\sigma = 10000$, $\kappa = 0.01$ and $\epsilon = 0.001$. Rotor speed is taken constant throughout the simulations. For the second part of the comparisons, the proposed adaptive PI controller is compared to a high-gain controller, where $k_h = 10, \beta_h = 21.2$ and $\epsilon_h = 10$, to solidify the performance of the proposed adaptive PI controller. The design steps of the high gain controller are given in Appendix.

Miscellaneous numerical simulations have been carried out for different references and rotor speeds. In the first comparison, each simulation results are illustrated with a duration of 0.1s. Adaptive PI controller does not take place in the first half of the simulations. In the second half, adaptation rules apply to the PI controller. Figure 3 and Figure 4 illustrate the results for constant and sinusoidal current reference at 500rpm constant rotor speed.

In these numerical results, each current, the error of currents, the controller input, the generated motor torque, the estimation parameter $\hat{\theta}$ and time-varying proportional controller gain are presented, respectively. Table 1 and Table 2 represent the numerical values, which were obtained from the simulations that are illustrated in Figure 3 – Figure 6. As illustrated in Figure 3 - Figure 6, the error presence is significant with conventional PI at lower and higher speeds both for constant and sinusoidal reference. However, as the adaptive PI is applied, the steady-state error is significantly compensated and the ripple widths in current, and error in torque response are decreased. Besides, it is also proved that the internal signals are converging to a constant value, as shown by the means of Lyapunov theory in Section 4. Table 1 and Table 2 demonstrate that with the proposed adaptive PI controller, the RMS value of the current error for constant current reference has been improved from 0.3442 to 0.0656 at 500rpm, and from 0.4703 to 0.1552 at 1500rpm. The RMS value of the current error for sinusoidal current reference has been improved from 0.3432 to 0.0670 at 500rpm, and from 0.4700 to 0.1677 at 1500rpm. Overall, the current error RMS value has improved by approximately 60% - 80% at high and low speeds, respectively. Additionally, the current error has been improved by around 7% during commutation period. It stands out that the control signal in both constant and sinusoidal current reference changes significantly as adaptive PI controller kicks in, as opposed to the conventional PI controller. This is due to the controller design parameters, especially sufficiently small ϵ value having significant effect on the magnitude of the control signals, which can be deduced from the adaptation rule given in (26).

In the second comparison, in the first half of the simulation, the proposed adaptive PI controller does not take place and a high-gain controller is utilized to regulate the system. In the second half of the simulation, the proposed adaptive PI controller takes place. Figure 7 and Figure 8 illustrate the comparison of high-gain controller and adaptive PI controller with constant and sinusoidal current reference at 1500rpm constant rotor speed. In these numerical results, each current, the error of currents, the controller input are presented, respectively. Additionally, in this case, small ϵ value is increased to 0.1 to observe the effects on control signal and the reference tracking performance. In Figure 7 and Figure 8, it is obvious that with the high-gain controller, the reference tracking performance has significantly increased compared to the first case. However, even the maximum value of the current response with high-gain controller is still under the current reference value, namely it still exists steady state error. Also, the control signal of high-gain controller has increased. In the second half of the simulation, proposed adaptive PI controller is applied. When adaptive PI is applied, the current response swiftly sits on the current reference value, outperforming the high-gain controller. It is also obvious that by increasing the small

ϵ value, the control input of the adaptive PI controller decreased significantly. Moreover, it even is smaller in magnitude compared to the high-gain controller, meaning that the proposed adaptive PI controller achieves better current response with less energy consumption in control input. In Table 3 and Table 4 numerical values, which were obtained from the simulations that are illustrated in Figure 7 and Figure 8, are represented. With the proposed method the RMS value of the current error has improved from 0.1853 to 0.1611 with constant current reference at 1500rpm. With sinusoidal current reference at 1500rpm, the RMS value of the current error has been improved from 0.1879 to 0.1720. Overall, the RMS of the current response and current error have been improved by approximately 9%. In addition to that, the designed controller seems to be a high-gain controller but it is a controller that consumes less energy and responds easily to a non-linear changing system. We especially see this phenomenon in the switching case of the system, which is due to that the adaptation in the designed controller is updated according to the system dynamics.

Consequently, numerical solutions solidify the success of the proposed adaptive PI controller on BLDCM drives by employing comparisons with a conventional PI controller and a high-gain controller, while ensuring the stability of the controller by Lyapunov theory and the ability to compensate for the effects of external disturbances, nonlinearities, and uncertainties.

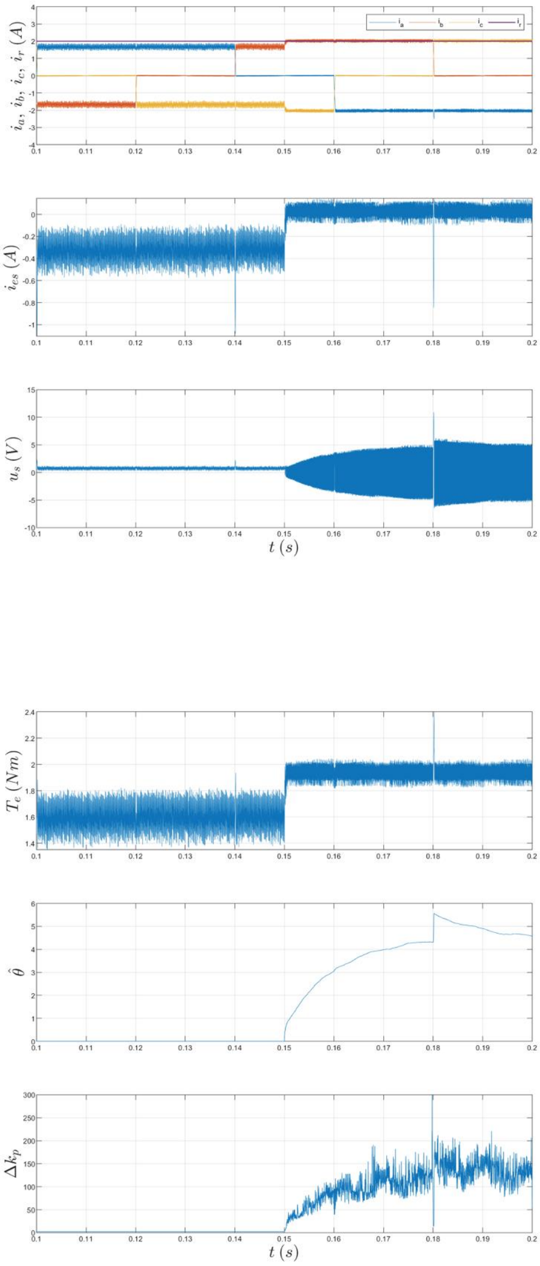

Figure 3. Simulation results for 2A constant current reference at 500 rpm constant speed. Change of the phase currents, current error, control input, torque, estimation of θ, and adaptation gain Δk_p, respectively from top to bottom.

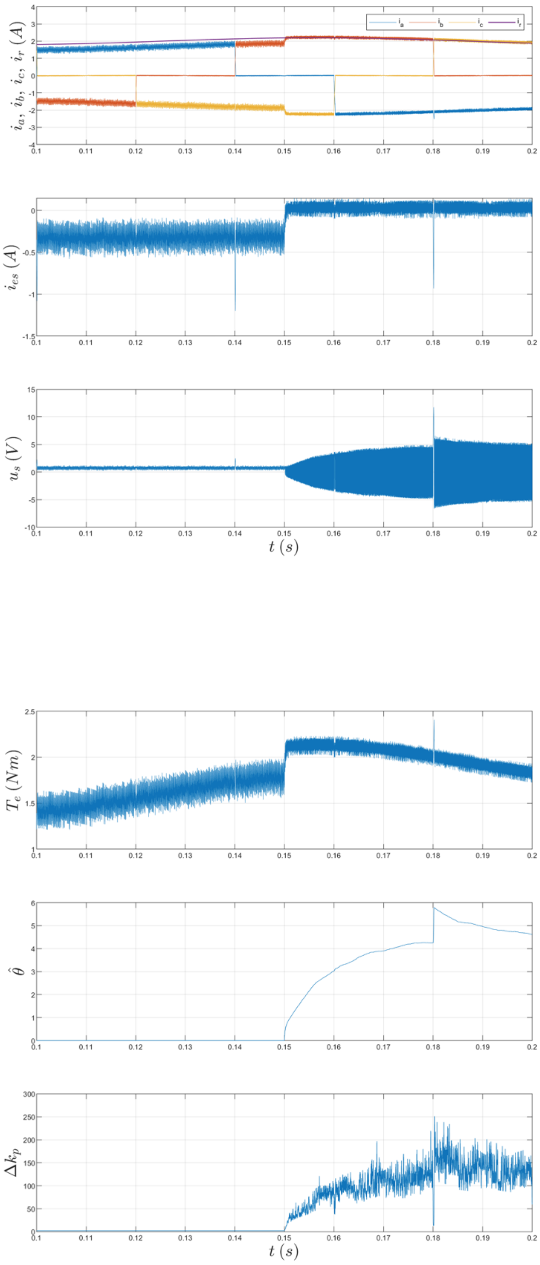

Figure 4. Simulation results for sinusoidal current reference at 500rpm constant speed. Change of the phase currents, current error, control input, torque, estimation of θ, and adaptation gain Δk_p, respectively from top to bottom.

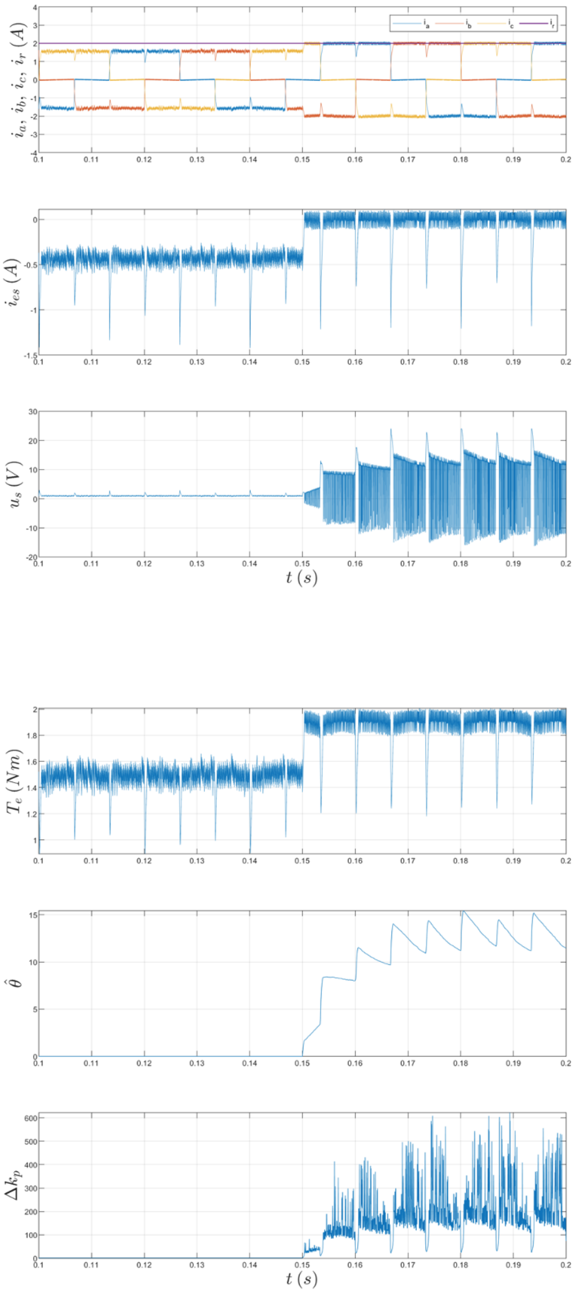

Figure 5. Simulation results for 2A constant current reference at 1500rpm constant speed. Change of the phase currents, current error, control input, torque, estimation of θ, and adaptation gain Δk_p, respectively from top to bottom.

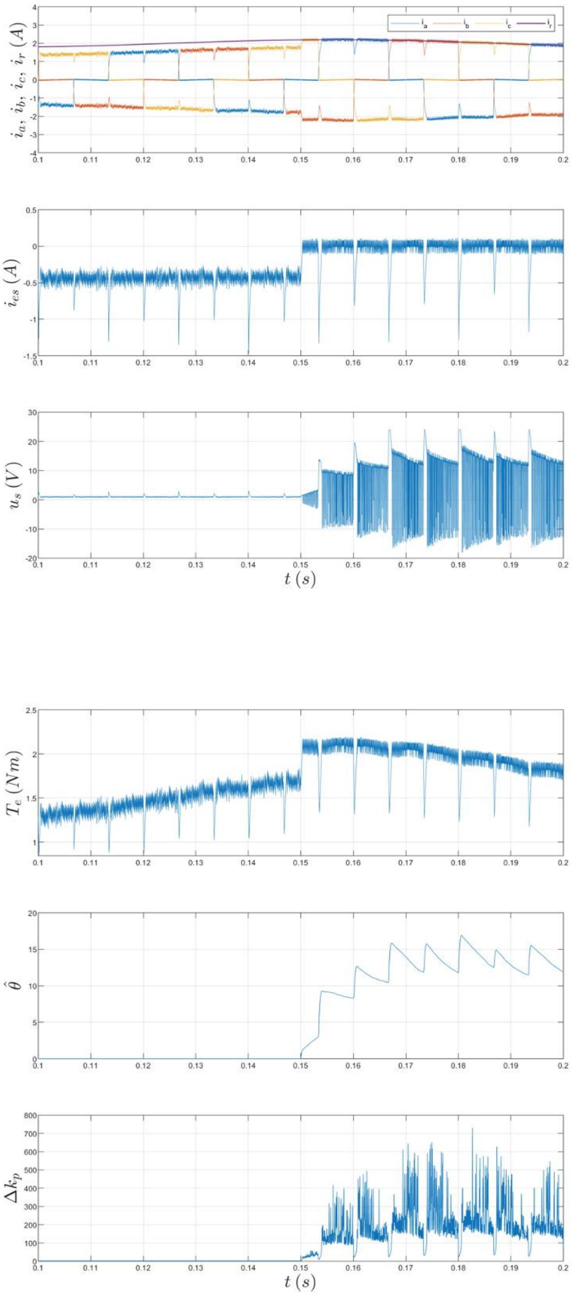

Figure 6. Simulation results for sinusoidal current reference at 1500rpm constant speed. Change of the phase currents, current error, control input, torque, estimation of θ, and adaptation gain Δk_p, respectively from top to bottom.

Table 1. Numerical simulation results for 2A constant current reference at different speeds.

	ω	$i_{s_{rms}}$	$i_{es_{rms}}$
Classical PI	500rpm	1.6757	0.3442
Adaptive PI	500rpm	2.0267	0.0656
Classical PI	1500rpm	1.5487	0.4703
Adaptive PI	1500rpm	1.9718	0.1552

Table 2. Numerical simulation results for sinusoidal current reference at different speeds.

	ω	$i_{s_{rms}}$	$i_{es_{rms}}$
Classical PI	500rpm	1.6818	0.3432
Adaptive PI	500rpm	2.1178	0.0670
Classical PI	1500rpm	1.5539	0.4700
Adaptive PI	1500rpm	2.0601	0.1677

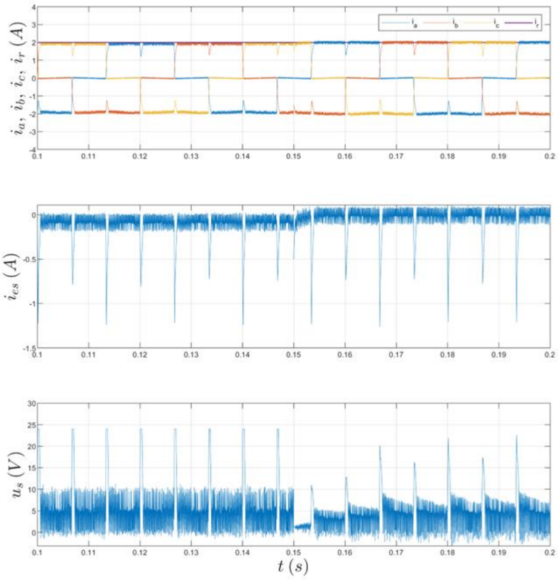

Figure 7. Simulation results of comparison of high-gain controller and adaptive PI for 2A constant current reference at 1500rpm constant speed. Change of the phase currents, current error, control input, respectively from top to bottom.

Table 3. Numerical simulation results of comparison of high-gain controller and adaptive PI for 2A constant current reference.

	ω	$i_{s_{rms}}$	$i_{es_{rms}}$
High-gain Controller	1500rpm	1.8915	0.1853
Adaptive PI	1500rpm	1.9628	0.1611

6. Conclusions

This paper proposes an adaptive PI controller for the regulation of currents in the torque loop of BLDCM drives. The proposed controller guarantees that all signals in the closed-loop dynamics remain bounded. Additionally, the trajectory tracking error of the currents tends to a very small neighborhood of the origin, which can be tuned by the adaptation rule. The convergence rate is adjusted with a pre-defined constant decreasing rate with the filtered variable. The proposed controller is tested with numerical simulations containing simulations that address nearly all practical issues, along with comparisons to the classical PI controller. When the PI controller is compared with the designed adaptive control, a better response in the regulation of currents of BLDCM observed a reduction in the root mean square (RMS) error current by 35.57% for a sinusoidal current reference at 1500 rpm when compared to the PI controller. In comparison, the reduction rate observed with the high-gain controller is approximately 9%. Future studies plan to extend the presented controller design to the torque loop of variable-speed brushless DC motor drives and implement the proposed controller in real-time on a BLDCM driver.

Appendix

In Appendix, the design steps of a high-gain nonlinear current controller based on Lyapunov function is presented to facilitate the comparative analysis.

First, the error expression can be re-defined as follows:

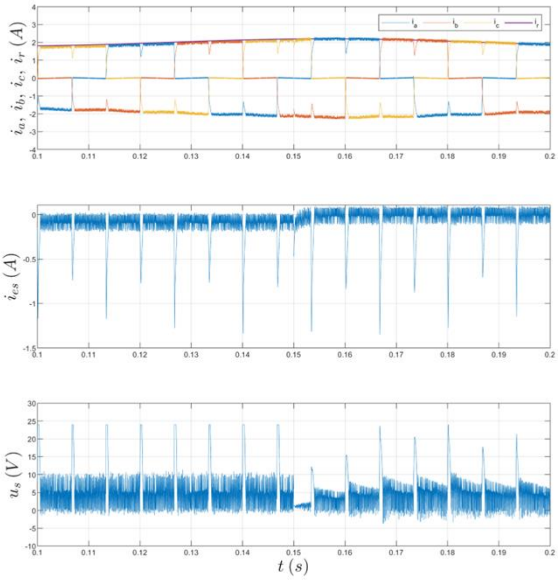

Figure 8. Simulation results of comparison of high-gain controller and adaptive PI for sinusoidal current reference at 1500rpm constant speed. Change of the phase currents, current error, control input, respectively from top to bottom.

Table 4. Numerical simulation results of comparison of high-gain controller and adaptive PI for sinusoidal current reference.

	ω	$i_{s_{rms}}$	$i_{es_{rms}}$
High-gain Controller	1500rpm	1.8938	0.1879
Adaptive PI	1500rpm	2.0515	0.1720

$$i_{es}(t) = i_s(t) - i_s^*(t) \tag{A-1}$$

where i_s^* is the desired sufficiently smooth current trajectory. Utilizing the equation (13), the current error dynamic is obtained as follows:

$$\frac{1}{g}\frac{di_{es}(t)}{dt} = \frac{f(i_s, e_s)}{g} + v_s(t) - \frac{1}{g}\frac{di_s^*(t)}{dt} \tag{A-2}$$

where the notations are defined in Section 3, and we assume that $0 \leq \frac{f(i_s,e_s)}{g} - \frac{1}{g}\frac{di_s^*(t)}{dt} \leq \beta_h$. In order to design a high-gain controller, we consider the following candidate Lyapunov function:

$$V(t) = \frac{1}{2g}{i_{es}}^2(t). \tag{A-3}$$

If the derivation of $V(t)$ with the respect to time is taken, it gives as follows:

$$\frac{dV(t)}{dt} = i_{es}(t)\left(\frac{f(i_s, e_s)}{g} + v_s(t) - \frac{1}{g}\frac{di_s^*(t)}{dt}\right). \tag{A-4}$$

Considering the equation (A-4), the controller input can be designed as:

$$v_s(t) = -k_h i_{es}(t) - \frac{\beta_h^2\, i_{es}(t)}{\epsilon_h}, \quad \epsilon_h > 0. \tag{A-5}$$

After the controller input given in (A-5) is proposed, the equation (A-4) turns into

$$\begin{aligned}\frac{dV(t)}{dt} &= -k_h i_{es}^2(t) - \frac{\beta_h^2\, i_{es}^2(t)}{\epsilon_h} + \frac{f(i_s, e_s)}{g} - \frac{1}{g}\frac{di_s^*(t)}{dt} \\ &\le -k_h i_{es}^2(t) - \frac{\beta_h^2\, i_{es}^2(t)}{\epsilon_h} + \beta_h |i_{es}(t)| \\ &= -k_h i_{es}^2(t) + \beta_h |i_{es}(t)| \left(1 - \frac{\beta_h\, |i_{es}(t)|}{\epsilon_h}\right) \end{aligned} \tag{A-6}$$

where if $\beta_h |i_{es}(t)| \ge \epsilon_h$, then $\frac{dV(t)}{dt} \le -k_h i_{es}^2(t)$ which means that $i_{es}(t)$ converges to zero. It is noticed that this case is satisfied under the condition of sufficiently high values of $\beta_h |i_{es}(t)|$.

Ethics committee approval and conflict of interest statement

This article does not require ethics committee approval. This article has no conflicts of interest with any individual or institution.

Acknowledgment

As authors, we are grateful to the Editor and three anonymous reviewers for their comments and suggestions, which contributed significantly to the improvement of the manuscript.

This article is part of the under-graduate thesis of C. Arslanoğlu (corresponding author).

Author Contribution Statement

Author 1 (corresponding author) conducted the literature review, wrote the manuscript focusing on conceptualization and results presentation, and developed and implemented the simulation works used in this article. Author 2 contributed to conduct the literature review, provided key insights for the paper's theoretical framework, contributed to writing and editing processes, and conducted a critical review offering feedback for improvement.

References

[1] Xia, C.-l. 2012. Permanent Magnet Brushless DC Motor Drives and Controls, John Wiley & Sons Singapore Pte. Ltd., 282s.

[2] Krishnan, R. 2009. Permanent Magnet Synchronous and Brushless DC Motor Drives, Taylor and Francis Group, LLC, 584s.

[3] Hemati, N., Leu, M. C. 1992. A complete model characterization of brushless DC motors, IEEE Transactions on Industry Applications, Vol. 28, p. 172-180, DOI: 10.1109/28.120227

[4] Sharma, P. K., Sindekar, A. S. 2016. Performance analysis and comparison of BLDC motor drive using PI and FOC, 2016 International Conference on Global Trends in Signal Processing, Information Computing and Communication (ICGTSPICC), Jalgaon, India, pp. 485-492.

[5] Hari, K. U., Rajeevan, P. P. 2022. A Direct Torque Control Scheme for BLDC Motor Drives with Open-end Windings, 2022 IEEE 1st Industrial Electronics Society Annual On-Line Conference (ONCON), Kharagpur, India, 1-6.

[6] İnan, R., Üzüm, O. M. 2022. Speed-Sensorless DTC of BLDC Motor with EKF-based Estimator Capable of Load Torque Estimation for Electric Vehicle. Avrupa Bilim Ve Teknoloji Dergisi, Vol.42, pp. 6-13. DOI: 10.31590/ejosat.1190197

[7] Ubare, P., Ingole, D., Sonawane, D.N. 2021. Nonlinear Model Predictive Control of BLDC Motor with State Estimation, IFAC-PapersOnLine, Vol. 54, pp. 107-112. DOI: 10.1016/j.ifacol.2021.08.531

[8] Ramesh, P., Ranjeev, A., Santhakumar, C., Vinoth, J., Bharatiraja, C. 2022. Sensor-less field orientation control for brushless direct current motor controller for electric vehicles, Materials Today: Proceedings, Vol. 65, pp. 277-284, DOI: 10.1016/j.matpr.2022.06.168

[9] Soni, U. K., Tripathi, R. K. 2017, Novel back EMF zero difference point detection based sensorless technique for BLDC motor, 2017 IEEE International Conference on Industrial Technology (ICIT), Toronto, ON, Canada, pp. 330-335

[10] John, M., Thomas, V. 2014. Position sensorless control of BLDC motor based on back EMF difference estimation method, 2014 Power And Energy Systems: Towards Sustainable Energy, Bangalore, India, pp. 1-6, DOI: 10.1109/pestse.2014.6805283

[11] Chowdhury, D., Chattopadhyay, M., Roy, P. 2013. Modelling and Simulation of Cost Effective Sensorless Drive for Brushless DC Motor, Procedia Technology, Vol. 10, pp. 279-286, DOI: 10.1016/j.protcy.2013.12.362

[12] Kalyani, S. T., Md, S. K. 2013. Simulation of sensorless operation of BLDC motor based on the zero-cross detection from the line voltage, International Journal of Advanced Research in Electrical, Electronics and Instrumentation Engineering, Vol.. 2, pp. 6185-619.

[13] Visoli, A., 2006. Practical PID Control, London: Springer-Verlag.

[14] Song, Y.D. 2018. Control of Nonlinear System via PI, PD and PID: Stability and Performance, CRC Press/Taylor & Francis Group.

[15] Türker, T. 2018. Fırçasız doğru akım motorunun hız kontrolü için uyarlamalı geri adımlamalı kontrolcü tasarımı, Pamukkale Üniversitesi Mühendislik Bilimleri Dergisi, Vol. 24, pp. 214–218, DOI: 10.5505/pajes.2017.72623

[16] Mamadapur, A., Unde Mahadev, G. 2019. Speed Control of BLDC Motor Using Neural Network Controller and PID Controller, 2nd International Conference on Power and Embedded Drive Control (ICPEDC), Chennai, India, pp. 146-151.

[17] Moradi, M., Ahmadi, A., Abhari, S. 2010. Optimal control based feedback linearization for position control of DC motor, 2nd International Conference on Advanced Computer Control, Shenyang, China, pp. 312-316.

[18] Shirvani Boroujeni, M., Arab Markadeh, G. Soltani, J. 2017. Adaptive Input-output feedback linearization control of Brushless DC Motor with arbitrary current reference using Voltage Source Inverter, 8th Power Electronics, Drive Systems & Technologies Conference (PEDSTC), Mashhad, Iran, pp. 537-542.

[19] Awadallah, M., Bayoumi, E., Soliman, H. 2009. Adaptive deadbeat controllers for brushless DC drives using PSO and ANFIS techniques. Journal of Electrical Engineering. Vol. 60, pp. 3-11.

[20] Baz, R., Majdoub, K. E., Giri, F., Taouni, A. 2022. Self-tuning fuzzy PID speed controller for quarter electric vehicle driven by In-wheel BLDC motor and Pacejka's tire model, IFAC-PapersOnLine, Vol. 55, pp.598-603, DOI: 10.1016/j.ifacol.2022.07.377

[21] Umam, M. K. Hasanah, R. N., Nurwati, T. 2022. PID-based Fuzzy Logic Theory Implementation on BLDC Motor Speed Control, 2022 International Seminar on Intelligent Technology and Its Applications (ISITIA), Surabaya, Indonesia, pp. 407-412.

[22] Kumar, B. H., Bhimasingu, R., Kumar, V. S. S. 2022. Fuzzy-PI based model predictive control for speed control of BLDC motor, 2022 IEEE International Conference on Power Electronics, Drives and Energy Systems (PEDES), Jaipur, India, pp. 1-6.

[23] Shahnazi, R., M. Akbarzadeh-T., R. 2008. PI Adaptive Fuzzy Control with Large and Fast Disturbance Rejection for a Class of Uncertain Nonlinear Systems, IEEE Transactions on Fuzzy Systems, Vol. 16, pp. 187-197, DOI: 10.1109/tfuzz.2007.903320

[24] Chang, W., Hwang, R., Hsieh, J. 2022. A self-tuning PID control for a class of nonlinear systems based on the Lyapunov approach, Journal of Process Control, Vol.12, pp. 233-242, DOI: 10.1016/s0959-1524(01)00041-5

[25] Song, Q., Song, Y.D. 2014. Generalized PI control design for a class of unknown nonaffine systems with sensor and actuator faults, Systems & Control Letters, v. 64, p. 86-95, DOI: 10.1016/j.sysconle.2013.11.011

[26] Y. Song, Y. Wang and C. Wen, "Adaptive Fault-Tolerant PI Tracking Control With Guaranteed Transient and Steady-State Performance," in IEEE Transactions on Automatic Control, Vol. 62, no. 1, pp. 481-487, Jan. 2017, DOI: 10.1109/TAC.2016.2554362.

[27] Song, Y. Huang, X. Wen, C. 2017. Robust Adaptive Fault-Tolerant PID Control of MIMO Nonlinear Systems With Unknown Control Direction, IEEE Transactions on Industrial Electronics, v. 64, p. 4876-4884, DOI: 10.1109/tie.2017.2669891

[28] Shi, J. Li, T., C. 2013. New Method to Eliminate Commutation Torque Ripple of Brushless DC Motor With Minimum Commutation Time, IEEE Transactions on Industrial Electronics, Vol. 60, pp. 2139-2146, DOI: 10.1109/tie.2012.2191756

[29] Lin, Y. -K., Lai, Y. S. 2011. Pulsewidth Modulation Technique for BLDCM Drives to Reduce Commutation Torque Ripple Without Calculation of Commutation Time, IEEE Transactions on Industry Applications, Vol. 47, pp. 1786-1793, DOI: 10.1109/tia.2011.2155612

[30] Türker, T. and Khudhair, I., O., K. 2017. A switched current controller with commutation delay compensation for the reduction of commutation torque ripple in BLDCM drives, Turkish Journal of

Electrical Engineering and Computer Sciences: Vol. 25, pp. 2635-2646 DOI: 10.3906/elk-1606-105

[31] Adıgüzel, F. Türker, T. 2017. A switching adaptive controller for the reduction of commutation torque ripple in BLDCM drives, 10th International Conference on Electrical and Electronics Engineering (ELECO), Bursa, Turkey, pp. 244-248.

[32] Haddad, W., M., VijaySekhar, C. 2008, Nonlinear Dynamical Systems and Control, Princeton University Press.

[33] Adıgüzel, F., Türker, T. 2022. A periodic adaptive controller for the torque loop of variable speed brushless DC motor drives with non-ideal back-electromotive force, Automatika, Vol.63:4, pp. 732-744, DOI: 10.1080/00051144.2022.2065802

[34] Adıgüzel, F., Türker, T. 2017. A switching adaptive current controller for BLDCM drives, 21st International Conference on System Theory, Control and Computing (ICSTCC), Sinaia, Romania, pp. 334-339.

DEU FMD 27(79) (2025) 72-79

Dokuz Eylül Üniversitesi Mühendislik Fakültesi Fen ve Mühendislik Dergisi
Dokuz Eylul University Faculty of Engineering Journal of Science and Engineering
Elektronik/Online ISSN: 2547-958X

RESEARCH ARTICLE / ARAŞTIRMA MAKALESI

Unleashing the Potential of Deep Learning Methods for Detecting Defective Expressions Using Hyperparameter Optimization Techniques

Anlatım Bozukluklarının Tespit Edilmesi için Hiperparametre Optimizasyon Teknikleri Kullanılarak Derin Öğrenme Yöntemlerinin Potansiyelinin Artırılması

Atilla Suncak [1*], **Özlem Varlıklar** [2]

[1] Department of Computer Technologies, Kastamonu Vocational Highschool, Kastamonu University, Kastamonu, TÜRKİYE
[2] Department of Computer Engineering, Faculty of Engineering, Dokuz Eylül University, İzmir, TÜRKİYE
Corresponding Author / Sorumlu Yazar *: atillasuncak@kastamonu.edu.tr

---

Abstract

Natural Language Processing (NLP) has emerged remarkable progress in the field of deep learning studies. Not only a superior alternative to rule-based NLP methods, deep learning-based techniques have also succeeded more accurate performances in various NLP tasks such as text classification, sentiment analysis or document clustering. Since the performance of a deep learning model undoubtedly depends on adjusting its hyperparameters ideally, tuning the most optimum hyperparameters determines the capability of the model learning in terms of meaningful pattern extraction from the input data. In this paper, hyperparameter optimization techniques of Bayesian Optimization, Random Search and Grid Search have been applied on the deep learning models of Long Short-Term Memory (LSTM) and Convolutional Neural Network (CNN) for the purpose of detecting defective expressions in Turkish sentences. The hyperparameters of previously implemented LSTM and CNN models for this purpose have been adjusted using trial-and-error approach, which is time-consuming and cannot guarantee the most ideal model in general. After these hyperparameters have been adjusted using optimization techniques, the performances in terms of accuracy have been increased from 87.94% to 92.82% and from 84.33% to 89.79% for the models of LSTM and CNN respectively.

Keywords: *Bayesian optimization, Grid search, Hyperparameter optimization, NLP, Random search, Turkish*

Öz

Doğal Dil İşleme (DDİ), derin öğrenme çalışmaları alanında dikkat çekici ilerlemeler ortaya koymuştur. Derin öğrenme tabanlı teknikler, yalnızca kural tabanlı DDİ yöntemlerine üstün bir alternatif olmakla kalmayıp, aynı zamanda metin sınıflandırma, duygu analizi veya belge kümeleme gibi çeşitli DDİ görevlerinde de daha doğru performanslar elde etmeyi başarmıştır. Bir derin öğrenme modelinin performansı, şüphesiz ki hiperparametrelerinin ideal şekilde ayarlanmasına bağlı olduğundan, en ideal hiperparametrelerin ayarlanması, girdi verilerinden anlamlı örüntü çıkarma açısından model öğrenmesinin kapasitesini belirler. Bu makalede, Türkçe cümlelerdeki anlatım bozukluklarını tespit etmek amacıyla Uzun Kısa-Süreli Bellek (UKSB) ve Evrişimsel Sinir Ağları (ESA) derin öğrenme modelleri üzerinde Bayesian Optimization, Random Search ve Grid Search hiperparametre optimizasyon teknikleri uygulanmıştır. Bu amaçla daha önce geliştirilmiş UKSB ve ESA modellerinin hiperparametreleri, zaman alan ve genel olarak en ideal modeli garanti edemeyen deneme-yanılma yaklaşımı kullanılarak ayarlanmıştı. Bu hiperparametreler, optimizasyon teknikleri kullanılarak ayarlandıktan sonra ise, doğruluk açısından performansları UKSB ve ESA modelleri için sırasıyla %87,94'ten %92,82'ye ve %84,33'ten %89,79'a yükseltilmiştir.

Anahtar Kelimeler: *Bayesian optimization, Grid search, Hiperparametre optimizasyonu, Doğal dil işleme, Random search, Türkçe*

---

1. Introduction

Deep learning has made a revolutionary effect on the field of artificial intelligence. It enabled crucial advancements in image processing, computer vision, natural language processing, and various other domains [1]. The success of deep learning comes from the powerful neural network that is capable of learning complex representations from vast amounts of data. However, optimal performance of deep learning models depends on careful hyperparameter tuning of them since it plays an important role for their behavior in shaping and generalizing capabilities [2].

Hyperparameter optimization has become a critical component when building a deep learning model. It encompasses tuning ideal hyperparameters for the model in order to maximize model performance. By adjusting the optimum values for the hyperparameters such as dropout, learning rate, optimizers, batch size, activation functions and etc., deep learning models can reach their full potential and provide superior results [3, 4]. Hyperparameter techniques are highly benefited in several kinds of studies such as parkinson disease prediction [5], sensor-based human activity recognition [6], malware classification [7] and sarcasm recognition [8].

DOI: https://doi.org/10.21205/deufmd.2025277910

Geliş Tarihi / Received: 11.03.2024
Kabul Tarihi / Accepted: 16.04.2024

Defective expression is the Turkish grammatical term which addresses the ambiguities in Turkish sentences. It can be caused by several semantic reasons such as using a redundant word, using a word in a wrong place, uncertainty in meaning of the sentence and etc. Furthermore, a defective expression may also be occurred by morphological reasons such as using wrong suffixes in a word (Since Turkish is an agglutinative language, suffixes are used in almost any grammatical issue.), missing element, conjunction errors and etc. [9, 10]. In education, mass-media, Turkish linguistic studies or literary works, defective expressions are always the problems that must be handled in Turkey. Considering other language ambiguities which are generally occurred by a synonym word which has several meanings, Turkish defective expressions show solid differences in terms of semantics and context.

Linguists rather than computer scientists have studied Turkish defective expressions throughout the literature. To give examples, the study of Büyükikiz [11] analyzed defective expressions in the essays, written by 8th grade students and the study of Özdem [12] analyzed local newspapers whether they have defective expressions or not. On the other hand, apart from the aforementioned manual analyze studies by linguists, the studies of Suncak and Aktaş [13-15] implemented deep learning models (LSTM [Long Short-Term Memory], CNN [Convolutional Neural Network] and Bi-LSTM [Bidirectional LSTM]) and machine learning classifiers (KNN [K-Nearest Neighbor], SVM [Support Vector Machine] and RF [Random Forest]) to detect defective expressions in Turkish sentences. The performance of deep learning models in terms of accuracy varies from 84% to 88%, while machine learning models provide 58% to 78% accuracy rates. However, the hyperparameters of these models have been adjusted using trial-and-error method, therefore it can be clearly declarable that these performances may be increased using the right optimization methods.

This article will discuss the hyperparameter optimization of CNN and LSTM deep learning models. This study's main objective and contribution are to provide more ideal performances for detecting defective expressions in Turkish sentences in comparison to the other models whose hyperparameters are empirically adjusted. Throughout the article, the impact of adjusting optimal values of key hyperparameters on model performances by using optimization techniques such as Bayesian Optimization (BO), Random Search (RS) and Grid Search (GS) will be analyzed in details. Each technique has its own strengths and limitations, therefore their applicability differs in consideration of amount of data, number of hyperparameters or other unforeseen reasons. By understanding the nuances of these optimization methods, the most suitable approach for a model can be selected [16].

In summary, hyperparameter optimization study in order to increase the performance of learning models to detect defective expressions in Turkish sentences have been served in this article. By understanding the importance of hyperparameter optimization, we aim to equip Turkish NLP (Natural Language Processing) researchers with the necessary tools and another point of view to unlock the full potential of deep learning models and push the boundaries of artificial intelligence. This article consists of five sections and the organization is as follows: Section Two explains dataset, data preparation and learning models and hyperparameter optimization methods used in this study. Section Three tells the results and performances of the models. Section Four provides discussion over the results and Section Five concludes the article.

2. Materials and Methods

In this article, the effectiveness of three popular hyperparameter optimization techniques, namely Bayesian optimization, random search, and grid search, have been analyzed for fine-tuning deep learning models. The implementation of the models has been performed using Python programming language with PyCharm IDE and its NLP and machine learning libraries such as Keras [17] and Tensorflow [18] have been benefited for the purpose.

2.1. Dataset

The data to train and test the models have been collected from various open-access web sources of courses, schools and education centers in addition to the official exam center of Turkey (ÖSYM). Each data is originally a sentence that belong to a multiple choice question related to defective expression. Thus, that sentence had already been determined by the expert of the institution whether it has defective expression or not since the answers have also been served related to each question. After a comprehensive search, 9710 Turkish sentences, 4299 of which consist of defective expressions and rest are grammatically proper, have been collected and each sentence according to having defective expression or not have been labelled as DEF or NON-DEF respectively, shown in Table 1.

Table 1. Sample of the sentences in dataset.

Sentence	Label
Dişçiye hiç ya da çok seyrek gidiyorlar.	DEF
Bu kursta, güzel konuşmanın inceliklerini öğreniyorum.	NON-DEF
Davete katılanların hemen hemen hepsini tanıyorum.	NON-DEF
Halk arasında da en iyi yaptığı işle sevilir sayılır duruma düştü.	DEF
Bu davranış insandan insana göre değişir.	DEF
Bu konuda yapılan açıklamaların anlaşılmayacak bir yanı bulunmuyor.	NON-DEF
Teknoloji ne kadar artarsa da el emeğinin önemi azalmıyor.	DEF
Toplumsal ve bireysel olaylara, yan tutmadan bakar.	NON-DEF
Yaptıklarını kendi ağzıyla itiraf etti.	DEF
İşe geç geleceğini hiç olmazsa bana haber verseydin bari.	DEF
İlgililer bu konuda görüş alışverişinde bulundular.	NON-DEF

Since that amount of data are inadequate for training an NLP-purposed learning model, the data have been augmented up to 29756 (13398 of them have defective expressions and 16358 of them are proper ones) using Turkish Synonym Dictionary [19], seen in Table 2.

Table 2. The number of sentences in dataset before and after data augmentation.

	Number of Sentences with Defective Expression	Number of Sentences without Defective Expression	Total
Before Augmentation	4299	5411	9710
After Augmentation	13398	16358	29756

In order to train and test a learning model for text operations, the data need the adequate preparation operations of NLP. For this reason, the text data have been applied some NLP techniques, seen in Figure 1, before feeding the models such as punctuation removal, normalization, stop-word removal and etc. However, we avoided stemming or lemmatization operations since suffixes may cause defective expression.

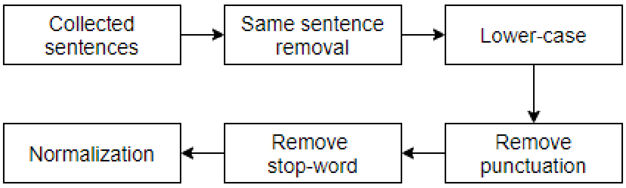

Figure 1. The flow diagram of data preprocess operations.

2.2. Word Vectors and Learning Models

Vectorising words or word embeddings refer to vectors for document vocabulary representation [20]. In this study, Word2vec technique has been used for word embedding extraction, introduced by Mikolov et al. [21] since word vectors are capable of providing better context information of the related word in comparison to the word itself. This technique considers the context of the word by its surrounding ones in the sentence for better semantic analysis [22]. In conclusion, each word of each sentence has been vectorised to train the learning models.

In order to detect defective expressions in Turkish sentences, the deep learning models of LSTM and CNN have been implemented. LSTM is known to be the most appropriate network for handling a long sequence of data among other RNN methods, introduced by Hochreiter and Schmidhuber [23]. Thanks to its memory cells, it has the capability of avoiding long term dependencies, which prevents vanishing gradient problem [24]. CNN is one of the most popular one among deep learning models for visual operations such as image classification or object detection, introduced by LeCun et al. [25]. On the other hand, CNN is also pretty applicable on text operations with considerably successful performances such as text classification, character level classification and etc.

The flow diagram of learning models is presented in Figure 2.

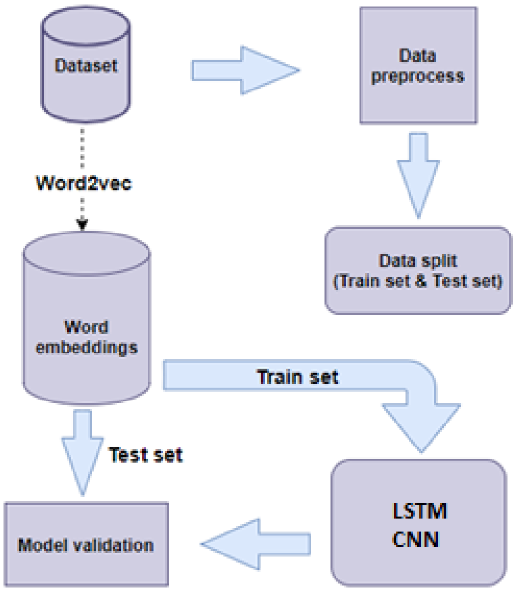

Figure 2. The flow diagram of learning models.

2.3. Evaluation Metrics

In order to measure the performance of each model; the metrics of accuracy, precision, recall and f1 score [26] have been applied, defined as Eqs. (1) - (2) - (3) - (4) respectively. The abbreviations of TP, TN, FP and FN refers to True-positive, True-negative, False-positive and False-negative respectively.

$$Accuracy = \frac{Number\ of\ correct\ predictions}{Total\ number\ of\ predictions} \tag{1}$$

$$Precision = \frac{TP}{TP + FP} \tag{2}$$

$$Recall = \frac{TP}{TP + FN} \tag{3}$$

$$F1\ Score = \frac{2 * precision * recall}{precision + recall} \tag{4}$$

Mean Squared Error (MSE) is the loss function of the models that calculates the average of the square of differences between original and predicted values of the data, defined as Equation (5). After several trials and errors with other loss functions, MSE resulted in better performances in terms of reducing loss.

$$MSE = \frac{1}{N}\sum_{i=0}^{n}(actual\ v. - predicted\ v.)^2 \tag{5}$$

In the equation of MSE, N refers to the total number of data and v means ‘values’. etc.

2.4. Hyperparameter Optimization Technique

The fact that both machine learning classifiers and deep learning models have a wide range of hyperparameters to be adjusted, it is undoubtedly crucial that tuning them in the most ideal of all the worlds in order to implement the optimum learning model and get the highest performance [27]. These techniques have both advantages and limitations according to the number of hyperparameter, the learning model that is applied on and etc. In this study, three popular hyperparameter optimization methods have been applied on the learning models, which are Grid Search (GS), Random Search (RS) and Bayesian Optimization (BO).

GS is a technique that has been widely used for hyperparameter tuning of learning models. It is known to be a straightforward approach that all combinations of the hyperparameters are defined in a grid and tried exhaustively [28]. Although it is simple, straightforward and exhaustive which guarantees that every hyperparameter combination will be calculated; there are important disadvantages such as being extremely computationally expensive and lack of flexibility which it cannot adapt to the observed result and limit the number of computations in addition to the fact that. In addition, the more the number of hyperparameters increases, the more the number of grid points grows exponentially, which results in inefficient performances [29, 30].

Despite being simple, RS is a powerful technique for hyperparameter optimization, introduced by Bergstra and Bengio [3]. This technique samples the parameter combinations randomly and discovers good configurations of hyperparameters by chance by exploring the search space in stochastic manner. Although GS is computationally expensive in high-dimensional spaces, RS is more effective in comparison. Despite the fact that it may not guarantee to find the optimum values, it provides efficient and perfect results with fewer calculations [31, 32].

BO is a well-known technique for being powerful and efficient for tuning hyperparameters and global optimization, introduced by Mockus [33] and his co-researchers [34]. This technique explores the search space by balancing exploration by benefiting the power of probabilistic modelling and Gaussian process. BO selects the most suitable combination to evaluate by considering both previously observed data and gained knowledge. This process leads to the exploration of ideal solution with fewer calculations, which makes BO suitable for the models that are time-consuming and exhaustive [35, 36].

The learning process highly relies on the success of the hyperparameter optimization. The flow of hyperparameter optimization process is depicted in Figure 3.

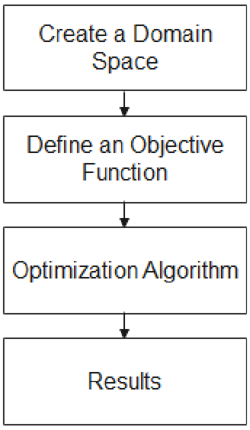

Figure 3. The flow diagram of learning models.

'Create a Domain Space' addresses the input values from the dataset. 'Define an Objective Function' represents the aim to increase the accuracy of learning models, therefore the objective function is the metric of 'accuracy'. 'Optimization Algorithm' is the method(s) used for hyperparameter optimization, therefore it addresses RS, GS and BO. Finally, 'Result' means the developed model after hyperparameter optimization technique is held.

3. Results

This section tells the performance results of the detection models when applying hyperparameter optimization techniques. It discusses them by comparing with the previous ones which the model hyperparameters have been adjusted with the approach of trial-and-error. Furthermore, each optimization technique has been applied using 10-fold cross validation in order to acquire more proper results and prevent overfitting. To start with, Table 3 depicts the hyperparameters of LSTM model with their ranges for each optimization technique applied.

Table 3. Hyperparameters of LSTM and their ranges for each optimization technique.

Hyperparameters	Bayesian Optimization	Random Search	Grid Search
Hidden Layer	32 to 512 (step = 32)	32 to 512 (step = 32)	64, 128, 256, 512
Dropout Rate	0.1 to 0.5 (step = 0.1)	0.1 to 0.5 (step = 0.1)	0.1, 0.3, 0.5
Activation Function	Softmax, Sigmoid, ReLu	Softmax, Sigmoid, ReLu	Softmax, Sigmoid, ReLu
Learning Rate	1e-4 to 1e-2 (log sampling)	1e-4 to 1e-2 (log sampling)	1e-4, 1e-3, 1e-2

Within the hyperparameters above, LSTM model have been optimized using each optimization technique and each technique resulted with top five best combinations. After that, each of these combinations have been applied on the model using 10-fold cross validation in order to prevent overfitting and get consistent performance. Table 4, Table 5 and Table 6 show the model performances when the best five hyperparameter combinations of Bayesian optimization, Random search and grid search are applied respectively.

CNN model, on the other hand, has been implemented using three convolution layers for the purpose of detecting defective expressions. Each layer has the hyperparameters of number of filters, kernel, pool size and dropout layer. The fact that there is too many hyperparameters with CNN model when multiplying by three, Grid search optimization has become a problem since it is originally an exhaustive approach; therefore, these too many hyperparameters made Grid search a grueling option and finally resulted in error due to the performance limitations of the device. As a result, only Bayesian optimization and Random search approaches could have been applied for hyperparameter optimization for CNN model. Table 7 tells the hyperparameters of CNN model with their ranges for each optimization technique applied.

Within the hyperparameters, given in Table 7, CNN model have been optimized using optimization techniques and each technique resulted with top five best combinations. After that, each of these combinations have been applied on the model using 10-fold cross validation in order to prevent overfitting and get consistent performance. Table 8, and Table 9 show the model performances when the best five hyperparameter combinations of Bayesian optimization and Random search are applied respectively. L.R. stands for Learning Rate and A.F. stands for Activation Function.

Table 4. Best five hyperparameter combinations of Bayesian optimization and their performances with LSTM

Hidden Layer	Dropout Rate	Learning Rate	Activation Function	Precision	Recall	F1 Score	Accuracy	Loss
416	0.1	0.004	Softmax	0.93	0.95	0.94	92.82	0.06
320	0.4	0.001	Softmax	0.94	0.94	0.94	92.78	0.06
192	0.4	0.0006	ReLu	0.93	0.94	0.93	91.85	0.06
320	0.3	0.002	Sigmoid	0.94	0.95	0.94	92.63	0.06
128	0.2	0.001	Sigmoid	0.93	0.93	0.93	91.57	0.07

Table 5. Best five hyperparameter combinations of Random search and their performances with LSTM.

Hidden Layer	Dropout Rate	Learning Rate	Activation Function	Precision	Recall	F1 Score	Accuracy	Loss
192	0.2	0.001	Sigmoid	0.94	0.93	0.93	92.14	0.07
480	0.4	0.003	Sigmoid	0.92	0.93	0.93	91.31	0.07
512	0.2	0.0002	Sigmoid	0.92	0.94	0.92	90.66	0.07
352	0.2	0.001	Softmax	0.94	0.95	0.94	92.49	0.06
352	0.5	0.008	Softmax	0.93	0.95	0.94	92.71	0.06

Table 6. Best five hyperparameter combinations of Grid search and their performances with LSTM.

Hidden Layer	Dropout Rate	Learning Rate	Activation Function	Precision	Recall	F1 Score	Accuracy	Loss
128	0.5	0.001	Softmax	0.92	0.92	0.92	90.45	0.08
64	0.5	0.0001	Softmax	0.84	0.89	0.86	82.92	0.14
352	0.2	0.001	Softmax	0.94	0.95	0.93	92.65	0.06
128	0.5	0.0001	Softmax	0.88	0.91	0.89	86.23	0.13
128	0.3	0.001	Sigmoid	0.93	0.94	0.93	91.74	0.08

Table 7. Hyperparameters of CNN and their ranges for each optimization technique.

Hyperparameters	Bayesian Optimization	Random Search
Number_of_filters_1	32 to 256 (step = 32)	32 to 256 (step = 32)
Kernel_Layer1	2 to 5 (step = 1)	2 to 5 (step = 1)
PoolSize_Layer1	2 to 3 (step = 1)	2 to 3 (step = 1)
Dropout_Layer1	0.1 to 0.5 (step = 0.1)	0.1 to 0.5 (step = 0.1)
Number_of_filters_2	32 to 256 (step = 32)	32 to 256 (step = 32)
Kernel_Layer2	2 to 5 (step = 1)	2 to 5 (step = 1)
PoolSize_Layer2	2 to 3 (step = 1)	2 to 3 (step = 1)
Dropout_Layer2	0.1 to 0.5 (step = 0.1)	0.1 to 0.5 (step = 0.1)
Number_of_filters_3	32 to 256 (step = 32)	32 to 256 (step = 32)
Kernel_Layer3	2 to 5 (step = 1)	2 to 5 (step = 1)
PoolSize_Layer3	2 to 3 (step = 1)	2 to 3 (step = 1)
Dropout_Layer3	0.1 to 0.5 (step = 0.1)	0.1 to 0.5 (step = 0.1)
Activation Function	Softmax, Sigmoid, ReLu	Softmax, Sigmoid, ReLu
Learning Rate	1e-4 to 1e-2 (log sampling)	1e-4 to 1e-2 (log sampling)

Table 8. Best five hyperparameter combinations of Bayesian optimization and their performances with CNN.

Layer 1	Layer 2	Layer 3	Others	Precision	Recall	F1 Score	Accuracy
Filters = 224 Kernel = 4 Dropout = 0.3 Pool Size = 2	Filters = 256 Kernel = 2 Dropout = 0.3 Pool Size = 2	Filters = 256 Kernel = 3 Dropout = 0.2 Pool Size = 3	L. R. = 0.0005 A. F. = ReLu	0.90	0.94	0.92	89.79
Filters = 160 Kernel = 4 Dropout = 0.1 Pool Size = 3	Filters = 224 Kernel = 4 Dropout = 0.3 Pool Size = 2	Filters = 160 Kernel = 4 Dropout = 0.1 Pool Size = 2	L. R. = 0.0001 A. F. = Softmax	0.89	0.93	0.92	88.89
Filters = 64 Kernel = 5 Dropout = 0.1 Pool Size = 2	Filters = 256 Kernel = 2 Dropout = 0.1 Pool Size = 3	Filters = 160 Kernel = 3 Dropout = 0.2 Pool Size = 3	L. R. = 0.002 A. F. = Softmax	0.89	0.93	0.91	88.40
Filters = 224 Kernel = 3 Dropout = 0.1 Pool Size = 3	Filters = 128 Kernel = 5 Dropout = 0.3 Pool Size = 3	Filters = 128 Kernel = 2 Dropout = 0.1 Pool Size = 2	L. R. = 0.0001 A. F. = Sigmoid	0.90	0.94	0.92	89.06
Filters = 64 Kernel = 2 Dropout = 0.1 Pool Size = 3	Filters = 256 Kernel = 2 Dropout = 0.1 Pool Size = 2	Filters = 128 Kernel = 3 Dropout = 0.2 Pool Size = 2	L. R. = 0.001 A. F. = ReLu	0.89	0.94	0.91	88.94

Table 9. Best five hyperparameter combinations of Random search and their performances with CNN.

Layer 1	Layer 2	Layer 3	Others	Precision	Recall	F1 Score	Accuracy
Filters = 128 Kernel = 5 Dropout = 0.2 Pool Size = 2	Filters = 224 Kernel = 4 Dropout = 0.5 Pool Size = 3	Filters = 64 Kernel = 2 Dropout = 0.2 Pool Size = 3	L. R. = 0.0002 A. F. = Softmax	0.88	0.93	0.92	89.08
Filters = 64 Kernel = 5 Dropout = 0.1 Pool Size = 3	Filters = 128 Kernel = 3 Dropout = 0.1 Pool Size = 2	Filters = 96 Kernel = 3 Dropout = 0.3 Pool Size = 3	L. R. = 0.001 A. F. = Sigmoid	0.89	0.91	0.91	88.80
Filters = 224 Kernel = 5 Dropout = 0.5 Pool Size = 2	Filters = 224 Kernel = 2 Dropout = 0.2 Pool Size = 2	Filters = 64 Kernel = 2 Dropout = 0.4 Pool Size = 2	L. R. = 0.0001 A. F. = ReLu	0.88	0.91	0.90	87.46
Filters = 160 Kernel = 4 Dropout = 0.4 Pool Size = 2	Filters = 128 Kernel = 3 Dropout = 0.3 Pool Size = 3	Filters = 224 Kernel = 3 Dropout = 0.3 Pool Size = 3	L. R. = 0.002 A. F. = Sigmoid	0.89	0.90	0.91	88.81
Filters = 128 Kernel = 3 Dropout = 0.2 Pool Size = 3	Filters = 32 Kernel = 2 Dropout = 0.2 Pool Size = 3	Filters = 256 Kernel = 2 Dropout = 0.5 Pool Size = 2	L. R. = 0.0006 A. F. = ReLu	0.91	0.92	0.92	89.21

4. Discussion

Applying optimization techniques on deep learning models has demonstrated a slight but important improvement in performance when comparing to existing results from trial-and-error technique. When comparing these two learning methods, LSTM comes into prominence in terms of performance due to the capabilities of long-term dependencies. On the other hand, CNN performed quite acceptable results and increased its performance. Table 10 shows the best performances of each hyperparameter optimization techniques applied on LSTM with the model, optimized by trial-and-error technique.

Even though the metric results of optimization techniques are all close to each other, it must be pointed out that BO provided completely different hyperparameters except activation function in comparison to RS and GS, which they adjusted exactly the same hyperparameters to get the ideal model. Due to the fact that BO benefits the power of probabilistic modelling and Gaussian process, it can implement the most ideal model with the hyperparameters in the search space that other techniques are not capable of. To conclude, all optimization techniques performed better than trial-and-error technique to provide the most ideal model of LSTM.

Table 10. Best performances using hyperparameter optimizations applied on LSTM model.

Optimization Technique	Hidden Layer	Dropout Rate	Learning Rate	Activation Function	Precision	Recall	F1 Score	Accuracy	Loss
Bayesian Optimization	416	0.1	0.004	Softmax	0.93	0.95	0.94	92.82	0.06
Random Search	352	0.2	0.001	Softmax	0.94	0.95	0.94	92.49	0.06
Grid Search	352	0.2	0.001	Softmax	0.94	0.95	0.93	92.65	0.06
Trial-and-error	256	0.3	0.001	Softmax	0.88	0.89	0.88	87.94	0.09

Table 11 depicts the best performances of each hyperparameter optimization techniques applied on CNN with the model, optimized by trial-and-error technique. As aforementioned, GS optimization could not be applied on CNN due to the fact that there are a lot of hyperparameters, thus thousands of combinations. The fact that GS performs an exhaustive search and the limitations of the machine to run the code, the computer could not handle the optimization. According to the results, it can be found out that the performances of CNN models, adjusted by BO and RS, showed close accuracy successes. BO comes into prominence with a slight difference for providing the most ideal model when comparing to RS technique. Both techniques, however, showed better performances in comparison to trial-and-error technique.

Table 11. Best performances using hyperparameter optimizations applied on CNN model.

Optimization Technique	Layer 1	Layer 2	Layer 3	Others	Precision	Recall	F1 Score	Accuracy	Loss
Bayesian Optimization	Filters = 224 Kernel = 4 Dropout = 0.3 Pool Size = 2	Filters = 256 Kernel = 2 Dropout = 0.3 Pool Size = 2	Filters = 256 Kernel = 3 Dropout = 0.2 Pool Size = 3	L.R. = 0.0005 A.F. = ReLu	0.90	0.94	0.92	89.79	0.10
Random Search	Filters = 128 Kernel = 3 Dropout = 0.2 Pool Size = 3	Filters = 32 Kernel = 2 Dropout = 0.2 Pool Size = 3	Filters = 256 Kernel = 2 Dropout = 0.5 Pool Size = 2	L.R. = 0.0006 A.F. = ReLu	0.91	0.92	0.92	89.21	0.11
Trial-and-Error	Filters = 128 Kernel = 3 Dropout = 0.3 Pool Size = 3	Filters = 128 Kernel = 3 Dropout = 0.3 Pool Size = 2	Filters = 128 Kernel = 2 Dropout = 0.3 Pool Size = 2	L.R. = 0.0001 A.F. = Softmax	0.80	0.88	0.84	84.33	0.12

5. Conclusion and Future Works

In this paper, we applied hyperparameter optimization techniques of Random search, Grid search and Bayesian optimization in order to adjust the learning models of LSTM and CNN to detect defective expressions in Turkish sentences. Previous studies showed that the hyperparameters of these models have been adjusted using trial-and-error technique, which requires an excessive time, knowledge and luck for providing the most ideal model. However, hyperparameter optimization techniques reduces this excessive spent time and selects the best hyperparameter combination out of search space, that has been created by each technique according to their own background algorithm.

Bayesian optimization benefits the power of probabilistic modelling and Gaussian process. Random search samples the parameter combinations randomly and discovers good configurations of hyperparameters in stochastic manner. Grid search, on the other hand, performs an exhaustive search, which guarantees the most ideal model; however, consumes an excessive time and requires a powerful machine. After these techniques are applied on learning models, both LSTM and CNN models performed more accurate than the previous models adjusted using trial-and-error technique.

This study contributes to Turkish NLP and is a great source for the researchers who study this area. In future, a more powerful machine must be considered for providing a larger search space using a wider hyperparameter interval, which will result higher number of combinations to implement more ideal models. Since more hyperparameters require more calculations, the number of process increases dramatically, therefore regular computers cannot handle and halts the process. What is more, this study can be turned into an application and serviced to the students and teachers who deals with Turkish education. Furthermore, this application also be used in mass-media workers. They can check their writings before publication whether there are any defective expressions in their writings or not.

Ethics committee approval and conflict of interest statement

This article does not require ethics committee approval and has no conflicts of interest with any individual or institution.

Acknowledgment

The authors would like to thank the editors and anonymous reviewers for providing insightful suggestions and comments to improve the quality of the research paper.

Author Contribution Statement

Author 1 (corresponding author) conducted the literature review, wrote the manuscript focusing on conceptualization and results presentation, and developed and implemented the code used in this study. Author 2 supervised the results from the learning models, contributed to writing and editing processes, and conducted a critical review offering feedback for improvement.

References

[1] LeCun, Y., Bengio, Y., & Hinton, G., 2015. Deep learning. Nature, Vol. 521(7553), pp. 436-444.

[2] Hinton, G.E., Srivastava, N., Krizhevsky, A., Sutskever, I., Salakhutdinov, R.R., 2012. Improving neural networks by preventing co-adaptation of feature detectors. arXiv preprint arXiv:1207.0580.

[3] Bergstra, J., Bengio, Y., 2012. Random search for hyper-parameter optimization. Journal of Machine Learning Research, Vol. 13(2).

[4] Smith, L.N., 2018. A disciplined approach to neural network hyper-parameters: Part 1--learning rate, batch size, momentum, and weight decay. arXiv preprint arXiv:1803.09820.

[5] Lilhore, U.K., Dalal, S., Faujdar, N., Margala, M., Chakrabarti, P., Chakrabarti, T., Velmurugan, H., 2023. Hybrid CNN-LSTM model with efficient hyperparameter tuning for prediction of Parkinson’s disease. Scientific Reports, Vol. 13(1), p. 14605.

[6] El Ghazi, M., Aknin, N., 2024. Optimizing Deep LSTM Model through Hyperparameter Tuning for Sensor-Based Human Activity Recognition in Smart Home. Informatica, Vol. 47(10).

[7] Mehta, R., Jurečková, O., Stamp, M., 2024. A natural language processing approach to Malware classification. Journal of Computer Virology and Hacking Techniques, Vol. 20(1), pp. 173-184.

[8] Palaniammal, M.A., Anandababu, P., 2024. Enhancing Sarcasm Recognition Using Chicken Swarm Optimization Algorithm with Graph Neural Network on Social Media.

[9] Demir, C., 2020. Lexical and structural ambiguities in student writing: An assessment and evaluation of results. Academic Education Research Journal, Vol. 8, pp. 100-108. DOI: 10.30918/AERJ.8S3.20.077.

[10] Göksel, A., Kerslake, C., 2004. Turkish: A comprehensive grammar. Routledge.

[11] Büyükikiz, K.K., 2007. İlköğretim 8. sınıf öğrencilerinin yazılı anlatım becerilerinin söz dizimi ve anlatım bozukluğu açısından değerlendirilmesi. Gazi University, Ankara, Turkey.

[12] Özdem, A., 2012. Çanakkale'deki yerel gazetelerin anlatım bozuklukları açısından incelenmesi. Çanakkale Onsekiz Mart University, Çanakkale, Turkey.

[13] Suncak, A., Aktaş, Ö., 2021. A novel approach for detecting defective expressions in Turkish. Journal of Artificial Intelligence and Data Science (JAIDA), Vol. 1, pp. 35-40.

[14] Suncak, A., 2022. Developing a new approach in natural language understanding to defect defective expressions in Turkish sentences. Dokuz Eylül University, İzmir, Turkey.

[15] Suncak, A., Aktaş, Ö., 2022. Detecting Defective Expressions in Turkish Sentences Using a Hybrid Deep Learning Method. Dokuz Eylül Üniversitesi Mühendislik Fakültesi Fen ve Mühendislik Dergisi, Vol. 24(72), pp. 825-834.

[16] Bergstra, J., Bardenet, R., Bengio, Y., Kégl, B., 2011. Algorithms for hyper-parameter optimization. Advances in Neural Information Processing Systems, Vol. 24.

[17] Chollet, F., 2015. Keras. GitHub. Retrieved from https://github.com/fchollet/keras.

[18] Abadi, M., et al., 2016. TensorFlow. GitHub. Retrieved from https://github.com/tensorflow.

[19] Aktaş, Ö., Birant, Ç.C., Aksu, B., Çebi, Y., 2013. Automated synonym dictionary generation tool for Turkish (ASDICT). Bilig, Vol. 65, p. 47.

[20] Muhammad, P.F., Kusumaningrum, R., Wibowo, A., 2021. Sentiment analysis using Word2vec and long short-term memory (LSTM) for Indonesian hotel reviews. Procedia Computer Science, Vol. 179, pp. 728-735.

[21] Mikolov, T., Sutskever, I., Chen, K., Corrado, G.S., Dean, J., 2013. Distributed representations of words and phrases and their compositionality. Advances in Neural Information Processing Systems, pp. 3111-3119.

[22] Fang, G., Zeng, F., Li, X., Yao, L., 2021. Word2vec based deep learning network for DNA N4-methylcytosine sites identification. Procedia Computer Science, Vol. 187, pp. 270-277.

[23] Hochreiter, S., Schmidhuber, J., 1997. Long short-term memory. Neural Computation, Vol. 9(8), pp. 1735-1780.

[24] Gers, F.A., Schmidhuber, J., Cummins, F., 2000. Learning to forget: Continual prediction with LSTM. Neural Computation, Vol. 12(10), pp. 2451-2471.

[25] LeCun, Y., Bottou, L., Bengio, Y., Haffner, P., 1998. Gradient-based learning applied to document recognition. Proceedings of the IEEE, Vol. 86(11), pp. 2278-2324.

[26] Hossin, M., Sulaiman, M.N., 2015. A review on evaluation metrics for data classification evaluations. International Journal of Data Mining & Knowledge Management Process, Vol. 5(2), p. 1.

[27] Feurer, M., Hutter, F., 2019. Hyperparameter optimization. Automated Machine Learning: Methods, Systems, Challenges, pp. 3-33.

[28] Michalski, R.S., Carbonell, J.G., Mitchell, T.M., 1984. Machine learning: An artificial intelligence approach. Springer-Verlag Berlin Heidelberg.

[29] Pontes, F.J., Amorim, G.F., Balestrassi, P.P., Paiva, A.P., Ferreira, J.R., 2016. Design of experiments and focused grid search for neural network parameter optimization. Neurocomputing, Vol. 186, pp. 22-34.

[30] Ensor, K.B., Glynn, P.W., 1997. Stochastic optimization via grid search. Lectures in Applied Mathematics, Vol. 33, pp. 89-100.

[31] Andradóttir, S., 2006. An overview of simulation optimization via random search. Handbooks in Operations Research and Management Science, Vol. 13, pp. 617-631.

[32] Andradóttir, S., 2014. A review of random search methods. Handbook of Simulation Optimization, pp. 277-292.

[33] Močkus, J., 1975. On Bayesian methods for seeking the extremum. In Optimization Techniques IFIP Technical Conference, pp. 400-404.

[34] Mockus, J., Mockus, J., 1989. The Bayesian approach to local optimization. Springer Netherlands, pp. 125-156.

[35] Frazier, P.I., 2018. Bayesian optimization. In Recent Advances in Optimization and Modeling of Contemporary Problems, pp. 255-278.

[36] Snoek, J., Larochelle, H., Adams, R.P., 2012. Practical Bayesian optimization of machine learning algorithms. Advances in Neural Information Processing Systems, Vol. 25.

Dokuz Eylül Üniversitesi Mühendislik Fakültesi Fen ve Mühendislik Dergisi
Dokuz Eylul University Faculty of Engineering Journal of Science and Engineering
Elektronik/Online ISSN: 2547-958X

RESEARCH ARTICLE / ARAŞTIRMA MAKALESI

The Effect of Different Mixing and Compaction Temperatures on the Particle (Cantabro) Loss in Porous Asphalt Pavements

Farklı Karıştırma ve Sıkıştırma Sıcaklıklarının Poroz Asfalt Kaplamaların Parça Kaybına Etkisi

Ahmet Bugra Ibis [1], **Burak Sengoz** [2], **Ali Almusawi** [3*], **Derya Kaya Ozdemir** [4], **Ali Topal** [5]

[1,2,4,5] Dokuz Eylul University, Department of Civil Engineering, , İzmir, TÜRKİYE
[3] Cankaya University, Department of Civil Engineering, Ankara, TÜRKİYE
Corresponding Author / Sorumlu Yazar *: ali.almusawi@cankaya.edu.tr

Abstract

Porous asphalt (PA) is a type of pavement with an open-graded aggregate that contains higher air voids than the conventional asphalt pavements after compaction, which allows precipitation waters to infiltrate from the pavement surface to the lower layers. The particle loss in the wear layer causes surface deterioration, which affects pavement performance. In addition, the porosity nature of porous asphalt leaves the pavement under the effect of air and water continuously, which accelerates the oxidation rate and affects the surface properties of the pavement. Moreover, these factors can affect the bitumen-aggregate bond strength and cause cohesion degradation within the asphalt film, causing the bitumen to peel from aggregate. The performance of porous asphalt, particularly strength and durability, is greatly affected by compaction temperature. Higher compaction temperatures can reduce the air voids of the mix, so the required mix densities may not be achieved. In this study, the particle loss of porous asphalt samples prepared at 3 different compaction temperatures by using unmodified bitumen, SBS®, Elvaloy®, and Sasobit® modified bitumen was investigated and the optimum mixing and compaction temperature was determined.

Keywords: *Porous asphalt, compaction temperature, particle loss, modified porous asphalt, porous asphalt design, polymers.*

Öz

Poroz asfalt, sıkıştırma sonrasında geleneksel asfalt kaplamalara göre daha yüksek hava boşlukları içeren, yağış sularının kaplama yüzeyinden alt katmanlara sızmasına izin veren, açık gradasyonlu agregaya sahip bir kaplama türüdür. Aşınma tabakasındaki parçacık kaybı, kaplama performansını etkileyen yüzey bozulmasına neden olur. Ayrıca poroz asfaltın gözenekli yapısı, kaplamayı sürekli olarak hava ve suyun etkisi altında bırakmakta, bu da oksidasyon hızını hızlandırmakta ve kaplamanın yüzey özelliklerini etkilemektedir. Ayrıca, bu faktörler bitüm-agrega bağ mukavemetini etkileyebilir ve asfalt film içinde kohezyonun bozulmasına neden olarak bitümün agregadan soyulmasına neden olabilir. Poroz asfaltın performansı, özellikle mukavemet ve dayanıklılık, sıkıştırma sıcaklığından büyük ölçüde etkilenir. Daha yüksek sıkıştırma sıcaklıkları karışımın hava boşluklarını azaltabilir, dolayısıyla gerekli karışım yoğunlukları elde edilemeyebilir. Bu çalışmada, modifiye edilmemiş bitüm ve SBS®, Elvaloy®, Sasobit® modifiyeli bitüm kullanılarak 3 farklı sıkıştırma sıcaklığında hazırlanan gözenekli asfalt numunelerinin parçacık kaybı araştırılmış ve optimum karıştırma ve sıkıştırma sıcaklığı belirlenmiştir.

Anahtar Kelimeler: *Poroz asfalt, sıkıştırma sıcaklığı, parça kaybı, modifiye poroz asfalt, poroz asfalt dizayn, polimerler.*

1. Introduction

Porous asphalt is a type of pavement designed with a higher percentage of air voids to allow water from precipitation or other factors to drainage the pavement surface faster than conventional asphalt pavement. Generally, the air void content is recommended to be between 18% and 25% to ensure adequate permeability during heavy rainfall [1]. The percentage of coarse aggregates is greater than 85% and creates a coarse-grained skeleton that develops stone-on-stone contact and high associated air void content, allowing water to flow through the internal structure of PA mixtures [2]. Porous asphalt has been widely used in flexible pavement construction in recent years. Bitumen or asphalt binders are used to bind the aggregate particles together. Binders are known to deform and flow at high temperatures but become brittle at low temperatures. While the abrasive effect of the vehicle wheel on the pavement surface, especially in high-stress areas, can initiate particle loss, it can also cause peeling with the effect of water. This leads to a pavement problem known as scattering, which is more dominant in porous asphalt than in dense asphalt [3,4]. The structure of porous asphalt causes faster oxidation and embrittlement of the binder compared to conventional dense mix [5]. The mixture's resistance to particle loss depends not only on the oxidation resistance of the binder, but also on binder film thickness, aggregate gradation, and percentage of air voids [6]. The effect of temperature is very important especially during mixing, laying and compaction processes in the construction of strong and durable pavements [7]. This is because the bitumen is heated to obtain the required viscosity to allow the aggregates to stick together better. However, prolonged heating will cause the

DOI: https://doi.org/10.21205/deufmd.2025277911

Geliş Tarihi / Received: 30.01.2024
Kabul Tarihi / Accepted: 07.05.2024

bitumen to oxidize and harden, resulting in serious damage to the pavement after paving [8]. Compaction number and compaction temperature are critical factors determining the performance of a porous asphalt mix. However, there is no widely accepted method for the design of PA mixtures, and the compression number and compression temperatures used in different institutions are not the same. It is essential to evaluate the effect of compaction on the performance of porous asphalt mixtures and to determine the optimum compaction and compaction temperature, and this is of great importance for the design of porous asphalt mixtures [9]. The Cantabrian test can simulate the rolling impact created by the traffic on the road [6]. The Cantabrian test is commonly used to evaluate the resistance to particle loss by abrasion and the effect of impact on porous mixes [10]. Abrasion loss is an important parameter for gauging bonding properties between aggregates and bitumen. This test is commonly used in Japan to evaluate the particle loss resistance of porous asphalt under winter conditions [11].

1.1. literature Review

Inadequate compaction of porous asphalt mixes causes the mix's stiffness to fall short of service prerequisites. In contrast, excessive compaction tends to crush the aggregate and alter the gradation, losing the pavement's drainage and noise reduction benefits. Consequently, controlling the road performance of a porous asphalt mixture requires sufficient compaction [12-13]. A specific temperature limit is established during the compaction of porous asphalt to ensure optimal pavement performance [12]. Maintaining a consistent temperature throughout the compaction process is essential for creating porous asphalt pavement with significant air void connectivity, ensuring solidity and longevity. The high viscosity of bitumen, which hinders compaction efforts, means that low compaction temperatures can affect both density and the bond between aggregate and bitumen [15]. According to Renken [16], reducing the compaction degree to achieve a higher void content is deemed inappropriate. This is because resistance to deformation and particle loss (raveling) heavily relies on a high degree of compaction. Conversely, Poulikakos et al. [17] reported that the Cantabro test is a distinctive porous asphalt evaluation method commonly used to assess mixture resistance to stripping and particle loss resulting from traffic impact and abrasion. Due to its exposure to significant moisture levels, porous asphalt is more susceptible to moisture damage compared to traditional dense mixtures. Previous studies on Polymer Modified asphalt have investigated the influence of mixing and compaction temperatures on the indirect tensile strength [18]. The indirect tensile strength provides insights into the tensile characteristics of the asphalt mixture, which are closely related to the pavement's susceptibility to cracking [19] [20]. Porous asphalt, designed to facilitate stormwater infiltration through interconnected air voids, presents unique challenges in compaction. Unlike conventional dense-graded asphalt mixes, which prioritize minimizing air voids, the compaction process for porous asphalt requires a nuanced approach to preserve its permeability. Achieving structural stability without compromising the integrity of the void network is paramount. Excessive compaction can lead to pore collapse and a subsequent reduction in permeability, undermining the pavement's intended functionality. Consequently, ongoing research endeavors to refine compaction techniques, focusing on adjustments in production temperature and rolling methods to optimize porous asphalt performance.

2. Materials and Methods

In this section, firstly, the determination methods of mixing and compaction temperature specifications adopted by different standards will be presented, followed by the properties of the bitumen, polymers, and the type of aggregates.

2.1. Materials

In this study, the base bitumen with 50/70 penetration grade, has been used. Some of the conventional tests have been applied to measure the physical properties, as illustrated in Table 1.

Table 1. Physical properties of the base bitumen

Test	Specification	Results	Specification limits
Penetration (25 ºC; 0.1 mm)	ASTM D5 EN 14264	65	50-70
Softening point (ºC)	ASTM D36 EN 1427	51	46-54
Ductility (25 ºC; cm)	ASTM D113	100	-
Specific gravity	ASTM D70	1.030	-
Flash point (ºC)	ASTM D92	260+	230 (min)
Penetration index (PI)	-	0.35	-
Rolling thin film oven test (RTFOT)	ASTM D2872-12		
Change of mass (%)	-	0.160	0.5 (max.)
Penetration after RTFOT (25 ºC; 0.1 mm)	ASTM D5 EN 1426	53	50 (min.)
Retained penetration after RTFOT (%)	ASTM D36 EN 1427	82	50 (min.)
Softening point after RTFOT (ºC)	ASTM D36 EN 1427	58	48 (min.)

Two different elastomeric type polymers; Styrene Butadiene Styrene (SBS®), Reactive Elastomeric Terpolymer type – Elvaloy® and organic warm mix asphalt (WMA) additive (Sasobit®) were utilized for the modification. SBS®, Elvaloy®, and Sosabit® contents were selected as 5%, 1.5% and 3% of bitumen weight, respectively. The polymer and WMA contents were determined based on past research [21-25]. Table 2 illustrates the physical properties of the SBS® and Elvaloy®. Additionally, Table 3 shows the physical and chemical properties of Sasobit®. The production conditions for PMB and WMA samples are provided in Table 4 [26-29].

The porous asphalt samples were prepared using two different aggregate types (limestone and basalt), which were collected from the Dere Beton/Izmir quarry. Some of the physical properties of the aggregates are presented in Table 5. The aggregate gradation has been chosen as a Type - 2 based on the Turkish Specifications.

Two aggregate series were utilized to manufacture the porous asphalt samples. The #1 series was formed using only limestone aggregate, while the #2 series was formed by mixing the coarse particles of the basalt with the fine particles of the limestone. The gradation of the two series was selected according to Turkish standards (Figure 1).

Table 2. The physical characteristics of SBS® and Elvaloy® polymers.

Physical properties	Specification	SBS® Kraton D 1101	Elvaloy® 4170
Molecular structure	-	Linear	Linear
Specific gravity	ASTM D792	0.94	-
Tensile strength at break (MPa)	ASTM D 412	31.8	31.8
Shore hardness (A)	ASTM D 2240	71	-
Physical form	-	Powder, pellet	Powder, pellet
Melt flow rate	ASTM D-1238	<1	8
Processing temperature (◦ C)	-	150–170	-
Elongation at break (%)	ASTM D 412	875	-
Density	-	-	0.557

Table 3. The physical and chemical properties Sasobit®.

Property	Sasobit®
Colour	Off-white to pale brown
Odor	Practically odorless
Congealing point	>90 C (ASTM D 938)
Molecular weight	Approx. 1000
Density at 25°C	0.9 g/cm^3
pH values	Neutral
Initial boiling point	271°C (ASTM 6352)
Flash point	285°C (ASTM D 92)

Table 4. Production detailed regarding the additives and modifications.

			Production Conditions		
Modifier Type		Per. (%)	Mixing Temp. (ºC)	Mixing Duration (min)	Shearing Rate (rpm)
Polymer	SBS Kraton® D1101	5	180±5	120	2000
	Elvaloy® 4170	1.5	190	120	200
WMA	Sasobit	3	120	10	1000

Table 5. The physical properties of limestone and basalt aggregates.

Test	Specification Limits	Test Standard	Limestone	Basalt
Resistance to fragmentation (Los Angeles), %	≤25	TS EN 1097-2	22.3	13.7
Resistance to abrasion (Micro-Deval), %	≤20	TS EN 1097-1	18	15
Fastness weathering (With MgSO$_4$ loss), %	≤10	TS EN 1367-2	9.2	7.7
Flakiness Index %	≤15	TS EN 933-3	6.6	4.8
Water Absorption %	≤2	TS EN 1097-6	1.05	0.6

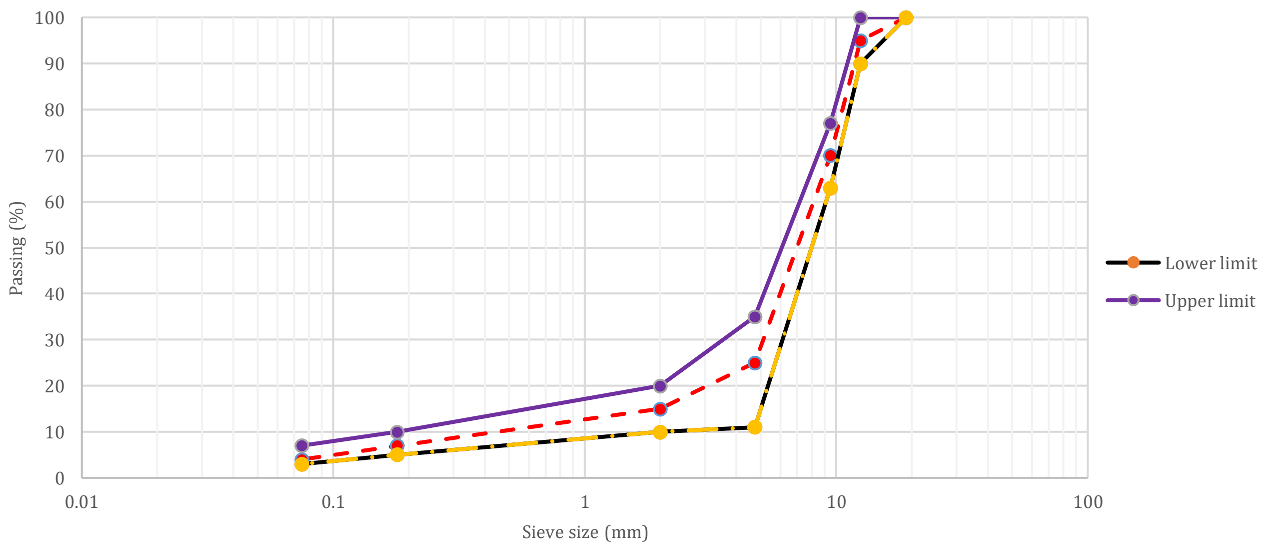

Figure 1. Utilized Aggregate Gradation.

2.2. Methods of Determining Mixing and Compaction Temperatures

The Equiviscous method (ASTM D 2493) is used while the mixing compression temperature is found for dense gradations. However, a special method has not been propounded for porous asphalt. In the porous asphalt specification used in Turkey, the compaction temperature is determined as 145±5 °C since modified bitumen is used. Since the mixing and compaction temperature is an important criterion in terms of pavement performance, it has been tried to suggest the optimum mixing and compaction temperature for porous asphalt designs, in addition to the specification, by making trials.

2.2.1.Equiviscous Method (ASTM D 2493)

The detailed procedure of this method is explained in the American Society for Testing and Materials under the Designation of D2493. The focus of the experiment is to measure the viscosity of the bitumen samples at two temperatures (135 °C and 165 °C). For this purpose, the Brookfield viscometer is suggested where the shear rate is fixed at 6.8 1/s. The obtained viscosity values are plotted on a log viscosity versus temperature chart. Mixing and compaction temperatures viscosity values correspond to 170 ± 20 mPa s and 280 ± 30 mPa s [30-31].

2.2.2.Proposed Method for Porous Asphalt Pavement

In the porous asphalt Turkish specification, the compression temperature is determined as 145±5 °C. However, determining an optimum mixing compression temperature is important in terms of piece loss of porous asphalt pavements. It is thought that the piece loss will give variable values according to the type of bitumen to be used, the bitumen modifying additive, and the type of aggregate. Therefore, a study was carried out within the compression temperature limits allowed by the specification. Porous asphalt samples were prepared using pure bitumen and SBS®, Elvaloy®, Sasobit® modified bitumen, and 2 different aggregate groups of limestone and limestone-basalt mixture. Mixtures prepared with polymer-modified bitumen are compaction at 140 °C, 145°C, and 150°C, and mixtures prepared with warm mix asphalt modified at 3 different temperatures, 120°C, 125°C, and 130°C, and the particle loss values of the mixtures are examined. The optimum mixing and compaction temperature was tried to be found.

2.3. Resistance to Abrasion Loss of Asphalt Samples

The Cantabro test is carried out to find the percentage of porous asphalt pavements particle loss against loads. Three Marshall samples are prepared for each design. The weights of the samples before the experiment are recorded as W1. Then, a single cylindrical sample is placed in the Los Angeles test device without metal balls and 300 cycles are made. When the number of cycles is completed, the sample is removed from the device and weighed W2. The test is repeated in the same way for each remaining sample. The particle loss value is found with the help of the formula in equation 1.

$$P = \frac{W_1 - W_2}{W_1} \times 100 \qquad (1)$$

Where;

P = Abrasion loss (%)

W1 = Mass before test (g)

W2 = Mass after test (g)

3. Results and Discussions

In general mixing-compaction temperatures of dense graded asphalt mixtures are determined by the conventional method depending on the viscosity value of the bitumen. Mixing-compaction temperatures of mixtures can be found by using different methods [30-31]. However, this method may not be suitable for porous asphalt, because it has a high void ratio due to its porous asphalt structure, the mixing-compaction temperatures determined by traditional methods may cause excessive compression and close the gaps and prevent the pavement from working for its intended purpose.

Worldwide specifications often do not specify a method for determining the mixing-compaction temperatures of porous asphalt. In Turkey, compaction temperature was determined as 145±5 °C when using modified bitumen. By using different mixing-compaction temperatures that support the specification, the optimum mixing and compaction temperature has been tried to determine as a result of the part loss values of the prepared mixtures.

With only limestone aggregate, 3 samples were prepared by adding bitumen at the rate of 4% of the mixture weight for each bitumen type at different mixing-compaction temperatures. The prepared porous asphalt mixtures were subjected to the abrasion test after being kept at room temperature for 2 days. Considering the effect of the room temperature in which the experiment was carried out on the test results, care was taken to conduct the test under appropriate conditions. Particle loss values of mixtures prepared with unmodified bitumen and SBS®, Elvaloy®, Sasobit® modified bitumen at 3 different mixing-compaction temperatures are given in Figure 2 and Figure 3. The results shown are the average values of 3 samples prepared for each bitumen.

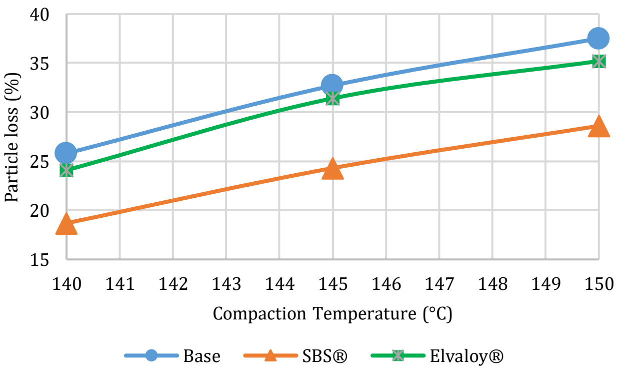

Figure 2. Particle loss results regarding limestone aggregate with PMB.

When analyzing the particle loss values of porous asphalt mixtures containing solely limestone aggregate, it is observed that the compaction temperature is set at 140°C when using base bitumen and SBS or Elvaloy modified bitumen, and at 120°C when Sasobit modified bitumen is employed. The main reason for determining these values is the compaction temperature at which the loss of parts is minimal.

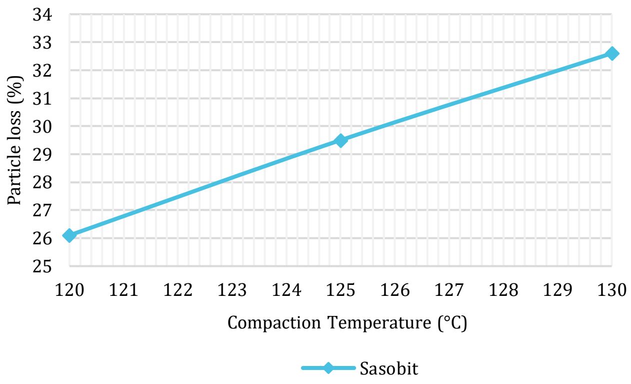

Figure 3. Particle loss results regarding limestone aggregate with Sasobit® WMA additive.

Samples were prepared with the limestone-basalt aggregate combination mixture, base bitumen and SBS®, Elvaloy®, Sasobit® modified bitumen, and samples containing bitumen up to 4% of the mixture weight at 3 different mixing-compaction temperatures. The values were found by taking the average of the particle loss results of the mixtures prepared as 3 samples for each bitumen variety. Relevant part loss values are shown in Figure 4 and Figure 5.

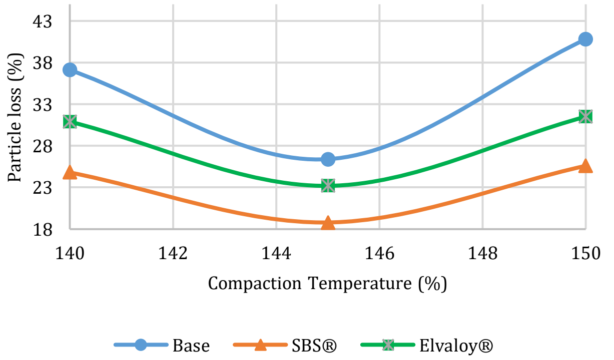

Figure 4. Particle loss results regarding basalt-limestone aggregate with PMB.

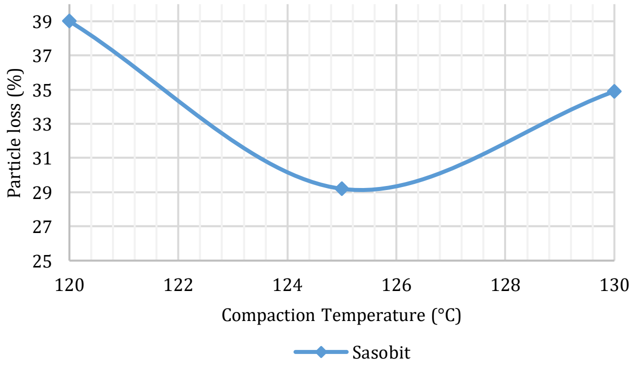

Figure 5. Particle loss results regarding basalt-limestone aggregate with Sasobit WMA additive.

4. Conclusion

The optimum compaction temperature was determined according to the particle loss values of the porous asphalt samples prepared using a limestone-basalt aggregate mixture. This design gave the minimum part loss value at a higher compaction temperature than the mixtures made using only limestone aggregate. It is thought that one of the reasons for this is the use of different gradation. For the design made with this aggregate mixture and using unmodified bitumen and SBS®, Elvaloy® modified bitumen, the optimum compaction temperature was determined as 145°C, and when Sasobit® modified bitumen was used, it was determined as 125°C. The compression temperature is the main factor in determining these temperatures, which gives the minimum value of particle loss.

When the results obtained using two different aggregate groups and four different bitumen types were compared, it was seen that a higher compaction temperature was required for the limestone-basalt aggregate mixture compared to the design using only limestone. The main reason is that a higher compression temperature is required to enable the aggregate particles to adhere to each other in the mixture so that two different aggregate types can perform as a single material.

It is considered necessary to find an optimum mixing-compaction temperature with the Cantabro loss approach within the limits of the compaction temperature specified in the specification in order to better represent the field conditions of the mixture to be designed and applied to the field.

The results indicate that gradation, aggregate type, types of bitumen modification and mixing-compaction temperature are factors that significantly affect abrasion loss. Porous asphalts are more prone to particle loss due to high air voids, resulting in less adhesion between aggregate particles. It is thought that the higher particle loss value of the warm mix asphalt additive is due to the fact that the aggregates do not stick to each other by compaction at low temperatures. Studies can be carried out on porous asphalt design by using different warm mix asphalt additives. In order to better represent the field conditions, the prepared porous asphalt samples should be tested with the conditioning method and the freeze-thaw effect in the field should be examined.

Ethics committee approval and conflict of interest statement

This article does not require ethics committee approval and has no conflicts of interest with any individual or institution.

Author Contribution Statement

All authors contributed equally to the conception, design, execution, and interpretation of the study, as well as the preparation and revision of the manuscript.

References

[1] Kamar, F.H.A., Sarif, J.N., 2009. Proc. of 13th Conf. of the Road Eng. Ass. of Asia and Australasia (REAAA), p. 9-07.

[2] Ma, X., Zhou, P., Jiang, J., Hu, X., 2020. High-temperature failure of porous asphalt mixture under wheel loading based on 2D air void structure analysis. Construction and Building Materials, Vol. 252, p. 119051. DOI: 10.1016/j.conbuildmat.2020.119051.

[3] Kandhal, P.S., Mallick, R.B., 1998. Open graded friction course: state of the practice. Washington, DC, USA: Transportation Research Board, National Research Council.

[4] Huber, G., 2000. Performance survey on open-graded friction course mixes. Transportation Research Board, Vol. 284.

[5] Herrington, P.R., Reilly, S., Cook, S., 2005. Porous asphalt durability test. Wellington: Transfund New Zealand.

[6] Kandhal, P.S., Mallick, R.B., 1999. Design of new-generation open-graded friction courses. NCAT Report, No. 99-3.

[7] Luxman, N.N., Hassan, N.A., Jaya, R.P., Warid, M.M., Azahar, N.M., Mahmud, M.Z.H., Ismail, S., 2019. Effect of compaction temperature on porous asphalt performance. IOP Conference Series: Earth and Environmental Science, Vol. 244(1), p. 012011. DOI: 10.1088/1755-1315/244/1/012011.

[8] Capitão, S.D., Picado-Santos, L.G., Martinho, F., 2012. Pavement engineering materials: Review on the use of warm-mix asphalt.

Construction and Building Materials, Vol. 36, pp. 1016-1024. DOI: 10.1016/j.conbuildmat.2012.06.038.

[9] Wang, X., Ren, J., Hu, X., Gu, X., Li, N., 2021. Determining optimum number of gyrations for porous asphalt mixtures using superpave gyratory compactor. KSCE Journal of Civil Engineering, Vol. 25(6), pp. 2010-2019. DOI: 10.1007/s12205-021-1005-x.

[10] Khedoe, R.N., Woldekidan, M.F., van de Ven, M., van Emst, G., 2006. Possible use of C-Fix in Special Applications: Porous Asphalt. In Wegbouwkundige Werkdagen 2006, pp. 1-10.

[11] Poulikakos, L.D., Partl, M.N., 2003. A comparison of Swiss and Japanese porous asphalt through various mechanical tests.

[12] Masad, E., Scarpas, A., Rajagopal, K.R., Kassem, E., Koneru, S., Kasbergen, C., 2016. Finite element modelling of field compaction of hot mix asphalt. Part II: Applications. International Journal of Pavement Engineering, Vol. 17(1), pp. 24-38.

[13] Cheng, Z., Li, X., Yang, Q., Liang, N., Chen, L., Zheng, S., Wang, D., 2023. Study on Compaction Properties and Skeleton Structural Characteristics of Porous Asphalt Mixture. Sustainability, Vol. 15(18), p. 13911.

[14] McDaniel, R.S., Thornton, W.D., Dominguez, J.G., 2004. Field evaluation of porous asphalt pavement. SQDH Report No. 2003-4. Purdue University.

[15] Hassan, A., Mahmud, M., Adi, N., Rahmat, N., Hainin, M., Jaya, R.P., 2016. Effects of air voids content on the performance of porous asphalt mixture. Journal of Engineering and Applied Sciences, Vol. 11(20), pp. 11884-11887.

[16] Renken, P., 2000. Perspective on optimisation of porous asphalt surface course. In Proceedings of the 2nd Eurasphalt and Eurobitume Congress, Book 2-Session 3.

[17] Takahashi, S., Poulikakos, L.D., Partl, M.N., 2003. Evaluation of improved porous asphalt by various test methods. In Sixth International RILEM Symposium on Performance Testing and Evaluation of Bituminous Materials, pp. 230-236.

[18] Tayfur, S., Ozen, H., Aksoy, A., 2007. Investigation of rutting performance of asphalt mixtures containing polymer modifiers. Construction and Building Materials, Vol. 21(2), pp. 328-337. DOI: 10.1016/j.conbuildmat.2005.08.014.

[19] Harish, L., 2014. The Permeability and Indirect Tensile Strength Characteristics of Porous Asphalt Mixes. Vol. 5, pp. 62-67.

[20] Luxman, N.N., Hassan, N.A., Jaya, R.P., Warid, M.M., Azahar, N.M., Mahmud, M.Z.H., Ismail, S., 2019. Effect of compaction temperature on porous asphalt performance. IOP Conference Series: Earth and Environmental Science, Vol. 244(1), p. 012011. DOI: 10.1088/1755-1315/244/1/012011.

[21] Sengoz, B., Isikyakar, G., 2008. Analysis of styrene-butadiene-styrene polymer modified bitumen using fluorescent microscopy and conventional test methods. Journal of Hazardous Materials, Vol. 150(2), pp. 424-432. DOI: 10.1016/j.jhazmat.2007.04.122.

[22] Topal, A., 2010. Evaluation of the properties and microstructure of plastomeric polymer modified bitumens. Fuel Processing Technology, Vol. 91(1), pp. 45-51. DOI: 10.1016/j.fuproc.2009.08.007.

[23] Almusawi, A., Sengoz, B., Topal, A., 2021. Evaluation of mechanical properties of different asphalt concrete types in relation with mixing and compaction temperatures. Construction and Building Materials, Vol. 268, p. 121140. DOI: 10.1016/j.conbuildmat.2020.121140.

[24] Ozdemir, D.K., Topal, A., McNally, T., 2021. Relationship between microstructure and phase morphology of SBS modified bitumen with processing parameters studied using atomic force microscopy. Construction and Building Materials, Vol. 268, p. 121061. DOI: 10.1016/j.conbuildmat.2020.121061.

[25] Kaya, D., Topal, A., Gupta, J., McNally, T., 2020. Aging effects on the composition and thermal properties of styrene-butadiene-styrene (SBS) modified bitumen. Construction and Building Materials, Vol. 235, p. 117450. DOI: 10.1016/j.conbuildmat.2019.117450.

[26] Oner, J., 2019. Rheological characteristics of bitumens prepared with process oil. Građevinar, Vol. 71(7), pp. 559-569. DOI: 10.14256/JCE.2587.2018.

[27] Topal, A., Sengoz, B., Kok, B.V., Yilmaz, M., Dokandari, P.A., Oner, J., Kaya, D., 2014. Evaluation of mixture characteristics of warm mix asphalt involving natural and synthetic zeolite additives. Construction and Building Materials, Vol. 57, pp. 38-44. DOI: 10.1016/j.conbuildmat.2014.01.093.

[28] Oner, J., Sengoz, B., 2018. Effect of polymers on rheological properties of waxy bitumens. Revista de la Construcción, Vol. 17(2), pp. 279-295. DOI: 10.7764/rdlc.17.2.279.

[29] Oner, J., Sengoz, B., Rija, S.F., Topal, A., 2017. Investigation of the rheological properties of elastomeric polymer-modified bitumen using warm-mix asphalt additives. Road Materials and Pavement Design, Vol. 18(5), pp. 1049-1066. DOI: 10.1080/14680629.2016.1206484.

[30] Almusawi, A., Sengoz, B., Topal, A., 2021. Investigation of mixing and compaction temperatures of modified hot asphalt and warm mix asphalt. Periodica Polytechnica Civil Engineering, Vol. 65(1), pp. 72-83.

[31] Almusawi, A., Sengoz, B., Topal, A., 2021. Evaluation of mechanical properties of different asphalt concrete types in relation with mixing and compaction temperatures. Construction and Building Materials, Vol. 268, p. 121140. DOI: 10.1016/j.conbuildmat.2020.121140.

DEU FMD 27(79) (2025) 86-98

Dokuz Eylül Üniversitesi Mühendislik Fakültesi Fen ve Mühendislik Dergisi
Dokuz Eylul University Faculty of Engineering Journal of Science and Engineering
Elektronik/Online ISSN: 2547-958X

RESEARCH ARTICLE / ARAŞTIRMA MAKALESI

The Effect of Internal and External MQL Methods Used for Environmentally Friendly Manufacturing on Machining Performance in Drilling AA2024 Alloys: A Comparison for ANN And Taguchi Analyzes

AA2024 Alaşımlarının Delinmesinde Çevre Dostu İmalat için Kullanılan İçten ve Dıştan MMY Yöntemlerinin İşleme Performansına Etkisi: YSA ve Taguchi Analizleri için bir Karşılaştırma

Ayşegül Çakır Şencan [1]*, Abdullah Duran [2], Ulvi Şeker [2], Müberra Rüveyda Koçak [1], Cevdet Şencan [3]

[1] Zonguldak Bulent Ecevit University, Faculty of Engineering, Department of Mechanical Engineering, Zonguldak,TÜRKİYE
[2] Gazi University Faculty of Technology, Department of Manufacturing Engineering, Ankara,TÜRKİYE
[3] Middle East Technical University, Institute of Natural and Applied Sciences, Department of Neuroscience and Neurotechnology, Ankara, TÜRKİYE

Corresponding Author / Sorumlu Yazar *: aysegulcakir@beun.edu.tr

Abstract

In recent years, the interest in sustainable manufacturing has created an increasing demand for the economical and environmentally friendly Minimum Quantity Lubrication (MQL) method. However, there are not enough studies comparing internal and external MQL applications in drilling operations. The aim of this study is to investigate the effects of internal and external MQL application on drilling performance. Using Taguchi L9 experimental design, AA2024 aluminum alloy was drilled under three different cooling conditions (internal MQL, external MQL, dry), three different cutting speeds (100, 125, 150 m/min) and three different feeds (0.10, 0.15, 0.20 mm/rev). Surface roughness (Ra) was determined as the performance criterion, 30 repetitions were made in each experiment and the average Ra values were calculated for each condition. At the end of the experiments, the lowest Ra value (0.5 µm) was obtained in the internal MQL condition where the lowest cutting speed (100 m/min) and feed (0.1 mm/rev) parameters were used. In the external MQL condition, Ra results close to dry cutting were observed. The ANOVA analysis revealed that the control factor with the greatest effect on Ra values was the cooling condition. In addition, tool wear after the 30th hole was examined with SEM images and minimum deformation was observed in the internal MQL. ANN and Taguchi analyses were applied to the Ra data measured in the experiments. It was observed that the measured Ra data were in agreement with the data estimated using the Taguchi approach by 97% and with the data estimated using the ANN approach by 99%.

Keywords: *Drilling, Internal MQL, External MQL, Taguchi, ANN*

Öz

Son yıllarda sürdürülebilir imalata olan ilgi, ekonomik ve çevre dostu Minimum Miktarda Yağlama (MMY) yöntemine artan bir talep oluşturmuştur. Ancak, delme operasyonlarında içten ve dıştan MMY uygulamalarını karşılaştıran yeterli çalışma bulunmamaktadır. Bu çalışmanın amacı, MMY yönteminin içten ve dıştan uygulanmasının delme performansı üzerindeki etkilerini incelemektir. Taguchi L9 deney tasarımı kullanılarak AA2024 alüminyum alaşımı, üç farklı soğutma koşulunda (içten MMY, dıştan MMY, kuru), üç farklı kesme hızı (100, 125, 150 m/dk) ve üç farklı ilerleme (0.10, 0.15, 0.20 mm/dev) ile delinmiştir. Yüzey pürüzlülüğü (Ra) performans kriteri olarak belirlenmiş, her deneyde 30 tekrar yapılmış ve her şart için ortalama Ra değerleri hesaplanmıştır. Deneyler sonunda, en düşük Ra değeri (0.5 µm), en düşük kesme hızı (100 m/dk) ve ilerleme (0.1 mm/dev) parametrelerinin kullanıldığı içten MMY koşulunda elde edilmiştir. Dıştan MMY koşulunda kuru kesmeye yakın Ra sonuçları gözlenmiştir. Yapılan ANOVA analizi, Ra değerleri üzerinde en büyük etkiye sahip kontrol faktörünün soğutma koşulu olduğunu ortaya koymuştur. Ayrıca, 30. delikten sonra takımların aşınması SEM görüntüleriyle incelenmiş ve içten MMY'de minimum deformasyon gözlenmiştir. Deneylerde ölçülen Ra verilerine YSA ve Taguchi analizleri uygulanmıştır. Ölçülen Ra verilerinin, Taguchi yaklaşımı kullanılarak tahmin edilen verilerle %97, YSA yaklaşımı kullanılarak tahmin edilen verilerle %99 uyum sağladığı görülmüştür.

Anahtar Kelimeler: *Delik delme, İçten MMY, Dıştan MMY, Taguchi, ANN*

1. Introduction

In addition to the fact that aluminum alloys are light, the fact that their various alloys have very good strength, electrical and thermal conductivity has made this type of material a fairly common building and engineering material in recent years. The lightness of this material group makes it preferred especially in the aviation and automobile industries. In addition, its resistance to corrosion increases the importance of this material in the health sector. Many studies have been carried out on the machining of aluminum alloys with a versatile combination of properties, and these studies are still continuing [1-4].

DOI: https://doi.org/10.21205/deufmd.2025277912

Geliş Tarihi / Received: 26.01.2024
Kabul Tarihi / Accepted: 08.05.2024

Machining conditions affect the machinability of aluminum alloys as well as the metallurgical structure of the material [3]. The most important problem encountered when machining these alloys is the control of the resulting chips. During the machining of some aluminum alloys, a fairly thick, strong, not easily broken continuous chip structure usually appears. This situation causes serious problems in the removal of chip, especially in the drilling process. In addition, the adhesion of the material to the tool due to its ductility also creates another machining problem [3, 4].

Drilling is the type of operation that has the most problems in machining, especially in removing the chip from the cutting area. In the drilling process, chip formation occurs in the closed area and cannot be seen. It is much more difficult to discharge of resulting chips and transmit the cutting fluid. Friction between chip and helical channel and friction between drill and machined surfaces is much greater. The chip angle varies throughout the mouth and therefore different cutting conditions occur throughout the mouth. For this reason, chip removal with a drill occurs in much more complex and severe conditions than with a single-mouth tool [4]. In the researches, when the hole drilling process is compared with other machining processes, it has been observed that the drilling process has a 33% application frequency [5].

The fact that hole drilling processes have such an important share among machining processes increases the importance of the studies to be carried out on the solution of the problems encountered in the hole drilling process. In this field, various studies have been conducted examining tool life and hole quality, especially in the drilling of ductile materials such as aluminum [6, 7].

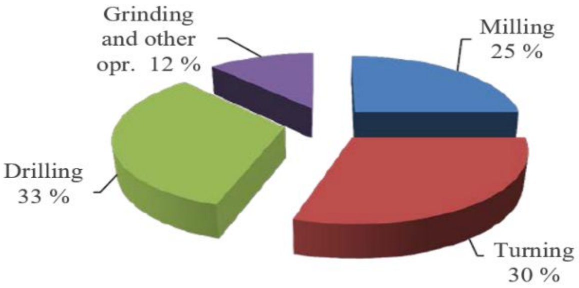

Figure 1. Comparison of drilling with other chip removal operations [5].

The metallurgical structure of the machined material, tool material and geometry, cutting parameters, cooling conditions, machine properties are the factors affecting the machining performance in machining. These factors are also effective in drilling performance as in other machining types [8, 9]. If a performance assessment is to be made in the drilling process, the evaluation criteria can be characterized by cutting tool life, hole quality (surface quality, measurement-shape accuracy in holes) and chip removal efficiency. The factors affecting these criteria are shown schematically in Figure 2.

The application of cutting/cooling fluid is very important to improve machining performance in the machining process. Because in this process, cutting fluids decelerate the heat generated in the cutting zone, while reducing friction on the tool-chip interface with a lubricating effect. It also helps the chip to move away from the cutting area. Thus, the application of cutting fluid increases the machining speed, as well as supply the tool life and improves product quality [10, 11].

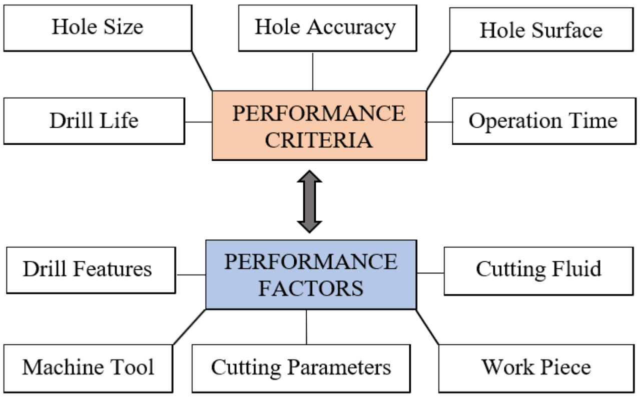

Figure 2. Factors affecting hole drilling performance criteria.

The economics of production, including product quality, production quantity and time, is not enough to describe a successful manufacturing process. In addition, nature and human health should not be adversely affected in this process [10-12]. In addition to its related advantages, the application of cutting fluid with traditional cooling conditions also causes negatives in the manufacturing process. When the waste management of cutting fluids with chemical content is not done well, it mixes with the soil and damages the nature. It has been observed that these chemical liquids that come into contact with the skin of employees on the production line also harm human health [12]. However, the fact that processes such as the supply, storage and disposal of cutting fluids cause additional costs also increases the total cost of production [13, 14].

It is clear that the control of the amount of coolant used in the machining process is important both in terms of its impact on nature and human health, and in terms of the total cost of production. Therefore, reducing the amount of coolant used is seen as a requirement related to the mentioned situations. However, while reducing the amount of coolant used, it is also necessary not to adversely affect the product quality and cutting tool life [15, 16]. The Minimum Quantity Lubrication (MQL) method, the use of which has become widespread in recent years, is a method applied to meet these requirements. In the literature research on the subject, it has been seen that this method provides much better results than dry cutting and close to traditional cooling in terms of tool life and surface quality. Dhar and Islam compared MQL with dry conditions when turning AISI 1040 steel and obtained much better results with MQL in terms of temperature in the cutting zone, tool wear and surface roughness. [16]. Srejit examined the machining performance of AA6061 alloy under three different conditions: dry cutting, MQL and conventional cooling, and found that MQL could be a good alternative to conventional cooling [17]. In addition, various studies have been conducted to determine the most accurate application of the MQL method. In these studies, the type of cutting fluid used, the flow rate and pressures to be applied were investigated. The effects of conditions such as nozzle position, cutting tool properties and cutting parameters on machining performance were also investigated in external MQL applications [18, 19]. Rahim and Sasahara used four different cooling conditions in high-speed drilling of TI6Al4V alloy. These are air cooling, conventional cooling, and application of palm oil and synthetic oil separately to the cutting area with MQL. According to their results, better processing performance was achieved when palm oil was applied to the cutting zone with MQL [19]. Bhowmick and Alpas compared MQL, dry and conventional cooling conditions in drilling 319 Al alloy. In experiments where they used HSS tools with different coating properties, they did not examine the relationship between the force and torque acting on the tools and the wear on the tools. At the end of the experiments, they were able to obtain better results with MQL than dry cutting [20]. In their study, Krishnan and Raj developed an MQL system and applied waste vegetable oils to the cutting zone in the AISI 304 alloy drilling process. They carried out various tests and CFD analyzes for the optimum nozzle design. At the end of the study, they compared the forces acting on the tool, wear on the tools and chip morphology with conventional cooling conditions. They observed that the high viscosity vegetable oil used in the MQL system could provide a reduction in forces [21]. Buss et al., examined the flow behavior of oil mist in the channels inside the tool through numerical analysis during the drilling process using the internal MQL method. As a result of multiphase dynamic analyses, they simulated that most of the oil mist could form an oil film in the regions at the channel entrance, and a small portion could form an oil film in the regions at the channel exits [22].

In machining operations where the cutting event takes place indoors, such as drilling holes, it is very important to choose the correct coolant application parameters. It is estimated that internal or external application of the MQL method in the hole drilling process can significantly affect the results. However, in the literature research, no studies were found that compared these different applications satisfactorily. In drilling, since it is difficult for the cutting fluid to reach the cutting zone, the application of cutting fluid with a small amount of oil mist, such as the MQL technique, may be insufficient. For this reason, in some studies where the MQL method was applied externally in the application of hole drilling, results close to dry cutting conditions were observed [23]. In other studies, conducted on the subject, better results were obtained than dry cutting when applying external MQL, especially in holes that are not deep [19, 20, 21]. On the other hand, it is understood that it is important to correctly adjust the flow rate and pressure parameters of internal MQL application in the drilling process [22].

In order to examine in more detail, the reasons for the different results obtained in the current studies on the effect of the MQL method on the drilling performance, this study was carried out. For this purpose, drilling experiments were carried out under three different conditions: external MQL method, internal MQL method and dry cutting. These conditions have been tested with different cutting parameters. As a workpiece material, AA2024 alloy, which is one of the aluminum alloy groups with a high tendency to plastering, was selected. Thus, a satisfactory comparison of the effect of internal application and external application of the MQL method on processing performance was made in the study.

2. Results and Dicussion

In this study, the effect of the application of the MQL method on the drilling of aluminum alloys was invest gated. In this context, AA2024 alloy was selected as the workpiece. The MQL application was applied from within the tool and from outside the tool (with a nozzle). By comparing these two conditions with dry cutting, experiments were conducted under 3 different cooling conditions in total. In order to examine the effect of different cooling conditions on the machining performance during the experiments, and to what extent different cutting parameters affect the experiments, the experiments were carried out at three different cutting speeds and three different feeds. While determining the cutting parameters, the recommendation of the cutting tool company and the applications in the literature were taken into consideration. The surface roughness values (Ra) of the holes obtained at the end of the experiments and the wear (w) data on the tools were determined as performance criteria. The control factors and levels determined for the experiments are given in Table 1.

Table 1. Control factors and levels for the experiments

Factors	Cooling condition (A)	Cutting speed *{m/min}* (B)	Feed *{mm/rev}* (C)
1.Level	Internal MQL	100	0.10
2.Level	External MQL	125	0.15
3.Level	Dry Cut	150	0.20

The experiments were designed according to the Taguchi L9 vertical array. In this way, the number of 27 experiments were reduced to 9. Table 2 shows the experimental design used when performing drilling experiments on alloy AA2024.

Table 2. Taguchi L9 vertical array experiment design for AA2024.

		A	B	C
Number of experiments	Variables	Cooling condition	Cutting speed *m/min*	Feed *mm/rev*
D1	A1B1C1	Internal MQL	100	0.10
D2	A1B2C2	Internal MQL	125	0.15
D3	A1B3C3	Internal MQL	150	0.20
D4	A2B1C3	External MQL	100	0.20
D5	A2B2C1	External MQL	125	0.10
D6	A2B3C2	External MQL	150	0.15
D7	A3B1C2	Dry Cutting	100	0.15
D8	A3B2C3	Dry Cutting	125	0.20
D9	A3B3C1	Dry Cutting	150	0.10

A total of 9 cutting tools were used by drilling with a new cutting tool under all conditions. Each experiment was repeated 30 times and it was aimed to observe the wear /plastering of the cutting tool used in each condition. The mean values of the relevant conditions were determined by taking the arithmetic average of the data obtained at the end of these 30 repetitions. AA2024 aluminum sheets with a thickness of 25 mm were used as the workpiece. The position of the test holes on the plates is as shown in Figure 4. The holes are positioned with the optimal distance to the workpiece.

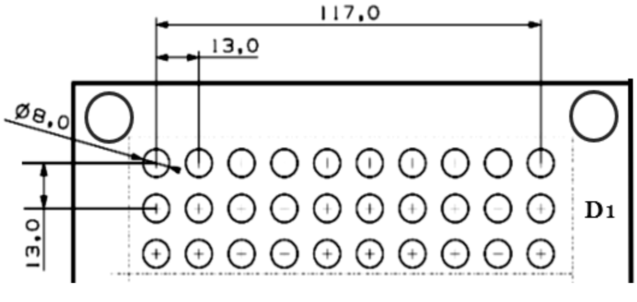

Figure 4. The position of the holes on the workpiece sample.

The chemical and physical properties of the used AA 2024 aluminum alloys are given in Table 3.

Helical, two-mouth, 8 mm diameter, cooling channel, uncoated carbide drills were used in the experiments. Cutting tools were selected as internal cooling channels because the internal MQL system was applied in the experiments. The measurements related to the cutting tools used are given in Figure 5.

The experiments were carried out at the ECOSPEED 2600 (HSM) high-speed machining center. Technical information about the machine tool is given in Table 4.

Table 3. Chemical and mechanical properties of AA2024 aluminum alloys.

Si	Cu	Mn	Mg	Cr	Zn
0.5	4.5	0.6	1.5	0.1	0.2
Heat treatment	Yield Stress *(MPa)*	Tensile Stress *(MPa)*	Elongation (%)	Stiffness Brinell	Modulus of Elasticity *(GPa)*
T4	315 - 330	440 – 465	20.0	120	73.1

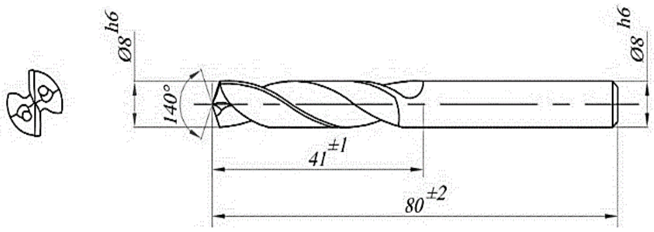

Figure 5. Uncoated carbide drills used in experiments

Table 4. The Technical characteristics of the ECOSPEED 2600 CNC machine tool

Name of the Machine	ECOSPEED 2600 HSM	
Control Unit	SIEMENS 840D	
Maximum speed	30 000	*rev/min*
Machining Table	2500 x 7000	*mm*
Feed on the Axes	X:65 000, Y ve Z:50.000	*mm/min.*
Axial Motion	X: 6800, Y: 2600, Z: 670 A: ±40º, B: ±40º	*mm*

The cooling system on the ECOSPEED 2600 (HSM) machine is the VOGEL Digital-Super MQL cooling system. This system is capable of cooling both from the inside and from the outside. Constant flow rates and pressures were used in the experiments. Haughton CDT MAX-ML 200 cutting oil was used in the experiments. The technical characteristics of the VOGEL brand MQL system used are given in Table 5.

Table 5. Technical characteristics of the VOGEL Digital Super MQL system

Application of cutting fluid	Internal/ External MQL	
	External MQL	
Number of nozzles	8	*piece*
Filter capacity	0.025	*mm*
Maximum flow rate	50	*L/min.*
Maximum pressure	5	*Bar*
	Internal MQL	
Maximum flow rate	20	*L/min.*
Maximum pressure	7	*Bar*

“Mahr” brand Perthometer M1 type, desktop and printable surface roughness measuring device was used for surface roughness measurements of the hole surfaces drilled into the samples. For the reliability of the measurements, four measurements were made from separate points for each measured hole. The average surface roughness (Ra) values were determined for each hole measured by taking the arithmetic mean of the values obtained as a result of the measurements.

The technical characteristics of the surface roughness measuring device used are given in Table 6.

Table 6. Technical characteristics of the surface roughness measuring device.

MODEL	Mahr Perthometer M1	
The principle of measurement	The spectator tip method	
Scanning speed	0.5	*(mm/s)*
Measuring range	100 – 150	
Profile resolution	12	
Filter	Gaussian	
Cut off	0.08 – 0.25 – 0.8 – 2.5	*(mm)*
Scan lengths	1.75 – 5.6 – 17.5	*(mm)*
Number of sampling lengths	1 – 5 can be selected	
Dimensions	190 x 170 x 75	*(mm)*
Approximate weight	900	*(gr)*

In order to measure the effect of process parameters on quality characteristics, the data obtained were subjected to variance analysis. In this study, surface roughness was chosen as the quality characteristic, and cooling condition, cutting speed and feed parameters were selected as process parameters. In addition, in order to determine the optimum conditions, the Signal/Noise (S/N) test was also applied to the data by using the "the smallest is the best" approach. In addition, the results of the experiment were evaluated with the artificial neural networks (ANN) approach and prediction models were obtained. The ANN model used is a feed-forward multilayer ANN model. Pythia software was used while creating the ANN model. Thanks to this software, a 3-6-5-1 network structure has been obtained that can give the closest result to reality. After a part of the data obtained from the experiments was reserved for testing and verifying the ANN model, the remaining part was used in the learning process. The activation function used in the ANN model is a sigmoid-logistic function called “Fermi”. In this function, data ranges from 0 to 1 and normalized data is used. The predictions made by the ANN model created for this study were tested with the separated data. Then, the “Absolute Percentage of Change (R2)" verification method was used to measure the prediction performance of the model. Finally, the estimates made by the Taguchi method and the estimates made by the ANN method were compared. The schematic view of the experimental setup, measurements and analyzes is as shown in Figure 6.

3. Results and Discussions

3.1 Analysis of surface roughness (Ra) data

In experiments where 30 drilling repetitions were performed for each cutting condition, 1., 15. and 30. The surface roughness of the three holes was measured for each condition. By taking measurements from 4 different places for each hole, the arithmetic mean of these 4 measurements was accepted as the surface roughness of that hole. Measurements were carried out in accordance with TS EN 10049 standard. In Table 7, the average Ra value obtained from the 1., 15. and 30. holes for each different condition and the arithmetic mean of these three Ra values are given.

In the graphics in Figure 7 in drilling AA2024 aluminum alloy using the internal MQL (a) external MQL (b) and dry cutting (c) methods, the resulting Ra values for 9 different cutting parameters with different cutting parameters (cutting speed - feed) combination in each cooling condition are given. The D1-D9 series used in the graphs express different cutting conditions. The values on the "Repeat Test" axis represent the 1st, 15th and 30th holes drilled using the same cutting condition and the same tool in the repeat tests.

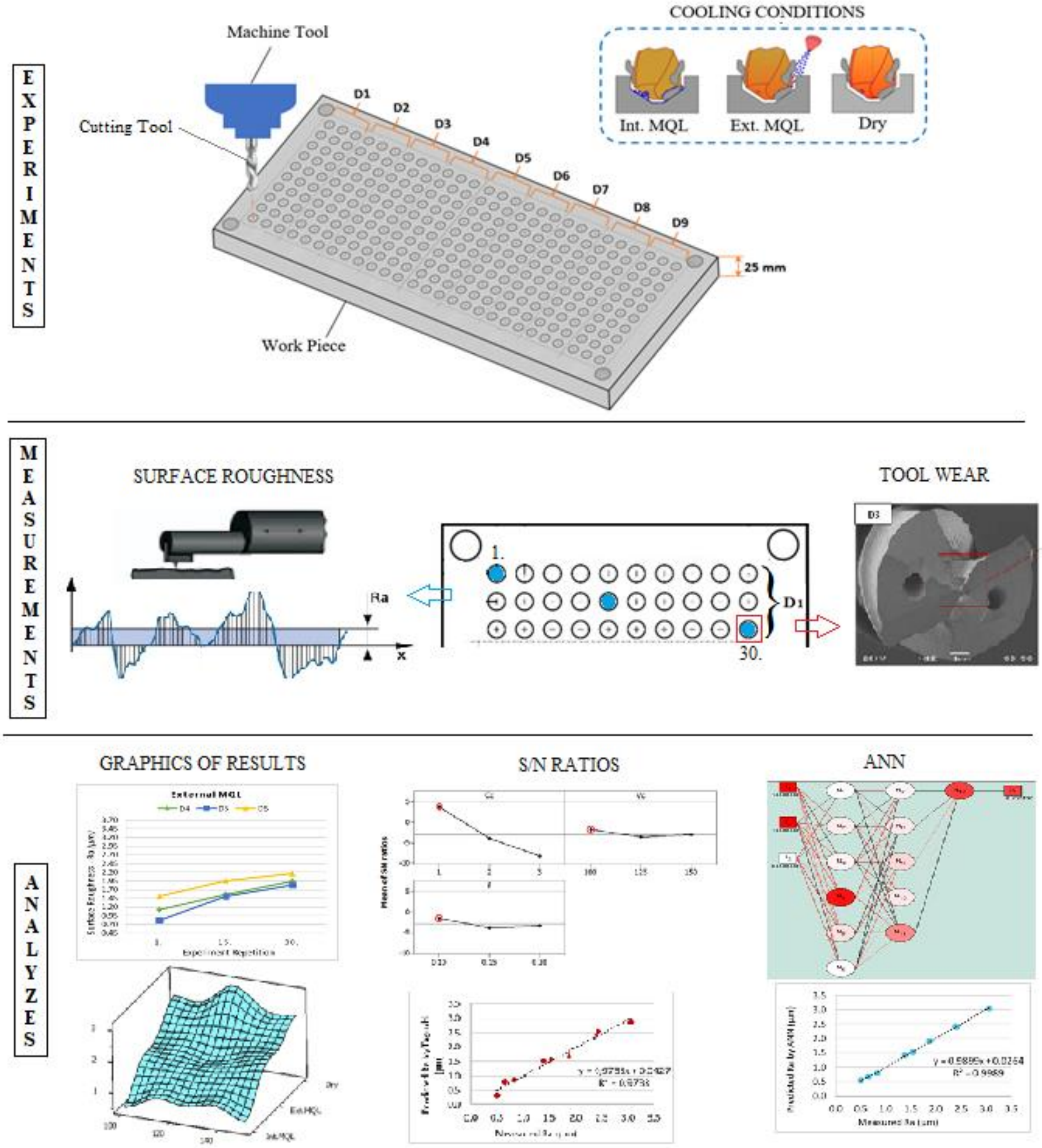

Figure 6. Schematic view of the experimental setup, measurement and analyzes.

In the graphs in Figure 7 it is seen that there is a slight increase in Ra surface roughness values from the first hole to the last hole for all cutting conditions. This means that a tool used in the repeat test could not perform on the 30. hole as it did on the 1st hole, that is, it was worn/smeared. It is an expected situation that the tool will begin to wear under repeated machining conditions [24]. The point that needs to be considered here is to what extent the applied cooling methods can prevent deformation in the tool. When the graphs in Figure 7 are examined, it is seen that the increase in Ra from the first hole to the last hole is below 20% in the internal MQL application in a graph, around 60% in the external MQL application in the b graph and around 50% in the dry cutting application in the c graph. It is thought that this increase, which is much higher in external MQL and dry cutting applications compared to internal MQL application, may be due to the higher level of smearing and/or wear on the cutting edges of the tools at the end of 30 holes. When external MQL and dry cutting conditions are compared, the values observed between 1-1.5µm in external MQL application at the beginning are seen to increase to 2-2.5µm values at the end of 30 holes. In dry cutting, the data that were initially observed as 2-2.5µm were observed to increase to 2.7-3.7µm after 30 holes. These results show that the external MQL and dry cutting conditions may be insufficient in the drilling process, the tool cannot maintain its property for a long time under these conditions and deforms quickly. For obtain average Ra value of a cutting condition, the surface roughness of the first, fifteenth and thirtieth repeated holes belonging to that cutting condition was measured and determined by taking the arithmetic average of the measured Ra values. Thus, by taking the arithmetic average of the surface roughness (Ra) values of these holes measured in 30 drilling operations repeated for 9 different cutting conditions, the average Ra values were calculated for each different condition.

Table 7. Estimated Ra values with measured Ra values

		A	B	C	Surface roughness results (μm)			
Number of experiments	Variables	Cooling condition	Cutting speed *(m/min)*	Feed *(mm/rev)*	1.	15.	30.	Avg.
D1	A1B1C1	Internal MQL	100	0.10	0.452	0.502	0.545	0.500
D2	A1B2C2	Internal MQL	125	0.15	0.764	0.825	0.912	0.834
D3	A1B3C3	Internal MQL	150	0.20	0.613	0.646	0.721	0.660
D4	A2B1C3	External MQL	100	0.20	1.129	1.556	1.943	1.543
D5	A2B2C1	External MQL	125	0.10	0.815	1.514	1.832	1.387
D6	A2B3C2	External MQL	150	0.15	1.503	1.953	2.165	1.874
D7	A3B1C2	Dry Cut	100	0.15	1.993	2.503	2.763	2.420
D8	A3B2C3	Dry Cut	125	0.20	2.505	3.005	3.666	3.059
D9	A3B3C1	Dry Cut	150	0.10	1.899	2.375	2.893	2.389

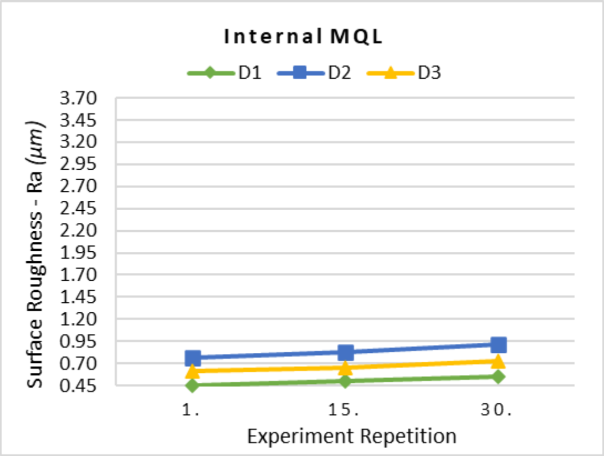

(a)

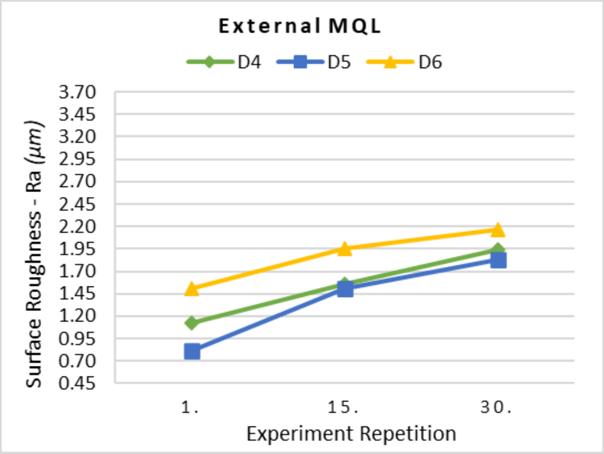

(b)

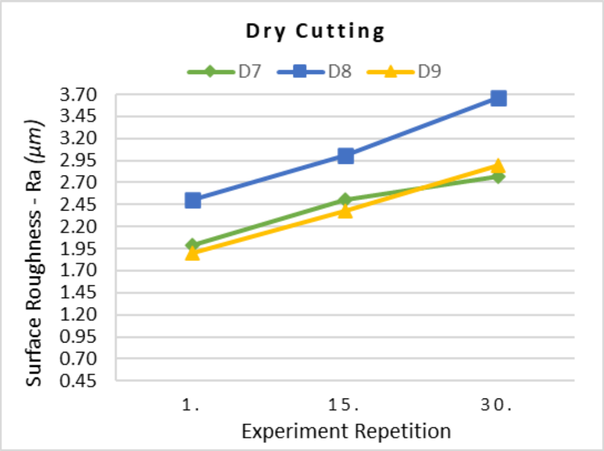

(c)

Figure 7. The change in surface roughness (Ra) values obtained from the 1st. 15th and 30th holes in 30 drilling repetitions for each cutting condition on AA2024 alloy.

3.2. Analysis of variance of average surface roughness (Ra) data

In order to see the effect of the process parameters (cooling condition, cutting speed and feed) on the surface roughness (Ra) determined as a quality characteristic; the relevant data were subjected to variance analysis. The ANOVA results obtained are given collectively in Table 8.

At the end of the analysis of variance. the P value obtained for the cooling condition was less than the value of α (0.05). Since P < α. the type of cooling condition, which is the process parameter, has a significant effect on the surface roughness. which is the quality characteristic. If we look at the degrees of influence of the process parameters from the PD column, it seems that the cooling condition affects the surface roughness the most with 92.5%. Therefore, it is seen that cooling conditions greatly affect the surface quality in drilling operations carried out in closed areas. Because, correctly applied MQL method reduces friction by lubricating the tool-chip and tool-workpiece interfaces. In addition, in the MQL method, compressed air applied to the cutting area helps remove the resulting chip without getting stuck in the hole [25]. For these reasons, it is thought that using the internal MQL method in hole drilling operations without reducing cutting and feed speeds will help to obtain a more error-free product in a shorter time.

Among the process parameters. the P values of the cutting speed and feed factors are 0.593 and 0.461, respectively, and are greater than the acceptable error rate of 0.05. Since the P value of the feed parameter is closer to 0.05, it seems that the effect on surface roughness is greater than the cutting speed. On the other hand, the cutting speed has a more unstable effect compared to other process parameters. While explaining the effect of cutting speed on Ra. increasing the cutting speed makes it easier to cut, thereby improving the surface quality. But the chip formed at the same time and the chip jammed in the unit area increase with the increase in the cutting speed. Jammed chips increase the loads and vibration that affect the tool. Therefore, while increasing the cutting speed facilitates cutting, on the other hand, it deforms the surface with more chip compression [2].

This situation is also considered to be the cause of the unstable effect observed in the ANOVA results.

3.3. Signal/Noise (S/N) analysis of average surface roughness (Ra) data

The Taguchi technique was used in the design of the experiment and in the analysis of the results obtained. Since the lowest surface roughness values will give the best results, in this study which uses the “Smallest is the best” approach. The smallest-best function used in the Taguchi method is given in Eq (1).

$$\eta = \frac{S}{N_s} = -10\log\left(\frac{1}{n}\sum_{i=1}^{n} y_i^2\right) \qquad (1)$$

The surface roughness data obtained by drilling the AA2024 alloy were subjected to Signal-to-Noise (S/N) analysis. In Table 9, the S/N ratios of the control factors according to the Ra results for AA2024 are given.

In Table 10, the analysis of each control factor for the average surface roughness values was performed with the S/N and mean response table. The maximum-minimum value in Table 10 is the difference between the maximum average of the respective levels of each parameter and the average of the minimum values. The higher this value. the greater the degree of influence of that factor [26]. In this context, when Table 10 is evaluated, it can be said that the most important factors affecting the average surface roughness data obtained by drilling the AA2024 alloy are the cooling condition, feed and cutting speed.

One of the important steps in the Taguchi technique is to determine the optimum levels. These levels are used to draw the effect graphs of the levels [26]. In the graph in Figure 8 where the highest S/N ratios express the optimal conditions, these optimal levels are clearly visible.

Table 8. ANOVA results (ANOVA results for surface roughness data obtained by drilling AA2024 alloy).

Source	DF	SS'	SS	MS	F	P	PD (%)
Cooling condition (C_c)	2	5.7562	5.7562	2.8781	35.32	0.028	92.5
Cutting speed (V_c)	2	0.1119	0.1119	0.0559	0.69	0.593	1.8
Feed (f)	2	0.1903	0.1903	0.0951	1.17	0.461	3.1
Error	2	0.1630	0.1630	0.0815			2.6
Total	8	6.2213					100.0

DF: Degree of freedom. SS: Pure sum of squares. SS: Sum of squares. MS: Mean square.
PD: Percentage distribution. F: F-Test statistics. P: Significance values
(S = 0.285454 R-Sq = 97.38% R-Sq(adj) = 89.52%)

Table 9. S/N ratios of control factors according to Ra results for AA2024

Number of experiments	C_c: Cooling Condition	V_c: Cutting Speed (m/min)	f: Feed (mm/rev)	Ra: Average Surface Roughness (µm)	Ra_p: Predicted Ra Values (µm)	S/N ratio
D1	1 (Internal MQL)	100	0.10	0.500	0.319	6.02060
D2	1 (Internal MQL))	125	0.15	0.834	0.875	1.57668
D3	1 (Internal MQL)	150	0.20	0.660	0.801	3.60912
D4	2 (External MQL)	100	0.20	1.543	1.584	-3.76732
D5	2 (External MQL)	125	0.10	1.387	1.528	-2.84153
D6	2 (External MQL)	150	0.15	1.874	1.693	-5.45539
D7	3 (Dry)	100	0.15	2.420	2.561	-7.67631
D8	3 (Dry)	125	0.20	3.059	2.878	-9.71159
D9	3 (Dry)	150	0.10	2.390	2.431	-7.56796

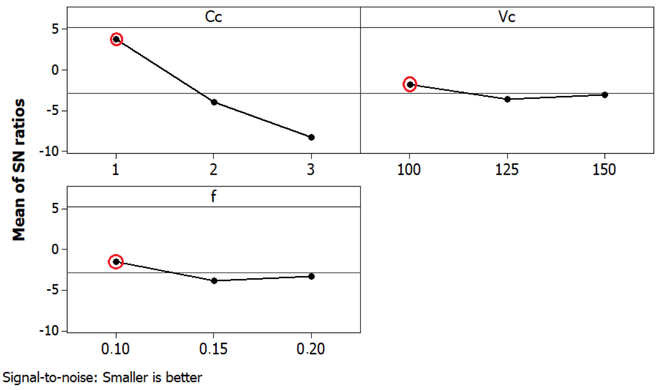

Figure 8. The main effect graph for S/N ratios according to Ra results obtained at AA2024 drilling

Table 10. Average S/N and mean responses for each of the levels of parameters.

Cutting parameters	Level 1	Level 2	Level 3	Max-Min
	S/N Levels			
A (Cooling Conditions C_c)	3.739	-4.021	-8.319	12.054
B (Cutting speed. Vc)	-1.808	-3.659	-3.138	1.851
C (Feed. f)	-1.463	-3.852	-3.290	2.389
	Mean Levels			
A (Cooling Conditions C_c)	0.6647	1.6013	2.6230	1.9583
B (Cutting speed. Vc)	1.4877	1.7600	1.6413	0.2723
C (Feed. f)	1.4257	1.7093	1.7540	0.3283

Table 11. Optimum levels of control factors for surface roughness (Ra).

Control factors	Symbol	Unit	Opt. level	Opt. value
Cooling condition (A)	Cc		1	Internal MQL
Cutting speed (B)	V_c	m/min	1	100
Feed (C)	f	mm/rev	1	0.1

The optimum results of the surface roughness values obtained using the Taguchi optimization method can be either any of the conditions used in the current experiments or a condition other than the current experiments. The optimum results obtained in this study are seen to be the experimental condition used in the experiments (First experiment: D1). In the Taguchi method, Eq (2) is used to estimate the surface roughness (Ra_p) of the optimum condition.

⍰⍰$_p$= (⍰$_1$ − ⍰$_{⍰⍰}$) + (⍰$_1$ − ⍰$_{⍰⍰}$) + (⍰$_1$ − ⍰$_{⍰⍰}$) + ⍰$_{⍰a}$ (2)

Here, A1, B1 and C1 are the optimum responses for Ra, and ⍰$_{⍰a}$ is the arithmetic mean of the Ra values measured in the experiments. When the values are put in place in the equation, Rap = 0.319 mm comes out. The calculation made using the related prediction module of the Minitab package program has also been confirmed. The optimum conditions calculated by the Taguchi method should be within the optimization result range. A confidence interval is needed to compare the Ra value calculated for the optimum condition with the Ra value measured in the experiment. The confidence interval in question can be expressed as in Eq. (3).

$$[Ra_p - CI] < Ra < [Ra_p + CI] \tag{3}$$

Here, in order to be able to calculate the CI value that determines the confidence interval, Eq (4) and Eq (5) is taken advantage of.

$$CI = \sqrt{F_{\alpha;1;f_e} v_e \left(\frac{1}{n_{eff}} + \frac{1}{r}\right)} \tag{4}$$

$$CI = \sqrt{F_{\alpha;1;f_e} v_e \left(\frac{1}{n_{eff}} + \frac{1}{r}\right)} \tag{5}$$

Where N is the number of experiments, T_{dof} is the degree of freedom of the main factors, n_{eff} is the number of effective repetitions, F_α is the ratio of F at the level of 1 and 95% confidence, α is the significance level, f_e is the degree of freedom of the error, and the variance of the error, and r is the number of repetitions for the verification test. For r = 3, N = 9, T_{dof} = 6, n_{eff} = 1.286 was calculated.

In Equation 4, the parameter determining the confidence interval was calculated as (CI) ±0.391 when the values $F_{0.05,1,2}$ = 18.51 (using the F test table), v_e =0.0815, n_{eff} = 1.286 were replaced.

For the confidence interval of the estimated mean optimal surface roughness at 95% reliability, when the values of CI, Ra and Rap are substituted in Equation 3 as follows:

[0,319 – 0,391] < 0,500 < [0,319 + 0,391] →-0,072 < 0,500 < 0,710

3.4. Comparison of Taguchi and Artificial Neural Network (ANN) methods in estimating Ra results

Artificial neural networks have become one of the prediction models used in recent years in the field of manufacturing. While creating the ANN model, it is necessary to determine the appropriate network structure, derive the most accurate equations, check the learning, test and prediction values, etc. operations need to be made. In this study, the ANN model was created using the Pythia package program. For the Ra output value, cooling conditions, cutting speed and feed were used as input values. The 3-6-5-1 network structure was used as the most suitable network structure. This network structure, which has 3 levels, has 2 hidden layers and a total of 12 neurons. This network structure used is as shown in Figure 9.

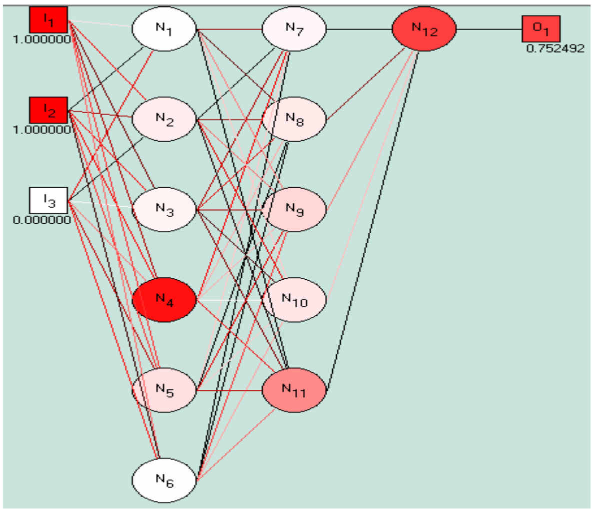

Figure 9. The 3-6-5-1 network structure used in the ANN model

The applied ANN model is feed-forward and a sigmoid function called “Fermi” is used as the transfer function. The Fermi transfer function used is as in Eq. (6):

$$N_{(i)} = \frac{1}{1 + e^{-4(E_i - 0.5)}} \tag{6}$$

Since normalization is required for the selected inputs to be in a comparable range, the input and output values are normalized between 0 and 1 by following Eq. (7).

$$N_v' = \left[\frac{N_i - N_{min}}{N_{max} - N_{\min}}\right] \tag{7}$$

After the input data is normalized with Eq. (7), to calculate the E_i (1) values of level 1 neurons in Eq. (6), Eq. (8) can be written as follows:

$$E_{i(1)} = w_{1i}C_c' + w_{i2}V_c'{}' + w_{i3}f' \tag{8}$$

E_i values for level 2 neurons were calculated with Eq. (9).

$$E_{i(2)} = w_{1i}N_1 + w_{2i}N_2 + w_{3i}N_3 + \cdots + w_{ii}N_i \tag{9}$$

For the level 3 neuron, the Ei value was calculated with Eq. (10).

$$E_{i(3)} = w_{7i}N_7 + w_{8i}N_8 + w_{9i}N_9 + \cdots + w_{ii}N_i \tag{10}$$

In the equations mentioned above, i expresses the number of neurons at that level. The adapted equation for the estimation of Ra values with ANN using the above equations is as follows:

$$N_{Ra} = \left(1 + e^{-4(-1.549869N_7 + 0.750294\,N_8 - 0.260733\,N_9 - 0.122533\,N_{10} + 1.786629\,N_{11} - 0.5)}\right)^{-1} \tag{11}$$

In order to calculate the reliability of the applied model, the absolute percentage of change expressed as R2 was used in the theoretical analysis of the model. For a reliable model, R2 is expected to be between 80% and 100% [27]. In the current study, the R2 value obtained from the YSA model for Ra is calculated as follows.

$$R^2 = 1 - \left[\frac{\sum i\left(Ra_i - N_{Ra_i}\right)^2}{\left(\llbracket (N \rrbracket_{Ra_i}\right)^2}\right] \tag{12}$$

The R2 value obtained from the ANN model for Ra in Eq. (12) was calculated as 99.86%.

A comparison between the estimated outputs and the measured Ra values by YSA and Taguchi analysis is given in Table 12 and Figure 10.

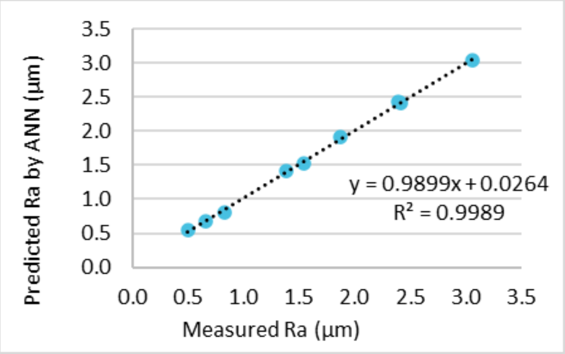

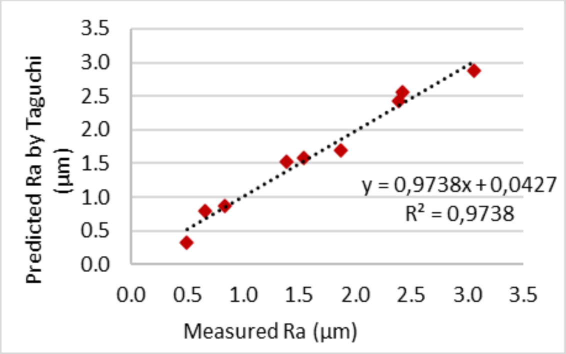

Figure 10. The compatibility of the estimated Ra values with the measured Ra value

Table 12. Estimated Ra values with measured Ra values

Test No	Variable	Measured Ra (µm)	Predicted Ra by ANN (µm)	Predicted Ra by Taguchi (µm)
D1	A1B1C1	0.500	0.552	0.319
D2	A1B2C2	0.834	0.801	0.875
D3	A1B3C3	0.660	0.684	0.801
D4	A2B1C3	1.543	1.530	1.584
D5	A2B2C1	1.387	1.409	1.528
D6	A2B3C2	1.874	1.910	1.693
D7	A3B1C2	2.420	2.406	2.561
D8	A3B2C3	3.059	3.039	2.878
D9	A3B3C1	2.390	2.426	2.431

According to these results, it can be said that the outputs obtained from the equations are normally distributed. Due to the high R^2 value in the reliability and validation test results of the models, mathematical models obtained with both YSA and Taguchi estimations can be used to predict the Ra results obtained in drilling AA2024 aluminum alloy. When the prediction performances for Taguchi analysis and artificial neural networks (ANN) are compared, it can be said that the ANN model gives closer to the correct outputs both in terms of theoretical analysis and graphical analysis.

3.5. Effect of cutting tool wear on surface roughness

The variation of these values according to different cutting parameters (Vc and f) and cooling conditions is shown in Figure 11

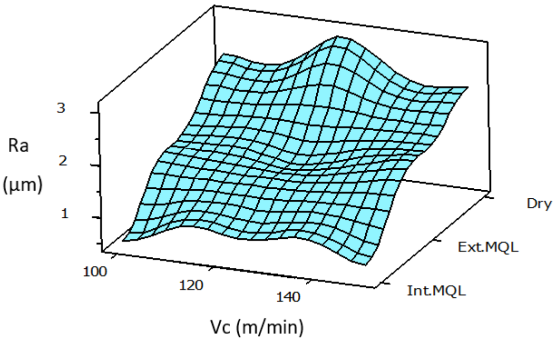

(a)

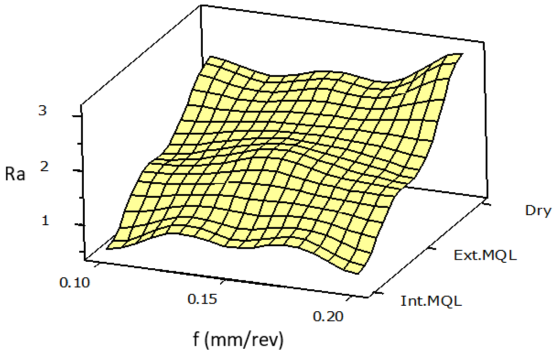

(b)

Figure 11. Change of surface roughness according to machining conditions: a) Change according to the cutting speed (Vc) and cooling condition. b) Change according to the feed (f) and cooling condition

Graph a in Figure 11 shows a clear increase in surface roughness as the feed value increases under all cooling conditions. When the effect of cooling conditions on surface roughness is examined in the same graph, it is seen that different cooling conditions used when machining with the same feed parameters have a significant effect on surface roughness. The highest surface roughness was observed under dry cutting conditions, while the lowest surface roughness, as expected, was observed during internal MQL application. The high smearing tendency caused by the high ductility characteristic of AA2024 alloy has been reduced by the application of internal MQL. It is thought that this decrease in the tendency to form built-up edge (BUE) combined with the low strength of the material has positive results on the surface quality [28, 29].

Figure 11 shows the effect of cutting speed and cooling conditions on surface roughness in graph B. When the graph is examined, it is seen that the change in cooling conditions seriously affects the surface roughness when machining at the same cutting speed. While the highest surface roughness is observed in dry cutting conditions, it is seen that the lowest surface roughness is obtained under internal cooling conditions. In the same graph, it is seen that the effect of the change in cutting speed on surface roughness is more unstable, especially under dry cutting and external cooling conditions. It is generally expected that the surface roughness will decrease with the increase of cutting speed in machining [30]. In the drilling process, the situation may be slightly different. Since the drilling process takes place in a closed area, an increase in the volume of chips released per unit time along with an increase in cutting speed can increase chip compression and plastering. In this case, the surface roughness may be more than expected [24, 31]. It is estimated that the uncertainty in the effect on the surface roughness of the cutting speed seen in the graph may be caused by the mentioned conditions of the drilling operation.

A separate cutting tool was used for each condition in the drilling tests performed under 9 different cutting conditions. In order to see the wear on the cutting tools used for each different condition, the experiment was repeated 30 times under the same condition with the same tool. At the end of the experiments, images were taken with Scanning Electron Microscope (SEM) in order to detect the wear of the tools. Detailed images taken from the cutting edges of the tools with SEM are given in Figure 12.

AA2024 aluminum alloy is a ductile and highly adhesive material. For this reason, it is very likely that it will be plastered to the team in drilling operations where chip evacuation is difficult because it takes place in a closed area. When the application of cutting fluid in the drilling process is not applied correctly, it will be inevitable that the ductile aluminum will be plastered onto the tool [2-4]. In dry cutting conditions, it is expected that aluminum will be plastered onto the tool during drilling. The main purpose of this study is to compare the effect of MQL application from within the tool and MQL application with nozzle from outside the tool on machining performance in drilling operations on ductile materials. When the surface roughness of the holes obtained from the experiments was examined in the previous sections, it was revealed that much smaller Ra data were obtained in the internal MQL application than in the external MQL application. The reason for the observation of much larger surface roughness data in the external MQL application compared to the internal MQL application is understood when looking at the SEM images of the cutting tools given in Figure 12. When looking at the SEM image (a) of the tool used in the D3 experiments in Figure 10 and where internal MQL application is applied, it is seen that the chisel edges retain their shape. Only a certain amount of chip accumulation (Built Up Layer -BUL) in the form of a layer on the chip surface of the tool is visible. Again, this time in Figure 12, when the SEM images (b) of the tool used in the D5 experiments and where external MQL application is applied are examined, it is seen that both the main cutting edges and the auxiliary cutting edge (chisel edge) have lost their form. It is seen that the workpiece material starts from the auxiliary cutting edge in the center of the tool and sticks to the tool markedly towards the main cutting edges, disrupting the cutting form of the tool. In addition to the Built-Up Edge (BUE) chips observed along cutting edges, there is also in the forms of layers built-up layer (BUL) on the chip surfaces. Due to the nature of the drilling process, the cutting speed decreases from the tool circumference to the center. Built-up edge formation is more common under low cutting speed conditions rather than high cutting speeds. In the machining of ductile materials, especially conditions where there is no or insufficient application of cutting fluid, such as dry cutting or external MQL, are suitable conditions for the formation of BUE [2-4, 20]. Especially in these cooling conditions, more BUE is seen towards the tool center where the cutting speed approaches zero. In internal MQL conditions, it is thought that the cutting fluid prevents the chip from sticking to the chisel edges because it successfully forms a film layer between the tool and the chip. Thus, it is evaluated that the roughness value is lower on the surfaces processed by the cutting tool that maintains its sharpness.

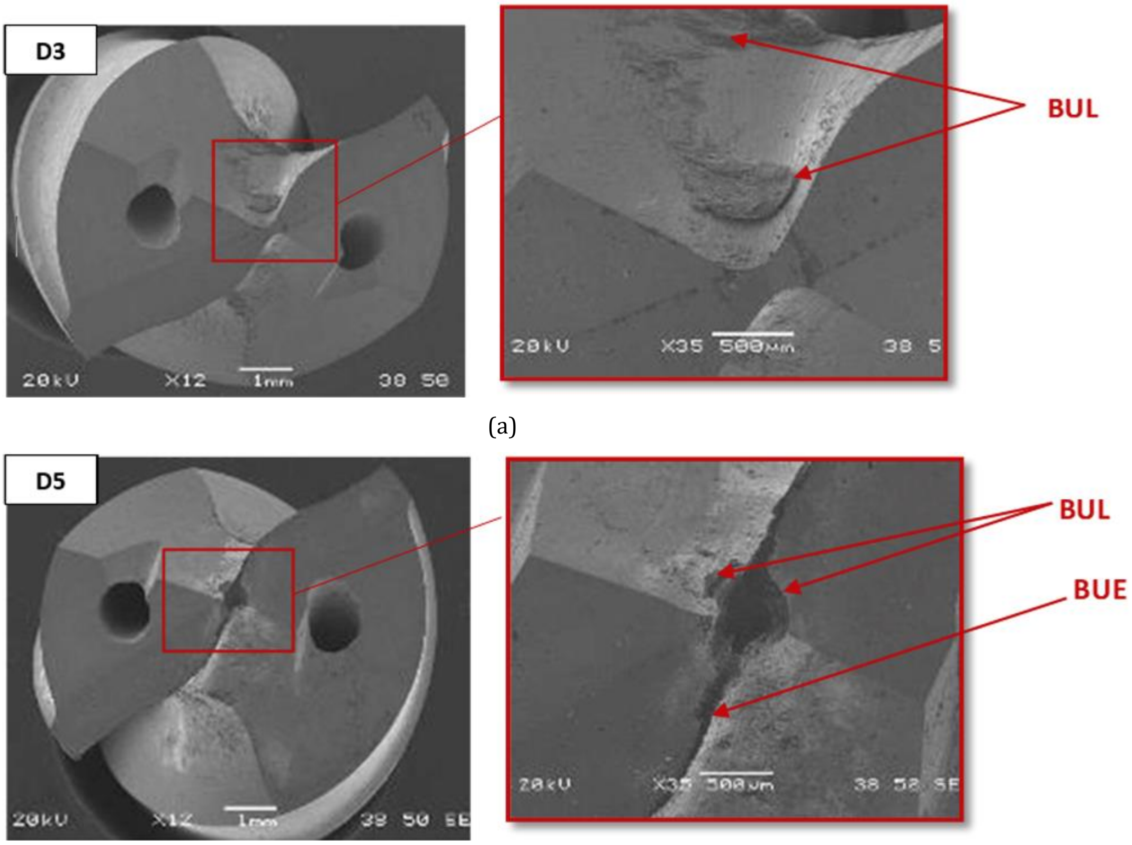

(a)

(b)

Figure 12. SEM photos of the drills used in the drilling of AA2024 alloy: (a) Internal MQL application. (b) External MQL application.

4. Conclusions

In this study, drilling tests were carried out on AA2024 aluminum alloys using uncoated carbide drills with internal cooling channels. In this study, in particular, the effect of the application of the MQL method through channels in the tool and its application with nozzles from outside the tool on the machining performance was compared. In order to evaluate the machining performance in drilling tests using different cutting parameters and cooling conditions, the surface roughness (Ra) of the holes and wear/plastering on the tools were examined. In order to clearly see the abrasions /plastering on the tools in the experiments carried out under 9 different cutting conditions, each condition was repeated 30 times. The results obtained at the end of the experiments can be summarized as follows:

- ✓ In the repeat experiments conducted for each different condition of the system, it was observed that the Ra values measured at the 30th hole under all cooling conditions were higher than those measured at the 1. hole.
- ✓ However, in these repeat experiments conducted for each different condition, it was determined that the amount of increase in surface roughness from the 1st hole to the 30th hole was very low in internal MQL application. It has been observed that the amount of increase in Ra values under external MQL conditions is close to dry machining conditions. In the re-experiments conducted, the surface roughness from the first hole to the last hole was significantly increased under these two conditions.
- ✓ The arithmetic average of the Ra results measured in 30 drilling repetitions for each different condition was taken. These averages are compared to evaluate the machining performance under each different condition. In the comparison carried out, it was determined that the most important factor affecting the surface roughness is the cooling condition. This situation is clearly demonstrated in the relevant graphs. In addition, the effect rate of the cooling condition in the analysis of variance on Ra data was 92%.
- ✓ The lowest average Ra values in the study were observed in conditions of internal MQL. On the other hand, slightly lower results were observed in external MQL application than in dry conditions. It has been revealed that the effect of cooling conditions on Ra is much more pronounced, especially in conditions where high cutting parameters are applied.
- ✓ The increase in these feed parameters, as expected, increased the surface roughness.
- ✓ It has been observed that the effect of the change in cutting speed on surface roughness is more unstable due to the difficulty experienced in chip evacuation during drilling (especially in dry cutting and external cooling conditions).
- ✓ According to the “Smallest is the best” approach. the L9 vertical index was used in the Taguchi experiment design and the number of 27 experiments was reduced to 9. At the end of these experiments, the optimum conditions obtained in the Signal/Noise (S/N) tests for the measured Ra data describe the best machining performance. According to the results obtained from the S/N tests, the internal MQL method (A1), which is the first level of cooling conditions, 100 m/min (B1), the first level of the cutting speed and 0.10 mm/rev (C1), the first level of the feed parameter, are the optimum

conditions. The 0.5 μm surface roughness amount measured under these conditions is the smallest Ra value measured under all conditions.

- ✓ In the SEM images of the tools used in the experiments, results consistent with the Ra data obtained under the conditions in which the corresponding tools were used were observed. It is observed that the chisel edge form is usually preserved in tools used in internal MQL conditions where small Ra values are observed. Due to the effect of the reduction of the cutting speed from the tool circumference to the tool center during drilling operations, more built-up edge (BUE) was observed. especially in the tool center than around it.
- ✓ In addition, ANN and Taguchi analyses were successfully applied to the data obtained from the experiments. At the end of these analyses, a 97% concordance was observed between the results obtained in the experiments and the estimated data obtained using the Taguchi approach, while a 99% concordance was observed between the estimated data obtained using the ANN approach. According to these results, it can be said that the estimates made with the ANN approach can give closer to the correct results.

As a result, it has been demonstrated by this study that the MQL method can be effective not only in turning and milling operations. But also, in drilling when the correct method is used. In this way, it is thought that by encouraging the MQL method to be used more frequently in the field of manufacturing. It can be ensured that environmentally friendly and sustainable production becomes widespread.

Ethics committee approval and conflict of interest statement

There is no need to obtain permission from the ethics committee for the article prepared. There is no conflict of interest with any person/institution in the article prepared.

Acknowledgments

The authors would like to thank the Technological Research Council of Turkey (TUBITAK) for this study supports under the program 1002-115M106 coded project finance. Also. the authors would like to thank the Turkish Aerospace Industries Corporation (TUSAŞ/TAI) for the possibility of using machines and equipment in their experiments.

Declaration of author contributions

Ayşegül Çakır Şencan: Experimental research, Methodology, Analysis, Writing, Original draft.
Abdullah Duran: Methodology, Review, Editing
Ulvi Şeker: Funding acquisition, Project management Methodology, Review, Editing.
Müberra Rüveyda Koçak, Writing, Editing, Original draft.
Cevdet Şencan: Review, Editing, Analysis.

References

[1] Çakır, A., 2009. AA7075 and AA6013 Investigation of cutting parameter on aluminium alloys during drilling operations. Gazi University, Graduate School of Natural and Applied Sciences, Master Thesis, Ankara.

[2] Çakır, A., 2015. Investigation of the effect of cooling conditions on cutting performance in drilling AA7075 and AA2024 aluminum materials. Gazi University, Graduate School of Natural and Applied Sciences, Ph.D. Thesis, Ankara.

[3] Mills, B., Redford, A.H., 1983. Machinability of Engineering Materials. Applied Sci. Publishers Ltd.

[4] Akkurt, M., 1998. Metal Cutting Methods and Machine Tools. Birsen Press, pp. 23-90.

[5] Tonshoff, H.L., Spintig, W., Konig, W., Neises, A., 1994. Machining of holes developments in drilling technology. Annals of the CIRP, Vol. 43(2), pp. 551-561.

[6] Ogawa, M., Inose, M., Arai, M., Saga, T., 1994. Micro drilling of 5056 wrought aluminum alloy. Journal of Japan Institute of Light Metals, Vol. 44(9), pp. 486-491. DOI: 10.2464/jilm.44.486.

[7] Pirtini, M., Lazoglu, I., 2005. Forces and hole quality in drilling. International Journal of Machine Tools & Manufacture, Vol. 45(1), pp. 1271-1281. DOI: 10.1016/j.ijmachtools.2005.01.004.

[8] Taşgetiren, S., Aslantaş, K., 2000. A new design of hard metal insert holder for cutting on turning. 3rd GAP Engineering Congress, pp. 150-157.

[9] Mendi, F., 1996. Machine tool theory and calculations. Gazi Bookstore, pp. 5-40.

[10] Demir, H., Ulaş, H.B., Zeyveli, M., 2009. Desired properties of cutting fluids used in machining. 5th International Advanced Technologies Symposium (IATS'09), 13-15 May, Karabük, pp. 1327-1331.

[11] Silliman, J.D., 1992. Cutting and grinding fluids: selection and application. Society of Manufacturing Engineers.

[12] Yücel, E., Günay, M., Ayyıldız, M., Erkan, Ö., Kara, F., 2011. Effects of cutting fluids used in machining on human health and sustainable use. 6th International Advanced Technologies Symposium (IATS'11), pp. 116-121.

[13] Çakır, A., Kavak, N., Şeker, U., 2017. Recycling of cutting fluids used in machining for sustainable production. Engineer and Machinery, Vol. 58(684), pp. 15-30.

[14] Autret, R., Liang, S.Y., 2003. Minimum quantity lubrication in finish hard turning. Proceedings of International Conference on Humanoid. Nano Technology, Information Technology, Communication and Control, Environment and Management (HNICEM'03), Manila, Philippines, pp. 1-9.

[15] Çakır, M.C., 2017. Modern methods of chip removal. Dora Publishing.

[16] Dhar, N.R., Ahmed, N.T., Islam, S., 2007. An experimental investigation on effect of minimum quantity lubrication in machining AISI 1040 steel. International Journal of Machine Tools & Manufacture, Vol. 47(5), pp. 748-753. DOI: 10.1016/j.ijmachtools.2006.09.017.

[17] Sreejith, P.S., 2008. Machining of 6061 aluminium alloy with MQL dry and flooded lubricant conditions. Materials Letters, Vol. 62(2), pp. 276-278.

[18] Çakır, A., Yağmur, S., Kavak, N., Küçüktürk, G., Şeker, U., 2015. The effect of minimum quantity lubrication under different parameters in the turning of AA7075 and AA2024 aluminium alloys. International Journal of Advanced Manufacturing Technology, Vol. 81, pp. 2515-2521. DOI: 10.1007/s00170-015-7878-4.

[19] Rahim, E.A., Sasahara, H.A., 2011. A study of the effect of palm oil as MQL lubricant on high-speed drilling of titanium alloys. Tribology International, Vol. 44(3), pp. 309-317. DOI: 10.1016/j.triboint.2010.10.032.

[20] Bhowmick, S., Alpas, A.T., 2008. Minimum quantity lubrication drilling of aluminium-silicon alloys in water using diamond-like carbon coated drills. International Journal of Machine Tools & Manufacture, Vol. 48(12-13), pp. 1429-1443. DOI: 10.1016/j.ijmachtools.2008.04.010.

[21] Krishnan, P.G., Raj, S.D., 2023. Machinability and tribological analysis of used cooking oil for MQL applications in drilling AISI 304 using a low-cost pneumatic operated MQL system. Journal of Manufacturing Processes, Vol. 104, pp. 348-371. DOI: 10.1016/j.jmapro.2023.09.028.

[22] Buss, L., Schumski, L., Sölter, J., Avila, K., Karpuschewski, B., Fritsching, U., 2023. Minimum Quantity Lubrication (MQL) multiphase dynamics of a vibration-assisted drilling process. Procedia CIRP, Vol. 117, pp. 420-425.

[23] Kuzu, A.T., Alma, U.A., Rahimzadeh Berenji, K., Bakkal, M., 2014. Experimental investigation of CGI drilling adapted with external MQL system. 16th International Conference on Machine Design and Production (UMTIK), June 30 – July 03, İzmir, p. 63.

[24] Han, S., Faverjon, P., Valiorgue, F., Rech, J., 2018. Prediction and modeling of thermal distortion in sequential MQL drilling of AlSi7 cylindrical parts. Procedia CIRP, Vol. 77, pp. 336-339. DOI: 10.1016/j.procir.2018.09.029.

[25] Ali, S.Y., Yao, Y., Wu, B., Zhao, B., Ding, W., Jamil, M., Khan, A., Baig, A., Liu, Q., Xu, D., 2024. Recent developments in MQL machining of aeronautical materials: A comparative review. Chinese Journal of Aeronautics. DOI: 10.1016/j.cja.2024.01.018.

[26] Chen, Y.H., Tam, S.C., Chen, V.L., Zheng, H.Y., 1996. Application of Taguchi method in the optimization of laser micro-engraving of photomask. International Journal of Material & Product Technology, Vol. 11(3-4), pp. 333-334. DOI: 10.1504/IJMPT.1996.036336.

[27] Çetin, M.H., Ozcelik, B., Kuram, E., Demirbas, E., 2011. Evaluation of vegetable-based cutting fluids with extreme pressure and cutting parameters in turning of AISI 304L by Taguchi method. Journal of Cleaner Production, Vol. 19, pp. 2049-2056. DOI: 10.1016/j.jclepro.2011.07.013.

[28] Cobden, R., 1994. Aluminium: Physical properties, characteristics and alloys. European Aluminium Association, TALAT-1501, pp. 36-252.

[29] Rogov, V.A., Siamak, G., 2013. Optimization of surface roughness and vibration in turning of aluminum alloy AA2024 using Taguchi technique. International Journal of Mechanical, Industrial Science and Engineering, Vol. 7(11), pp. 869-878.
[30] Trent, E.M., 1989. Metal cutting. Butterworths Press, pp. 1-171.
[31] Kıvak, T., 2012. Investigation of the effects of cryogenic treatment applied to cutting tools on the drillability of Ti-6Al-4V alloy. Gazi University, Ph.D. Thesis, Ankara.

DEU FMD 27(79) (2025) 99-109

Dokuz Eylül Üniversitesi Mühendislik Fakültesi Fen ve Mühendislik Dergisi
Dokuz Eylul University Faculty of Engineering Journal of Science and Engineering
Elektronik/Online ISSN: 2547-958X

ARAŞTIRMA MAKALESI / RESEARCH ARTICLE

X-Işını Görüntüleri Kullanılarak Omuz İmplantlarının Tespiti ve Sınıflandırılmasında YOLOv5 Modellerinin Performanslarının İncelenmesi

Investigation of The Performance of Yolov5 Models In The Detection and Classification of Shoulder Implants Using X-Ray Images

Elif Baykal Kablan

Karadeniz Teknik Üniversitesi Mühendislik Fakültesi, Yazılım Mühendisliği, Trabzon, TÜRKİYE
Sorumlu Yazar / Corresponding Author : ebaykal@ktu.edu.tr

Öz

Total Omuz Artroplastisi (TOA), omuz eklemindeki hasara bağlı ağrı ve hareket kısıtlanması yaşayan hastalarda omuzun hasar görmüş kısmının protez implant ile değiştirildiği cerrahi işlemdir. Zamanla protez implantların aşınması veya zarar görmesi durumunda, protez üreticisi ve model bilgisine ihtiyaç duyulur, ancak tıbbi kayıtlardaki eksiklikler nedeniyle bu bilgiler genellikle belirsiz olabilmektedir. Bu nedenle, uzman kişiye bağımlılığı azaltarak hızlı ve doğru bir şekilde protez bilgilerini sağlayacak otomatik sistemlere ihtiyaç duyulmaktadır. Bu çalışmada, omuz implantı üreticilerinin X-ışını görüntüleri kullanılarak tespiti ve sınıflandırılması için otomatik bir sistem önerilmiştir. Sistemde YOLOv5n, YOLOv5s, YOLOv5m ve YOLOv5l modelleri kullanılarak implant baş bölgesi tespiti ve sınıflandırma işlemleri gerçekleştirilmiş ve elde edilen sonuçlar karşılaştırılmıştır. Veri dengesizliği nedeniyle bazı sınıfların diğerlerinden daha iyi temsil edildiği sınıf ağırlıklandırma tekniği de kullanılmıştır. Bu tekniğin modelin sınıflandırma performansını önemli ölçüde artırdığı tespit edilmiştir. Karşılaştırma sonucunda sınıf ağırlıklandırmalı YOLOv5l modelinin mAP@0.5, mAP@0.5:0.95, kesinlik, duyarlılık ve F1-ölçütü değerlerinde en yüksek performansı gösterdiği görülmüştür ve bu değerler sırasıyla 98.3, 85.9, %97.0, %95.7 ve %96.3 olarak elde edilmiştir. Önerilen YOLOv5l modeli, literatürdeki diğer hibrit makine öğrenmesi yaklaşımlarına göre düşük maliyetli ve yüksek performanslı bir çözüm sunmaktadır. Bu sayede, YOLOv5 modellerinin omuz implantlarının tespit ve sınıflandırmasında değerli bir araç olarak etkinliği gösterilmiştir. Ayrıca, önerilen sistem sayesinde radyologlar ve cerrahlar için verimli ve güvenilir analiz süreçleri sunulması ve iş yükünün azaltılması beklenmektedir.

Anahtar Kelimeler: *Derin Öğrenme, Total Omuz Artroplastisi, X-ray, YOLOv5*

Abstract

Total Shoulder Arthroplasty (TSA) is a surgical procedure in which the damaged part of the shoulder is replaced with a prosthetic implant in patients with pain and restriction of movement due to damage to the shoulder joint. If prosthetic implants wear out or become damaged over time, prosthesis manufacturer and model information is needed, but this information can often be unclear due to deficiencies in medical records. Therefore, there is a need for automated systems to provide prosthesis information quickly and accurately, reducing reliance on specialists. In this study, an automatic system is proposed for the detection and classification of shoulder implant manufacturers using X-ray images. In the system, implant head region detection and classification processes were performed using YOLOv5n, YOLOv5s, YOLOv5m, and YOLOv5l models and the results obtained were compared. The class weighting technique was also used, where some classes are better represented than others due to data imbalance. It was found that this technique significantly improves the classification performance of the model. As a result of the comparison, it was observed that the YOLOv5l model with class weighting showed the highest performance in mAP@0.5, mAP@0.5:0.95, precision, sensitivity, and F-measure values, and these values were obtained as 98.3, 85.9, 97.0%, 95.7% and 96.3% respectively. The proposed YOLOv5l model offers a low-cost and high-performance solution compared to other hybrid machine learning approaches in the literature. Thus, the effectiveness of YOLOv5 models as a valuable tool in the detection and classification of shoulder implants has been demonstrated. Furthermore, the proposed system is expected to provide efficient and reliable analysis processes and reduce the workload for radiologists and surgeons.

Keywords: *Deep Learning, Total Shoulder Arthroplasty, X-ray, YOLOv5*

EXTENDED ABSTRACT

Introduction

The Shoulder, the most mobile joint in the human body, often requires surgical intervention for conditions like osteoarthritis and rheumatoid arthritis, leading to Total Shoulder Arthroplasty (TSA). The objective of TSA is pain alleviation and restoration of normal shoulder functions. Surgical decisions, including prosthesis choice, are commonly guided by X-ray images. However, despite advancements in prosthetics, wear and loosening may necessitate periodic reviews or replacements. This paper addresses the challenge of prosthetic wear or damage,

DOI: https://doi.org/10.21205/deufmd.2025277913

Geliş Tarihi / Received: 26.01.2024
Kabul Tarihi / Accepted: 15.05.2024

emphasizing the importance of knowing the prosthesis manufacturer and model for efficient replacement. Current gaps in medical records often lead to uncertainties, requiring additional X-ray imaging and expert examinations. Automatic diagnostic systems are crucial for early interventions, and recent advances in deep learning, especially YOLOv5, have shown promising results in medical image processing.

The study conducts a comprehensive comparison of YOLOv5's nano, small, medium, and large versions for both implant detection and classification, surpassing recent studies in classification accuracy. Utilizing a publicly shared dataset, this work stands as the most extensive comparative analysis in the literature. By introducing YOLOv5 for joint implant classification from X-ray images, this study contributes to the growing body of research in deep learning applications for medical image analysis.

Materials and Methods

In this study, the investigation revolves around a publicly available dataset introduced by Urban et al. in 2020, featuring 597 X-ray images specifically focused on shoulder implants from four distinct manufacturers—Cofield (83 images), Depuy (294 images), Tornier (71 images), and Zimmer (149 images). The dataset presents several challenges, including variable and relatively low image resolution, diverse aspect ratios, and imbalances in class distribution. These challenges underscore the complexity of the problem. The dataset was chosen due to its recent introduction, open accessibility, and widespread adoption in the literature. A systematic split allocated 90% of the data to the training set and the remaining 10% to the testing set. A 5-fold cross-validation strategy was implemented, ensuring each class had representation across training and testing sets. For labeling, the LabelImg annotation tool was used to mark implant head regions with rectangular bounding boxes, aligning with YOLO algorithms. YOLOv5, with its four variants (n, s, m, and l), served as the primary deep learning framework, each trained for 400 epochs with consistent hyperparameters. The study concludes with a comparative analysis of YOLOv5 variants' performance, providing insights into their effectiveness in shoulder implant detection.

Results and Discussion

The proposed YOLOv5-based approach for shoulder implant detection and classification is evaluated against state-of-the-art methods, encompassing all its sub-versions. Utilizing transfer learning for efficient training, each YOLOv5 model is fine-tuned on a dataset of X-ray images containing shoulder implants, leveraging pre-trained weights from the COCO dataset. The models undergo 400 epochs with specific hyperparameters, including a batch size of 8, momentum of 0.9, decay of 0.0005, and a learning rate of 0.001. Quantitative assessments, employing metrics such as precision, recall, F1-score, and mAP, highlight the superior performance of the YOLOv5l model with detection metrics of 98.7% mAP@0.5, 85.7% mAP@0.5:0.95, 93.4% precision, 94.6% recall, and 93.9% F1-score, as presented in Table 3. The convergence of precision and recall to 100% during training and validation is visualized in Figure 5. Qualitatively, true positive detection results of the YOLOv5l model on selected test images are illustrated in Figure 6. A comprehensive comparison with previous studies on the same dataset is provided in Table 4, affirming the proposed YOLOv5 model's efficacy for accurate shoulder implant detection and classification.

Conclusion

The YOLOv5 models achieve a low-cost and high-performance objective compared to other hybrid machine learning approaches in the literature, showcasing their effectiveness in medical imaging applications like shoulder implant detection and classification. The models are envisioned to offer an efficient and reliable analysis process for radiologists and surgeons, potentially alleviating their workload. However, a notable limitation is the limited diversity in implant manufacturer classes within the dataset, providing an opportunity for expansion by increasing this diversity. Moreover, exploring model performance enhancements through testing on larger datasets and diverse imaging conditions remains a promising avenue for future research.

---

1. Giriş

Omuz vücuttaki tüm eklemler arasında en yüksek hareketliliğe sahip karmaşık yapılı bir eklemdir. Total Omuz Artroplastisi (TSA), omuz ekleminde özellikle kireçlenme ve romatoid artrit hastalıkları nedeniyle meydana gelen hasara bağlı ciddi ağrısı ve hareket kısıtlanması olan hastalarda uygulanan bir ameliyat türüdür. Bu ameliyatın amacı ağrıyı gidermek ve hastaya normal omuz fonksiyonlarını yeniden kazandırarak yaşam kalitesini artırmaktır [1-3]. TSA ameliyatı ile fonksiyonunu yitirmiş ve istenen potansiyelde çalışamayan eklem çıkarılarak yerine protez implant yerleştirilmektedir. Ameliyat sırasında hangi protezin yerleştirileceğine karar vermek için X-ışını görüntüleri kullanılmaktadır. Günümüzde birkaç farklı protez üreticisi olmakla birlikte her bir üretici vakaya ve hastaya özgü birkaç farklı model sunmaktadır. Mevcut kullanılan protez ürünleri, malzemeleri ve cerrahi teknikler oldukça gelişmiş olsa da protezler zamanla aşınabilmekte ya da gevşeyebilmektedir. Dolayısıyla cerrahi işlem uygulandıktan sonra protez durumunun belirli zaman aralıklarıyla tekrar gözden geçirilmesi ve gerektiği takdirde yeniden yerleştirilmesi gerekmektedir [4]. Ayrıca kaza gibi bazı durumlarda mevcut protez zarar görmüş ise değiştirilmektedir. Protezin iyileştirilmesi veya değiştirilmesi durumunda sürecin hızlı ve başarılı bir şekilde ilerlemesi açısından protez üreticisi ve model bilgisi hasta veya doktor tarafından bilinmelidir. Ancak bu gibi durumlarda genellikle tıbbi kayıtlardaki eksiklikler sebebiyle belirsizlik durumu ortaya çıkmaktadır. Dolayısıyla hastadan tekrar X-ışını görüntüsü alınarak tıbbi uzman tarafından detaylı bir inceleme ile üretici ve model bilgisi doğrulanmaktadır. Bu incelemenin uzman kişiye bağlı, zaman alıcı ve yorucu olmasından dolayı otomatik sistemlere ihtiyaç duyulmaktadır.

Otomatik tanı sistemleri erken tedavi ve cerrahi işlem ile protezde daha fazla bozulmayı önlemek açısından kritik öneme sahiptir. Son zamanlarda, derin öğrenme yöntemleri geniş bir yelpazede tıbbi görüntü işleme görevlerinde yüksek performans sergilemektedir. Örneğin, derin sinir ağları, kanser teşhisi için meme kanseri, akciğer kanseri, beyin tümörü gibi çeşitli tıbbi görüntü sınıflandırma görevlerinde etkileyici sonuçlar elde etmiştir. Derin öğrenme yöntemleri, organ segmentasyonu, lezyon tespiti ve yoğunluk tahmini gibi tıbbi görüntü analizi alt alanlarında da başarılı olmuştur. Derin öğrenme modelleri, büyük miktarda veriyi etkili bir şekilde öğrenerek karmaşık ilişkileri ve özellikleri yakalayabilme yeteneğine sahiptir. Derin sinir ağlarının katmanlı yapısı, özelliklerin hiyerarşik olarak çıkarılmasını sağlar ve bu da tıbbi görüntülerdeki anatomik yapıların ve patolojik bölgelerin daha iyi temsil edilmesine yardımcı olur. Ayrıca, derin öğrenme modelleri, veri artırma teknikleri ve transfer öğrenme gibi yöntemlerle de desteklendiğinde daha da güçlenir. Bu sayede, sınırlı veriye sahip tıbbi görüntü veri setleri üzerinde bile yüksek performans elde edilebilir. Sonuç olarak, derin öğrenme yöntemleri, tıbbi görüntü işleme alanında etkileyici sonuçlar veren güçlü bir araç haline gelmiştir. Daha detaylı bir tartışma ve karşılaştırma için okuyucular, araştırma makalelerine başvurabilirler [5-6]. Literatürde X-ışını görüntülerinden omuz implantlarının tespiti ve sınıflandırılması amacıyla önerilen derin öğrenme tabanlı birkaç çalışma mevcuttur [4, 7-12].

Urban vd. [7] omuz implantlarını sınıflandırmak amacıyla 6 farklı derin öğrenme tabanlı CNN mimarisini (VGG-16, VGG-19, ResNet-50, ResNet-152, NASNet, DenseNet-201) uygulamışlardır. Veri seti, dört farklı protez üreticisine ait 16 farklı modelin kullanıldığı 597 adet omuz implantı X-ışını tarama görüntüsünden oluşmaktadır. CNN mimarilerinin ImageNet [13] gibi büyük boyutlu veri seti üzerinde önceden eğitilmesinin ve daha sonra omuz implantlarının X-ışını görüntülerini içeren bir veri setinde ince ayar yapılmasının iyi sonuçlar sağladığını belirtmişlerdir. En yüksek sınıflandırma performansını 10-kat çapraz doğrulama uygulayarak %80,4 doğrulukla NASNet [14] mimarisi ile elde etmişlerdir. Yi vd. [8] beş farklı implant modeli içeren toplam 482 adet omuz implantı X-ışını tarama görüntüsü kullanmışlardır. Tüm modelleri tek bir sınıflandırıcı ile eğitmek yerine sırasıyla her implant modeli için beş ayrı ResNet-152 mimarisini ikili sınıflandırıcı olarak eğitmişlerdir. 20-kat çapraz doğrulama uygulayarak Solar için 0,86'dan Zimmer için 1,0'a kadar değişen AUC-ROC değeri elde etmişlerdir. Yilmaz [9] literatürden farklı olarak en öne çıkan özellik filtrelerini seçmek amacıyla yeni bir kanal seçim katmanı (channel selection layer) kullanan çok kanallı bir CNN modeli önermiştir. Model her görüntü için kanallar arasında uygulanan en etkili özellik seçimi ile doğruluk oranını önemli ölçüde artırmıştır. Önerilen yöntem %97,2 doğruluk oranı ile diğer çalışmalara göre daha iyi performans göstermiştir. Sultan vd. [10] omuz implantlarını sınıflandırmak amacıyla CNN ağ topluluğu mimarisine dayalı bir yöntem önermişlerdir. Rotasyonel olarak veri artırma uygulayarak eğitim veri setini 36 kat artırmışlardır. Modifiye edilmiş ResNet ve DenseNet ağ modellerini DRE-Net ağ topluluğu mimarisini oluşturmak için derinlemesine birleştirmişlerdir. DRE-Net mimarisi ile 10-kat çapraz doğrulama ile %85,92 doğruluk, %84,69 F1-ölçütü, %85,33 kesinlik ve %84,11 duyarlılık elde etmişlerdir. Efeoglu vd. [11] 3 farklı üreticiye ait omuz implantlarını sınıflandırmak amacıyla 12 farklı sınıflandırıcının performansını karşılaştırmıştır. 10-kat çapraz doğrulama uygulanarak K-NN algoritmasının %74 doğruluk ile diğer algoritmalara göre daha iyi performans sağladığı görülmüştür. Bu sonuç derin öğrenme tabanlı yöntemlerin klasik makine öğrenmesi yöntemlerine göre oldukça başarılı olduğunu göstermiştir. Sivari vd. [4] derin öğrenme ve makine öğrenmesi algoritmalarının birleşiminden oluşan 10 farklı hibrit sınıflandırıcı model oluşturmuş ve istatistiksel olarak test etmişlerdir. Deneysel sonuçlara göre DenseNet201 + Lojistik Regresyon modeli kullanılarak %95,07 doğruluk sağlamışlardır. Karaci [12] diğer tüm yöntemlerden farklı olarak YOLOv3 nesne tespiti modeli ile omuz implantlarının baş bölgesini tespit ettikten sonra bu bölgeleri çeşitli CNN mimarilerine giriş olarak vermiştir. Sonuç olarak YOLOv3 nesne tespiti modeli ile implantın baş bölgesine odaklanmanın sınıflandırma doğruluğunu artırdığı görülmüştür. YOLOv3 ile DenseNet201 modelinin birlikte kullanımı ile %84,76 doğruluk elde etmişlerdir.

Nesne tespiti, birçok görüntü sınıflandırma tabanlı çalışmanın temel taşı olup bilgisayarlı görüntü alanında yoğun olarak çalışılmaktadır. Nesne tespitinde temel amaç, verilen bir giriş görüntüsü içerisinde tespit edilmesi istenen nesnelerin konumunu sınırlayıcı kutu ile belirlemek ve hangi sınıfa ait olduklarını belirlemektir [15]. Literatürde bu amaçla önerilen yöntemler tek-adımlı ve iki-adımlı olmak üzere iki sınıf altında toplanmaktadır. Tek-adımlı yöntemler bölge önerilerinin oluşturulması ve bu bölgelerin sınıflandırılması olmak üzere iki adımda çalışmaktadır. SSD [16] ve YOLO [17] yöntemlerinde ise hem bölge önerme hem de sınıflandırma tek adımda gerçekleştirildiğinden tek-adımlı olarak adlandırılmaktadır. Bu özellik SSD ve YOLO yöntemlerinin hızlı çalışmasını ve böylece gerçek zamanlı uygulamalarda daha çok tercih edilmesini sağlamaktadır [18]. YOLO, R-CNN [19], Fast R-CNN [20] ve Faster R-CNN [21] gibi diğer popüler CNN tabanlı nesne algılama yönteminin algılama süresini azaltmayı amaçlamıştır. YOLO, hız ve doğruluk açısından güçlü performans sağlar ve gerçek zamanlı nesne algılama uygulamasında uygulanabilmektedir. Önerilen ilk YOLO yöntemi üzerinde yapılan gelişmeler sonucunda literatürde YOLOv2 (YOLO9000) [22], YOLOv3 [23], YOLOv4 [24] ve YOLOv5 [25] olmak üzere hızı ve doğruluğu yüksek gerçek zamanlı birçok nesne algılama yöntemi önerilmiştir. YOLO'nun tüm beş versiyonu birçok uygulamada yaygın olarak kullanılmış ve başarılı şekilde uygulanmıştır.

X-ışını görüntülerinden omuz implantı sınıflandırma alanında ise yalnızca Karaci vd. [12] YOLO'nun üçüncü sürümü olan YOLOv3 yöntemini implantın baş bölgesini tespit etmek amacıyla önermiştir. Sınıflandırma işlemini ise ayrıca tespit ettiği baş bölgelerini CNN mimarilerine giriş olarak vererek gerçekleştirmiştir. Bu çalışmada ise, hem implantın baş bölgesinin tespit edilmesi hem de sınıflandırılması amacıyla en güncel YOLOv5 yöntemi önerilmektedir. Önerilen çalışma kapsamında YOLOv5 modelinin YOLOv5n (nano), YOLOv5s (küçük), YOLOv5m (orta) ve YOLOv5l (büyük) olmak üzere dört alt versiyonu kullanılarak bu mimarilerin algılama ve sınıflandırma performansları karşılaştırılmıştır. YOLOv5 modelinin her versiyonu farklı model derinliklerine sahiptir ancak aynı ağ yapısı temel alınarak tasarlanmıştır. Çalışmada kullanılan omuz implant veri setinin dengesiz yapısı nedeniyle, sınıf ağırlıklandırma tekniği de kullanılmıştır. Sınıf ağırlıklandırma tekniği, veri dengesizliği nedeniyle bazı sınıfların diğerlerinden daha iyi temsil edilmesi problemini ele almayı amaçlamaktadır.

Çalışmanın ana katkıları aşağıdaki gibidir:

• X-ışını görüntülerinden omuz implantı sınıflandırmak amacıyla YOLO yaklaşımlarını hem algılama hem de sınıflandırma amacıyla öneren bilindiği kadarıyla ilk çalışmadır.

• Literatürde herkese açık paylaşılan veri setini kullanan diğer birçok güncel çalışmadan daha yüksek sınıflandırma performansı elde edilmiştir.

• YOLOv5n (nano), YOLOv5s (küçük), YOLOv5m (orta) ve YOLOv5l (büyük) olmak üzere dört farklı YOLOv5 versiyonu kullanılarak sonuçlar karşılaştırmalı olarak sunulmuş ve tartışılmıştır.

• Literatürde bu alanda yapılan diğer çalışmalarla bilindiği kadarıyla en kapsamlı karşılaştırmayı sağlayan çalışmadır.

Bu makalenin geri kalanı şu şekilde organize edilmiştir. Bölüm 2, ilk olarak çalışmada yararlanılan herkese açık X-ışını veri setini tanıtmaktadır. İkinci olarak X-ışını görüntülerinden omuz implantı tespiti ve sınıflandırılması için kullanılan YOLOv5 yöntemini alt versiyonlarıyla birlikte ayrıntılı olarak açıklamaktadır. Son olarak değerlendirme metriklerini tanıtmaktadır. Deneysel sonuçlar ve sonuçların ayrıntılı analizi

Bölüm 3’te verilmektedir. Son olarak, Bölüm 4’te sonuçlar ve gelecek çalışmalar için öneriler tartışılmaktadır.

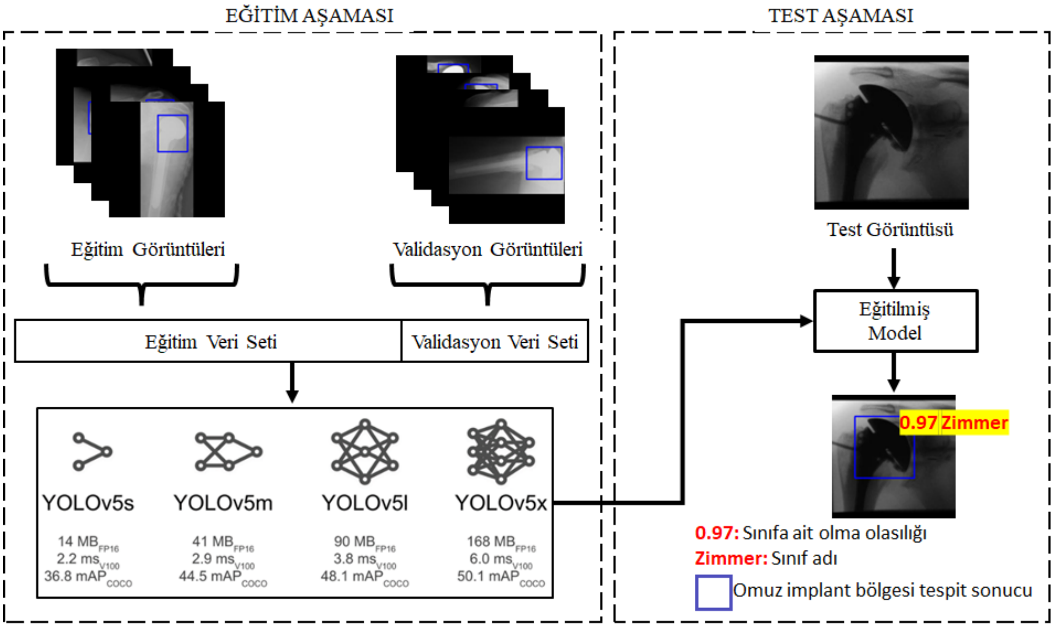

Şekil 1. Önerilen sistemin iş akışı.

Figure 1. Workflow of the proposed system.

2. Materyal ve Metot

Önerilen sistemin iş akışı Şekil 1’de gösterilmektedir. İş akışı eğitim (eğitim ve validasyon) ve test olmak üzere iki aşamadan oluşmaktadır. Tüm deneyler, Intel(R) Core(TM) i9-11900K 3.50 GHz CPU ve NVIDIA GeForce RTX 3080 12GB GPU donanımlı bir bilgisayarda gerçekleştirilmiştir. Çalışmada yararlanılan herkese açık X-ışını veri seti, önerilen YOLOv5 yöntemi ve alt versiyonlarının mimarileri, bu mimarilerin eğitim, validasyon ve test aşamalarının ayrıntıları, sınıflandırıcı modifikasyonu ve performans değerlendirmesinde kullanılan ölçütler alt başlıklarda sunulmaktadır.

2.1. Veri kümesi tanıtımı

Çalışmada kullanılan herkese açık veri seti Urban vd. [7], omuz implantlarını içeren 597 X-ışını görüntüsü içermektedir. Veri setinde 83 Cofield, 294 Depuy, 71 Tornier, 149 Zimmer olmak üzere 4 farklı omuz implant üreticisine ait X-ışını görüntüleri bulunmaktadır. Şekil 2'de veri setindeki 4 sınıfa ait X-ışını görüntüsü örnekleri verilmiştir.

Veri setinin içerdiği çeşitli zorluklardan biri, değişken ve nispeten düşük görüntü çözünürlüğe sahip olmasıdır. Görüntülerin çoğunun en uzun boyutu 250 pikseli geçmemekle birlikte en-boy oranları da farklıdır. Diğer zorluklar ise, değişken ve bazen çok düşük görüntü kontrastı ve her bir sınıfa ait örnek sayısı dengesizliğidir. Tüm bu zorluklar önerilen problemin zorluğunu açıkça ortaya koymaktadır. Bu çalışmada, bu veri setini seçmemizin sebebi 2020 yılında önerilen herkese açık güncel bir veri seti olması ve literatürde en güncel çalışmaların bu veri setini kullanıyor olmasıdır. Bu veri setini kullanan tüm çalışmalar Bölüm 3'te sunulacaktır.

Veri seti %90 eğitim ve %10 test olmak üzere iki parçaya ayrılmıştır. Ayrıca, eğitim seti beş gruba ayrılarak 5-kat çapraz doğrulama gerçekleştirilmiştir. Dört set alt eğitim için, bir set ise validasyon için kullanılmıştır. Veri seti bölünürken her sınıftan rastgele görüntüler seçilmiştir. Ayrıca her bir çapraz doğrulama katında, doğrulama için seçilen tüm örneklerin tamamen bir sınıfa ait olması veya bir sınıftan hiç örnek olmaması gibi durumlar engellenmiştir. Veri setinin kullanımına göre her sınıftaki görüntü sayısı Tablo 1'de verilmiştir.

Şekil 2. Veri setindeki farklı üreticilerden bazı örnek görüntüler (a) Cofield (b) Depuy (c) Tornier (d) Zimmer

Figure 2. Some sample images from different manufacturers in the dataset (a) Cofield (b) Depuy (c) Tornier (d) Zimmer

Yukarıda bahsedilen zorluklardan biri olan veri dengesizliğini çözmek amacıyla Sivari vd. [4] çalışmalarında veri artırma uygulamış ancak daha düşük sonuçlar elde etmişlerdir. Daha düşük sonuçların ise yapay örneklerden elde edilen özelliklerin gelişigüzel olması ve yapay örnek sayısının orijinal örnek sayısından fazla olması gibi nedenlerden kaynaklanıyor olabilir olduğunu belirtmişlerdir. Bu çalışmada, veri dengesizliği sorununu ele almak için sınıf ağırlıklandırma tekniği uygulanmıştır. Bu yöntem, veri setindeki sınıfların frekansına dayalı olarak farklı ağırlıkların atanmasını ve böylece az temsil edilen sınıflara daha fazla vurgu yapmayı amaçlamaktadır. Matematiksel olarak, w_i ile ifade edilen sınıf i'ye atanmış ağırlık şu şekilde hesaplanmıştır.

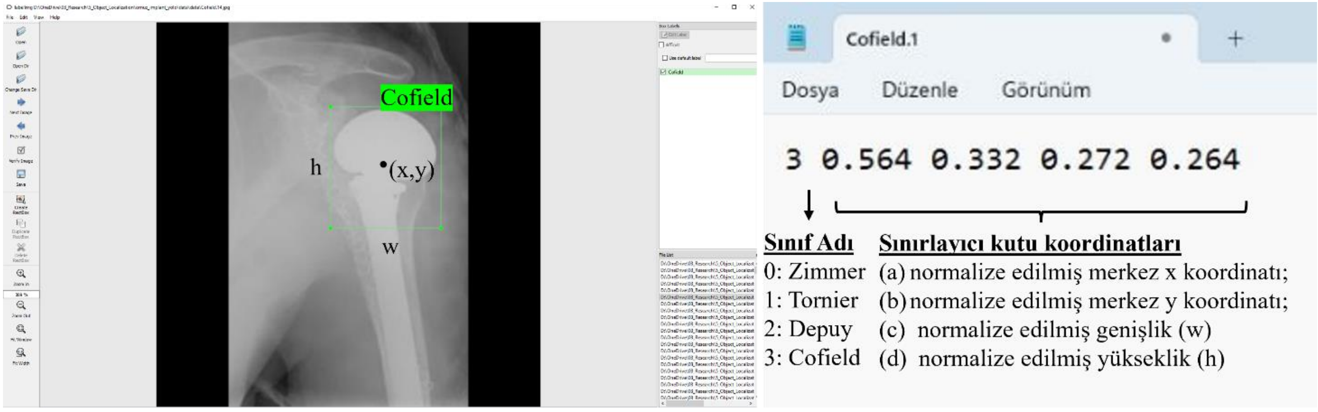

```
3 0.564 0.332 0.272 0.264
```

Sınıf Adı	Sınırlayıcı kutu koordinatları
0: Zimmer	(a) normalize edilmiş merkez x koordinatı;
1: Tornier	(b) normalize edilmiş merkez y koordinatı;
2: Depuy	(c) normalize edilmiş genişlik (w)
3: Cofield	(d) normalize edilmiş yükseklik (h)

Şekil 3. Veri kümesi içinde etiketlenmiş görüntülere bir örnek.

Figure 3. An example of labelled images within the dataset.

$$w_i = \frac{N}{n_i \times C} \tag{1}$$

Burada N toplam örnek sayısını, n_i sınıf i'deki örnek sayısını ve C toplam sınıf sayısını temsil etmektedir. Elde edilen sınıf ağırlıkları, eğitim sırasında hata fonksiyonuna dahil edilerek modelin azınlık sınıflara daha fazla dikkat etmesi teşvik edilmiş ve böylece genel performans artırılmıştır.

Tablo 1. Veri setinin kullanımına göre her sınıftaki görüntü sayısı.

Table 1. Number of images in each class according to the use of the dataset.

Üretici	Train	Test
Cofield	75	8
Depuy	264	30
Tornier	64	7
Zimmer	134	15
Toplam	537	60

Karaci vd. [12] çalışmasında önerildiği gibi implantın baş bölgesini tespit etmek amacıyla veri setindeki tüm görüntüler etiketlenirken LabelImg etiketleme aracı kullanılmıştır. Etiketleme yöntemi olarak dikdörtgen sınırlayıcı kutu tekniği kullanılmıştır. Çünkü YOLO algoritmaları bu tür dikdörtgen etiketli verilerle çalışmaktadır. Her çizilen dikdörtgen sınırlayıcı kutuya ilgili implant sınıf adı verilerek etiketleme tamamlanmıştır.

Etiketleme aracıyla gerçekleştirilen bir görüntü etiketleme örneği Şekil 3'te gösterilmiştir. Etiketleme işlemi tamamlandıktan sonra araç çıktı olarak her bir görüntü için o görüntü üzerinde etiketlenen bölgelerin sınırlayıcı kutu koordinatlarını ve sınıf bilgilerini vermektedir. Bu etiketler PASCAL VOC veya YOLO formatında txt dosyaları olarak kaydedilmektedir. ImageNet ve MS COCO veri setine ait etiketler PASCAL VOC formatında kaydedildiği için, bu çalışmada LabelImg aracı ile elde edilen etiketler PASCAL VOC formatında kaydedilmiştir. Görüntüdeki sınırlayıcı kutu ilgili .txt dosyasında depolanan veri satırına karşılık gelmektedir. Satırdaki beş adet sayısal değer sırasıyla sınıf adını ve görüntü üzerindeki sınırlayıcı kutu bilgilerini temsil etmektedir. Sınırlayıcı kutu koordinatları ise sırasıyla (a) normalize edilmiş merkez x koordinatı, (b) normalize edilmiş merkez y koordinatı, (c) normalize edilmiş genişlik ve (d) normalize edilmiş yüksekliği temsil etmektedir. Sınırlayıcı kutunun sol alt köşe koordinatı (x_1, y_1), sağ üst köşe koordinatı (x_2, y_2), görüntü genişlik w ve yüksekliği h olmak üzere değerler aşağıdaki gibi hesaplanmıştır.

$$a = \frac{(x_1 + x_2)/2.0}{w} \tag{2}$$

$$b = \frac{(y_1 + y_2)/2.0}{h} \tag{3}$$

$$c = \frac{x_2 - x_1}{w} \tag{4}$$

$$d = \frac{y_2 - y_1}{h} \tag{5}$$

2.2. YOLOv5

Çalışmada YOLOv5 ağının YOLOv5n (nano), YOLOv5s (küçük), YOLOv5m (orta) ve YOLOv5l (büyük) olmak üzere dört alt versiyonu kullanılmıştır. Alt versiyonlar adlandırılırken s, m, l ve x, ağ mimarisinin artan derinliğini göstermektedir. YOLOv5 ağının her bir versiyonu farklı model derinliklerine sahiptir, ancak genel olarak omurga, boyun ve kafa olmak üzere üç ana bölümden oluşan aynı ağ yapısı temel alınarak tasarlanmıştır. YOLOv5 model omurgası, belirli bir girdi görüntüsünden temel özellikleri çıkarmak için kullanılmaktadır. Elde edilen özellikler kullanılarak özellik haritası oluşturulur. Yüksek doğruluk sağlarken ve modellerin işlem süresini azaltırken üst düzey özellikleri çıkarmayı amaçlayan Çapraz Aşamalı Kısmi Ağ (Cross Stage Partial Network, CSPNet) [26] mimarisine dayalı olarak tasarlanmıştır. Model boynu, özellik piramitleri oluşturmak amacıyla model omurgasının farklı aşamalarından elde edilen özellik haritalarını toplar. YOLOv5 özellik piramitlerini elde etmek için model boynu içinde Yol Toplama Ağ (PANet) [27] mimarisini kullanmaktadır. Özellik piramitlerinin en önemli katkısı, modelin farklı boyut ve ölçeklerdeki aynı türdeki nesneleri tanımlamasına ve eşleştirmesine yardımcı olmaktır. Son olarak, model kafası, YOLOv5'in nihai nesne algılama parçası olarak işlev görmektedir. YOLOv3 ve YOLOv4 ile aynı mimaride tasarlanmıştır. Model kafası, son özellik haritalarına çapa (anchor) kutuları uygular ve nesnellik puanları, sınıf ait olma olasılıkları ve algılanan nesneleri çevreleyen sınırlayıcı kutuların koordinatları ile nihai çıktı vektörlerini oluşturur.

YOLOv5'in tüm alt versiyonlarının çekirdek temel yapısı olarak kullandığı ağ mimarisi Şekil 4'te verilmiştir. Şekilde de görüldüğü gibi, YOLOv5 birçok anahtar modüle sahiptir.

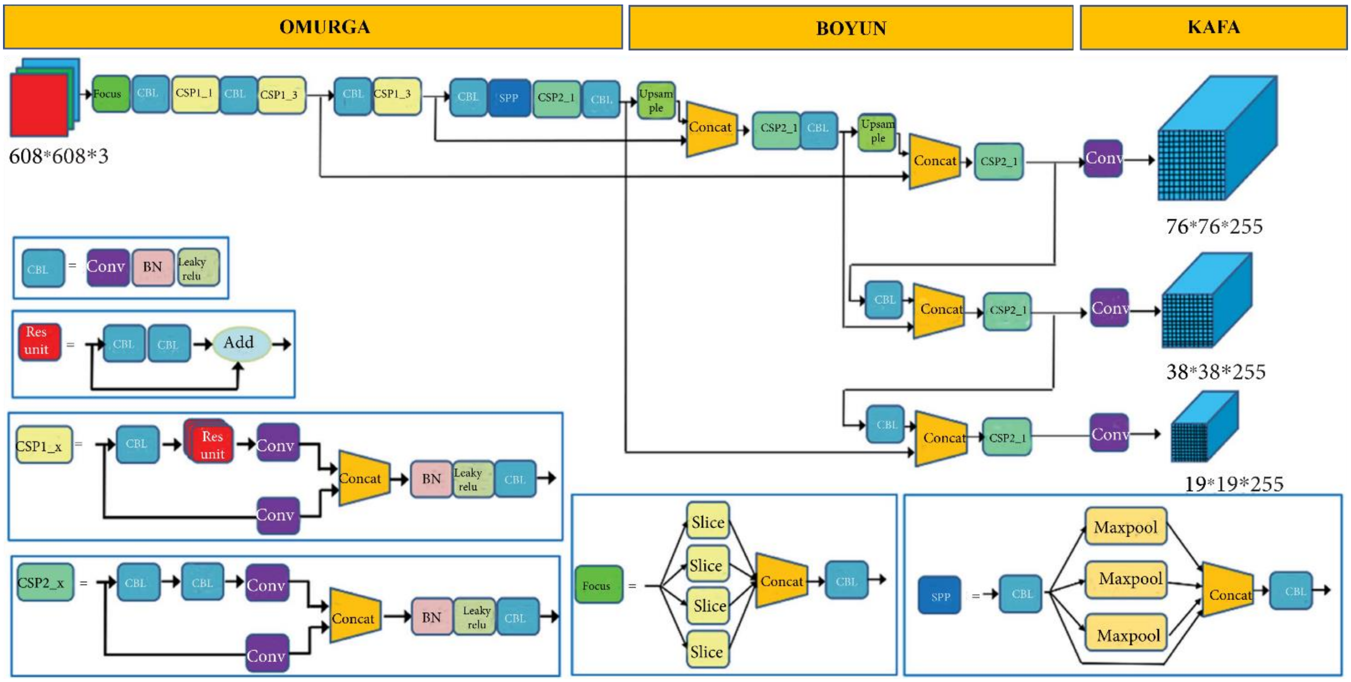

Şekil 4. YOLOv5 mimarisi.

Figure 4. YOLOv5 architecture.

- Odak (Focus) modülü, giriş görüntüsünü dört adet en boy oranları aynı paralel dilimlere böler ve daha sonra bu dilimler derinlik olarak birleştirilir ve özellik haritalarını oluşturmak üzere CBL modülüne aktarılır.

- CBL modülü, özellik çıkarma için sırasıyla konvolüsyon işlemi (Conv), paket normalizasyonu (batch normalization, BN) ve sızıntılı doğrultulmuş doğrusal birim (leaky rectified linear unit, LeakyReLU aktivasyon fonksiyonu kullanan temel bir modüldür.

- CSP modülü, üst düzey özellikleri çıkararak modelin öğrenme kapasitesini geliştirmek için kullanılan CSPNet tabanlı bir modüldür. YOLOv5, CSP1 ve CSP2 olmak üzere iki tip CSP modülü içerir. CSP1 modülü model omurgasında kullanılırken CSP2 modülü ise model boynunda kullanılmaktadır.

- CSP1_n ile gösterilen CSP modülü, bir adet CBL modülü ve n adet RES (artık) blok içerir. CSP2_n ile gösterilen CSP modülü ise, n + 1 adet CBL modülü içerir. Daha fazla RES bloğu ve CBL modülü, ağ mimarisinin derinliğini artırmaktadır. YOLOv5 ağlarının dört alt versiyonunda kullanılan CSP modül yapıları Tablo 2'de verilmiştir.

- SPP modülü, mekansal özellikleri karıştırmak ve havuzlamak için model omurgasında kullanılan bir modüldür. Giriş özelliklerini üç paralel maksimum havuzlama katmanı aracılığıyla aşağı örnekledikten sonra başlangıç özellikleri ile birleştirmektedir.

Her bir YOLOv5 alt versiyonu 400 epoch boyunca aynı hiper parametre seti kullanılarak eğitilmiştir. Hiper parametreler batch boyutu = 16, momentum = 0.9, decay = 0.0005 ve öğrenme oranı = 0.001 olarak ayarlanmıştır.

Tablo 2. YOLOv5 ağının alt versiyonlarında kullanılan CSP modülleri.

Table 2. CSP modules used in sub-versions of the YOLOv5 network.

CSP Modülü	YOLOv5s	YOLOv5m	YOLOv5l	YOLOv5x
CSP1	CSP1_1	CSP1_2	CSP1_3	CSP1_4
CSP1	CSP1_3	CSP1_6	CSP1_9	CSP1_12
CSP1	CSP1_3	CSP1_6	CSP1_9	CSP1_12
CSP2	CSP2_2	CSP2_4	CSP2_6	CSP2_8
CSP2	CSP2_2	CSP2_4	CSP2_6	CSP2_8
CSP2	CSP2_2	CSP2_4	CSP2_6	CSP2_8
CSP2	CSP2_2	CSP2_4	CSP2_6	CSP2_8
CSP2	CSP2_2	CSP2_4	CSP2_6	CSP2_8

2.3. Sınıflandırıcı modifikasyonu

YOLOv5 mimarisi COCO veri kümesi [28] üzerinde 80 nesne kategorisini sınıflandırmak için eğitildiğinden çıkış tensörünün boyutu 3 × (5 + 80) = 255'tir. Burada 3, her ızgara tahmini için üç şablon kutusunu, 5 ise her tahmin kutusunun koordinatlarını (x, y, w, h) ve güvenirliği (güven, c) temsil etmektedir. Omuz implantı sınıflandırma probleminde ise Cofield, Depuy, Tornier ve Zimmer olmak üzere 4 farklı nesne mevcuttur. Bu nedenle YOLOv5 sınıflandırıcısını 4 sınıflı probleme uyarlamak gerekmektedir. Çıktı boyutu 3 × (5 + 4) = 27 olacaktır. Bu çalışmada, COCO veri seti üzerinde önceden eğitilmiş YOLOv5 versiyonları omuz implantı veri seti üzerinde ince ayarlanmıştır. Bunun sebebi, veri setinde bulunan örnek sayısının az olması ve modelin rastgele başlatılan ağırlıklarla sıfırdan eğitildiği takdirde, yakınsamasının uzun sürebilecek olmasıdır. Bu durumda bile, yüksek doğruluk elde edilmeyebilmektedir. Önceden eğitilmiş YOLOv5 modellerinin ince ayarlanması, transfer ögrenme olarak adlandırılmaktadır ve modelin transfer ögrenme ile eğitilmesi daha yüksek başarı sağlamakla birlikte daha az zaman almaktadır.

2.4. Değerlendirme metrikleri

Bu çalışmada YOLOv5 versiyonlarının omuz implantı tespit performansını nicel olarak değerlendirmek amacıyla doğruluk, ortalama kesinlik (mean Average Precision, mAP), kesinlik (precision), duyarlılık (recall) ve F1-ölçütü olmak üzere beş metrik kullanılmıştır. Doğruluk, tüm örnekler içerisinde modeller tarafından doğru olarak tespit edilen örneklerin oranını ölçer. Ortalama kesinlik (Average Precision, AP), her bir sınıf için kesinlik-duyarlılık eğrisi üzerinde farklı duyarlılık değerlerine karşılık gelen kesinlik değerlerinin ortalaması olarak hesaplanmakta, ortalama kesinlik değerlerinin ortalaması (mean Average Precision; mAP) ise, bütün sınıflara ait kesinlik değerlerinin ortalaması olarak ifade edilmektedir. mAP@0.5, nesne tespitlerinin kesinlik ve duyarlılık oranını Intersection over Union (IoU) eşiği 0.5'ten büyük olan tahminler üzerinde değerlendirir. Öte yandan, mAP@[0.5:0.95], 0.5 ile 0.95 arasındaki farklı IoU eşiklerini dikkate alarak modelin performansını daha kapsamlı bir şekilde değerlendirir. Kesinlik, modeller tarafından pozitif olarak tespit edilen örnekler içerisinde gerçek pozitif örneklerin oranını ölçerken, duyarlılık ise veri kümesindeki pozitif örneklerin içinde gerçek pozitif tespitlerin oranını ölçmektedir. F1-ölçütü, kesinlik ve duyarlılık başarı değerlendirme ölçütlerinin birlikte değerlendirilmesi olup, kesinlik ve duyarlılık değerlerinin harmonik ortalamasıdır. Bu ölçütler (6-11) eşitlikleri kullanılarak hesaplanmaktadır. Eşitliklerde DP, DN, YP ve YN sırasıyla, doğru pozitif, doğru negatif, yanlış pozitif ve yanlış negatif sayısını ifade etmektedir. P, R, N değerleri ise sırasıyla tüm kategorilerdeki kesinliği, duyarlılığı ve toplam sınıf sayısını temsil etmektedir.

$$Doğruluk = \frac{TP + TN}{TP + FP + TN + FN} \quad (6)$$

$$Kesinlik = \frac{TP}{TP + FP} \quad (7)$$

$$Duyarlılık = \frac{TP}{TP + FN} \quad (8)$$

$$F - \text{ölçütü} = 2 \times \frac{Kesinlik \times Duyarlılık}{Kesinlik + Duyarlılık} \quad (9)$$

$$AP = \int_0^1 P(R)dR \quad (10)$$

$$AP = \frac{\sum_{i=1}^{N} AP_i}{N} \quad (11)$$

3. Bulgular ve Tartışma

Bu bölümde, omuz implantlarının tespiti ve sınıflandırılması için önerilen YOLOv5 tabanlı yaklaşımın (tüm alt versiyonlarıyla birlikte) performansı en son teknoloji yöntemlerin performansı ile karşılaştırılmıştır. Bir ağın eğitiminde yüksek doğruluk seviyesine ulaşmak için sıfırdan eğitim yapıldığı takdirde gereken zaman ve veriden tasarruf etmek amacıyla transfer öğrenme kullanılmaktadır. YOLO versiyonlarında transfer öğrenme COCO veri seti üzerinde önceden eğitilmiş ağırlıklar kullanılarak yapılmaktadır. Bu çalışmada, her bir YOLOv5 versiyonu, COCO veri seti üzerinde önceden eğitilmiş ağırlıklar kullanılarak omuz implantları içeren X-ışını görüntülerinden oluşan bir veri seti üzerinde ince ayarlanmıştır. YOLOv5 modelinin tüm alt versiyonları 400 epoch boyunca eğitilmiştir veağların öğrenme sürecinde hiper-parametre set şöyle ayarlanmıştır: batch boyutu = 8, momentum = 0.9, decay = 0.0005 ve öğrenme hızı = 0.001.Tüm modeller için eğitim süreci, validasyon kayıpları belirli iterasyon boyunca değişmediğinde veya 400 epoch tamamlandığında durdurulmuştur ve adil karşılaştırma için aynı test veri kümesi üzerinde test edilmiştir ve hiper-parametreler sabit tutulmuştur. Performans hem niceliksel hem de niteliksel olarak karşılaştırılmıştır.

Nicel performans değerlendirmesi için, IoU metriği, her bir omuz implant bölgesinin tespit doğruluğunu belirlemek kullanılmıştır. IoU, tahmin edilen sınırlayıcı kutu (A_{pred}) ile kesin referans sınırlayıcı kutu (A_{gt}) arasındaki örtüşmeyi ölçer ve Eşitlik 12'deki gibi hesaplanır.

$$IoU = \frac{A_{pred} \cap A_{gt}}{A_{pred} \cup A_{gt}} \quad (12)$$

Bu çalışmada, 0.6 veya daha büyük IoU değeri ile sınıflandırılan nesne tespit sonuçları, IoU değeri 0.6'dan büyükse doğru pozitif (TP) olarak kabul edilmiştir. IoU değeri 0.6'dan küçükse sonuç yanlış pozitif (FP) olarak değerlendirilmiştir. IoU çıktısı kullanılarak kesinlik, duyarlılık, F1-ölçütü ve mAP metrikleri sınıflandırma performansını hesaplamak için kullanılmıştır.

YOLOv5 modellerinin alt versiyonlarının deneysel sonuçlarını araştırmak için 60 görüntü test seti olarak kullanılmıştır. Sonuçlar 5-kat çapraz doğrulama uygulanarak elde edilmiştir. 4 farklı modelin ve YOLOv5l modelinin sınıf ağırlıklandırmalı versiyonunun dayanıklılığını değerlendirmek için elde edilen kesinlik, duyarlılık, F1-ölçütü ve mAP değerleri Tablo 3'te özetlenmiştir. Modelin sınıflandırma performansını değerlendirmek için kesinlik, duyarlılık, F1-ölçütü ve mAP kullanılmıştır. Tabloda sunulan tüm değerler, sınıfların ayrı ayrı kesinlik, duyarlılık, F1-ölçütü ve mAP değerlerinin makro ortalamasını temsil etmektedir. Makro ortalama, her sınıfın performansını eşit olarak kabul etmektedir. Tüm modeller, 5-kat çapraz doğrulama ile elde edilen veri kümeleri üzerinde eğitilmiştir. Karşılaştırma sonuçları, YOLOv5n modeli diğer modellere göre en düşük performans göstermiştir. Bu modelin mAP@0.5, mAP@0.5:0.95, kesinlik, duyarlılık ve F1-ölçütü sırasıyla 94.8, 82.2, %91.3, %79.8 ve %85.1 olarak tespit edilmiştir. Diğer modeller arasında ise YOLOv5l modelinin sınıf ağırlıklandırma tekniği ile birlikte uygulandığında önemli ölçüde daha iyi bir performans sergilediği görülmüştür. Bu modelin mAP@0.5, mAP@0.5:0.95, kesinlik, duyarlılık ve F1-ölçütü sırasıyla 98.3, 85.9, %97.0, %95.7 ve %96.3 olarak tespit edilmiştir.

Tablo 3. YOLOv5n, YOLOv5s, YOLOv5m ve YOLOv5l modellerinin performans karşılaştırması.

Table 3. Performance comparison of YOLOv5n, YOLOv5s, YOLOv5m and YOLOv5l models.

Model	**Sınıf**	**Kesinlik(%)**	**Duyarlılık(%)**	**F1-ölçütü(%)**	**mAP (0.5%)**	**mAP (0.5:0.95%)**
YOLOv5n	Cofield	84.1	66.7	74.4	94.0	77.5
	Depuy	96.3	86.7	91.2	96.8	84.2
	Tornier	94.7	85.7	89.9	94.4	84.9
	Zimmer	90.1	80.0	84.8	93.9	82.1
	Ortalama	91.3	79.8	85.1	94.8	82.2
YOLOv5s	Cofield	100.0	62.4	76.8	91.0	72.1
	Depuy	93.2	93.3	93.2	98.8	81.4
	Tornier	84.7	100.0	91.7	97.8	88.6
	Zimmer	78.2	86.7	82.2	95.8	82.2
	Ortalama	89.1	85.6	86.0	95.8	81.1
YOLOv5m	Cofield	100.0	75.3	85.9	97.1	84.6
	Depuy	90.6	93.3	91.9	96.8	83.7
	Tornier	90.1	100.0	94.8	99.5	91.3
	Zimmer	71.4	93.3	80.9	94.0	84.1
	Ortalama	88.0	90.5	88.4	96.9	85.9
YOLOv5l	Cofield	100.0	89.9	94.7	99.5	86.5
	Depuy	91.1	96.7	93.8	98.5	86.4
	Tornier	95.3	100.0	97.6	99.5	85.6
	Zimmer	87.3	92.0	89.6	97.1	84.1
	Ortalama	93.4	94.6	93.9	98.7	85.7
YOLOv5l + Class Weight	Cofield	96.5	87.5	91.77	96.2	80.9
	Depuy	99.4	96.7	98.03	98.9	85.3
	Tornier	100.0	98.8	99.39	99.5	93.7
	Zimmer	91.9	100.0	95.77	98.7	83.6
	Ortalama	**97.0**	**95.7**	**96.34**	**98.3**	**85.9**

Model performansları sınıf bazlı değerlendirildiğinde ise, Cofield sınıfında, YOLOv5s, YOLOv5m ve YOLOv5l modellerinin %100 kesinlikle en yüksek başarıya ulaştığı dikkat çekmiştir. Aksine, YOLOv5n modeli, Cofield sınıfında %84.1 ile en düşük kesinlik değerine sahiptir. Depuy sınıfında, YOLOv5l modeli sırasıyla %99.4 ve %96.7 olmak üzere en yüksek kesinlik ve duyarlılık değerlerine sahiptir. Aynı şekilde Tornier sınıfında YOLOv5l modeli sırasıyla %100.0 ve %98.8 ile en yüksek kesinlik ve duyarlılık değerlerine sahiptir. Son olarak, Zimmer sınıfında, YOLOv5l modelinin duyarlılık değeri diğer modellere kıyasla daha yüksektir. F-ölçütünde ise YOLOv5l modeli tüm sınıflarda en yüksek başarıyı sağlamıştır.

Genel olarak, bu sonuçlar sınıf ağırlıklandırmalı YOLOv5l modelinin en iyi performansı gösterdiğini ve daha küçük modellerin (YOLOv5n, YOLOv5s ve YOLOv5m) bazı sınıflarda daha düşük başarıya sahip olduğunu göstermektedir.

Şekil 5'te YOLOv5l modelinin eğitim ve validasyon grafiklerinin değişim sonuçları görülmektedir. Kesinlik ve duyarlılık değerlerinin hem eğitim hem de validasyon kümesinde hızlı bir şekilde %100'e, hata oranının da benzer hızda 0'a yakınsadığı görülmüştür.

Nitel performans değerlendirmesi için, test setinden rastgele seçilen birkaç görüntü üzerinde YOLOv5l modeli ile elde edilen tespit etme ve sınıflandırma sonuçları Şekil 6'da verilmiştir.

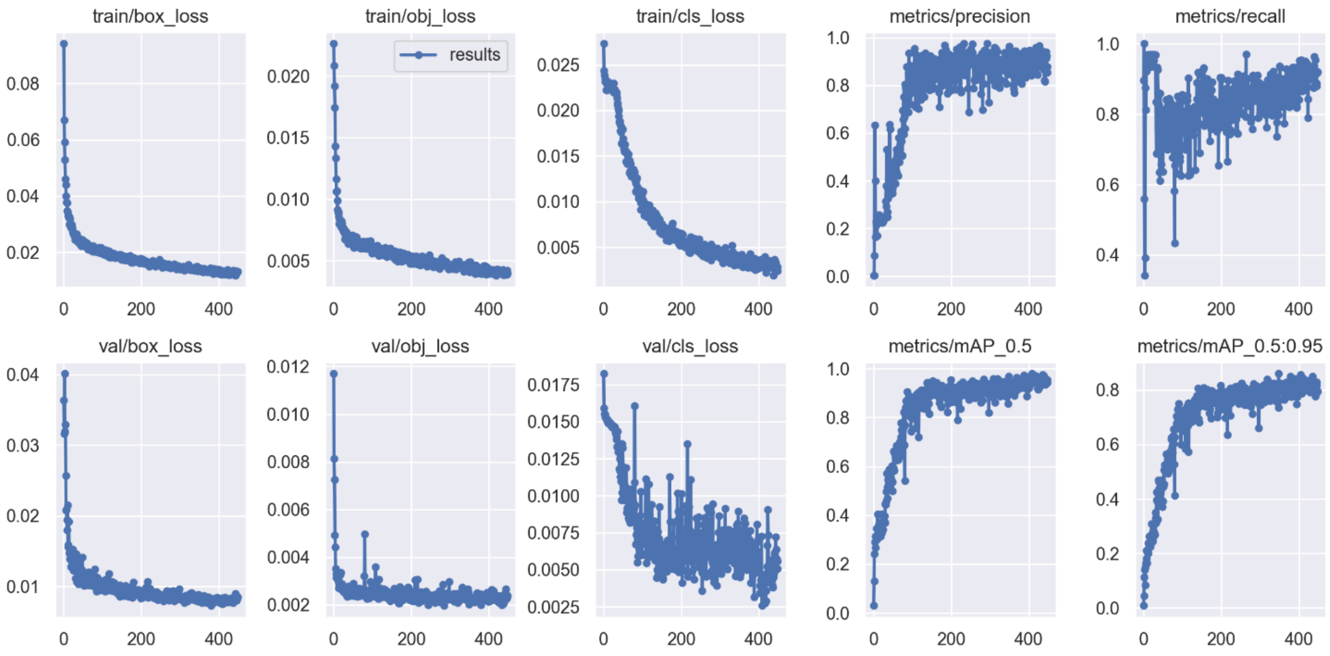

Şekil 5. YOLOv5l modelinin eğitim ve validasyon grafiklerinin değişim sonuçları.

Figure 5. Change results of the training and validation graphs of the YOLOv5l model.

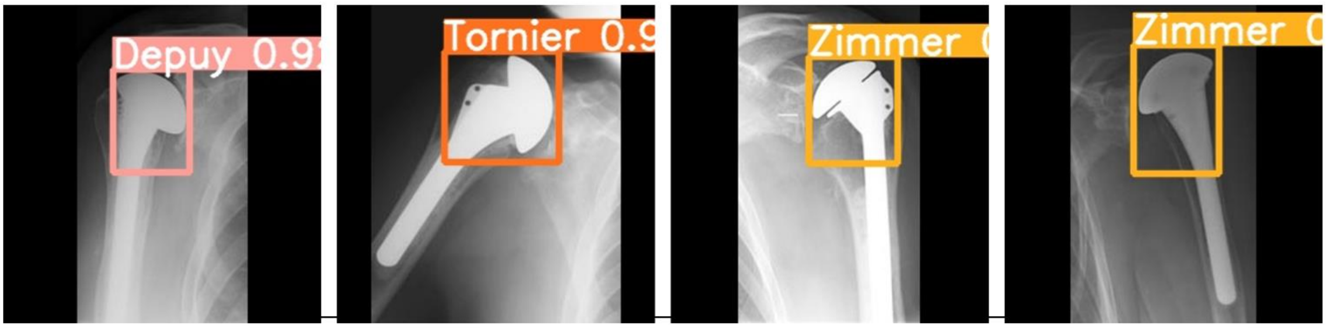

Şekil 6. Veri setine ait bazı test görüntüleri üzerinde YOLOv5l modeli ile elde edilen doğru pozitif algılama ve sınıflandırma sonuçları.

Figure 6. True positive detection and classification results obtained with the YOLOv5l model on some test images of the dataset

YOLOv5l, omuz implantlarının farklı kategorileri için iyi bir tanıma performansına sahiptir çünkü konvolüsyonel sinir ağı algoritması manuel özellik çıkarma gerektirmemekle birlikte ve genelleme yeteneğini artırmaktadır.

Tablo 4, omuz implantı üreticilerinin tespiti ve sınıflandırılması amacıyla önerilen sınıf ağırlıklandırmalı YOLOv5 modelinin aynı veri kümesi üzerinde önerilen önceki çalışmalarla kapsamlı bir karşılaştırmasını sunmaktadır. Önceki çalışmalarda genellikle bireysel makine öğrenmesi, bireysel derin öğrenme yaklaşımları ve hibrid yaklaşımlar önerilmiştir. Bu çalışmalar oldukça güncel olup derin öğrenme ve makine öğrenmesi yaklaşımlarının doğru ve güvenilir sınıflandırma sonuçları elde etmek için etkili oldukları açıktır. Sonuçlar incelendiğinde en yüksek çapraz doğrulama doğruluk, kesinlik ve duyarlılık değerleri [9] çalışmasında sırasıyla %97.2, %98.6 ve %98.0 olarak elde edilmiştir. Öte yandan diğer en iyi sonuçların elde edildiği Sivari vd. [4] çalışmasında da belirtildiği gibi, [9] çalışmasında veri kümesi test ve doğrulama setine ayrılmamakla birlikte, yalnızca 5 kat çapraz doğrulama sonuçları verilmiştir. Doğrulama veri setinin amacı modelin hiper parametrelerini ayarlamak ve modelin yeteneklerini ölçmektir. Dolayısıyla Sivari vd. [4] çalışmasında sonuç değerlendirmesinin tarafsız bir test setinde gerçekleştirilmesi önerilmiştir. Bu öneri doğrultusunda %95.0 doğruluk, %97.0 kesinlik ve %95.7 duyarlılık değerleri elde edilmiştir. Önerilen yöntem literatürdeki diğer çalışmalarla kıyaslandığında karşılaştırılabilir düzeyde oldukça başarılı sonuçlar elde edilmiştir.

4. Sonuçlar

Bu çalışmada, omuz implantı üreticilerinin otomatik tespiti ve sınıflandırılması için önerilen sistemde, YOLOv5n, YOLOv5s,YOLOv5m ve YOLOv5l modelleri kullanılarak model implant baş bölgesi tespiti ve sınıflandırma gerçekleştirilmiş ve sonuçlar karşılaştırılmıştır. Ayrıca, veri dengesizliği problemini çözmek amacıyla önerilen sınıf ağırlıklandırma tekniğinin modelin sınıflandırma performansını önemli ölçüde artırdığı tespit edilmiştir. Yapılan karşılaştırmada, en yüksek mAP@0.5, mAP@0.5:0.95, kesinlik, duyarlılık ve F1-ölçütü değerleri sınıf ağırlıklandırmalı YOLOv5l modeli ile sırasıyla 98.3, 85.9, %97.0, %95.7 ve %96.3 olarak elde edilmiştir.

Tablo 4. Aynı veri seti üzerinde yapılan literatürdeki diğer çalışmaların karşılaştırması.

Table 4. Comparison of other studies in the literature on the same data set.

Çalışma	Veri seti, Sınıf bilgisi	Yöntem	Doğruluk (%)	Kesinlik(%)	Duyarlılık(%)
Urban vd. [7]	597: Cofield, Depuy, Tornier, Zimmer	NasNet	80.0	80.0	75.0
Sultan vd. [10]	597: Cofield, Depuy, Tornier, Zimmer	DRE-Net	85.92	85.33	84.11
Yilmaz [9]	597: Cofield, Depuy, Tornier, Zimmer	Çok kanallı CNN	97.2	98.6	98.0
Efeoglu vd. [11]	349: Cofield, Depuy, Zimmer	K-NN	74.0	64.16	56.1
Karaci [12]	597: Cofield, Depuy, Tornier, Zimmer	YOLOv3 + DenseNet201	84.76	82.37	80.35
Sivari vd. [4]	597: Cofield, Depuy, Tornier, Zimmer	DenseNet201 + Lojistik Regresyon	95.07	96.77	91.64
Önerilen Çalışma	597: Cofield, Depuy, Tornier, Zimmer	YOLOv5l	95.0	97.0	95.7

Önerilen YOLOv5 modelleri, literatürdeki diğer hibrit makine öğrenmesi yaklaşımlarına göre düşük maliyetli ve yüksek performanslı bir hedefe ulaşmaktadır. Dolayısıyla, omuz implantlarının tespiti ve sınıflandırılması gibi tıbbi görüntüleme uygulamalarında YOLOv5 modellerinin etkili bir araç olduğunu göstermiştir. Ayrıca, radyologlar ve cerrahlar için verimli ve güvenilir bir analiz süreci sağlayabileceği ve iş yükünü azaltabileceği öngörülmüştür. Bu çalışmanın önemli bir sınırlaması, veri kümesindeki implant üretici sınıflarının sayısının sınırlı olmasıdır. Veri kümesindeki implant üreticilerinin çeşitliliğinin artırılması, çalışmanın genişletilmesi için bir fırsat sunmaktadır. Öte yandan, daha geniş veri kümelerinde ve farklı görüntüleme koşullarında test edilerek, modellerin performanslarının daha da geliştirilmesi mümkündür.

Etik kurul onayı ve çıkar çatışması beyanı

Hazırlanan makalede etik kurul izni alınmasına gerek yoktur. Hazırlanan makalede herhangi bir kişi/kurum ile çıkar çatışması bulunmamaktadır.

Kaynaklar

[1] Cofield, R. H., 1984. Total shoulder arthroplasty with the Neer prosthesis. JBJS, Cilt. 66(6), s. 899-906. DOI: 10.2106/00004623-198466060-00010.

[2] Sanchez-Sotelo, J., 2011. Total shoulder arthroplasty. The Open Orthopaedics Journal, Cilt. 5, s. 106. DOI: 10.2174/1874325001105010106.

[3] Sukjamsri, C., 2015. The effect of implant misalignment on shoulder replacement outcomes. Doctoral dissertation, Imperial College London. DOI: 10.25560/28581.

[4] Sivari, E., Güzel, M. S., Bostanci, E., Mishra, A., 2022. A novel hybrid machine learning-based system to classify shoulder implant manufacturers. Healthcare, Cilt. 10(3), s. 580. DOI: 10.3390/healthcare10030580.

[5] Sahoo, D. P., Rout, M., Mallick, P. K., Samanta, S. R., 2022. Comparative analysis of medical images using transfer learning based deep learning models. International Conference on Advancements in Smart, Secure and Intelligent Computing (ASSIC), s. 1-8.

[6] Sistaninejhad, B., Rasi, H., Nayeri, P., 2023. A review paper about deep learning for medical image analysis. Computational and Mathematical Methods in Medicine, Cilt. 2023.

[7] Urban, G., Porhemmat, S., Stark, M., Feeley, B., Okada, K., Baldi, P., 2020. Classifying shoulder implants in X-ray images using deep learning. Computational and Structural Biotechnology Journal, Cilt. 18, s. 967-972. DOI: 10.1016/j.csbj.2020.04.005.

[8] Yi, P. H., Kim, T. K., Wei, J., Li, X., Hager, G. D., Sair, H. I., Fritz, J., 2020. Automated detection and classification of shoulder arthroplasty models using deep learning. Skeletal Radiology, Cilt. 49, s. 1623-1632. DOI: 10.1007/s00256-020-03463-3.

[9] Yılmaz, A., 2021. Shoulder implant manufacturer detection by using deep learning: Proposed channel selection layer. Coatings, Cilt. 11(3), p. 346. DOI: 10.3390/coatings11030346.

[10] Sultan, H., Owais, M., Park, C., Mahmood, T., Haider, A., Park, K.R., 2021. Artificial intelligence-based recognition of different types of shoulder implants in X-ray scans based on dense residual ensemble-network for personalized medicine. Journal of Personalized Medicine, Cilt. 11, p. 482.

[11] Efeoğlu, E., Gürkan, T. U. N. A., 2021. Radyografi görüntüleri ve sınıflandırma algoritmaları kullanılarak omuz protezlerinin üreticilerinin belirlenmesi. Kırklareli Üniversitesi Mühendislik ve Fen Bilimleri Dergisi, Cilt. 7(1), s. 57-73. DOI: 10.34186/klujes.906660.

[12] Karaci, A., 2022. Detection and classification of shoulder implants from X-ray images: YOLO and pretrained convolution neural network-based approach. Journal of Faculty of Engineering and Architecture of Gazi University, Cilt. 37, s. 283-294. DOI: 10.17341/gazimmfd.888202.

[13] Deng, J., Dong, W., Socher, R., Li, L. J., Li, K., Fei-Fei, L., 2009. Imagenet: A large-scale hierarchical image database. IEEE Conference on Computer Vision and Pattern Recognition, s. 248-255. DOI: 10.1109/CVPR.2009.5206848.

[14] Zoph, B., Vasudevan, V., Shlens, J., Le, Q. V., 2018. Learning transferable architectures for scalable image recognition. IEEE Conference on Computer Vision and Pattern Recognition, s. 8697-8710. DOI: 10.1109/CVPR.2018.00907.

[15] Sahin, O., Ozer, S., 2022. YOLODrone+: Improved YOLO Architecture for Object Detection in UAV Images. IEEE Signal Processing and Communications Applications Conference (SIU), s. 1-4. DOI: 10.1109/SIU55565.2022.9864746.

[16] Liu, W., Anguelov, D., Erhan, D., Szegedy, C., Reed, S., Fu, C. Y., Berg, A. C., 2016. SSD: Single shot multibox detector. ECCV 2016, Cilt. 14, s. 21-37. DOI: 10.1007/978-3-319-46448-0_2.

[17] Redmon, J., Divvala, S., Girshick, R., Farhadi, A., 2016. You only look once: Unified, real-time object detection. IEEE Conference on Computer Vision and Pattern Recognition, s. 779-788.

[18] Jintasuttisak, T., Edirisinghe, E., Elbattay, A., 2022. Deep neural network based date palm tree detection in drone imagery. Computers and Electronics in Agriculture, Cilt. 192, p. 106560. DOI: 10.1016/j.compag.2021.106560.

[19] Girshick, R., Donahue, J., Darrell, T., Malik, J., 2014. Rich feature hierarchies for accurate object detection and semantic segmentation. IEEE Conference on Computer Vision and Pattern Recognition, s. 580-587.

[20] Girshick, R. (2015). Fast r-cnn. In Proceedings of the IEEE international conference on computer vision (s. 1440-1448).

[21] Ren, S., He, K., Girshick, R., Sun, J., 2015. Faster R-CNN: Towards real-time object detection with region proposal networks. Advances in Neural Information Processing Systems, Cilt. 28.

[22] Redmon, J., Farhadi, A., 2017. YOLO9000: better, faster, stronger. IEEE Conference on Computer Vision and Pattern Recognition, s. 7263-7271.

[23] Redmon, J., Farhadi, A., 2018. YOLOv3: An incremental improvement. arXiv preprint arXiv:1804.02767.

[24] Bochkovskiy, A., Wang, C. Y., Liao, H. Y. M., 2020. YOLOv4: Optimal speed and accuracy of object detection. arXiv preprint arXiv:2004.10934.

[25] Nelson, J., Solawetz, J., 2020. YOLOv5 is here: State-of-the-art object detection at 140 fps. Roboflow.

[26] Wang, C. Y., Liao, H. Y. M., Wu, Y. H., Chen, P. Y., Hsieh, J. W., Yeh, I. H., 2020. CSPNet: A new backbone that can enhance learning capability of CNN.

IEEE/CVF Conference on Computer Vision and Pattern Recognition Workshops, s. 390-391.

[27] Liu, S., Qi, L., Qin, H., Shi, J., Jia, J., 2018. Path aggregation network for instance segmentation. IEEE Conference on Computer Vision and Pattern Recognition, s. 8759-8768.

[28] Lin, T. Y., Maire, M., Belongie, S., Hays, J., Perona, P., Ramanan, D., Zitnick, C. L., 2014. Microsoft COCO: Common objects in context. ECCV 2014, Cilt. 13, s. 740-755. DOI: 10.1007/978-3-319-10602-1_48.

DEU FMD 27(79) (2025) 110-120

Dokuz Eylül Üniversitesi Mühendislik Fakültesi Fen ve Mühendislik Dergisi
Dokuz Eylul University Faculty of Engineering Journal of Science and Engineering
Elektronik/Online ISSN: 2547-958X

ARAŞTIRMA MAKALESI / RESEARCH ARTICLE

Buğday Samanı ve Kenevir Lifi ile Üretilen Miselyum Biyokompozitleri

Mycelium Biocomposites Produced by Using Wheat Straw and Hemp Fiber

Merve Mocan *, Rukiye Akış, Nurseda Akgürsu, İlayda Albayrak

Gebze Teknik Üniversitesi, Malzeme Bilimi ve Mühendisliği Bölümü, Gebze/Kocaeli, TÜRKİYE

Sorumlu Yazar / Corresponding Author *: mmocan@gtu.edu.tr

Öz

Genleştirilmiş polistiren (EPS) köpük, dayanıklılığı, hafifliği ve uygun maliyeti nedeniyle sıklıkla tercih edilen bir ambalaj malzemesidir. Bununla birlikte düşük yoğunluğu, geri dönüşümünün ekonomik sebeplerle tercih edilmemesine yol açmakta ve doğada bozunmayan yapısı nedeniyle çevrede yüksek miktarda plastik kirliliğine sebep olmaktadır. Bundan dolayı, birçok ülke EPS ambalaj ürünlerini yasaklamaya başlamıştır. Çevresel etkiyi azaltmak için EPS'nin biyo-esaslı ve biyobozunur alternatiflerle değiştirilmesi gerekmektedir. Miselyum esaslı malzemeler tamamen biyo-esaslı ve biyobozunur oldukları için, boyutsal kararlılığa sahip köpüğümsü yapısı ile EPS ambalaj için güçlü bir aday olarak sunulabilirler. Ancak, malzeme özelliklerinin halen geliştirilmesi gerekmektedir. Besiyeri olarak kullanılan doğal liflerin türü ve boyutu değiştirilerek, miselyum esaslı biyokompozitlerin son ürün özellikleri ayarlanabilir ve geliştirilebilir. Bu çalışmada, Pleurotus ostreatus miselyumu, kenevir lifi ve buğday samanı kullanılarak tamamen biyo-esaslı ve biyobozunur biyokompozit köpük ürünleri üretilmiştir. Bu doğal liflerin türünü ve boyutunu değiştirerek elde edilen biyokompozitlerin özellikleri incelenmiştir. Pleurotus ostreatus miselyumuna kenevir lifi ve buğday samanının ayrı ayrı ve birlikte ve farklı boyutlarda katılması ile malzemelerin yapısal, mekanik, ısıl, morfolojik, su emme ve yanıcılık özelliklerine etkisi ilk kez karakterize edilmiş olup besiyer çeşidine göre basma dayanımı 21-30 kPa, su emme %147-348 arasında değişmiş, 234-552 °C'ye kadar sıcaklık dayanımı göstermiş, 90 saniyeye kadar süren yanma testinde kenevir içeren numunelerde tutuşma görülmemiş olup kenevir ve buğday samanının birlikte kullanılması ürün özelliklerinin geliştirilmesinde sinerjistik etki tespit edilmiştir. Miselyum esaslı biyokompozitlerin petrol esaslı ve doğada bozunmayan polimerlere sürdürülebilir bir alternatif olarak güçlü bir potansiyel taşıdığı gösterilmiştir.

Anahtar Kelimeler: *Miselyum Biyokompozit, Tarım Atıkları, Buğday Samanı, Kenevir Lifi, Sürdürülebilir Biyo-esaslı Biyobozunur Köpük Ambalaj, Döngüsel Ekonomi.*

Abstract

Expanded polystyrene (EPS) foam is a frequently preferred packaging material due to its durability, lightness and affordable cost. However, its low density makes recycling not preferred for economic reasons, and due to its non-biodegradable nature, it causes high amounts of plastic pollution in the environment. Therefore, many countries have started to ban EPS packaging products. EPS needs to be replaced with bio-based and biodegradable alternatives to reduce environmental impact. Since mycelium-based materials are completely bio-based and biodegradable, they can be presented as a strong candidate for EPS packaging with their dimensionally stable foam structure. However, material properties still need to be improved. By changing the type and size of natural fibers used as medium, the end product properties of mycelium-based biocomposites can be adjusted and improved. In this study, completely bio-based and biodegradable biocomposite foam products were produced using Pleurotus ostreatus mycelium, hemp fiber and wheat straw. For the first time, the effects of adding hemp fiber and wheat straw separately, together, and in different sizes to Pleurotus ostreatus mycelium on the structural, mechanical, thermal, morphological, water absorption, and flammability properties of materials have been characterized. Depending on the substrate type, the compression strength ranged from 21 to 30 kPa, while water absorption varied between 147% and 348%. The materials exhibited temperature resistance up to 234-552°C. No ignition was observed in samples containing hemp during the combustion test lasting up to 90 seconds. Furthermore, in the improvement of product properties a synergistic effect was identified when hemp and wheat straw were used together and it has been shown that mycelium-based biocomposites have the potential as a sustainable alternative to petroleum-based and non-biodegradable polymers.

Keywords: *Mycelium Biocomposites, Agricultural Residues, Wheat Straw, Hemp Fiber, Sustainable Bio-based Biodegradable Foam Packaging, Circular Economy.*

EXTENDED ABSTRACT

Introduction

Expanded polystyrene (EPS) is a commonly used plastic packaging material due to its lightweight, insulation properties, and impact resistance, benefiting food preservation and transportation. However, its non-biodegradable nature, low recycling rates, and potential health risks linked to its production

DOI: https://doi.org/10.21205/deufmd.2025277914

Geliş Tarihi / Received: 11.01.2024
Kabul Tarihi / Accepted: 20.05.2024

chemicals have raised environmental concerns, leading to EPS bans in various countries[1]. This has triggered the search for alternative packaging materials to address the growing need for sustainable packaging solutions[2].

Mycelium biocomposites (BCs), as being strong alternatives to non-biodegradable packaging, are created by allowing mycelium, the filamentous substance in fungal roots, to grow on organic materials such as wheat straw, sawdust, wood chips, cotton, and rice husk [3]. As the fungus colonizes the substrate, its hyphae absorb nutrients and form connections within the organic material's cellulose, hemicellulose, and lignin-rich components [4]. After full colonization, the substrate undergoes heat treatment to deactivate the organism. The resulting product is mycelium biocomposite, which exhibits an inert, lightweight and foamy structure[5]. Mycelium-based materials have gained attention especially for being fully bio-based, possessing a lightweight foam-like structure with sufficient dimensional stability, cost-effective raw materials, high fire resistance, and thermal and sound insulation properties. These materials also offer a complete biodegradability which enables organic recycling and their low carbon and energy footprint that aid in combating global warming by utilizing low-energy production and agricultural residues without competing with food resources[4]. Despite the potential, further development is needed to match the properties of petroleum-based plastics for a complete replacement.

This research aims to investigate the production of mycelium biocomposites by valorizing agricultural residues by blending hemp fibers and wheat straw with Pleurotus ostreatus mycelium, known for rapid growth[6]. The compatibility known between hemp fibers and mycelium enhances material properties in composites, resulting in increased bending strength[7]. Wheat straw supports mycelium growth and enhances composite durability. While prior research explores natural fibers' roles in mycelium growth, this study bridges gaps by investigating the final products' properties [8]. This study investigates mycelium biocomposites utilizing hemp and wheat straw independently and in combination, examining the influence of various wheat straw sizes on the final product. The study analyzes chemical structure, morphological, mechanical, thermal, water absorption, and flammability characteristics to gauge the potential of these biocomposites in practical applications. In the literature, a mycelium biocomposite study encompassing all of these characterizations for hemp and wheat straw substrates has not been observed.

Materials and Methods

Materials: Pleurotus ostreatus (oyster mushroom) mycelium, was purchased from the Yalova Atatürk Horticultural Central Research Institute, Türkiye. Wheat straw kindly provided from a farm in Manisa, while hemp fibers were kindly provided by Ketene Bitkisel Üretim Tekstil San. Tic. A.Ş. Türkiye. Wheat straw was ground to two separate sizes, thick (30.34 ± 5.86 mm) and thin (8.90 ± 7.10 mm), using a Demsan Brader HC 1500 GR blade mill at standard speed for 15 and 30 seconds, respectively. Hemp was reduced to a single size (34.20 ± 5.60 mm) by cutting with scissors. (Figure 1). The lengths and standard deviation values were determined by measuring at least 100 samples using calipers.

Production of Mycelium Biocomposites: The wheat straw and hemp, intended for use as substrates, underwent sterilization at 121°C for 40 minutes. All equipment, including the workbench and gloves, was sterilized with a 95% ethyl alcohol solution to prevent sample contamination. The mycelium was combined with the substrate in a sterilized plastic container and left to grow under dark conditions at 25 °C and 80% relative humidity. Different substrates were tested: fine wheat straw (İBBK), coarse wheat straw (KBBK), hemp (KBK), and a combination of fine wheat straw with hemp (İB-K). The growth process took approximately 12-14 days, followed by drying at room temperature for four days. Additionally, some samples were dried in an oven at 70 °C to examine the effect of drying conditions on material properties.

Chemical Structure Analysis: FTIR spectroscopy (Perkin Elmer Spectrum 100) was used to analyze the chemical structure of the biocomposite samples. Measurements were taken at multiple points on each sample to generate representative spectra.

Mechanical Properties: Compression testing of mycelium biocomposites was performed using an Instron 5569 universal testing machine. Three samples from each test set (100 mm × 100 mm × 50 mm) were analyzed to determine the compression stress at 10% deformation and the slope of the linear elastic region, providing the elastic modulus values.

Morphological Properties: Morphological analysis of the sample surfaces was conducted using a Philips XL30 SFEG scanning electron microscope (SEM). The specimens were coated with a thin layer of gold to prevent charge effects, and at least five different regions were analyzed to capture representative images. The measurements on the images were determined using the ImageJ software.

Flammability Characteristics: For the combustion test, conducted by modifying the TS EN ISO 6941 standard. A single flame source was used vertically, positioning the sample to be tested 4.5 cm above the flame source and parallel to the ground. Samples were exposed to the flame source for 10, 30, 60, and 90 seconds.

Water Absorption Properties: The water absorption capacity of the mycelium biocomposite materials was assessed following a modified version of ASTM C272/C272M−18 standard. Samples were immersed in pure water at 22 ± 1°C for 2 and 24 hours to measure absorption. The change in weight after immersion was measured.

Thermal Properties: Thermogravimetric analysis (TGA) was performed using a Netzsch STA 449 F3 Jupiter device. The biocomposite samples were heated in air at a rate of 10°C/min up to 800 °C to assess their thermal stability.

Results and Discussion

Chemical Structure Analysis

FTIR spectra revealed the molecular characteristics in mycelium biocomposites (Figure 9). Peaks represented diverse components, including polysaccharides, proteins, lignocellulosic structures, chitin, and specific structural vibrations within protein, lignin, and cellulose compounds [4, 9, 10]. The composition analysis indicated a higher cellulose content in hemp, while wheat straw demonstrated a higher amount of lignin, as supported literature [11],[12].

Mechanical Properties

Compressive strength and elastic modulus differed among biocomposites (Table 1). Thin wheat straw-based biocomposite exhibited the highest compressive strength, followed by thin wheat-hemp, hemp, and thick wheat straw biocomposite aligning with findings in the literature (Table 3). Parallel trends were observed in elastic modulus, further emphasizing the effect of drying conditions on the mechanical properties [13].

Morphological Properties

Morphological analyses showed distinct structural variations among biocomposites (Figure 11). Thick wheat straw biocomposite displayed intermittent mycelium layer and large voids, while the thin wheat straw-based biocomposite exhibited a tighter structure with a well-connected mycelium. Hemp biocomposite demonstrated a good adhesion [7].

Flammability Properties

Samples were exposed to a flame for durations of 10, 30, 60, and 90 seconds in the combustion test (Figure 12). Notably, styrofoam caught fire even before completing 10 seconds, while all other biocomposite samples only exhibited slight charring without ignition during this period. At 30 seconds, no ignition was observed, but there was increased charring compared to the previous stage. Despite no ignition in any sample after 60 seconds, intensified charring was evident. Hemp and hemp-wheat straw biocomposite samples did not ignite even at the 90 second period, while wheat straw in both dimensions ignited at 75 seconds. Additionally, hemp-containing biocomposites exhibited less charring, possibly due to the tighter mycelium coverage, containing chitin, which is known to delay combustion [14, 15]. This is likely attributed to the elevated chitin content of the mycelium, potentially influenced by the high cellulose content present in the hemp substrate [16]. The lower flammability of all mycelium biocomposites compared to styrofoam is another superior property of these novel materials.

Water Absorption Properties

Water absorption values for mycelium-based biocomposite samples are presented in Figure 13 for 2 hours and 24 hours. Results showed that within 2 hours, samples containing thin wheat straw absorbed more water than those with thick wheat straw (IBBK: 314.44%; KBBK: 259.94%), nearly equalizing after 24 hours (IBBK: 346.59%; KBBK: 348.56%). This difference is attributed to the greater surface area per unit mass of thin wheat straw compared to thick wheat straw in IBBK. Hemp biocomposite (KBK) absorbed less water than both dimensions of wheat straw biocomposite samples for both durations. Biocomposites with wheat straw and hemp together showed the lowest water absorption (2 hours: 147.33%; 24 hours: 167.58%), The synergy observed between hemp and thin wheat straw, as discussed earlier, may stem from hemp's high cellulose content, promoting chitin production. Moreover, thin wheat introduces additional voids, facilitating mycelium growth. This combination likely yields a dense mycelial structure rich in hydrophobic chitin, thus decreasing water absorption.

Thermal Properties

Thermogravimetric analysis examined the onset and completion temperatures of decomposition for the produced biocomposites and styrofoam (Figure 14, Table 2). Styrofoam began decomposing the latest but completed decomposition quickly. Among the biocomposites, KBBK showed the earliest decomposition and weakest mechanical properties, followed by IBBK with a 12°C difference. KBK exhibited slightly more resistance than IBBK. When thin wheat straw and hemp were used together (IB-K), the highest thermal resistance was achieved (234.44°C). In line with previous findings, the thermal stability results further highlight the synergistic effect of utilizing hemp and thin wheat straw together as a substrate. The completion temperature of decomposition was 255°C higher for styrofoam than the highest thermal resistance observed in thick wheat straw biocomposite (663.45°C).

Conclusion

This study explores mycelium biocomposites made from wheat straw and hemp, separately or together, as potential alternatives to non-biodegradable styrofoam. Their structural, mechanical, combustion, water absorption, and thermal properties were examined. Hemp had higher cellulose and lower lignin compared to wheat straw. Thin wheat straw mycelium biocomposites (IBBK) exhibited superior strength, whereas thick wheat straw biocomposite (KBBK) fell behind. Wheat straw biocomposites seemed to contain more voids, while hemp formed tighter bonds with no observed effect on the mechanical properties. Hemp-containing biocomposites (KBK) resisted ignition for up to 90 seconds. IBBK absorbed more water than KBBK, with thin wheat-hemp mixtures (IB-K) showing the least absorption. Substrate choice notably impacted thermal resistance, with IB-K being the most robust. Mycelium biocomposites decompose without any harmful chemicals occurs during the thermal degradation of EPS, offering another environmental advantage. Combining hemp and thin wheat (IB-K) created synergy, providing flame resistance, lower water absorption, and higher thermal resistance. Tailoring substrates shapes mycelium biocomposites for specific properties, offering an eco-friendly, low-flammability alternative to EPS with room for further enhancement.

1. Giriş

Plastik ambalajlar gıda işleme, depolama, taşıma için, gıdayı bozulmadan korumak için ve ambalajlanan malzemeyi dış etkenlerden korumak için sıklıkla tercih edilen malzemelerdir. Ambalaj malzemeleri Avrupa'nın en büyük plastik pazarı olup %40,5'ini oluşturmaktadır [2]. Bu plastiklerin de büyük çoğunluğunu genleştirilmiş polistiren (EPS) adı verilen petrol-esaslı stiren monomerinin polimerizasyonuyla elde edilen kapalı gözenekli polistiren köpük veya strafor afını verdiğimiz malzeme oluşturmaktadır. EPS kolay ve ucuz üretilebilen, oldukça hafif, iyi yalıtım özelliklerine sahip olup ambalajlanan ürünü darbelere karşı korumaktadır. Bunlarla beraber EPS oldukça yanıcı olup üretiminde kullanılan malzemelerin özelliklerinin önemli dezavantajları mevcuttur. Polistirenin monomeri olan stirene maruz kalmanın yemek borusu, pankreas, lenf ve kan kanseri riskini artırdığı tespit edilmiştir [17]. EPS şişirici ajanı olarak kullanılan pentan gazının kimyasal ürünlerin tehlikelerini tanımlayan, sınıflandıran Küresel Uyumlaştırılmış Sınıflandırma ve Kimyasalların Etiketlenmesi Sistemi'ne (GHS) göre yutulduğunda ve solunum sistemine girmesi durumunda halinde ölümcül olup (H304) uyuşukluğa veya baş dönmesine neden olabildiği (H336), ayrıca sucul ortamda uzun süre kalıcı, toksik etkiye sebep olduğu (H411) ve oldukça yanıcı bir malzeme (H225) olduğu malzeme güvenlik formlarında belirtilmektedir. Ayrıca çoğu plastik malzemede olduğu gibi EPS de doğada bozunmamakta ve birikerek çevre kirliliği yaratmaktadır. Kıyılarda yığılan plastiklerin %23'ünün EPS olduğu [1] 1970'lerde incelenen bir çalışmada bile 14 çeşit balığın 8'inin sindirim sisteminde EPS tespit edilmiştir [18] günümüzde bu rakamların çok daha yüksek olduğunu tahmin etmek güç değildir.

Doğada bozunmayan plastik malzemelerin sadece %21,3'ü geri dönüştürülmekte %21,8'i yakılmakta, %53,8'i ise doğaya çöp olarak bırakılmaktadır [19]. Termoplastik olması dolayısıyla geri dönüşüme oldukça elverişli olan EPS'in geri dönüşümünün neredeyse hiç gerçekleştirilmemesi yoğunluğu çok düşük olmasından dolayı (Köpüğün %2'sini polistiren ve %98'i hava içermektedir) bu malzemenin geri dönüşümünde elde edilecek kazancın düşük olmasıdır. Yukarıda bahsedilen sorunların ortadan kalkmasına yönelik EPS kullanımı birçok ülke tarafından yasaklanmaya başlanmıştır [1]. Bununla beraber günlük hayata kattığı avantajlardan dolayı ambalaj malzemesi ihtiyacı artarak devam etmekte olduğu için alternatif malzemelerin araştırılması gerekmektedir.

Son yıllarda miselyum esaslı malzemeler; tamamen biyo-esaslı, boyutsal kararlılığa sahip oldukça düşük yoğunluklu köpüğümsü bir yapıya sahip olmaları, hammaddelerinin düşük maliyeti ve bol bulunabilmesi, yüksek yanmazlık, ısıl ve ses yalıtım özellikleri ve ambalajdan inşaata geniş potansiyel uygulama olanakları nedeniyle yoğun ilgi görmektedir [20]. Miselyum biyokompozitleri mantar kökündeki ipliksi bir madde olan hiflerin birleşiminden meydana gelen miselyumun organik malzemeler üzerinde gelişmesine izin verilerek üretilir. Buğday samanı, tahta talaşı, odun parçacıkları, pamuk ve pirinç kabuğu gibi çeşitli organik maddeler, miselyum biyokompozitlerin yetiştirilmesi için yaygın olarak kullanılan besiyerleri arasındadır [3]. Fungusun besiyeri işgal etmesi sırasında, hifleri selüloz, hemiselüloz ve lignin açısından zengin materyal içinde iç içe geçerek besinleri emer ve bağlantılar oluşturur [4]. Besiyer tamamen miselyum tarafından işgal edildiğinde, organizmanın kritik bir sıcaklık eşiğinin üzerinde deaktivasyonu için bir ısı işlemine tabi tutulur. Sonuç olarak elde edilen ürün, inert, hafif, köpüğümsü ve biyobozunur bir malzeme olan miselyum biyokompozittir [21]. Miselyum biyokompozitler doğada tamamen bozunabilmekte ve daha fazla biyokompozit hammadde eldesi için organik geri dönüşümü mümkün kılarak döngüsel ekonomi sağlamaktadır. Aynı zamanda üretimi sırasında düşük enerji gereksinimi ve tamamen doğal malzemelerden elde edilmesi nedeniyle miselyum esaslı biyokompozitler, oldukça düşük karbon ve enerji ayak izine sahip ürünler olup küresel ısınma sorununa sürdürülebilir bir çözüm olarak önerilebilir. Miselyumun üretilmesi için kullanılan besiyeri gıda ürünleri olabileceği gibi tarım atıklarında mevcut olan doğal liflerden de faydalanılabilmesi gıda ile rekabet oluşturulmaması, düşük maliyet ve atık yönetimi sağlanarak aynı zamanda atıklardan katma değerli ürün eldesini sağlaması açısından avantaj oluşturmaktadır [4]. Besiyeri olarak değerlendirilen bu doğal lifler miselyum tarafından beslenmek amacıyla tüketilmekte iken aynı zamanda henüz tüketilmeyen kısmı malzemeyi mekanik olarak takviye ederek; anafazı miselyum, takviye malzemesi doğal lif olan bir tür biyokompozit (BK) malzemeyi oluşturmaktadır. Bununla beraber bu biyo-esaslı malzemeler petrol-esaslı alternatiflerine göre özellikleri biraz daha zayıf kalabilmektedir. Biyo-esaslı ve biyobozunur malzemelerin petrol-esaslı plastiklerin yerini alabilmeleri için özelliklerinin geliştirilmesi gerekmektedir.

Bu çalışma kapsamında, biyolojik etkinliği yüksek olan ve hızlı lif oluşturabilen mantar türlerinden biri olan Pleurotus ostreatus (istiridye mantarı) türüne ait miselyum [6] ve besiyeri olarak kenevir lifi ve buğday samanının kullanılarak bu tarım atıklarının katma değerlerinin artırılması hedeflenmiştir. Bir kompozit malzemede malzeme özelliklerinin daha iyi olmasına sebep olan en önemli faktör bileşenler arasındaki yüksek uyumdur. Besiyeri olarak kullanılan kenevir lifleri ve miselyum arasında yüksek uyum olduğu bilinmektedir [7]. Ayrıca Pleurotus ostreatus ve kenevir liflerinin kombinasyonunun verimli büyüme sağladığı dolayısıyla üretim zamanını hızlandırdığı ve kenevir miselyum uyumu kaynaklı olarak elde edilen ürünün yüksek eğilme mukavemetine sahiptir [8].

Ülkemizde yıllık artan bir oranla 20 milyon tona yakın buğday üretilmektedir [22]. Bu üretim sonucunda açığa çıkan buğday samanı oldukça yüklü miktarda bir tarım atığı olarak ortaya çıkmaktadır. Buğday samanının miselyum gelişiminde verimli bir ortam sağlama avantajına sahip olduğu bilinmektedir [6]. Buğday samanı gibi tarımsal atıklar malzemelerin aşınma direncini artırmasından dolayı kompozit ürünün daha uzun ömürlü olmasını sağlamaktadır [23]. Bunun yanında kolay işlenebilirlik ve düşük yoğunluk gibi fiziksel özelliklerinden dolayı da tercih edilmiştir.

Literatürde buğday samanı, kenevir ve benzeri doğal liflerin çeşitli mantar miselyumlarının büyüme veriminde nasıl rol oynadığı incelenmiş olsa da [24] biyokompozit son ürünlerin özellikleri incelenmemiştir. Aynı şekilde buğday samanı, kenevir lifi kullanarak farklı mantar miselyumları ile gerçekleştirilen biyokompozit üretim çalışmaları varsa da [4],[6] bu iki doğal lifin bir arada kullanıldığı ve farklı besiyer boyutlarının ürün özelliklerine etkisinin incelendiği bir çalışmaya rastlanmamıştır.

Bu çalışmada kenevir ve buğday samanını ayrı ayrı ve birlikte miselyum biyokompoziti üretiminde kullanılmıştır, ayrıca farklı boyutlarda buğday samanı kullanımının elde edilen ürün özelliklere etkileri incelenmiştir. Miselyum biyokompozitinin kimyasal yapı özellikleri Fourier dönüşümlü kızılötesi (FTIR) spektoskopisi, yapıbilim özellikleri taramalı elektron mikroskopu (SEM), mekanik özellikleri basma testi, ısıl özellikleri termogravimetrik analiz (TGA) cihazı ile analiz edilmiş olup ürünün su emme ve yanıcılık özellikleri de incelenmiştir. Literatürde kenevir ve buğday samanı besiyeri için bu karakterizasyonların tamamını kapsayan bir miselyum biyokompozit çalışması gözlemlenmemiştir (Tablo 3).

2. Materyal ve Metot

2.1. Kullanılan Malzemeler

Pleurotus ostreatus (istiridye mantarı) miselyumları Yalova Atatürk Bahçe Kültürleri Merkez Araştırma Enstitüsü'nden temin edilmiştir. Buğday samanı, Manisa'da bulunan bir çiftlikten ve kenevir lifleri Ketene Bitkisel Üretim Tekstil San. Tic. A.Ş. tarafından bilâbedel temin edilmiştir. Buğday samanı kalın (30,34 ± 5,86 mm) ve ince (8,90 ± 7,10 mm) olacak şekilde iki ayrı boyutta Demsan Brader HC 1500 GR bıçaklı öğütücüde standart hızda sırayla 15 ve 30 saniye boyunca ufaltılmış, kenevir tek boyutta (34,20 ± 5,60 mm) kesilerek küçültülmüştür. Kenevirin küçültülmesi daha çok tüylenme şeklinde gerçekleşmiştir (Şekil 1).

Şekil 1. Buğday samanının (a) temin edildiği, (b) ince kıyılmış ve (c) kalın kıyılmış hâli. Kenevirin (d) temin edildiği ve (e) boyutları küçültülmüş hâli.

Figure 1. Wheat straw (a) as supplied, (b) finely chopped and (c) coarsely chopped. Hemp (d) as supplied and (e) reduced in size.

Uzunluklar ve standart sapma değerleri en az 100 adet numunenin kumpas ile ölçülmesiyle tespit edilmiştir. Temin edilen EPS 0,0064 g/cm^3 yoğunluğa sahip olup karakterizasyonlar aynı boyutlardaki miselyum biyokompozit ve EPS numuneleri ile gerçekleştirilmiştir.

2.2. Miselyum Biyokompozitlerin Üretimi

Öncelikle besiyeri olarak kullanılması planlanan buğday samanı ve kenevir küçük ölçülere getirildi. Hammaddelerin 121 °C'de ve 40 dakika boyunca otoklavda sterilizasyonu sağlanmıştır. Tezgâh, eldiven ve diğer tüm ekipmanlar, numunelerin bulaşını önlemek için %95 etil alkol çözeltisi ile temizlenerek kullanılmıştır.

Miselyum, besiyeriyle birleştirilmesi için etil alkol ile arındırılmış plastik bir kaba (13 cm × 6 cm × 10 cm) aktarılmış (uzun dönem kullanımlarda daha kolay sterilizasyon için cam tavsiye edilir.) ve besiyeri ile karıştırılıp kapağı kapatılmıştır. Her bir deneme için 20 gram besiyeri ve 200 gram mantar miseli miktarı kullanılmıştır. Besiyerlerinin etkilerini gözlemlemek için tekli ve çiftli olarak besiyerleri kullanılmıştır. Tekli denemelerde ince buğday samanı (İBBK), kalın buğday samanı (KBBK), kenevir (KBK) miselyum biyokompozitleri üretilmiştir. Çiftli denemelerde ince buğday samanı ve kenevir lifi (İB-K) biyokompoziti bu besiyerlerin eşit ağırlıkta eklenmesi ile elde edilmiştir. Miselyumun gelişim gösterebilmesi için ihtiyaç duyduğu ortamın sıcaklığı 25 °C ve bağıl nemi %80 [25] olarak karanlık koşullarda büyümeye bırakılmıştır ve desikatör içinde istenen ortam sağlanmıştır (Şekil 2).

Şekil 2. (a) İstiridye mantar miselyumunun temin edildiği şekli, (b) bir parçası. Üretimde kullanılan (c) desikatör ve (d) otoklav.

Figure 2. Oyster mushroom mycelium (a) as provided, (b) one piece. (c) Desiccator and (d) autoclave used in production.

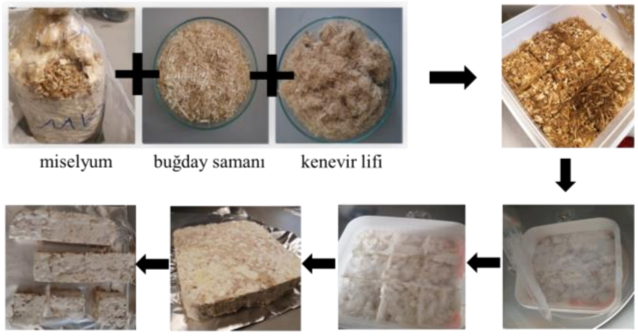

Şekil 3. Miselyum biyokompozit üretim aşamaları.

Figure 3. Production stages of mycelium biocomposite.

Desikatörün içerisine numunelerle birlikte nemölçer ve istenilen ortam nemini sağlaması için bir beher içerisine yaklaşık 50 mL doymuş sodyum bromür (NaBr) çözeltisi eklenmiştir. Üretim süreci 12-14 gün aralığında gerçekleştirilmiş olup kuruması için gereken süre oda sıcaklığında 4 gün olarak belirlenmiştir. Ayrıca numuneler 70 °C'deki bir etüvde 12 saat bekletilerek de kurutulmuş olup ve kurutmanın malzeme özellikleri üzerindeki etkisi kenevir lifi ile hazırlanmış miselyum biyokompozit için incelenmiştir.

2.3. Kimyasal Yapı Analizi

Perkin Elmer Spectrum 100 FTIR spektrofotometresinde (Şekil 4) 650 ila 4000 cm^{-1} tarama aralığında gerçekleştirilmiştir. Temsili bir spektrumuna sahip olmak için ölçümler her bir biyokompozit numunelerinin en az üç noktasında gerçekleştirilmiştir.

Şekil 4. FTIR spektrofotometresi.

Figure 4. FTIR spectrophotometer.

2.4. Mekanik Özellikler

Miselyum biyokompozitlerin basma testi Instron 5569 cihazı (Şekil 5) ile yapılmıştır. Köpük malzemelerin boşluklu ve esnekliklerinin düşük olmasından dolayı çekme testine nazaran sonuçları malzeme kusurlarından daha bağımsız olan basma testi tercih edilmiştir. Test, 100 mm × 100 mm × 50 mm numune ölçüleriyle ISO 844 standardı baz alınarak her bir deney setinden üçer numune için gerçekleştirilmiştir. Numunelere ait %10 deformasyona ait basma gerilimi ve doğrusal olarak elde edilen elastik bölgenin eğimi alınarak elastik modül değerleri tespit edilmiştir.

Şekil 5. Basma testi cihazı.

Figure 5. Compression test device.

2.5. Yapıbilim Özellikleri

Numunelerin yüzeylerine ait yapıbilim (morfolojik) analizi, Philips XL30 SFEG taramalı elektron mikroskobu (SEM) cihazı (Şekil 6) ile gerçekleştirilmiştir. Şarj etkilerini önlemek için tüm örnekler altın bir tabaka ile kaplanarak görüntüler 15 kV hızlandırma gerilimi kullanılarak elde edildi. Temsili bir görüntü elde etmek için en az beş farklı bölge analiz edildi. Fotoğraf üzerindeki boyutlar ImageJ programı kullanılarak tespit edildi.

Şekil 6. Taramalı Elektron Mikroskobu (SEM).

Figure 6. Scanning Electron Microscope (SEM).

2.6. Yanma Özellikleri

Yanma testi TS EN ISO 6941 standardının modifiye edilmesi ile gerçekleştirilmiş, düzenekte tek bir alev kaynağı dikey olarak kullanılmış, deneye tabi tutulacak numune alev kaynağından 4,5 cm yukarıda ve zemine paralel olarak konumlandırılmıştır. Numuneler; 10, 30, 60 ve 90 saniye boyunca alev kaynağına maruz bırakılmıştır [6].

2.7. Su Emme Özellikleri

Miselyum biyokompozit malzemelerin su emme kapasitelerini belirlemek için ASTM C272/C272M– 18 standardının modifiye edilmiş şekli kullanılmıştır. Bir kap içerisine sıcaklığı 22 ± 1°C olan saf su doldurularak ve numune alttan desteklenen bir ağırlık ile suyun yüzeyinden 25 mm aşağıda olacak şekilde konumlandırılmıştır (Şekil 7). Oda sıcaklığında 5 gün kurutulduktan sonra numune 2 saat ve 24 saat süresince su içerisinde bekletilmiştir. Bu sürelerin sonunda kaptan çıkarılıp suyun fazlası alınarak hassas terazi ile ölçülüp suya daldırma öncesi ağırlığı ile kıyaslanmıştır [6].

Şekil 7. Su emme test düzeneği.

Figure 7. Water absorption test setup.

2.8. Isıl Özellikler

Biyokompozit numunelerinin ısıl kararlılığının ölçümü için Netzsch STA 449 F3 Jupiter cihazı ile termogravimetrik analiz (TGA) cihazı (Şekil 8) gerçekleştirilmiş olup hava ile 10 °C/dak hız ile 800 °C'ye kadar ısıtılmıştır.

Şekil 8. Termogravimetrik analiz cihazı.

Figure 8. Thermogravimetric analyzer.

3. Bulgular ve Tartışma

3.1. Kimyasal Yapı Analizi

Kalın buğday samanı, ince buğday samanı, kenevir ve kenevir ile ince buğday samanı ile hazırlanmış miselyum biyokompozitlerinin FTIR spektrumlarında (Şekil 9) tespit edilen 3200 cm^{-1} piki polisakkaritlerin O-H gerilmesi ve proteinlerdeki amid gruplarının N-H gerilim titreşimine tekabül etmektedir. 2800-2900 cm^{-1} Aralığında lignoselülozik yapıların ve kitine ait C-H gerilmesi gözlemlenmektedir.

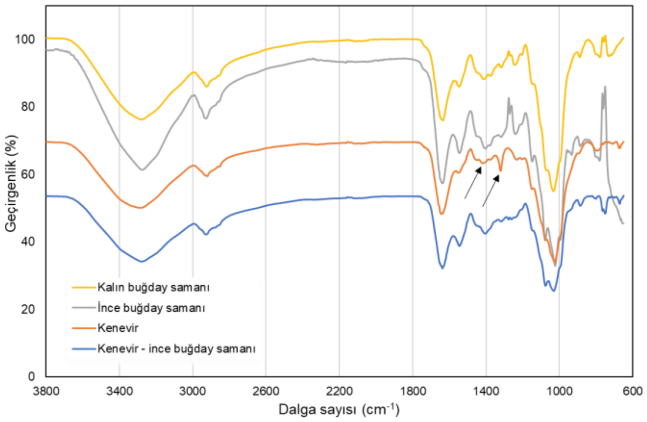

Şekil 9. a) Kalın buğday samanı, b) ince buğday samanı, c) kenevir ve d) kenevir-ince buğday miselyum biyokompozitlerinin FTIR spektrumları.

Figure 9. FTIR spectra of a) thick wheat straw, b) thin wheat straw, c) hemp and d) hemp-thin wheat mycelium biocomposites (from top to bottom).

1630 cm^{-1} civarlarındaki pik elde edilen protein yapısındaki amid I'e ait C=O gerilmesi, aminoasitlere ait C=C gerilmesi ve/veya N-H bükülmesine ait olabilir[10]. 1545 cm^{-1} piki proteinde bulunan amid II yapısına (N-H bükülme, C-N gerilme) [9, 10], 1400-1450 cm^{-1} civarındaki piklerin lignin ve karbohidratlarda bulunan CH_2 bükülmesi ait olduğu tespit edilmiştir[4]. 1370 cm^{-1} selüloz ve hemiselülozda bulunan CH deformasyon titreşimine ait olmakla beraber [26] miselyumun selüloz ile beslenmesinin sonucu kitin oluşumunun da gözlemlendiği bölge olarak da verilmektedir [10]. 1310-1320 cm^{-1} selülozdaki CH_2 burkulması [4], 1230-1250 cm^{-1} Aralığında pikin lignine ait metoksil gruplarındaki C-O gerilmesine ait olup, 1150 cm^{-1} C-O gerilmesine, 1070 cm^{-1} civarlarındaki absorpsiyon piki C=O gerilmesine[26], 1020-1030 cm^{-1} bölgesi ise C=O bükülmesine [10] tekabül etmektedir. 880 cm^{-1} civarındaki absorpsiyon pikleri monosakkaritlere ait glikosidik bağlara ve selülozun amorf bölgesine ait olduğu belirtilmektedir[26]. 750-790 cm^{-1} aralığında gözlemlenen absorpsiyon piklerinin polisakkaritlerde bulunan anomerik karbona ait olduğu düşünülmektedir [10]. Tüm numunelerin benzer yerlerde absorpsiyon pikleri vermektelerse de buğday samanı içeren biyokompozitlerde absorpsiyon pikinin 1410 cm^{-1} civarlarında, kenevir içeren biyokompozitlerde ise 1320 cm^{-1}'lerdeki pikin daha şiddetli olduğu tespit edilmiştir. Yukarıda 1410 cm^{-1}'larda pikin lignine, 1320'lerdeki pikin ise selüloza ait olduğu belirtilmişti. Bu şiddetler arasındaki farkın kenevirin selüloz içeriğinin buğdaya göre yüksek olması ve buğdaydaki ligninin de kenevirdeki miktardan daha fazla olmasından kaynaklandığı düşünülmektedir (kenevir: %74,1 selüloz, %7,6 hemiselüloz, %2,2 lignin[11]; buğday samanı: %32-45 selüloz, %20-45 hemiselüloz, %11-26 lignin[12]).

3.2. Mekanik Özellikler

Basma dayanımı için %10 deformasyondaki basma gerilimi ve elastik modül için elastik bölgedeki eğim hesaplanmıştır. Kalın buğday samanı, ince buğday samanı, kenevir ve kenevir- ince buğday samanı ile hazırlanan miselyum biyokompozitlerinin basma testleri sonuçları Tablo 1'deki gibidir.

Tablo 1. Miselyum BK'ler ve EPS'nin mekanik özellikleri.

Table 1. Mechanical properties of mycelium BCs and EPS.

	Elastik modül (kPa)	Basma gerilimi (%10 gerinim) (kPa)
İnce buğday BK	3,91 ± 0,02	30,36 ± 3,78
Kalın buğday BK	2,83 ± 0,76	21,00 ± 2,36
Kenevir BK	3,45 ± 0,10	23,88 ± 4,36
İnce buğday-kenevir BK	3,00 ± 0,15	24,26 ± 0,15
EPS	5,13 ± 0,12	54,82 ± 4,97

Miselyum biyokompozitler arasında ince buğday BK en yüksek basma değerine sahiptir (30,36 kPa). Bunu sırayla buğday-kenevir bileşimi, kenevir ve kalın buğday BK takip etmektedir. İBBK'nın basma gerilimi KBBK'ya göre %45 daha yüksek elde edilmiştir. İB-K BK'nın basma gerilimi ise yine KBBK'ya göre %15 daha yüksektir. Kalın buğday besiyerinin miselyum ile temas eden yüzey alanının daha düşük olması, daha fazla hacim kaplamasından ötürü daha boşluklu bir yapıya sahip olduğu ve bu nispeten büyük boşlukların miselyum ile besiyerin yapışmasını azaltarak miselyumun beklenilen yoğunlukta gelişememesine sebep olduğunu düşünülmektedir [6]. Optimum boyutlardaki buğday samanının malzemeye daha yüksek miktarda takviye sağladığı görülmektedir. Elde edilen basma dayanımı değerleri literatürde kullanılan buğday samanı ve kenevir içeren miselyum biyokompozitlerin çoğuna benzer özellik göstermektedir (Tablo 3). Elastik modül değerleri incelendiğinde miselyum BK'lar arasında basma gerilimi en yüksek İBBK (3,91 kPa) iken bunu KBK ve İB-K BK ve takip etmektedir. En düşük elastik modülü en düşük basma gerilimine de sahip olan KBBK'ya aittir. İBBK elastik modülü KBBK'dan %38, KBK'nin ise %22 daha yüksek elde edilmiştir.

Kenevirin içine ince buğday samanının katılması kenevir BK'nın basma dayanımını artırmışsa da yine de değer ince buğday samanı BK'nınkine ulaşamamıştır. Bunlarla beraber BK'ların basma dayanımının ve elastik modül değerlerinin EPS ile yarışabilir düzeye ulaşması için daha fazla artırılması gerektiği görülmektedir. Devam etmekte olan çalışmalarımız bu değerlere yaklaşıldığını göstermektedir.

Ayrıca miselyum biyokompozitlerin kurutma şekillerinin malzeme özelliklerine etkisini incelemek için KBK üretiminde iki farklı kurutma yolu denenmiştir. İlki yukarıda sonuçları sunulmuş olan oda sıcaklığında 4 gün bekletme ile kurutma yöntemi diğeri de 70 °C'deki etüv ortamında kurutma olup oda sıcaklığında kurutulan numunelerde bir fark görülmezken etüvde kurutulan numunelerde koku ve renk değişimi (sararma) muhtemel bir küflenme gözlemlendi. Etüvlenmiş numune birkaç gün oda sıcaklığında beklediğinde ise numunenin dağıldığı ve sabit yapının korunmadığı görüldü (Şekil 10). Etüvde kurutulan BK'nin elastik modül ve basma gerilimi değerleri sırasıyla 1,09 ve 11,78 kPa olup kurutma farkı mekanik özelliklerde %68 ve %51 gibi ciddi azalmaya sebep olmuştur.

Etüvde kurutulan BK'nın duyusal (görünüm, koku) ve mekanik özelliklerinde ciddi düşme tespit edilmesiyle literatürde sıklıkla belirtilen[13] etüv ile kurutmanın aslında malzemeye yarardan çok zarar getirdiği görülmüştür. Burada yüksek sıcaklık ürüne olumsuz etki edebildiği gibi biyokompozitlerin kuruma hızının küfün üreme hızından daha yavaş olduğu düşünülmüştür. Ayrıca etüvde hava devridaiminin olmamasının küflenmeye yol açabileceği ve hava devridaiminin sağlanması durumunda daha farklı sonuçların elde edilebileceği de düşünülmektedir. Devridaimsiz bir etüv varlığında numunelerdeki yüksek nemin öncelikle açık havada bir miktar kurutulup kalan eser miktarda nem ve aktivitenin sonlandırılması için yüksek sıcaklıkta kurutma daha faydalı olabilir.

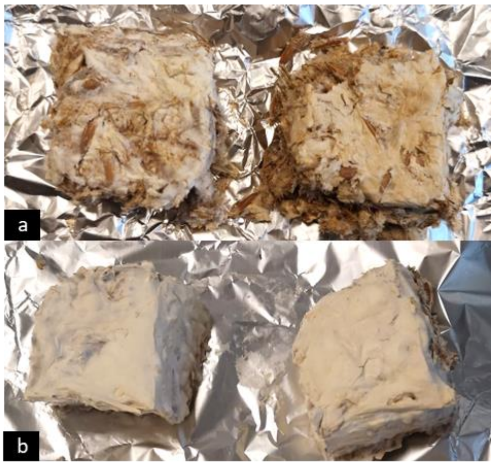

Şekil 10. (a) Etüvde ve (b) açık havada kurutulmuş kenevir miselyum biyokompozit numunelerinin görünümü.

Figure 10. Appearance of hemp mycelium biocomposite samples dried (a) in the oven and (b) in the open air.

3.3. Yapıbilim (Morfoloji) Özellikleri

BK'lerin yapıbilim özelliklerini incelendiğinde ilk dikkat çeken KBBK'nın yapısıdaki miselyumların belli bölgelerde küme şeklinde toplandığı 60 µm boyutlarında boşluklar içermesidir (Şekil 11). Buna karşın İBBK'nın yapısının daha sıkı, miselyumların birbirine daha bağlı olduğu ve boşlukların boyutlarının daha küçük olduğu (13,55±6,31 µm) gözlenmektedir. Bu yapı farkının etkisi, elde edilen mekanik özelliklerde de doğrulanmıştır. İBBK'da birbirine daha bağlı halde görülen yapının malzemenin basma dayanımında da artışa sebep olduğu düşünülmektedir. KBK yüzeyinin de miselyum tarafından tamamen kaplanmış olduğu görülmüştür. İB-K BK ise

KBBK’dan daha yoğun yapılı olmakla beraber bazı iri boşluklar (31,84±8,32 µm) ve tüm yapı boyunca köpük gibi küçük boşluklar da (8,00±2,36 µm) içermektedir.

Morfolojik analiz buğday samanı içeren BK’lerin daha fazla boşluk içerdiğini ve kenevirin daha sık olarak bağlandığını göstermektedir. Bu, kenevir liflerinin güçlü bir yapışma yeteneği gösterdiğini ve kenevirin besi yeri olarak kullanıldığı kompozit malzemelerde miselyum büyümesinin daha başarılı olduğunu göstermekte olup literatürde de doğrulanıyor olsa da [27] bu yapı özelliği ince buğdayın ekstradan kattığı mekanik avantajlardan dolayı malzemenin mekanik özelliklerine yansımamıştır.

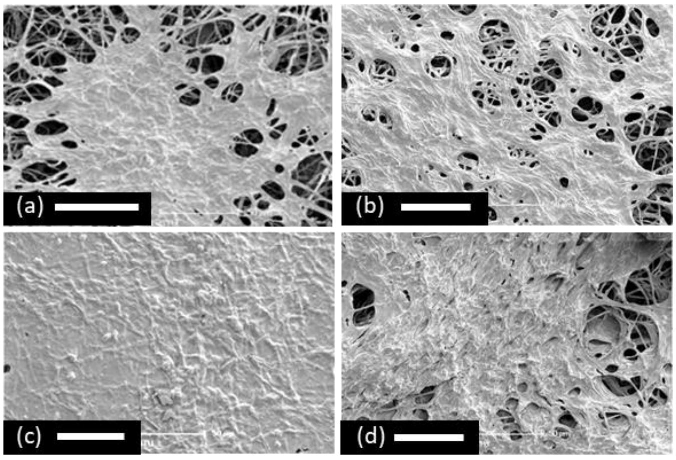

Şekil 11. (a) Kalın buğday samanı, (b) ince buğday samanı (c) kenevir (d) ince buğday samanı-kenevir BK SEM görüntüleri. Ölçek 50 µm.

Figure 11. SEM images of (a) thick wheat straw, (b) thin wheat straw (c) hemp and (d) thin wheat straw-hemp BC. Scale 50 µm.

3.4. Yanma Özellikleri

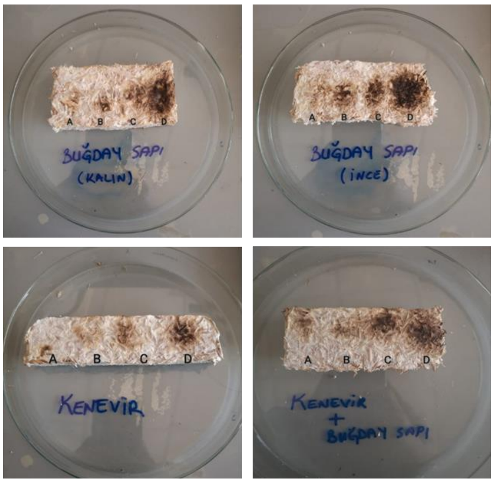

Şekil 12. a)10 sn, b)30 sn, c)60 sn ve d)75-90 sn’de miselyum BK’lerin yanmazlık özelliklerinin gösterimi.

Figure 12. Demonstration of the fireproof properties of mycelium BKs at a)10 sec, b)30 sec, c)60 sec and d)75-90 sec.

Yanma testinin yapılması için hazırlanan deneyde kullanılan numuneler sırasıyla 10, 30, 60 ve 90 saniye boyunca alev kaynağına maruz bırakılmıştır (Şekil 12). İlk olarak, 10 saniye boyunca alev kaynağına maruz bırakılan straforun 10 saniye tamamlanmadan tutuştuğu, diğer tüm BK numunelerin bu sürede tutuşma olmadan sadece hafif karardığı gözlenmiştir. İkinci olarak, 30 saniye boyunca alev kaynağına maruz bırakıldığında da hiçbir numunede tutuşmanın olmadığı gözlenmiştir. Ancak bir öncekinden daha fazla kararma olmuştur. 60 saniye boyunca alev kaynağına maruz bırakıldığında hiçbir numunede yine tutuşma olmamış ama öncekilere göre daha yoğun bir kararma gözlemlenmiştir. Kenevir ve ince buğday samanı-kenevir BK numunelerinde 90. saniyede bile tam tutuşma gözlenmemiş olup buğday samanının BK’nin iki boyutu için de 75. saniyesinde tutuşmanın başladığı gözlenmiştir. Ayrıca kenevir içeren BK’de daha az kararma oluştuğu gözlemlenmiştir. Kenevirin gerçekleştirdiği bu avantajların morfolojik analizde de görüldüğü gibi miselyum ile daha sıkı kaplanması olduğunu düşündürmektedir. Zira miselyumun yapısında bulunan kitin yanmayı geciktirici bir malzeme olarak bilinmektedir [14, 15]. Muhammad Haneef ve çalışma ark. yaptıkları araştırmada saf selüloz ile beslenen miselyumun kitin miktarının daha fazla olduğuna dikkat çekmiş olup [16] kenevirdeki selüloz miktarının buğdaya nazaran daha fazla olduğu FTIR analizinde bahsedilmişti. Dolayısıyla kenevir içeren besiyeri tüketen miselyumların yapısında daha fazla kitin oluşturmasına, bunun da yanmazlığa olumlu etki etmesine sebep olduğu düşünülmektedir.

Burada kullanılan tüm miselyum BK’lerin strafordan daha az yanıcı olması bu malzemelerin üstün özelliklerinden biridir. Literatürde kenevir ve buğday samanı besiyeri kullanılarak üretilen miselyum biyokompozitlerinin yanmazlık test sonuçları oldukça sınırlı olup Fusarium oxysporum ile besiyeri olarak kullanılmış kağıt ve bayat kahve atıklarının kullanılarak hazırlandığı miselyum biyokompozitinde 80 saniyeye kadar tutuşmanın gözlenmediği, bu çalışmadan farklı olarak 80 saniye ardından malzemenin 30 dakika boyunca için için yanarak tükendiği belirtilmiştir[28].

3.5. Su Emme Özellikleri

Deneylerde kullanılan miselyum esaslı biyokompozit numunelerin su emme değerlerine ilişkin değerler Şekil 13’te verilmiştir.

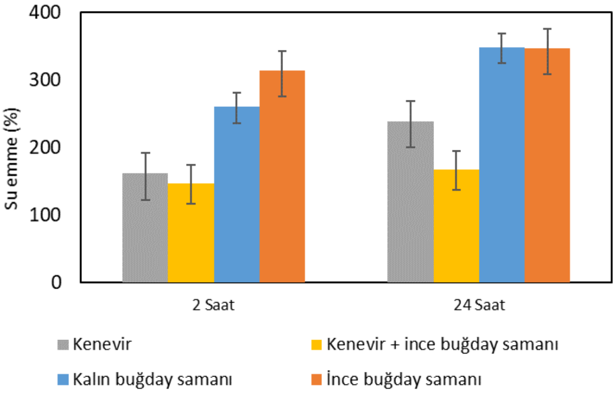

Şekil 13. Miselyum BK’lerin su emme davranışları.

Figure 13. Water absorption behavior of mycelium BCs.

Su emme testi 2 saat ve 24 saat için gerçekleştirilmiştir. Bu deneyden elde ettiğimiz verilere göre 2 saat içinde ince buğday samanı içeren numunelerin kalın buğday samanına göre daha fazla su emdiği (İBBK: %314,44; KBBK: %259,94) 24 saat süre sonunda birbirleriyle neredeyse eşitlendiği görülmektedir (İBBK: %346,59; KBBK: %348,56). İBBK’nin KBBK’ye göre daha fazla su emmesinin sebebi ince buğdayın birim kütleye düşen yüzey alanının kalın buğday besiyerine göre daha fazla olması şeklinde açıklanabilir. Kenevir biyokompozit (KBK) numunesinin su emme miktarı iki süre için de iki farklı boyuttaki buğday samanı BK numunelerinden daha azdır.

Buğday samanı ve kenevirin birlikte kullanıldığı numunelerinde (İB-K) ise su emme miktarının en az olduğu (2 saat: %147,33; 24 saat: %167,58) tespit edilmiştir. Kenevir ile ince buğdayın birlikte bu sinerjiyi oluşturmasının muhtemel sebebi bir önceki başlıkta da tartışılmış olduğu gibi kenevirdeki yüksek miktarda selülozun yüksek oranda kitin üretimine sebep olması, bununla beraber ince buğdayın da yapıya ekstra boşluklar getirerek miselyum büyümesine alan açması ve elde edilen hidrofobik olan kitin miktarı yüksek ve yoğun miselyum yapısının su emmeyi azaltması olduğu düşünülmektedir.

3.6. Isıl Özellikler

Üretilen biyokompozitlerin ve straforun termogravimetrik analizlerinde bozunmaya başladığı ve bozunmanın bittiği sıcaklıklar incelenmiştir (Şekil 14, Tablo 2).

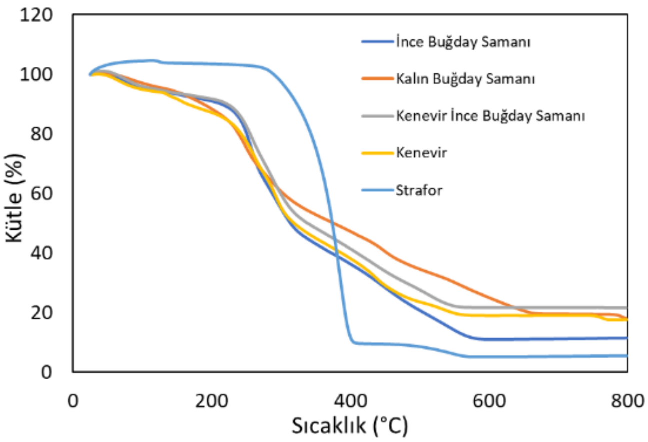

Şekil 14. Miselyum BK'lerin termal davranışları.

Figure 14. Thermal behavior of mycelium BCs.

Tablo 2. TGA analizi sonuçları.

Table 2. TGA analysis results.

	Bozunmaya başladığı sıcaklık (°C)	Bozunmanın bittiği sıcaklık (°C)
İnce buğday BK	227,15	582,92
Kalın buğday BK	214,64	663,45
Kenevir BK	230,21	558,45
Buğday-kenevir BK	234,44	552,15
EPS	312,55	407,92

Bu sonuçlara göre strafor en geç bozunmaya başlamışsa da bozunması erken tamamlanmıştır. Üretilen biyokompozitlerde en erken bozunan mekanik özelliklerde de en zayıf özelliği gösteren KBBK'dir. Onu 12 °C fark ile İBBK takip etmektedir. KBK, İBBK'den birkaç derece daha dayanıklıdır. İnce buğday ile kenevir birlikte kullanıldığında (İB-K) ise en yüksek sıcaklık dayanımı elde edilmiştir (234,44 °C). Yanmazlık, su emme testlerinde olduğu gibi bu sonuçlarda da bu iki besiyerinin kullanımı ürünün sıcaklık dayanımında yukarıda tartışılmış olan sinerjistik etkiyi oluşturduğunu göstermektedir. Strafor daha geç bozunmaya başlamış olsa da 407,92 C'de oldukça hızlı bir şekilde bozunmaya uğramıştır. En yüksek sıcaklık dayanımına sahip olan besiyerin strafordan 255 °C daha yüksek olacak şekilde kalın buğday samanı BK'ye ait olduğu görülmektedir (663,45 °C).

Tablo 3. Bu çalışmadaki ve literatürde kenevir ve buğday samanı içerikli çalışmaların karakterizasyon sonuçları.

Table 3. Characterization results of this study and studies containing hemp and wheat straw in the literature.

Miselyum Türü	Besiyer	Basma Dayanımı (kPa) (% def.)	Yanmazlık Testi	Su emme (%)	Bozunmaya başladığı sıcaklık (°C)	Uygulama	Ref
Pleurotus ostreatus	Buğday samanı	20 (%20)	-	-	-	Mimari	[29]
Trametes versicolor	Kenevir	17-33 (%10)	-	24s 24-27	-	Yalıtım malzemesi	[4]
Pleurotus ostreatus, Oudemansiella radicata, Acremonium sp.	Buğday kepeği, pamuk sapı	70-240 (%10)	-	2s 58-95 24s 138-145	250-270 °C	İnşaat ve yapı malzemesi	[30]
Ganoderma lucidum	Buğday samanı	70 (%25)	-	-	-	İnşaat ve yapı malzemesi	[31]
Ganoderma lucidum	Kenevir, buğday samanı ayrı (preslenmemiş)	16-25 (%10)	-	-	-	Yeşil malzeme	[32]
Trametes versicolor	Buğday tanesi, pirinç kabuğu	-	Tutuşma Buğday tanesi: 7 sn Pirinç kabuğu: 12 sn	-	-	İnşaat ve yapı malzemesi	[33]

Pleurotus ostreatus	Buğday samanı	-	Tutuşma 67 sn	2s 256,64 24s 257,46	-	Yeşil malzeme	[6]
Pleurotus ostreatus	Kenevir lifi, buğday samanı ve birlikte	21-30 (%10)	Tutuşma Buğday samanı: 75 sn Tutuşma yok Kenevir: 90 sn Kenevir-buğday samanı: 90 sn	2s 147-314 24s 167-348	215-234 °C	Ambalaj	Bu çalışma

4. Sonuçlar

Bu çalışmada tarım atıkları olan buğday samanı ve kenevirin farklı boyutları, ayrı veya karışım halinde hazırlandıklarında yapısal, mekanik, morfolojik, yanma, su emme, ısıl özelliklerde nasıl değişiklikler gerçekleştiği incelenmiş olup biyobozunur olmayan strafor malzemesinin yerine geçiş potansiyeli değerlendirilmiştir.

Yapısal değerlendirmede kenevir lifinin buğday samanına göre selüloz içeriğinin daha yüksek ve lignin oranının daha düşük olduğu gözlemlenmiştir.

Morfolojik analiz buğday samanı içeren BK'lerin daha fazla boşluk içerdiğini ve kenevirin daha sık olarak bağlandığını göstermiştir. Miselyum biyokompozitler arasında ise en yüksek elastik modül ve basma dayanımının İBBK'ya ait olduğu en düşük değerlerin ise KBBK'ya ait olduğu görülmektedir. Kenevirin içine ince buğday samanının katılması kenevir BK'nın basma dayanımını artırmışsa da yine de değer ince buğday samanı BK'ya ulaşamamıştır. Zira İBBK, miselyumun daha sık büyümesini sağlayan kenevirden daha iyi bir doğal lif takviyesini sağlandığı düşünülmektedir. Etüvde kurutulan BK'nın duyusal (görünüm, koku) ve mekanik özelliklerinde ciddi düşmeye sebep olmasından dolayı devridaimi olmayan 70 °C'deki bir etüvde kurutulması tavsiye edilmemektedir.

Yanma testinde üretilen tüm biyokompozitlerin 75. saniyeye kadar tutuşmadığı, kenevir içerenlerin 90. saniyede dahi tutuşma göstermediği tespit edilmiştir. Bunun muhtemel sebebi kenevirde buğday samanından daha fazla miktarda bulunan selülozun hidrofobik olan kitin içeriği yüksek yoğun miselyum oluşumunu sağlamasıdır. Yanmazlık özelliği miselyum biyokompozitlerin özellikle inşaat gibi kullanım alanlarında EPS'ye üstünlüklerinden biridir.

Su emme testlerinde İBBK'nin KBBK'ye göre daha fazla su emme göstermiş olup, en düşük su emmenin miselyum ile daha sık bağlanmış olan İB-K karışımı BK'lere ait olduğu görülmüştür. Miselyum biyokompozit üretiminde kullanılan besiyerinin ürünün ısıl dayanımına önemli etkiler oluşturduğu ve en dayanıklı miselyum BK'nin İB-K olduğu görüldü. Ayrıca EPS bozunma ürünleri arasında stiren, pentan gibi çevreye ve sağlığa zararlı kimyasallar mevcutken miselyum biyokompozitlerde bu türde kimyasalların varlığı söz konusu değildir.

Sonuç olarak mekanik özellik olarak en iyi dayanımı ince buğday miselyum BK'leri gösterirken kenevirin yapısal olarak miselyumun daha fazla bağlanmasını sağlayarak ince buğday ile oluşan biyokompozitinin birlikte sinerjistik etki göstererek yanmazlık, düşük su emme, yüksek ısıl dayanıma sahip olduğu görülmüştür. Bu sinerjistik etkinin kenevir içinde daha yüksek miktarda bulunan selülozdan kaynaklı olduğu düşünülmektedir. Farklı boyutlarda farklı besiyerler kullanarak istenen özelliklerde miselyum biyokompozitlerin üretilmesinin mümkün olduğu gösterilmiştir. Çevreci ve düşük yanıcılık/yanmazlık özelliklerinden dolayı miselyum kompozitleri özellikleri daha da geliştirilerek EPS'ye alternatif olmaya en yakın malzemelerdendir.

Etik kurul onayı ve çıkar çatışması beyanı

Hazırlanan makalede etik kurul izni alınmasına gerek yoktur. Hazırlanan makalede herhangi bir kişi/kurum ile çıkar çatışması bulunmamaktadır.

Teşekkür

Bu çalışma 1919B012112643 nolu "Miselyum esaslı biyokompozitlerinden ambalaj malzemesi eldesi" başlıklı 2209A projesi kapsamında TÜBİTAK tarafından desteklenmiştir. FTIR analizi için Dr. İpek ÖMEROĞLU, TGA ve basma testlerinin gerçekleştirilmesinde Adem ŞEN ve SEM analizleri için Ahmet NAZIM'a teşekkür ederiz.

Yazar katkılarının beyanı

MM: Fikir oluşturma, literatür taraması, deney tasarımı, danışmanlık, metodoloji, görselleştirme, yazım: orijinal taslak, düzenleme, eleştirel inceleme. RA, NA, İA: Literatür taraması, deney tasarımı, veri toplama, deneylerin ve analizlerin gerçekleştirilmesi, yazım: orijinal taslak

Kaynaklar

[1] Chan, H.H.S., Not, C., 2023. Variations in the Spatial Distribution of Expanded Polystyrene Marine Debris: Are Asian's Coastlines More Affected? Environmental Advances, Cilt. 11, s. 100342.

[2] Europe, P., 2021. Plastics—The Facts 2021: An Analysis of European Plastics Production, Demand and Waste Data. Plastics Europe Association of Plastics Manufacturers.

[3] Zimele, Z., et al., 2020. Novel Mycelium-Based Biocomposites (MBB) as Building Materials. Journal of Renewable Materials, Cilt. 8(9), s. 1067-1076.

[4] Elsacker, E., et al., 2019. Mechanical, Physical and Chemical Characterisation of Mycelium-Based Composites with Different Types of Lignocellulosic Substrates. PLoS One, Cilt. 14, e0213954. DOI: 10.1371/journal.pone.0213954

[5] Elsacker, E., et al., 2020. A Comprehensive Framework for the Production of Mycelium-Based Lignocellulosic Composites. Science of the Total Environment, Cilt. 725, s. 138431.

[6] Kutbay, N. H., Yavuzcan, H. G., Aktaş, S., 2022. Mantarın Bağlayıcı Olarak Kullanıldığı Bir Kompozit Malzemenin Üretilmesi ve Tutuşma Süresi ile Su Alma Özelliklerinin Tespiti. Politeknik Dergisi, Cilt. 25(4), s. 1701-1711.

[7] Li, Y., Pickering, K.L., Farrell, R.L., 2009. Determination of Interfacial Shear Strength of White Rot Fungi Treated Hemp Fibre Reinforced Polypropylene. Composites Science and Technology, Cilt. 69(7), s. 1165-1171.

[8] Etinosa, O.P., 2019. Design and Testing of Mycelium Biocomposite. African University of Science and Technology, Materials Science and Engineering, Doktora Tezi, 150s, Nigeria.

[9] Haksoy, H., et al., 2020. Deli Bal ve Grayanotoksin'in Karaciğer Dokusu Üzerindeki Etkilerinin Zamana Bağlı Araştırılması. Konuralp Tıp Dergisi, Cilt. 12(1), s. 97-111.

[10] Chulikavit, N., et al., 2022. Influence of Growth Rates, Microstructural Properties and Biochemical Composition on the Thermal Stability of Mycelia Fungi. Scientific Reports, Cilt. 12(1), s. 15105.

[11] Dorez, G., et al., 2014. Effect of Cellulose, Hemicellulose and Lignin Contents on Pyrolysis and Combustion of Natural Fibers. Journal of Analytical and Applied Pyrolysis, Cilt. 107, s. 323-331.

[12] Zhang, L., et al., 2022. Comparison of Lignin Distribution, Structure, and Morphology in Wheat Straw and Wood. Industrial Crops and Products, Cilt. 187, s. 115432.

[13] Jiang, L., et al., 2017. Manufacturing of Biocomposite Sandwich Structures Using Mycelium-Bound Cores and Preforms. Journal of Manufacturing Processes, Cilt. 28, s. 50-59.

[14] Moussout, H., et al., 2016. Kinetics and Mechanism of the Thermal Degradation of Biopolymers Chitin and Chitosan Using Thermogravimetric Analysis. Polymer Degradation and Stability, Cilt. 130, s. 1-9.

[15] Pan, H., et al., 2015. Formation of Self-Extinguishing Flame Retardant Biobased Coating on Cotton Fabrics via Layer-by-Layer Assembly of Chitin Derivatives. Carbohydrate Polymers, Cilt. 115, s. 516-524.

[16] Haneef, M., et al., 2017. Advanced Materials from Fungal Mycelium: Fabrication and Tuning of Physical Properties. Scientific Reports, Cilt. 7(1), s. 41292.

[17] Program, R.T.P.N.N.T., 2021. National Toxicology Program. 15th Report on Carcinogens.

[18] Carpenter, E.J., et al., 1972. Polystyrene Spherules in Coastal Waters. Science, Cilt. 178(4062), s. 749-750.

[19] Tsakona, M., Rucevska, I., 2020. Baseline Report on Plastic Waste: Basel Convention. United Nations, s. 1–68.

[20] Yang, L., Park, D., Qin, Z., 2021. Material Function of Mycelium-Based Bio-Composite: A Review. Frontiers in Materials, Cilt. 8.

[21] Elsacker, E., et al., 2020. A Comprehensive Framework for the Production of Mycelium-Based Lignocellulosic Composites. Science of the Total Environment, Cilt. 725, s. 138431

[22] TÜİK, 2022. Bitkisel Üretim İstatistikleri, 2022. TÜİK.

[23] Mengeloğlu, F., Alma, M.H., 2002. Buğday Saplarının Kompozit Levha Üretiminde Kullanılması. KSÜ Fen ve Mühendislik Dergisi, Cilt. 5(2), s. 37-48.

[24] Yang, W., Guo, F., Wan, Z., 2013. Yield and Size of Oyster Mushroom Grown on Rice/Wheat Straw Basal Substrate Supplemented with Cotton Seed Hull. Saudi Journal of Biological Sciences, Cilt. 20(4), s. 333-338.

[25] Jose, J., et al., 2021. Investigations into the Development of a Mycelium Biocomposite to Substitute Polystyrene in Packaging Applications. Arabian Journal for Science and Engineering, Cilt. 46(3), s. 2975-2984.

[26] Vârban, R., et al., 2021. Comparative FT-IR Prospecting for Cellulose in Stems of Some Fiber Plants: Flax, Velvet Leaf, Hemp and Jute. Applied Sciences, Cilt. 11(18), s. 8570.

[27] Precious, E.O., 2019. Design and Testing of Mycelium Biocomposite. African University of Science and Technology, Materials Science and Engineering, Doktora Tezi.

[28] Iordache, O.G., et al., 2018. Novel Myco-Composite Material Obtained with Fusarium Oxysporum.

[29] Ghazvinian, A., et al., 2019. Mycelium-Based Bio-Composites for Architecture: Assessing the Effects of Cultivation Factors on Compressive Strength. 37 Education and Research in Computer Aided Architectural Design in Europe and XXIII Iberoamerican Society of Digital Graphics, Joint Conference. Blucher Design Proceedings, s. 505-514.

[30] Gou, L., et al., 2021. Morphological and Physico-Mechanical Properties of Mycelium Biocomposites with Natural Reinforcement Particles. Construction and Building Materials, Cilt. 304, s. 124656.

[31] Răut, I., et al., 2021. Fungal-Based Biopolymer Composites for Construction Materials. Materials, Cilt. 14(11), s. 2906.

[32] Buntsma, J., 2019. An Exploration on Cellulose and Weed Residues from Biomass to Mycelium Composite. Stowa, Amersfoort, Netherlands.

[33] Jones, M., et al., 2018. Waste-Derived Low-Cost Mycelium Composite Construction Materials with Improved Fire Safety. Fire and Materials, Cilt. 42(7), s. 816-825.

DEU FMD 27(79) (2025) 121-125

Dokuz Eylül Üniversitesi Mühendislik Fakültesi Fen ve Mühendislik Dergisi
Dokuz Eylul University Faculty of Engineering Journal of Science and Engineering
Elektronik/Online ISSN: 2547-958X

RESEARCH ARTICLE / ARAŞTIRMA MAKALESI

Structural and Nanomechanical Properties of Silicon Single Crystals Grown by the Czochralski Method

Czochralski Metodu ile Büyütülen Silisyum Tek Kristalinin Yapısal ve Nanomekanik Özellikleri

Tuncay Dikici [1,2,3*], **Serdar Yıldırım** [2,3,4]

[1]Dokuz Eylül University, Torbalı Vocational School, Welding Technology Program, Izmir, TÜRKİYE
[2] Dokuz Eylül University, The Graduate School of Natural and Applied Sciences, Department of Nanoscience and Nanoengineering, Izmir, TÜRKİYE
[3] Dokuz Eylül University, Center for Fabrication and Application of Electronic Materials, Izmir, TÜRKİYE
[4]Dokuz Eylül University, Department of Metallurgical and Materials Engineering, Izmir, TÜRKİYE

Sorumlu Yazar / Corresponding Author *: tuncay.dikici@deu.edu.tr

Abstract

The rapid advancements in the fields of artificial intelligence, cloud computing, big data analysis and internet of things have expanded the use of electronic devices and increased the demand for semiconductors. The Czochralski method, the most common and effective production technique for these materials, allows the production of single-crystal forms of elements such as Silicon (Si), Germanium (Ge), and various semiconductor compounds. In this study, the crystal structure, surface morphology and mechanical properties of a Si wafer, prepared by slicing a single crystal Si ingot grown by the Czochralski method, were determined by x-ray diffraction (XRD), scanning electron microscopy (SEM), atomic force microscopy (AFM) and nanoindentation methods, respectively. XRD analysis of the silicon wafer confirmed its single-crystal structure, showing a cubic lattice structure and a single peak on the (100) plane, while SEM and AFM analyses determined that the surface is smooth, even, and undamaged. Hardness and elastic modulus values for the Si wafer, calculated from indentation tests using a Berkovich tip under different loads, were determined to be an average of 19 GPa and 255 GPa, respectively. These results hold vital importance for the advancement of semiconductor technologies. The design and production of electronic devices with superior performance and durability can be achieved with a comprehensive understanding of the mechanical properties of the materials.

Keywords: *Silicon single crystal, Czochralski method, Nanoindentation, Hardness*

Öz

Yapay zeka, bulut bilişim, büyük veri analizi ve nesnelerin interneti alanlarındaki hızlı gelişmeler, elektronik cihazların kullanımını genişletmiş ve yarıiletkenlere olan talebi artırmıştır. Bu malzemelerin üretiminde en yaygın ve etkili yöntem olan Czochralski yöntemi, Silisyum (Si), Germanyum (Ge) gibi elementlerin ve çeşitli yarı iletken bileşiklerin tek kristal formunda üretilmesine olanak sağlar. Bu çalışmada, Czochralski yöntemi ile büyütülen silisyum tek kristal ingottan kesilerek hazırlanan Si plakanın (wafer) kristal yapısı, yüzey morfolojisi ve mekanik özellikleri sırasıyla x-ışınları kırınımı (XRD), taramalı elektron ve atomik kuvvet mikroskobu (SEM ve AFM) ve nanoindentasyon yöntemi ile tespit edilmiştir. Silisyum plakanın XRD analizi, kübik kafes yapısını ve (100) düzleminde tek bir pik göstererek tek kristal yapısını doğrularken, SEM ve AFM analizleriyle, yüzeyin düzgün, pürüzsüz ve hasarsız olduğu belirlenmiştir. Farklı yüklerde Berkovich tip uç kullanılarak yapılan indentasyon testleri sonucunda Si plakaya ait sertlik ve elastisite modülü değerleri ortalama 19 GPa ve 255 GPa olarak hesaplanmıştır. Bu sonuçlar, yarıiletken teknolojilerin ilerlemesi için hayati öneme sahiptir. Üstün performans ve dayanıklılığa sahip elektronik cihazların tasarımı ve üretimi, malzemelerin mekanik özelliklerinin kapsamlı bir şekilde anlaşılmasıyla gerçekleştirilebilir.

Anahtar Kelimeler: *Silisyum tek kristal, Czochralski yöntemi, Nanoindentasyon, Sertlik*

1. Introduction

Single crystal silicon is the most commonly used semiconductor material as a substrate in microelectronics and optoelectronic applications. The growth technology of single crystal silicon has made rapid progress in recent years. The process of crystal growth is essentially an interdisciplinary field involving metallurgy and materials engineering, mechanical engineering, chemical engineering, physics, and so on [1]. The requirement for bigger wafer diameters and the desire to increase the mass quality of crystals are the driving forces behind the development of silicon crystal growth technology. [2]. Single crystal materials exhibit superior properties compared to polycrystalline or amorphous equivalents. There are generally two main groups in the methods of growing single crystals, which are growth from solution and growth from melt. The methods used in growth from melt are also known as the Czochralski, Bridgman-Stockbarger, and Verneuil methods, named after their inventors [3,4]. Jan Czochralski invented the Czochralski method of single crystal formation in 1917 [5]. Despite being a rapid growth technique, Czochralski is frequently employed in optical applications for semiconductors and oxide/fluoride materials. This method

DOI: https://doi.org/10.21205/deufmd.2025277915

Geliş Tarihi / Received: 29.02.2024
Kabul Tarihi / Accepted: 20.05.2024

allows for the production of excellent and homogeneous crystals. The Czochralski crystal growth technique is a melt growth technique that involves the solidification of a liquid phase [6]. Since the melting point of silicon is 1412°C, the furnace is heated above 1500°C. A diminutive seed crystal, possessing the requisite crystallographic orientation, is submerged into the liquefied silicon. Subsequently, it is gradually retracted by the mechanism designed for crystal extraction. In the pursuit of fabricating a monocrystalline ingot, the preservation of homogeneity is paramount. This is accomplished by concurrently rotating and extracting the seed crystal. In contrast, the furnace is subjected to a rotation counter to the direction of the crystal puller. As the molten silicon adheres to the seed crystal and is retracted, it commences solidification, mirroring the orientation of the seed crystal. As a result, a monocrystalline ingot is successfully procured. In the event that a doped crystal is required, dopant material is infused into the molten silicon, thereby enabling its integration into the burgeoning crystal lattice. The withdrawal rate, as well as process controls such as the rotation speed of the crystal puller, are crucial for obtaining high-quality single crystals. Si-based MEMS technologies commonly utilize Si wafers oriented in the [100] direction. In other words, the surface of the Si wafer is the (100) crystallographic plane. Less frequently, wafers oriented in the [111] or [110] directions are used [7].

The progression of Microelectromechanical Systems (MEMS) technology has necessitated the appraisal of the mechanical attributes of semiconductor Si plates and their associated thin films. These components are integral to the structural integrity of the devices, thereby ensuring their reliability. Over the years, a multitude of testing methodologies have been devised to scrutinize the mechanical properties of these materials, which can be broadly categorized into direct and indirect techniques. Direct methodologies encompass a spectrum of tests, including tensile, bending, and compression tests. These techniques offer a straightforward approach to deciphering the stress-strain relationships inherent in Si plates, bearing a resemblance to traditional testing methodologies employed for bulk materials. However, the implementation of such tests on Si plates is fraught with challenges due to their inherent brittleness and extreme sensitivity to the minutest of defects. Additional complexities associated with this approach include the fabrication of test-suitable plates and the difficulties encountered in their gripping, manipulation, and alignment. To circumvent these challenges, indirect methodologies, such as nanoindentation testing, have been developed. This technique provides a reliable avenue for assessing the mechanical properties of surface layers of bulk materials, inclusive of the thin films that are deposited on Si plates. It offers consistent measurements of parameters such as hardness, elastic modulus, and fracture toughness. A significant advantage of this methodology is its simplicity, obviating the need for intricate sample preparation [8].

Indentation is a non-destructive testing method used to determine mechanical properties. A rigid and non-deformable penetrating tip (indenter) is used to apply a mechanical load (P, load) to the surface of the material to be tested. This loading results in a permanent indentation mark on the material. In nanoindentation technique, it is possible to determine the mechanical properties of thin films and small-scale materials such as hardness and elastic modulus by creating smaller indentation depths with smaller loads. A loading-unloading curve, which represents the characteristic behavior of the material depending on the applied load (P) and the indentation depth (h), is created, and the mechanical properties are calculated based on this curve. In the domain of material science, the advent of the nanoindentation technique can be traced back to the mid-1970s. Nevertheless, it was the pioneering research conducted by Oliver and Pharr, employing a Berkovich-type indenter, that ignited an unprecedented wave of interest in probing the hardness and elastic modulus of materials at a minuscule scale. This technique of mechanical testing has demonstrated its efficacy in deciphering the complex mechanical behavior of a diverse spectrum of materials, encompassing ceramics, composites, alloys, coated surfaces, and thin films [9-11]. It is imperative to underscore that the mechanical attributes of the silicon substrate not only govern the mechanical performance of the device, but also significantly impact its electrical and optical characteristics [12]. In this study, the mechanical properties such as hardness and elastic modulus of a single crystal silicon wafer produced by the Czochralski method were determined using a nanoindentation device at different loads.

2. Materials and Methods

The undoped single crystal Si ingot used for nanomechanical studies was grown at the PVA Tepla Czochralski laboratory-scale single crystal ingot growth machine located at Dokuz Eylül University, Center for Electronic Materials Production and Application (EMUM) (Figure 1). The materials and specifications required for the preparation of Si single crystal plates are given in Table 1.

The schematic diagram illustrating the growth of a single crystal silicon ingot is shown in Figure 2. The process consists of loading polycrystalline silicon, melting, shoulder, neck, body, and cone formation stages. After loading the polycrystalline silicon into the quartz crucible, the melting process was conducted at a temperature of 1560 °C. Once the molten silicon reached a homogeneous structure, a [100]-oriented single crystal seed silicon was immersed into the molten silicon pool at the solid-liquid phase equilibrium temperature of 1427 °C, and the formation of neck and shoulder was observed in the crystallization process. Upon reaching the desired diameter for shoulder formation, the pulling and rotation speeds were adjusted to proceed to the body formation stage. The ingot production was completed by varying the parameters of temperature, rotation, and pulling speeds. The entire process took approximately 18 hours, resulting in the production of an undoped single crystal Si ingot with dimensions of 300 mm in length and 110 mm in width [13].

Table 1. Materials and properties for the manufacture of single-crystal silicon wafers

Aim	Materials	Properties
Czochralski process (Ingot production)	Polycrystalline silicon (Si)	Pure silicon (99.9999%), loaded 5 kg.
	Crucible	Polished Quartz (SiO_2) crucible
	Argon gas	99.999% purity, 50 L, 3 tubes were used.
Wafer preparation (ingot slicing, lapping, polishing and cutting)	Colloidal alumina	9 µm Al_2O_3 + deionized water (1/10), cast plate surface [Lapping]
	Colloidal cerium oxide	3 µm Ce_2O_3 + deionized water (1/10), cast plate surface [Lapping]
	Colloidal nano silica	Nano SiO_2 (40 nm) + deionized water + H_2O_2 on pad surface [Polishing]

Figure 1. PVA Tepla Czochralski laboratory scale single crystal ingot growth device [13].

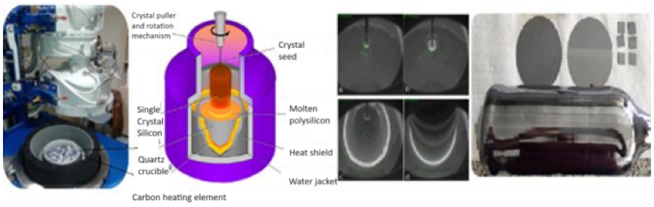

Figure 2. Schematic diagram of the Czochralski crystal growth process [13].

The single crystal Si ingot obtained after the Czochralski process underwent slicing, lapping, polishing, cutting, and cleaning processes using the materials listed in Table 1. The ingot slicing process was performed using a precision slicing machine (STX 1202) with the assistance of a diamond particle-coated wire. Lapping and polishing procedures were conducted on a Logitech machine, where the Si wafer was placed on a casting substrate to achieve desired smooth and flat surfaces. In these processes, Al_2O_3 and CeO_2 powders, as well as SiO_2 suspension, were utilized [13]. The polished Si wafers were subsequently cut into 20mm x 20mm squares, as shown in Figure 2. Following each stage, the samples were cleaned in acidic and alkaline baths, rinsed, and dried. The obtained square cross-section Si samples were subjected to various structural and mechanical tests.

The Thermo-Scientific ARL X'TRA model X-ray diffraction (XRD) instrument was used to determine whether the samples were single crystals after magnification and to explore their phase structure. The analysis was conducted using monochromatic Cu-Kα X-ray radiation (λ=1.54055 Å) at voltage of 45 kV and current of 44 mA, with a scanning rate of 2 °/min and angles ranging from 2θ=10-75°. The surface morphology of the samples was examined using a COXEM EM-30 scanning electron microscope (SEM) and a Nanosurf easyScan 2 atomic force microscope (AFM).

The IBIS nanoindentation device was used to determine the hardness and elastic modulus of the silicon substrate. Prior to testing, calibration tests were performed on a fused silica reference sample. Nanoindentation tests were conducted on the substrate surface at ten different loads (30-300 mN), and loading-unloading curves were extracted from the results to calculate the values of hardness and elastic modulus.

3. Result and Discussion

3.1. Crystalline Structure and Phase analysis

The XRD pattern of the sliced plate from a single crystal Si ingot produced by the Czochralski method is shown in Figure 3. Crystal orientation is examined in XRD analysis to determine if a material is a single crystal. Polycrystalline silicon with a cubic lattice structure (JCPDS 27-1402) contains crystals on different planes [14] However, the single crystal silicon plate produced by the Czochralski process exhibited a single peak at 69.46° on the (100) plane. This indicates that all planes of the produced ingot are oriented in a single direction, confirming it is a single crystal. As can be seen from the figure, no other peaks were observed. This is supported by the literature [15-18].

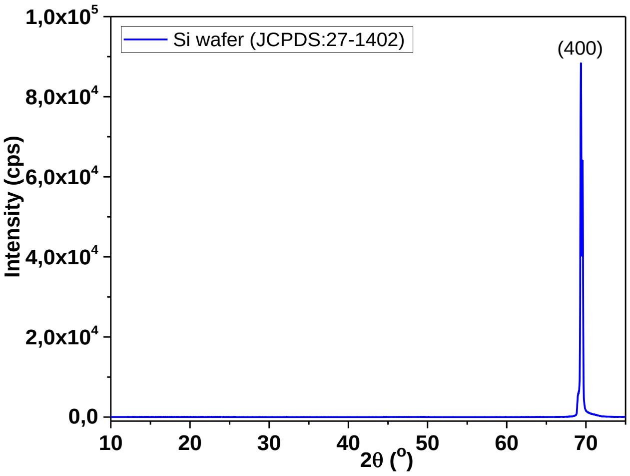

Figure 3. XRD pattern drawing and phase analysis of a single crystal Si wafer.

3.2. Surface Morphology

Surface roughness, morphology, and topography are important factors for Si substrates and thin films. In principle, these factors strongly influence the surface coating quality. In this regard, SEM (surface morphology and topography) and AFM (surface morphology and roughness) images of Si plates are discussed in Figure 4. Figure 4a shows a secondary electron image of the Si plate taken at a magnification of 1000X under a 20 kV accelerating voltage after the polishing process. Upon examining the morphology, it can be observed that the surface is smooth, polished, and free of any scratches or cracks. Figure 4b presents two- and three-dimensional 20 µm x 20 µm AFM micrographs of the surface. The study conducted for surface roughness and morphology determined linear and areal roughness values of 6 nm and 3.4 nm, respectively. The obtained values indicate that the surface is prepared in an extremely smooth and polished manner. Similar surface images and roughness values have also been reported in the literature [19-20].

3.3. Mechanical Properties

The indentation method is a characterization technique in which a rigid, sharp indenter typically made of a mechanically known, extremely hard material like diamond penetrates a homogeneous solid material at a depth of h from the surface under an applied indentation load P. During a loading-unloading cycle, the values of P-h are continuously recorded in a computer environment to characterize the process.

In this study, loading-unloading curves for different loads applied to the wafer are presented in Figure 5a. It has been observed that the indentation depth increases with increasing load (Figure 5b). At the lowest load of 30 mN, this value was measured as 0.302 µm ± 0.013, while at the highest load of 300 mN, it was measured as 1.050 µm ± 0.003. Nanoindentation tests revealed an intriguing observation in the form of a "pop-out" phenomenon that appeared during the unloading phase, indicating the occurrence of inelastic deformation. This behavior can be attributed, as suggested by Vodenitcharova and Zhang's theory, to a sudden volumetric increase resulting from a phase transformation within the material [8].

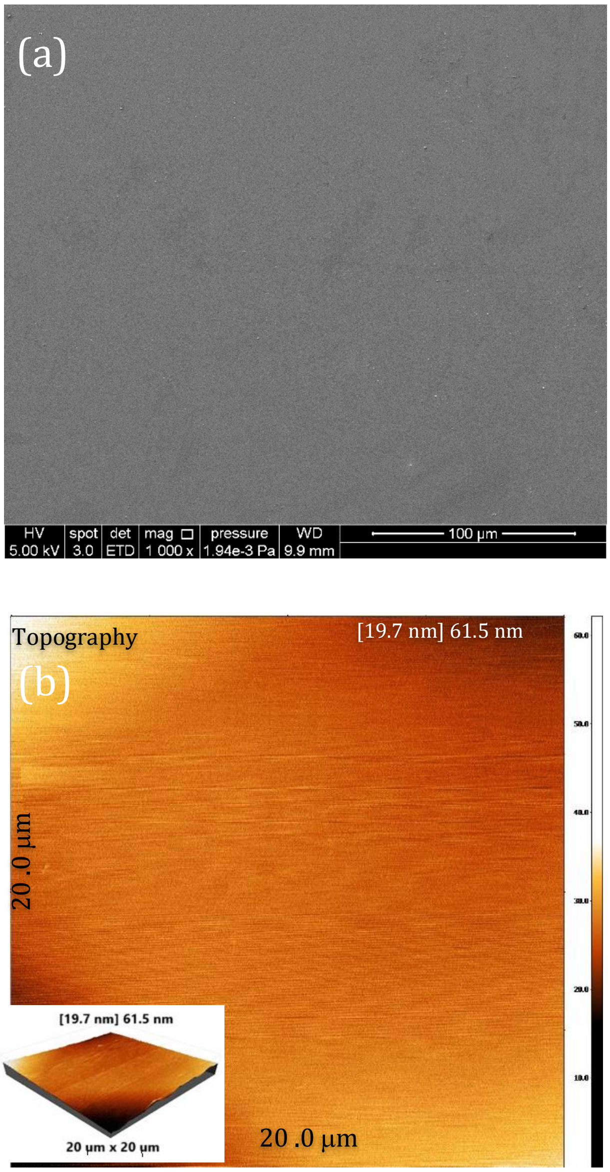

Figure 4. Micrographs of a single crystal Si wafer SEM (a) and AFM (b).

The hardness values of the Si plate at different loads obtained from the nanoindentation test are shown in Figure 6. In the measurements conducted, the average highest hardness value at three different loads was determined as 21.8 ± 1.35, while the lowest hardness value was calculated as 18.90 ± 0.24. Based on the result obtained from the graph, we can say that the hardness value of the Si plate is ~19 GPa. It is expected that the hardness result will be higher at lower loads. Given that the Berkovich diamond indenter's practical tip has a finite sharp point radius, the elastic modulus and hardness rise with contact depth at lesser depths. For bulk Si wafers, indentation depth values of 100 nm and more are typically considered to be accurate, especially in light of the potential for the surface to be oxidized [21]. However, the range where the hardness values begin to stabilize provides us with the true result.

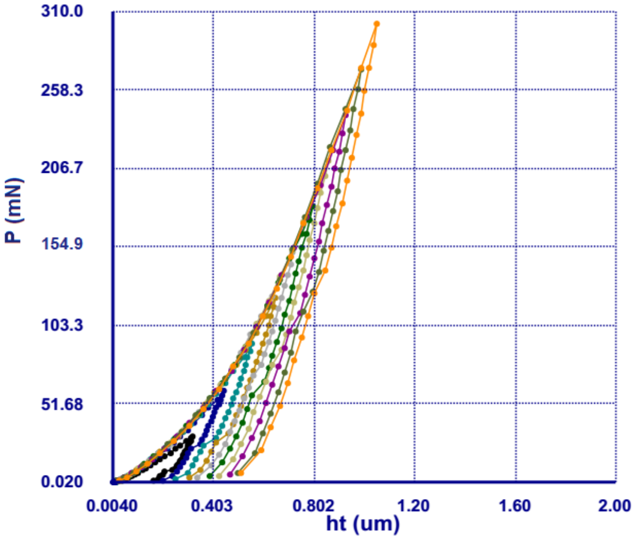

P (mN)	ht (μm)$_{mean}$
30	0,302±0,013
60	0,437±0,004
90	0,551±0,005
120	0,644±0,005
150	0,719±0,004
180	0,795±0,003
210	0,860±0,002
240	0,926±0,003
270	0,982±0,008
300	1,050±0,003

Figure 5. Loading-unloading curve (a) and Loading-mean penetration values (b) of the silicon wafer.

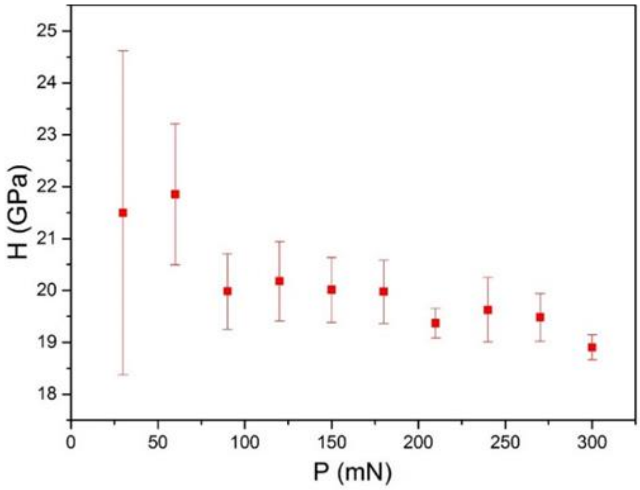

Figure 6. Hardness values of silicon wafer at different loads.

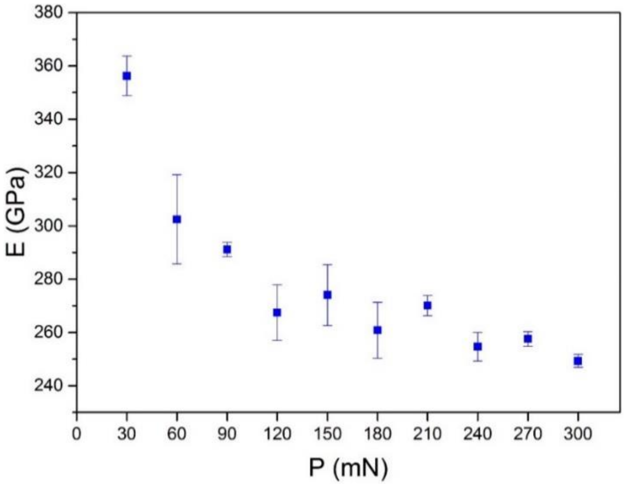

Figure 7. Elastic modulus values of silicon plate at different loads.

The results of the nanoindentation test conducted on Si plates at different loads are presented in Figure 7. According to the results, the average highest elastic modulus is calculated as 356 ± 7.4 GPa, while the lowest elastic modulus value is measured as 249 ± 2.3 GPa. The elastic modulus value for the Si plate can be read from the graph to be ~255 GPa.

4. Conclusion

This study examined the mechanical properties of plates obtained from single crystal silicon ingots produced by the Czochralski method. These plates are the preferred circuit elements for integrated circuit manufacturing and photovoltaic solar cell production in semiconductor technology. Analyzes conducted using SEM and AFM devices to evaluate the surface quality of the plates have determined that the surface morphology is smooth and uniform. Since surface roughness and morphology are critical factors for surface coatings, these findings indicate a successful surface treatment process. The hardness and elastic modulus of the plates were measured using the nanoindentation technique. This procedure was conducted at 10 different loads ranging from 30 mN to 300 mN. As the load increased, an initial decrease in hardness and elastic modulus values was observed, but the rate of change subsequently decreased. According to the obtained results, the hardness value of the silicon plates was approximately 19 GPa, and the elastic modulus was calculated to be approximately 255 GPa. These findings demonstrate the suitability of such silicon plates for semiconductor and photovoltaic applications. In conclusion, significant findings have been discovered that contribute to the design and production of electronic devices with improved performance and durability, advancing semiconductor technologies.

Ethics committee approval and conflict of interest statement

This article does not require ethics committee approval. This article has no conflicts of interest with any individual or institution.

Acknowledgment

We would like to express our gratitude to Dokuz Eylül University, Center for Electronic Materials Production and Application, for their support in the production and characterization studies of this work.

Author Contribution Statement

All authors contributed equally to the writing, conceptualization, literature review, data collection, validation and critical review of this manuscript.

References

[1] Vegad, M., Bhatt, N.M., 2014. Review of Some Aspects of Single Crystal Growth Using Czochralski Crystal Growth Technique. Procedia Technology, Vol. 14, pp. 438-446.

[2] Wu, L., 2008. Numerical Simulation of Czochralski Bulk Crystal Growth Process: Investigation of Transport Effects in Melt and Gas Phases. PhD Thesis, Catholic University of Louvaine, Belgium, 190p.

[3] Rudolph, P., 2014. Handbook of crystal growth: Bulk crystal growth. Second Edition, Elsevier.

[4] Kasap, S.O., Capper P., 2017. Springer Handbook of Electronic and Photonic Materials. New York: Springer.

[5] Czochralski, J., 1917. A New Method for the Measurement of the Crystallization Rate of Metals. Zeitschrift des Vereines Deutscher Ingenieure, Vol. 61, pp. 245–351.

[6] Schneemeyer, L.F., 2003. Crystal Growth. In: Meyers, R., Third, E., (Eds.), Academic Press, New York, USA.

[7] Tilli, M., Paulasto-Kröckel, M., Petzold, M., Theuss, H., Motooka, T., Lindroos, V. (Eds.), 2020. Handbook of Silicon Based MEMS Materials and Technologies. Elsevier.

[8] Li, X., Ding, G., Ando, T., Shikida, M., Sato, K., 2006. Mechanical Properties of Mono-Crystalline Silicon Thin Films Measured by Different Methods. IEEE International Symposium on Micro Nano Mechanical and Human Science, Nagoya, Japan, pp. 1-6.

[9] Poon, B., Rittel, D., Ravichandran, G., 2008. An Analysis of Nanoindentation in Linearly Elastic Solids. International Journal of Solids and Structures, Vol. 45(24), pp. 6018-6033.

[10] Oliver, W.C., Pharr, G.M., 1992. An Improved Technique for Determining Hardness and Elastic Modulus Using Load and Displacement Sensing Indentation Experiments. Journal of Materials Research, Vol. 7(6), pp. 1564-1583.

[11] Sattler, K.D. (Ed.), 2010. Handbook of Nanophysics: Functional Nanomaterials. CRC Press.

[12] Lee, W.S., Chen, T.H., Chang, S.L., 2009. Nanoindentation Response and Microstructure of Single-Crystal Silicon under Different Loads. IEEE 3rd International Conference on Nano/Molecular Medicine and Engineering, pp. 164-167.

[13] Yıldırım, S., 2017. Production and Development of Implant Dosimeters in Radiotherapy. PhD Thesis, Graduate School of Natural and Applied Sciences, Dokuz Eylül University, İzmir, 190p.

[14] Lin, N., Han, Y., Zhou, J., Zhang, K., Xu, T., Zhu, Y., Qian, Y., 2015. A Low Temperature Molten Salt Process for Aluminothermic Reduction of Silicon Oxides to Crystalline Si for Li-Ion Batteries. Energy & Environmental Science, Vol. 8(11), pp. 3187-3191.

[15] Lam, Y.C., Zheng, H.Y., Tjeung, R.T., Chen, X., 2009. Seeing the Invisible Laser Markings. Journal of Physics D: Applied Physics, Vol. 42(4), p. 42004.

[16] Ren, W., Wang, Y., Zhang, Z., Tan, Q., Zhong, Z., Su, F., 2016. Facile Patterning Silicon Wafer by Rochow Reaction over Patterned Cu-Based Catalysts. Applied Surface Science, Vol. 360, pp. 192–197.

[17] Shen, J., Yu, X., Zhang, Y., Zhong, H., Zhang, J., Qu, M., Le, X., 2015. Novel Microstructures on the Surfaces of Single Crystal Silicon Irradiated by Intense Pulsed Ion Beams. Nuclear Instruments and Methods in Physics Research, Section B: Beam Interactions with Materials and Atoms, Vol. 365, pp. 26–29.

[18] Xia, Y., Pu, X., Liu, J., Liang, J., Liu, P., Li, X., Yu, X., 2014. CuO Nanoleaves Enhance the c-Si Solar Cell Efficiency. Journal of Materials Chemistry A, Vol. 2(19), pp. 6796.

[19] Pandey, K., Pandey, P.M., 2017. Chemically Assisted Polishing of Monocrystalline Silicon Wafer Si (100) by DDMAF. Procedia Engineering, Vol. 184, pp. 178-184.

[20] Pandey, K., Pandey, P.M., 2019. An Integrated Application of Chemo-Ultrasonic Approach for Improving Surface Finish of Si (100) Using Double Disk Magnetic Abrasive Finishing. The International Journal of Advanced Manufacturing Technology, Vol. 103, pp. 3871-3886.

[21] Sun, Y.L., Zuo, D.W., Li, D.S., Chen, R.F., Wang, M., 2008. Mechanism of Brittle-Ductile Transition of Single Silicon Wafer Using Nanoindentation Techniques. Key Engineering Materials, Vol. 375, pp. 52-56.

Dokuz Eylül Üniversitesi Mühendislik Fakültesi Fen ve Mühendislik Dergisi
Dokuz Eylul University Faculty of Engineering Journal of Science and Engineering
Elektronik/Online ISSN: 2547-958X

ARAŞTIRMA MAKALESI / RESEARCH ARTICLE

Lavvar Tesis Artıklarının Flokülasyon ve Filtrasyonla Susuzlandırılması

Dewatering of Coal Processing Plant Tailings by Flocculation and Filtration

Çağrı Çerik

Dokuz Eylül Üniversitesi Mühendislik Fakültesi, Maden Mühendisliği Bölümü, Cevher Hazırlama Anabilim Dalı, İzmir, TÜRKİYE
Sorumlu Yazar / Corresponding Author : cagri.cerik@deu.edu.tr

Öz

Bu çalışmada, kömür zenginleştirme tesis atıklarının çeşitli flokülantlar ve dozajlarla ön koşullandırmasının, filtrasyon testleri ve filtre kekinin nem içeriği üzerindeki etkisi incelenmiştir.. Bu amaçla, tesis artıkları üzerinde anyonik (Praestol 2540, Cyfloc A-150) ve noniyonik (Cyfloc N-100) flokülantlar kullanarak katıların çökelme ve filtrasyon davranışları gözlemlenmiştir. Deney sonuçları incelendiğinde anyonik flokülantların lavvar tesis atıklarını susuzlandırma için daha etkili olduğu gözlemlenmektedir. Deneylerde susuzlandırma için en etkili flokülantın 100 g/t dozajda Praestol 2540 olduğu belirlenmiştir.

Anahtar Kelimeler: *Kömür tesis artıkları, flokülasyon, filtrasyon, susuzlandırma*

Abstract

In this study, the effect of preconditioning of coal preparation plant tailings with various flocculants and dosages on filtration kinetics and moisture content of the filter cake was examined. For this purpose, anionic (Praestol 2540, Cyfloc A-150) and nonionic (Cyfloc N-100) treatments were used on the tailings. Sedimentation and filtration behaviors of solids were observed using flocculants. As a result, it is observed that anionic flocculants are more effective for dewatering. In the experiments, it was determined that the most effective flocculant for dewatering was Praestol 2540 at a dosage of 100 g/t.

Keywords: *Coal preparation plant tailing, flocculation, filtration, dewatering*

EXTENDED ABSTRACT

Introduction

Coal waste dewatering typically involves the use of thickeners and filters [1]. While filtration yields more water, it is an expensive process. Therefore, initially using thickeners and slightly increasing the solid content helps reduce dewatering costs [2].

The waste in coal washing plants contains minerals such as kaolin, illite, muscovite, and quartz. Due to the slow natural settling of these minerals, flocculants are required. Flocculants are used in most coal washing plants to separate fine wastes and water [3].

The effect of flocculants on dewatering varies significantly due to differences in clay content, mineral composition, and properties of the pulp water in coal wastes [4]. Surface charges of particles affect flocculation mechanisms, thus influencing floccule size and efficiency [5-7].

Flocculants increase operating costs. Therefore, it is essential to carefully select the type and amount of flocculant to be used when obtaining waste with low moisture content

Materials and Methods

In experimental studies 0.1% flocculant solutions were prepared, mixed with tailings and the settling was allowed, followed by measuring the interface height over time.

In filtration experiments, a solid content of 30% was used to simulate the plant thickener output. The pulp obtained from sedimentation tests was fed into the vacuum filter. The amount of water filtered over time in the vacuum filter was measured.

Results and Discussion

Results showed that higher sedimentation rates were achieved when Praestol 2540 and Cyfloc A-150 were used. Anionic flocculants form larger flocs compared to other types of flocculants, resulting in higher sedimentation rates [4].

The amount of flocculant added to cover half of the particle surface area is referred as the optimum dosage. When more flocculant is added than the optimum dosage, there is no space left on the particle surface for the flocculants to attach. In this case, the flocculant is prevented from bridging between particles, and adversely affecting the flocculation process [10-12]. To avoid exceeding the optimum dosage and to mitigate the cost of flocculants, a maximum of 200 g/t of reagent was used in the experiments.

The filtration process depends on the cake structure. Surface moisture can be removed by applied pressure, but removing absorbed and capillary water from the surface due to high internal capillary pressure is challenging [13,14]. As the particle size increases, the dewatering efficiency increases, so flocculants are used to reduce the moisture content of the filter cake [14].

DOI: https://doi.org/10.21205/deufmd.2025277916

Geliş Tarihi / Received: 16.04.2024
Kabul Tarihi / Accepted: 10.06.2024

Larger flocs reduce the available surface area, thereby reducing the amount of surface water.

Conclusion

In this study the dewatering of fine-sized coal preparation plant tailings through flocculation and filtration was investigated. It was observed that anionic flocculants increased both sedimentation and filtration rates. Experiments conducted with Praestol 2540 at a dosage of 100 g/t yielded a sedimentation rate of 570 mm/min and filtration was completed in approximately 10 minutes. On the other hand, experiments with Cyclof A-150 with a dosage of 200 g/t resulted in a sedimentation rate of 545 mm/min and a filtration time of approximately 13 minutes. Due to its lower dosage requirement and higher effectiveness, Praestol 2540 was determined to be more suitable for this material.

1. Giriş

Son yıllarda kazı mekanizasyonunun gelişmesiyle ve çevresel etkileri nedeniyle daha kaliteli kömür talebinin artmasıyla ince malzeme üretimi artmıştır. Endüstri ve termik santral kullanımı için, kömürün düşük nem, kül ve kükürt değerlerine ve yüksek kaloriye sahip olması gerekmektedir. Kaliteli kömür üretmek için malzeme ufalanarak kül ve diğer gang mineralleri serbest hale getirilmelidir. Fakat tane boyutunun azalmasıyla aynı zamanda elde edilen artıklarda daha ince olmakta ve susuzlandırılması bir sorun hale gelmektedir.

Kömür artıklarının susuzlandırmasında genellikle tkiner ve filtreler kullanılmaktadır [1]. Filtrasyon ile daha fazla su kazanılmasına rağmen pahalı bir işlemdir. Bu nedenle öncelikle tkiner kullanılması ve katı oranının bir miktar artırılması susuzlandırma maliyetlerinin azalmasın sağlamaktadır [2].

Kömür yıkama tesislerindeki atıklar içerisinde kaolin, illit, muskovit ve kuvars gibi mineraller bulunmaktadır. Bu minerallerin doğal çökelme süresi çok yavaş olduğundan flokülantlarlara ihtiyaç duyulmaktadır. Flokülantlar çoğu kömür yıkama tesisinde ince artıklar ve suyun ayrılmasında kullanılmaktadır [3].

Kömür artıklarındaki kil oranı, mineral yapısı ve pülpü oluşturan suyun özelliklerinin farklı olması nedeniyle flokülantların susuzlandırmaya etkisi oldukça değişkendir [4]. Tanelerin yüzey yükleri, flokülasyon mekanizmalarını etkilemekte ve böylece flok boyutunu ve flokülasyon verimliliğini etkiler [5-7].

Flokülantlar işletme maliyetlerini artırmaktadır. Bu nedenle düşük nem oranına sahip tesis atığı elde ederken kullanılacak flokülant türünü ve miktarını iyi belirlemek gerekmektedir.

Bu çalışmada farklı miktarda ve türde flokülantların susuzlandırmaya etkisi araştırılmıştır. Kömür artıklarına çöktürme ve sonrasında filtrasyon işlemi yapılarak nihai ürünün nem oranı incelenmiştir.

2. Materyal ve Metot

2.1. Materyal

Bu çalışmada kullanılan kömür zenginleştirme artıkları Soma bölgesinde faaliyet gösteren bir lavvar tesisinden elde edilmiştir. Numuneler %10 katı oranına sahip pülp şeklinde alınmıştır. Numuneye ait elek analizi sonuçları Tablo 1'de verilmektedir.

Çöktürme testler için standart 1 lt'lik mezür kullanılırken filtrasyon testlerinde vacuubrand rs8 vakum filtre (Şekil 1) kullanılmıştır. Flokülant olarak Praestol 2540 (Solenis), Cyfloc A-150 ve Cyfloc N-100 (Cytec) kullanılmıştır.

2.2. Metot

Deneylerde kullanılmak üzere %0,1 flokülant çözeltileri hazırlanmıştır. Miktara göre flokülant çözeltisi ve pülp numunesi mezürde karıştırılmıştır. Numunelerin karışması için mezürün ağzı kapatılarak 10 kez aşağı yukarı çevrilmiş ve çökelmeye bırakılıp süreye bağlı arayüz yüksekliği ölçülmüştür.

Filtrasyon deneylerinde tesis tkiner çıkışını simüle etmek için %30 katı oranında çalışılmıştır. Çökelme testlerinden elde edilen pülp vakum filtreye beslenmiştir. Vakum filtrede zamana bağlı olarak süzülen su miktarı ölçülmüştür.

Flokülasyon ve filtrasyon testleri doğal pH değeri olarak 7,8 de yapılmıştır.

Tablo 1. Numunenin tane boyut dağılımı

Table 1. Particle size distribution of the sample

Tane Fraksiyonu (μm)	Ağırlık (%)
106-75	4,48
75-53	7,52
53-38	3,24
38-25	5,25
-25	79,51
Toplam	100

Şekil 1. Laboratuvar tip vakum filtre

Figure 1. Laboratory vacuum filter

3. Bulgular ve Tartışma

3.1. Flokülasyon Testleri

Lavvar tesis atıklarının susuzlandırılmasında anyonik flokülant olarak Praestol 2540 ve Cyfloc A-150 non-iyonik flokülant olarak Cyfloc N-100 kullanılmıştır. Deneylerde doğal pH değeri olan 7,8'de çalışılmıştır. Praestol 2540, Cycloc A-150 ve N-100 ile yapılan deneylere ait zamana ve dozaja bağlı çökelme grafikleri sırasıyla Şekil 2, 3 ve 4'de verilmektedir.

Praestol 2540 kullanılarak yapılan deneyler incelendiğinde 100 g/t kullanımdan sonra çökelme hızında anlamlı bir artış gözlemlenmemiştir. Sabit çökelme hızı, grafiğin başlangıcındaki lineer kısımdan hesaplanabilir [8]. 100 g/t ve 200 g/t dozajlardaki çökelme hızları sırasıyla 570 mm/dk ve 592 mm/dk olarak bulunmuştur. Bu nedenle bu flokülant için 100 g/t dozajın yeterli olduğuna karar verilmiştir.

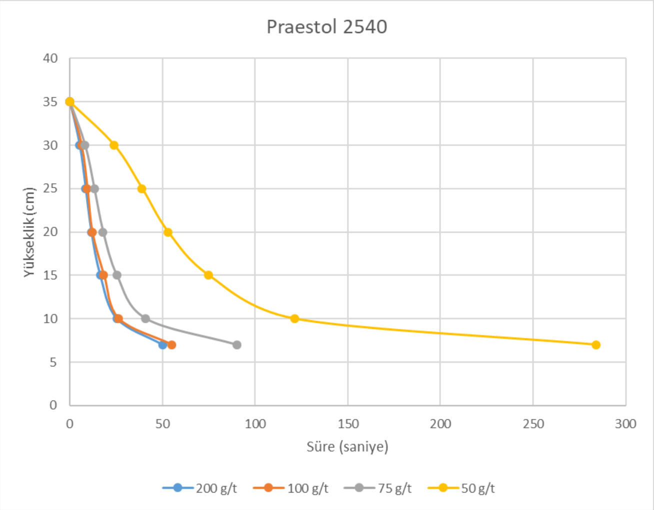

Şekil 2. Praestol 2540 zamana ve dozaja bağlı çökelme eğrileri.

Figure 2. Praestol 2540 settling curves against time and dosage.

Cyfloc A-150 HMW kullanılarak yapılan deneyler incelendiğinde çökelme hızı 200 g/t reaktif miktarına kadar artış göstermektedir. 200 g/t dozajdaki çökelme hızları sırasıyla 545 mm/dk olarak bulunmuştur (Şekil 3).

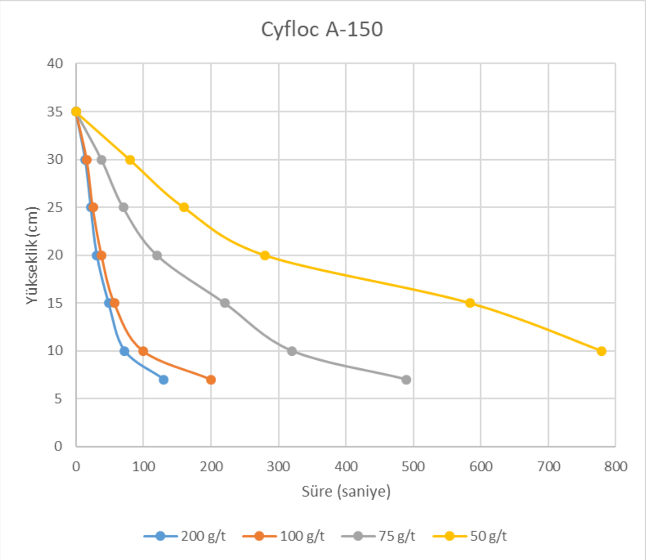

Şekil 3. Cyfloc A-150 zamana ve dozaja bağlı çökelme eğrileri.

Figure 3. Cyfloc A-150 settling curves against time and dosage.

Cyfloc N-100 reaktifine ait çökelme grafiği Şekil 4'de verilmektedir. Reaktif miktarının artmasına rağmen çökelme hızında anlamlı bir artış gözlemlenmemiştir. Çökelme hızı en yüksek 200 g/t dozajda 13 mm/dk olarak elde edilmiştir. Bu değer diğer anyonik reaktiflerle karşılaştırıldığında çok yavaş olduğundan sonraki testlerde kullanılmamıştır.

Taneler ve non-iyonik flokülantlar arasındaki etkileşimler asidik süspansiyonlarda daha güçlü, hidroliz reaksiyonlarından dolayı alkali süspansiyonlarda daha zayıftır. Yüksek pH değerlerinde, non-iyonik flokülantların aktif grupları, bir anyonik yapı oluşturmak üzere kısmen veya tamamen hidrolize olur [9].

Sonuçlar incelendiğinde, Praestol 2540 ve Cyfloc A-150 kullanıldığında daha yüksek çökelme hızlarına ulaşıldığı görülmektedir. Anyonik flokülantlar diğer flokülant türlerine göre daha büyük flok oluşturduğu için daha yüksek çökelme hızlarına sahiptir [5].

Tane yüzey alanının yarısını kaplayacak şekilde eklenen flokülant miktarı, optimum dozaj olarak ifade edilmektedir. Optimum dozajdan daha fazla flokülant eklendiğinde tanelerin yüzeyinde flokülantların tutunabilmesi için hiç boşluk kalmamaktadır. Bu durumda flokülantın taneler arasında köprü kurması engellenmekte ve flokülasyon işlemini olumsuz yönde etkilemektedir [10-12]. Flokülantların pahalı olması ve optimum dozajı aşmaması için deneylerde en fazla 200 g/t reaktif kullanılmıştır.

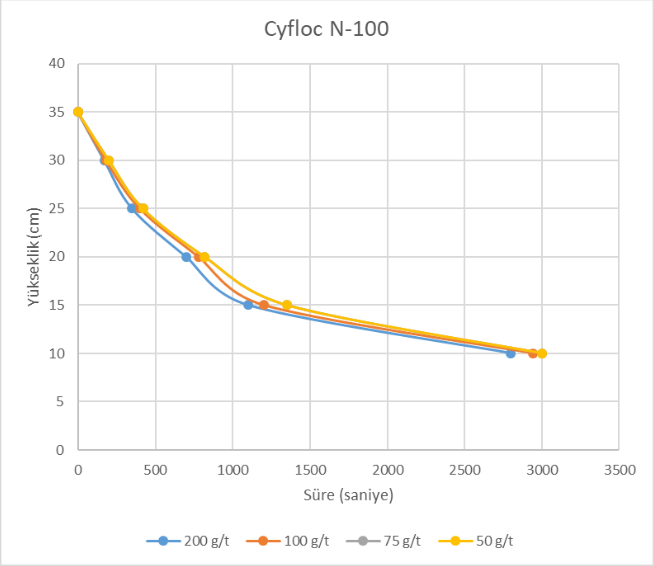

Şekil 4. Cyfloc N-100zamana ve dozaja bağlı çökelme eğrileri.

Figure 4. Cyfloc N-100 settling curves against time and dosage.

3.2. Filtrasyon Testleri

Filtrasyon testleri, flokülasyon testlerinde iyi sonuç veren Praestol 2540 ve Cyfloc A-150 kullanılarak %30 katı oranında yapılmıştır. Flokülantların filtrasyona etkisini gözlemlemek amacıyla reaktif kullanmadan da deney yapılmıştır. Deney sonuçları Şekil 5'de verilmektedir.

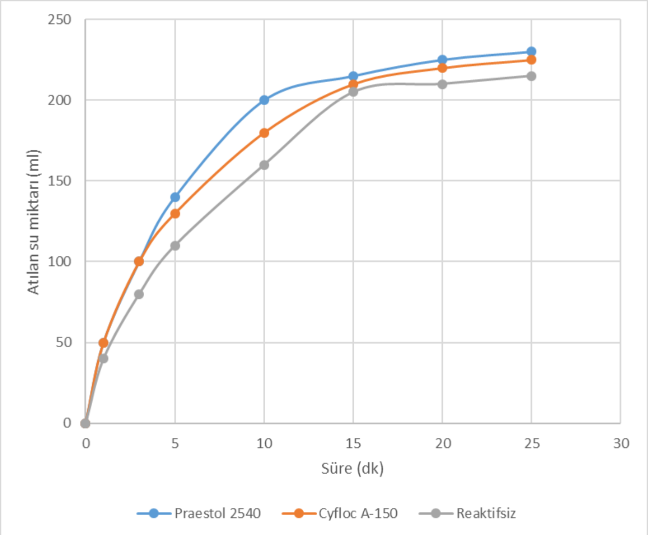

Şekil 5. Zamana ve reaktife bağlı susuzlandırma eğrileri.

Figure 5. Dewatering curves against time and reagent.

Filtrasyon testleri incelendiğinde 200 ml su atıldıktan sonra filtrasyon hızının önemli ölçüde düştüğü gözlemlemektedir. Bu da %50 katı oranına denk gelmektedir. 100 g/t Praestol 2540 ve 200 g/t Cycfloc A-150 kullanıldığında, Praestol 2540'ın daha etkili sonuç verdiği görülmektedir. Ayrıca reaktif kullanılmadan yapılan test ile karşılaştırıldığında, flokülasyon işleminde kullanılan reaktiflerin filtrasyon işlemine de etki ettiği görülmektedir.

Filtreleme işlemi kekin yapısına bağlıdır. Yüzey nemi, uygulanan basınçla uzaklaştırılabilirken, yüksek iç kılcal basınç nedeniyle yüzeye adsorbe olan ve kapiler suyun çıkarılması zordur [13,14]. Tane boyutunun artmasıyla susuzlaştırma verimliliği arttığından filtre kekinin nem içeriğini azaltmak için flokülant kullanılmaktadır [14]. Daha büyük floklar mevcut yüzey alanının azalmasına sebep olmakta ve bu nedenle yüzey suyu miktarı azalmaktadır.

4. Sonuçlar

Bu çalışmada ince boyutlu lavvar artıklarının flokülasyon ve filtrasyon ile susuzlandırılması araştırılmıştır. Sonuçlar incelendiğinde anyonik flokülantların, çökelme hızı ve filtrasyon hızını arttırdığı gözlemlenmiştir. Praestol 2540 ile yapılan deneylerde 100 g/t dozajda 570 mm/dk çökelme hızı ve yaklaşık 10 dk sürede filtrasyon işlemi tamamlanmıştır. Cyclof A-150 ile yapılan deneylerde ise, 200 g/t dozajda 545 mm/dk çökelme hızı ve yaklaşık 13 dk filtrasyon süresi değerleri elde edilmiştir. Bu malzeme için hem daha düşük dozajlarda kullanılması hem de daha etkili olması nedeniyle Praestol 2540'ın daha uygun olduğu belirlenmiştir.

Etik kurul onayı ve çıkar çatışması beyanı

Hazırlanan makalede etik kurul izni alınmasına gerek yoktur. Hazırlanan makalede herhangi bir kişi/kurum ile çıkar çatışması bulunmamaktadır.

Kaynaklar

[1] Hogg, R., 2000. Flocculation and Dewatering. International Journal of Mineral Processing, Cilt. 58, s. 223-236.

[2] Lockhart, N.C., Veal, C.J., 1996. Coal Dewatering: Australian R&D Trends. Coal Preparation, Cilt. 17, s. 5–24. DOI: 10.1080/07349349608905254.

[3] Das, B., Prakash, S., Biswal, S.K., Reddy, P.S.R., 2006. Settling Characteristics of Coal Washery Tailings Using Synthetic Polyelectrolytes with Fine Magnetite. The Journal of the Southern African Institute of Mining and Metallurgy, Cilt. 106, s. 707-716.

[4] Alam, N., Ozdemir, O., Hampton, M.A., Nguyen, A.V., 2011. Dewatering of Coal Plant Tailings: Flocculation Followed by Filtration. Fuel, Cilt. 90, s. 26–35.

[5] Sabah, E., Cengiz, I., 2004. An Evaluation Procedure for Flocculation of Coal Preparation Plant Tailings. Water Research, Cilt. 38, s. 1542–1549.

[6] Sabah, E., Erkan, Z.E., 2006. Interaction Mechanism of Flocculants with Coal Waste Slurry. Fuel, Cilt. 85, s. 350–359.

[7] Nasser, M.S., James, A.E., 2006. The Effect of Polyacrylamide Charge Density and Molecular Weight on the Flocculation and Sedimentation Behaviour of Kaolinite Suspensions. Separation and Purification Technology, Cilt. 52(2), s. 241–252.

[8] Hoşten, Ç., 2010. Cevher Hazırlama ve Zenginleştirme Temel İşlemlerinin Tasarımı. 2. Baskı, ODTÜ Basım İşliği, Ankara, 450s.

[9] Alptekin, A.M., 2006. Doğal Taş Atık Sularının Flokülasyon/Koagülasyon Yöntemiyle Arıtılması. Afyon Kocatepe Üniversitesi, Fen Bilimleri Enstitüsü, Yüksek Lisans Tezi, 77s., Afyonkarahisar.

[10] Somasundaran, P., Das, K.K., 1998. Flocculation and Selective Flocculation – An Overview. In: Innovations in Mineral and Coal Processing, Atak, S., Önal, G., Çelik, M.S. (Eds.), Balkema, Rotterdam, s. 185-203.

[11] Çiftçi, H., Işık, S., 2017. Farklı Anyonik, Katyonik ve Noniyonik Flokülantların İnce Boyutlu Lavvar Tesisi Atıklarının Çökelme Davranışlarına Etkileri. Süleyman Demirel Üniversitesi Fen Bilimleri Enstitüsü Dergisi, Cilt. 21, Sayı. 1, s. 13-19.

[12] Tao, D., Groppo, J.G., Parekh, B.K., 2000. Effects of Vacuum Filtration Parameters on Ultrafine Coal Dewatering. Coal Preparation, Cilt. 21(3), s. 315–335. DOI: 10.1080/07349340008945624.

[13] Selomulya, C., Liao, J.Y.H., Bickert, G., Amal, R., 2006. Micro-Properties of Coal Aggregates: Implications on Hyperbaric Filtration Performance for Coal Dewatering. International Journal of Mineral Processing, Cilt. 80(2–4), s. 189–197.

[14] Tao, D., Parekh, B.K., Liu, J.T., Chen, S., 2003. An Investigation on Dewatering Kinetics of Ultrafine Coal. International Journal of Mineral Processing, Cilt. 70(1–4), s. 235–249.

Dokuz Eylül Üniversitesi Mühendislik Fakültesi Fen ve Mühendislik Dergisi
Dokuz Eylul University Faculty of Engineering Journal of Science and Engineering
Elektronik/Online ISSN: 2547-958X

ARAŞTIRMA MAKALESI / RESEARCH ARTICLE

Vakum Destekli Reçine İnfüzyon Kalıplama ile Kompozit Parça Üretiminde Hava Kaçak Lokasyon Tespiti

Detection of Air Leak Locations in Composite Part Production Using Vacuum Assisted Resin Infusion Molding

Berkay Aydoğan, **Yeliz Pekbey** *

Ege Üniversitesi Mühendislik Fakültesi Makine Mühendisliği, İzmir, Türkiye
Sorumlu Yazar / Corresponding Author *: yeliz.pekbey@ege.edu.tr

Öz

Kompozit parça üretiminde yaygın olarak kullanılan vakum destekli reçine infüzyon kalıplama metodolojisinde, yapıda boşluğa sebebiyet vererek parça kalitesine olumsuz etki eden hava kaçaklarının tespiti ve müdehalesi üretim öncesi veya sırasında çok önemlidir. Kompozit parça içerisine ihtiva etmiş hava boşlukları, endüstriyel uygulamalarda işletmeler için zaman kaybı, yapısal sorunlar ve dolayısıyla maliyet anlamına gelmektedir. Bu çalışmada endüstrideki kaçak tespiti yöntemleri incelenmiş ve hava akış sensörleri ile heterojen geçirgenliğe sahip kompozit parça üretimlerinde kullanılmak üzere bir algoritma geliştirilerek kaçak tespiti üzerine çalışmalar yapılmıştır. Çalışmalarda termal kütle akış ölçerleri kullanılmış olup, Parçacık Sürü Optimizasyonu (PSO) ve çeşitli matematiksel optimizasyon yöntemleri kullanılmıştır. Geliştirilen bu sistem endüstriyel ölçekte kullanılabilecek şekilde tasarlanmış ve doğrudan hat üzerine montaja uygun biçimde testlere tabi tutulmuştur. Yapılan çalışmalar vakum destekli reçine infüzyon kalıplama ile heterojen yapıdaki laminalı kompozit parça üretiminde hava kaçak tespitinin zorluklarını açıkça ortaya koymuş bu zorlukların hangi yaklaşımlarla ortadan kaldırılabileceği konusunda öneriler vermiştir. Çalışma sonucunda homojen yapıdaki laminalı kompozit parça üretiminde %9,2 heterojen yapıdaki laminalı kompozit parça üretiminde %16,5 ortalama hata oranı ile sonuç verebilen bir hava kaçak tespit sistemi geliştirilmiştir.

Anahtar Kelimeler: *Kompozit parça üretimi, Vakum destekli reçine infüzyon kalıplama, Hava kaçak tespiti, PSO, Termal kütle akış ölçer.*

Abstract

In composite part production, particularly using vacuum assisted resin infusion molding methodology, detecting and addressing air leaks that cause voids in the structure and negatively affect part quality is crucial before or during the manufacturing process. Air voids within composite parts lead to time losses, structural issues, and increased costs in industrial applications. This study examines industrial leak detection methods and develops an algorithm using airflow sensors for detecting leaks in composite parts with heterogeneous permeability. The research utilized thermal mass flow meters and applied Particle Swarm Optimization (PSO) along with various mathematical optimization methods. The developed system is designed for industrial-scale use and tested for direct assembly on production lines. The study highlights the challenges of detecting air leaks in the vacuum assited resin infusion of laminated composite parts with heterogeneous structures and provides recommendations on how to overcome these challenges. As a result of the study, a leak detection system was developed, achieving an average error rate of 9.2% for homogeneous laminated composite parts and 16.5% for heterogeneous laminated composite parts.

Keywords: *Composite manufacturing, Vacuum infusion, Air leak detection, Thermal mass flow sensors, PSO, Laminated composites*

EXTENDED ABSTRACT

Introduction

This study focuses on the detection of air leaks in composite parts produced using vacuum assisted resin infuion molding methods, which are critical for maintaining the quality and integrity of the final product. Air leaks can lead to voids and defects, impacting the structural performance of composite materials. The research evaluates current industrial methods and proposes a novel algorithm integrating thermal mass flow sensors and Particle Swarm Optimization (PSO) to accurately identify air leaks during the manufacturing process. The developed system has been validated through rigorous testing and shows promising results, especially in handling the complexities of heterogeneous laminated composites.

In the realm of composite part manufacturing, particularly with vacuum assisted resin infusion molding techniques, air leaks pose significant quality control challenges. These leaks can introduce voids within the composite structure, compromising the mechanical properties and overall integrity of the final product. Detecting and mitigating these leaks during the manufacturing process is crucial to ensuring high-quality outcomes. This research aims to explore existing industrial leak detection methods and develop a sophisticated algorithm that

DOI: https://doi.org/10.21205/deufmd.2025277917

Geliş Tarihi / Received: 30.05.2024
Kabul Tarihi / Accepted: 18.06.2024

utilizes thermal mass flow sensors to enhance the detection accuracy of air leaks in laminated composite parts.

Composite materials produced through vacuum assisted resin infusion molding are widely used in various industries due to their superior mechanical properties and lightweight characteristics. However, the presence of air leaks during the manufacturing process can lead to voids, which compromise the structural integrity of the composite parts. Traditional leak detection methods often fall short in identifying these defects accurately, especially in composites which have heterogeneous permeability lamination. Thus, there is a significant need for a reliable and efficient method to detect air leaks during the manufacturing process.

Materials and Methods

The methodology involves the use of thermal mass flow sensors coupled with PSO, a robust optimization technique, to pinpoint air leaks in composite laminates. Thermal mass flow sensors are employed due to their sensitivity and accuracy in detecting minute changes in airflow, which are indicative of leaks. PSO is an optimization algorithm inspired by the social behavior of birds flocking or fish schooling, and it is utilized to enhance the detection accuracy by optimizing the sensor data interpretation.

The experimental setup included laminated composites made from bi-axial glass fiber fabrics with varying layer densities and incorporated high-permeability polypropylene distribution meshes to simulate industrial conditions. Three different laminate configurations were tested: 2 layers, 10 layers, and 50 layers. Artificial air leaks were introduced using medical needles, creating controlled punctures to test the system's detection capabilities. The performance of the system was evaluated based on its ability to detect these leaks accurately.

Initial algorithmic attempts (MHADG) using fixed airflow values proved inadequate, particularly in regions with high permeability. The MHADG algorithm did not account for variations in airflow over time, which led to inaccuracies. Consequently, the algorithm was refined to account for time-dependent airflow values (ZBADG), enhancing the accuracy by considering the temporal aspect of airflow readings. This approach allowed for a more dynamic and responsive detection system.

Further improvements led to the development of the IZBADG algorithm, which integrated the area under the flow rate curve over time, significantly improving the precision of leak detection. By calculating the area under the curve, the algorithm could better account for variations in airflow that occur due to leaks, providing a more reliable detection method. The IZBADG algorithm was designed to adapt to the specific conditions of each test scenario, making it robust and versatile for different composite configurations.

Results and Discussion

The IZBADG algorithm demonstrated substantial improvements in detecting air leaks within both homogeneous and heterogeneous laminated composites. The average error rates were reduced to 9.2% for homogeneous composites and 16.5% for heterogeneous composites. The presence of distribution meshes and the number of laminate layers were critical factors influencing detection accuracy. The enhanced algorithm effectively minimized these error rates, showcasing its potential for industrial application.

The findings highlight the complexity of air leak detection in vacuum assisted resin infusion molding processes, especially in heterogeneous laminated composites. The integration of thermal mass flow sensors with PSO optimization offers a viable solution for real-time leak detection, significantly improving manufacturing quality and reducing defect-related costs. The study also underscores the importance of sensor placement and algorithmic adjustments to accommodate varying material permeabilities and structural configurations.

The experimental results revealed that the IZBADG algorithm could effectively detect leaks introduced in various laminate configurations. For the 2-layer configuration, the algorithm showed a high degree of accuracy due to the relatively simple structure and low permeability. In the 10-layer configuration, the presence of more layers introduced additional complexity, but the algorithm still maintained a reasonable error rate. The 50-layer configuration posed the most significant challenge due to its high permeability and complexity, yet the algorithm adapted well, demonstrating its robustness.

The presence of high-permeability polypropylene distribution meshes significantly impacted the detection accuracy. These meshes are used to facilitate resin flow during the resin infusion process, but they also introduce additional pathways for air leaks, complicating detection. The IZBADG algorithm's ability to account for these complexities and maintain accuracy highlights its effectiveness and potential for real-world applications.

Conclusion

The conclusion should summarize the main findings of your study and their implications. It should also restate the purpose of your study and the specific research questions or hypotheses that you addressed. Make sure your extended abstract is free of grammatical, spelling, and punctuation errors. An impactful extended abstract will ensure the readability and citation of your paper.

---

1. Giriş

Vakum yardımıyla üretilen kompozit bileşenlerin üretim sürecinde, üretilen parçanın takviye ve matris malzemelerinin istenen oranda birleştirilmesi ve parçanın yüzeyine homojen bir basınç dağılımı oluşturulması için bir vakum folyosu gereklidir. Temel görevi, laminat ve ortam arasında yalıtımsal bir sınır oluşturmaktır. Esnek yapısı ve isostatik basınç prensibi sebebiyle, basınç farkı ile oluşan kuvvetler yüzeye eş oranlı ve yüzeyin normali yönünde etki eder.

Üretimi yapılacak olan parçanın içerisine ihtiva etmiş hava kabarcıkları son ürün mekanik özelliklerini düşürmektedir [1]. Fiber takviyeli kompozit yapılardaki %1,5'luk bir hava içeriğinin kayma mukavemetini %50'ye kadar, kayma modulusünü de %10'a kadar düşürebileceğini belirtmiştir [2]. Frascino ve Zabulon (1994) yaptıkları çalışmalarda karbon takviyeli kompozit yapılarda artan hava içeriğinin yapı içerisinde rijitlik kaybına, dolayısiyle eğilme mukavemetinde ciddi düşüşlere sebebiyet verdiğini belirtmiştir [3]. Frascino ve Zabulon (1994) yaptıkları çalışmalarda kullanılan hava içerikli panellerin hava içerikleri Tablo 1'de, eğilme mukavemeti değerleri de Tablo 2'de verilmektedir. Bu hava kabarcıkları, yapıya, folyo üzerindeki hasarlardan veya folyoyu kalıba yapıştırıp yalıtımı tamamlamakta kullanılan yapıştırıcı bant ile kalıp yüzeyi arasından girebilir. Bu sebeple parçayı dış ortama karşı koruyan bu yalıtımsal sınırın parça kalitesi açısından önemi büyüktür.

Tablo 1. Çalışma yapılan panellerin hava içerikleri [3].

Table 1. Air content of the studied panels [3].

Plaka No	**Numune No**					**Ortalama (%Vv)**
	1	2	3	4	5	
1	1,39	1,28	1,46	1,22	1,33	1,34
2	4,26	4,33	4,34	3,83	4,32	4,22
3	5,41	5,78	5,37	5,12	4,87	5,31
4	5,81	6,02	5,69	6,06	5,74	5,86

Tablo 2. Çalışma yapılan panellerin eğilme mukavemetleri [3].

Table 2. Flexural strengths of the studied panels [3].

Plaka No	**Eğilme Mukavemeti (MPa)**					**Ortalama**
	1	2	3	4	5	
1	1403	1451	1457	1416	1388	1423
2	1319	1360	1260	1274	1357	1314
3	1190	1219	1280	1209	1177	1215
4	1167	1257	1138	1263	-	1206

Vakum paketleme üretim yöntemlerinde çoğunlukla kullanılan malzemeler Şekil 1'de gösterilmiştir. Vakum folyosu, yalıtım bandı kaçak kaynağını oluşturabilmeleri, emme kumaşı ise bir hava iletim katmanı görevi görmesi sebebiyle kaçak tespitinde büyük önem taşımaktadırlar.

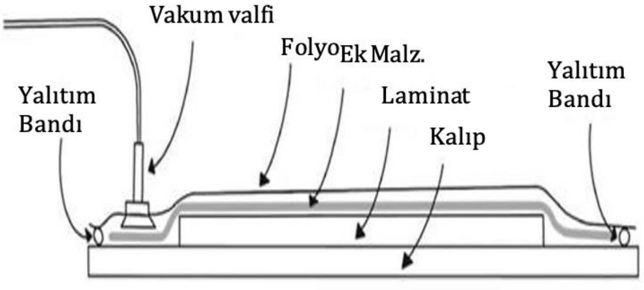

Şekil 1. Vakum paketleme şematiği [4,5].

Figure 1. Vacuum packing schematic [4,5].

Vakumlu paketleme üretim yöntemlerinde uygulama yüksek oranda el işçiliği ile yapılmaktadır. Yalıtım bantları ile yapıştırılan vakum folyosu üzerine yeteri kadar baskı uygulamama, folyo çekilirken meydana gelecek kırışıklıklar, folyo yüzeyine delici/kesici malzemelerle baskı uygulanması, kalıp yüzeyinde meydana gelen mikro çatlaklar gibi sebeplerden dolayı laminasyon içerisine hava kaçakları olmaktadır. Bu hava kaçakları zamanında tespit edilip ilgili tamir veya düzeltmeler uygulanmaz ise mekanik mukavemet düşüşüne sebebiyet vererek kalitesizlik maliyetini ve doğal olarak atık miktarını artırır. Bu sebeplerden dolayı bir kaçak tespiti sisteminin vakumlu paketleme ile kompozit parça üretimi sırasında oluşturulması çok büyük önem arz etmektedir.

Vakumlu paketleme ile kompozit parça üretiminde ticarileşmiş kaçak tespit sistemleri ticari olmayan araştırma veya patent aşamasında olan kaçak tespit sistemlerine göre daha azdır. Mikro ölçekte hava kaçak tespiti için maliyetler artmakta ve tespit süresi ise azalmaktadır. Meskell ve Eret [6] geleneksel olarak kullanılan ultrasonic mikrofonlu detektörler ve basınç düşümü testini, hassas ultrasonik mikrofon düzeneği kullanarak geliştirmiş ve ses frekanslarını optimize ederek mikro ölçekteki sızıntı şeklindeki hava kaçaklarını tespit edebilmiştir. Bu yöntem ile vakumlu paketleme ile üretim yapılacak bir kalıpta mobil bir ekipmanda harcanacak zaman kaybının önüne geçmek mümkündür. Ancak fabrika endüstriyel ölçekte düşünüldüğünde ortamdaki gürültü bu yöntemin tarama alanı veya hassasiyetine olumsuz etki edecektir. Haschenburger ve Heim 'in [7] testlerini gerçekleştirdiği hibrit bir yapısı olan vakum kaçak folyosu ile kaçak tespiti yöntemi, hızlı tepki süresi ile yine testini yaptıkları mürekkep yöntemi ve gaz detektörü yönteminin önüne geçmektedir. Ancak büyük çaplı vakumlu paketleme uygulamalarında yüksek maliyet ve zaman kaybına sebebiyet verecektir.

Convergent firması, hava kaçak tespitinde Kütle akış sensörlerini, kaçak tespiti algoritmasıyla kullanarak hızlı ve doğru tespiti sağlamıştır [8]. Bu yöntemde yüksek maliyetli bir çözümdür ancak hassas ve hızlı hava kaçak tespiti yapabilmektedir. Haschenburger vd. [4] bu yaklaşımı geliştirerek sisteme termal kameraların entegresi ve trilateration yönteminin uygulanmasıyla kaçak lokasyonunun tespit hassasiyetini artırmıştır. Petricevic [9] piezoelektrik sensörler kullanarak vakum folyosunun basınç değişimini incelemiştir. Bu basınç değişimi sırasında üzerindeki sinyal değişiminin tespit ederek kaçak tespitini gerçekleştirmiş ve daha basit bir düzenek ile prototip denemelerini gerçekleştirmiştir.

Kızılötesi termografi yöntemi ile de kaçak tespiti yapılabilmektedir. Bu metot Joule-Thompson etkisine dayanmaktadır ve Alman Havacılık ve Uzay Merkezi tarafından patentlenmiştir [4,10]. Kaçak tespit folyosu ile de kaçak tespiti yapılabilmektedir. Bu metotta vakum folyosunun altında, içerisinde oksijene tepki veren ve gaz geçirgenliği olan bir membran malzemesi bulunmaktadır. Hava kaçağı meydana geldiğinde ve bu malzeme oksijen ile temasa geçtiğinde görünüşü değişmekte ve hava kaçakları görsel olarak tespit edilebilmektedir [11].

Vakumlu paketleme uygulamaları için maliyet, çevrim süresi, ölçüm hassasiyeti hesaba katıldığında hava akış sensörü ile kaçak tespit sistemlerinin bu üretim metoduna daha verimli sonuçlar verebileceği öngörülmüştür. İlgili metotlar detaylıca incelenmiş olup, Tablo 3'te maliyet, hassasiyet ve süre parametreleri hesaba katılarak karşılaştırmalı olarak verilmiştir.

Bu çalışmada, vakum destekli reçine infüzyon kalıplama ile kompozit parça üretiminde oluşabilecek hava kaçaklarının lokasyonunu tespit edebilecek bir algoritma geliştirilerek hava kaçak tespit sistemi oluşturulmuştur. Kompozit parça üretiminde yaygın olarak kullanılan vakumlu paketleme metodolojisinde, yapıda boşluğa sebebiyet vererek parça kalitesine olumsuz etki eden hava kaçaklarının tespiti ve müdahalesi için üretim öncesi veya üretim sırasında sırasında bir algoritma geliştirilmiştir [12]. Bu amaca yönelik olarak endüstrideki kaçak tespiti yöntemleri incelenmiş ve bir rüzgâr türbin kanadı imalatında kullanılan cam elyaf kat sayıları ve infüzyon planları referans alınmıştır. Geliştirilen algoritma ile Parçacık Sürü Optimizasyonu (PSO) ve çeşitli matematiksel optimizasyon yöntemleri kullanılarak kaçak tespiti gerçekleştirilmiştir. Elde edilen sonuçlar endüstriyel ölçekte kullanılabilecek şekilde tasarlanmış ve doğrudan hat üzerine montaja uygun biçimde testlere tabi tutularak sonuçlar deneysel olarak kıyaslanmıştır.

Tablo 3. Kaçak tespit sistemlerinin büyük çaplı vakum destekli reçine infüzyon kalıplama üretimlerine uygulanabilirliğinin karşılaştırılması.

Table 3. Comparison of the applicability of leak detection systems to large scale vacuum assisted resin infusion moulding productions.

Kaçak Tespit Sistemi	Tahmini Yatırım Maliyeti	Tarama Alanı	Tespit Süresi
Mobil UT Mikrofon ve Basınç Düşümü Testi	Düşük	Düşük	Yüksek
Kızılötesi Termografi [4]	Orta	Orta	Düşük
Kaçak Tespit Folyosu [8]	Yüksek	Yüksek	Orta
UT Mikrofon Düzeneği [9]	Orta	Düşük	Düşük
Piezoelektrik Sensör Sistemi [10]	Orta	Orta	Düşük
Özel Mürekkep ile Tespit [7]	Düşük	Düşük	Yüksek
Gaz Detektörü ile Tespit [7]	Orta	Orta	Orta
Kütle Akış Hızı Sensörleri ile Tespit [11]	Orta	Yüksek	Düşük
Termal Kamera ve Akış Hızı Sensör Sistemi [4]	Yüksek	Yüksek	Düşük

Düşük: Maliyet <10k $, Tarama alanı <5m^2, Tespit süresi >20 dk. Orta: 10k $<Maliyet<100k $, 5m^2<Tarama alanı<50 m^2, 10dk<Tespit süresi<20dk. Yüksek: 100k $<Maliyet, Tarama alanı>50 m^2, 10dk>Tespit süresi

2. Materyal ve Metot

Yapılacak testlerde bir kompozit parça olarak kabul edilen rüzgâr türbin kanatlarının vakum destekli reçine infüzyon kalıplama yöntemi ile imalatı referans alınmıştır. Bu bağlamda rüzgâr türbin kanatlarında kullanılan biaksiyal 1000 g/m^2 cam fiber kumaşlar test düzeneklerinde 2,10 ve 50 katman olarak ayrı paketlerde test edilmesi kararlaştırılmıştır. Ek olarak yüksek permabiliteli ayırıcı olarak ise elmas konfigürasyonlu polipropilen dağıtıcı file kullanılmıştır.

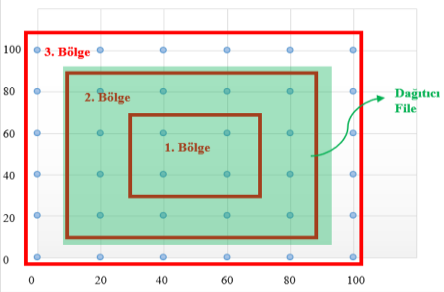

Şekil 2. Test düzeneğinde bölgelerin gösterimi.

Figure 2. Representation of the zones in the test setup.

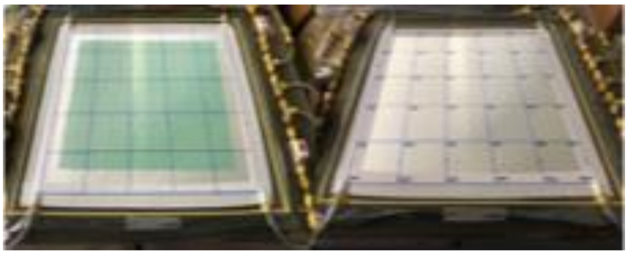

Şekil 3. Dağıtıcı fileli (sol) ve dağıtıcı filesiz (sağ) laminalı görseller.

Figure 3. Laminated images with (left) and without (right) diffusing mesh.

Her bir test konfigürasyonunda, paketlerde oluşacak bir hava kaçağını simüle etmek için 0,8 mm çaplı medikal iğneler kullanılmış olup 1000x1000 mm'lik bir laminada toplamda Şekil 2'de gösterildiği gibi 36 adet delik açılması kararlaştırılmıştır. Vakum destekli reçine infüzyon kalıplama ile kompozit parça üretiminde vakum kanallarına olası matris malzeme (testlerde epoksi reçine kullanılmıştır) kaçağını engellemek adına reçine tuzakları konulur. Yapılan testlerde hava kanalları iki adet reçine tuzağına bağlanmış ve bu tuzaklar ise vakum pompasına bağlanmıştır.

Şekil 3'te görüldüğü üzere paketlerin dört köşesine yerleştirilen akış ölçerler ile deney seti hazırlanmıştır. Dağıtıcı fileli pakette dağıtıcı filenin pozisyonu kenar kısımlardan(kumaş bitiş köşesi) 100 mm uzaklıkta(paket merkezine doğru) olacak şekilde belirlenmiştir. Bir rüzgâr türbin kanadının üretimi sırasında uygulanan infüzyon planları incelendiğinde kabukların ön ve arka keplerine kadar pozisyonlandırılan dağıtıcı fileler, kalıbın bitiş noktalarından ortalama 100 mm boşluk bırakılarak ve paket içerisine vakumu iletebilmek için kenar hatlar boyunca yerleştirilen geçirgenlik seviyesi yüksek cam elyaf emme kumaşları yerleştirilmektedir. Deney çalışmasında bu durum dikkate alınmış ve benzer durum 1000x1000 mm'lik deney çalışmalarında simüle edilmiştir.

Kurulan sistem, her bir sensördeki akış hızları üzerinde hortum uzunluklarının etkisini en aza indirmek için eşit uzunlukta hortumlar kullanarak ve oluşabilecek sensör okuma sapmalarını en aza indirmek için Şekil 4'te görülebileceği şekilde tasarlanmıştır.

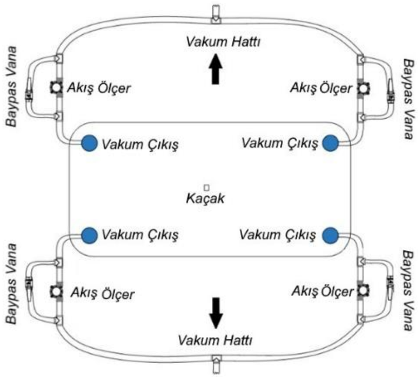

Şekil 4. Kurulan sistemin şeması.

Figure 4. Schematic of the installed system.

Sistemde her sensör vakum hattı girişinin dört adet baypas vana hattı mevcuttur. Bu hatlar her çalışma öncesinde sensör okumalarını eşitlemek(sıfırlamak) için kullanılmıştır. Kaçak lokasyonunu tespit edecek hesaplama algoritması parçacık sürü optimizasyonu (PSO) olarak belirlenmiş ve kaynak koda yazılmıştır.

3. Bulgular ve Tartışma

Bu bölümde vakum destekli reçine infüzyon kalıplama ile kompozit parça üretiminde oluşabilecek hava kaçaklarının lokasyonunu tespit edebilecek bir algoritma geliştirilerek hava kaçak tespit sistemi oluşturulmuştur. Bu algoritma test sonuçları ile yakınsayıp yakınsamadığı belirlenmiştir. Bu bölümde 2, 10 ve 50 katlı paketlerde BX1000 dağıtıcı fileli ve filesiz test sonuçlarından kaçak tespit dağılımı, mutlak hava akış, zamana bağlı akış, iyileştirilmiş zamana bağlı değerlerine göre kaçak tespit dağılımı anlatılacaktır. Ayrıca, kumaş kat sayısının ve dağıtıcı filenin yapılmış algoritma etkinliği üzerindeki etkisi de tartışılacaktır.

3.1 Mutlak hava akış değerlerine göre (MHADG) yapılan çalışmalar

Bu çalışmada vakum destekli reçine infüzyon kalıplama ile kompozit parça üretiminde oluşabilecek hava kaçaklarının lokasyonunu tespit edebilecek bir algoritma geliştirilerek hava kaçak tespit sistemi oluşturulmuştur. Bu algoritma test sonuçları ile yakınsayıp yakınsamadığı belirlenmiştir. Bu bölümde, 2, 10 ve 50 katlı paketlerde BX1000 dağıtıcı fileli ve filesiz test sonuçlarından kaçak tespit dağılımı, mutlak hava akış, zamana bağlı akış, iyileştirilmiş zamana bağlı değerlerine göre kaçak tespit dağılımı anlatılacaktır. Ayrıca, kumaş kat sayısının ve dağıtıcı filenin yapılmış algoritma etkinliği üzerindeki etkisi de değerlendirilecektir.

Bu çalışmada amaç fonksiyonu minimize edilecek şekilde belirlenmiştir. Amaç fonksiyonunun hazırlanması, optimizasyon problemi kurulumunun kritik bir parçasıdır. Ana varsayım, havanın en yakın vakum portuna gitmesiydi. Bunu formüle etmek için, her bir kaçak konumu ile her bir ilgili vakum portundan geçen akış arasındaki mesafe çarpılarak hesaplanır. Ardından, tüm bu değerler bir kümede toplanır. Mesafe arttıkça, akış hızı azalır. Bunlar ters orantılıdır. Bu değer, birçok nedenden dolayı öngörülemeyeceğinden (kaçak deliği boyutu, paket içindeki basınç, kaçak sayısı vb.) elde edilen mesafe ve akış hızı çarpımı kümesinin standart sapması olarak hesaplanır.

$$\Phi = StdDev\left\{\sqrt{(X_i - X_l)^2 + (Y_i - Y_l)^2}F_i \middle| i = 1, n\right\} \qquad (1)$$

Denklem 1, Φ amaç fonksiyonunu ifade etmektedir. X_i,(i). portun x koordinatını; Y_i, (i). portun y koordinatını; X_l, hava kaçağının x koordinatını; Y_l, hava kaçağının y koordinatını temsil eder. F_i ise (i). porttaki hava akış hızını, n ise toplam akış ölçer sayısını belirtir. Bu parametreler, hava kaçaklarının en yakın vakum portuna olan uzaklıklarını ve portlardaki hava akış hızlarını hesaplamak için kullanılır.

Deney seti 1000x1000 mm lik bir alanda dağıtıcı fileli ve dağıtıcı filesiz olarak 2,10 ve 50 kat cam elyaflı paketler olmak üzere toplam 6 adet yapılmıştır. Paket vakum folyosu ile yalıtılmış ve vakum pompası çalıştırılmıştır. Paket full basınç seviyesine ulaştığında sisteme bağlanan hava akış sensörleri baypas hatları yardımı ile aynı seviyeye(kalibrasyon) getirilmiştir. Her bir testte 36 adet 0,8 mm çaplı yapay kaçak deliği oluşturulmuş ve bu delik koordinatları kaydedilmiştir. Sırasıyla her bir delik lokasyonundan delikler açılmış sensörlerden alınan veriler kaydedilmiştir. Bu esnada, oluşturulan arayüz üzerinden de algoritmanın kaçağı tespit ettiği lokasyon kontrol edilmiştir. Her açılan delik sonrası veri alımı tamamlandıktan sonra delik macun ile kapatılıp bir sonraki delikte aynı işlem tekrarlanmıştır.

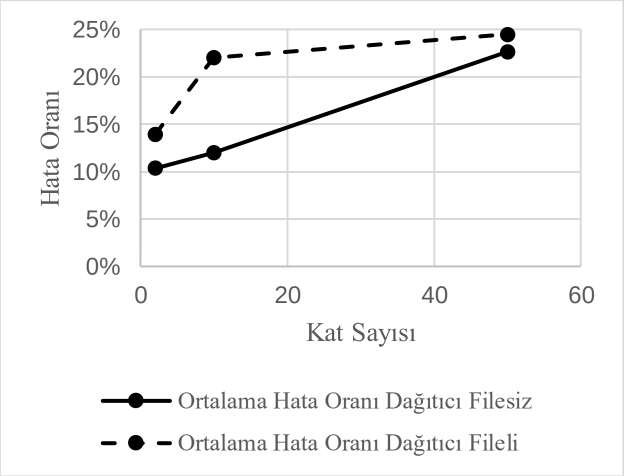

Şekil 5. Kumaş katı sayısının ve dağıtıcı filenin MHADG yapılmış algoritma etkinliği üzerindeki etkisi.

Figure 5. The effect of the number of fabric solids and dispersive mesh on the efficiency of the MHADG algorithm.

Şekil 5 incelendiğinde mutlak hava akış değerleriyle yapılmış algoritmanın 2, 10 ve 50 katlık paketlerde kaçak tespit hata oranı kapsamında artan bir eğilim göstermektedir. Bu artış, 50 katlık laminasyonlarda özellikle dağıtıcı filesiz yani geçirgenlik homojenliği bulunan paketlerde daha fazla olarak gözükmektedir. Heterojen geçirgenliğe sahip yani dağıtıcı fileli paketlerde 10 kattan 50 kata geçişte dikkate değer bir değişkenlik bulunamamıştır. 2 ve 50 katlı paketlerde dağıtıcı filenin etkisi 10 katlı paketlere göre daha azdır. Bu durum paket içerisindeki cam elyaf yoğunluğunun çok az veya çok fazla olmasının toplam paket geçirgenliği üzerindeki etkisini göstermektedir.

Tablo 4. Katsayısı ve dağıtıcı file varlığına göre MHADG testlerden elde edilen hata oranları.

Table 4. Error rates obtained from MHADG tests according to the coefficient and the presence of dispersive mesh.

BX1000 Kat Sayısı	Ortalama Hata Oranı (%)	
	Dağıtıcı Filesiz	Dağıtıcı Fileli
2	10,33	13,92
10	11,97	22,03
50	22,64	24,49
Ortalama (%)	14,98	20,14

Tablo 4'teki sonuçlara göre, PSO algoritması ve hava akış sensörleri kullanılarak tasarlanmış bir kaçak tespit sisteminin kaçak tespitini dağıtıcı filesiz bir laminada(homojen) mutlak hava akış değerleri kullanılarak ortalama (2,10 ve 50 katlık çalışma ortalaması) %15, dağıtıcı fileli bir laminada ortalama (2,10 ve 50 katlık çalışma ortalaması) %20,1 hata oranıyla tespit edebilmiştir. Ek olarak kalınlık artışının hava kaçağı durumunda ortalama hata oranını olumsuz etkilediği sonucuna varılabilir. Ayrıca, dağıtıcı filenin varlığı geçirgenlik değerini değiştirdiği için bir diğer hata oranına olumsuz etki eden parametre olarak değerlendirilebilir.

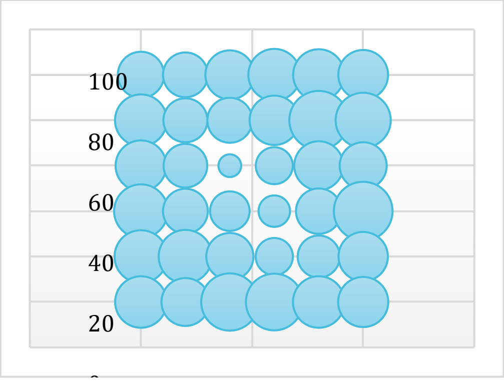

Şekil 6. MHADG Yapılan Çalışmanın Ortalama Hata Oranı Dağılımı.

Figure 6. MHADG average error rate distribution of this study.

Hava akış sensörleriyle mutlak akış değerleri analiz edildiğinde, bir dağıtıcı filenin varlığı, bu alanın merkezinde hatanın azaldığını, merkezden uzaklaşıldıkça hata oranının yükseldiğini göstermiştir. Geçirgenlik seviyesi çok daha yüksek bu ağsı yapının paket içerisine giren havayı kendi üzerinde eşit şekilde dağıttığı tespit edilmiştir. Bu durumun geçirgenliği yüksek materyaller üzerinde hava kaçak lokasyon tespitini zorlaştırdığı açıktır. Şekil 6 incelendiğinde 1. bölgede (merkez) ortalama hata oranının düştüğü, 2. ve 3. bölgelerde arttığı görülebilir. Yapılan değerlendirme sonucunda sensörlerden mutlak değerler yerine zamana bağlı verilerin kullanılması uygun görülmüştür.

3.2 Zamana bağlı akış değerlerine göre (ZBADG) yapılan çalışmalar

Bir önceki test çalışmalarından elde edilen veriler değerlendirilmiş ve hava akış sensörlerinin kabiliyetleri de göz önüne alınarak algoritma güncellenmiştir. Güncellenen algoritmada akış sensörlerinden saniyede 1 kez bir veri alma frekansında hava akışı bilgisi alınmış ve çalıştırılan kodda hava kaçak lokasyonu tespiti yapılmıştır.

MHADG yapılan çalışmada sabitlenen hava akış değerleri algoritmada kullanılmıştı. MHDAG yapılan çalışmada sabitlenen akış değerleri özellikle geçirgenlik seviyesi çok yüksek olan dağıtıcı file alanı üzerinden yüksek hata oranı vermiştir. Bu durumun önüne geçmek ve hata oranını düşürmek için sensörlere gelen hava akışının ne zaman geldiği de algoritma tarafından kaydedilmiş ve zamana bağlı olarak elde edilen akış değerleri kaçak lokasyonunu bulmak için kullanılmıştır. Akış değerleri stabil hale geldiğinden manuel olarak kayıtlar durdurulmuştur. Veri akışı takip edilerek kontrollü bir şekilde deney gerçekleştirilmiştir.

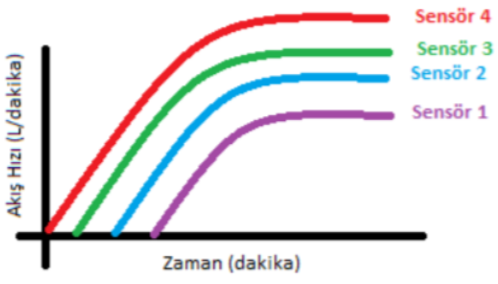

Şekil 7. Zamana bağlı akış değerlerine göre sensörlerin ayrımı.

Figure 7. Separation of sensors according to time-dependent flow values

Şekil 7'de görülebileceği gibi dört adet sensöre farklı zamanlarda gelen akış değerleri aralarında bir fark yaratacak ve amaç fonksiyonuna etkisi olacaktır.

$$\phi = \left\{ \sqrt{(X_i - X_l)^2 + (Y_i - Y_l)^2} \Delta t_i \middle| i = 1, n \right\} \qquad (2)$$

Denklem 2'de görülebileceği gibi zamanın etkisi amaç fonksiyonuna Δt_i olarak eklenmiştir.

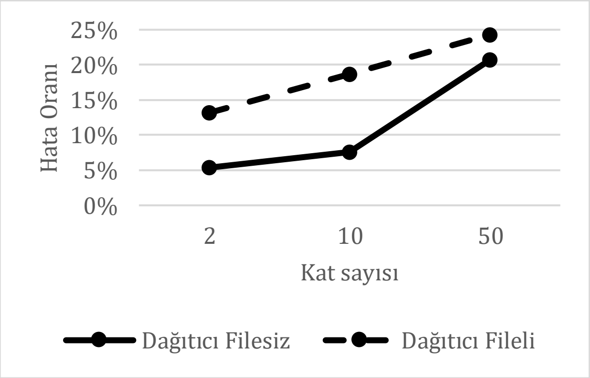

Şekil 8. Kumaş katı sayısının ve dağıtıcı filenin ZBADG yapılmış algoritma etkinliği üzerindeki etkisi.

Figure 8. The effect of the number of fabric solids and dispersive mesh on the efficiency of the ZBADG algorithm.

Şekil 8 incelendiğinde, zamana bağlı hava akış değerleriyle yapılmış algoritmanın 2, 10 ve 50 katlık paketlerde kaçak tespit hata oranı artan bir eğilim göstermektedir. Heterojen geçirgenliğe sahip yani dağıtıcı fileli paketlerde 2 kattan 10 kata geçişte %42, 10 kattan 50 kata geçişte hata oranı %30 artmıştır. 50 katlı paketlerde dağıtıcı filenin etkisi diğer paketlere göre çok daha azdır. Bu durum MHADG çalışmasındaki gibi paket içerisindeki cam elyaf yoğunluğunun çok fazla olmasının total paket geçirgenliği üzerindeki etkisini göstermektedir.

Tablo 5. Katsayısı ve dağıtıcı file varlığına göre ZBADG testlerden elde edilen hata oranları.

Table 5. Error rates obtained from ZBADG tests according to the coefficient and the presence of dispersive mesh.

BX1000 Kat Sayısı	**Ortalama Hata Oranı (%)**	
	Dağıtıcı Filesiz	**Dağıtıcı Fileli**
2	5,36	13,17
10	7,63	18,70
50	20,71	24,30
Ortalama (%)	11,24	18,72

Tablo 5'teki sonuçlara göre, PSO algoritması ve hava akış sensörleri kullanılarak tasarlanmış bir kaçak tespit sisteminin kaçak tespitini dağıtıcı filesiz bir laminada(homojen) zamana bağlı akış değerleri kullanılarak ortalama (2,10 ve 50 katlık çalışma ortalaması) %11,2, dağıtıcı fileli bir laminada ortalama (2,10 ve 50 katlık çalışma ortalaması) %18,7 hata oranıyla tespit edebilmiştir. Bir önceki mutlak hava akış değerlerine göre yapılan çalışmaya göre dağıtıcı filesiz paketlerde ortalama(2,10 ve 50 katlık çalışma ortalaması) hata oranında %3,8 dağıtıcı fileli paketlerde ortalama hata oranında%1,4 düşüş yakalanmıştır. Ek olarak kalınlık artışının hava kaçağı durumunda ortalama hata oranını olumsuz etkilediği sonucuna tekrar varılabilir. Dağıtıcı filenin varlığı geçirgenlik değerini değiştirdiği için bir diğer hata oranına olumsuz etki eden parametre olarak değerlendirilebilir. Bu durum, algoritmanın ilk varsayımını (kaçak yoluyla hava, en yakın vakum portlarına daha fazla akar) ihlal edeceği için algoritmanın tahmininde hata oluşacaktır.

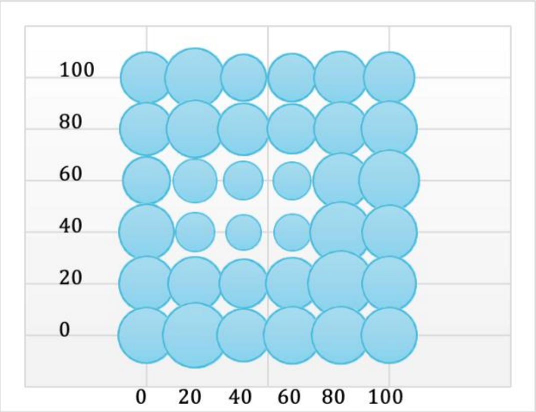

Şekil 9. ZBADG Yapılan Çalışmanın Ortalama Hata Oranı Dağılımı.

Figure 9. Average error rate distribution of the ZBADG study.

Hava akış sensörleriyle zamana bağlı akış değerleri analiz edildiğinde bir dağıtıcı filenin varlığı, bu alanın merkezinde hatanın azaldığını, merkezden uzaklaşıldıkça hata oranının yükseldiğini tekrar göstermiştir. Geçirgenlik seviyesi çok daha kabiliyetleri de göz önüne alınarak algoritma tekrar güncellenmiştir. Güncellenen algoritmada akış sensörlerinden saniyede 1 kez bir veri alma frekansında hava akışı bilgisi alınmış ve bu veriler veri akışı grafiğinin altında kalan alan hesaba katılarak yani belirli bir veri alım süresi sonunda integral değerlerinin algoritmada çalıştırılması amaçlanmıştır. Çalıştırılan kodda hava kaçak lokasyonu tespiti yapılmıştır.

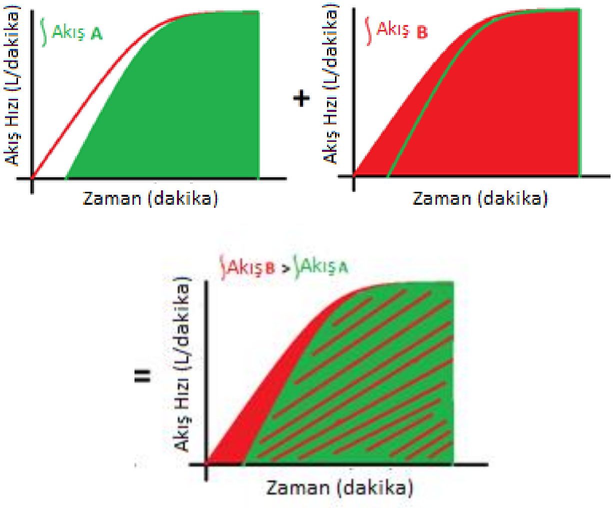

Şekil 10. İyileştirilmiş zamana bağlı akış değerlerine göre hesaplama yapan algoritma değişikliği.

Figure 10. Modification of the algorithm calculating according to the optimised time-dependent flow values.

MHADG yapılan çalışmada sabitlenen hava akış değeleri, ZBADG yapılan çalışmada ise sensörlere gelen ilk akış zamanı algoritmada kullanılmıştı. Yüksek geçirgenliğe sahip malzemeler (dağıtıcı file gibi) tüm akışların benzer değerlere yakınsamasına neden olmasına rağmen, sensörlere giden akışın başlangıç zamanı ve akışın yükselme hızı farklıdır. Akış hızının integral değeri hesaplandığında, benzer stabil değere sahip olan iki akış sensörünün birbirleri arasındaki fark ayırt edilebilir. Şekil 10'da görülebileceği üzere iki farklı zamanda ve eğimde hareket eden hava akışı eğimin altında kalan alanın algoritmaya dahil edilmesi ile daha düşük hatalı sonuç verecektir. Şekil 10'da Akış B'nin, Akış A'dan daha fazla alana sahip olduğu görülmektedir. Bu durumda algoritma B akışının ilgili sensöre daha yakın olduğunu hesaplayacaktır.

$$\phi = \left\{\sqrt{(X_i - X_l)^2 + (Y_i - Y_l)^2} \int F_i \,\middle|\, i = 1, n\right\} \qquad (3)$$

Denklem 3'te görülebileceği gibi akış değerlerinin oluşturduğu eğimin altında kalan alanlar amaç fonksiyonuna $\int F_i$ olarak eklenmiştir.

Veri akışını otomatik olarak kayıt altına alıp manuel işlemi engellemesi adına algoritmada son on akış değerinin standart sapmasının belirli bir değerin (algoritmada 1 değeri kullanılmıştır) altına inmesi durumu limit olarak belirlenmiştir.

$$\delta = \sqrt{\sum (Q_i - \mu)^2 / N} \qquad (4)$$

Denklem 4'de Q_i (i). gözlemdeki akış değerini, μ ortalama akış değerini(tüm gözlemlerin ortalaması) ve N gözlem sayısını göstermektedir. Elde edilen grafikler incelendiğinde standart sapma yaklaşımının verimli sonuçlar verdiği görülmüştür.

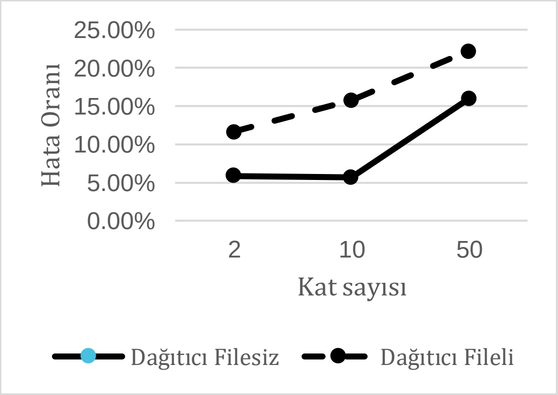

Şekil 11. Kumaş katı sayısının ve dağıtıcı filenin İZBADG yapılmış algoritma etkinliği üzerindeki etkisi.

Figure 11. The effect of the number of fabric solids and dispersive net on the efficiency of the IZBADG algorithm.

Şekil 11 incelendiğinde iyileştirilmiş zamana bağlı hava akış değerleriyle yapılmış algoritmanın 2, 10 ve 50 katlık paketlerde kaçak tespit hata oranı artan bir eğilim göstermektedir. Heterojen geçirgenliğe sahip yani dağıtıcı fileli paketlerde 2 kattan 10 kata geçişte hata oranı %35, 10 kattan 50 kata geçişte hata oranı %41 artmıştır. 50 katlı paketlerde dağıtıcı filenin etkisi diğer paketlere göre çok daha fazladır. Bu durum yine MHADG ve ZBADG yapılan çalışmalarda olduğu gibi paket içerisindeki cam elyaf yoğunluğunun çok fazla olmasının total paket geçirgenliği üzerindeki etkisini göstermektedir.

Tablo 6'daki sonuçlara göre, PSO algoritması ve hava akış sensörleri kullanılarak tasarlanmış bir kaçak tespit sisteminin kaçak tespitini dağıtıcı filesiz bir laminada(homojen) iyileştirilmiş zamana bağlı akış değerleri kullanılarak ortalama (2,10 ve 50 katlık çalışma ortalaması) %9,2, dağıtıcı fileli bir laminada ortalama (2,10 ve 50 katlık çalışma ortalaması) %16,6 hata oranıyla tespit edebilmiştir. Bir önceki zamana bağlı hava akış değerlerine göre yapılan çalışmaya göre dağıtıcı filesiz paketlerde ortalama (2,10 ve 50 katlık çalışma ortalaması) hata oranında %2, dağıtıcı fileli paketlerde ortalama hata oranında %2,2 düşüş yakalanmıştır.

Tablo 6. Katsayısı ve dağıtıcı file varlığına göre İZBADG testlerden elde edilen hata oranları.

Table 6. Error rates obtained from IZBADG tests according to the coefficient and the presence of dispersive mesh.

BX1000 Kat Sayısı	Ortalama Hata Oranı (%)	
	Dağıtıcı Filesiz	Dağıtıcı Fileli
2	5,84	11,67
10	5,67	15,74
50	15,96	22,23
Ortalama (%)	9,16	16,55

Ek olarak kalınlık artışının hava kaçağı durumunda ortalama hata oranını olumsuz etkilediği sonucuna tekrar varılabilir. Dağıtıcı filenin varlığı geçirgenlik değerini değiştirdiği için bir diğer hata oranına olumsuz etki eden parametre olarak değerlendirilebilir. Bu durum, algoritmanın ilk varsayımını (kaçak yoluyla hava, en yakın vakum portlarına daha fazla akar) ihlal edeceği için algoritmanın tahmininde hata oluşacaktır.

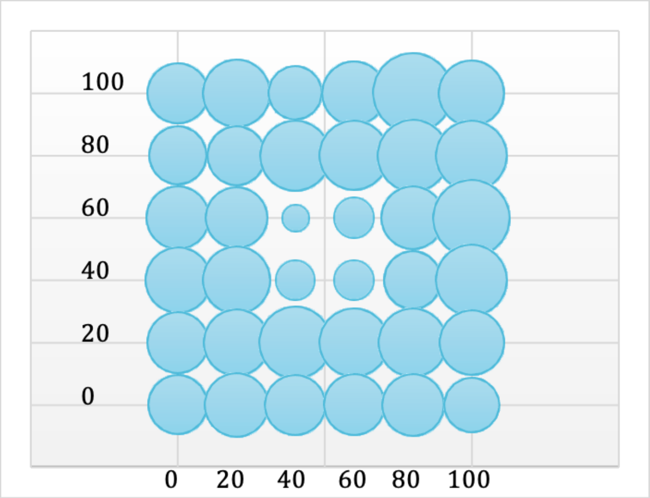

Şekil 12. İyileştirilmiş zamana bağlı akış değerlerine göre Yapılan Çalışmanın Ortalama Hata Oranı Dağılımı.

Figure 12. Average error rate distribution of the study according to the optimised time-dependent flow values.

Hava akış sensörleriyle iyileştirilmiş zamana bağlı akış değerleri analiz edildiğinde, bir dağıtıcı filenin varlığı, yine MHADG ve ZBADG yapılan çalışmalarda olduğu gibi bu alanın merkezinde hatanın azaldığını, merkezden uzaklaşıldıkça hata oranının yükseldiğini göstermiştir. Geçirgenlik seviyesi çok daha yüksek bu ağsı yapının paket içerisine giren havayı kendi üzerinde eşit şekilde dağıttığı tespit edilmiştir. Bu durumun geçirgenliği yüksek materyaller üzerinde hava kaçak lokasyon tespitini zorlaştırdığı açıktır. Yapılan tüm çalışmalar arasında iyileştirilmiş zamana bağlı akış değerlerine göre yapılmış çalışmalar en düşük standart sapma ve hata oranı değerlerini vermiştir.

4. Sonuçlar

Yapılan çalışmalar sonucunda PSO algoritması ve iyileştirilmiş zamana bağlı akış değerlerine göre 1000x1000 mm boyutlarında ve farklı laminasyon kalınlıklarında kaçak tespitleri gerçekleştirilmiştir. Bu tespitlere göre kat sayısının artışı hata oranını artırmaktadır. Ek olarak geçirgenliği cam elyaf geçirgenliğinden çok daha fazla olan dağıtıcı filenin varlığı özellikle bulunduğu bölgede hata oranını artırmaktadır.

Şekil 13'te görülebileceği üzere yapılan çalışmalar ve algoritma iyileştirmeleriyle 2,10 ve 50 kat laminasyonlarda hava kaçağı tespiti hata oranında düşüş elde edilmiştir. En yüksek hata oranları sırasıyla 50, 10 ve 2 katlık laminalardan elde edilmiş olup kat sayısının major etkisi bu sonuca sebebiyet vermiştir.

Şekil 14'te bu azalım ortalama verilere göre ifade edilirse son durumda dağıtıcı fileli laminatlarda %16,5 dağıtıcı filesiz laminatlarda %9,2 seviyelerine getirilmiştir. Algoritma iyileştirmelerinin dağıtıcı filesiz çalışmalarda hata oranını ortalama %5,8, dağıtıcı fileli çalışmalarda ortalama %3,6 düşürdüğü görülmektedir.

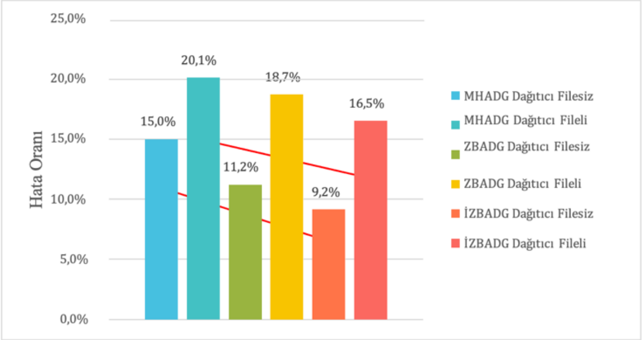

Şekil 13. Algoritmaların 2,10 ve 50 katlık çalışmalardaki ortalama hata oranları.

Figure 13. Average error rates of the algorithms in 2,10 and 50-fold runs.

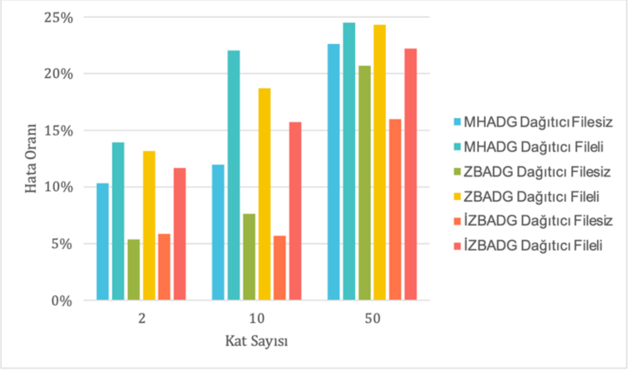

Şekil 14. Algoritmaların hata üzerindeki etkisi.

Figure 14. The effect of algorithms on error.

Elde edilen sonuçlar aşağıdaki gibi özetlenebilir:

- Çalışmanın hedefi olan heterojen geçirgenliğe sahip paketler içerisinde gerçekleşen hava kaçağı tespitini, 2 katlı laminasyonlar için ortalama %11,7, 10 katlı laminasyonlar için ortalama %15,7 ve 50 katlı laminasyonlar için ortalama %22,2 lik hata oranlarıyla gerçekleştirmiştir.
- Laminasyon kat sayısının artışı hava akış sensörleri ile kaçak tespitini zorlaştırmaktadır.
- Yüksek geçirgenliğe sahip dağıtıcı filenin varlığı sistem içerisinde hava yönelim hızını major olarak tesir etmekte ve bölgesel olarak hata oranlarına etki etmektedir.
- Çalışmadan elde edilen verilerin daha fazla deney ile desteklenmesi ve özellikle dağıtıcı filenin 1000x1000 mm 'lik bir laminatta 800x800 mm'lik bir alan içerisinde kullanıldığı hesaba katılarak daha büyük boyutlarda deneylerin gerçekleştirilmesi önerilmektedir. Bu yapılacak deneylerde dağıtıcı filenin boyutunun artması dikkatle incelenmeli ve artan boyutta hava kaçağının hareket hızı kayıt altına alınmalıdır. Bu adım sonrasında

elde edilecek veriler analiz edilip bir yapay zeka algoritması ile desteklenmeli ve sonuçlar bölümünde bahsedilen düzensizliklerin hata oranına etkisi azaltılmalıdır.

Etik kurul onayı ve çıkar çatışması beyanı

Hazırlanan makalede etik kurul izni alınmasına gerek yoktur. Hazırlanan makalede herhangi bir kişi/kurum ile çıkar çatışması bulunmamaktadır.

Teşekkür

Yazarlar, deneysel testlerin gerçekleştirilmesindekiekipman desteklerinden dolayı TPI Kompozit SAN. ve TİC. A.Ş. teşekkürlerini sunarlar.

Yazar katkılarının beyanı

İlk yazar, literatür taraması, makale yazımı, deney tasarımı ve analizlerin gerçekleştirilmesi konularında görev almış, ikinci yazar ise metodolojinin geliştirilmesi, düzenlenmesi ve denetlemesini gerçekleştirmiştir.

Kaynaklar

[1] Medikhani, M., Gorbatikh, L., Verpoest, I., Lomov, S., 2019. Voids in Fiber-Reinforced Polymer Composites: A Review on Their Formation, Characteristics, and Effects on Mechanical Performance. Journal of Composite Materials, Cilt. 53(12), s. 1579-1669. DOI: 10.1177/0021998318772152

[2] Hancox, N.L., 1977. The Effects of Flaws and Voids on the Shear Properties of CFRP. Journal of Materials Science, Cilt. 12, s. 884–892. DOI: 10.1016/0010-4361(78)90377-4

[3] Frascino, Mfiller de Almeida, Zabulon dos Santos Nogueira, 1994. Neto Effect of Void Content on the Strength of Composite Laminates. Composite Structures, s. 139-148. DOI: 10.1016/0263-8223(94)90044-2

[4] Haschenburger, A., Menke, N., Stüve, J., 2021. Sensor-Based Leakage Detection in Vacuum Bagging. International Journal of Advanced Manufacturing Technology, Cilt. 116(7-8), s. 2413-2424. DOI: 10.1007/s00170-021-07505-5

[5] Lengsfeld, H., Altstadt, V., Wolff-Fabris, F., Kramer, J., 2014. Composite Technologien. DOI: 10.3139/9783446440807

[6] Meskel, C., Eret, P., 2012. Microphone Arrays for Compressed Air Leakage Detection. Evaluation of On-Site Energy Generation for Manufacturing Industry in a Decarbonized Energy System. 4th Berlin Beamforming Conference, 22-23 Kasım, Berlin, s. 6-9.

[7] Haschenburger, A., Heim, C., 2019. Two-Stage Leak Detection in Vacuum Bags for the Production of Fibre-Reinforced Composite Components. CEAS Aeronautical Journal, Cilt. 10(3), s. 885-892. DOI: 10.1007/s13272-018-00357-y

[8] David, M., Ee, V., Edvin, M., Bernstein, J.R., Wagner, J.W., 2021. Detection, Monitoring, and Management of Gas Presence, Gas Flow, Gas Leaks in Composites Manufacturing. Convergent Manufacturing Technologies Inc., EP2861411A1, 5s.

[9] Petricevic, R., Radestock, O., 2015. Technical Report: Leakage-Detection and -Localization with Vacuum-Autoclave-Processing of FRPs (iNDTact).

[10] Bolke, J., Uçan, H., Stefaniak, D., Krombholz, C., Gramm, L., 2012. Leckageerkennung. DE102011100096B4, s. 1-7.

[11] Finley, M., Michael, B., Kenneth, D., 2010. Leak Detection in Composite Tools. The Boeing Company, US 2010/0170326A1, s. 1-5. https://worldwide.espacenet.com/patent/search/family/043981096/publication/US2010170326A1?q=US20100170326A1 (Erişim Tarihi: 21.12.2024)

[12] Aydoğan, B., 2024. Vakum İnfüzyon ile Heterojen Yapıdaki Laminalı Kompozit Parça Üretiminde Hava Akış Sensörleri Kullanılarak Hava Kaçak Lokasyon Tespiti. Ege Üniversitesi, Lisansüstü Eğitim Enstitüsü, Yüksek Lisans Tezi, 103s, İzmir.

DEU FMD 27(79) (2025) 139-146

Dokuz Eylül Üniversitesi Mühendislik Fakültesi Fen ve Mühendislik Dergisi
Dokuz Eylul University Faculty of Engineering Journal of Science and Engineering
Elektronik/Online ISSN: 2547-958X

ARAŞTIRMA MAKALESI / RESEARCH ARTICLE

Çevre Dostu Manyetik Pektin Nanobiyokompozitleri Kullanarak Toryum(IV) İyonlarının Giderilmesi

Removal of Thorium(IV) Ions Using Environmentally Friendly Magnetic Pectin Nanobiocomposites

Sabriye Yuşan [1*], **Çağkan Özçivit** [1,2], **İkbal Gözde Kaptanoğlu** [1]

[1] Ege Üniversitesi Nükleer Bilimler Enstitüsü 35100 Bornova, İzmir, TÜRKİYE
[2] Slimstock Türkiye PS Plaza, Kozyatağı Mah. Bayar Cad, Gülbahar Sk. No:17/96 Kat:9 Kadıköy, İstanbul, TÜRKİYE

Sorumlu Yazar / Corresponding Author *: sabriye.doyurum@ege.edu.tr

Öz

Bu çalışmada, sucul ortamlardan toryumun uzaklaştırılması için etkili, güvenli, çevre dostu ve toksik olmayan pektin-manyetik (Fe_3O_4) nanobiyokompozitler birlikte çöktürme yöntemiyle sentezlenmiş ve karakterize edilmiştir. Optimum özelliklere sahip manyetik nanobiyokompozit adsorban ile toryumun sulu çözeltilerden uzaklaştırılması için, pH, toryum konsantrasyonu, sıcaklık ve temas süresi gibi ana deneysel parametrelerin etkisi kesikli yöntemlerle incelenmiştir. Langmuir, Freundlich ve Dubinin-Radushkevich izotermleri kullanılarak adsorpsiyon modeli belirlenmiş ve ilgili parametreler hesaplanmıştır. Ayrıca, adsorpsiyonun termodinamik parametreleri olan entalpi, Gibbs serbest enerji değişimi ve entropi hesaplanmıştır.

Anahtar Kelimeler: *Pektin, Nanobiyokompozit, Toryum, Adsorpsiyon*

Abstract

In this study, effective, safe, environmentally friendly and non-toxic pectin-magnetic (Fe_3O_4) nanobiocomposites were synthesised and characterised by co-precipitation method for the removal of thorium from aquatic environments. The effect of main experimental parameters such as pH, thorium concentration, temperature and contact time on the removal of thorium from aqueous solutions by magnetic nanobiocomposite adsorbent with optimum properties was investigated by batch methods. The adsorption model was determined using Langmuir, Freundlich and Dubinin-Radushkevich isotherms and the related parameters were calculated. In addition, the thermodynamic parameters of adsorption such as enthalpy, Gibbs free energy change and entropy were calculated.

Keywords: *Pectin, Nanobiocomposite, Thorium, Adsorption*

EXTENDED ABSTRACT

Introduction

With the advancement of nuclear technology, the release of radioactive materials with high radiological, biological and chemical toxicity into the environment in unexpected accidents constitutes a significant source of risk for human health and the environment. After a nuclear power plant accident, the radioactive fallout is dispersed and accumulated in the environment, exposing individuals to significant internal and external contamination. Intrinsically ingested radioactive materials can cause both acute and chronic radiation damage, thus threatening the health of individuals. [1].

The environmental risk of radiological contamination can be safely and effectively reduced by the use of new and effective sorbents. In recent years, research on the design and synthesis of nanocomposites and nanomagnetic composites using non-toxic natural polymers of biological origin and the removal of heavy metals has gained importance. In the process of transition to nuclear technology in our country, the preparation and application of effective, safe, economical, fast, environmentally friendly and non-toxic radionuclide removal and immobilisation agents to be used in the control of possible nuclear contamination in the future is of great importance. [2-4].

Thorium (Th) is an important natural radioactive element found in higher quantities than uranium, especially among actinides. Human activities such as the recovery of nuclear fuel and the utilisation of thorium-related ores, nuclear weapons and laboratory work can lead to the accumulation of this radionuclide as waste. The toxic property of thorium, even in trace amounts, can lead to acute toxic effects and harmful diseases, making it a public health problem. Therefore, it is important to remove thorium from aqueous solutions. [5,6].

Magnetite iron oxide nanoparticles have long been used as potential components of biomaterials because of their biocompatibility, biodegradability and low toxicity. [7]. However, there are some unavoidable problems with magnetic nanoparticles. In their natural state, metallic nanoparticles are chemically active, have a high oxidation tendency and tend to aggregate together to reduce their energy. To solve these problems, nanoparticles are often coated with polymer, silica or other materials. This prevents agglomeration and oxidation of

DOI: https://doi.org/10.21205/deufmd.2025277918

Geliş Tarihi / Received: 12.06.2023
Kabul Tarihi / Accepted: 01.07.2024

magnetic nanoparticles, while at the same time allowing the surfaces of the nanoparticles to be functionalised and thus gain new properties. [9-13].

Various particle stabilisation methods have been reported to increase sorption capacity and prevent agglomeration of nanoparticles. [14,15]. Pectin is among the prominent stabilisers as an effective, economical and environmentally harmless material. Literature studies show that pectin-based magnetic nanoparticles increase physical stability and sorption capacity. In a study conducted by Gong et al. [16], pectin-iron oxide magnetic nanocomposite was used as adsorbent for the removal of Cu(II) ions. Kadam et al. [17] used pectin-stabilised magnetic graphene oxide Prussian blue nanocomposite for the removal of cesium from aqueous solutions. In another study, pectin obtained from citrus fruits and carbon coated magnetic nanocomposite were synthesised and used as adsorbent for the removal of methylene blue [18].

In this study, it is aimed to develop, characterise and investigate the adsorption properties of effective, safe, environmentally friendly and non-toxic pectin-based magnetic-nanobiocomposite materials that can be used for the removal of Th(IV) ions from nuclear waste solutions. Currently, no studies exist concerning this synthesis method and the application of this method to the adsorption of thorium on effective, safe, environmentally friendly, and non-toxic nanobiocomposite. These materials can be rapidly separated from solutions thanks to their magnetic properties and do not harm the environment.

Materials and Methods

In this study, magnetic pectin (pectin Fe_3O_4) nanobiocomposite was prepared by co-precipitation method. In the synthesis process, firstly, the bidistilled water to be used was passed through nitrogen gas for 30 minutes. Then, 35 mL of 3.2% $FeCl_3$ solution in 0.12 N HCl was prepared and stirred to obtain a homogeneous mixture. Then, 25 mL of 0.5% pectin solution was slowly added and stirred in a magnetic stirrer until a homogeneous mixture was obtained. Afterwards, freshly 25 mL of 0.7% Na_2SO_3 solution was slowly added to the $FeCl_3$+pectin solution. At this stage the colour of the solution changed from yellow to red. Then, 14 mL of 14% NH_3 solution was slowly added dropwise and the colour of the solution changed to black. The solution was stirred in the magnetic stirrer for another 2 hours. The solution was then washed with bidistilled water until pH neutral, filtered through a membrane under vacuum and the solid sample was freeze-dried.

Batch method was used in adsorption studies. In the experiments, 10 mL of Th(IV) solutions at appropriate concentrations and 0.01 g of adsorbent were subjected to adsorption in a thermostat shaker. Different pH values, interaction times, Th(IV) initial concentrations and temperature values were tested to determine the factors affecting the adsorption efficiency. After adsorption, solid-liquid separation was performed externally with the help of a magnet and the Th(IV) concentrations remaining in the solutions were determined by ICP-OES. All experiments were performed with at least three parallel samples and the averages of the results obtained were used. According to the data obtained, the adsorption efficiency was calculated by the following formula.

$$\text{Adsorption (\%)} = \frac{(C_o - C_e)}{C_e} \text{x} 100$$

where Ci is the initially loaded thorium concentration (mg/L) and Ce is the thorium concentration (mg/L) remaining in the solution after adsorption.

Results and Discussion

In this study, nanobiocomposites with magnetite iron oxide nanoparticles were synthesised using pectin biopolymer to improve adsorbent capacity, metal ion selectivity and ease of separation from the solution. Then, the removal of thorium ions from aqueous solutions with the nanobiocomposite selected according to the optimum synthesis conditions was investigated by batch method.

X-ray diffraction (XRD) method was used to investigate the crystal structures of the synthesised nanobiocomposite. Figure 1a shows Fe_3O_4 magnetic nanoparticles and 1b shows the XRD spectrum of pectin-Fe_3O_4 nanobiocomposite. The characteristic peaks at 2θ values of 31.92°, 35.76°, 43.32°, 57.34° and 63.08° support the presence of the spinal structure of Fe_3O_4 [19,20]. In the XRD spectrum of the pectin/Fe_3O_4 nanobiocomposite, some peaks disappeared due to the presence of the pectin matrix and possible interaction, and some peaks are wider and less intense. In the light of the data obtained from the XRD spectrum, the crystallite size of the pectin/Fe_3O_4 nanobiocomposite was calculated as 5.76 nm using the Debye-Scherrer equation.

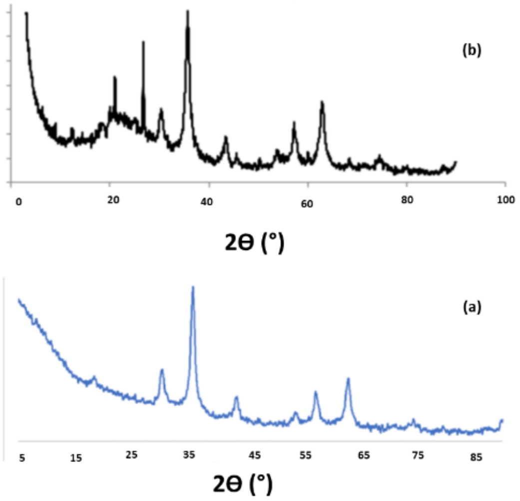

Figure 1. XRD spectrum of Fe_3O_4 (a) and pectin-Fe_3O_4 nanobiocomposite(b).

According to the BET surface area result, other characterisation analyses were performed for the the material with a particle size of 5.76 nm and a surface area of 94.651 m^2/g. According to SEM/EDX results, it can be stated that the surface of pectin/Fe_3O_4 nanobiocomposites is porous and rough due to the presence of cross-linked starch in pectin/Fe_3O_4 nanocomposites and Fe_3O_4 nanoparticles are embedded in the pectin matrix.

The SEM analysis of the pectin/Fe_3O_4 nanobiocomposites show that the surface of the pectin/Fe_3O_4 nanocomposite has a porous, rough structure due to the presence of pectin and Fe_3O_4 nanoparticles are embedded in the pectin matrix [21]. The presence of C along with Fe and O in Energy Dispersive X-Ray Analysis (EDX) confirms the binding of pectin to the magnetite structure.

The magnetic property of pectin-Fe_3O_4 nanobiocomposite was characterised by vibrating sample magnetometer (VSM) at room temperature. According to this result, the synthesised nanobiocomposite shows superparamagnetic properties at room temperature.

Batch method was used in adsorption studies. In the experiments, 10 mL of Th(IV) solutions at appropriate concentrations and 0.01 g of adsorbent were subjected to adsorption in a thermostat shaker. Different pH values, interaction times, Th(IV) initial concentrations and temperature values were tested to determine the factors affecting the adsorption efficiency. It was determined that pH 5, 60 minutes contact time, 100 mg/L Th(IV) initial concentration were the optimum working conditions for magnetic-pectin nanobiocomposite

According to the adsorption isotherms drawn according to the data obtained, Langmuir, Freundlich and D-R model correlation values were calculated as 0.9975, 0.2627 and 0.0771, respectively. According to these values, it was determined that the adsorption process was in accordance with the Langmuir model. According to Langmuir isotherm, the maximum sorption capacity was found to be 166.66 mg/g. The adsorption energy calculated from the D-R isotherm model for the adsorbent was calculated as 4.82 kJ/mol. Since adsorption mechanisms with energy values less than 8 kJ/mol are considered as physical, physical adsorption can be mentioned for this system. According to the data obtained in the studies on adsorption thermodynamics, it was determined that the adsorption process can be both physical and chemical adsorption for the adsorbent.

Conclusion

In this study, pectin-Fe_3O_4 nanobiocomposite was synthesized for the removal of thorium ions from aqueous solutions and the structure and morphology of the material were characterised by XRD, BET, SEM-EDX, FT-IR and VSM methods. Various adsorption experiments were carried out using the synthesised nanobiocomposite adsorbent and the results obtained were evaluated. In the study, optimum conditions for solution pH, contact time, initial Th(IV) ion concentration and temperature values were determined. According to the data obtained, it was determined that pH 5, 60 minutes contact time, 100 mg/L Th(IV) initial concentration were the optimum working conditions for magnetic-pectin nanobiocomposite and temperature did not affect the adsorption efficiency.

In addition, it was found that the Langmuir, Freundlich and D-R isotherm models were in accordance with the Langmuir model with high correlation coefficient and the adsorption was monolayer. The maximum sorption capacity was calculated as 166.67 mg/g. Thermodynamic studies show that the adsorption process is endothermic and spontaneous.

1. Giriş

Nükleer teknolojinin ilerlemesiyle birlikte, yüksek radyolojik, biyolojik ve kimyasal toksisiteye sahip radyoaktif maddelerin beklenmedik kazalarda çevreye salınması, insan sağlığı ve çevre için önemli bir risk kaynağı oluşturur. Bir nükleer santral kazası sonrasında ortaya çıkan radyoaktif serpinti, çevresel ortamlarda dağılarak birikir, bu da bireyleri önemli ölçüde içsel ve dışsal kontaminasyona maruz bırakır. İçsel olarak alınan radyoaktif maddeler, hem akut hem de kronik radyasyon zararına neden olabilir, böylece bireylerin sağlığını tehdit edebilir. [1].

Radyolojik kontaminasyonun çevresel riski, yeni ve etkili sorbentlerin kullanımıyla güvenli ve etkili bir şekilde azaltılabilir. Son yıllarda, biyolojik kökenli, toksik olmayan doğal polimerlerin kullanıldığı nanokompozitlerin ve nanomanyetik kompozitlerin tasarlanması, sentezlenmesi ve ağır metallerin giderilmesindeki araştırmalar önem kazanmıştır. Ülkemizde nükleer teknolojiye geçiş sürecinde, gelecekte olası nükleer kontaminasyonların kontrolünde kullanılmak üzere etkili, güvenli, ekonomik, hızlı, çevre dostu ve toksik olmayan radyonüklit giderme ve immobilizasyon ajanlarının hazırlanması ve uygulanması büyük önem taşımaktadır. [2-4].

Toryum (Th), özellikle aktinitler arasında uranyumdan daha yüksek miktarlarda bulunan önemli bir doğal radyoaktif elementtir. Nükleer yakıtın geri kazanımı ve toryumla ilişkili cevherlerin kullanılması gibi insan faaliyetleri, nükleer silahlar ve laboratuvar çalışmaları, bu radyonüklidin atık olarak birikmesine neden olabilir. Toryumun toksik özelliği, eser miktarda olsa bile akut toksik etkilere ve zararlı hastalıklara yol açabilir, bu da bir halk sağlığı sorunu haline gelir. Bu yüzden, toryumun sulu çözeltilerden uzaklaştırılması önemlidir. [5,6].

Manyetit demir oksit nanoparçacıkları, biyomateryallerin potansiyel bileşenleri olarak uzun süredir kullanılmaktadır çünkü biyouyumlulukları, biyobozunabilirlikleri ve düşük toksisiteleri vardır. [7].

Bunun yanı sıra, küçük partikül boyutu, geniş özgül yüzey alanı ve yüksek sorpsiyon kapasitesi sayesinde manyetik nanopartiküller, kirlenmiş toprak ve sular içerisindeki ağır metallerin sorpsiyonunda büyük bir potansiyele sahiptir [8]. Ancak, manyetik nanopartiküllerle ilgili bazı kaçınılmaz sorunlar vardır. Doğal hallerinde, metalik nanoparçacıklar kimyasal olarak aktiftir, yüksek bir oksidasyon eğilimine sahiptir ve enerjilerini azaltmak için bir araya gelme eğilimindedirler. Bu sorunları çözmek için, nanopartiküller genellikle polimer, silika veya diğer materyallerle kaplanır. Bu, manyetik nanopartiküllerin topaklanmasını ve oksidasyonunu önlerken aynı zamanda nanopartiküllerin yüzeylerinin fonksiyonlandırılmasına olanak tanır ve böylece yeni özellikler kazanmasını sağlar. [9-13].

Sorpsiyon kapasitesini artırmak ve nanopartiküllerin topaklanmasını önlemek için çeşitli partikül stabilizasyon yöntemleri rapor edilmiştir. [14,15]. Pektin, etkili, ekonomik ve çevreye zararsız bir materyal olarak öne çıkan stabilizatörler arasındadır. Yapılan literatür çalışmaları, pektin bazlı manyetik nanopartiküllerin fiziksel stabiliteyi arttırdığını ve sorpsiyon kapasitesini artırdığını göstermektedir. Gong ve ark. [16] tarafından gerçekleştirilen bir çalışmada, pektin-demir oksit manyetik nanokompoziti Cu(II) iyonlarının giderimi için adsorban olarak kullanılmıştır. Kadam ve ark. [17] pektin ile stabilize edilmiş manyetik grafen oksit Prusya mavisi nanokompozitini sulu çözeltilerden sezyum giderimi için kullanmışlardır. Bir diğer çalışmada turunçgillerden elde edilen pektin ile karbon kaplı manyetik nanokompozit sentezlenmiş ve metilen mavisinin giderimi için adsorban olarak kullanılmıştır [18].

Bu çalışmada, nükleer atık çözeltilerinden Th(IV) iyonlarının giderimi için kullanılabilecek etkili, güvenli, çevre dostu ve toksisitesi olmayan pektin tabanlı manyetik-nanobiyokompozit malzemelerin geliştirilmesi, karakterizasyonu ve adsorpsiyon özelliklerinin incelenmesi amaçlanmaktadır. Bu malzemeler, manyetik özellikleri sayesinde çözeltilerden hızlı bir şekilde ayrılabilmekte ve çevreye zarar vermemektedir.

2. Materyal ve Metot

Bu çalışmada, manyetik pektin (pektin Fe_3O_4) nanobiyokompoziti birlikte çöktürme yöntemiyle hazırlanmıştır.

Sentez sürecinde, öncelikle kullanılacak bidistile su, 30 dakika boyunca azot gazıyla geçirilmiştir.
Ardından, 35 mL %3,2'lik $FeCl_3$ çözeltisi, 0,12 N HCl içinde hazırlanmış ve buna karıştırılarak homojen bir karışım elde edilmiştir. Daha sonra, üzerine 25 mL %0,5 konsantrasyondaki pektin çözeltisi yavaşça eklenmiş ve manyetik karıştırıcıda homojen bir karışım elde edilene kadar karıştırılmıştır. Sonrasında, taze olarak hazırlanmış 25 mL %0,7'lik Na_2SO_3 çözeltisi, $FeCl_3$+pektin çözeltisine yavaşça eklenmiştir. Bu aşamada çözeltinin rengi sarıdan kırmızıya dönmüştür. Daha sonra, 14 mL %14'lük NH_3 çözeltisi yavaşça damla damla eklenmiş ve çözeltinin rengi siyaha dönmüştür. Çözelti, 2 saat daha manyetik karıştırıcıda karıştırılmıştır. Daha sonra, pH nötr oluncaya kadar bidistile su ile yıkanmış, vakum altında membranla süzülmüş ve katı örnek freeze-dryer ile kurutulmuştur.

2.1. Th(IV) Alım Denemeleri Bulgular ve Tartışma

Adsorpsiyon çalışmalarında kesikli (batch) yöntemi kullanılmıştır. Denemelerde uygun derişimlerde 10 mL Th(IV) çözeltileri ve 0,01 g adsorban kullanılarak termostatlı çalkalayıcıda adsorpsiyona işlemine tabi tutulmuştur. Adsorpsiyon verimini etkileyen faktörlerin belirlenmesi için farklı pH değerleri, etkileşim süreleri, Th(IV) başlangıç konsantrasyonları ve sıcaklık değerleri denenmiştir. Adsorpsiyon sonrasında katı-sıvı ayrımı, dışsal olarak mıknatıs yardımıyla yapılmış ve çözeltilerde kalan Th(IV) konsantrasyonları ICP-OES cihazı ile tayin edilmiştir. Tüm denemeler en az üç paralel numune ile yapılmış ve elde edilen sonuçların ortalamaları kullanılmıştır. Elde edilen verilere göre adsorpsiyon verimi aşağıdaki formülle hesaplanmıştır.

$$\text{Adsorpsiyon Verimi} = \frac{(C_i - C_e)}{C_i} \times 100 \qquad (1)$$

burada, C_i başlangıçta yüklenen toryum konsantrasyonunu (mg/L), C_e adsorpsiyondan sonra çözeltide kalan toryum konsantrasyonunu (mg/L) göstermektedir.

3. Bulgular

3.1. Pektin- Fe_3O_4 Nanobiyokompozitinin Karakterizasyonu

Sentezlenen nanobiyokompozitin kristal yapılarını araştırmak için X-ışını kırınım (XRD) yöntemi kullanılmıştır. Şekil 1a'da Fe_3O_4 manyetik nanoparçacıkları ve 1b'de pektin-Fe_3O_4 nanobiyokompozitinin XRD spektrumu gösterilmektedir. 2θ değerleri 31,92°, 35,76°, 43,32°, 57,34° ve 63,08°'de karakteristik tepe noktaları Fe_3O_4'ün spinal yapısının varlığını desteklemektedir [19,20]. Pektin-Fe_3O_4 nanobiyokompozitinin XRD spektrumunda, pektin matrisinin varlığı ve olası etkileşim nedeniyle bazı pikler kaybolmuş ve bazıları daha geniş ve daha az şiddette görülmektedir. XRD spektrumundan elde edilen veriler ışığında aşağıda verilen Debye-Scherrer eşitliği kullanılarak Pektin-Fe_3O_4 nanobiyokompozitinin kristalit boyutu 5.76 nm olarak hesaplanmıştır.

$$L = \frac{0.9\lambda}{\beta cos\theta} \qquad (2)$$

burada, L kristalit boyutu (nm), λ kullanılan X-ışınının dalga boyu (1,5405 Å), β yarı şiddet genişliği ve ϴ, X ışınlarının kristalde oluşturduğu kırınım açısıdır.

Nanobiyokompozit malzemelerin adsorpsiyon veriminde önemli etkenlerden olan yüzey alanı ve gözenek yapılarının tespiti için Brunauer, Emmet ve Teller (BET) analizi gerçekleştirilmiştir. Pektin-Fe_3O_4 nanobiyokompozitinin yüzey alanı 94,65 m^2/g, por hacmi 0,15 cm^3/g ve por boyutu 65,40 Å olarak bulunmuştur.

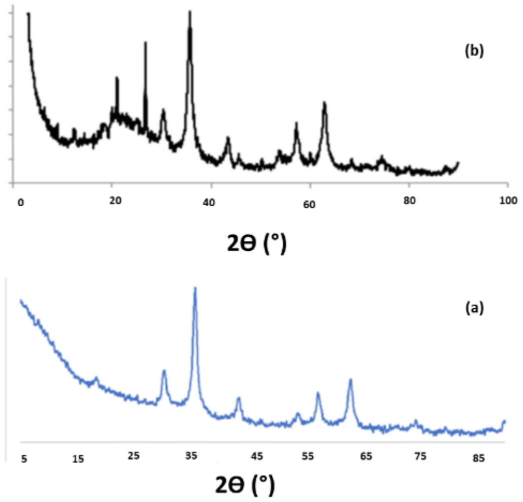

Şekil 1. Fe_3O_4 (a) ve pektin-Fe_3O_4 nanobiyokompozitinin (b) XRD spektrumu.

Figure 1. XRD spectrum of Fe_3O_4 (a) and pectin-Fe_3O_4 nanobiocomposite(b).

Pektin-Fe_3O_4 nanobiyokompozitinin morfolojik karakterizasyonu taramalı elektron mikroskobu (SEM) ile gerçekleştirilmiştir. Şekil 2'de yer alan Pektin/Fe_3O_4 nanobiyokompozitlerinin SEM görüntülerinden pektin-Fe_3O_4 nanokompozitinin yüzeyinin, pektin varlığından dolayı gözenekli, pürüzlü yapıda olduğu ve Fe_3O_4 nanoparçacıklarının pektin matrisine gömülü olduğu görülmektedir [21]. Enerji Dağıtıcı X-Işını Analizinde (EDX) Fe ve O ile birlikte C'nin varlığı, pektinin manyetit yapıya bağlandığını doğrulanmaktadır (Şekil 2).

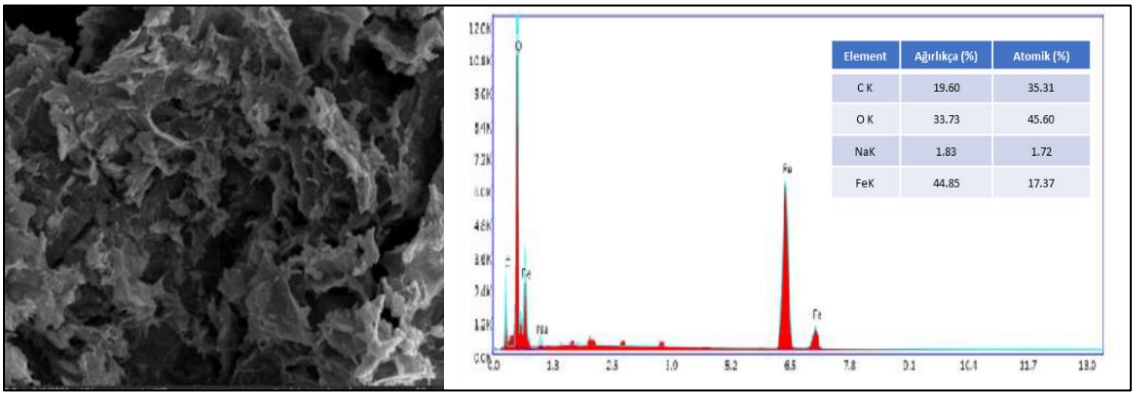

Element	Ağırlıkça (%)	Atomik (%)
C K	19.60	35.31
O K	33.73	45.60
NaK	1.83	1.72
FeK	44.85	17.37

Şekil 2. Pektin-Fe_3O_4 nanobiyokompozitinin SEM görüntüsü ve EDX spektrumu.

Figure 2. SEM image and EDX spectrum of pectin-Fe_3O_4 nanobiocomposite.

Yapıdaki fonksiyonel gruplar FT-IR analizi ile tespit edilebilmektedir. Şekil 3'de pektinin FT-IR spektrumunda, 3340 cm^{-1}'deki pik, pektin içindeki -OH germe titreşimlerine karşılık gelmektedir [6]. Hidrojen bağları ile dimerlere bağlanan COOH serbest karboksillerinde O – H germe titreşimine atanan 2900 cm^{-1} civarında daha küçük bir geniş omuza sahiptir. Pektin, COOH'nin C-O gerilmesine (1732 cm^{-1}) atanmış çok güçlü bir bandına sahiptir. Pektinin FT-IR spektrumu, daha zayıf asimetrik karboksiletest germe bandına sahiptir (1606 cm^{-1}). Pektin-Fe_3O_4 nanobiyokompozitinin FT-IR spektrumunda görüldüğü gibi, 1596 cm^{-1}'de bir tepe ile birlikte 1418 cm^{-1} dalga sayısında orta derecede bir tepe gözlemlenmiştir. Bu, hem simetrik hem de asimetrik COO – gerilmelerinin gözlemlendiğini gösterir. Bunun nedeni, demir oksit nanoparçacıklarına ticari pektin eklenmesi olabilir. Ayrıca Fe_3O_4 yapısı Fe–O germe titreşimi (543 cm^{-1}) pikleri ile desteklenmektedir.

Pektin-Fe_3O_4 nanobiyokompozitinin manyetik özelliği, oda sıcaklığında titreşen numune manyetometresi (VSM) ile karakterize edilmiş ve grafiği Şekil 4'te verilmiştir. Bu sonuca göre, sentezlenen nanobiyokompozit, oda sıcaklığında süperparamanyetik özellik göstermektedir (50 emu/g).

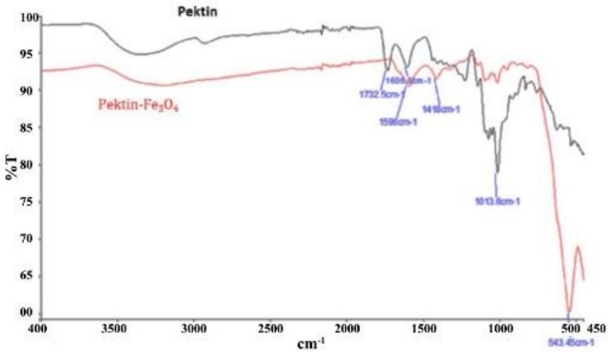

Şekil 3. Pektin ve pektin-Fe_3O_4 nanobiyokompozitinin FT-IR spektrumu.

Figure 3. FT-IR spectrum of pectin and pectin-Fe_3O_4 nanobiocomposite

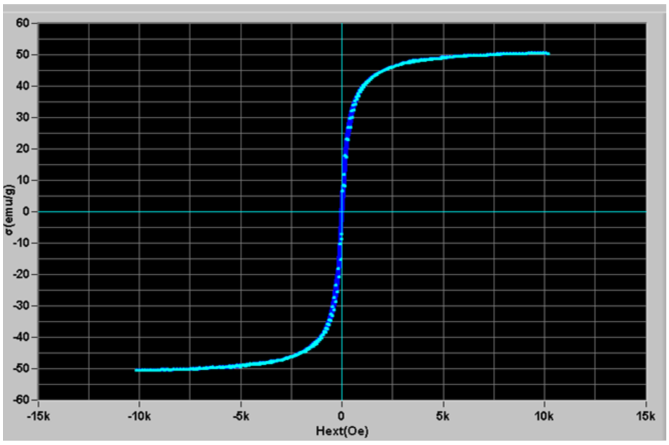

Şekil 4. Pektin-Fe_3O_4 nanobiyokompozitinin VSM grafiği.

Figure 4. VSM plot of pectin-Fe_3O_4 nanobiocomposite.

3.2. Toryum(IV) Adsorpsiyon Çalışmaları

Yapılan çalışmada, adsorpsiyon verimini etkileyen parametrelerden çözelti pH'ı, temas süresi, başlangıç Th(IV) iyonu konsantrasyonu ve sıcaklık değerleri için optimum koşullar araştırılmıştır. Adsorpsiyon sürecinde en önemli faktörlerden biri pH'dır. pH seviyesi, metal iyonlarının sulu çözeltilerden çözünmesini etkiler ve adsorban maddenin yüzey yükünü değiştirir [22]. Pektin-Fe_3O_4 adsorbanının Th(IV) sorpsiyon performansına pH'ın etkisini incelenmek üzere pH'ları 2 ile 6 arasında olacak şekilde ayarlanan, 50 mg Th(IV)/L'lik çözeltiler ile gerçekleştirilen adsorpsiyondan elde edilen sonuçlar, Şekil 5'de gösterilmektedir. Maksimum Th(IV) alımı pH 5'de %99,49 ve 49,74 mg Th(IV)/g olarak elde edilmiştir. Bu durum şu şekilde açıklanabilir: Düşük pH değerlerinde, adsorbanın yüzey yükü pozitiftir ve bu da toryum(IV) iyonlarının adsorpsiyonu için elverişli değildir. Bu arada, hidrojen iyonları aktif bölgeler için metal toryum(IV) iyonlarıyla güçlü bir şekilde rekabet ederek daha az metal adsorpsiyonuna neden olur. Çözelti pH'ı 2,0 ile 5 arasında olduğunda, hidrojen iyonlarının rekabetçi etkisi azalır, bunun yerine toryum(IV) iyonlarının adsorpsiyonu artar. pH 5 olduğunda, çok sayıda aktif adsorpsiyon bölgesi serbest kalır ve maksimum sayıda adsorpsiyon bölgesi elde edilir, bu da toryum (IV) iyonlarının saldırısı için çok sayıda fırsat sağlar, bu nedenle pH 5'te maksimum toryum (IV) adsorpsiyon verimliliği görülmüştür. pH'ın daha da artmasıyla, çözünmeyen toryum hidroksit çökelmeye başlamaktadır [23]. Elde edilen veriler literatür ile uyumludur [24, 25].

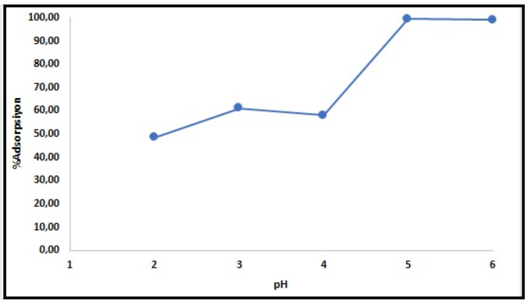

Şekil 5. pH'ın adsorpsiyon verimine etkisi.

Figure 5. Effect of pH on adsorption efficiency.

Şekil 6'da 10-250 mg/L başlangıç Th(IV) konsantrasyonu içeren çözeltiler ile pektin-Fe_3O_4 nanobiyokompoziti için pH 5'de konsantrasyonun adsorpsiyona etkisi incelenmiştir. Buna göre başlangıç Th(IV) konsantrasyonu arttıkça % adsorpsiyon verimi azalmaktadır. Pektin-Fe_3O_4 adsorbanı için en yüksek alım verimi 100 mg/L Th(IV) konsantrasyonunda %99,9 olarak hesaplanmıştır.

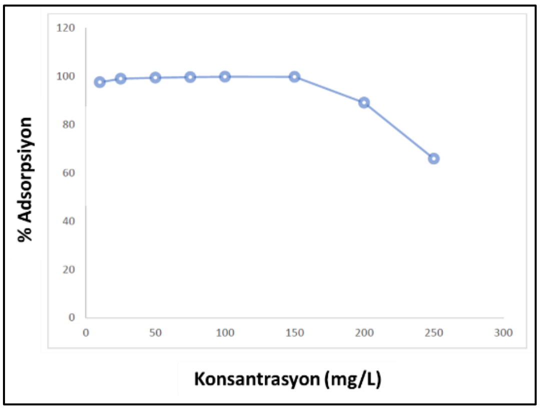

Şekil 6. Başlangıç Th(IV) konsantrasyonun adsorpsiyon verimine etkisi.

Figure 6. Effect of initial Th(IV) concentration on adsorption efficiency.

Adsorpsiyon prosesinde optimum temas süresinin tespiti için, 100 mg/L Th(IV) çözeltisi ile pH 5'de 15-180 dk. aralığında termostatlı çalkalayıcıda adsorpsiyon prosesi gerçekleştirilmiştir. Yapılan çalışmalar sonucunda elde edilen veriler Şekil 7'de gösterilmektedir.

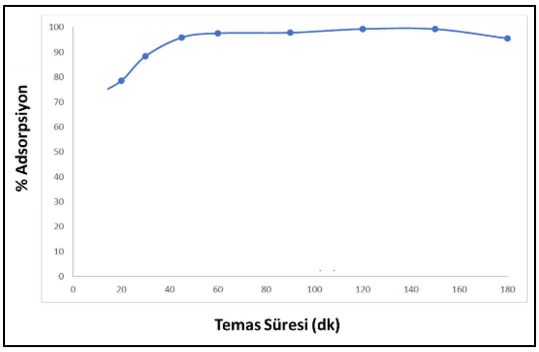

Şekil 7. Adsorpsiyon verimine temas süresinin etkisi.

Figure 7. Effect of contact time on adsorption efficiency.

Deneysel sonuçlara göre Th(IV) iyonlarının sulu çözeltilerden gideriminde en yüksek verim 120 dakikada %99,35 olarak belirlenmiştir. Ancak adsorpsiyon prosesinin ekonomikliği açısından adsorpsiyon prosesinin dengeye ulaştığı 60 dakika optimum temas süresi olarak belirlenmiştir.

Adsorpsiyon verimini etkileyen parametrelerden sıcaklığın etkisinin tespiti için 100 mg/L Th(IV) çözeltisi pH 5'de, 60 dakika süre ile 30, 35 ve 40°C derece sıcaklıklarda adsorpsiyon süreci gerçekleştirilmiştir. Elde edilen veriler Şekil 8'de gösterilmektedir. Yapılan çalışmalardan elde edilen verilere göre sıcaklığın adsorpsiyon prosesinde anlamlı bir etkisi olmadığı görülmüştür. Bu nedenle 25°C optimum değer olarak seçilmiştir.

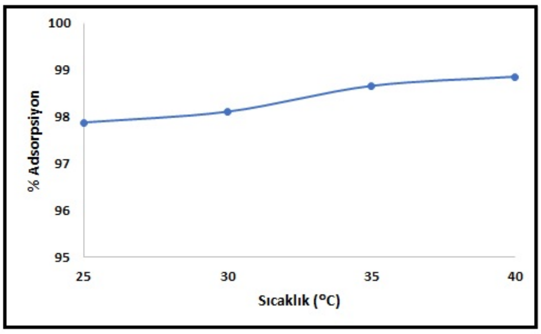

Şekil 8. Sıcaklığın adsorpsiyon verimine etkisi.

Figure 8. Effect of temperature on adsorption efficiency.

Langmuir modeli, adsorban yüzeyinde belirli sayıda aktif merkeze homojen doygun tek tabakalı adsorpsiyonu kabul eden ve belirli bir kirletici derişiminde yüzeyin doygunluğa ulaştığını varsayan teorik bir modeldir. [26]. Bu model, adsorpsiyon dengesinin dinamik bir denge olduğunu yani bir dt zamanı içinde adsorplanan madde miktarının, adsorban yüzeyinden ayrılan madde miktarına eşit olduğunu varsayar. Langmuir modeli aşağıdaki eşitlikle ifade edilir.

$$\frac{\mathrm{C_e}}{\mathrm{q_e}} = \frac{\mathrm{C_e}}{Q_0} + \frac{1}{Q_0 \mathrm{b_L}} \tag{3}$$

burada, C_e denge derişimi (mg/L) ve q_e sorbentin birim miktarı başına adsorplanan Th(IV) iyonu miktarı (mg/g), Q_0 (mg/g) ve b_L (L/mg) olmak üzere kapasite ve enerji ile ilişkili Langmuir sabitlerini göstermektedir.

R_L faktörü, sorbentin araştırılan metallere afinitesini gösterir ve metal iyonlarının güçlü bağlanmasını belirtir ve aşağıdaki eşitlikle ifade edilir.

$$\mathrm{R_L} = \frac{1}{1 + \mathrm{bC_0}} \tag{4}$$

burada, b Langmuir sabiti ve C_0 başlangıç konsantrasyonunu göstermektedir. $0<R_L<1$ olması adsorpsiyon sürecinin elverişliliğine işaret etmektedir.

Freundlich tarafından geliştirilen ve izotermal adsorpsiyonu ifade eden Freundlich izotermi, heterojen yüzey enerjileri için özel bir durumu açıklar. Genel olarak, Freundlich modeli, adsorplanan maddenin derişimi arttıkça dengede adsorplanan miktarların arttığı heterojen yüzeylerdeki adsorpsiyonu tanımlayan bir modeldir. [27]. Freundlich izoterm modeli aşağıdaki eşitlikle ifade edilir.

$$\mathrm{lnq_e} = \mathrm{lnK_F} + \frac{1}{n_F} lnC_e \tag{5}$$

burada, q_e sorbentin birim miktarı başına adsorplanan Th(IV) iyonu (mg/g), C_e denge derişimi (mg/mL), K_F adsorbanın kapasitesi (mg/g) ve n_F Freundlich sabitidir.

Dubinin-Radushkevich (D-R) izoterm modeli, düşük konsantrasyon aralıklarında uygulanabilir ve hem homojen hem de heterojen yüzeyleri tanımlamak için kullanılır. D-R izotermi, yüzey adsorpsiyonunda gözeneklerin küçükten büyüğe doğru sırasıyla dolduğu düşüncesiyle türetilmiş ve mikrogözeneklerin hacim dağılımını veren bir modeldir. [28]. D-R izoterm modeli aşağıdaki eşitlikler ile ifade edilir.

$$\mathrm{ln}q_e = \mathrm{lnX_m} - \beta\varepsilon^2 \tag{6}$$

$$\varepsilon = \mathrm{RT}\left(\frac{1}{1 + \mathrm{C_e}}\right) \tag{7}$$

$$\mathrm{E} = \frac{1}{\sqrt{-2\beta}} \tag{8}$$

burada, ε Polanyi potansiyeli, , β ortalama sorpsiyon enerjisi, X_m teorik adsorpsiyon kapasitesi, T mutlak sıcaklık (Kelvin), R evrensel gaz sabiti (J/mol K), C_e denge konsantrasyonunu (mg/mL), E, sorpsiyon enerjisini göstermektedir.

Pektin-Fe_3O_4 nanobiyokompoziti kullanılarak, 25-250 mg/L konsantrasyon aralığında, optimum koşullarda ve sabit sıcaklıkta (25°C) sulu çözeltilerden adsorplanan toryumun elde edilen deneysel verilerinin Langmuir, Freundlich ve D-R izotermlerine uygunluğu Şekil 9'da incelenmiş ve elde edilen veriler Tablo 1'de sunulmuştur.

Tablo 1'de sunulan verilere göre Langmuir, Freundlich ve D-R modeli korelasyon değerleri (R^2) sırasıyla 0,997, 0,263 ve 0,077 olarak hesaplanmıştır. Bu değerlere göre adsorpsiyon prosesinin Langmuir modeline uygun olduğu tespit edilmiştir. Langmuir izotermine göre maksimum sorpsiyon kapasitesi 166,67 mg/g olarak bulunmuştur. 0,007 olarak bulunan R_L değeri Th(IV)'un manyetik-pektin üzerindeki verimli sorpsiyonunu doğrulamaktadır.

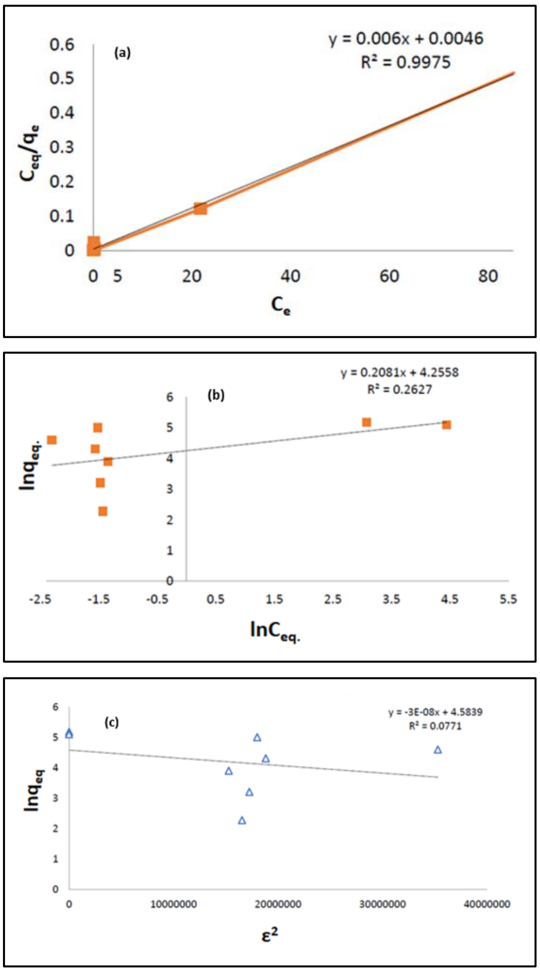

Şekil 9. Langmuir (a), Freundlich (b) ve D-R (c) İzotermleri.

Figure 9. Langmuir (a), Freundlich (b) and D-R (c) Isotherms.

Tablo 1. Langmuir, Freundlich ve D-R İzotermlerine ilişkin sabitler.

Table 1. Constants for Langmuir, Freundlich and D-R Isotherms.

İzoterm modelleri	Parametreler	Pektin-Fe_3O_4
Langmuir	Q_0 (mg/g)	166,67
	b_L (L/mg)	1,30
	R_L	0,007
	R^2	0,997
Freundlich	K_F (mg/g)	70,51
	n_F	4,80
	R^2	0,263
D-R	X_m (mg/g)	97,89
	E (kJ/mol)	4,08
	R^2	0,077

Adsorpsiyon termodinamiğinin incelenmesi için deneyler 25-40°C arasında ve 100 mg/L Th(IV) çözeltileri ile gerçekleştirilmiştir. Adsorpsiyon prosesinin termodinamik modelini belirlemek için ΔG^0 standart Gibbs serbest enerjisi, ΔH0 standart entalpi ve ΔS^0 standart entropi değerlerinden yararlanılmıştır. Bu parametrelerin hesaplanmasında aşağıdaki eşitlikler kullanılmıştır.

$$\Delta G^0 = -RT \times \ln K \tag{9}$$

$$\ln K_d = \frac{-\Delta H^0}{RT} + \frac{\Delta S^0}{R} \tag{10}$$

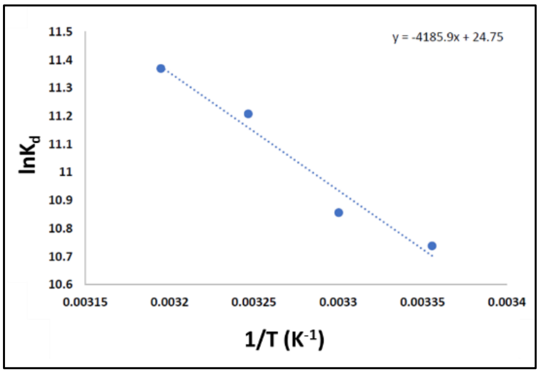

Şekil 10. Pektin-Fe_3O_4 nanobiyokompozitinin Th(IV) adsorpsiyonunda sıcaklığa karşı lnK_d grafiği.

Figure 10. Plot of lnK_d versus temperature in Th(IV) adsorption of pectin-Fe_3O_4 nanobiocomposite.

Tablo 2. Th(IV) adsorpsiyonuna ait termodinamik parametreler

Table 2. Thermodynamic parameters of Th(IV) adsorption

T (°C)	ΔH^0 (kJ/mol)	ΔS^0 (kJ/molK)	ΔG^0 (kJ/mol)
25	34,8	0,21	-26,52
30			-27,55
35			-28,58
40			-29,61

Tablo 2'deki verilere göre, ΔH^0 değerinin pozitif olması, adsorpsiyona ait dengenin endotermik bir reaksiyon olduğunu; ΔG^0 değerinin negatif olması ise, adsorpsiyon işleminin kendiliğinden gerçekleştiğini gösterir. Sıcaklığın artmasıyla ΔG0 değerinin daha büyük negatif değerlere sahip olması, yüksek sıcaklıklarda adsorpsiyon prosesinin kendiliğinden gerçekleştiğini ve toryum iyonlarının adsorbana istemli olarak tutunduğunu gösterir. ΔS^0 değerinin pozitif olması, katı-sıvı ara yüzeyindeki düzensizliğin adsorpsiyon süresince arttığını gösterir. Ayrıca, ΔS^0'un pozitif olması, toryum iyonlarının adsorbana olan ilgisini gösterir. [29].

Termodinamik çalışmalar, adsorpsiyon mekanizması hakkında fikir verir. Genel olarak, fizisorpsiyon için Gibbs serbest enerjisindeki değişimin mutlak büyüklüğü -20 ile 0 kJ/mol arasında ve kemisorpsiyon için -80 ile -400 kJ/mol arasındadır [30]. Bu çalışmada elde edilen sonuçlara göre, Pektin-Fe_3O_4 nanobiyokompoziti ile gerçekleşen adsorpsiyon prosesi 25-40°C aralığında hem fiziksel hem de kimyasal karakter taşımaktadır. [29].

4. Tartışma ve Sonuç

Bu araştırmada, sulu çözeltilerden toryum iyonlarının giderilmesi için pektin-Fe_3O_4 nanobiyokompoziti sentezlenmiş ve malzemenin yapı ve morfolojisi XRD, BET, SEM-EDX, FT-IR ve

VSM yöntemleriyle karakterize edilmiştir. Sentezlenen nanobiyokompozit adsorbanı kullanılarak çeşitli adsorpsiyon deneyleri yapılmış ve elde edilen sonuçlar değerlendirilmiştir. Çalışmada, adsorpsiyon verimini etkileyen parametrelerden çözelti pH'ı, temas süresi, başlangıç Th(IV) iyonu konsantrasyonu ve sıcaklık değerleri için optimum koşullar belirlenmiştir. Elde edilen verilere göre, manyetik-pektin nanobiyokompoziti için pH 5, 60 dakika temas süresi, 100 mg/L Th(IV) başlangıç konsantrasyonunun optimum çalışma koşulları olduğu ve sıcaklığın adsorpsiyon verimini etkilemediği belirlenmiştir. Ayrıca, çizilen Langmuir, Freundlich ve D-R izoterm modellerinden yüksek korelasyon katsayısı ile sırasıyla Langmuir modeline uygun olduğu ve adsorpsiyonun tek tabakalı olduğu anlaşılmıştır. Maksimum sorpsiyon kapasitesi 166,67 mg/g olarak hesaplanmıştır. Termodinamik çalışmalar, adsorpsiyon sürecinin endotermik ve kendiliğinden gerçekleştiğini göstermektedir.

Etik kurul onayı ve çıkar çatışması beyanı

Hazırlanan makalede etik kurul izni alınmasına gerek yoktur. Hazırlanan makalede herhangi bir kişi/kurum ile çıkar çatışması bulunmamaktadır.

Yazar katkılarının beyanı

Sabriye YUŞAN: Fikir Oluşturma, Araştırma, Fizibilite Çalışması, Yazım, Veri Toplama ve Revizyon
Çağkan ÖZÇİVİT: Deneysel Çalışma, Araştırma, analizlerin gerçekleştirilmesi.
İkbal Gözde KAPTANOĞLU: Kontrol, Gözden Geçirme, Yazım

Kaynaklar

[1] Nyberg, A. G., Stricklin, D., Sellström, A., 2011. Mass casualties and health care following the release of toxic chemicals or radioactive material—Contribution of modern biotechnology. International Journal of Environmental Research and Public Health, Cilt. 8(12), s. 4521–4549.

[2] Kaptanoglu, I. G., Yusan, S., 2023. Synthesis and characterization of graphene oxide/alginate and application of central composite design in the adsorption of Th(IV) on the nanobiocomposites. Radiochimica Acta, Cilt. 111(10), s. 751-763.

[3] Adman, N., Yusan, S., 2023. Synthesis and characterization of graphene oxide/alginate and application of central composite design in the adsorption of Th(IV) on the nanobiocomposites. Radiochimica Acta, Cilt. 111(2), s. 117-128.

[4] Kaptanoglu, I. G., Yusan, S., 2023. Adsorption of uranium ions from aqueous solutions by graphene-based zinc oxide nanocomposites. Journal of Radioanalytical and Nuclear Chemistry, Cilt. 332(11), s. 4705-4719.

[5] Pamukoglu, M. Y., Kirkan, B., Senyurt, M., 2017. Removal of thorium(IV) from aqueous solution by biosorption onto modified powdered waste sludge: Experimental design approach. Journal of Radioanalytical and Nuclear Chemistry, Cilt. 314, s. 343–352.

[6] Jyothi, R. K., Costa De Melo, L. G. T., Santos, R. M., et al., 2023. An overview of thorium as a prospective natural resource for future energy. Frontiers in Energy Research, Cilt. 11, p. 1132611.

[7] Grumezescu, A. M., Andronescu, E., Ficai, A., Ficai, D., Huang, K. S., Gheorghe, I., Chifiriuc, C. M., 2012. Water soluble magnetic biocomposite with potential applications for antimicrobial therapy. Biointerface Research in Applied Chemistry, Cilt. 2(6), s. 469-475.

[8] Saharan, P., Chaudhary, G. R., Mehta, S. K., et al., 2014. Removal of water contaminants by iron oxide nanomaterials. Journal of Nanoscience and Nanotechnology, Cilt. 14(1), s. 627-643.

[9] Rathore, B. S., Chauhan, N. P. S., Panneerselvam, P., et al., 2022. Synthesis and characterization of Ch-PANI-Fe2O3 nanocomposite and its water remediation applications. Water, Cilt. 14(22), p. 3615.

[10] Prill, B., Yusan, S., Sedir, U., et al., 2022. Strontium (II) biosorption studies on starch-functionalized magnetic nanobiocomposites using full factorial design method. Journal of Polymers and the Environment, Cilt. 30(12), s. 5148-5162.

[11] Akbas, Y. A., Yusan, S., Sert, S., et al., 2021. Sorption of Ce(III) on magnetic/olive pomace nanocomposite: Isotherm, kinetic and thermodynamic studies. Environmental Science and Pollution Research, Cilt. 28(40), s. 56782-56794.

[12] Oral, A. E., Aytas, S., Yusan, S., et al., 2020. Preparation and characterization of graphene-based magnetic nano composite for adsorption of lanthanum ions from aqueous solutions. Analytical Letters, Cilt. 53(11), s. 1812-1833.

[13] Akbas, Y. A., Yusan, S., 2020. Development and characterization of non-treated and chemically modified olive pomace biosorbents to remove Ce(III) ions from aqueous solutions. Journal of Radioanalytical and Nuclear Chemistry, Cilt. 323(2), s. 763-772.

[14] Amstad, E., Textora, M., Reimhult, E., 2011. Stabilization and functionalization of iron oxide nanoparticles for biomedical applications. Nanoscale, Cilt. 3, p. 2819.

[15] Laurent, S., Forge, D., Port, M., et al., 2008. Magnetic iron oxide nanoparticles: Synthesis, stabilization, vectorization, physicochemical characterizations, and biological applications. Chemical Reviews, Cilt. 108(6), s. 2064–2110.

[16] Gong, J. L., Wang, X. Y., Zeng, G. M., et al., 2012. Copper (II) removal by pectin–iron oxide magnetic nanocomposite adsorbent. Chemical Engineering Journal, Cilt. 185, s. 100–107.

[17] Kadam, A. A., Jang, J., Lee, D. S., 2016. Facile synthesis of pectin-stabilized magnetic graphene oxide Prussian blue nanocomposites for selective cesium removal from aqueous solution. Bioresource Technology, Cilt. 216, s. 391–398.

[18] Zhang, W., Zhang, L. Y., Zhao, X. J., et al., 2016. Citrus pectin derived ultrasmall Fe_3O_4@ C nanoparticles as a high-performance adsorbent toward removal of methylene blue. Journal of Molecular Liquids, Cilt. 222, s. 995–1002.

[19] Wang, S., Zhang, C., Chang, Q., 2017. Synthesis of magnetic crosslinked starch-graft-poly (acrylamide)-co-sodium xanthate and its application in removing heavy metal ions. Journal of Experimental Nanoscience, Cilt. 12, s. 270–284.

[20] Liang, Z., Wu, X., Xie, Y., et al., 2012. A facile approach to fabricate water-soluble Au-Fe_3O_4 nanoparticle for liver cancer cells imaging. Chinese Journal of Chemistry, Cilt. 30, s. 1387–1392.

[21] Naushad, M., Ahamad, T., Sharma, G., et al., 2016. Synthesis and characterization of a new starch/SnO2 nanocomposite for efficient adsorption of toxic Hg2+ metal ion. Chemical Engineering Journal, Cilt. 300, s. 306–316.

[22] Han, R., Zou, W., Wang, Y., et al., 2007. Removal of uranium (VI) from aqueous solutions by manganese oxide coated zeolite: Discussion of adsorption isotherms and pH effect. Journal of Environmental Radioactivity, Cilt. 93, s. 127–143.

[23] Yang, S. K., Tan, N., Yan, X. M., et al., 2013. Thorium(IV) removal from aqueous medium by citric acid treated mangrove endophytic fungus Fusarium sp. #ZZF51. Marine Pollution Bulletin, Cilt. 74(1), s. 213-219.

[24] Tuzen, M., Sarı, A., Saleh, T. A., 2020. Synthesis, characterization, and evaluation of carbon nanofiber modified-polymer for ultra-removal of thorium ions from aquatic media. Chemical Engineering Research and Design, Cilt. 163, s. 76-84.

[25] Anirudhan, T. S., Rijith, S., Tharun, A. R., 2010. Adsorptive removal of thorium(IV) from aqueous solutions using poly(methacrylic acid)-grafted chitosan/bentonite composite matrix: Process design and equilibrium studies. Colloids and Surfaces A: Physicochemical and Engineering Aspects, Cilt. 368(1–3), s. 13-22.

[26] Langmuir, I., 1918. The adsorption of gases on plane surfaces of glass, mica, and platinum. Journal of the American Chemical Society, Cilt. 40, s. 1361–1403.

[27] Yusan, S. D., Erenturk, S. A., 2011. Sorption behaviors of uranium (VI) ions on α-FeOOH. Desalination, Cilt. 269, s. 58–66.

[28] Yusan, S. D., Akyil, S., 2008. Sorption of uranium (VI) from aqueous solutions by akaganeite. Journal of Hazardous Materials, Cilt. 160, s. 388–395.

[29] Yusan, S., Gok, C., Erenturk, S., et al., 2012. Adsorptive removal of thorium (IV) using calcined and flux calcined diatomite. Applied Clay Science, Cilt. 67, s. 106–116.

[30] Jaycock, M. J., Parfitt, G. D., 1981. Chemistry of Interfaces. Ellis Horwood Ltd., Onichester. Retrieved from https://agris.fao.org/agris-search/search.do?recordID=US201300325033 (Erişim Tarihi: 18 Ekim 2021).

DEU FMD 27(79) (2025) 147-151

Dokuz Eylül Üniversitesi Mühendislik Fakültesi Fen ve Mühendislik Dergisi
Dokuz Eylul University Faculty of Engineering Journal of Science and Engineering
Elektronik/Online ISSN: 2547-958X

RESEARCH ARTICLE / ARAŞTIRMA MAKALESI

Investigating the Relationship between Soil Gas Radon and Soil Permeability by Using Artificial Neural Networks

Yapay Sinir Ağları Kullanılarak Toprak Gazı Radonu ve Toprak Geçirgenliği arasındaki İlişkinin Araştırılması

Selin Erzin

Dokuz Eylul University, Science Faculty, Physics Department, 35390, İzmir, TÜRKİYE

Corresponding Author /Sorumlu Yazar : selin.erzin@deu.edu.tr

Abstract

This study aims to explore the relationship between soil gas radon concentration (C_{Rn}) and soil permeability (k). To accomplish this, a single linear regression analysis (SLRA) model and an artificial neural network (ANN) model were built from 142 soil gas C_{Rn} and k measurements collected from the literature. When soil gas C_{Rn} values predicted by both models were compared with those measured, the ANN model outperformed the SLRA model. Furthermore, several performance metrics, including correlation coefficient, root mean square error, relative absolute error, and mean absolute error were determined to examine the prediction capabilities of SLRA and ANN models. The metrics obtained demonstrated that the ANN model exhibited superior performance to the SLRA model, thereby showing the accuracy and applicability of the ANN model for forecasting soil gas C_{Rn} values. The study's findings indicated that the developed ANN model may be utilized to forecast soil gas C_{Rn} values based on soil k values.

Keywords: *Soil gas radon, Soil permeability, Artificial neural networks*

Öz

Bu çalışmanın amacı, toprak gazı radon konsantrasyonu (C_{Rn}) ile toprak geçirgenliği (k) arasındaki ilişkiyi araştırmaktır. Bunu gerçekleştirmek için, literatürden toplanan 142 toprak gazı C_{Rn} ve k ölçümünden bir tek doğrusal regresyon analizi (SLRA) modeli ve bir yapay sinir ağı (YSA) modeli oluşturulmuştur. Her iki model tarafından tahmin edilen toprak gazı C_{Rn} değerleri ölçülenlerle karşılaştırıldığında, YSA modeli SLRA modelinden daha iyi performans göstermiştir. Ayrıca, SLRA ve YSA modellerinin tahmin yeteneklerini incelemek için korelasyon katsayısı, kök ortalama kare hatası, bağıl mutlak hata ve ortalama mutlak hata dahil olmak üzere çeşitli performans ölçütleri belirlenmiştir. Elde edilen ölçütler, YSA modelinin SLRA modelinden daha üstün performans sergilediğini ve böylece toprak gazı C_{Rn} değerlerinin tahmininde YSA modelinin doğruluğunu ve uygulanabilirliğini göstermiştir. Çalışmanın bulguları, geliştirilen YSA modelinin toprak k değerlerine dayalı olarak toprak gazı C_{Rn} değerlerini tahmin etmek için kullanılabileceğini göstermiştir.

Anahtar Kelimeler: *Toprak gazı radonu, Toprak geçirgenliği, Yapay sinir ağları*

1. Introduction

Radon, a radioactive gas prevalent in the environment, is a potential health concern for humans. The natural radionuclides ^{235}U, ^{232}Th, and ^{238}U release radon through their decay chains [1]. There are three radon isotopes: ^{222}Rn, ^{220}Rn, and ^{219}Rn. The most common isotope of radon is ^{222}Rn, which is formed when radium (^{226}Ra) decays in the ^{238}U chain. Consequently, the term "radon" refers to ^{222}Rn in the vast majority of cases, including this study.

^{222}Rn is present in all soils and rocks in the Earth surface. The disintegration of ^{222}Rn creates alpha particles and other radionuclides, which can be breathed by humans. The ionizing radiation's adverse effects on human health are widely known. ^{222}Rn is a significant natural source of ionizing radiation, accounting for approximately fifty percent of the natural radiation dosage because of ionizing radiation [2]. Recent research has connected long-term exposure to relatively low levels of ^{222}Rn concentration (C_{Rn}) to an increased risk of cancer [3-6]. To prevent human exposure, it is vital to anticipate regions with elevated natural radiation levels. Radon potential indicators include soil permeability (k) and soil gas C_{Rn}, which are especially essential in urbanized areas.

Artificial neural networks (ANNs) are intended to mimic the decision-making processes seen in the human brain by simulating the functions of biological neurons. ANNs are composed of linked neurons, which evaluate information and learning patterns from data to make predictions or decisions [7]. The intrinsic complexity and nonlinearity of the ANN structure facilitate the resolution of complex issues, including those involving uncertainties, especially when the fundamental relationship of data is very complicated [8]. Therefore, ANNs are widely employed and regarded as intelligent tools for solving complex issues [9].

In this work, the use of both a single linear regression analysis (SLRA) model and an ANN model to estimate soil gas C_{Rn} values using the soil k values was investigated. To accomplish this, the data of 142 soil gas C_{Rn} and k measurements acquired from the

DOI: https://doi.org/10.21205/deufmd.2025277919

Geliş Tarihi / Received: 31.05.2024
Kabul Tarihi / Accepted: 02.07.2024

literature [1, 10-12] were used. The soil gas C_{Rn} values measured were compared to those predicted by the ANN and SLRA models to assess the efficiency of both models in predicting soil gas C_{Rn} values from the soil *k* values.

2. Materials and Method

2.1. Artificial Neural Networks

An ANN is a sort of machine learning model based on the human brain's structure [13]. ANNs are made up of linked neurons that collaborate for processing information. Neurons are separated into three layers: input, hidden layer(s) and output. The input layer receives input data from the outside world and transmits it into the network [14]. The hidden layer(s) do different computations on the data provided through the input layer, and the results are sent to the output layer [14]. The output layer transmits the data learned by the network to the outside world [15]. Each neuron in a layer is connected to all the other neurons in the layer above it via weighted connections. This form of ANN is also known as a multi-layer feed-forward perceptron (MLP) [16].

ANN performance is highly dependent on the number of hidden layers [17]. In particular, for complex problems where accuracy and the time complexity are the primary limitations, determining the hidden layers' number is an important challenge in the construction of ANNs [18]. ANN models with fewer than three hidden layers exhibited lower accuracy, whereas those with more than three hidden layers were demonstrated to be suboptimal in terms of time complexity [18]. Additionally, the hidden neurons' number is also crucial while developing ANN model. This number is selected based on the intricacy of the input-output relationship [17]. As the relationship develops more complicated, more hidden neurons should be used [17]. As observed by Choobasti et al. [14], using an excessively large number of hidden neurons result in the ANN model's performance in predicting being reduced due to overfitting.

MLP learning is an unconstrained optimization problem that attempts to lower overall error values based on the synaptic weights of the ANN [16]. Using input-output vectors as training data, a learning algorithm iteratively adjusts the synaptic weight values in an MLP to approach the desired behavior [19]. This technique is generally completed in two phases using the backpropagation learning method [17]. To create outputs, data is sent into the ANN through the input layer in the first step [17]. In the second phase, any discrepancies in the expected and actual outputs are communicated from the output layer to the previous layers, with the connection weights modified to lower the error value [20]. After training, ANNs keep learning weights of each neuron in their memory. During the testing phase, a new and previously untested dataset is fed into the ANN to provide forecasts based on the saved learning weights [20]. Finally, the actual values are compared to the predicted values by the ANN to evaluate its prediction ability [20].

2.2. Development of Artificial Neural Network Model

In this study, the use of ANNs to determine the relationship between the soil gas C_{Rn} and soil *k* values was investigated. To accomplish this, the data of 142 soil gas C_{Rn} and *k* measurements acquired from the literature [1, 10-12] were used. In creating the ANN model, the measured *k* value was used as an input parameter, while the determined soil gas C_{Rn} value was used as an output parameter. The details of input and output parameters used in this study are listed in Table 1.

Random samples were selected from the dataset for training and testing. While training dataset was used to build an ANN model and identify its learning weights, testing dataset was used to select the best ANN architecture based on the identified learning weights. To do this, 142 data sets were divided into 20% and 80% sets for testing and training purposes. It has been demonstrated that data preparation before network training can enhance the ANN performance [17, 21]. Thus, the data in this study was normalized from -0.9 to 0.9 using Equation (1) with the ranges given in Table 1.

$$\mathrm{x_{norm}} = 1.8 \times \left(\frac{\mathrm{x} - \mathrm{x_{min}}}{\mathrm{x_{max}} - \mathrm{x_{min}}}\right) - 0.9 \tag{1}$$

where $\mathrm{x_{norm}}$ and x denote normalized and actual values, respectively, while $\mathrm{x_{max}}$ and $\mathrm{x_{min}}$ denote the experimental data's highest and lowest values, respectively.

Table 1. The details of the input and output parameters used in the ANN model developed.

Parameters used	**Minimum**	**Maximum**	**Mean**	**Range**	**Std. Deviation**	**Kurtosis**	**Skewness**
Input parameter							
Soil *k*	5.2×10^{-14}	2.4×10^{-11}	3.16×10^{-12}	2.40×10^{-11}	5×10^{-12}	3.48	6.92
Output parameter							
Soil gas C_{Rn}	0.37	319.40	38.96	319.03	58.73	2.10	2.51

The purpose of an ANN design is to find the optimal architecture of ANNs for a given task. The trial-and-error approach was employed to examine the optimum design of ANNs. Three primary hyperparameters to consider while selecting the best architecture for ANNs are the number of hidden layers, the number of hidden neurons per hidden layer, and the transfer function of each hidden and output layers [22]. These hyperparameters have a vital role in improving the network's prediction accuracy [22]. The hidden layers' number varies with the problem's nature and complexity [23]. When hidden layers' number rises, the ANN model tends to overfit [24]. As a result, in this work, ANN models were created with one to three hidden layers. As mentioned before, determining the number of hidden neurons in the hidden layer(s) is challenging. In this work, the number of hidden neurons in each hidden layer(s) varied from 1 to 5 by one. To obtain optimal ANN performance throughout the stages of training and testing, most often utilized transfer functions (hyperbolic tangent sigmoid (tansig) and logistic sigmoid (logsig) functions) were employed. The Levenberg-Marquardt back-propagation algorithm was employed during the phase of training. The performance of ANN models was then investigated to determine the best ANN structure. Mean absolute error (MAE) was used to evaluate each generated network size's performance until no appreciable improvement was discovered. The best ANN model consists of three hidden layers, each with five hidden neurons, a tansig transfer function in the hidden layers' neurons and output layer neuron and 78 epochs.

2.3. Simple linear regression analysis

Simple linear regression analysis (SLRA) is the most basic form of RA and is used to examine the relationship between two variables. SLRA was employed in this study to assess the relationship between soil gas C_{Rn} and soil k values, with the SPSS 16.0 software program. The 142 data sets utilized in creating the best ANN model were additionally employed for developing the SLRA model, which resulted in the equation below.

$$\text{Soil gas } C_{Rn} = 25.369 + 4\times10^{12} \times \text{soil } k \qquad R^2=0.134 \qquad (2)$$

In Eq. (2), soil k is in m^2 and soil gas C_{Rn} is in kBq m^{-3}.

3. Results and Discussion

The ANN model's predicted soil gas C_{Rn} values were compared to those obtained experimentally in Figs. 1 and 2 for training and testing samples. Almost all of the forecasts in Figs 1 and 2 are close to the perfect prediction line, which is shown as a solid diagonal line. The coefficient of correlation (r) measures the strength of a linear relationship between two variables.

The following guideline was proposed by Smith [25] for |⍰| values:

$|r| \leq 0.2$ There is a weak correlation between the variables.

$0.2 < |r| < 0.8$ There is a correlation between the variables.

$|r| \geq 0.8$ There is a strong correlation between the variables.

The r values of 0.84 and 0.88 obtained for the training and testing samples in Figs. 1 and 2 demonstrate a significant correlation between the predicted and measured soil gas C_{Rn} values based on Smith [25]. In other words, the predicted and measured C_{Rn} values are not significantly disparate. The results also demonstrate that the soil gas C_{Rn} value can be accurately predicted using the constructed ANN model, provided that the soil k value is known.

The SLRA model (Eq. (2)) has an R^2 value of 0.134, based on the SLRA results. The predicted soil gas C_{Rn} values from Eq. (2) were compared to the experimentally obtained soil gas C_{Rn} values in Fig. 3 for all samples to evaluate the SLRA model's prediction performance. The r value of 0.37 in Fig. 3 illustrates that there is a correlation between the predicted and measured values based on Smith [25]. Furthermore, Fig. 3 shows that the SLRA model cannot accurately estimate soil gas C_{Rn} values from soil k values.

In reality, the r value between predicted and measured soil gas C_{Rn} values is a useful indication of the ANN and SLRA models' prediction ability. In this study, two performance metrics (relative absolute error and root mean square error, denoted as *RAE* and *RMSE*) were calculated using the formulae described below to assess the prediction accuracy of the ANN and SLRA models.

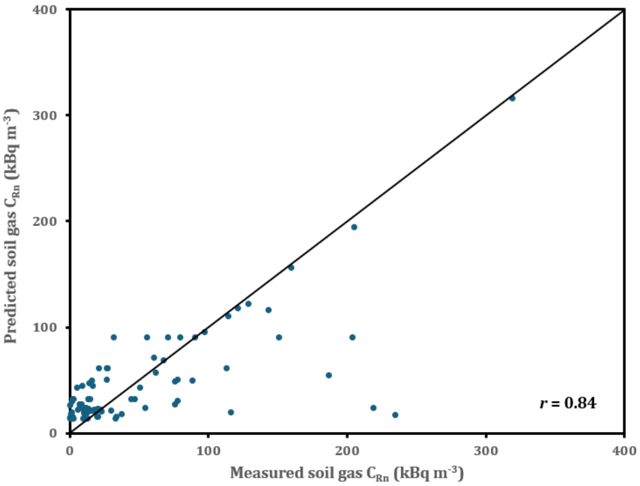

Figure 1. Comparison of the measured soil gas C_{Rn} values with the predicted soil gas C_{Rn} values from the ANN model for training samples.

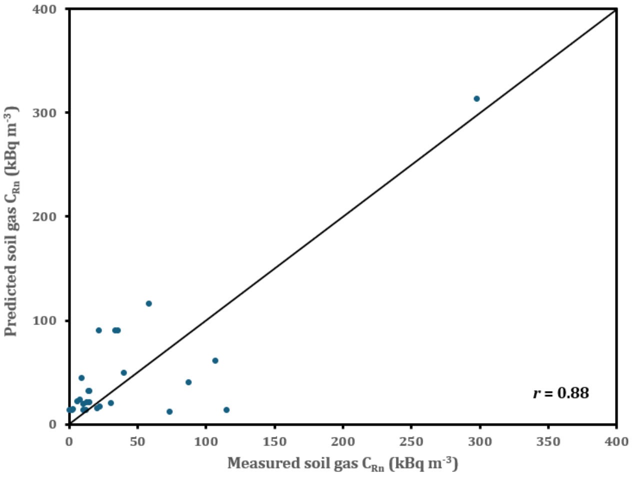

Figure 2. Comparison of the measured soil gas C_{Rn} values with the predicted soil gas C_{Rn} values from the ANN model for testing samples.

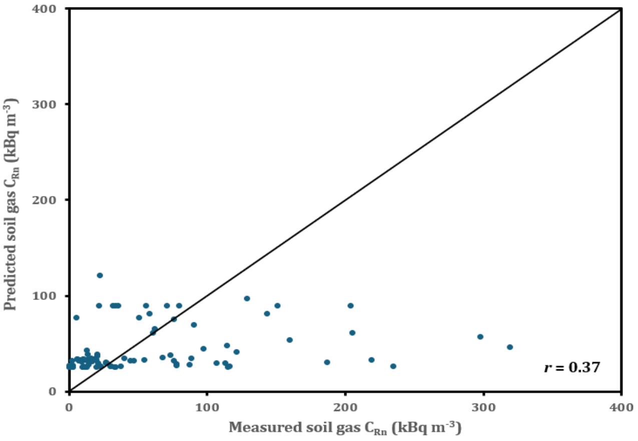

Figure 3. Comparison of the measured soil gas C_{Rn} values with the predicted soil gas C_{Rn} values from the SLRA model for all samples.

$$RAE = \frac{\sum_{i=1}^{N}\left|\left((C_{Rn})_{Pre} - (C_{Rn})_{Exp}\right)\right|}{\sum_{i=1}^{N}\left|\left((C_{Rn})_{Exp} - (C_{Rn})_{Exp\,Mean}\right)\right|} \tag{3}$$

$$RMSE = \sqrt{\frac{1}{N}\sum_{i=1}^{N}\left((C_{Rn})_{Exp} - (C_{Rn})_{Pre}\right)^2} \tag{4}$$

where $(C_{Rn})_{Exp}$ is the measured soil gas C_{Rn}value; $(C_{Rn})_{Pre}$ is predicted soil gas C_{Rn}value; $(C_{Rn})_{Exp\,Mean}$ is the measured soil gas C_{Rn}values' mean value; and N is the sample number. In a perfect forecast, the *RAE* value is 0; the *RAE* value increases as the model prediction error increases. The closer the *RMSE* is to zero, the smaller the difference between forecasts and observations.

Table 2 illustrates the developed ANN and SLRA models' performance metrics. The ANN model performed better in terms of prediction accuracy than the SLRA model based on the computed metrics in Table 2. This result also shows that the developed ANN model is effective and beneficial in predicting soil gas C_{Rn} values. As a result, the soil gas C_{Rn} values can be accurately predicted using the trained ANN structures from the soil *k* values.

Table 2. Performance metrics of the ANN and SLRA models developed in this study.

Model	Data	*r*	*MAE* (kBq m^{-3})	*RMSE* (kBq m^{-3})	*RAE* (kBq m^{-3})
ANN	Training set	0.84	21.66	38.76	0.52
	Testing set	0.88	25.61	35.48	5.45
SLRA	All set	0.37	35.00	54.50	13.30

4. Conclusion

This research investigates the use of SLRA and ANN models to estimate soil gas C_{Rn} values from soil *k* values. To do this, data including 142 soil gas C_{Rn} and soil *k* measurements from the available literature were used. The soil gas C_{Rn} values predicted from ANN and SLRA models were compared to the measured soil gas C_{Rn} values to assess the models' predictive ability. The comparison results demonstrated a better performance of the ANN model than the SLRA model in predicting soil gas C_{Rn} values. In accordance with the study's findings, the developed ANN model may be applied to forecast soil gas C_{Rn} values using the soil *k* values. This study demonstrates the effectiveness of the ANNs to acquire and illustrate complex relationships among the parameters.

Ethics committee approval and conflict of interest statement

This article does not require ethics committee approval. This article has no conflicts of interest with any individual or institution.

References

[1] Nuhu, H., Hashim, S., Aziz Saleh, M., Syazwan Mohd Sanusi, M., Hussein Alomari, A., Jamal, M.H., Abdullah, R.A., Hassan, S.A. 2021. Soil Gas Radon and Soil Permeability Assessment: Mapping Radon Risk Areas in Perak State, Malaysia, PLoS One, Vol. 16(7), e0254099.

[2] WHO. 2011. Guidelines for drinking water quality. World Health Organization, Copenhagen. 2011 Vol 1. 3rd edition).

[3] Alonso, H., Rubiano, J.G., Guerra, J.G., Arnedo, M.A., Tejera, A., Martel, P. 2019. Assessment of Radon Risk Areas in the Eastern Canary Islands using Soil Radon Gas Concentration and Gas Permeability of Soils, Science of The Total Environment, Vol. 664, p. 449–460.

[4] Giustini, F., Ciotoli, G., Rinaldini, A., Ruggiero, L., Voltaggio, M. 2019. Mapping the Geogenic Radon Potential and Radon Risk by Using Empirical Bayesian Kriging Regression: A Case Study from A Volcanic Area of Central Italy. Science of The Total Environment, Vol. 661, p. 449–464.

[5] ICRP. 2010. Lung Cancer Risk from Radon and Progeny and Statement on Radon. ICRP Publication 115. Ann. ICRP, Vol. 40(1), p. 1–64.

[6] UNSCEAR. 2006. Effects of Ionizing Radiation-Volume II: Scientific Annexes C, D and E. United Nations, New York.

[7] Sharshir, S.S., Abd Elaziz, M., Elsheikh, A. 2023. Augmentation and Prediction of Wick Solar Still Productivity Using Artificial Neural Network Integrated with Tree–Seed Algorithm, International Journal of Environmental Science and Technology, Vol. 20, p. 7237–7252.

[8] Araei, A.A. 2013. Artificial Neural Networks for Modeling Drained Monotonic Behavior of Rockfill Materials. International Journal of Geomechanics, Vol. 14(3), 04014005.

[9] Khandelwal, M., Singh, T.N. 2009. Prediction of Blast-Induced Ground Vibration Using Artificial Neural Network. International Journal of Rock Mechanics and Mining Sciences, Vol. 46(7), p. 1214-1222.

[10] Neznal, M., Neznal, M., Matolin, M., Barnet, I., Miksova, J. 2006. The New Method for Assessing the Radon Risk of Building Sites. Project report. State Office for Nuclear Safety, Prague

[11] Cosma, C., Cucoş-Dinu, A., Papp, B., Begy, R., Sainz, C. 2013. Soil and Building Material as Main Sources of Indoor Radon in Băiţa-Ştei Radon Prone Area (Romania), Journal of Environmental Radioactivity, Vol. 116, p. 174-179.

[12] Beltrán-Torres, S., Szabó, K.Z., Tóth, G., Tóth-Bodrogi, E., Kovács, T., Szabó, C. 2023. Estimated Versus Field Measured Soil Gas Radon Concentration and Soil Gas Permeability, Journal of Environmental Radioactivity, Vol. 265, 107224.

[13] Ünal, H.T., Başçiftçi, F. 2022. Evolutionary Design of Neural Network Architectures: A Review of Three Decades of Research, Artificial Intelligence Review, Vol. 55, p. 1723–1802.

[14] Choobbasti AJ, Farrokhzad F, Barari A (2009) Prediction of Slope Stability Using Artificial Neural Network (A Case Study: Noabad, Mazandaran, Iran). Arabian Journal of Science and Engineering, Vol. 2, p. 311–319

[15] Guo, Z., Uhrig, R.E. 1992. Use of Artificial Neural Networks to Analyze Nuclear Power Plant Performance, Nuclear Technology, Vol. 99, p. 36–42

[16] Goktepe B, Agar E, Lav AH (2004) Comparison of Multilayer Perceptron and Adaptive Neuro-Fuzzy System on Backcalculating the Mechanical Properties of Flexible Pavements ARI: The Bulletin of Istanbul Technical University, Vol. 54, p. 65–77.

[17] Erzin, S. 2024. Prediction of the Radon Concentration in Thermal Waters Using Artificial Neural Networks, International Journal of Environmental Science and Technology, Vol. 21(3), p. 7321–732.

[18] Uzair, M., Jamil, N. 2020. Effects of Hidden Layers on the Efficiency of Neural networks. 2020 IEEE 23rd International Multitopic Conference (INMIC), 1-6.

[19] Gopalakrishnan, K. 2010. Effect of Training Algorithms on Neural Networks Aided Pavement Diagnosis, International Journal of Engineering Science and Technology, Vol. (2), p. 83-92.

[20] Erzin, Y., Rao, B.H., Singh, D.N. 2008. Artificial Neural Network Models for Predicting Soil Thermal Resistivity, International Journal of Thermal Sciences, Vol. 47(10), p. 1347–1358.

[21] Motahar, S., Sadri, S. 2021. Applying Artificial Neural Networks to Predict the Enhanced Thermal Conductivity of a Phase Change Material with Dispersed Oxide Nanoparticles, International Journal of Energy Resources, Vol. 45, p. 15092–15109.

[22] Mahmoud, B., Pete, B., Majid, H., Sahar, H. 2021. Ten-Year Estimation of Oriental Beech (Fagus Orientalis Lipsky) Volume Increment in Natural Forests: A Comparison of An Artificial Neural Networks Model, Multiple Linear Regression and Actual Increment, Forestry: An International Journal of Forest Research, Vol. 94(4), p. 598–609.

[23] Muhammad Waseem, A., Monjur, M., Yacine, R. 2017. Trees vs Neurons: Comparison Between Random Forest and ANN for High-Resolution Prediction of Building Energy Consumption, Energy and Buildings, Vol. 147, p. 77-89, ISSN 0378-7788.

[24] Kaastra, I., Boyd, M. 1996. Designing a Neural Network for Forecasting Financial and Economic Time Series. Neurocomputing, Vol. 10(3), p. 215-236.

[25] Smith, G.N. 1986. Probability and Statistics in Civil Engineering: An Introduction, Collins, London

DEU FMD 27(79) (2025) 152-159

Dokuz Eylül Üniversitesi Mühendislik Fakültesi Fen ve Mühendislik Dergisi
Dokuz Eylul University Faculty of Engineering Journal of Science and Engineering
Elektronik/Online ISSN: 2547-958X

RESEARCH ARTICLE / ARAŞTIRMA MAKALESI

An Energy-efficient Parallel ASIC Implementation of Advanced Encryption Standard (AES) Algorithm Robust against Side-channel Attacks

Gelişmiş Şifreleme Standardı (AES) Algoritmasının Yan-Kanal Saldırılarına Dayanıklı ve Enerji Verimliliği Yüksek Paralel ASIC Uygulaması

Serdar Ünal [1], **Faik Başkaya** [2*]

[1] Fraunhofer Institute for Integrated Circuits IIS, Fraunhofer-Gesellschaft, Erlangen, GERMANY
[2] Department of Electrical and Electronics Engineering, Boğaziçi University, İstanbul, TÜRKİYE
Corresponding Author / Sorumlu Yazar *: faik.baskaya@bogazici.edu.tr

Abstract

Encryption becomes more crucial than ever in an increasingly interconnected world. Advanced Encryption Standard (AES) is still considered secure after more than 20 years thanks to its mathematical properties. However, side-channel attacks (SCA) threaten improper AES implementations. In this paper, different AES implementations are introduced, and their resistances against power SCA, namely Correlation Power Analysis (CPA) attack, are shown. For energy efficiency, the increase in power consumption due to the extras added for countering SCA was minimized by register-level organizations and process-related optimizations. Different AES implementations were constructed and processed through Cadence ASIC flow (TSMC 65 nm LP technology). SCA resistance was evaluated using the ChipWhisperer platform operating on realistic power consumption values obtained after RTL-to-GDSII flow. The results demonstrate that pipelining and unrolling the AES rounds increase the SCA resistance at the expense of a minimal reduction in energy efficiency. The proposed implementations are suitable for use with different side-channel attack countermeasures.

Keywords: *ASIC Implementation of Advanced Encryption Standard (AES), Hardware Security, Digital CMOS Design, Side-Channel Attacks, Correlation Power Analysis (CPA), ChipWhisperer*

Öz

Şifreleme, giderek birbirine bağlanan bir dünyada her zamankinden daha önemli hale gelmektedir. Gelişmiş Şifreleme Standardı (AES), matematiksel özellikleri sayesinde 20 yıldan fazla bir süre sonra hala güvenli kabul edilmektedir. Ancak yan kanal saldırıları (SCA), uygunsuz AES uygulamalarını tehdit etmektedir. Bu çalışmada farklı AES uygulamaları tanıtılmakta ve bunların güç Yan-Kanal Saldırısı'na (SCA), spesifik olarak Korelasyon Güç Analizi (CPA) saldırısı, karşı dirençleri gösterildi. Enerji verimliliği açısından, yan-kanal saldırısına karşı yapılan eklemeler nedeniyle güç tüketiminde meydana gelen artış, yazmaç düzeyindeki organizasyonlar ve çip akışı bazlı optimizasyonlar ile minimuma indirildi. Farklı AES uygulamaları oluşturuldu ve Cadence ASIC akışı (TSMC 65 nm LP teknolojisi) aracılığıyla işlendi. Yan-Kanal Saldırısı direnci, RTL'den GDSII'ye çip akışından sonra elde edilen gerçekçi güç tüketimi değerleri üzerinde çalışan ChipWhisperer platformu kullanılarak değerlendirildi. Sonuçlar, AES turlarının boru hattına yerleştirilmesinin ve açılmasının (unroll), enerji verimliliğinde minimum azalma karşılığında Yan-Kanal Saldırısı direncini arttırdığını göstermektedir. Önerilen uygulamalar farklı Yan-Kanal Saldırısı savunma önlemleriyle kullanılmaya uygundur.

Anahtar Kelimeler: *Gelişmiş Şifreleme Standardı (AES) ASIC Uygulaması, Donanım Güvenliği, Dijital CMOS Tasarımı, Yan-Kanal Saldırıları, Korelasyon Güç Analizi (CPA), ChipWhisperer*

1. Introduction

As the world turns into a global village, communication between people around the world is increasing. A tremendous amount of information flows through many channels at every time instant. Although communication security has been an important issue since very old times, security concerns are growing more than ever with increasing communication volume. Encryption is a method that is used to eliminate or reduce security concerns. In encryption, the plain text messages are converted to cipher text messages using a cipher key so that an adversary who intercepts the unintelligible cipher text message from the communication channel cannot understand the real message. There are two types of encryptions, namely symmetric and asymmetric encryption. In symmetric encryption, the same key is used for both encryption and decryption, whereas in asymmetric encryption a different key is used for each of the encryption and decryption actions. The focus of this work is the power side-channel attack on AES algorithm, which is a symmetric encryption algorithm. AES algorithm was developed after a competition organized by the US National Institute of Science and Technology (NIST) in 2000. The winner of the competition was the Rijndael algorithm [1], which has been called AES since then, and it was published as Federal Information Processing Standard (FIPS) in 2001 [2]. Since its declaration as Type-1 Suite-B Encryption Algorithm, it has been accepted as suitable for securing classified and unclassified information worldwide [3]. AES algorithm contains four fundamental operations: SubBytes, ShiftRows, MixColumns, and AddRoundKey. These operations are combined to form a round

DOI: https://doi.org/10.21205/deufmd.2025277920

Geliş Tarihi / Received: 13.05.2024
Kabul Tarihi / Accepted: 28.07.2024

that is executed multiple times using round keys, which are obtained using KeyExpansion routine from the initial cipher key. For more than 20 years, AES has successfully resisted attacks directed against its mathematical structure [4]. However, side-channel attacks that utilize unintended leakages from the implementation such as power consumption, electromagnetic radiation, execution time, sound, etc., are also posing a threat to AES implementations. These leakages are used together with knowledge about the system to disclose secret information [5]. Numerous papers have been published about side-channel attacks on AES [6-8]. In this paper, an ASIC simulation environment that enables the evaluation of power side-channel resistance of an IC design before fabrication is introduced. In addition, the effects of architectural decisions such as pipelining the rounds or unrolling the rounds on the power side-channel attack resistance are also examined. The main objective of this work is to design a power side-channel attack resistant AES block. This paper is organized as follows. Section 2 provides the underlying theoretical principles of obtaining a side-channel attack resistant and energy-efficient design and the methods to achieve these objectives. Section 3 describes the implemented AES versions. Section 4 presents the design environments and evaluation of the implemented AES versions according to the design objectives. Section 5 concludes the paper.

2. Methodology

The applied methods for improving side-channel resistance and energy efficiency are explained in Section 2.1 and Section 2.2, respectively.

2.1. Applied methods to increase side-channel attack resistance

A power side-channel attack is the main focus of this paper. More specifically, Correlation Power Analysis (CPA), initially developed by Brier [9], was executed on the power traces collected from the simulation of the AES blocks. In general, CPA uses the Pearson correlation function to calculate the correlation values of different power traces [9,10]. The Pearson correlation function can be formulated as

$$C(T,P) = \frac{\mu(\mathrm{TP}) - \mu(\mathrm{T})\mu(\mathrm{P})}{\sqrt{\sigma^2(T)\sigma^2(P)}} \tag{1}$$

where T is the set of power traces, P is the set of estimated power values from the power model, μ is the population mean, and σ is the standard deviation. A set of power traces was obtained using the Cadence environment while running encryption on 500,000 random inputs. The estimated power consumption values according to the power model corresponding to each random input were calculated via ChipWhisperer's functions. Depending on the attack point, either Hamming Weight (HW) or Hamming Distance (HD) functions are used to model the corresponding power consumption for a given register state or register transition, respectively. HW is directly obtained by adding all the bit values in a register; therefore, having more 1's in the register bits means a higher power consumption value. On the other hand, HD is calculated as the number of bits that have flipped between two consecutive states of a register [11]. Since the bit values and bit changes give information about the processed information, the pipelining method was employed to mix power consumption values of different inputs with each other by taking advantage of processing different inputs simultaneously. Unrolling the AES rounds, i.e. making them a feedforward combinational path that spans from the first round to the last, was also employed in order to make state transitions less visible as all the rounds execute at the same clock period instead of waiting for the next clock edge.

2.2. Applied techniques for improving energy efficiency

Lowering the power consumption is the key to achieve energy efficiency. In this work, several techniques were applied to reduce power consumption. The consumed power is proportional to (α), which is the activity factor as shown in

$$P_{static} = I_{static} V_{DD} \tag{2}$$

$$P_{dynamic} = \alpha C V_{DD}^2 f + V_{DD} I_{sc} \tag{3}$$

$$P_{total} = P_{static} + P_{dynamic} \tag{4}$$

where P=power, I=current, V_{DD}=supply voltage, α =activity factor, C=load capacitance, f=switching frequency, I_{sc}=short circuit current [12]. As visible in Eq. (3), the activity should be decreased to reduce the dynamic power consumption. In order to accomplish this, RTL was coded in such a way that the switching activity of the modules was reduced by the enable signals and fixing of the module inputs. In addition, clock gating was enabled in ASIC flow to decrease the unnecessary switching activity. TSMC 65 nm via Europractice offers two types of processes: General Purpose (GP), and Low Power (LP) [13]. LP process was preferred in this work to further reduce the overall power consumption. Another approach for power reduction is the utilization of different threshold voltage standard cells. There are three standard cell types in the LP process according to the threshold voltage of transistors they are built from: low threshold voltage cells (LVT), standard threshold voltage cells (SVT), and high threshold voltage cells (HVT). Power consumption is proportional to the MOSFET current, which has a relation with the threshold voltage as explained in the following formula

$$i_D = \frac{1}{2} k_n' \left(\frac{W}{L}\right) (V_{GS} - V_t)^2 \tag{5}$$

where i_D is the MOSFET current in saturation, k_n' is the process transconductance parameter, (W/L) is the transistor aspect ratio, V_{GS} is the gate-to-source voltage, and V_t is the threshold voltage [14]. Decreasing the threshold voltage (V_t) increases i_D which means the transistor switches faster but at the cost of a higher current. The design tools were adjusted to favor the use of HVT cells over LVT and SVT cells whenever possible.

3. Constructed AES Versions

In this work, four different AES versions were constructed to observe their power side-channel attack resistance performances. RTL codes for all designs were simulated using xsim from Vivado Design Suite (version 2020.2). Vivado Design Suite was used only as an RTL simulator as the focus of this work is ASIC design instead of FPGA design. Test vectors from NIST "The Advanced Encryption Standard Algorithm Validation Suite" (AESAVS) [15] were used to validate the designs.

3.1. Rolled version

The first version is called the rolled version. This is the base version of AES, and it is used as a reference point in this work. The block diagram of the rolled version can be seen in Figure 1. The different blocks contained in each round are SubBytes, ShiftRows, MixColumns, and AddRoundkey, which are shown in Figure 2 in their processing order. In the rolled version, only one hardware round block is used for nine rounds, where each round takes one clock cycle. To complete the encryption, one more round that is missing the MixColumns block from the original round is required to process the 128-bit block. The rolled version is compact; however, more cycles are required to complete each encryption. Besides, it does not contain any specific side-channel attack countermeasure.

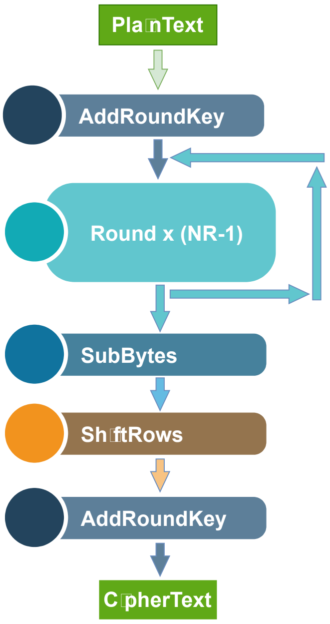

Figure 1. AES block diagram.

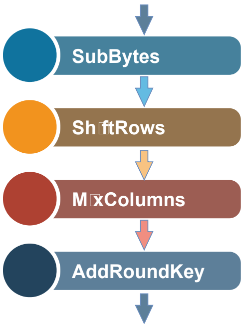

Figure 2. Block diagram of each AES encryption round.

3.2. Pipelined versions

Two different pipelined versions were implemented in this work. The pipelined versions are named 32-bit pipelined and 64-bit pipelined according to the bus widths of the input/output interfaces of the implementation, while both versions process 128-bit plain texts internally. Figure 3 depicts the block diagram of the 32-bit pipelined version. In this implementation, the nine rounds of the rolled version are executed in three identical blocks, which also serve as stages of the pipeline, and the remaining processing is completed combinationally with AddRoundkey, SubBytes, ShiftRows, and AddRoundkey blocks. Figure 4 describes a detailed view of these blocks, which are called "main round" in this work.

Main round block of the pipelined version consists of the same blocks as the round block of the rolled version; however, AddRoundkey block has the first order here as opposed to the last order in the rolled version round block. Main round block also has two inputs and two outputs as opposed to the single-input single-output round block of the rolled version. Every clock cycle, one of the two inputs is routed into the 128-bit input register of the main round block, selected by the 2-to-1 multiplexer. Using this multiplexer, main round block either accepts a new input from the previous stage of the pipeline or uses its own output as its new input, effectively processing the same input for another round. Multiplexer select input is received from a simple shift register called S_{count}, which is four bits for the 32-bit pipelined version and two bits for the 64-bit pipelined version; thus, receiving a new input from the previous pipeline stage once every four cycles or once every two cycles, respectively. This means that every main round block processes a 128-bit input for four cycles if it is a 32-bit pipelined implementation and for two cycles if it is a 64-bit pipelined implementation. This decision for the number of cycles per stage was made based on the bus width; receiving the 128-bit input plain text takes four clock cycles and two clock cycles with a 32-bit bus and 64-bit bus, respectively.

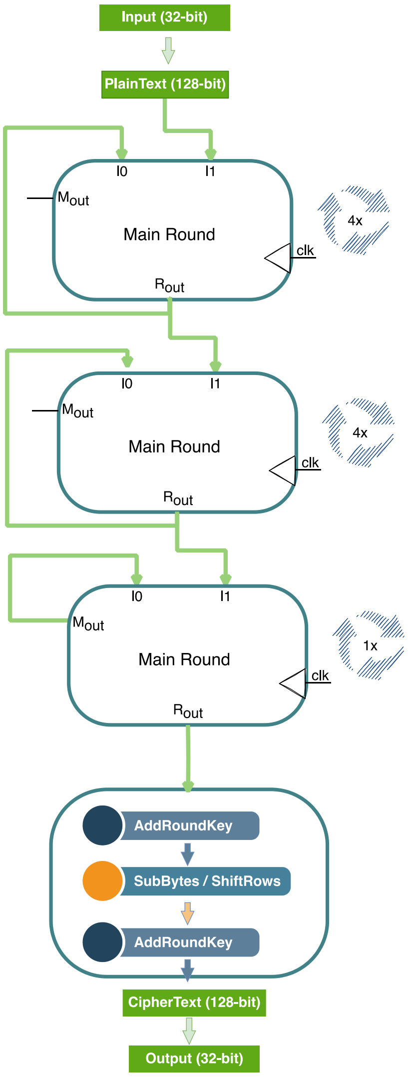

Figure 3. 32-bit pipelined AES implementation.

Since each main round block processes a given input for four cycles or two cycles before forwarding the output to the next stage, three main round blocks are required for the 32-bit pipelined implementation and five main round blocks are required for the 64-bit pipelined implementation. The last main round block in both implementations process only one round of the 9 total rounds. This irregularity is handled by bypassing the processing blocks in the last main round blocks for the cycles a new input is not being received using the M_{out} output port instead of R_{out}. Thanks to M_{out} & R_{out} combination, design simplicity was obtained by using the same main round block despite the mentioned irregularity for the last stage.

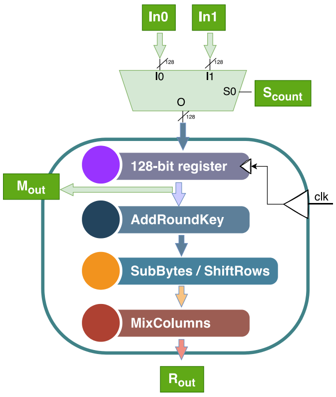

Figure 4. Block diagram of 32-bit pipelined AES implementation main round.

The pipelined configuration allows concurrent processing of three or five inputs in the 32-bit or 64-bit versions, respectively. This increases the throughput and the side-channel attack resistance because of the power consumption interference of individual inputs with each other at the expense of additional hardware and power consumption. A new cipher text can be obtained once every four or two cycles using the 32-bit or 64-bit pipelined configurations, respectively.

3.3. Unrolled version

In the unrolled version, each round of the rolled version is implemented as a separate block with no hardware reuse, and there are no registers between the blocks of different rounds, which effectively turns the entire AES into a purely combinational circuit that can encrypt the input plain text in a single clock cycle. Since the encryption operation fits into one clock cycle, the unrolled version requires a longer clock period. In addition, it occupies the largest area among all versions because of the high number of hardware blocks used. The unrolled version uses a 32-bit interface that is similar to the interfaces of the rolled and 32-bit pipelined versions.

4. Design Environments and Evaluation

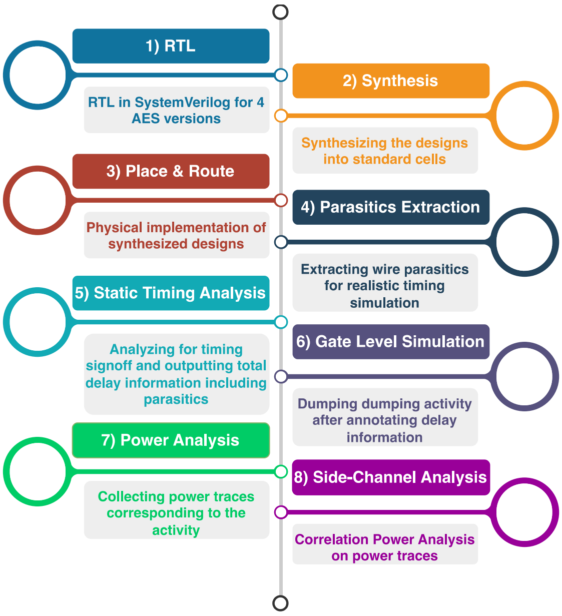

Figure 5. Experiment flow.

All four AES versions explained in Section 3 were processed through the ASIC flow using Cadence tools. ChipWhisperer from NewAE Technology, which is an open-source toolchain containing target hardware, capture hardware, firmware, and software, was used for side-channel attack resistance evaluation. Since power results were obtained by simulation outputs, only the analyzer [16] module of ChipWhisperer was used in this work. The experiment flow summarized in Figure 5 is explained in detail in Section 4.1, Section 4.2, and Section 4.3.

4.1. ASIC environment

TSMC 65 nm LP technology was used for the RTL-to-GDSII flow of different AES implementations. The versions and purposes of the used IC tools are as follows: Genus Synthesis Solution (v19.11) for synthesis, Innovus Implementation System (v19.11) for Place & Route (P & R), Quantus Extraction Solution (v19.1.3) for RC parasitics extraction, Tempus Timing Signoff Solution (v19.11) for Static Timing Analysis (STA), Xcelium Logic Simulation (v19.03) for gate-level simulation, Voltus IC Power Integrity Solution (v19.11) for power analysis.

There is a single functional mode and five different Process-Voltage-Temperature (PVT) corners used in this work, which can be found in Table 1. The corners are listed as Best Case (BC), Low Temperature (LT), Typical Case (TC), Worst Case (WC), and Worst Case Low Temperature (WCL). These PVT corners were combined with the RC extraction corners to obtain the delay corners. The operating frequencies of the designs were chosen to satisfy timing constraints for all the mentioned delay corners after Multi-Mode Multi-Corner (MMMC) analysis.

Table 1. Process, Voltage & Temperature (PVT) corners.

Corners	Process	Voltage (Volts)	Temperature (°C)
BC	FF	1.32	0
LT	FF	1.32	-40
TC	TT	1.2	25
WC	SS	1.08	125
WCL	SS	1.08	-40

For each version, the P & R tool is configured to use 60% standard cell density; therefore, the resulting area is (10/6) times the combined area of the standard cells obtained from the synthesis stage. Six out of nine available metal layers were used in this work as the blocks were designed to be IP's suitable to be integrated into top-level System-on-Chip (SoC).

Design statistics for all versions after P & R can be inspected in Table 2, where logical instances values increase from left to right implying increased hardware usage from the rolled version to the pipelined versions, and to the unrolled version. The unrolled version requires a higher clock period because of the combinational nature of the design completing the entire encryption in a single clock cycle. Positive Worst Negative Slack (WNS) and Worst Hold Slack (WHS) ensure that the signals do not arrive too late or too early so that the flip-flops can receive the correct values. The tool was configured to use HVT cells as much as possible since they consume less power, as explained in Section 2.2. Yet, some LVT cells were still required in the timing-critical paths. The HVT proportion is greater than 50% for all four versions, in line with the energy-efficient target. The layout of the 32-bit pipelined version at the end of the P & R can be seen in Figure 6, which was partitioned to show the approximate locations of the major components of the design. Different colors in the layout correspond to different metal layers. The seemingly regular pattern of nets shows power and ground lines. The yellow arrows at the perimeter of the block correspond to inputs and outputs at the interface of the block.

Table 2. Design statistics after P & R.

	Rolled	Pipe. 32	Pipe. 64	Unrolled
Logical Inst.	20,808	35,986	50,809	80,062
Period (ns)	8	8	8	40
WNS (ns)	0.297	0.086	0.264	0.124
WHS (ns)	0.094	0.090	0.080	0.056
LVT (%)	4.3	11.5	10.0	20.1
SVT (%)	2.2	10.2	7.9	21.4
HVT (%)	93.4	78.3	82.1	58.4

4.2. Trace collection

A test bench containing encryption operation of 500,000 random inputs with the cipher key 128'h2b7e151628aed2a6abf7158809cf4f3c was used for the simulation. The gate-level simulation was made after annotating the gate-level netlist received from Innovus with cell delays and interconnect delays using information from Quantus and Tempus tools so that the parasitic effects are taken into account and the simulation is more realistic. Activity information resulting from the test bench was dumped in multiple Value Change Dump (VCD) files from Xcelium tool, which store the switching activity of nets by recording the times each net switch at. It is important to annotate switching information during power analysis to obtain realistic power consumption values. The power analysis was done at the typical corner. The current drawn by the AES blocks while encrypting 500,000 random inputs was dumped with 50 ps time steps during power analysis in Voltus tool, which provides enough precision for the side-channel attack analysis of both 8 ns (rolled and pipelined) and 40 ns (unrolled) period cases. The current values were interpreted as power values assuming constant supply voltage. The output text files were collected to be used in the power side-channel attack resistance evaluation. To give an insight into the time required to collect power traces, the average Voltus runtime for power analysis of 100,000 input encryption is 5.84 days for the rolled version in a server.

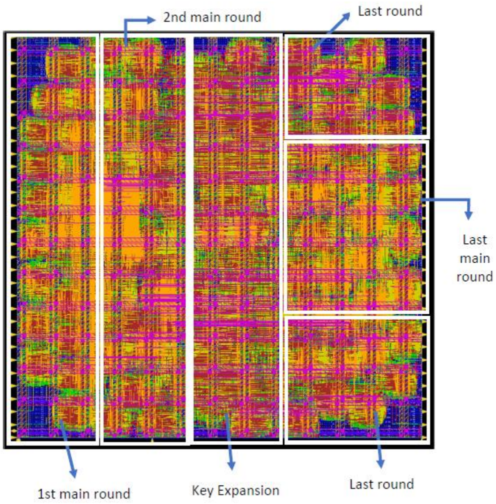

Figure 6. 32-bit pipelined AES implementation layout.

4.3. Side-channel attack resistance evaluation

The outputs from the Voltus tool were prepared to be used by the ChipWhisperer tool, which was used to evaluate side-channel attack resistance from the generated traces. 500,000 input values, 500,000 key values (all the same 128-bit value), and 500,000 trace sets are stored as MATLAB arrays. Each trace set corresponds to the time interval where their respective input is encrypted. These arrays are converted into NumPy arrays and transferred to the ChipWhisperer program. The program uses Correlation Power Analysis (CPA) attack by utilizing the Pearson correlation function [17], as explained in Section 2.1 The software model of AES is already available in the program. The power consumption is modeled by calculating Hamming Weight or Hamming Distance according to the bits of the intermediate values that are generated by the functions of the AES software model. For a particular leakage model (e.g. AddRoundKey output), the power consumption is calculated targeting that point, and the result is compared with the actual traces for every possible key byte combination. Different byte values are tested and ranked according to the correlation value coming from Eq. (1). If the model and the actual power traces are consistent with each other, the correlation value increases. There are many different leakage models targeting different parts of the AES algorithm. The attack point in time is also detected using correlation. As the other time instants give a low correlation with the guessed key byte combination while comparing traces belonging to the different outputs, the correct attack time becomes pinpointed with a high correlation value [18]. To give an insight about the time required to do side-channel analysis, the ChipWhisperer runs for approximately 31.5 hours to analyze 400,000 traces of rolled version for the round_1_2_state_diff_sbox leakage model in a desktop computer with 32 GB RAM and 12 CPU threads. ChipWhisperer results for the rolled version with 500,000 random inputs and round_1_2_state_diff_sbox leakage model can be seen in Table 3, where five most likely guesses for every byte of the cipher key are shown. The guesses that matched the original cipher key were highlighted with a yellow color.

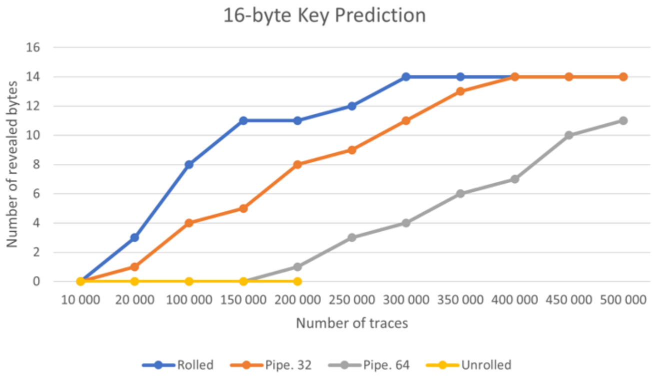

Figure 7. Results of side-channel attacks on all AES versions.

ChipWhisperer results with eleven different input spaces (10,000 - 50,000, - 100,000 - 150,000 - 200,000 - 250,000 - 300,000 - 350,000 - 400,000 - 450,000 - 500,000) can be observed in Figure 7. The revealed bytes are the correct bytes that are visible in the first row of their tables similar to the presented values in Table 3. That is, if the correct byte is the most-correlated guess for a particular byte of the cipher key, it is counted into the number of revealed bytes. Figure 7 compares different AES versions according to the round_1_2_state_diff_sbox leakage model, which appears to be the most successful attack for the collected traces. Different leakage models from ChipWhisperer were also tried but after a small number of inputs round_1_2_state_diff_sbox leakage model starts to dominate and becomes the most effective leakage model for different versions. Therefore, side-channel attack resistances of all four versions were compared using the round_1_2_state_diff_sbox leakage model, which focuses on the Hamming distance between the first and the second round SubBytes outputs. It should be noted that the trace number in the analysis of the unrolled version was limited to 200,000 in these tests, since its larger area & higher standard cell count makes trace collection & side-channel attack testing prohibitively resource-intensive. The worst performing version is the rolled version as expected since it does not contain any specific side-channel attack countermeasure. In general, more bytes are revealed as the input size is increased. However, the number of revealed bytes may not change even after a large number of traces, since some bytes are revealed easily, and some bytes need many more traces to be disclosed as can be seen in results where the number of revealed bytes appears as saturated indicating remaining bytes need much more traces. The pipelined versions perform better with a smaller number of revealed bytes compared to the rolled version. The 64-bit pipelined version is more resistant than the 32-bit pipelined version, as expected. The best-performing version is the unrolled version when the comparison is made at 200,000 traces. The purely combinational encryption approach of the unrolled version leaves little space for attackers, which comes at the cost of a significant increase in area.

Table 3. Byte prediction results after 500,000 traces collected from the rolled AES version.

f	*e*	*d*	*c*	*b*	a	9	8	7	6	5	4	3	2	1	0
2b	7e	15	16	28	9e	c2	a6	ab	f7	15	88	09	cf	4f	3c
31	9a	c1	db	22	ae	62	3b	4e	43	f1	cf	3e	5c	57	02
8f	db	17	3d	53	f3	c5	30	05	2d	c9	a6	74	ab	42	7c
05	7c	aa	3c	71	4d	d2	64	84	7b	3a	3d	e7	48	1f	a7
9b	14	6d	a4	d0	3f	ff	b6	3b	28	b1	48	9b	3c	2b	78

The unrolled and pipelined designs are compared against six designs from the literature in Table 4. The designs from the literature contain different countermeasures for the AES against the power SCA. The effectiveness of our unrolled and pipelined implementations was evaluated comparatively with these countermeasures using Power-Performance-Area (PPA) and SCA resistance metrics. Four of the designs were fabricated and side-channel attacks were executed on the hardware [19-21, 23]. On the other hand, the design Ref. [22] used simulation to evaluate side-channel attack resistance similar to our work. The design Ref. [24] was fabricated but the results are from simulation. Measurements-to-Disclosure (MTD) in Table 4 is the number of traces required for differentiating the correct secret key from all wrong key guesses [25]. It can be reported as the number of traces needed to disclose either one byte from the cipher key or all bytes of the cipher key. In this work, the all-bytes approach was chosen, i.e., "≥ 500K" means, 500,000 traces were collected, analyzed, and still not all of the bytes were disclosed after 500,000 traces. Trace numbers were restricted to 500,000 as collecting traces in simulation with numbers comparable to attacks executed directly on hardware is impractical. Besides, fewer traces in a noise-free simulation environment gives enough insight into the design compared to the noisy hardware setup where the noise requires more traces to be collected for revealing the key. It is reported in Ref. [26] that 160 times more measurements were necessary for a real hardware attack compared to the simulated attack. Therefore, MTD values found in simulations should be scaled by such a large number for a fair comparison of simulation and hardware results unless advanced techniques are employed for reducing noise in hardware setups. In addition, the design Ref. [22] in Table 4, which use simulation to evaluate side-channel resistance, do not report MTD value at all. There is also Ref. [27] that again uses simulation to evaluate SCA resistance against a countermeasure. It has high throughput, but it was not added to the table as it lacks area, power, and MTD information. Ref. [28] uses the same ChipWhisperer Analyzer module but in addition to being done on the FPGA, it also lacks area and power information.

4.4. Energy efficiency evaluation

Energy efficiencies of different designs are compared via a Figure of Merit (FoM) metric, which has a unit of (Gbps/mW). The metric was developed to enable a fair comparison between different designs in different technologies as smaller technology nodes enable higher frequency designs which also result in higher dynamic power consumption. The FoM is calculated as follows:

$$FOM = \frac{throughput(Gpbs)}{power\ consumption(mW)} \tag{7}$$

According to the results reported in Table 4, The 64-bit pipelined version has a throughput greater than Refs. [19], [21], [22], [23], and [24]. Ref. [20] has a throughput higher than the 64-bit pipelined version, but its power consumption is more than three times higher. In terms of area, pipelined versions are the smallest except Ref. [22], [24] which are in the advanced nodes where transistor sizes are smaller. The number of gates in Ref. [22] is also fewer indicating a compact design; however, with less throughput and higher power consumption compared to the 64-bit pipelined version. Operating frequencies in this work are suitable for applications in different domains. Since the frequencies are not very high, the power consumption is smaller and the design does not require special very high-frequency signal handling issues when integrated into the top-level designs while still providing comparable throughput. As far as energy efficiency is concerned, pipelined designs have a higher FoM compared to the unrolled version as well as the designs from the literature except Ref. [24]. However, the design in Ref. [24] has much lower MTD value compared to the pipelined versions. The rolled version has a slightly higher FoM than the pipelined versions; however, it does not contain any specific power side-channel attack countermeasures and it tends to reveal more bytes than the pipelined and unrolled versions as demonstrated in Figure 7.

Table 4. Comparison of different AES implementations.

	Rolled	*Unrolled*	*Pipe. 32*	*Pipe. 64*	[19]	[20]	[21]	[22]	[23]	[24]
Technology (nm)	65	65	65	65	130	65	180	22	130	16
Area (mm^2)	0.134	0.415	0.208	0.278	1.37	0.291	0.67	0.0169	N.A	0.0012
Gates	21K	80K	36K	51K	N.A	N.A	N.A	16K	N.A	N.A
Power (mW)	5.0	21.5	16.0	32.2	44.34	98	12	41.6	11.02	0.08
Clock Cycles	10	1	4	2	11	10	11	10	10	204
Frequency (MHz)	125	25	125	125	110	1320	24	400	38.8	300
Throughput (Gbps)	1.6	3.2	4	8	1.28	16.9	0.28	5.12	0.50	0.18
MTD	≥ 500K	≥ 200K	≥ 500K	≥ 500K	≥ 10M	940K	≥ 800K	N.A	≥ 500K	15983
FoM (Gbps/mW)	0.32	0.15	0.25	0.25	0.03	0.17	0.02	0.12	0.05	2.25

5. Conclusions

Four different implementations were analyzed in this work to address the side-channel attack resistance of the AES algorithm. The rolled version is the baseline implementation where a single hardware unit is used to complete all nine rounds, one round at a clock cycle. This is used as a reference point in this work. The following two versions are 32-bit pipelined and 64-bit pipelined implementations containing additional hardware to allow more than one input to be processed simultaneously within the same clock cycle. Pipelined versions enhance resistance to side-channel attacks through increased parallelism via processing consecutive input samples simultaneously and mixing the sum of their power consumption values. Since the attacker can observe only the total power consumption, calculating correlation due to distinct inputs becomes more difficult, increasing the MTD values. The last version is the unrolled version containing purely combinational rounds with no hardware reuse. Since there is no clock transition between the different AES steps, the unrolled version benefits from a complex, non-repetitive power profile, and it becomes more difficult to differentiate the different steps from each other in the power traces. In all proposed cases; namely, the unrolled and pipelined versions, the unique power trace characteristics of each step in the standard AES implementation are obfuscated by processing multiple inputs or multiple steps simultaneously. Therefore, correlation power analysis approach effectiveness is reduced, resulting in lower correlation values.

Taking the power consumptions of the different approaches into account, pipelined versions provide a reasonably strong resistance against side-channel attacks at a reasonably low power consumption, resulting in the best FoM for 65nm or earlier technology nodes. In order to improve energy efficiency, RTL was coded to favor lower switching activity. In addition, TSMC Low Power (LP) process was chosen, and higher threshold standard cells were used as long as the timing constraints were satisfied.

All versions were designed from RTL-to-GDSII in TSMC 65 nm using Cadence tools, and the power traces obtained from Voltus tool were evaluated in ChipWhisperer program against Correlation Power Analysis (CPA). The unrolled version performed the best side-channel attack resistance at the expense of the highest area and logical standard cell count. Thanks to the efficient utilization of hardware blocks, 32-bit and 64-bit pipelined versions achieved high throughput with a lower area compared to the unrolled version. Their 16.0 mW and 32.2 mW power consumptions stand lower compared to the existing designs in the literature as well. It was demonstrated that pipelined and unrolled implementations of the AES algorithm have higher side-channel attack resistances compared to the baseline rolled implementation of AES at the expense of a minor reduction in energy efficiency.

Ethics committee approval and conflict of interest statement

This article does not require ethics committee approval. This article has no conflicts of interest with any individual or institution.

Acknowledgment

This research was conducted while the first author was an employee of TUBITAK BILGEM. We thank TUBITAK BILGEM for allowing us to use the ASIC tools required to complete this work.

Author Contribution Statement

Faik Baskaya: project administration, conceptualization, supervision, writing (review & editing). Serdar Unal: conceptualization, methodology, software, validation, formal analysis, investigation, resources, data curation, visualization, writing (original draft).

References

[1] Daemen, J., Rijmen, V. 2000. The Block Cipher Rijndael. In J.-J. Quisquater, B. Schneier ed. Smart Card Research and Applications. Springer Berlin Heidelberg, Berlin, Heidelberg, pp. 277–284. DOI: https://doi.org/10.1007/10721064_26

[2] National Institute of Standards and Technology. 2016. Cryptographic Standards and Guidelines AES Development. https://csrc.nist.gov/projects/cryptographic-standards-and-guidelines/archived-crypto-projects/aes-development (Accessed: 23.07.2022).

[3] Alghazzawi, D. M., Hasan, S. H., Trigui, M. S. 2014. Advanced Encryption Standard - Cryptanalysis research. 2014 International Conference on

Computing for Sustainable Global Development (INDIACom), pp. 660–667. DOI: 10.1109/IndiaCom.2014.6828045

[4] Socha, P., Brejník, J., Bartik, M. 2018. Attacking AES implementations using correlation power analysis on ZYBO Zynq-7000 SoC board. 2018 7th Mediterranean Conference on Embedded Computing (MECO), pp. 1–4. DOI: 10.1109/MECO.2018.8406034

[5] Zhou, Y., Feng, D. 2005. Side-Channel Attacks: Ten Years After Its Publication and the Impacts on Cryptographic Module Security Testing. IACR Cryptol. ePrint Arch., 388. http://eprint.iacr.org/2005/388 (Accessed: 23.07.2022).

[6] Ghandali, S., Ghandali, S., Tehranipoor, S. 2021. Deep K-TSVM: A Novel Profiled Power Side-Channel Attack on AES-128. IEEE Access, Vol. 9, pp. 136448–136458. DOI: 10.1109/ACCESS.2021.3117761

[7] Mushtaq, M., Akram, A., Bhatti, M. K., Rais, R. N. B., Lapotre, V., Gogniat, G. 2018. Run-time Detection of Prime + Probe Side-Channel Attack on AES Encryption Algorithm. 2018 Global Information Infrastructure and Networking Symposium (GIIS), pp. 1–5. DOI: 10.1109/GIIS.2018.8635767

[8] Guo, S., Zhao, X., Zhang, F., Wang, T., Shi, Z. J., Standaert, F.-X., Ma, C. 2014. Exploiting the Incomplete Diffusion Feature: A Specialized Analytical Side-Channel Attack Against the AES and Its Application to Microcontroller Implementations. IEEE Transactions on Information Forensics and Security, Vol. 9(6), pp. 999–1014. DOI: 10.1109/TIFS.2014.2315534

[9] Brier, E., Clavier, C., Olivier, F. 2004. Correlation Power Analysis with a Leakage Model. In M. Joye, J.-J. Quisquater ed. Cryptographic Hardware and Embedded Systems - CHES 2004. Springer Berlin Heidelberg, Berlin, Heidelberg, pp. 16–29. DOI: https://doi.org/10.1007/978-3-540-28632-5_2

[10] Kundrata, J., Fujimoto, D., Hayashi, Y., Barić, A. 2020. Comparison of Pearson correlation coefficient and distance correlation in Correlation Power Analysis on Digital Multiplier. 2020 43rd International Convention on Information, Communication and Electronic Technology (MIPRO), pp. 146–151. DOI: 10.23919/MIPRO48935.2020.9245325

[11] Brown, S. D., Vranesic, Z. G. 2012. Fundamentals of Digital Logic with VHDL Design. 3rd edition. McGraw Hill Education, p. 624.

[12] Weste, N. H. E., Harris, D. 2005. CMOS VLSI Design: A Circuits and Systems Perspective. 3rd edition. Pearson Education, pp. 188-191, 196.

[13] TSMC Technologies. https://europractice-ic.com/technologies/asics/tsmc/ (Accessed: 23.07.2022).

[14] Sedra, A. S., Smith, K. C. 2011. Microelectronic Circuits. 6th edition. Oxford University Press, New York, pp. 362-366.

[15] Bassham, L. E. 2002. The Advanced Encryption Standard Algorithm Validation Suite (AESAVS). https://csrc.nist.gov/CSRC/media/Projects/Cryptographic-Algorithm-Validation-Program/documents/aes/AESAVS.pdf (Accessed: 23.07.2022).

[16] NewAE Technology. 2022. Analyzer. https://chipwhisperer.readthedocs.io/en/latest/analyzer-api.html (Accessed: 08.05.2023).

[17] NewAE Technology. 2018. Correlation Power Analysis. https://wiki.newae.com/Correlation_Power_Analysis (Accessed: 23.07.2022).

[18] O'Flynn, C. 2016. Introduction to Side-Channel Power Analysis (SCA, DPA). https://www.youtube.com/watch?v=OlX-p4AGhWs (Accessed: 11.05.2023).

[19] Tokunaga, C., Blaauw, D. 2009. Secure AES Engine with a Local Switched-Capacitor Current Equalizer. 2009 IEEE International Solid-State Circuits Conference - Digest of Technical Papers, pp. 64-65,65a. DOI: 10.1109/ISSCC.2009.4977309

[20] Lu, S., Zhang, Z., Papaefthymiou, M. 2015. 1.32GHz High-Throughput Charge-Recovery AES Core with Resistance to DPA Attacks. 2015 Symposium on VLSI Circuits (VLSI Circuits), pp. C246–C247. DOI: 10.1109/VLSIC.2015.7231274

[21] Miura, N., Fujimoto, D., Korenaga, R., Matsuda, K., Nagata, M. 2014. An Intermittent-Driven Supply-Current Equalizer for 11x and 4x Power-Overhead Savings in CPA-Resistant 128bit AES Cryptographic Processor. 2014 IEEE Asian Solid-State Circuits Conference (A-SSCC), pp. 225–228. DOI: 10.1109/ASSCC.2014.7008901

[22] Chou, Y.-H., Lu, S.-L. L. 2019. A High Performance, Low Energy, Compact Masked 128-Bit AES in 22nm CMOS Technology. 2019 International Symposium on VLSI Design, Automation and Test (VLSI-DAT), pp. 1–4. DOI: 10.1109/VLSI-DAT.2019.8741835

[23] Kar M., Singh A., Mathew S. K., Rajan A., De V., Mukhopadhyay S. 2018. Reducing Power Side-Channel Information Leakage of AES Engines Using Fully Integrated Inductive Voltage Regulator. IEEE Journal of Solid-State Circuits, Vol. 53(8), pp. 2399-2414. DOI: 10.1109/JSSC.2018.2822691

[24] Dhanuskodi, S. N., Holcomb, D. 2019. Enabling Microarchitectural Randomization in Serialized AES Implementations to Mitigate Side Channel Susceptibility. 2019 IEEE Computer Society Annual Symposium on VLSI (ISVLSI), Miami, FL, USA, pp. 314-319. DOI: 10.1109/ISVLSI.2019.00064

[25] Tiri, K., Hwang, D., Hodjat, A., Lai, B.-C., Yang, S., Schaumont, P., Verbauwhede, I. 2005. Prototype IC with WDDL and Differential Routing -- DPA Resistance Assessment. In J. R. Rao, B. Sunar ed. Cryptographic Hardware and Embedded Systems -- CHES 2005. Springer Berlin Heidelberg, Berlin, Heidelberg, pp. 354–365. DOI: https://doi.org/10.1007/11545262_26

[26] Ors, S. B., Gurkaynak, F., Oswald, E., Preneel, B. 2004. Power-Analysis Attack on an ASIC AES Implementation. International Conference on Information Technology: Coding and Computing, 2004. Proceedings. ITCC 2004., Vol. 2, pp. 546-552. DOI: 10.1109/ITCC.2004.1286711

[27] Peng, Y., Zhao, H., Sun, X., Sun, C. 2017. A Side-Channel Attack Resistant AES with 500Mbps, 1.92pJ/Bit PVT Variation Tolerant True Random Number Generator. 2017 IEEE Computer Society Annual Symposium on VLSI (ISVLSI), pp. 249–254. DOI: 10.1109/ISVLSI.2017.51

[28] Lagasse, J., Bartoli, C., Burleson, W. 2019. Combining Clock and Voltage Noise Countermeasures Against Power Side-Channel Analysis. 2019 IEEE 30th International Conference on Application-Specific Systems, Architectures and Processors (ASAP), pp. 214–217. DOI: 10.1109/ASAP.2019.00009

https://dergipark.org.tr/en/pub/deumffmd

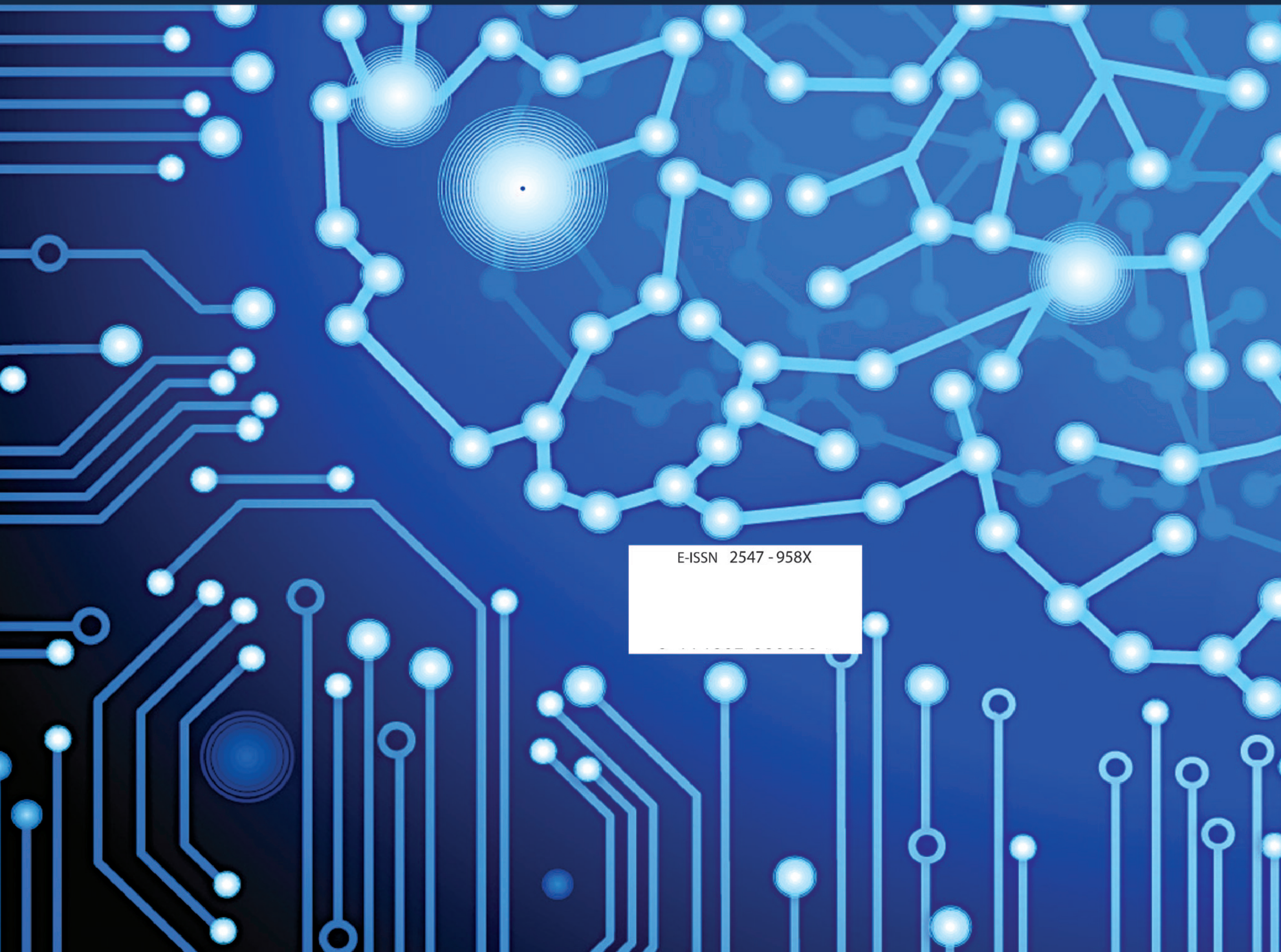

E-ISSN 2547 - 958X